Optimization of a single-phase liquid xenon Compton camera for 3γ medical imaging

Lucia Gallego Manzano

Thèse de Doctorat

Lucía Gallego Manzano

Mémoire présenté en vue de l'obtention du
grade de Docteur de l'École des Mines de Nantes
sous le label de L'Université Nantes Angers Le Mans

École doctorale : 3MPL - Matière, Molécules, Matériaux en Pays de la Loire

Discipline : Constituants élémentaires et physique théorique
Spécialité : Physique nucléaire expérimentale
Unité de recherche : Laboratoire SUBATECH - UMR 6457

Soutenue le 21 Juillet 2016 à Nantes
Thèse N° : 2016EMNA0276

Optimization of a Single-Phase Liquid Xenon Compton Camera for 3γ Medical Imaging

JURY

Rapporteurs :	**M. Paul Lecoq**, Professeur, Organisation Européen pour la Recherche Nucléaire (CERN), Genève (Suisse)
	M. Fabrice Retière, Chercheur, TRIUMF, Vancouver (Canada)
Examinateurs :	**M. Fernando Arqueros Martínez,** Professeur à l'Universidad Complutense de Madrid (Espagne)
	Mme. Laurence Le Coq, Professeur à l'École des Mines de Nantes (France)
Invité(s) :	**M. Jean-François Chatal,** Professeur Emérite en Médecine Nucléaire à l'Université de Nantes (France)
Directeur de Thèse :	**M. Ginés Martínez García,** Directeur de recherche CNRS, Subatech, Nantes (France)
Co-directeur de Thèse :	**M. Jean-Pierre Cussonneau,** Maître-assistant, École des Mines de Nantes (France)

Acknowledgements

Et tels qu'ils devraient être, mes derniers mots sont dédiés à tous ceux qui ont contribués à ce moment. Je ne peux pas, même si j'aimerais bien, personnaliser chacun des moments et des situations particulières pour lesquels je vous dois beaucoup à chacun d'entre vous, car il serait un peu bizarre que les remerciements soient plus longs que le manuscrit lui-même. Mais je voudrais vous dire que sans vous je n'en serai pas ici aujourd'hui et que cette thèse n'aurait pas été possible. Pour tout ça :

¡GRACIAS!

Je tiens en premier lieu à remercier Laurence Le Coq de m'avoir fait l'honneur de présider mon jury de thèse. Un grand merci à Fabrice Rètiere et à Paul Lecoq pour avoir accepté la lourde tâche d'en être les rapporteurs. Merci á Fernando Arqueros et Jean-François Chatal d'avoir aussi accepté de faire parti de ce jury. Merci à Ginés Martínez d'avoir accepté être mon directeur de thèse et d'avoir attendu un petit moment avant de lire ce précieux livre de «Aprendre à dire non». Gracias Ginés pour ton soutien et ta gentillesse depuis mon arrivée à Nantes.

Je tiens à adresser mes plus sincères remerciements à Dominique Thers et à Jean-Pierre Cussonneau pour leur soutien et pour m'avoir offert l'opportunité de réaliser une thèse dans un domaine aussi passionnant. Je les remercie pour les «vient discuter cinq minutes», qui n'étaient jamais cinq minutes, mais qui m'ont obligés à pousser toujours plus loin mes connaissances sur des sujets très différents. Merci aussi pour les, parfois difficiles mais toujours productives, discussions sur ce travail et pour m'avoir donné la liberté et la force d'explorer de nouvelles idées. Merci pour votre disponibilité, votre patience, votre confiance et vos conseils. Un grand merci en particulier à Jean-Pierre pour avoir accepté d'encadrer cette thèse et pour avoir toujours pris le temps de répondre à mes nombreuses questions ou quelque fois à la même question plusieurs fois, mais toujours avec le sourire. Je tiens aussi à exprimer ma profonde gratitude à Eric Morteau pour m'avoir pris sous son aile, pour m'avoir fait confiance avec la manip et ainsi que pour avoir su me guider et montrer les routes mystérieuses de l'électronique et du development de détecteurs. Merci d'avoir répondu à toutes mes innombrables questions et de m'avoir appris à regarder le vent d'un nouvel œil. Merci !

Je voudrais également exprimer toute ma gratitude aux autres membres du groupe Xénon. Merci à Nicolas Beaupere pour ta gentillesse et ta générosité. Merci à ma compagne de voyage Sara Diglio pour ta simplicité, ta générosité et tous tes précieux conseils et discussions autour d'un café. Comment ne pas exprimer ma gratitude à Jean-Sébastien Stutzmann et Patrick Leray pour leur soutien, leur bonne humeur même dans les moments les plus désespérantes et pour leur appui technique tout au long de ces années. Je remercie Loïck Virone et Kevin Micheneau pour m'avoir supporté pendant toutes ces années dans le même bureau. Merci aussi à Julien Masbou et Luca Scotto-Lavina. J'ai beaucoup appris avec vous

et de vous, mais surtout merci à l'ensemble du groupe d'avoir fait de ces années toute une aventure !

Je remercie également les anciens membres du groupe Xénon avec qui j'ai eu le plaisir de travailler. Merci Aurélien, Maxime, Olivier et Abdul. Des remerciements spéciaux à Jérôme pour m'avoir aidé dans mes premiers mois après mon arrivée à Subatech. Je tiens aussi à remercier les étudiants du groupe Xénon avec qui j'ai eu l'opportunité de travailler dans le cadre de leur stage de Master. Merci à Yajing, Arthur, Erwann, Guillaume, Pawan et Zhao. Je vous souhaite à tous le meilleur pour l'avenir.

Je suis redevable à de nombreux personnes qui, avec le temps, sont devenus mes amis et sans lesquels mon temps passé à Subatech n'aurait pas été le même. Merci à ma petite jumelle Charlotte, Florian, Jose, Lucile, Martin, Aurélien et Diego. Je suis certaine que la fin de la thèse n'est pas la fin de nos aventures ensemble.

Merci à l'ensemble des thésards et post-docs de Subatech, présents ou passés, avec qui j'ai eu le plaisir de partager de nombreuses pauses café, soirées et de trés bons moments. Merci Fanny, Alexandre S., Alexandre P., Grégoire, Loïc, Dani, Thorben, Thiago, Roland, Guillaume, Maryam, Benjamin A., Audrey, Gabriel, Florian, Benjamin G., Benjamin S., Jennifer, Antoine, Alexis et Zak.

Je dis un grand merci aux membres du groupe Plasma : Ginés, Diego, Philippe, Guillaume, Laurent, Astrid, Patrice et Denise pour votre gentillesse et pour m'avoir accueillie dans vos barbecues comme un membre du groupe.

Un grand merci à Jean-Pierre, Richard et Nöel pour m'avoir permis d'avoir de l'experience en enseignement à l'École des Mines de Nantes. Merci aux étudiants du projet PIST pour m'avoir donné l'opportunité de superviser votre travail et pour votre patience avec mon, pas tout le temps très compressible, Français.

Un grand merci à la direction du laboratoire pour m'avoir donné l'opportunité de réaliser ma thèse au sein du laboratoire Subatech. Merci aux filles de l'administration. Merci aussi au service informatique pour sa patience avec mes «memory leaks». Merci Michelle Dauvé et Delphine Turlier pour votre disponibilité et les services rendus. Et un grand merci aussi aux autres personnes du laboratoire qui ont fait de mon séjour à Subatech un moment toujours plus agréable.

Je remercie également Olivier Gevin pour son aide avec le «zouzou» responsable de nombreux maux de tête. Dans le cadre de cette thèse, j'ai eu la chance d'aller au Japon, en particulier au centre de recherche KEK, pour échanger et surtout améliorer mes connaissances dans la cryogénie du xénon liquide. Je remercie à Toshiaki Tauchi, Satoshi Mihara et Katsuyu Kasami pour cette opportunité et leur accueil pendant notre séjour. Thank you very much.

Y cambiamos de lengua para dar mi más profundo agradecimiento a Fernando Arqueros, Jaime Rosado y Paco Ramos. Muchas gracias por darme la oportunidad de empezar en el mundo de la investigración, por vuestra confianza, apoyo y sobre todo, por haber dedicado tiempo a formarme. Sin duda esta tesis no hubiera sido posible sin vosotros, por todo ello: ¡Gracias!

Gracias a mi «familia nantesa»: Rocio, Tatán, Sara, Jean-Pascal y Jose, por vuestra amistad, por recordarme que en esta vida hay cosas más importantes que el trabajo y por todos los momentos (y los que nos quedan) juntos. Nos vemos en Madrid!

Gracias a mis amigos. A aquellos que forman parte de mi vida desde que tengo memoria; desde el momento tortilla en el Gorongoro o las tardes de domingo en el parque de la Fuente del Berro, y a aquellos más recientes, pero no por ello menos importantes. En cualquier caso, gracias Julito, Lafren, Santi, Ire, Lalo, Raquel ... y mis «pitutis» Ali y Ele, porque a pesar del tiempo o la distancia, estar con vosotros siempre es como estar en casa. Gracias también a Celes, Gloria, Paula, Leti, Rachel y Azahara. Gracias por ser una risa asegurada y porque a pesar de los años, cuando estoy con vosotras es como si el tiempo no pasara.

Y por último, pero no por ello menos importante, gracias a mi familia. Gracias a mis padres y a mi hermano Pablo, a los que les dedico este trabajo. Vuestro apoyo, cariño y confianza me ha dado la fuerza para seguir adelante y siempre querer superarme y sacar lo mejor de mi misma. Por entenderme (o al menos intentarlo) cuando a veces ni yo misma lo hago. Gracias a mis abuelos, por quererme tal y como soy.

Y muchas gracias a ti, Javi, por mucho más de lo que podría escribir.

Table of Contents

Introduction

The rapid evolution of the different medical imaging techniques, particularly in the areas of instrumentation and image processing, marked the beginning of the 21st century. This is in part due to the significant technological advances, and the continuous interplay between the worlds of scientific research and industry. The application of fundamental nuclear and particle physics to medical applications is essential in modern medicine and it has deeply influenced its development. Many devices currently used in medical imaging have their roots directly borrowed from experiments in nuclear and particle physics. However, despite the very good images currently obtained in clinical practice, the increasing life expectancy and the desire to always move forward in that direction pose new challenges, especially for functional imaging techniques used in nuclear medicine. The reduction of the radiation dose administered to the patient, the decrease of the time required to perform an exam and the therapeutic follow-up of certain diseases are three clear vectors to guide future improvements. It is in this context that Subatech proposed a new medical imaging technique, called 3γ imaging. The 3γ imaging technique is an innovative functional medical imaging modality, which is based on two new concepts: the joint use of a new technology based on a liquid xenon Compton telescope, and a new radiopharmaceutical labeled with Sc-44, which aims to reduce the activity injected to the patient to unprecedented limits.

The principle of the 3γ imaging technique is based on the use of a specific radioisotope, the ^{44}Sc, which emits a positron and a γ-ray of 1.157 MeV in spatial and temporal coincidence. After the annihilation of a positron with an electron of the surrounding matter, two γ-rays are produced back-to-back with an energy of 511 keV. The detection in coincidence of these two photons forms a line of response (LOR) between the two interactions. In 3γ imaging, we use the intersection between the LOR and a Compton cone obtained after the interaction of the third γ-ray, coming from the decay of ^{44}Sc, with a Compton telescope. With the additional information provided by the third photon, it is possible to constrain the position of the source along the LOR and hence, directly obtain the distribution of the radioactive source in 3D. The benefit of this new technique is expressed directly in terms of reducing the number of disintegrations necessary to obtain the image and therefore, the activity injected to the patient and / or the exam time are significantly reduced.

In order to consolidate and provide an experimental demonstration of the use of a liquid xenon Compton camera for 3γ imaging, a first phase of research and development (R&D) has been carried out. This initial step is the starting point of the XEMIS project (XEnon Medical Imaging System), which involves both fundamental research and the development and implementation of innovative technologies. A first prototype of a liquid xenon Compton telescope, called XEMIS1, was successfully developed and tested at Subatech laboratory. The choice of liquid xenon as detection medium is motivated by the fact that the detection techniques currently available in nuclear medicine, mostly based on the use of scintillation crystal for the detection of γ-rays, are not well suited for 3γ imaging. Moreover, the fundamental physical properties of liquid xenon, high density and atomic number, give it a

high stopping power for ionizing radiation, which makes liquid xenon a perfect candidate as a γ-ray detector in the energy range from several tens of keV to tens of MeV. Liquid xenon is both an excellent active medium for an ionizing radiation detector and an excellent scintillator, with the advantage of making possible the construction of large scale, massive and homogeneous detectors. These are the main reasons why liquid xenon has gained relevance, not only in medical imaging, but also in diverse fields such as in fundamental particle physics and astrophysics.

The present document details the characterization and optimization of a single-phase liquid xenon Compton camera for 3γ imaging applications. It provides the experimental evidence of the feasibility of the 3γ imaging technique through the small-scale prototype XEMIS1. This work has been focused in the extraction of the ionization signal in liquid xenon and the device optimization. The obtained results have contributed to substantial advancements in our understanding of the detector performances and ionization signal extraction, which has led to the final design and construction of a second prototype dedicated to small animal imaging. This larger-scale device called XEMIS2, is a monolithic cylindrical camera filled with liquid xenon placed surrounding the small animal. The geometry of XEMIS2 is optimized to measure the three γ-rays with very high sensitivity and a wide field of view.

The work presented in this document was performed at Subatech laboratory under the scientific advice of Dr. Jean-Pierre Cussonneau and the supervision of Dr. Ginés Martinez. This document is divided in seven chapters, each of them as stand-alone as possible.

Chapter 1 is devoted to an introduction of the general properties of liquid xenon as radiation detector material. We overview the physics of particle interaction and the production of ionization and scintillation signals in liquid xenon. A general review of various liquid xenon-based detectors used in different experimental research fields is presented. Then, we perform a brief introduction to nuclear medical imaging and in particular to the two most used nuclear functional medical imaging techniques, single positron emission computed tomography and positron emission tomography. We describe the basics of Compton imaging and we carry out a detailed description of the principle of the 3γ-imaging technique. Finally, we introduce the basic requirements of a liquid xenon Compton camera for medical imaging.

In **Chapter 2**, we present an overview of the basic principle of a liquid xenon time projection chamber. Liquid xenon time projection chambers are one of the most promising technologies for the study of rare phenomena, from dark matter searches to neutrino detection. XEMIS is a single-phase liquid xenon time projection chamber, which design has been optimized for medical applications. We lay out the basic principle and the advantages of these kind of detectors for nuclear medical imaging. The different mechanisms that affect the production and detection of the ionization signal in liquid xenon such as diffusion, recombination and impurities attachment are discussed. Finally, we present a brief summary of the formation process of the ionization signal in the segmented anode, starting from the interaction of an ionizing particle with the detector to the collection of the signal by the front-end electronics. The discussion is supported by some experimental results along with results reported by other authors.

Chapter 3 gives a detailed description of the XEMIS1 camera. This includes a description of the light detection and charge collection systems and the cryogenic infrastructure, developed

to liquefy and maintain the xenon in stable temperature and pressure conditions during long data taking periods. The purity of the liquid xenon is a major concern is this kind of detectors where electrons must travel relative long distance without being attached to impurities. We describe the purification and circulation system used in XEMIS. Then, we introduce the main characteristics of the new liquid xenon Compton camera, XEMIS2. Building and operating a large scale detector for medical applications involves an entirely new set of challenges, from experimental condition stability, safety conditions to data acquisition and processing. An innovative cryogenic infrastructure, called ReStoX (Recovery and Storage of Xenon), has been especially developed to recuperate and store the xenon in liquid state.

Chapter 4 is devoted to the data acquisition system used in XEMIS1. The system has been developed to record both the ionization and scintillation signals with a minimum dead time. The design and performance of the readout front-end electronics used in XEMIS1 is introduced. We present a detailed study of the electronics response. The ASIC shows excellent properties in terms of gain linearity (in the energy range up to 2 MeV), baseline stability and electronic noise. In particular, my work was focused on the description of the measurement of the ionization signal. Special attention is paid to the optimization of the time and amplitude measurements of the ionization signals. In this thesis, a Monte Carlo simulation of the output signal of the IDeF-X LXe has been implemented. The obtained results have contributed to the development of an advanced acquisition system for the measurement of the ionization signal in XEMIS2. Finally, a description of the main characteristics of this new analog ASIC, called XTRACT, is presented.

The use of a Frisch grid, located between the cathode and the anode, is essential to remove the position-dependence of the collected signals. A complete study of the performances of a Frisch grid ionization chamber is presented in **Chapter 5**. During this work, three effects have been identified as possible factors that have a direct impact on the extraction of the ionization signal: electron transparency, inefficiency of the Frisch grid and indirect charge induction in non-collecting pixels. These processes and the studies performed in this thesis are explained in detail. Moreover, experimental data have been used to set an upper bound of their impact in the quality of the collected signals. A Monte Carlo simulation has been developed in order to study the effect of charge induction on a segmented anode.

In **Chapter 6**, a detailed description of the experimental set-up and trigger system used in XEMIS1 for the detection of 511 keV γ-rays from a ^{22}Na source is presented. We describe the data acquisition system and data processing protocol used in XEMIS1. A detailed description of the analysis and calibration method developed in this thesis to determine the noise for each individual pixel is discussed. The results obtained from this study are used to correct the raw data and to set a threshold level for event selection. Finally, the off-line methods used for clustering and data analysis is presented.

In **Chapter 7** we present and discuss the results obtained during this work with XEMIS1. The results presented in this section intent to provide a complete understanding of the response of XEMIS1 to 511 keV γ-rays. We study the energy, timing, position and angular resolutions with a monochromatic beam of 511 keV γ-rays emitted from a low activity ^{22}Na source. The evolution of the energy resolution and ionization charge yield with the applied electric field and the drift length are analyzed. Then, a preliminary calibration of the response of the detector for different γ-ray energies is presented. Transport properties

of electrons in LXe such as electron drift velocity and diffusion are discussed. Finally, we present a Monte Carlo simulation as an useful tool to understand the impact of diffusion on the measured signal on a pixelated detector, and to estimate the position resolution.

In conclusion, the work performed during this thesis has allowed to reach a very low electronic noise (lower than 100 electrons), a time resolution of 44 ns for 511 keV photoelectric events equivalent to a longitudinal spatial resolution of 100 μm, an energy resolution of 3.9 % (σ/E) at 511 keV and an electric field of 2.5 kV/cm, and a transverse spatial resolution smaller than 1 mm. All these results are compatible with the necessary requirements for small animal imaging with XEMIS2, and very promising for the future of the 3γ imaging technique.

Chapter 1

Liquid xenon as detection medium and its application to nuclear medical imaging

Contents

The study of the structure of matter, the origin of the universe or the fundamental laws of nature has captivated the interests of our species from the very beginning. The desire to understand and predict the behavior of nature has indeed incited many of the scientific and technological breakthroughs. In the field of experimental physics, new devices are continuously developed to apprehend new observations where the limits of our knowledge are tested.

Liquid noble gases and more particularly liquid xenon have proven to be a perfect detector medium to answer some of these fascinating questions. That is why, for the past few decades, many leading experiments in the field of particle physics, γ-ray astronomy and astrophysics

use liquid xenon as radiation detector medium showing its superiority over other materials. Moreover, its excellent properties for γ-ray detection have extended its use to other fields such as medical imaging applications.

In this chapter, we will first introduce the general properties of liquid xenon as radiation detector material. The physics of particle interactions and the production of ionization and scintillation signals in liquid xenon are also discussed in detail. Then, applications of liquid xenon detectors in several past and present experiments will be reviewed. The last part of this introductory chapter is devoted to a more extensive description of the application of liquid xenon to nuclear medical imaging. To conclude we will present the 3γ imaging technique, an innovative medical imaging modality developed at Subatech laboratory, that requires the use of liquid xenon as detection medium.

1.1 Fundamental properties of liquid xenon as radiation detection medium

Liquid noble gases, especially liquid xenon (LXe) and liquid argon (LAr) have shown their potential for particle detection since several decades [1]. Their high densities and short radiation lengths confer them a high stopping power for penetrating radiation. In addition, they present an unique response to ionizing radiation by the simultaneous emission of a scintillation and an ionization signals. These properties makes them a well suited medium not only for the detection of γ-rays but also for the discovery of rare events, such as direct dark matter search or neutrinoless double-beta decay.

In particular, LXe presents some very interesting properties, which made it one of the most extended target medium for both position-sensitive detectors and calorimeters. In this section, we will first present the fundamental properties of LXe as radiation detector. A brief reminder of the main interaction processes of γ-rays and charged particles with liquid xenon is also included. An introduction to both signal production channels, ionization and scintillation, is also presented in this section.

1.1.1 Main properties of liquid xenon

The relevant properties of the liquefied rare gases suitable for radiation detection are presented in Table 1.1. Among liquid noble gases, xenon (Xe) appears to be the most attractive candidate for particle detection in a wide range of applications [2]. Even though radon (Rn) has the highest atomic number (86), which is an important requirement for high stopping power detectors, its very high intrinsic radioactivity has excluded it so far for radiation detection. Therefore, omitting radon, Xe has the highest atomic number and density, which implies the highest absorption coefficient for γ-rays in the energy range of hundreds of keV to tens of MeV.

A review of some of the fundamental properties of LXe as detection medium is made in Table 1.2. LXe has a small radiation length of 2.77 cm which, together with its high atomic number provides good capabilities as electromagnetic calorimeter [3]. Moreover, among all noble gases, LXe has the highest ionization yield. Indeed, the high electron mobility in LXe

and the low energy required to produce an electron-ion pair, make it also very attractive as ionization detector medium. The high ionization density results in enough electron-ion pairs per unit length to generate a detectable ionization signal.

Element	**LHe**	**LNe**	**LAr**	**LKr**	**LXe**	**Ref**
Atomic number Z	2	10	18	36	54	[4]
Average atomic weight A	4.00	20.18	39.95	83.80	131.30	[4]
Density ($g.cm^{-3}$)	0.145	1.2	1.40	2.41	3.06	[4]
Boiling point at 1 atm (K)	4.22	27.1	87.3	119.9	165.0	[5, 6]
Average ionization energy W (eV)	41.3	29.2	23.6	18.4	15.6	[2, 4]
Light yield (photons/MeV)	15000	30000	40000	25000	42000	[5, 7]

Table 1.1 – Main properties of several liquid noble gases.

LXe also presents excellent scintillation properties with a high scintillation yield and fast decay times. The number of photons emitted per MeV with zero electric field is around 42000. This value is comparable to that of the most commonly used scintillator crystals such as NaI, and around two times bigger than the Lutetium Oxyorthosilicate (LSO), widely used in Positron Emission Tomography (PET) [8, 9]. In addition, the fast scintillation response implies good time resolution, making it ideal for time-of-flight (TOF) applications [10].

From the radioactive point of view, unlike krypton (Kr) and argon (Ar), which suffer from ^{85}Kr and ^{39}Ar at a level of 1MBq/kg and 1 Bq/kg respectively [11], Xe is intrinsically clean since no long-live naturally radioisotopes are present. This is a crucial requirement for those experiments for which low background is needed.

Another advantage of using liquid noble gases as radiation detection is the possibility to construct large monolithic detection volumes at a reasonable cost with high detection efficiency, which is not yet possible with other detector media such as semiconductor detectors. This fact, together with the previously mentioned characteristics, make liquid noble gases suitable media to produce high-sensitivity detectors with a large Field-Of-View (FOV). However, one constrain of using liquefied noble gases as particle detector is the need of good cryogenics and purification systems. LXe has a small temperature operating range of only 4 K. At a pressure of 1 bar, xenon becomes liquid at a temperature of 165 K and solid at 161 K. This small temperature interval requires constant pressure and temperature monitoring. Nevertheless, compared to the other liquid noble gases, LXe has a relative high temperature. The fast development of new and effective cryogenics systems in the recent years has made the technical aspects accessible.

Xenon properties	Values	Ref
Atomic number Z	54	[12]
Average atomic weight A	131.3	[12]
Density (g.cm^{-3})	3.06	[13]
Radiation length X_0 (cm)	2.77	[14]
Ionization potential in liquid phase (eV)	9.28	[4]
Average ionization energy W-value (eV)	15.6 ± 0.3	[15]
W_{ph} in liquid for relativistic e^- (eV)[a]	21.6	[2]
W_{ph} in liquid for alpha particles (eV)[a]	17.9	[2]
Peak emission wavelength (nm)	178	[2, 16]
Refractive index (at 178 nm)	[1.6,1.72]	[17, 18]
Fast decay time (singlet state τ_s) (ns)	2.2	[2, 16]
Slow decay time (triplet state τ_s) (ns)	27	[2, 16]
Recombination time (τ_r) (ns)	45	[16]

Table 1.2 – Main properties of Liquid xenon as radiation detector medium

[a]In the absence of electric field.

1.1.2 Response of liquid xenon to ionizing radiation

When an ionizing particle passes through matter, it loses its energy by interaction with the atoms of the medium. The type of interaction and the amount of deposited energy depend on the kind of incident particle, its energy and also on the type of material. Charged particles and photons mainly interact with matter via electromagnetic processes, principally through inelastic collisions with the atomic electrons [19]. Neutrons, on the other hand, interact with nuclei of the absorbing material via the strong interaction [20]. For the purpose of this thesis, only the principal electromagnetic mechanisms are considered.

Charged particle interactions in matter

Charged particles, such as α-particles, protons or electrons, lose their energy mainly by ionization and atomic excitation. When a charged particle penetrates in LXe, it will interact with the electrons and nuclei present in the material through the Coulomb force. Depending on whether this interaction is an inelastic collisions with the atomic electrons or an elastic scattering from nuclei, the incoming particle will lose its energy or it will just suffer a deflection from its incident direction. Inelastic collisions with the bound electrons of the atoms are in general the predominant processes by which heavy charged particles, such as α-particles and protons, interact with matter. These type of interactions will cause either ionization or excitation of the atoms of the medium depending on the transferred energy in each collision.

Since charged particles can transfer only a small fraction of the total energy in a single electronic collision, they interact with many electrons of the medium continuously losing their energy before being stopped [19]. Moreover, in the case of heavy charged particles, collisions with the atomic electrons are not enough to cause a significant deflection from the incoming direction. This implies that the trajectory of a heavy charged particle, defined as the average distance traveled by a particle before coming to rest, can be approximated by a straight line. On the other hand, electrons and positrons are less ionizing than heavy charged particles and thus, they can travel longer distances before slow down. For example, a 5.5 MeV α-particle will lose all its energy in 42.5 μm of LXe, while an electron of the same energy will travel around 1.3 cm of LXe before being stopped [13]. In addition, electrons and positrons are more susceptible to multiple scattering by nuclei than heavy charged particles, and also a larger fraction of their energy can be lost in a single interaction producing larger scattering angles. As a result, electrons and positrons suffer from larger deviations from the electron path than heavy charged particles, resulting in erratic trajectories. Figure 2.16 shows the trajectory of a 511 keV electron in LXe obtained by simulation.

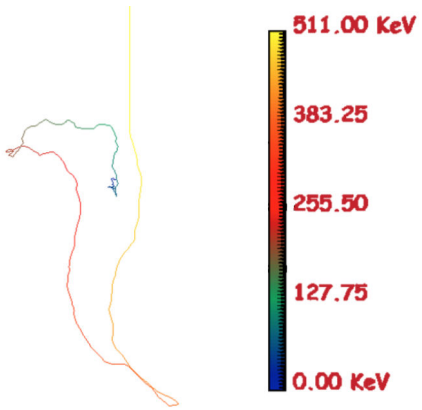

Figure 1.1 – Example of a 511 keV electron recoil track obtained by simulation. Energy loss along the track is represented by the the color palette [21].

Collisional energy loss is not the only mechanism by which charged particles lose their energy when interacting with matter. Electrons due to their small mass also lose their energy by inelastic collisions with nuclei, resulting in the emission of electromagnetic radiation (bremsstrahlung). However, at the energies we are interested in, of the order of 1 MeV, the radiative stopping power[1] mostly due to bremsstrahlung ($8.217 \times 10^{-2}\ MeVcm^2/g$) is about one order of magnitude smaller than that from collision interactions ($1.122\ MeVcm^2/g$) [13]. Thereby, the bremsstrahlung process becomes negligible and thus, it can be ignored from this discussion. The total mass stopping power and CSDA[2] range for electrons in xenon are shown in Figures 1.2 and 1.3 respectively. Then, the predominant interaction processes of electrons and positrons with matter at these energies are ionization and atomic excitation through inelastic collisions with the atomic electrons. Other mechanisms such as the emission of Cherenkov radiation and nuclear reactions are also irrelevant in this thesis. For a pedagogical review of these processes please refer to [19, 22].

[1]Rate of energy loss per unit length in the medium.

[2]Approximation of the average path length travelled by a charged particle before it slow down to rest [13].

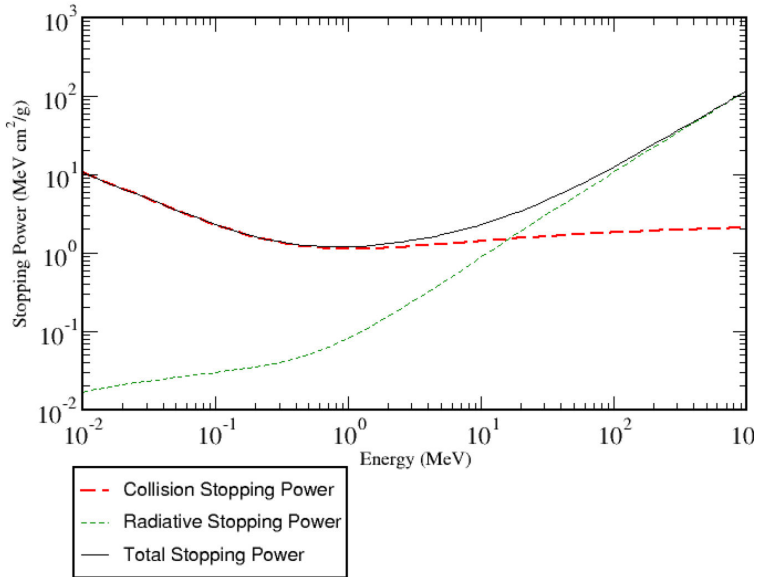

Figure 1.2 – Stopping power for electrons in xenon. Data from [13].

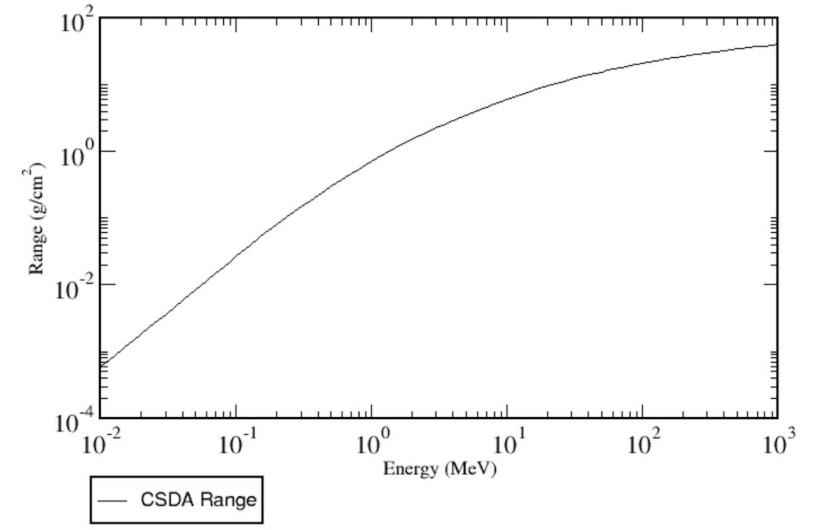

Figure 1.3 – CSDA range for electrons in xenon. Data from [13].

Photon interactions in matter

The lack of electric charge of photons, in our case X-rays and γ-rays, makes the interaction processes with matter completely different from those of charged particles. Unlike electrons, photons do not lose their energy continuously via Coulomb interactions with atomic electrons, but instead they travel relatively long distances before a partial or total transfer of their energy to the medium in a single interaction. Photons interact with LXe mainly via photoelectric effect, Compton scattering, Rayleigh effect and pair production. The relative contribution of this processes in xenon as a function of the photon energy is illustrated in Figure 1.4.

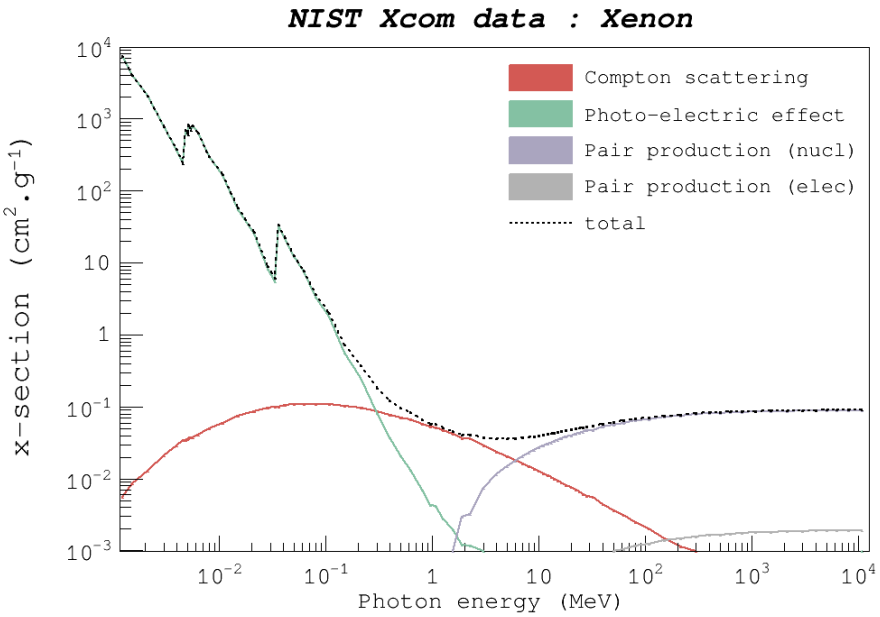

Figure 1.4 – Calculated photoelectric, total Compton scattering and pair production cross sections in xenon as a function of the photon energy. The values are taken from [13].

Photoelectric effect

In the photoelectric effect, the total energy of the incoming photon is transferred to a bound electron of the atom producing the complete absorption of the photon and the consequent ejection of the electron from the atom. The energy of the emitted electron is then equal to the energy of the incoming photon minus the binding energy of the electron on its atomic shell. Since the electrons are bounded, the momentum is conserved by the recoil of the entire atom.

This phenomenon was first observed and reported by Heinrich Hertz in 1887 after observing electric sparks when a metal was illuminated with a light of an specific wavelength. However, it was not until 1905 when a plausible explanation of the photoelectric effect was given by Albert Einstein, awarded in 1921 with the Nobel Prize in physics for its contribution to explain this effect.

The photoelectric effect is graphically depicted in Figure 1.5. After the ejection of the electron, the atom remains in an excited state with an inner shell electron vacancy. The atom will return to the ground state by filling the vacancy with a less tightly electron from an upper shell with lower binding energy. In such a transition, the emission of a characteristic X-ray or an Auger electron is produced. The direction in which the electron is ejected from the atom depends on the energy of the photon. For low energies the electron is emitted perpendicular to the direction of incidence, whereas for high energies the electron is ejected forward in the direction of the incident photon [19, 23]. At energies we are interested in, above 100 keV, the recoil electron is emitted almost in the same direction as the incident photon. Fluorescence radiation is, on the other hand, emitted isotropically.

For the photoelectric absorption to occur, the energy of the incident photon must be greater or equal to the binding energy of the involved electron. The probability of

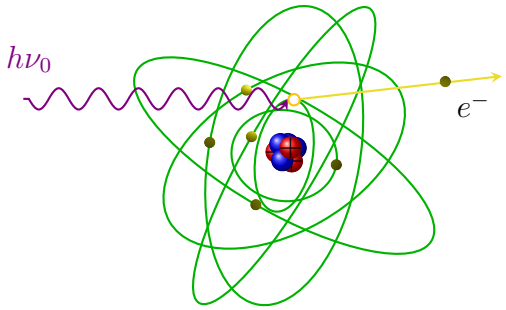

Figure 1.5 – Photoelectric effect

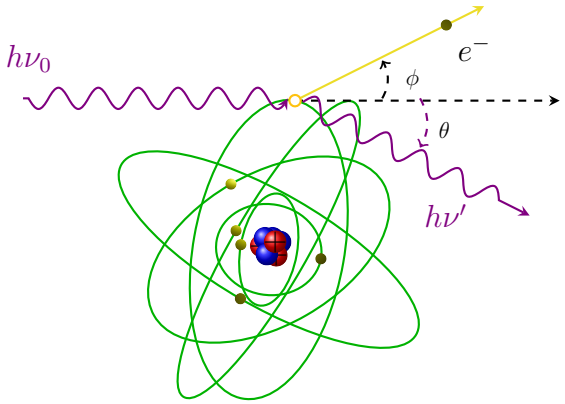

Figure 1.6 – Compton scattering.

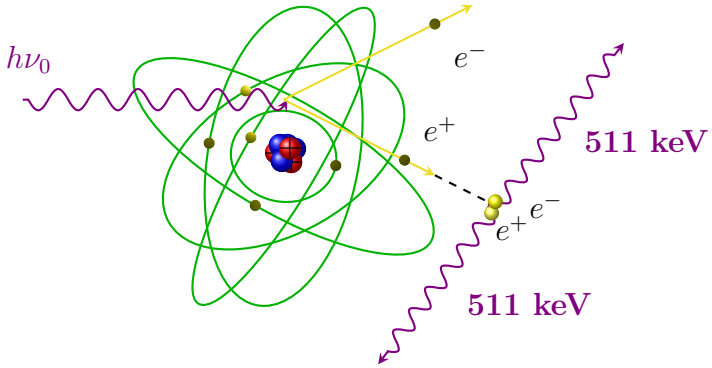

Figure 1.7 – Pair production

photoelectric absorption depends, therefore, on the electron binding energy, being greater for more tightly bound electrons. The photoelectric effect takes place predominantly in the K-shell. In fact, if the energy of the photon is higher than the K-electron binding energy, 85 % of the photoelectric interactions results in the ejection of an electron from the K-shell. Figure 1.4 shows the photoelectric cross section in LXe as a function of the photon's energy. As we can see, the probability of interaction increases as the energy of the photon decreases. In the figure the absorption edges corresponding to the K, L and M atomic shells are visible at energies of around 34 keV, 5 keV and 2 keV respectively. At these energies the photoelectric cross section rapidly increases, which means that "the maximum absorption takes place for photon with just enough energy to eject the electron" [19].

As presented in Figure 1.4, the photoelectric effect dominates over the other interaction processes at low photon energies or high atomic numbers Z. This is because the photoelectric cross section shows a strong dependency on the energy of the incident photon and on the atomic number of the material. Despite the complexity of the theoretical estimation of the photoelectric cross section, it can be roughly approximated as:

$$\tau \simeq const \ \frac{Z^n}{(h\nu)^3} \tag{1.1}$$

where τ is the photoelectric mass attenuation coefficient. At the energy range of interest, the dependency on Z varies between Z^4 to Z^5 depending on the energy of the photon. As a

result, materials with high atomic number are better candidates for γ-ray absorbers. For a complete discussion of the theoretical estimation of the photoelectric cross section please refer to [24].

Compton scattering

Compton scattering was first reported by Arthur H. Compton in 1923 [25] after a series of experiments concerning the scattering of X-rays from electrons in a carbon target. Its discovery made Compton recipient of the Nobel Prize in physics in 1927. Unlike photoelectric effect, in Compton scattering the incident photon with energy hν does not transfer all of its energy to a bounded electron, but instead, only a portion of its energy is transferred to a recoil electron which is considered to be at rest and unbound. The free electron approximation is only valid if the energy of the photon is much higher than the binding energy of the electron. After the collision, the photon is deflected with respect to its original direction and emitted with a lower energy $h\nu'$ that depends on the diffusion angle θ. Figure 1.6 illustrates the Compton scattering process. Applying momentum and energy conservation, the energy of the scattered photon $h\nu'$ is given by Equation 1.2:

$$h\nu' = \frac{h\nu}{1+\alpha(1-cos\ \theta)} \tag{1.2}$$

where $\alpha = h\nu/m_e c^2$. The electron recoils at an angle ϕ with a kinetic energy T_e given by:

$$\begin{aligned} T_e &= h\nu - h\nu' \\ &= h\nu\frac{\alpha(1-cos\ \theta)}{1+\alpha(1-cos\ \theta)} \end{aligned} \tag{1.3}$$

The directions of the scattered photon and the electron depend on the amount of energy transferred to the electron during the collision. The scattering angles of both the incoming photon and the released electron can be expressed as:

$$cos\ \theta = 1 - \frac{2}{(1+\alpha)^2 + \tan^2\phi + 1} \tag{1.4}$$

$$\cot\phi = (1+\alpha)\tan\frac{\theta}{2} \tag{1.5}$$

The energy transferred to the electron can vary from zero, when electron is scattered at right angles ($\phi \backsimeq 90°$), to a maximum value obtained for an scattering angle $\theta = 180°$ (back scattering). In such a collision, the electron moves forward in the direction of the incident photon, which conserves the minimum energy. The maximum energy that can be transferred to the scattered electron is given by Equation 1.6:

$$T_{e,max} = h\nu\frac{2\alpha}{1+2\alpha} \tag{1.6}$$

Figure 1.4 shows the total Compton scattering cross section as a function of the energy of the incident photon in xenon. The Compton scattering probability becomes important at energies of the order of 100 keV with a maximum at around 1.5 MeV and then, rapidly decreases as the energy of the incident photon increases. Because Compton scattering involves free electrons, the probability of Compton absorption is nearly independent of the atomic number Z, although is directly proportional to the number of electrons per gram Z/A, which is nearly constant for all materials. Regardless the probability of the interaction, the amount of energy transferred during the collision depends on the energy of the incident photon. Low-energy photons are scattered with small angles $\theta \backsimeq 0°$ going almost forward with respect to the direction of the incident photon with a small energy transfer to the electron. On the other hand, if the energy of the incident photon is large, 10 to 100 MeV, most of the energy is transferred to the recoil electron.

Rayleigh scattering

The phenomenon of Rayleigh scattering also known as coherent scattering, was named in honour of J. W. S. Rayleigh, who in 1871 published a paper describing, at that time unknown, effect [26, 27]. A full understanding of the process is, however, the result of collective efforts carried out by many authors during the first half of the 20th century [28]. Nevertheless, a rigorous mathematical formulation of the Rayleigh scattering had to wait until 1965 (Kleinman, 1975, 1978) [29].

The Rayleigh scattering is produced between an incident photon and a tightly bound atomic electron, in which both particle interact coherently. After the collision, the atom is neither ionized nor excited. The photon is deflected without energy transfer. The Rayleigh scattering mostly occurs at low energies and for high atomic number materials. The average scattering angle decreases with increasing energy. In xenon the probability of coherent scattering is very small even for low photon energies, so it can be ignored.

Pair production

Figure 1.7 illustrates the pair production mechanism. This effect, which is based on the conversion of a photon into an electron-positron pair, was first confirmed by Patrick M.S. Blackett and Giuseppe P.S. Occhialini after the discovery of the positron by Carl D. Anderson in 1932 [30]. Blacket was awarded for his work with the Nobel Prize in physics in 1948 [31].

For the pair production to occur, the incident photon must have an energy above $2m_ec^2$ (1.022 MeV). The photon, passing near the nucleus of an atom, can interact with the Coulomb field of the atomic nucleus to be transformed into an electron-positron pair. The electron and the positron are not scattered, but created from energy conservation after the photon disappears. The excess energy after the creation of the pair, which is equal to the difference between the energy of the incident photon and the minimum energy required to create the pair ($2m_ec^2$), is shared by the electron and the positron. After their emission, both particles will rapidly slow down inside the material. The positron will annihilate with an electron releasing two back-to-back γ-rays with energies of 511 keV.

The pair production mechanism can also occur in the field of an atomic electron if the energy of the incident photon is greater than $4m_ec^2$ (2.044 MeV). In such an interaction

called triplet production, the recoil electron is also ejected from the atom resulting in the emission of two electrons and a positron.

The probability of a photon to undergo a pair production increases rapidly with the photon energy and varies approximately as the square of the atomic number Z. In the case of xenon, pair production starts to dominate at energies above 10 MeV.

1.1.3 Ionization properties

As we have seen in Section 1.1.2, when an ionizing particle interacts with LXe it loses part of its energy mainly by ionization and atomic excitation. This implies that, regardless the type of incoming particle, charged particles or photons with the consequent emission of a recoil electron, a certain number of electron-ion pairs (N_i), excited atoms (N_{ex}) and free electrons (sub-excitation electrons) are created after the interaction with the LXe. The energy deposited by the scattering particle E_0 can be expresses in terms of the number of excited and ionized xenon atoms through the Platzman equation [32]:

$$E_0 \;=\; N_{ex}E_{ex} \;+\; N_iE_i \;+\; N_i\epsilon \tag{1.7}$$

where the energies E_{ex} and E_i correspond to the average energy needed to produce atomic excitation or an electron-ion pair respectively, and the remaining term ϵ corresponds to the kinetic energy of the sub-excitation electrons.

The average energy W needed to create an electron-ion pair in LXe can be expressed as follows:

$$W \;=\; \frac{E_0}{N_i} \tag{1.8}$$

Applying Equation 1.8:

$$W \;=\; E_i \;+\; E_{ex}\frac{N_{ex}}{N_i} \;+\; \epsilon \tag{1.9}$$

The value of W in LXe is $15.6 \pm 0.3\ eV$ [15]. Compared to that of LAr, which is $23.6 \pm 0.3\ eV$ [33], the significantly smaller W-value for LXe implies a much larger ionization yield. In fact, LXe has the highest ionization yield of ∼64000 pairs/MeV (for an infinite electric field) among all liquefied noble gases.

1.1.4 Scintillation mechanism

Scintillation light emission in LXe has been investigated in detail by many authors since the pioneering studies carried out by Doke [1]. Light is of major importance because its fast production mechanism, of the order of a few ns, makes photons useful to provide the event trigger information, which corresponds to the interaction time. Moreover, the number of produced photons is proportional to the deposited energy by the interacting particles and hence, it can provide calorimetric information.

Scintillation photons are produced either by atomic ionization or atomic excitation. Both ways lead to Xe_2^* excimer formation, in a molecular excited state singlet $^1\sum_u^+$ or triplet $^3\sum_u^+$, which eventually de-excites producing VUV photon. The two scintillation production processes can be summarized as follows:

1. Direct excitation of xenon atoms followed by an excited molecule formation and de-excitation:

$$\begin{aligned} Xe + e^- &\rightarrow Xe^* + e^- \\ Xe^* + Xe + Xe &\rightarrow Xe_2^* + Xe \\ Xe_2^* &\rightarrow 2Xe + h\nu \end{aligned} \tag{1.10}$$

   The recoiling electron emitted after the interaction via a photoelectric effect or a Compton scattering of a γ-ray with the LXe, may excite the encountered xenon atoms. The excited atoms Xe^* will combine with another xenon atom creating an excited di-xenon molecule or dimer Xe_2^*. After some time, depending on whether the molecule is on a singlet or triplet excited state, the dimer will return to the ground state through the dissociation in two neutral atoms and the emission of a VUV photon. The typical time needed for the formation of a Xe_2^* excimer is of the order of few picoseconds.

2. Molecular state formation through recombination between electrons and Xe^+ ions:

$$\begin{aligned} Xe + e^- &\rightarrow Xe^+ + 2e^- \\ Xe^+ + Xe &\rightarrow Xe_2^+ \\ Xe_2^+ + e^- &\rightarrow Xe^{**} + Xe \\ Xe^{**} &\rightarrow Xe^* + heat \\ Xe^* + Xe + Xe &\rightarrow Xe_2^* + Xe \\ Xe_2^* &\rightarrow 2Xe + h\nu \end{aligned} \tag{1.11}$$

   The ejected electrons can otherwise transfer enough energy to a neutral atom to create an electron-ion pair. The Xe^+ may recombine with another atom creating an ionized dimer Xe_2^+. The molecular ion Xe_2^+ will capture a free electron leading to the formation of a Xe_2^* excimer and the eventually emission of a UVU scintillation photon in the same way as in the direct excitation process. This process takes, however, more time for the Xe_2^* excimer formation.

No matter the origin of the scintillation emission process, the scintillation light spectrum is in the vacuum ultraviolet (VUV) region, with a peak around $\lambda = 178 \pm 1\ nm$ (FWHM = 14 nm) [34]. Moreover, a strong peculiarity of liquid noble gases is that they are transparent to their scintillation light, since the emitted VUV photons have an energy which is appreciably lower than the minimum necessary energy required for atomic excitation. The scintillation mechanism in LXe is schematically illustrated in Figure 1.8.

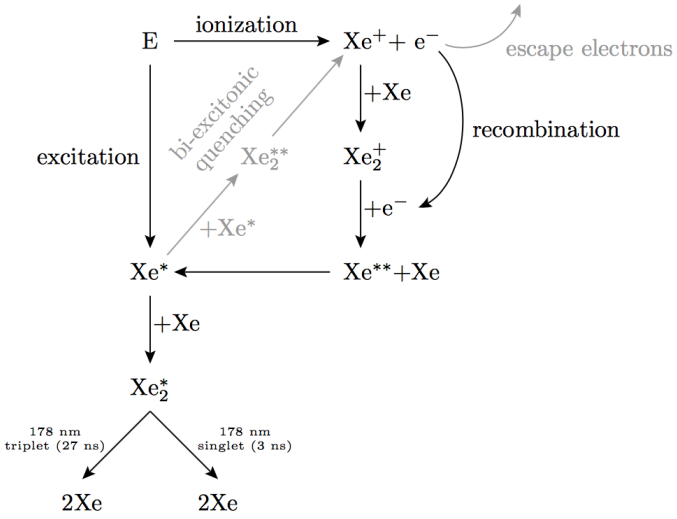

Figure 1.8 – Scintillation mechanism in LXe. Figure taken from [35].

Scintillation decay components

Both ions Xe^+ and excited atoms Xe^* lead to the formation of excited dimers Xe_2^*. The excimers may exist in two different energetic states, the singlet state ${}^1\sum_u^+$ and the triplet state ${}^3\sum_u^+$, which eventually decay to the ground state ${}^1\sum_g^+$. The associated relaxation times are then different, depending on which excited state the excimer is. For relativistic electrons, the lifetimes of the singlet and triplet excited states are 2.2 ns and 27 ns respectively [36]. These values referred as the fast and slow decay components depend slightly on the nature of the recoiling particle. Figure 1.9 illustrates the decay curves of the scintillation light in LXe for electrons, alpha particles and fission fragments without applied electric field. For electrons and without electric field, the scintillation light shows only a decay component of 45 ns [37, 38]. Since this component disappears in presence of an electric field as reported by Kubota et al. [37], its origin is most likely due to the recombination between electron and ions [39]. The comparison of the scintillation decay curves with and without applied electric field is shown in Figure 1.10. With an electric field of 4 kV/cm, the decay curve exhibits roughly a double exponential decay form, characterized by the fast and slow lifetimes of the single and triplet excited states. Scintillation light in LXe is therefore characterized by three different decay components: a fast component with a time constant of $\tau_s = 2.2 \pm 0.3\ ns$, a slow component with a lifetime of $\tau_t = 27 \pm 1\ ns$ and a third component due to electron-ion recombination with time constant of $\tau_r = 45\ ns$ (at 173 K). Table 1.3 lists the lifetime differences for electrons, alpha particles and fission fragments.

Incident particle	τ_s **(ns)**	τ_t **(ns)**	τ_r **(ns)**	I_s/I_t	**Ref**
Electrons:	2.2 ± 0.3	27.0 ± 1.0	~ 45	0.05	[37, 38]
Alpha particles:	4.3 ± 0.6	22.0 ± 1.5		0.45 ± 0.07	[38]
Fission fragments	4.3 ± 0.5	21.0 ± 2.0		1.6 ± 0.2	[38]

Table 1.3 – Decay times for the fast, slow and recombination time constants for electrons, α-particles and fission fragments

.

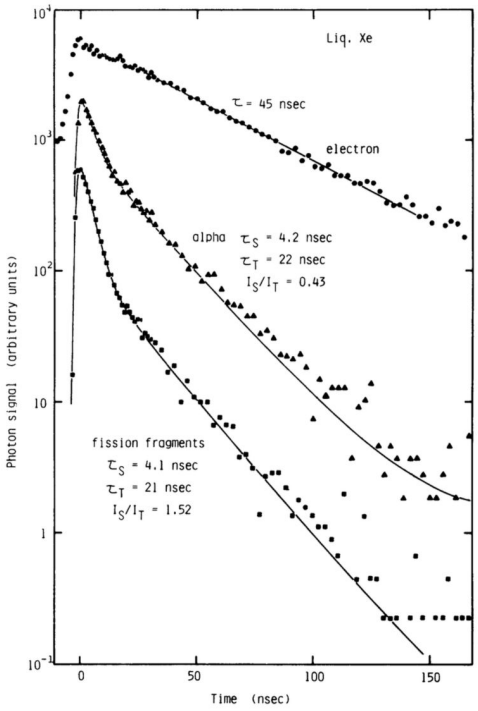

Figure 1.9 – Decay curves of the scintillation light for electrons, α-particles and fission fragments in LXe, without applied electric field [36, 38].

For electrons, 71 % of the VUV scintillation photons are produced by ionization of the xenon atoms, whereas the remaining 29 % is due to pure atomic excitation [37]. The later does not depend on the applied electric field and the ratio I_s/I_t between the number of produced photons from the two excited states, singlet (I_s) and triplet (I_t), was found to be 0.05 [38]. Under the influence of an electric field, on the other hand, the proportion of scintillation light due to recombination decreases. For an electric field of 2 kV/cm, for example, only the ∼46 % of the maximum scintillation light is produced (see Figure 1.11). Since the fraction of light due to direct excitation remains constant regardless the electric field, 63 % of the scintillation yield is therefore emitted with a time constants of 2.2 ns and 27 ns, while the remaining 37 % of the emitted photons have a decay time of 45 ns.

Although the decay times does not depend much on the ionization density, the proportion between the two excited states, singlet and triplet, depends on the recoiling particle. The energy loss per unit length for heavy particles such as α-particles is much higher than that

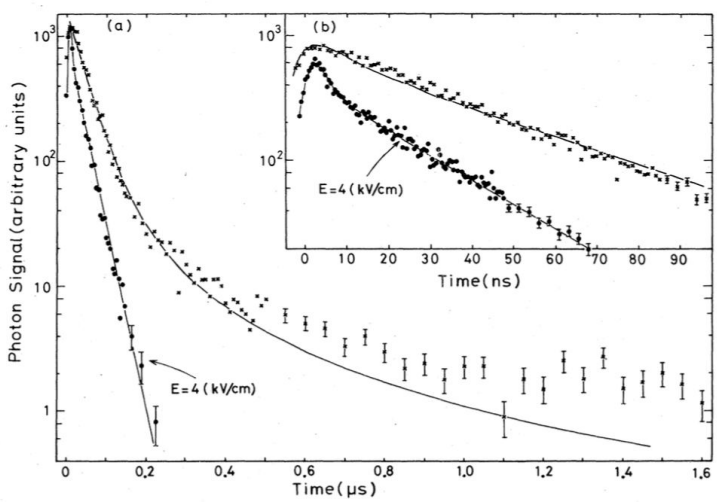

Figure 1.10 – Decay curves of the scintillation light for electrons in LXe with and without an applied electric field [39].

for electrons, leading to a much higher ionization density. The recombination yield will be higher and the recombination process will occur faster for heavy recoiling particles than for recoiling electrons. The recombination decay component become thus negligible and the scintillation decay times are dominated by the de-excitation of the singlet and triplet states. The ratios I_s/I_t are found to be 0.45 ± 0.07 and 1.6 ± 0.2 under α-particle and fission-fragment excitation, respectively, showing an enhancement of $^1\sum_u^+$ formation with higher ionization density.

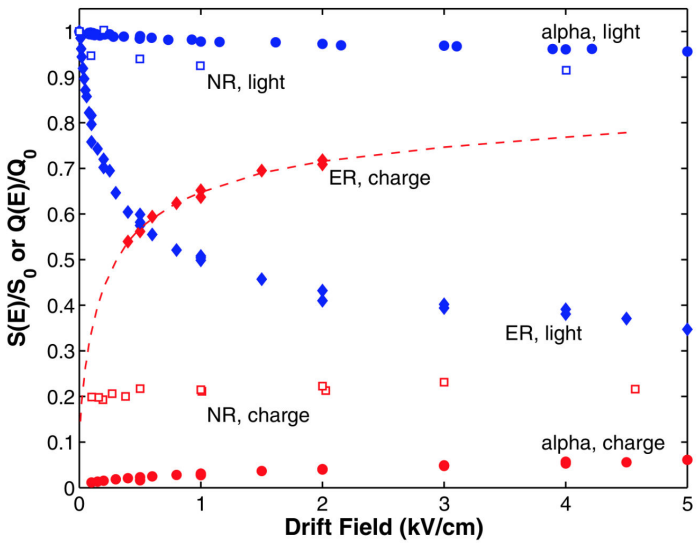

Figure 1.11 – Evolution of the charge and scintillation light yields with the electric field in liquid xenon for 122 keV electron recoils (ER), 56 keVr nuclear recoils (NR) and α-particles. Figure taken from [40].

Scintillation yield

The number of VUV scintillation photons, N_{ph}, emitted after the interaction of an ionizing particle with the LXe is characterized by the minimum average energy W_{ph} required to emit a scintillation photon. Liquid noble gases are in general very good scintillators. The scintillation yield for electron with 1 MeV of energy has been estimated between 40000 photons to 50000 photons [41]. LXe light yield is therefore comparable to that of the NaI scintillation crystal (43000 photons/MeV). For low energy electrons (20 - 100 keV), the light yield in LXe increases significantly producing nearly 70000 photons/MeV. Nevertheless, to date, there is not an accurate measurement of the value of W_{ph} due to the difficulty of the measurement.

The average energy for a scintillation photon emission depends on the number of electron-ion pairs produced by ionization, N_i, and on the number of excited atoms N_{ex}. Assuming that all electron-ion pairs recombine ($\vec{E} = 0\ kV/cm$), the average energy W_{ph} can be expressed as follows:

$$W_{ph} \;=\; \frac{E_0}{N_{ph}} \;=\; \frac{E_0}{N_i \;+\; N_{ex}} \;=\; \frac{W}{1 \;+\; \dfrac{N_{ex}}{N_i}} \tag{1.12}$$

where E_0 is the energy of the incident particle and W is the average energy required to generate an electron-ion pair. The maximum value of W_{ph} published by Doke et al. [42] in 2002 was estimated to be $13.8 \pm 0.9\ eV$, corresponding to a photon yield of $\sim$ 72000 $photons/MeV$. More recent studies agrees with the result of Doke et al. [42], showing results of $13.45 \pm 0.29\ eV$ [43] and $13.7 \pm 0.2\ eV$ [44]. This value corresponds to the minimum possible energy needed to produce a scintillation photon without escape electrons or scintillation quenching. For relativistic electrons (1 MeV) a value of 21.6 eV has been estimated [42]. A compilation of the existing experimental and theoretically estimated W_{ph} values for LXe can be found in [41].

The scintillation yield depends on the recoiling particle since the recombination process between electrons and positive ions depends on the density of electron-ion pairs. The estimated value of W_{ph} for α-particles in LXe is 21.6 eV with a production ratio β/α of 0.81 [45].

Photon attenuation in LXe

There are two main aspects besides recombination that can affect the collection of the produced scintillation light in a LXe detector: the absorption of electron by impurities (λ_{abs}) and the photon elastic scattering ($\lambda_{rayleigh}$). The total attenuation coefficient of photons can be expressed according to Equation 1.13:

$$\frac{1}{\lambda_{att}} \;=\; \frac{1}{\lambda_{abs}} \;+\; \frac{1}{\lambda_{rayleigh}} \tag{1.13}$$

Thus, the variation of the number of produced photons N_{ph} with the distance can be expressed as an exponential function which depends on the total attenuation coefficient, λ_{att}, also referred as the mean free path of scintillation photons:

$$N(z) \;=\; N_{ph}\; e^{\frac{-z}{\lambda_{att}}} \tag{1.14}$$

LXe is transparent to its own scintillation light since the absorption band of free exciton is at a higher energy than the scintillation light emission band, which is $\sim 0.6\ eV$ [46]. However, the presence of impurities in the liquid can absorb a large fraction of the scintillation photons. Water is the most serious contaminant due to its high absorption cross section. A concentration of the order of 10 ppm (parts per million) is enough to attenuate 90 % of the scintillation light in two cm [47]. O_2 can also contribute to the scintillation photon loss, although its influence is more important for the ionization signal. Photon attachment to impurities can be successfully reduced by installing a purification system (see Chapter 3, Section 3.1.4).

The Rayleigh scattering length in LXe also affects the collection of scintillation light. Its influence is especially important for large volume detectors. The travelled length by a photon through the LXe before undergoing a Rayleigh scattering is strongly dependent on the wavelength of the light as well as on the optical properties. For LXe, the Rayleigh scattering length has been experimentally determined as $\lambda_{rayleigh} = 29\ cm$ [48], which is in good agreement with the theoretical calculations. For a detector with the dimensions as the one reported in this thesis, the Rayleigh scattering contribution can be considered negligible.

1.2 Next generation of LXe detectors

Liquefied rare gases are an attractive option for radiation and particle detection thanks to their very interesting and suitable properties previously discussed in this chapter. Among liquid noble gases, LXe and LAr are widely used in modern physics experiments despite the difficulties associated with handling low temperature detectors. In particular, LXe has gained importance in different research fields from medical imaging applications to physics beyond the standard model. Following the success of current LXe-based detectors such as XENON100, EXO, LUX, XMASS, Panda-X..., LXe technology has gained a lot of interest in the scientific community, which has led to the development of a new generation of large-scale LXe detectors. In fact, the possibility of building big massive monolithic detectors makes liquid noble gases very interesting for the study of rare phenomena such as the measurement of low-energy solar neutrinos and direct dark matter search.

The development of large-scale LXe detectors aims to push the performances and sensitivity of the current technology beyond the existing limits. However, ultra-sensitive detectors bring along new technological challenges. These include fast and efficient purification systems, high applied electric fields along long drift distances of the order of 1 m and effective background rejection both environmental and intrinsic to the detectors.

In this section we perform a brief overview of some past, present and future LXe detectors dedicated to the dark matter search, neutrinoless double β decay detection, γ-ray astrophysics and nuclear medicine imaging.

Dark Matter Direct Detection

LXe is one of the most extended target materials used in the direct detection of dark matter. Weakly Interacting Massive Particles (WIMPs) are a particularly interesting candidate for the dark matter *"problem"*, which is one of the remaining unknowns in the universe. The WIMP particle is predicted by many supersymmetric extensions of the standard model [49]. They interact only through the weak nuclear force and gravity, and can have masses from 40 GeV to 3.2 TeV [49]. The WIMP interacts with matter through elastic collisions producing a nucleus recoil. LXe has shown its potential to discriminate nuclear recoils generated by elastic scattering of a WIMP or neutrons, from electronic recoils produced by, for example, γ-rays, which are the major source of background. The predicted interaction cross sections are in the range of $10^{-42} - 10^{-46}\ cm^2$, which translates into a interaction rate of the order of 10^{-4} event/LXe kg. The extremely low interaction cross sections require large target volumes, with the main challenges being the detection of low-energy signals in the keV-scale and unprecedented levels of sensitivity with a huge control of the background.

Beyond the ongoing direct dark matter experiments based on LXe detectors, we can mention the XENON, ZEPLIN, LUX and XMASS projects. All of them as exception of XMASS, are based on a dual-phase LXe/GXe detector. The main advantage of using a two phase-detector compared to a single-phase technique is the capability to reject background. However, single-phase detectors are technological simpler. The scaling to larger devices of dual-phase detectors might become relatively complicated. Moreover, the presence of a double liquid-gaseous phase limits the possible geometrical designs of the detector. The performances of a single-phase xenon detector depend on whether it relays on measuring exclusively the scintillation light as the XMASS experiment, or both scintillation and ionization signals as in dual-phase technology. The combination of both scintillation-light and ionization-electron signals provides better energy resolution and position sensitivity.

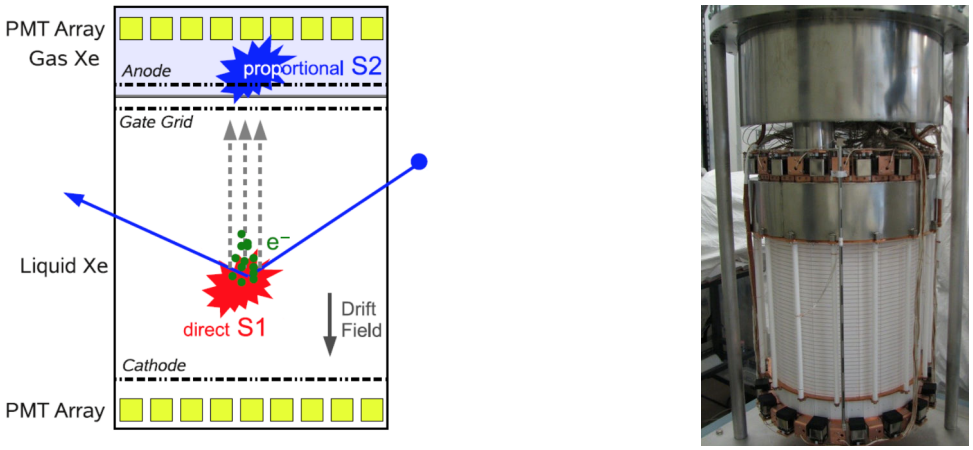

(a) **(b)**

Figure 1.12 – (a) Schematic principle of a dual phase xenon Time Projection Chamber (TPC) [50] and (b) the XENON100 TPC (from XENON collaboration).

In the XENON Dark Matter Search collaboration, two detectors, XENON10 and XENON100, have already been successfully tested, and a larger scale detector XENON1T is currently in the qualification stage. All of them operate underground at the Gran Sasso laboratory (LNGS) in Italy. The XENON100 detector [51] consists of a dual-phase time-projection chamber (TPC) that contains about 70 kg of LXe. Figure 1.12 shows a sketch of the basic principle of a dual-phase xenon TPC (left) and the XENON100 TPC (right). The LXeTPC exploits both the scintillation and ionization signals produced after the interaction of an ionizing particle with the LXe. The bulk volume of the detector is liquid with a drift length of 30 cm, whereas the top is based on a thin layer of gaseous xenon. Both the top and bottom parts of the detector are covered by two arrays of photomultiplier tubes (PMT) to detect both the primary scintillation light (S1) and the secondary scintillation photons (S2). The proportional scintillation light S2 is locally produced in the gas phase located above the liquid level. An electric field applied between the cathode and the anode forces the ionization electrons to drift towards the gas phase. A second electrical field called extraction field, which is higher than the drift field, is applied to convert the electrons into a proportional amount of electroluminescence photons. The time difference between the prompt signal S1 and the S2 signal from the ionization electrons is used to reconstruct the Z position of the interaction points inside the detector. The XY position is determined from the distribution of the S2 signal in the PMTs. Finally, the ration between both S1 and S2 signals is used to discriminate between electronic and nuclear recoils. A more detailed description of the principle of a TPC is performed in the Chapter 2.

Similarly, the LUX (Large Underground Xenon) detector [52] is a two-phase TPC filled with 370 kg of LXe (100 kg of target mass) contained in a titanium vessel. The detector is based on the same principle as the XENON detector. LUX is placed underground at the Sanford Underground Laboratory of the Homestake Mine, in South Dakota and it is operational since 2009. The next step on the LUX experiment is a new detector called LZ from LUX-ZEPLIN that merge two dark matter experiments LUX and ZEPLIN (ZonEd Proportional scintillation In Liquid Noble gases). The LZ detector will hold a target mass twenty times higher than that of LUX (7 tons), and which promises a sensitivity much greater [53]. An artistic design of the future LZ detector is depicted in Figure 1.13.

The XMASS experiment [54], on the other hand, is based on a single-phase TPC with a fiducial volume of $\sim$100 kg of LXe used to measure exclusively the scintillation signal. Thereby, the entire LXe volume is surrounded by PMTs to efficiently measure the scintillation light. The XMASS detector is depicted in Figure 1.14. The XMASS project was developed for double beta decay, pp and ^{7}Be solar neutrinos, in addition to the direct detection of dark matter. The future of the XMASS experiment is the XMASS1.5 detector with 5 tons of LXe (3 tons fiducial).

Gamma-Ray Astrophysics

The application of LXe in γ-ray astronomy was first investigated in the late 1980s, following the encouraging results in terms of sensitivity, energy resolution and signal collection of LXe for γ-ray observation in the energy range from 200 keV to 25 MeV [45]. The first attempts of astrophysics observations with LXe were carried out with the Liquid Xenon Gamma-Ray

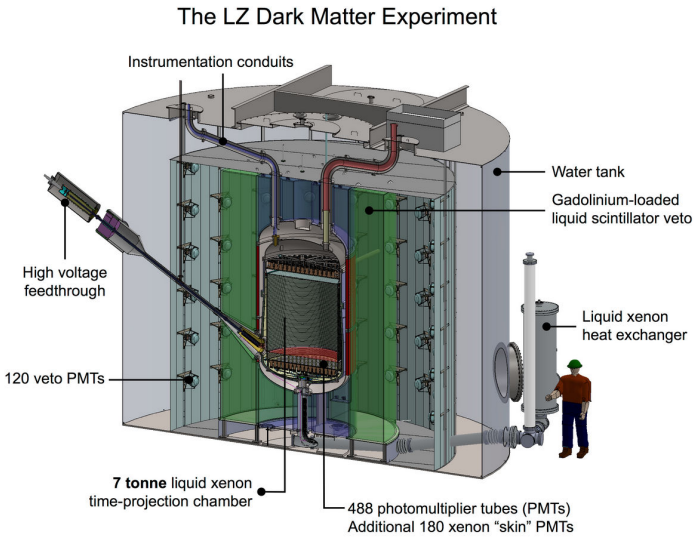

Figure 1.13 – Cutaway drawing of the LZ dark matter detector within the outer detector and water tank. Figure from LZ collaboration.

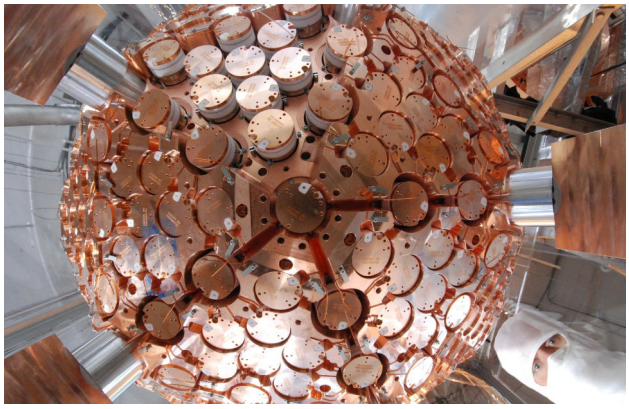

Figure 1.14 – The 800 kg XMASS detector. Figure from XMASS collaboration.

Imaging Telescope (LXeGRIT) [55]. LXeGRIT is a Compton telescope based on a LXe time projection chamber (TPC) used as a balloon-borne instrument. The development of LXeGRIT was the start of a novel concept of Compton telescope, different from standard Compton imaging systems.

The device was based on a single monolithic detector that exploited both scintillation and ionization signals. A schematic drawing of the LXeGRIT detector is depicted in Figure 1.15. The detector consists of a gridded ionization chamber with an active zone of 400 cm^2 and a drift length of 7 cm filled with ultra-pure LXe. The scintillation light generated after the interaction of an ionizing particle with the LXe is detected by four VUV-sensitive photomultiplier tubes (PMT) and used as the event trigger for the data acquisition. A uniform electric field of 1 keV/cm is applied between the cathode and the anode to force electrons to drift towards the anode. The ionization signal is collected by four independent electrodes placed at 9 mm from a shielding grid used as a Frisch grid. A set of two parallel wired planes is installed to provided information of the X and Y position of the interaction point inside the fiducial volume of the detector.

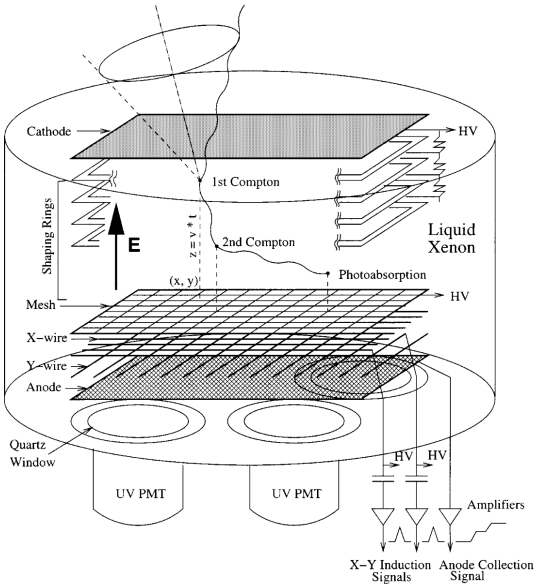

Figure 1.15 – Schematic design of the LXeGRIT LXeTPC. Figure taken from [56].

LXeGRIT was tested in three different balloon flights. After a first short duration flight in 1997 for engineering tests and calibration purposes, the feasibly of LXeGRIT was successfully demonstrated in two longer duration flights in 1999 and 2000 [57, 58]. LXeGRIT showed good performances as γ-ray detector, with a spatial resolution of 1 mm, an energy resolution of 8.8 % FWHM at 1 MeV and an angular resolution of 4° at 1.8 MeV [59].

At the moment there are not ongoing experiment for γ-ray astronomy based on LXe detectors. However, the important developments around LXe technologies in the past years, has renewed the interest of using LXe as detection medium for astronomy observations.

Particle Physics

LXe is also a very suitable candidate for particle physics experiments such as the detection of low-energy solar neutrinos, neutrinoless double beta decay search and the measurement of neutrino-nucleus scattering.

The EXO-200 (Enriched Xenon Observatory) is a good example of a LXe detector dedicated to the study of neutrinoless double beta decay [60]. It is based on a 200 kg TPC filled with LXe enriched in the ^{136}Xe isotope to 80 %, developed for the detection of the double beta decay transition via the $0\nu\beta\beta$ channel [61]. A schematic drawing of the EXO-200 TPC is presented in Figure 1.16. The TPC is divided in two symmetric zones separated by an optically transparent shared cathode. Both regions are equipped with induction and collection wire planes. The crossed wires are placed at the endcaps of the TPC. An electric field of 376 V/cm is applied between the cathode and the anodes to drift the ionization charges towards the wires. The scintillation light is detected by two sets of Large Area Avalanche Photodiodes (LAAPD) also located at the ends of the TPC and parallel to the cathode. The double beta decay of ^{136}Xe is therefore detected by the collection of both the ionization signal and the scintillation light. The detector is located at the Waste Isolation Pilot Plant (WIPP) in New Mexico, and it has been operational since 2011. The EXO-200

experiment reported the first observation of the two-neutrino double beta decay $2\nu\beta\beta$ of ^{136}Xe and pursued the search of the neutrinoless double beta decay [62]. nEXO from *next* EXO is a large scale 5 tons LXe detector design with the aim of increasing the sensibility achieved with its predecessor EXO-200 in at least an order of magnitude.

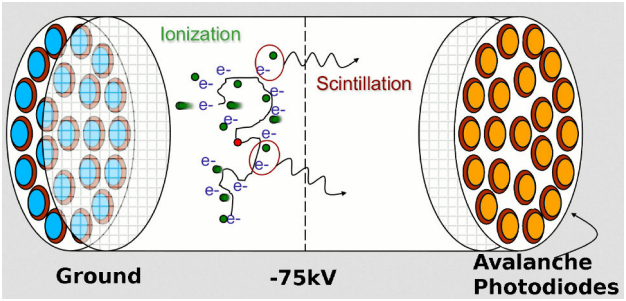

(a)

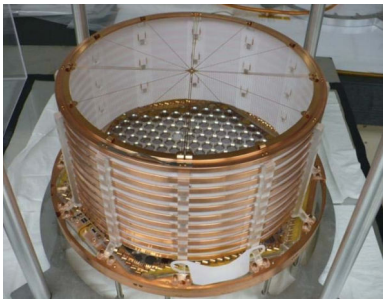

(b)

Figure 1.16 – (a) Schematic principle of the EXO-200 TPC and (b) EXO-200 TPC. Figures from EXO collaboration.

The PandaX experiment with 125 kg of LXe (37 kg of fiducial volume), and the MEG experiment based on a 900 liter LXe scintillation detector, are other examples of the upgrade of large scale LXe-based detectors, dedicated to observe double beta decays and $\mu^+ \rightarrow e^+ + \gamma$, respectively.

Medical Imaging

The potential of LXe for medical imaging was already considered in the early 1970s. Most part of the LXe detectors in medical imaging have been focused on Positron Emission Tomography (PET) scanners, where the coincidence of the 511 keV γ-rays emitted in opposite directions after the annihilation of a positron with an electron are used to reconstruct the emission point of a radioactive source (see Section 1.3.3). Although, some attempts have been also made in gamma-cameras for Single Positron Emission Computed Tomography (SPECT) (see Section 1.3.2). A successful LXe gamma-camera was developed in 1983 by Erogov et al. [63]. The detector showed comparable energy and spatial resolutions of the order of 15 % at 122 keV and 2.5 mm respectively, than the values obtained with a standard gamma-camera based on scintillation crystals [64].

First experiments related to the use of liquid xenon detectors for PET were made almost 40 years ago [65]. Later, in the 90s, the group of A.J.P.L. Policarpo and V. Chepel developed the first prototype of a LXe TPC for PET [66, 67]. The detector was based on a multiwire chamber design to detect both the ionization and scintillation signals. Other groups have also worked in this direction based on the detection of both production channels [68, 69, 70] or only the scintillation light [71]. Thanks to the excellent scintillation properties of LXe, its application for Time of Flight PET (TOF-PET) has been also considered by several authors [10, 65]. The first prototype of a LXe TPC for TOF-PET was developed in 1997 by Waseda *et.al.* [10]. In 2004, our group proposed the idea of using a LXeTPC

for the detection in coincidence of three γ-rays emitted quasi-simultaneously from specific 3γ-emitting radionuclides [72]. This nuclear imaging technique is presented in the next section. The proposed technology is a single-phase LXeTPC that exploits both charge and light yields of electronic recoils. The detector has been developed to fulfill the requirements of a device dedicated to medical applications: high energy resolution, high detector granularity to increase the spatial resolution, the ability to discriminate single from multiple scatter interactions, and very low electronic noise. A detailed description of the detector is presented in Chapter 3.

1.3 3γ imaging: a new medical imaging technique

1.3.1 A brief introduction to nuclear medical imaging

Nuclear medicine is a medical specialty that uses radioactive substances for the diagnosis and treatment of diseases. The radionuclides (label) are chemically bound to a biologically active molecule (tracer) forming a radiopharmaceutical or radiotracer, which is introduced into the patient. Once the radiotracer is administered to the patient, the molecule concentrates at specific organs or cellular receptors with a certain biological function. The choice of a specific radioisotope depends on the actual biological function or organ we are interested in. The concentration of the radioactive substance in the region of interest, allows nuclear medicine to image the location and extent of a certain disease in the body, besides the evaluation of its functional activity from a morphological point of view. The ability to evaluate physiological functions is the main difference between nuclear medicine imaging and traditional anatomic imaging techniques, such as Computed Tomography (CT) or conventional Magnetic Resonance Imaging (MRI). To provides the best available information on tumor staging and assessment of many common cancers, functional imaging is usually combined with anatomical imaging techniques [73].

The origin of nuclear medicine is the result of many scientific discoveries that date back from the end of the XIX century. The discovery of the X-rays by Wilhelm Röntgen in 1895 represented one of the greatest revolution in medicine through the incorporation of the use of ionizing radiation for the diagnosis and treatment of many different diseases [74]. Its discovery triggered the development of medical imaging techniques, which provided an actual image of the inside of the human body. The beginning of image-based diagnosis supposed a greatly increase of our life expectancy, health and welfare. A few years after the breakthrough of the X-rays, many fundamental findings followed, that opened the path to the understanding of the structure of matter and its fundamental interactions. The discovery of natural radioactivity by Henri Becquerel in 1896 and the finding, two years later, of two new radioactive elements polonium and radium by Marie and Pierre Curie laid the foundations of this new medical specialty known as *Nuclear Medicine* [75]. The use of radioactive substances in medicine was driven, in the coming years, by a series of scientific discoveries such as the finding of artificial radioactivity in 1934 by Irène Joliot-Curie and Frédéric Joliot-Curie, and the production of radionuclides for medical use in 1946 by the Oak Ridge National Laboratory. Nuclear Medicine won official recognition as a potential medical specialty in 1946 after the successful treatment with radioactive iodine (^{131}I) in a patient

with thyroid cancer [76]. The use of radioactive iodine was later extended to the diagnosis and treatment of thyroid diseases including the production of images of the thyroid gland, which provided visual information of thyroid disorders.

Nuclear medicine imaging was shaped by the development of scintillation detectors and scintillation cameras, which facilitated external imaging and measurement of radionuclides distributed within the body. The invention in 1950 of the rectilinear scanner by Benedict Cassen, followed by the development of the first scintillation camera, also known as Anger Camera (Hal Anger, 1958), suppose a revolutionary breakthrough in medical diagnosis [77]. The significant technological advances in the following years opened a new window to the study of human physiology, which gave medical imaging, until then exclusively anatomical, a functional character. By the 50s, the use of nuclear medicine was widespread for clinical use. In particular, nuclear imaging techniques experienced a rapid development during the mid 1960s. The initial scintillation camera evolved into modern imaging systems such as PET and SPECT. These two functional imaging techniques are widely used in clinical practice. Currently, nuclear medicine imaging has extend from organ imaging for tumor localization, to the diagnosis of a great variety of diseases including the diagnosis of cardiovascular diseases and neurological disorders [78].

During the 60s, a new detector for imaging solar neutrinos was proposed independently by Pinkau (1966) and White (1968). This detector, called Compton camera, exploited the physics of Compton scattering for imaging purposes. The possible application of a Compton telescope in nuclear medicine was first proposed by Todd, Nightingale and Everett in 1974 [79], although the potential of Compton scattered imaging in medicine was already been noticed back in 1959 by Lale [80]. The detector proposed by Todd *et. al.* was based on a combination of a standard Anger camera and a pixelated germanium detector. Compton imaging provides high sensitivity, high spatial resolution and 3D information.

One of the main limitations of nuclear imaging techniques is the risk of radiation exposure. The biological effect of ionizing radiation was first observed in 1897 after a prolonged exposure to a source of X-rays. In 1927, H. J. Muller reported the resulting genetic effects and the increase of cancer risk [81]. In the past years, additional efforts have been focused at reducing the radiation dose by the improvement of the actual instrumentation, the implementation of low-dose protocols and the development of new imaging techniques. The goal is to obtain same quality images with a significant reduction of the dose administered to the patient. An innovative nuclear medicine imaging technique was proposed in 2004 by Thers *et.al.* [72]. This technique called 3γ imaging consists in measuring the position of a radioactive source in 3D using the simultaneous detection of three γ-rays by means of a LXe Compton camera. The 3γ imaging technique exploits the benefits of the Compton imaging providing high sensitivity and very good spatial resolution with an important reduction of the administered dose [82].

In this section, a brief description of the two main functional imaging techniques PET and SPECT is performed. The explanation includes some notions of the physics background, detection system and main radiopharmaceuticals used in clinical practice. The principle of a Compton telescope and the basics of the Compton imaging are also discussed in this section. Finally, we introduce the concept of the 3γ imaging technique and the possible 3γ emitter radionuclides that can be used.

1.3.2 Single Photon Emission Tomography

Single Photon Emission Computed Tomography (SPECT) is a non-invasive functional medical imaging technique, which provides 3D information of the distribution of a radiotracer inside the body [83]. The SPECT technique requires a radiopharmaceutical labeled with a γ-emitter radionuclide. An external detector is used to measure the radiation emitted from the radiotracer and generate an image.

The SPECT imaging is based on the principle of the Anger camera [84]. A standard scintillation camera consists of a large scintillation crystal, usually NaI(Tl), coupled to an array of PMTs. Figure 1.17 illustrates the principle of operation of a scintillation camera. Since γ-rays are emitted isotropically, a collimator is placed between the patient and the radiation detector to relate the detected γ-ray to the emission point. The collimator only allows photons from certain directions to reach the detector and thus, limits the acceptance angle and defines the spatial distribution of the photons detected by the scintillation crystal. Collimators are made of high atomic number materials, usually lead or tungsten, to efficiently absorb those γ-rays emitted with a certain angle with respect to the collimator holes. A widely-used collimator is the parallel-hole which provides a two-dimensional parallel projection of the source distribution with a constant FOV. Such a collimator only allows photons emitted in the normal direction with respect to the crystal surface to reach the detector, whereas the rest of photons are absorbed. Other types of collimators used in clinical practice are illustrated in Figure 1.18. Collimators are therefore necessary to obtain information of the incoming direction of the emitted γ-rays, at the expense of being the major limitation to the spatial resolution and the sensitivity of SPECT detectors. The adequate choice of a collimator depends on the image purposes in terms of energy resolution, sensitivity and spatial resolution.

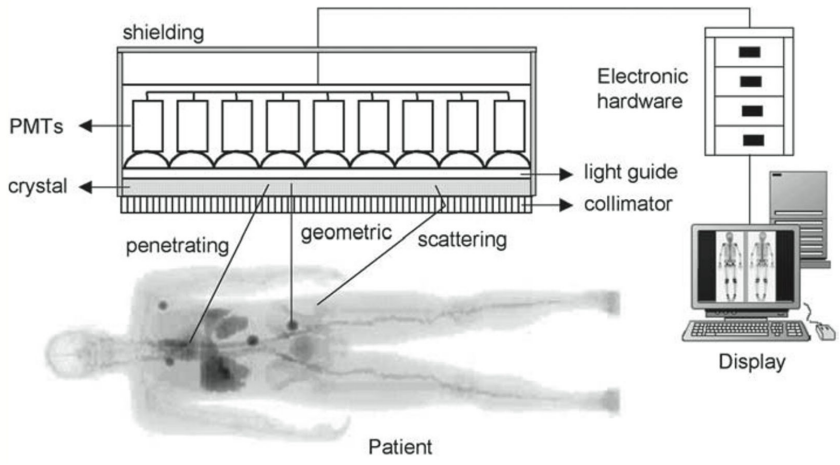

Figure 1.17 – Schematic description of the principle of an Anger scintillation camera. Figure taken from [85].

The advantage of SPECT imaging compared to planar scintigraphy is the tomographic character of the SPECT technique. In SPECT, the gamma camera moves around the patient following a circular, elliptical or contoured orbit. By rotating the detector, two-dimensional

projections are acquired from many different angles. These multiple projections are then reconstructed using either analytic or iterative reconstruction algorithms that generate a 3D image slice by slice.

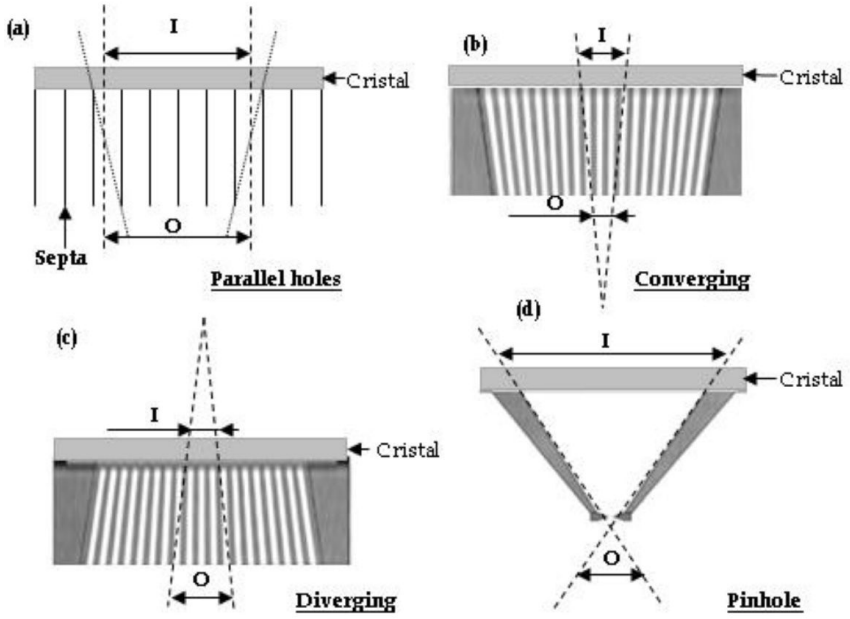

Figure 1.18 – Different types of collimators used in SPECT. Figure taken from [86].

Scintillators

The basic radiation detectors used in SPECT imaging are scintillation detectors that transform the incident γ-rays into optical photons. Historically, the Anger camera was based on a NaI scintillation crystal, commonly doped with thallium to improve the scintillation performances. γ-rays interact with the molecules and atoms of the detector either by photoelectric effect or Compton scattering, leading the crystal in excited state. The excited atoms return to the ground state with the consequent emission of a fluorescence photon. The fluorescence emission process depends on whether the detector is based on an organic or inorganic scintillation crystal [20]. In particular, the NaI(Tl) is an inorganic scintillation detector characterized by the emission of visible photons with a primary decay constant at 230 ns and maximum emission wavelength at 410 nm [87]. The main characteristics of the NaI(Tl) as scintillation detector are listed in Table 1.4.

An ideal scintillation crystal should have high detection efficiency, large light output and good energy and time resolutions. Particularly, the NaI(Tl) has a high scintillation yield, in average 40 photons are emitted per keV, and a high detection efficiency for the energies typically used in SPECT (below 200 keV). For example, 85% of the incoming 140 keV γ-rays from the decay of ^{99m}Tc deposit all their energy in the detector. The energy resolution of the NaI(Tl) is of the order of 7-8% at 1 MeV [86]. Associated with the light yield requirement, a large fraction of the emitted scintillation photons should be detected. This implies that the optical self-absorption of the scintillation crystal should be minimal. The NaI(Tl) is

relatively transparent to its own light, with about the 30% of the emitted photon detected by the PMT [86]. Due to its good scintillation properties, the NaI(Tl) remains as one of the most used scintillation detector in SPECT, even 60 years later of the development of the first Anger camera.

Photodetectors

The photons emitted by the scintillation crystal are detected by a photosensor, typically a PMT, and converted into an electrical signal. The principle of a PMT is schematically represented in Figure 1.19. Incident photons strike the photocathode located at the entry window of the PMT, which emit a number of photoelectrons as a result of photoelectric absorption. These electrons are directed by a focusing electrode towards a series of electrode called dynodes, where electrons are multiplied by means of secondary emission. The geometry of the dynode chain is such that an increasing number of electrons is produced after each collision. Electrons are accelerated towards the next dynode under the influence of an intense electric field established along the dynodes chain. Each dynode is held at a more positive voltage than the previous one. The electrons reach the first dynode with a kinetic energy equal to the potential difference between the photocathode and the dynode. This energy is sufficient to extract more secondary electrons from this dynode and create an avalanche of electrons. At the end of the multiplication chain, a large number of electrons is produced and collected by the last dynode, called anode. The total number of electrons that arrive to the anode for each photoelectron ejected from the photocathode is defined as the gain of a PMT. Gains of the order of 10^5 to 10^8 are usually reached with these devices. The total collected charge in the anode results in a sharp current pulse that contains the timing information of the arrival of a photon at the photocathode. The amplitude of the pulse delivered by the PMT is proportional to the number of scintillation light that reached the PMT surface, which is proportional to the deposited energy [20].

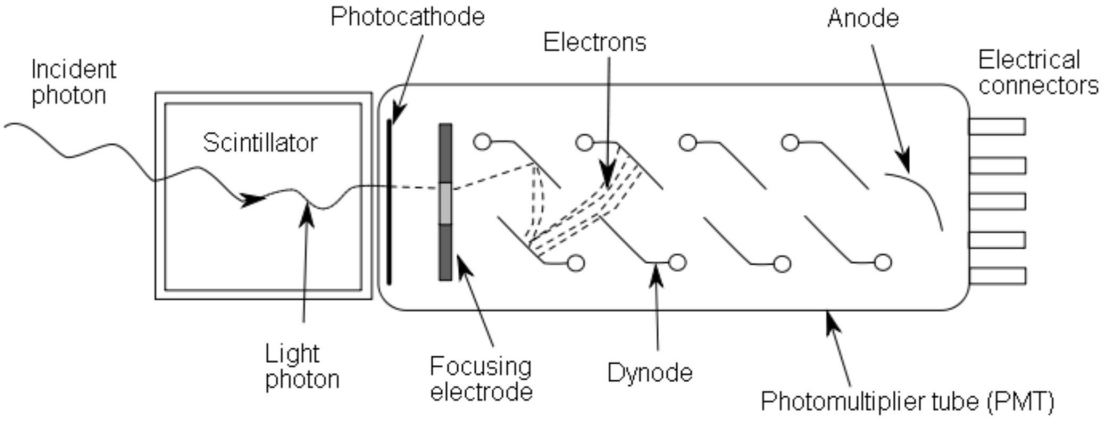

Figure 1.19 – Principle of operation of a photomultiplier tube (PMT) [20].

Other photodetectors such as Silicon PhotoMultipliers (SiPM) are also widely used in many different applications [88]. The insensitivity to magnetic field of SiPMs compared to the standard PMTs, is one of the most interesting advantages of this kind of photosensors,

which has given rise to the development of hybrid systems PET-MRI. This new medical imaging technique combines the functional imaging of PET with the high contrast in soft tissues of the MRI [89].

1.3.3 Positron Emission Tomography

Positron Emission Tomography (PET) [90] is a nuclear medicine imaging technique widely used in the diagnosis and staging of many sorts of cancers [91]. PET is based on the decay of β^+-emitting radionuclides. The emitted positron annihilates with an electron of the surrounding matter, resulting in the emission of two γ-rays in opposite directions, each of them with an energy equal to the rest mass of the emitted particles ($mc^2 = 511\ keV$). The principle of the PET imaging is therefore based on the detection in coincidence of these two 511 keV γ-rays. The devices used in PET are commonly based on a circular array of detectors arranged in a ring configuration around the patient (see Figure 1.20). The registration in coincidence of these two γ-rays defines a line of response (LOR) which contains information about the annihilation position. With a full angular coverage of the patient, the information collected in every LOR is processed and used to produce an image of the functionality of the organism.

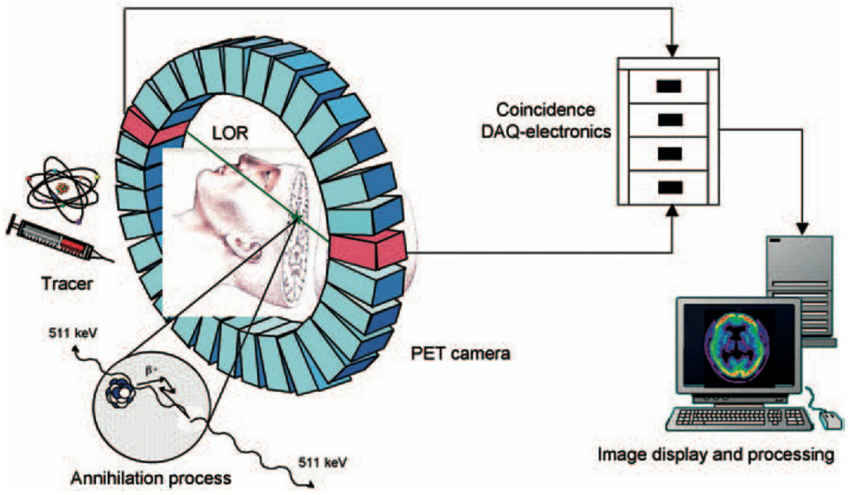

Figure 1.20 – Schematic description of the principle of a PET system. Figure taken from [85].

A PET scanner consists of a set of scintillation crystals positioned in a cylindrical gantry. Each scintillation crystal is coupled to a PMT usually attached via a light guide. Unlike in SPECT, the radiation detector is not an unique monolithic crystal, but it is composed by a array of several rectangular crystals separated from each other by a reflective material like Teflon. Crystal segmentation allows to increase the spatial resolution of the detector. The choice of the crystal dimensions requires, however, a compromise between sensitivity and spatial resolution [92].

To obtain a signal, the system requires interactions in two independent detectors within a short time window. This information is extracted thanks to a coincidence circuit established

between the different detectors that compose the tomograph. Besides the coincidental time window, a narrow energy windows is normally set around the 511 keV photoelectric peak to determine a true coincidence. Energy and time conditions depend on the characteristics of the scintillation crystal used in the system. After a coincidence, an annihilation is assumed to have taken place somewhere along the LOR between the two crystals. The information measured by each coincidental unit at different angles is reconstructed providing 3D information of the distribution of the radiotracer inside the body. Moreover, if the study is performed over successive temporal intervals, a temporal distribution of a metabolic function is obtained, allowing dynamic studies.

Same as in SPECT, the scintillation crystals used in PET should have a high detection efficiency for 511 keV γ-rays, i.e. high density, large photon emission rate and good energy and time resolutions. The NaI(Tl) used in SPECT is not a good candidate for PET imaging, due to its poor detection efficiency at higher energies than 200 keV. At 511 keV, for example, only 12% of the detected γ-rays deposit all their energy in the detector. PET requires higher density crystals in order to increase the photoelectric absorption. Some of the scintillation crystals commonly used in PET are the Bismuth Germanate (BGO), Lutetium Oxyorthosilicate (LSO) and Lutetium Yttrium Orthosilicate (LYSO). Their basic properties are summarized in Table 1.4. Compared to the NaI(Tl), these scintillation crystals have lower light output, whereas they show high detection efficiency for 511 keV photons and faster scintillation emission, which results in an important improvement in the counting-rate capability of the detector.

	NaI(Tl)	BaF_2	LSO	GSO	LYSO	$LaBr_3$	LFS	LuAP	LuI_3
Effective atomic no. (Z)	51	54	66	59	60	47	63	65	60
μ (cm^{-1})	0.34	0.44	0.87	0.62	0.86	0.47	0.82	0.9	~0.56
Density (gm cm^{-3})	3.67	4.89	7.4	6.7	7.1	5.3	7.3	8.34	5.6
Index of refraction	1.85	-	1.82	1.85	1.81	1.88	1.78	1.95	-
Light yield (% NaI(Tl))	100	5	75	30	80	160	77	16	190
Peak wavelength (nm)	410	220	420	430	420	370	430	365	470
Decay constant (ns)	230	0.8	40	65	41	25	35	18	30
Hygroscopic	yes	slight	no	no	no	no	no	no	yes

Table 1.4 – Properties of some scintillators used in functional medicine imaging. Table taken from [93].

PET performances

Due to the limited energy and time resolutions of the system, there are also some limitations in the coincidence detection technique that cause image degradation in PET. Figure 1.21 illustrates the main coincidence event types. A **true event** is considered when the two detected photons come from the same annihilation point (Figure 1.21 a). However, if one or both of the detected photons interact with the surrounding matter before being detected, they may have changed their direction producing an error in the reconstructed position. This kind of events are known as **scattered events** (Figure 1.21 e). Nevertheless, since scatter produces energy loss, scattered events can be substantially reduced by the energy window condition. **Random coincidences** between two γ-rays from two different annihilation processes within the coincidence window are also possible, generating a LOR that does not include useful information about the radiotracer distribution (Figure 1.21 d). Finally, **multiple coincidences** may occur when three or more photons are detected simultaneously within the coincidence window (Figure 1.21 b). These pile-up events cause an ambiguity between possible valid photon pairs, and therefore are usually discarded from the reconstructed data. Equally, **single coincidences** are produced when only one of the emitted photons is detected, which are directly rejected from the reconstruction (Figure 1.21 c).

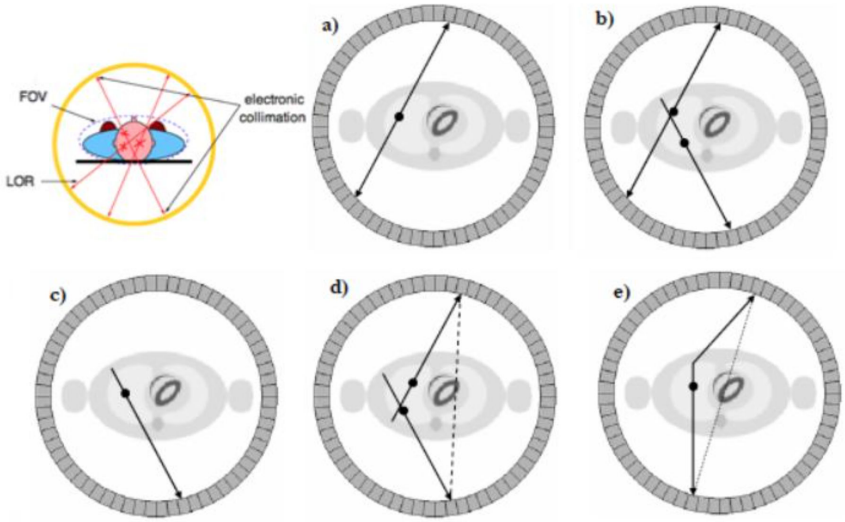

Figure 1.21 – Illustration of the main coincidence event types: a) true; b) multiple; c) single; d) random and e) scattered. Figure adapted from [90].

Since the detection of the two γ-rays is made via the coincidence between the two back-to-back 511 keV γ-rays, there is no need of collimator. Therefore, the sensitivity of a PET scanner is several times higher than that of SPECT. However, there are other factors that ultimately affect the spatial resolution in PET. The emitted positron travels some distance before it annihilates with an electron. The distance from the emission point to the annihilation point is known as positron range and it depends both on the energy of the emitted positron and the surrounding materials. Since PET imaging reconstructs the annihilation sites and not the positron emission points, the non-zero positron range is one of the main limiting factors to the spatial resolution [94]. Another factor that affects the

performances of the PET technique is related to the fact that not all of the positrons are at rest when the annihilation occurs. Since the majority of annihilations occur with both positron and electron at thermal energies, by energy and momentum conservation, the two 511 keV γ-rays are emitted with an angle of approximately 180° [95]. However, there is a non negligible probability that the annihilation occurs when the positron is not at rest. This causes a non-collinearity between the emitted γ-rays that adds some uncertainty in the identification of the annihilation position [95]. This non-collinearity may be of the order of 0.5°. The combination of both effects affects the intrinsic spatial resolution of the PET imaging technique. For example, for the ^{18}F, which is one of the most used positron-emitting radionuclides in PET, this limitation is less than 1 mm. Nevertheless, on a PET system the major constraint to the spatial resolution is still the intrinsic spatial resolution of the PET detector.

1.3.3.1 Time-of-Flight PET

The Time of Flight PET or TOF-PET exploits the time difference Δt between the two detected photons to provide information of the depth of interaction inside the crystal. In PET, there is a uniform probability that the emission point lays along the entire length of the LOR. The accurate measurement of the arrival time of the two back-to-back 511 keV γ-rays constrains the position of the annihilation point along the LOR between two coincidental pairs [96, 97, 98]. Figure 1.22 illustrates the basic principle of the TOF-PET technique. The time information correlates to the position of the annihilation point with respect to the center of the FOV according to the formula:

$$\Delta x \;=\; \frac{c}{2}\,\Delta t \tag{1.15}$$

where c is the speed of light. The position constraint achieved by adding the time of flight information is not enough to highly improve the spatial resolution or to avoid the image reconstruction process. The existing commercially available TOF-PET systems achieve timing resolutions of the order of 450 ps to 900 ps allowing a position resolution of 6.75 to 13.5 cm (FWHM) along the LOR [99, 100, 101]. In the case of small animal imaging, the annihilation position can be estimated with a resolution of the order of 2 - 3 cm.

The exploitation of timing information to calculate the emission point along the LOR was introduced in the 1960s, along with the development of PET [103]. However, its application for clinical use had to wait until the 1980s with the development of the first TOF-PET system [104]. The TOF-PET modality has suffered a very tortuous trajectory until its complete acceptance in the clinical practice. The early TOF-PET systems were based on cesium fluoride (CsF) and barium fluoride (BaF_2) scintillation crystals that provided good timing resolutions compared to the standard NaI(Tl) or BGO crystals. However, due to their low detection efficiency and low scintillation yield, the research around TOF-PET was paused and almost forgotten in the early 1990s. Later, in the 2000s, the development of new and faster scintillation crystals such as the LSO, reawoke the interest for this imaging modality for both industry and research. The incorporation of new photodetectors, electronics and more precise image reconstruction techniques have also contributed to the improvement of

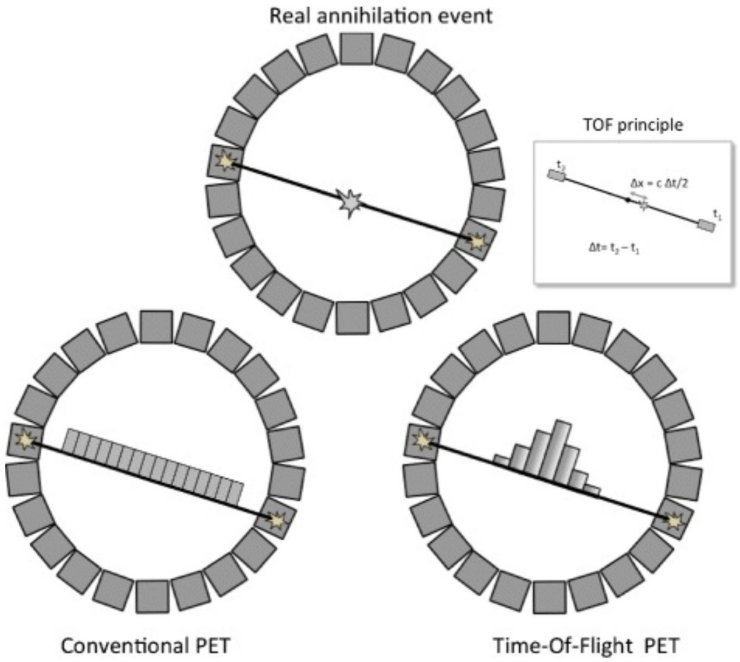

Figure 1.22 – Comparison between conventional PET and TOF-PET. The measured time-of-flight difference (Δt) between the arrival photons in TOF-PET allows to constraint the annihilation point along the LOR [102].

TOF-PET imaging. LYSO crystals combined with SiPMs have shown a great potential with achievable timing resolutions of between 200 - 300 ps [105, 106]. However, even today, there are still some technological limitations that avoid reaching the desired timing requirements of the TOF-PET.

To obtain subcentimeter spatial resolution, a coincidence timing precision of less than 50 ps is necessary. However, this is hard to accomplish with the existing technology. On the other hand, the additional timing information has demonstrated to improve the Signal to Noise Ratio (SNR) in the reconstructed images, which is one of the limitations of PET imaging. The statistical noise reduction factor or *gain* of the TOF-PET with respect to the Non-TOF mode can be approximated as:

$$\frac{SNR_{TOF}}{SNR_{Non-TOF}} = \sqrt{\frac{D}{\Delta x}} \tag{1.16}$$

where D is the size of the emission source. The SNR improvement of the TOF-PET for a time resolution of 500 ps and a patient with 40 cm in diameter is about $\sim$2.3. Since this gain is related to the object size, a largest improvement is expected in heavy patients. No improvement in terms of SNR is, however, obtained for small animal imaging technologies.

Over the recent years, the results show that the advantages of TOF-PET should be focused on the improvement in terms of lesion detection, shortening of the total imaging time and reduction of the injected dose [99].

PET and SPECT Radionuclides

Radioactive tracers are based on a specific biological active molecule coupled to a radioactive isotope, that allow the assessment of physiological and metabolic functions in the organism and the diagnosis of diseases. The type of carrier molecule depends greatly on the purpose of the scan, which can vary from bone imaging ($Na^{18}F$), myocardial perfusion ($^{82}RbCl$) or glucose metabolism (^{18}FDG). Properties such as decay scheme, effective half-life, energy and chemical properties make radionuclides appropriate for certain applications.

Radioactive tracer employed in SPECT are all γ-emitting radionuclides. The most common radioactive marker is the ^{99m}Tc, which is characterized by a half-life of 6 hours and the emission of a main γ rays of energy 140 keV. The ^{99m}Tc is produced by the decay of ^{99}Mo that has a much longer half- life of 66 hours. This allows the use of ^{99}Mo$-^{99m}$Tc generators, which make ^{99m}Tc daily available in hospitals. Other frequently used radioisotopes in SPECT are listed in Table 1.5.

Radionuclide	Half-life	Energy (keV)
^{99m}Tc	6.02 hours	140.5
^{123}I	13 hours	159
^{201}Tl	73 hours	170, 135
		e^- capture 69 - 80 keV
^{67}Ga	3.26 days	93.3, 185.6, 300
^{111}In	2.81 days	171.3, 245.4

Table 1.5 – Physical properties of the main radioisotopes used in SPECT.

PET requires β^+-emitting radionuclides. The most frequently used are listed in Table 1.6 with some of their physical characteristics. Among them, the ^{18}F, characterized by a half-life of 110 minutes and positron range of less than 0.7 mm in water, is the most commonly used radionuclide in neurology, cardiology and in the diagnosis and staging of many sorts of cancer. The most frequently used ^{18}F-labeled radiopharmaceutical is 18-fluoro-deoxy-glucose (FDG), which is an analogue of glucose. The other relevant PET isotopes are characterized by much shorter half-lives with respect to ^{18}F, so they have to be produced in the same center where the medical exam is performed. The positron energy and its resulting range in water are inversely correlated with the PET image resolution.

1.3.4 Future trends in functional imaging

The perspectives of nuclear medical imaging are in constant growth thanks to the technological advances and the development of new radiopharmaceutical. In the past few years, the progress in functional imaging is focused, not so much in the constant improvement of image resolution, which is probably nearing its limit, but in its consolidation as a routine clinical technique. The reduction of the injected dose and the shortening of the imaging time have also become

Radionuclide	Half-life (min)	Production	Range in water (mm)		Max. Emission energy (MeV)
			Max	Mean	
^{11}C	20.4	cyclotron	4.1	1.1	0.959
^{13}N	9.97	cyclotron	5.1	1.5	1.197
^{15}O	2.03	cyclotron	7.3	2.5	1.738
^{18}F	109.8	cyclotron	2.4	0.6	0.633
^{82}Rb	1.25	generator	14.1	5.9	3.400
^{68}Ga	68	generator	8.9	2.9	1.899

Table 1.6 – Physical properties of positron emitters radionuclides used in PET. Figure taken from [107].

of great importance to reduce the radiation exposure of the patients and working personnel during a medical exam. To overcome some of the limitations of PET and SPECT, which show a relative poor anatomical detail, the development of multimodal imaging system offers more reliable images. Multimodality is based on the combination of two or more different imaging techniques to take advantage of complementary information provided by each independent modality. Anatomical imaging ensures very good spatial resolution of less than 1 mm. However, for the diagnosis and staging of certain diseases, morphological information is not always enough, since functional changes may occur in the absence of any associated structural change. Accordingly, multimodal imaging is currently a preferred approach. Nowadays, there are commercially available PET-CT, SPECT-MR and PET-MR multimodal systems [108, 109, 110]. In particular, the coupling of PET and CT has become a standard in clinical practice due to the improved quality image and robustness of the diagnosis [111].

1.3.5 Medical imaging with a Compton Camera

Compton imaging is a well-know technique that exploits the kinematics of Compton scattering for the reconstruction of the origin of incoming γ-rays [112]. The original direction of the incident particle can be determined from the coordinate point (x_i, y_i, z_i) and the energy deposited (E_i) at each individual interaction i. Figure 1.23 depicts the principle of Compton imaging for a single γ-ray. The basic useful event for a Compton scattering system consists of two interactions, a Compton scattering and a photoelectric absorption. In the first interaction, the incoming γ-ray with energy E_γ is deflected from its initial trajectory after losing some of its energy to an atomic electron. The resulting energy E_1 can be determined from the scattering formula:

$$E_{\gamma'} = \frac{E_\gamma}{1 + E_\gamma(1 - cos\ \theta)/m_e c^2} \tag{1.17}$$

From the energy conservation, the energy deposited after the first interaction is: $E_1 = E_\gamma - E_{\gamma'}$. After the second interaction, the scattered γ-ray with energy $E_{\gamma'}$ is completely absorbed. Assuming that both events are calorimetrized inside the detector, the incident energy E_γ is equal to the sum of the deposited energies in both interactions: $E_\gamma = E_1 + E_2$. Applying energy and momentum conservation, the deflection angle for the first interaction can be computed using the Compton scatter formula:

$$\cos\theta = 1 + m_e c^2 \left(\frac{1}{E_1 + E_2} - \frac{1}{E_1} \right) \tag{1.18}$$

The incident direction of the incoming γ-ray cannot be directly determined, but it theoretically falls in the surface of a cone with opening angle θ and an axis direction that can be determined from the spatial coordinates (x_1, y_1, z_1) and (x_2, y_2, z_2) of the first and second interactions, represented by the subscripts 1 and 2 respectively. Therefore, the spatial location of the interaction points combined with the deflection angle, constraint the possible location of the emission point. Each detected γ-ray is expected to have different reconstructed Compton cones from different scatter angles and axis. The intersection of the cones resulting from multiple incident γ-rays, reveals the probable location of the radiation source. For an accurate reconstruction, the correct sequence of the two interactions must be known.

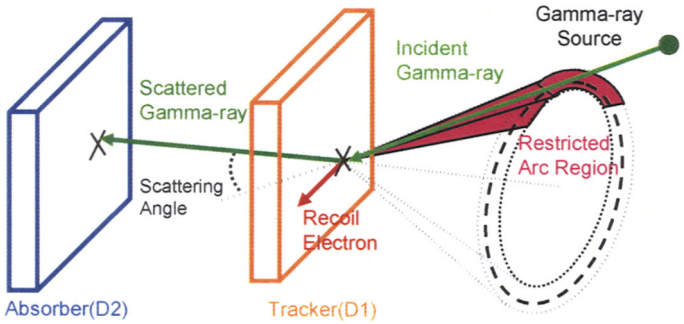

Figure 1.23 – Basic principle of a Compton camera [113].

Compton imaging systems, also known as Compton cameras are widely used to image sources of gamma radiation in a variety of applications such as nuclear medicine imaging, hadrontherapy, γ-ray astronomy and homeland security. Traditional Compton cameras consist of, at least, two independent position-sensitive detectors working in coincidence. The γ-ray undergoes a Compton scattering in the first detector, known as the scatterer, and is completely absorbed in the second module or absorber as illustrated in Figure 1.23. In nuclear medicine, Compton cameras have the potential to overcome some of the inherent physical limitations of standard SPECT and PET systems in terms of system sensitivity and image resolution. The direct triangulation of the position of the radioactive source, allows the possibility of imaging the source distribution without the use of mechanical collimators and reconstruction algorithms. Compton imaging also provides large field of view, good background rejection, direct 3D imaging and an increase of the detection efficiency over a large energy range between hundreds of keV to tens of MeV. However, an accurate reconstruction of the Compton cones requires high spatial and energy resolutions. Some

technological limitations have prevented Compton imaging to become a suitable medical imaging alternative in clinical practice. In the recent years, the development of new detectors and optimized technologies have renewed the interest of Compton imaging for medical applications. The use of solid state detectors seems very promising to fulfill the requirements of Compton imaging. The choice of LXe as detection medium has also shown its potential for γ astronomy with the LXeGRIT experiment [114] and in nuclear medical imaging [115], which is the purpose of this dissertation.

1.3.6 The 3γ imaging technique

As mentioned in the introduction, one of the increasing concerns in nuclear medicine is the radiation exposure of the patients during a medical exam. Typical $^{18}F-FDG$ injected activities in human PET studies are in the range from ∼370 to 740 MBq [116], while in small-animal PET, activities of the order of 4 - 40 MBq are typically applied [117]. These injected activities lead to effective doses on the order of ∼10 mSv. The administered doses and the examination times, which are of the order of 10 - 45 min depending on the scanner, disease, patient and image reconstruction method, are prohibitive for monitoring disease progression and the assessment of the response of a disease to treatment. A new medical imaging technique called 3γ imaging was proposed to improve not only the spatial resolution of standard nuclear imaging techniques, but also to reduce the administered dose maintaining image quality with reasonable scanning times. This technique opens a new window in the future of medical imaging in which low dose is required.

The 3γ imaging technique is based on the triple coincidence between the two 511 keV γ-rays generated after the annihilation of a positron with an electron, and an additional γ-ray emitted from a specific 3γ-emitting radioisotope. The notion of the triple coincident Compton imaging was introduced for the first time in 1987 by Liang et al. [118]. However, due to the limited available technology at that time, no further research was performed around this technique. Later in 2001, Kurfess and Phlips [119] resumed the research work based on solid-state detectors. Independently, in 2004 Thers *et.al.* [72] proposed the idea of the 3γ imaging and the potential of using a large monolithic LXe Compton camera as γ-detector. To consolidate and show the advantages of the 3γ imaging technique, a first phase of research and development (R&D) has been carried out within a research project called XEMIS (XEnon Medical Imaging System). This initial phase involves both fundamental research and the implementation of novel technologies. Currently, 3γ imaging with LXe is in the early stages of the pre-clinical phase with the development and characterization of a small animal LXe Compton imaging system called XEMIS2. Furthermore, the application of the 3γ imaging modality has been recently adopted by other authors such as [120], who propose the use of a standard Compton camera based on solid state detectors and $LaBr_3$ scintillator crystals as detection system.

In this section, we describe the basic principle of the 3γ imaging technique. The physical requirements of a LXe Compton camera to achieve an accurate reconstruction of the position of the radioactive source are also discussed. Finally, we present the features required by a 3γ-emitting radionuclide as a possible candidate for this medical imaging modality.

Principle of the 3γ imaging technique

3γ imaging is a new functional medicine imaging technique based on the detection in coincidence of three γ-rays. This medical imaging modality aims to obtain a precise 3D location of a radioactive source with both good energy and spatial resolutions, and a significant reduction of the dose administered to the patient. The principle of the 3γ imaging technique consists in measuring the position of a radioactive source in 3D using the simultaneous detection of three γ-rays. Consequently, this technique requires the use of a specific radionuclide that emits a γ-ray and a positron in quasi-coincidence [121]. Assuming that the positron and the γ-ray are emitted simultaneously, the position of the radionuclide is then obtained by the intersection between the LOR, given by the two back-to-back 511 keV γ-rays resulted from the positron annihilation, and the Compton cone defined from the interaction of the third γ-ray with a Compton telescope. The Compton cone surface contains the incident direction of the third γ-ray and it can be directly inferred from the Compton kinematics as explained in the previous section. The aperture angle of the cone, θ, is given by the Compton scattering formula (see Equation 1.18), whereas the axis of the cone is determined by the first two interaction points of the incoming photon inside the detector. Figure 1.24 illustrates the principle of the 3γ imaging technique.

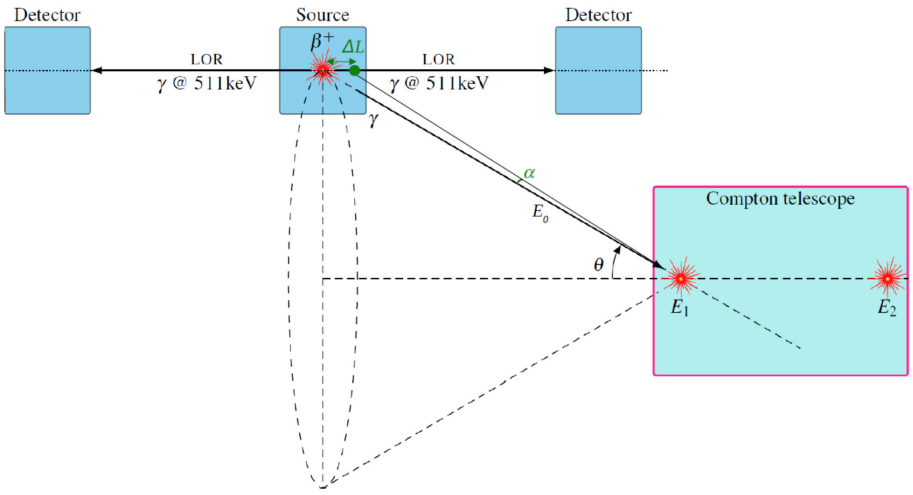

Figure 1.24 – Schematic illustration of the principle of the 3γ imaging technique with a LXe Compton telescope. The difference between the position of the source and a reconstructed intersection point (green point) is represented as ΔL. This difference can be also expressed in terms of the angle α [82].

Thanks to the additional information brought by the third photon, in contrast to the previously mentioned medicine imaging techniques SPECT and PET, the 3γ imaging allows real-time detection and the direct reconstruction in 3D of the emitter position at a low counting rate. The potential of this new medicine imaging modality lies directly in the reduction of the number of radioactive decays needed to obtain an image. The time required to perform an exam and the radioactive dose received by the patient should be therefore significantly reduced.

Modern small animal PET imaging systems can reach spatial resolution of the order of 1 - 2 mm (FWHM) with sensitivities of 1% to 15% for a point source at the center of the FOV [122]. The combination of the positron annihilation with a prompt γ-ray enables to reach submillimiter spatial resolution in the 3D with high sensitivity. Previous results showed that a uniform sensitivity of around 5% to 7% along the full FOV are expected with a monolithic LXe Compton camera design for small animal imaging [123].

Moreover, 3γ imaging shows the potential to overcome certain limitations of the standard functional imaging techniques. The additional information supplied by the third photon allows to efficiently separate the reconstructed true events from background. Therefore, the spatial uncertainty introduced by the positron range and Compton scattering of the γ-rays within the object before reaching the detector can be strongly reduced. A detailed simulation of the detector have shown the possibility of obtaining good property images only by the triangulation of the position of the source from the interaction of the three γ-rays in a simulated rat phantom, without any additional reconstruction algorithms. First raw images shows very good results with a sensibility of 7%. Furthermore, to increase the quality of the reconstructed image, a deconvolution technique using the ML-EM iterative algorithm has been also implemented showing that good properties images of the whole animal can be obtained with only 20 kBq of injected activity, 100 less of activity than a conventional small animal functional imaging exam.

Requirements of the 3γ imaging technique

To exploit the advantages of the 3γ imaging technique the Compton telescope requires a high Compton scattering efficiency and a high spatial and energy resolutions on each γ interaction. As discussed in the previous section, for each coincidence event, a Compton cone is reconstructed. The precision on the reconstruction of the intersection point between the cone and the LOR is what determines the image spatial resolution of the detector. The errors on the reconstruction of the cone involve the uncertainty on the cone apex ($\sigma^2_{\theta_p}$), and opening angle ($\sigma^2_{\theta_E}$), that can be quantified as an angular resolution on the emission point along the LOR (σ_θ). In fact, the angular resolution can be considered as one of the most important parameters to characterize the image performances of a Compton camera. Assuming that each contribution is Gaussian-distributed and uncorrelated, the total angular resolution can be expressed as:

$$\sigma^2_\theta \;=\; \sigma^2_{\theta_p} \;+\; \sigma^2_{\theta_E} \;+ \sigma^2_{\theta_{DB}} \tag{1.19}$$

where $\sigma^2_{\theta_{DB}}$ represents the intrinsic limitation to the angular resolution due to the Doppler broadening effect (see Chapter 2, Section 2.3.2). Therefore, there are three sources of error that limits the angular resolution of a Compton camera: the position resolution, which limits the precision in measuring the the direction of the scattered γ-ray, the energy resolution, which affects the determination of the scatter angle, and the inherent resolution given by the Doppler broadening.

Energy resolution

The aperture angle of the reconstructed cone is computed using Equation 1.18, that can be expressed in terms of the energy transferred to the ejected electron E_e according to the following expression:

$$\begin{aligned} \cos\theta &= 1 \; + \; m_e c^2 \left(\frac{1}{E_\gamma} \; - \; \frac{1}{E_1} \right) \\ &= \; 1 \; + \; m_e c^2 \left(\frac{1}{E_\gamma} \; - \; \frac{1}{E_\gamma \; - \; E_e} \right) \end{aligned} \tag{1.20}$$

where E_γ is the energy of the incoming photon. Therefore, any error in the determination of the deposited energy affects the value of the Compton angle. The contribution of the energy resolution can be estimated by applying error propagation to Equation 1.20 and assuming that E_γ is known:

$$\sigma^2_{\theta_E} \; = \; \left(\frac{\partial \theta}{\partial E_e} \, \sigma_{E_e} \right)^2 \tag{1.21}$$

where σ_{E_e} is the energy resolution of the detector. The energy contribution to the angle θ is therefore given by:

$$\frac{\partial \theta}{\partial E_e} \; = \; \frac{1}{\sin\theta} \, \frac{m_e c^2}{(E_\gamma \; - \; E_e)^2} \tag{1.22}$$

The energy resolution in a LXe Compton telescope depends on three main factors:

$$\sigma^2_{E_e} \; = \; \sigma^2_{LXe} \; + \; \sigma^2_{el} \; + \; \sigma^2_{others} \tag{1.23}$$

The first contribution σ_{LXe} is the intrinsic energy resolution of LXe and it comes from statistical fluctuations in the charge carrier formation (see Chapter 2, section 2.2). The number of electron-ion pairs produced by an ionizing particle in the LXe is proportional to the deposited energy, E_0, in such interaction: $N_i = E_0/W$. However, the number N_i of generated charge carriers fluctuates statistically, which results in a physical limit to the energy resolution of the detector. In a first approach, it can be expected that this number fluctuates according to Poisson statistic. However, due to the correlation between the events along the track of the recoiling electron, they can not be treated independently. The deviation from the Poisson limit is quantified by the Fano factor, F, that depends on the target material [124]. The energy resolution of a detector expressed in terms of the full width at half maximum (FWHM), can be inferred from the Fano factor through the following formula:

$$\sigma_{E_e} \; = \; 2.35 \frac{\sqrt{F N_i}}{N_i} = \; 2.35 \sqrt{\frac{FW}{E_0}} \tag{1.24}$$

LXe has an estimated low Fano factor of 0.041 [1], which predicts a theoretical energy resolution of about 2 keV (FWHM) at 1 MeV, of the order of that of germanium detectors. However, it has been demonstrated experimentally that this value is underestimated since several contributions are missing. In LXe the lifetime of the electrons in the detector is limited by the recombination between electrons and positive ions. The recombination rate depends on the applied electric field along the drift length of the detector as discussed in Section 2.2, and it introduces an additional source of uncertainty in the measurement of the energy resolution. The best published result in LXe, combining scintillation light and ionization electrons, is 1 % (σ/E) for 1.33 MeV γ-rays, measured by Stephenson et al. [125] at an electric field of 0.2 kV/cm. With our LXe TPC, an energy resolution of 5 % (σ/E) has been obtained for 511 keV ^{22}Na γ-rays at an electric field of 1 keV/cm [82, 115].

The second contribution to the energy resolution σ_{el} comes from the electronic noise introduced by the readout electronics (see Chapter 4) and its value does not depend on the energy. The electronic noise must be minimized to increase the SNR and to allow the detection of low deposited energies. A electronic noise of the order of 100 e^- has already been reported with our experimental set-up [115]. Such low electronic noise is necessary to recuperate all the deposited energy after an interaction that may be shared by multiple neighboring pixels. An electronic noise of less than 100 e^- is negligible with respect to the contribution due to the intrinsic energy resolution, which results in a measured energy resolution of 5 % at 511 keV [82]. Finally, the last term σ_{others} accounts for other contributions to the energy resolution such as the inefficiency of the Frisch grid or pulse rise time variations (see Chapter 5).

Position resolution

The axis of the Compton cone is determined from the intersection point between the first and second interactions of the incoming γ-ray inside the detector. The position of the source $\vec{r}$ is related to both interaction positions via the following geometric expression:

$$\cos\theta \;=\; \frac{(\vec{r}_2 \;-\; \vec{r}_1).(\vec{r}_1 \;-\; \vec{r})}{||\vec{r}_2 \;-\; \vec{r}_1||.||\vec{r}_1 \;-\; \vec{r}||} \tag{1.25}$$

The spatial resolution is thus proportional to separation distance between the two interactions. The impact of the position to the opening angle can be approximated by:

$$\sigma_p^2 \;=\; \sigma_{(x_1,y_1)}^2 \;+\; \sigma_{(x_2,y_2)}^2 \tag{1.26}$$

where $\sigma_{(x_1,y_1)}$ and $\sigma_{(x_2,y_2)}$ represent the spatial resolution of the first and second interaction points respectively. The uncertainty on the position of each interaction depends on the geometry of the collecting electrode. In the case of a pixelated anode, the lateral spatial resolution depends on the pixel size as well as on the size of the electron cloud. If the charge cloud is completely detected by a single pixel, the position of the interaction is referred to the center of the pixel. On the other hand, if the charge cloud is spread over several pixels due

to the charge sharing effect, the interaction point is calculated as the centroid position of the charge distribution. Either way the pixel size introduces an error on the determination of the interaction point which depends on the pixel size. Considering a uniform spatial resolution with the energy and the drift distance of about $\sigma_s \simeq 500$ μm ($\sigma_x \approx \sigma_y \approx \sigma_z$), the impact of the position resolution can be approximated as:

$$\sigma_p \;=\; \sqrt{2}\,\frac{\sigma_s}{d(E_{\gamma'})} \tag{1.27}$$

where $d(E_{\gamma'})$ is the 3D separation between the two interaction vertex that depends on the deposited energy in the first interaction point, which in turn depends on the scatter angle θ. The distance d increases with the energy of the scattered photon. To estimate the contribution of the position resolution, the value of d for an incident γ-ray of 1.157 MeV should take into account the minimum possible distance due to both the pixel size and the electronic shaping time to avoid pile-up. 1.157 MeV corresponds to the energy of the third γ-ray emitted from a source of ^{44}Sc (see next section). The anode is divided in 64 pixels of 3.125×3.125 mm^2 each. Therefore, two interaction will be separated only if the distance between them is at least 3.125 mm along the two dimensions X-Y. Moreover, to consider the separation along the drift length, the collected signals from each interaction point should be separated a minimum time that comprises the rise and fall times of the integrated pulses, which is of the order of 7 to 8 μs. A minimum distance of 1 cm was then considered.

This separation between two consecutive interaction also depends on the deposited energy in the first interaction. The higher the deposited energy, the smaller the remaining energy of the scattered γ-ray, a thus smaller the distance between interaction. This average distance is determined by the mean free path of the scattered γ-ray.

Doppler broadening

Doppler broadening constitutes an irreducible limitation to the angular resolution in a Compton telescope. The effect of Doppler broadening is higher for target materials of larger atomic number, such as Ge or Xe, compared to Si or liquid scintillators [126]. In the case of LXe and for γ-rays with incident energies of 1.157 MeV, its contribution is very small and can be directly neglected [58]. For a more detailed description of the Doppler broadening effect see Chapter 2, Section 2.3.2.

Angular resolution

Taking into account the contributions of the energy and spatial resolutions, we can estimate the angular resolution of a LXe Compton camera. Figure 1.25 shows the angular resolution as a function of the scatter angle determined from Equation 1.19, where the term due to Doppler broadening is zero. The energy (red line) and position (green line) resolutions as a function of the scatter angle were obtained using Equations 1.21 and 1.27 respectively, for an incoming energy of 1.157 MeV. As we can see, the angular resolution is dominated by the contribution of the energy resolution. For scatter angles up to $\sim 60°$, the angular resolution is less than 3°and improves for more forward scatterings. The energy resolution

has a minimum value at around $\sim 7°$. For smaller values of the scatter angle, the energy resolution worsens and diverges at very small values of θ. Equally, for scatter angles bigger that 60°, the energy resolution increases. This can be better understood from Figure 1.26 that shows the energy of the recoil electron as a function of the scatter angle obtained from Equation 1.3.

The energy transferred to the electron varies from zero, when the electron is scattered at right angles, to a maximum value obtained for a scattering angle of 180°(see Figure 1.26). In a backscattering collision, the electron moves forward in the direction of the incident photon. At high electron energies the term $(E_\gamma - E_e)^2$ from Equation 1.22 dominates and thus, the angular resolution degrades at higher scatter angles. This can be also deduced from the slope of the curve on Figure 1.26. A small error in the calculation of the electron energy, implies a significant error in the scatter angle determination. Similar results are observed at small Compton scattering angles. For small electron energies, i.e. small scatter angles, the term $1/\theta$ of Equation 1.22 dominates, which tends to infinity as the angle decreases.

The dependence of the angular resolution on the interaction point separation is shown in the green line of Figure 1.25. As we can see the position resolution is almost constant with the scatter angle. This implies that, for the typical separation between interaction of the order of few cm used to estimate the contribution of the spatial resolution, a position resolution of millimeters is required for good imaging performance.

From Figure 1.25 we can deduce that not all scatter angles are thus valid to perform the Compton cone reconstruction. Fair values of the angular resolution are, therefore, for scattering angles between $\sim 10°$ to 60°, which translate into a deposited energy between 40 keV - 610 keV (see Figure 1.26). This implies that an additional cut on the clusters energy should be included in the analysis.

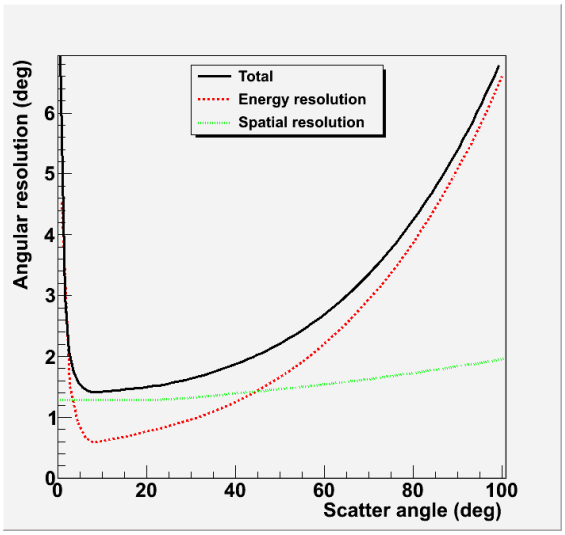

Figure 1.25 – Expected angular resolution of XEMIS as a function of the scatter angle for an electric field of 2 kV/cm (black line). The electronic noise was fixed to 150 e^-/cluster and the intrinsic energy resolution σ_{LXe} was parametrized using the results of [115].

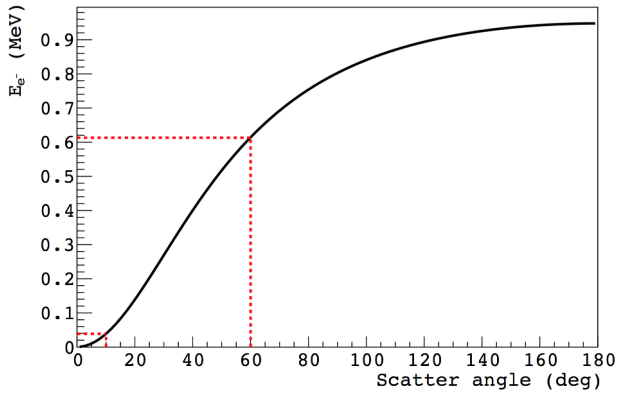

Figure 1.26 – Energy of the recoil electron as a function of the scatter angle obtained from Equation 1.3. The red dashed lines represent the energy interval associated with an acceptable angular resolution.

3γ emitter radionuclides. The ^{44}Sc

The 3γ imaging technique requires a specific radioisotope that emits a positron and γ-ray in quasi-coincidence. Among the possible candidates the radionuclide must present a series of specific characteristics. After the emission of the positron, the daughter nuclide should remain in an excite state to follow a transition to its ground state with the consequent emission of a γ-ray. The decay time to the ground state should be fast enough to consider that both emissions, positron and γ-ray, are almost simultaneous. This feature is important to exploit the temporal coincidence of the three γ-rays. The branching ratios of the positron and gamma emissions should be close to 100% to increase the detection efficiency. Moreover, it is preferable that the de-excitation of the daughter nuclide is followed by the emission of an unique γ-ray, to reduce the dose administered to the patient, the noise background and the counting rate of the detector. The energy of the emitted photon should also be higher than the energy of the two 511 keV γ-rays produced after the annihilation of the positron, to favor the Compton scattering and avoid mispositioning the emission source. The limitation due to attenuation within the patient before reaching the detector is also reduced as the energy of the emitted photon increases. Finally, although the information of the third γ-ray, which comes directly from the source, helps to reduce the spatial uncertainty produced by the positron range, the energy of the emitted positron is also relevant for 3γ imaging. Higher positron energies implies higher average positron ranges.

There are a large number of radioisotopes like ^{94m}Tc, ^{67}Br, ^{124}I, ^{86}Y, ^{152}Tb, ^{52}Mn, ^{82}Rb, ^{22}Na and ^{44g}Sc that are possible candidates for the 3γ imaging technique. Table 1.7 list the properties of some of these radionuclides. Beyond them, the ^{44g}Sc seems to be a particularly attractive choice. The ^{44g}Sc has a half life of ∼4 hours, which is good for clinical practice. In contrast, the ^{14}O and ^{82}Rb have too short half lives, whereas the ^{22}Na has a extremely long half life of 3 years. The ^{94m}Tc has also a relative adequate half life of ∼ 1 hour. However, the probability of positron decay is only 67.6 % with the emission of one or more γ-rays with energies between 871.05 keV to 2740.1 keV. The ^{44}Sc, on the other hand, decays 94.27 % of the time in a positron (5.73 % by electron capture), with a γ-ray emission probability of 99.9 % [127]. Figure 1.27 shows the decay scheme of ^{44g}Sc.

	^{14}O	^{22}Na	^{44g}Sc	^{82}Rb	^{94m}Tc
Half life:	70.6 s	2.6 years	3.97 hours	1.273 min	52 min
β^+ BR[a] (%):	99.249	90.326	94.27	13.13	67.6
				81.76	
E_{max} β^+ (keV):	1808.24	545.7	1474.3	2601	2439
				3378	
E_γ (keV):	2312.6	1274.5	1157	776.52	871.5
					993.19
					1522.1
					1868.7
					2740.1
					3129.1
γ BR (%):	99.38	99.94	99.9	15.08	94.2
					2.21
					4.5
					5.7
					3.5
					2.21

Table 1.7 – Physical properties of some 3γ-emitting radionuclides [127].

[a]Branching Ratio.

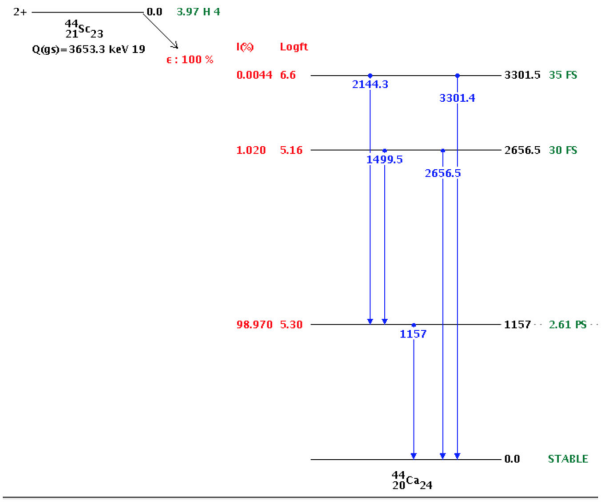

Figure 1.27 – Decay scheme of ^{44g}Sc. Figure from [127].

The ^{44g}Sc decays to excited ^{44}Ca by β^+-decay emission. The positron is emitted with a maximum energy of 1.474 MeV. Then, the excited ^{44}Ca decays in about 2.61 ps to the ground state by emitting an unique γ-ray of 1.157 MeV. This path is followed 99.9% of the

time. Due to the fast emission of the third photon, we can assume that they are emitted simultaneously.

The ^{44g}Sc can be directly produced from a $^{44}Ti/^{44}$Sc generator ($T_{1/2} = 60.4\ years$) [128]. However, nowadays the production of ^{44}Ti is limited for clinical use. An alternative via of production is based on the irradiation of natural calcium or enriched calcium-44 targets [129, 130]. Currently, ^{44g}Sc is produced at the ARRONAX cyclotron (Nantes, France) via the irradiation of a $^{44}CaCO_3$ target with 16 MeV deuterons, through the production of the ^{44}Sc/^{44g}Sc in-vivo generator [131]. This projectile and energy allow to avoid the production of ^{43}Sc, a radioisotope with the same half-live as the ^{44g}Sc.

The disadvantage of this method is, however, the co-production of longer-lived radioactive impurities such as ^{44m}Sc ($T_{1/2} = 58.6\ hours$). The ^{44m}Sc mainly decays by internal transition to its ground state (98.80%). Due to its long half life, the use of a $^{44m}Sc/^{44}Sc$ generator can be an interesting option for the tracking of long-lived radioisotopes for targeted therapy with monoclonal antibodies (mAbs). However, for the 3γ imaging technique, only the ^{44g}Sc is interesting. Therefore, it requires a production route that limits the production of both ^{44m}Sc and ^{43}Sc. Indeed, these isotopes will result in an undesirable source of background in the detector, and an unnecessary increase of radiation exposure to the patient. The concentration of impurities depends on the energy of the particle beam. Duchemin et al. [130] showed that the production of ^{43}Sc and ^{44m}Sc can be reduced by irradiating a ^{44}Ca target with protons of 15 MeV. The use of ^{44g}Sc labeled to DOTAT-conjugated peptides has already been tested in pre-clinical [132] and clinical trials [133] showing promising results. The ^{44}Sc is a particularly promising element for nuclear medicine since several radioisotopes are suited for both therapy and/or diagnosis. The physical properties of the scandium isotopes suitable for nuclear medicine are listed in Table 1.8.

	^{43}**Sc**	^{44g}**Sc**	^{44m}**Sc**	^{47}**Sc**
Half life:	3.89 hours	3.97 hours	2.44 days	3.35 days
Emitter:	β^+ (88 %)	β^+ (94.27%)	γ (98.8 %)	β^- (100 %)
E_{max} β (keV):	1200	1474	-	440.9 (68.4 %)
				600.3 (31.6 %)
E_γ (keV):	372.8 (23 %)	1157 (99.9 %)	270	159 (68 %)
Production:	$^{43}Ca(p,n)$	$^{44}Ca(p,n)$	$^{44}Ca(p,n)$	$^{48}Ti(p,2p)$
	$^{42}Ca(d,n)$	$^{44}Ca(d,2n)$	$^{44}Ca(d,2n)$	
	$^{nat}Ca(\alpha,X)$	$^{44}Ti/^{44}Sc$ gen.		
	$^{nat}Ca(\alpha,Xn)^{43}Ti$			
Clinical use:	diagnosis	diagnosis	diagnosis	therapy

Table 1.8 – Main properties of the scandium isotopes of interest for nuclear medicine [131, 134].

1.4 Conclusions Chapter 1

In this chapter, the main characteristics as a detection medium of liquefied noble gases and in particular liquid xenon have been discussed. One of the most basic advantages of liquid xenon is its high density and atomic number, which results in a high stopping power for ionizing radiation. Moreover, the simultaneous emission of both a scintillation and an ionization signals after the interaction of an ionizing particle, is a particular interesting property of this kind of media. Among liquid noble gases, liquid xenon has the smallest W-values and thus, the highest ionization and scintillation yields. In addition to the large light yield, the fast response of liquid xenon to radiation, which is of the order of a few ns, makes it suitable for timing applications.

Liquid xenon has proven to be a perfect candidate as a γ-ray detector in the energy range from several tens of keV to tens of MeV due to its ideal properties. For this reason, its use as radiation detection medium has increased in the recent years in numerous applications in particle physics, astrophysics and medical imaging. A short overview of some of the currently liquid xenon-based detectors used in the detection of rare events, such as neutrinoless double beta decay or the direct detection of dark matter, γ-ray astronomy and functional medical imaging is also presented in this chapter.

In fact, liquid xenon is considered as a promising detection medium for medical applications since the 1970s. Early approaches were focused on the use of liquid xenon as a detector medium in SPECT and PET. These two medicine imaging modalities, based on standard scintillation crystals, are well established in the clinical practice. A brief description of these two functional imaging techniques is presented in Section 1.3.1.

The potential of LXe has led to the development of a new concept of nuclear medical imaging based on the precise 3D location of a radioactive source by the simultaneous detection of 3γ-rays. To take advantage of this imaging technique called 3γ imaging, a detection device based on a single-phase liquid xenon Compton telescope and a specific (β^+,γ) emitter radionuclide, ^{44}Sc, are required.

The XEMIS project (XEnon Medical Imaging System) developed at Subatech laboratory, has started a research program that revolves around the feasibility of the 3γ imaging concept for its future in pre-clinical and clinical applications, and the development of new technologies around liquid xenon detection and cryogenic systems. The biggest advantages of this technique are the improvements in detection sensitivity, position resolutions and reduction of the injected activity to the patient. The basic principle and the main requirements of the 3γ imaging technique are discussed in Section 1.3.6.

A first prototype of a liquid xenon time projection chamber called XEMIS1 has been successfully developed. A second phase for small animal imaging has already begun with the construction and calibration of a larger-scale liquid xenon Compton camera called XEMIS2. The characteristics of both XEMIS1 and XEMIS2 are presented in Chapter 3. In the next chapter, we introduce the basic principle of a liquid xenon time projection chamber and the main transport properties of charge carriers in liquid xenon.

Chapter 2

Development of a liquid xenon Time Projection Chamber for medical applications

Contents

Due to the signal generation properties of LXe, which can produce simultaneously both ionization and scintillation signals after the passage of an ionizing particle through the medium, LXe detectors can be divided into three different categories according to which kind of signal they detect: the ionization signal, the scintillation signal, or both [2]. Ionization detectors have been commonly used since the first half of the 20th century to detect and measure only the ionization signal [135]. However, the difficulties associated with the scintillation light detection mainly due to the emission wavelength (178 ns) and the very low working temperature of xenon-based detectors, made the measurement of the light signal much complicated. During the last half of the 20th century, the development of new photodetectors with UV sensitivity and capable of withstanding the temperature of LXe, launched the development of a new generation of LXe detectors. LXe Time Projection

Chambers (TPC) belong to the category where both ionization and scintillation signals are simultaneously detected. A TPC is a sophisticated ionization detector that provides accurate information of individual events. They are extensively used in modern nuclear and particle physics experiments due to their ability to provide spatial information of the position of the particle track with high resolution, energy deposit information, as well as particle identification.

This chapter summarizes the fundamentals of the LXe TPC detection technology. This includes a discussion of the different mechanisms that affect the ionization signal production. The diffusion of the electron cloud during the drifting process and the electron-ion recombination are two factors that have a direct impact in the performances of a detector of the characteristics of XEMIS. Moreover, the range of the primary electrons, the X-ray emission and the Doppler broadening effect are other processes that affect the measurement of the ionization signal in a LXe TPC. The theoretical explanation of some of these processes is supported by experimental results reported by other authors including some of our work. The last part of this introductory chapter is devoted to technical considerations, such as the presence of impurities inside the LXe, that can degrade the measurement of the ionization signal.

2.1 Liquid xenon Time Projection Chamber

The 3γ imaging technique requires a detector that provides high sensitivity to emitted radiation, precise interaction localization and high energy resolution in order to obtain an image of the source with an acceptable SNR. As discussed in Section 1, a LXe Compton telescope is a perfect candidate to exploit the benefits of both the LXe and the 3γ imaging technique. However, Compton sequence reconstruction requires precise information of the 3D position and deposited energy of each individual interaction in the detector. To provide these informations the XEMIS detector is based on a Time Projection Chamber (TPC).

The concept of TPC was first introduced by D. Nygren at Berkeley in 1974 for the study of electron-positron collisions at the PEP colliding-beam ring at the SLAC National Accelerator Laboratory [136]. The original design of the Nygren's TPC is presented in Figure 2.1. The detector was based on a cylindrical chamber of 2 m long and 2 m in diameter filled with methane gas. In 1977, the concept of the TPC technology using a liquid instead of a gas was first proposed by C. Rubbia for the ICARUS project [137]. The detector was a large-volume TPC of 600 ton filled with LAr dedicated to the study of the properties of neutrino interactions. But it was not until 1989 when E. Aprile proposed for the first time the use of LXe as detection medium in a TPC for γ-ray spectroscopy and Compton imaging (see Section 1.2) [45].

In this section we introduce the basic principle of a LXe TPC. A more detailed description of the characteristics of the TPC used in XEMIS is presented in Chapter 3.

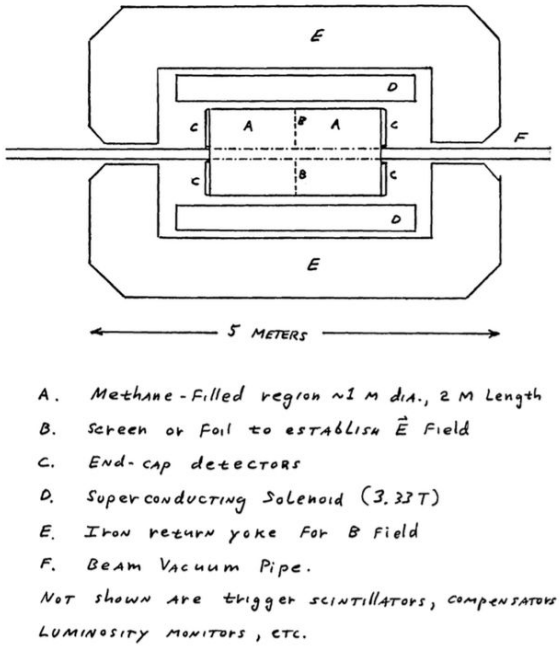

Figure 2.1 – Detector schematics of the TPC proposed for the first time by D. Nygren in 1974. Figure taken from [136].

2.1.1 Basic principle of a TPC

A TPC is a homogenous large-volume tracking detector that provides three-dimensional event reconstruction and energy information. Figure 2.2 illustrates the principle of a LXe TPC. The basic design of a TPC consist of two parallel plane electrodes (anode and cathode) separated by a certain distance d and filled filled with a gas or a liquid.

When an ionizing particle such as a γ-ray crosses the sensitive volume of the TPC, it ionizes the medium producing a track of electron-ion pairs. A uniform electric field of the order of several kV/cm applied between the two opposed electrodes prevents the recombination between electrons and ions. The electric field forces the electrons to drift towards the anode where they are collected by a pixelated array. The segmented anode provides two-dimensional information of the interaction inside the fiducial volume (X-Y coordinates). The third coordinate Z defined along the TPC axis, represents the distance from the point of interaction to the collecting electrode and is given by the drift time of the ionization electrons, as presented in Equation 2.1:

$$Z = \int_{t_0}^{t} \vec{v}_{drift}(t', \vec{E})\, dt' \tag{2.1}$$

where $\vec{v}_{drift}$ is the electron drift velocity, which depends on the applied electric field $\vec{E}$, t_0 is the time when the interaction occurs or trigger time, and t is the electron collection time. For a uniform electric field Equation 2.1 can be simplified by: $Z = v_{drift}(t - t_0)$.

An advantage of using LXe as detection medium is the simultaneous production of a scintillation signal that provides to the detector self-triggering capabilities. Due to the fast

scintillation light emission in LXe of the order of a few ns, t_0 can be obtained from the scintillation signal detection by for example a VUV sensitive PMT.

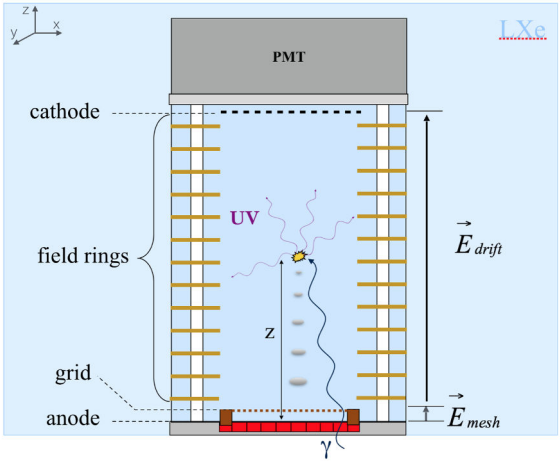

Figure 2.2 – Schematics drawing of the principle of a TPC.

Signal amplification is commonly used in TPCs due to the reduced amount of charge carriers produced per interaction. The charge amplification was traditionally accomplished by multi-wire proportional chambers (MWPCs). However, in the last decades the development of micropatterns detectors such as Gas Electron Multiplier (GEM) [138] and MICROMEsh GAseous Structure (MICROMEGAS) [139], have become a successful alternative in TPCs. These kind of detectors include a micro-mesh located at several hundreds of μm from the collecting electrode. The small gap between the mesh and the collecting electrode, also called amplification zone, is intended to amplify the ionization signal by applying a large electric field.

In LXe no charge multiplication in necessary, so the collected charge corresponds directly to the amount of charge produced by ionization, which in turn is proportional to the energy lost by the interacting particle in the medium. Therefore, the information of the deposited energy can be directly extracted from the amplitude of the ionization signal. Instead of using one of these amplification systems, we use a Frisch grid to collect the generated charges. The grid is placed between the cathode and anode to shield the anode from the motion of positive ions inside the sensitive volume (see Figure 2.2). Electrons start inducing a signal on the anode after passing through the grid, so the signals are independent of the position of the interaction with respect to the anode. To measure the amplitude and drift time of the collected signals, even in high-multiplicity events, fast read-out electronics are required.

2.1.2 Waveform formation

The information of the 3D position and deposited energy of each individual interaction is directly obtained from the waveforms generated by the read-out electronics. A brief summary of the signal formation process from the interaction of radiation with the detector to the charge collection by the electronics is presented in this section.

As discussed in Chapter 1, after the passage of an ionizing particle through the detector, the deposited energy E_0 is converted into a number of electron-ion pairs due to ionization.

The number of produced charge carries is given by the expression: $N_0 = E_0/W$ where W is the average energy needed to create an electron-ion pair. The small W-value in LXe implies high ionization yield and thus, the deposited charge can be directly measured from the amplitude of the signals.

Several effects such as electron-ion recombination and the purity of the medium play also an important role in the electron collection. Due to electron-ion recombination, a fraction of the produced electrons recombine before arriving to the anode. The recombination rate depends on the ionization density and on the applied electric field (see Section 2.2.1). On the other hand, electron attachment to electronegative impurities dissolved in the LXe may also reduce the number of ionization electrons that reach the anode. Similarly, the scintillation light may be absorbed by impurities dissolved in the LXe (Section 2.2.3). Both effects should be therefore minimized in order to increase the energy resolution of the detector by an adequate purification system and a relative high electric field.

The remaining charges drift towards the anode under the influence of the electric field. A pixelated anode gives directly the information of the X and Y position of each interaction point. The granularity of the anode limits the spatial resolution of the detector. The number of fired pixels per interaction affects the transverse spatial resolution of the detector and depends on several factors, such as the electron diffusion and the size of the electron cloud. A criteria concerning the location of the fired pixels and the arrival time of electrons to the anode should be established to identify those pixels that may be triggered by the same interaction. The regrouping of pixels from the same interaction vertex is called *clustering*.

Charges start inducing a current in the anode from the moment they start drifting. A Frisch grid placed between the cathode and the anode shields the anode from the movement of ions and partially removes the position dependence of the induced signal with respect to the collecting electrode. Ideally, electrons induce a signal in the anode from the moment the pass through the grid. The induced current is then processed by a charge sensitive preamplifier and filtered by a second order low-pass filter. A more detailed description of the read-out electronics is presented in Chapter 4. After processing, the amplitude of the output signal is proportional to the number of collected electrons, which in turn it is proportional to the deposited energy in the detector. The drift time and thus the Z coordinate along the drift length, are also deduced from the waveform of the output signal.

Besides the intrinsic energy resolution of LXe, the electronic noise and the energy threshold used in the data analysis will also play an important role in the final energy resolution of the detector. Both contributions should be as low as possible, although in the case of the threshold level the volume of data due to noise events should be reduced before being registered.

2.2 Ionization Signal Production in Liquid Xenon

When charged particles travel through the LXe, they produce a track of electron-ion pairs by ionization. On a TPC a uniform electric field is applied to force electrons and ions to drift in opposite directions towards the TPC electrodes. This electric field contributes to reduce the recombination between the electrons and the ions during migration. The

recombination fraction depends on both the number of electron-ion pairs created and the applied electric field. The recombination effect and the influence of the electric field on the charge and scintillation light productions are described in this section. Inside LXe, as well as the recombination effect, other factors such as electron diffusion may also influence the final charge collection. Doppler broadening effect, X-ray emission and the spread of the electron cloud are discussed in the next section. Some of these properties have been experimentally studied during this work. A more detailed description can be found in the following Chapters.

2.2.1 Electron-ion recombination

The number of electron-ions pairs generated by radiation in LXe or ionization yield, depends on many different factors such as the energy of the incident particle (see Section 1.1.3), the applied electric field which is related to electron-ion recombination, and the purity of the medium. Charge loss due to either ionization carriers recombination or electron capture by electronegative impurities must be minimized in order to increase the energy resolution of the detector.

Besides the dependence of electron-ion recombination on the applied electric field, the fraction of recombined electrons also depends on the local ionization density, being greater at low fields and in dense ionization tracks. Understanding the mechanism of electron-ion recombination is of primary importance in order to predict the response of liquefied noble gas detectors. To date there are three main models that pretend to explain the phenomenon of recombination in liquid noble gases: the germinate recombination model proposed by Onsanger, which is based on the Coulomb interaction between the charge carriers [140], the columnar model of Jaffé [141] and the Thomas and Imel box model [142, 143]. Beyond them, the Thomas and Imel approach uses more realistic assumptions regarding liquid noble gases, and it is typically used to describe the energy resolution limitation observed in LXe beyond the Fano-limit [2] (see next section). In fact, this model was originally developed in 1987 to explain the mechanism of recombination in liquid xenon and liquid argon.

The fraction of collected electrons, i.e. those escaping recombination, predicted by the Thomas-Imel box model is given by Equation 2.2:

$$\frac{Q(E)}{Q_0} \;=\; \frac{1}{\xi}\,\ln\left(1 \;+\; \xi\right) \tag{2.2}$$

in which the free parameter ξ is defined as:

$$\xi \;=\; \frac{N_0\alpha}{4a^2\mu_- E} \tag{2.3}$$

where N_0 is the initial number of electron-ion pairs, μ_- is the electron mobility, α is the recombination coefficient and E is the applied electric field. In this model, electron diffusion is ignored and the positive ions are treated as stationary due to their slow motion compared to electrons. In addition, Thomas and Imel assumed that the initial number of produced electron-ion pairs N_0 is distributed in a three-dimensional box of size a, in contrast to the

Jaffé columnar model in which electrons are assumed to be uniformly distributed in a column of charge [142]. Equation 2.3 states that the probability of electron recombination decreases with increasing the applied electric field. At an infinite electric field the parameter $\xi \to 0$, which means that all electrons are collected, whereas at zero applied electric field $\xi \to \infty$.

The ionization density dependence of the recombination rate implies a non-linear ionization yield. Along a particle track, the ionization density is determined by the electronic stopping power of the primary electrons, which refers to the amount of energy loss per distance traveled [22]. Figure 1.2 shows the stopping power as a function of energy for electrons in LXe. Since the stopping power depends on the particle's energy, the ionization density distribution varies as the recoiling electron losses its energy. The specific energy loss of the primary electron along its track increases as its velocity decreases. The "single density model of charge collection" proposed by Thomas and Imel, presented in Equation 2.2, does not take into account these ionization density fluctuations along the trajectory of the recoiling electrons, in addition to the random emission of δ-rays along the track of the ionizing particle. These δ-rays are secondary electrons with enough energy to ionize the medium and produce more lower energy δ electrons. δ-rays loss most of their energy at the end of their trajectory creating a minimum ionizing region followed by a high local charge density region or *blob* at the end of the trajectory. These non-uniformities along the electron traces caused by the presence of δ-rays affect the recombination rate, and thus limits the intrinsic energy resolution of LXe.

A better description of the experimental data that takes into account ionization density fluctuations and δ-ray production was later proposed by Thomas et al. [143] by adding a second term to Equation 2.2, which depends on an additional recombination parameter:

$$\frac{Q(E)}{Q_0} = \frac{E_c}{E_p} = \left(a \frac{\ln(1 + \xi_0)}{\xi_0} + (1 - a) \frac{\ln(1 + \xi_1)}{\xi_1} \right) \tag{2.4}$$

$$a \equiv \left(\frac{\ln\left(\frac{E_2}{E_1}\right) - \frac{E_2}{E_p} + 1}{\ln\left(\frac{E_p}{E_0}\right)} \right) \tag{2.5}$$

As described in detail in T. Oger [115], the Thomas and Imel model accounts for two different rates of recombination. The minimum ionizing region is described by the parameter ξ_1, whereas the high charge density blob at the endpoint of the δ electron tracks is described by ξ_0. In Equation 2.4, E_p is the energy of the primary particle, E_c is the actual charge collected by the anode and E_0 is the minimum kinetic energy of a δ electron before thermalization. The parameter a given by Equation 2.5, represents the fraction of the total charge that is distributed along a δ-ray track, which depends on the initial energy of the secondary electron. Three δ electron energy intervals are considered in the Thomas and Imel model, which are defined by the parameters E_0, E_1 and E_2.

Influence of electron-ion recombination on the energy resolution

The energy resolution of a detector depends on the number of collected electrons. As discussed in Chapter 1, the statistical fluctuations in the number of generated electron-ion pairs do not follow a Poisson distribution, but they can be described as a function of the Fano factor. The energy resolution can, therefore, be expressed as a function of the Fano factor, F, according to the following expression [22]:

$$\frac{\sigma_E}{E_p} = \sqrt{\frac{F.W}{E_p}} \tag{2.6}$$

where W = 15.6 eV is the average energy required to produce an electron-ion pair [15], and E_p is the energy of the ionizing particle. The Fano factor in the case of LXe is predicted to be 0.041 [1], Without δ-electron production, the theoretical energy resolution based on the Fano factor is of the order of 2 keV (FWHM) at 1 MeV [144]. However, charge loss due to electron-ion recombination limits the intrinsic energy resolution of LXe. Based on the Thomas and Imel model, a more realistic description of the energy resolution is given by the expression:

$$\sigma_E(\%) = \frac{b}{\sqrt{E_p}}\left(\frac{\ln(1+\xi_1)}{\xi_1} - \frac{\ln(1+\xi_0)}{\xi_0}\right)\frac{E_p}{E_c} \tag{2.7}$$

where

$$b \equiv \frac{\sqrt{E_p\, F(E_p)\left(2E_2 - E_1\,\frac{E_2^2}{E_p}\right)}}{F(E_p)\ln(\frac{E_p}{E_0})} \tag{2.8}$$

In Equation 2.8, the factor $F(E_p)$ is a function of the energy of the ionizing particle, that for the particular case of LXe can be approximated by the formula [143]:

$$F(E_p) = -5.12.10^{-6}\,E_p^2 + 7.84.10^{-2}\,E_p + 4.28 \quad (E_p/eV) \tag{2.9}$$

Other factors such as the attachment of free electrons to electronegative impurities and the electronic noise also contribute to the energy resolution of the detector. These two contributions are taken under consideration in Section 2.2.3 and 4.2 respectively.

The free parameters of the Thomas and Imel model have been determined experimentally and reported by different authors. The authors themselves tested their model with 976 keV conversion electrons from a ^{207}Bi source showing good agreement with the experimental data [143]. The values of $\xi_0 E$, $\xi_1 E$, a and b were obtained by a simultaneous fit of the collected charge (Equation 2.2) and the energy resolution (Equation 2.7). Figures 2.3 and 2.4 show the relative ionization yield and the energy resolution of LXe versus the electric field strength for 570 keV γ-rays from a ^{207}Bi source and 662 keV γ-rays from a ^{137}Cs source

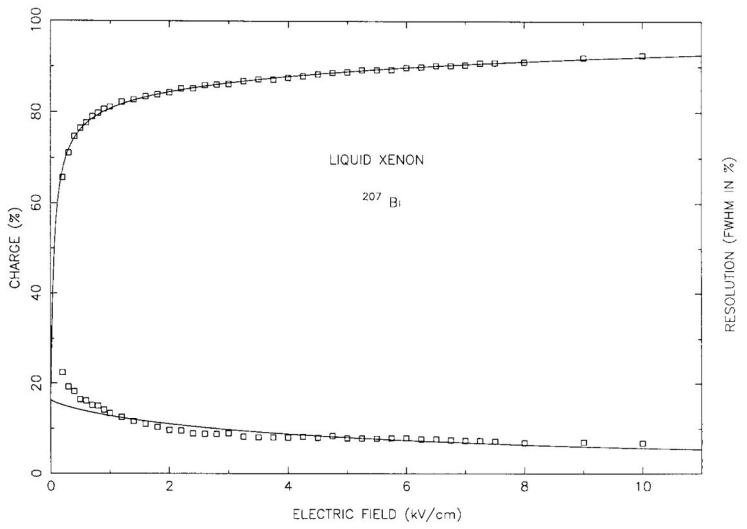

Figure 2.3 – Simultaneous fit of the Thomas and Imel recombination model to the charge yield and energy resolution for 570 keV γ-rays as a function of the electric field in LXe. Figure is taken from [145].

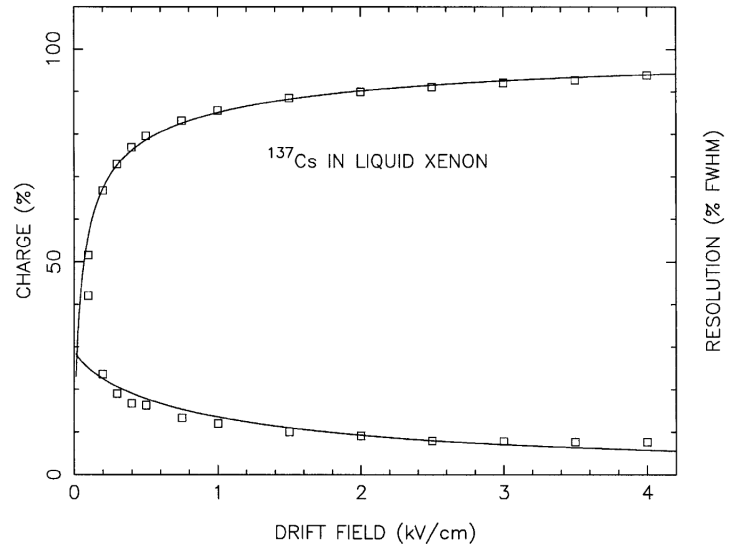

Figure 2.4 – Simultaneous fit of the Thomas and Imel recombination model to the charge yield and energy resolution for 662 keV γ-rays as a function of the electric field in LXe. Figure from [146].

reported by [145] and [146] respectively. Both curves have been fitted by the Thomas and Imel model. In both cases the collected charge is well described by Equation 2.2, whereas the electric field dependence of the energy resolution seems to saturate at high field strengths. The Thomas and Imel model cannot completely explain the electron-ion recombination observed in LXe. The discrepancies between the model and the experimental data may be related to the assumption that the electron drift velocity is directly proportional to the electric field strength. In LXe the electron drift velocity varies very slowly with the applied electric field and tends to saturate at fields higher than 3 kV/cm. Nevertheless, the hypothesis of a non-uniform distribution of the secondary electrons along the track of the

primary electrons seems necessary in order to explain the experimental results. The analysis of our experimental data using the Thomas and Imel model is presented in Chapter 7.

2.2.2 Influence of the electric field on charge and light yields

As discussed previously, the presence of an electric field of the order of several kV/cm reduces the recombination rate between electrons and positive ions, which implies an increase in the collected charge (see Figure 2.3 and 2.4). However, this effect is always accompanied by a reduction of the scintillation signal since the recombination component of the scintillation light is suppressed by the influence of the electric field. Figure 2.5 shows the field dependence of both light and charge yields for 662 keV γ-rays from a ^{137}Cs source in LXe [147]. As we can observe, the scintillation light yield, in contrast to the ionization yield, decreases as the electric field increases. The electric field dependence of the ionization and scintillation yields in LXe and LAr was first observed by S. Kubota and A. Nakamoto [39]. The results presented by the authors showed a reduction of the scintillation light by a 74 % at an electric field of 12.7 kV/cm, followed by a saturation of the collected charge. This provided a strong evidence of the recombination luminescence in LXe.

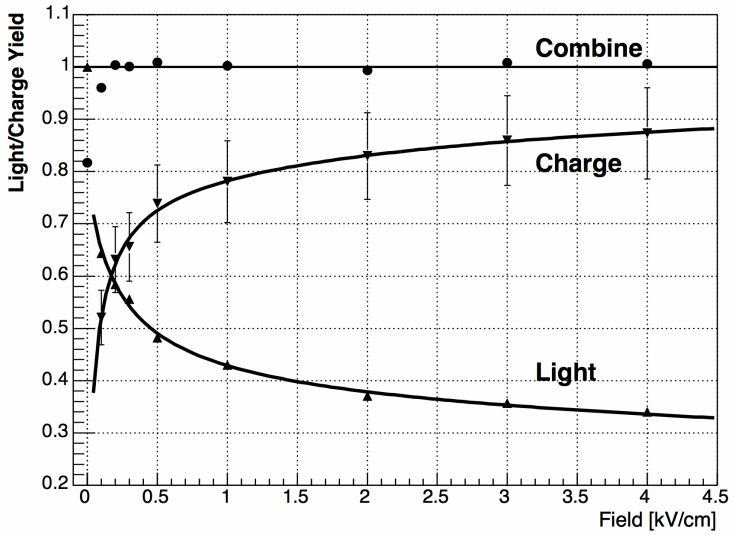

Figure 2.5 – Scintillation and ionization yields as a function of the drift field for 662 keV γ-rays from a ^{137}Cs source. Figure taken from [148].

The simultaneous increase of the collected charge and the decrease of the scintillation signals in liquid noble gases implicate a correlation between the ionization and the scintillation yields. The strong light and charge anti-correlation was first measured for relativistic electrons in LXe by E. Conti et al. [147] (see Figure 2.6). This anti-correlation effect is explained by the fact that high charge density regions imply a higher recombination rate between electrons and ions, which produces a large number of scintillation photons accompanied by a reduction in the number of free electrons. The correlation between charge and light in LXe has been used by many authors to improve the energy resolution of the detector, since the individual fluctuations of the ionization and scintillation signals are compensated when both signals are combined [148]. E. Aprile et al. reported, for example, an energy resolution

of 1.7 % from the combination of the two signals for 662 keV γ-rays from a ^{137}Cs source, whereas energy resolutions from charge and light spectra of 4.8 % and 10.3 % respectively were obtained when the signals were treated separately.

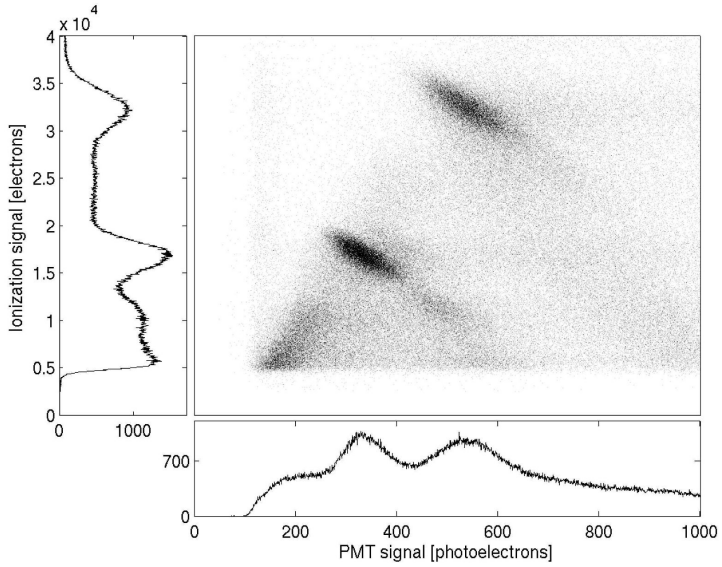

Figure 2.6 – Anti-correlation between scintillation and ionization signals for a ^{207}Bi source at a drift field of 4 kV/cm. Figure taken from [147].

2.2.3 Transport properties of charge carriers in LXe

Electrons and positive ions which escape recombination drift in opposite directions under the influence of the applied electric field. The drift velocity of the charge carriers depends thus on the applied electric field but also on the temperature and density of the medium. Furthermore, electrons diffuse while they drift towards the anode causing a certain spread of the electron cloud. In this section a brief summary of the electron and ion transport properties is presented. Other aspects that may affect the time development of the ionization signal are discussed in the following sections.

Electron drift velocity in LXe

The transport characteristic of charge carriers as a function of the applied electric field in LXe and LAr have received considerable experimental and theoretical attention since the last decades [149, 150, 151, 152, 153, 154, 155]. In a LXe TPC, since the Z coordinate along the drift length is directly determined by the product of the electrons drift time and the electrons drift velocity v_{drift}, an accurate knowledge of v_{drift} is important. The electron drift velocity in a LXe TPC depends on the electric field applied between the cathode and the anode. The variation of the electron drift velocity in LXe and gaseous xenon (GXe) as a function of the density-normalized electric field is presented in Figure 2.7. Similarly, the electron drift velocity dependence with the electric field for solid xenon (SXe) compared to LXe is presented in Figure 2.8. In all three cases, the electron drift velocity has a linear

field dependence at low-field strengths, while at high applied fields, above a few kV/cm, the electron drift velocity is no longer linear with the field and tends to saturate. In the low-field region the electron mobility becomes constant and the electron drift velocity can be approximated by:

$$\vec{v}_{drift} = \mu_{-}\vec{E} \tag{2.10}$$

where μ_{-} is the electron mobility in LXe and $\vec{E}$ is the electric field. For example, at 1 kV/cm, the drift velocity of electrons in LXe is approximately 2 mm/μs. Equation 2.10 is a good approximation since at low electric fields the electrons are assumed to be in equilibrium with the medium. However, as the strength of the electric field increases, the electrons are no longer in thermal equilibrium and the electron mobility becomes dependent of the applied electric field. A theoretical description of the electron drift velocity dependence with the applied electric field has been addressed by several authors [155, 156]. A correct description of experimental data in LXe and LAr has been provided by the Cohen-Lekner theory [151, 152], which takes into account the properties of the medium. However, the behavior of the electron drift velocity at high electric fields is still not fully understood.

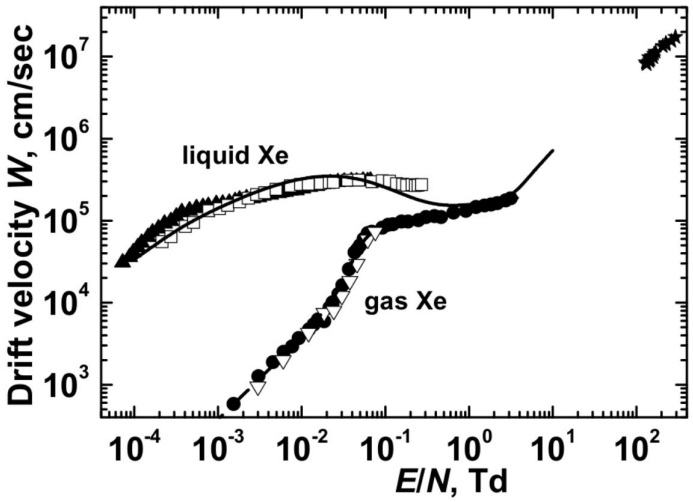

Figure 2.7 – Electron drift velocity in liquid and gaseous xenon as a function of the reduced electric field. Figure is taken from [155]. The x-axis represents the drift field over the number density of atoms, where 1 $Td = 10^{-17}\ Vcm^2$. The solid lines show the calculations by Atrazhev et al. and the points are experimental data from [157, 158, 159, 160].

Figures 2.7 and 2.8 also show that the electron drift velocity in LXe is higher than that in gaseous state in the whole field range presented in Figure 2.7, whereas higher values of v_{drift} are obtained for SXe. This effect can be explained due to the dependence of the electron mobility with density. The drift velocity of a charge carrier depends on the number of collisions per unit length. The probability that an electron undergoes a collision along its path is given by the scattering cross section, which is inversely proportional to the drift velocity. The scattering cross section depends on both the energy of the electron and the number of atoms per unit of volume N, i.e. the density of the medium. For xenon, the

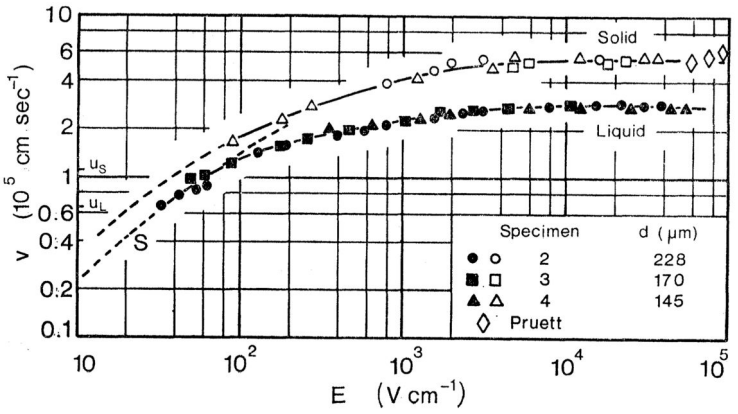

Figure 2.8 – Electron drift velocity in liquid (163 K) and solid (157 K) xenon as a function of the electric field strength. Figure is taken from [150].

scattering cross section for the liquid state is smaller than that for the gas, which implies a higher drift velocity. This makes LXe a more suitable detector medium for an ionization detector [155].

Besides the dependency on the electric field, the mobility of electrons in LXe also depends on the density of the medium, which implies a dependency on the pressure and temperature of the system and thus, on the experimental conditions of the detector. Figure 2.9 shows the electron mobility as a function of the temperature for liquid and solid xenon and argon. At a temperature of 165 K, the mobility of electrons in LXe is around 2200 $cm^2V^{-1}s^{-1}$, whereas at 195 K the mobility rapidly increases to ∼4500 $cm^2V^{-1}s^{-1}$ [150]. As a consequence, the electron drift velocity slightly depends on the temperature of the medium as presented in Figure 2.10. Moreover it was observed that contaminations with certain molecules such as carbon hydroxides can enhance the electron drift velocity [2].

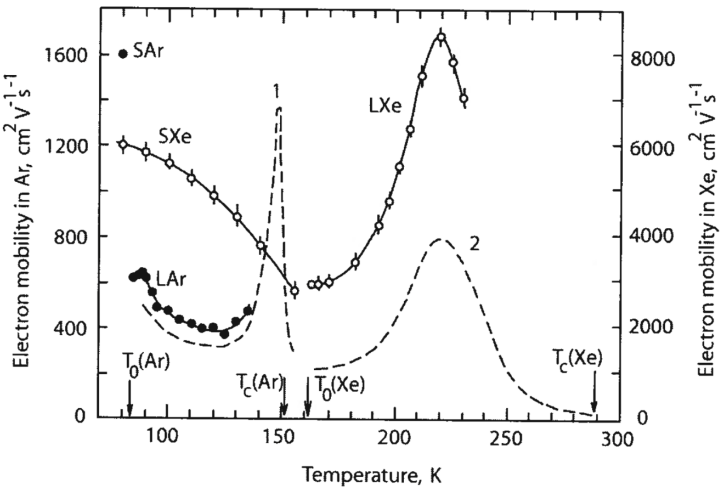

Figure 2.9 – Electron mobility in liquid and solid xenon and liquid argon as a function of the temperature. T_0 and T_c are the triple and critical points respectively. The dashed lines are the theoretical predictions from [161] for the Xe and [162] for the Ar. The point represents the experimental values reported by [158]. Figure is taken from [4]. Original figure is from [158].

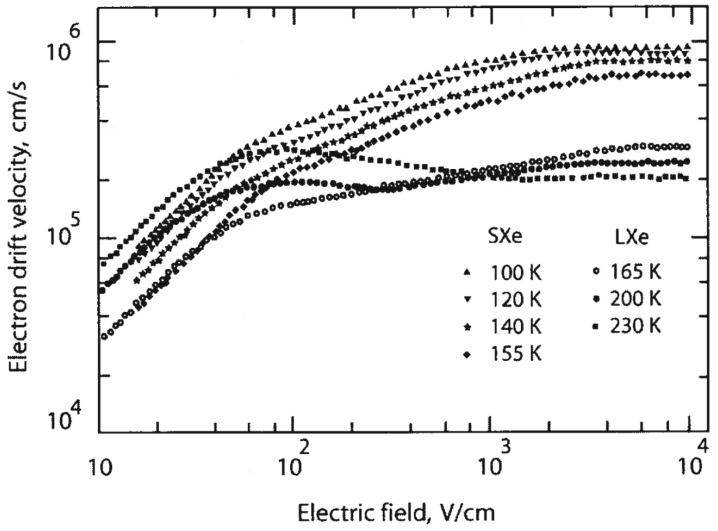

Figure 2.10 – Electron drift velocity in solid and liquid xenon as a function of the temperature. Figure taken from [158].

Holes and positive ions mobility in LXe

For the case of positive carries, which in LXe are positive Xe_2^+ ions and holes, the mobility is significantly lower than for electrons. For positive ions the mobility is of the order of 3.10^{-4} $cm^2V^{-1}s^{-1}$, which is around 10^{-5} times smaller than the electron mobility [163]. Whereas, the hole mobility is about 40.10^{-4} $cm^2V^{-1}s^{-1}$. The dependence of the hole mobility with temperature is depicted in Figure 2.11. As a result of the slow mobility of positive charge carriers in LXe, the induced charge due to the motion of positive charge carriers has a very slow rise time and it can be easily rejected with an appropriate front-end electronics.

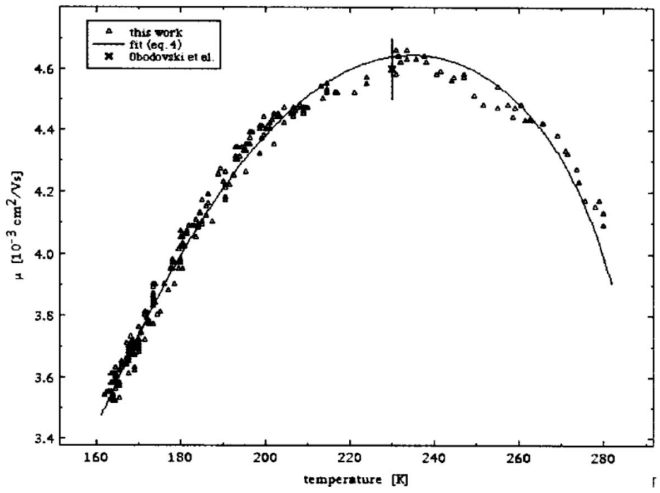

Figure 2.11 – Variation of the positive hole mobility in LXe as a function of temperature. Figure taken from [164].

Electron diffusion in LXe

Positive ions and free electrons produced after the interaction of an ionizing particle with LXe diffuses as they drift through the volume of the detector. This diffusion of the charge cloud is the result of the collision of the charges with the atoms and molecules of the liquid, which leads to a random motion of charge carriers during migration. The diffusion process is more important for electrons than for ions due to slower mobility of ions in the liquid. According to the kinetic theory, the spread of an initial point-like electron cloud can be described by a Gaussian distribution with a standard deviation equivalent to the diffusion of charge carriers along a certain axis $\vec{x}$. Therefore, the diffusion can be described according to:

$$\sigma_{\vec{x}} = \sqrt{2\ D_{\vec{x}}\ t_{drift}} \tag{2.11}$$

where $D_{\vec{x}}$ is diffusion coefficient along the axis $\vec{x}$ expressed in $cm^2 s^{-1}$ and t_{drift} is the electron drift time. The spread of the electron cloud depends on the electrons collection time, which is related to the travelled distance by the electron through the LXe (d_{drift}) and the electron drift velocity (v_{drift}). Therefore, Equation 2.11 can be expressed in terms of the distance according to:

$$\sigma = \sqrt{2\ D\ \frac{d_{drift}}{v_{drift}}} \tag{2.12}$$

Since the electron drift velocity depends on the applied electric field, a small spread of the electron cloud is expected at higher fields strengths. Moreover, the electron diffusion coefficient $D_{\vec{x}}$ also depends on the magnitude and direction of the applied electric field. Diffusion takes place along the three spatial dimensions. In LXe, the transverse diffusion coefficient D_T (perpendicular to the drift direction) is much larger than the longitudinal diffusion coefficient D_L defined along the drift direction [2]. As a consequence, the electron cloud will not maintain its original shape as it drifts through the LXe, but it will result is an ellipsoid with minor axis along the drift direction.

The values of the longitudinal and transverse diffusion coefficients obtained experimentally as a function of the electric field in LXe are presented in Figure 2.12. According to the results, the longitudinal diffusion coefficient is around ten times smaller than the transverse diffusion coefficient, so we can assume that its contribution to the electron cloud spread is negligible [2]. Unfortunately, the results available so far are not conclusive due to the difficulty of the measurement. Doke et al. [3] measured a value of D_T which varies between 44 $cm^2 s^{-1}$ to 80 $cm^2 s^{-1}$ with the electric field, resulting in a transverse diffusion of the order of $210 \mu m \sqrt{cm}$ to $270 \mu m \sqrt{cm}$ [115]. The experimental results as well as the values obtained for LAr as a function of the electric field are depicted in Figure 2.13. In a study carried out by our group [165] with a small dimension LXe TPC (see Chapter 3), a transverse diffusion coefficient of 37 $cm^2 s^{-1}$ was measured for an electric field of 0.5 kV/cm ($E/N = 5.5.10^{-18}\ V cm^2$), which is in good agreement with the value reported by Doke et al. [3] as can be deduced from Figure 2.13. Our results of the variation of the spread of the electronic cloud with the applied electric field are shown in Figure 2.14. For an electric

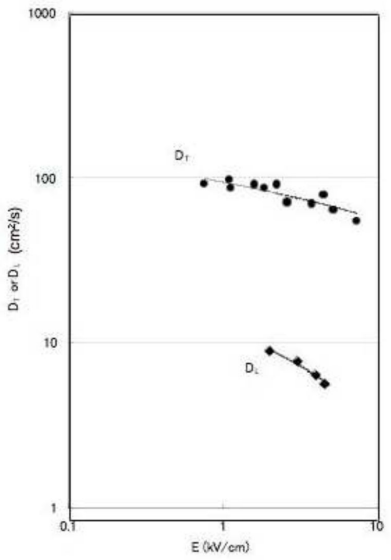

Figure 2.12 – Transverse (D_T) and longitudinal (D_L) diffusion coefficients for liquid xenon as a function of the electric field. Figure taken from [2].

field of 1 kV/cm, we estimated a lateral diffusion of the order of 170 $\mu m\sqrt{cm}$. This means that in our LXe Compton telescope, for an interaction that takes place close to the cathode, i.e. 12 cm far from the segmented anode, the diffusion process will typically expand the electron cloud on the order of 600 μm in the x-y plane with an almost negligible spread along the drift direction.

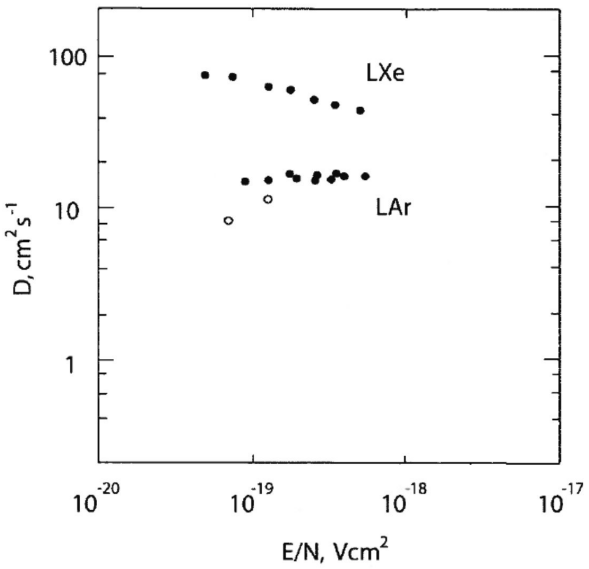

Figure 2.13 – Transverse diffusion coefficient for liquid xenon and liquid argon as a function of the density-normalized electric field. Figure is taken from [3].

Electron diffusion may affect the collection of the ionization signal. The transverse diffusion of the electrons may, on one side, limit the intrinsic spatial resolution of the detector and, on the other side, increase the number of multiple-pixel events, i.e. events with more

than one fired pixel per interaction. Whether or not this is a problem depends on the electron cloud size, the position of the cloud with respect to the anode and the deposited energy in the interaction. If a small amount of charge is shared with a neighboring pixel the reconstruction may be difficult and part of the charge may be lost due to the pulse selection threshold. Longitudinal diffusion along drift length of the detector, on the other hand, may produce a smearing of the collected signal due to the spread in the drift time between arrival electrons. In the case of LXe, the later can be neglected due to the small longitudinal diffusion coefficient.

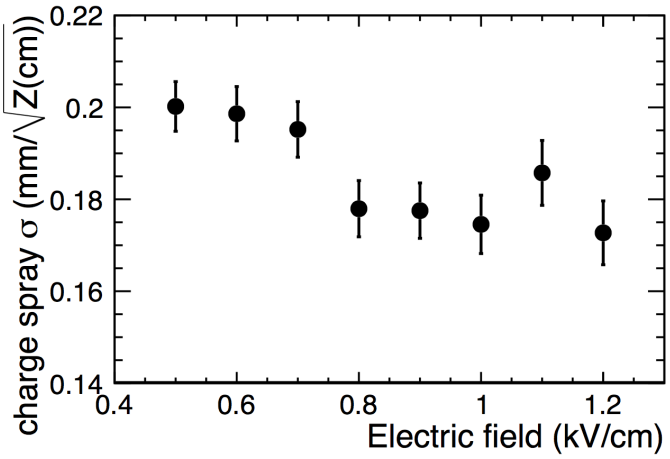

Figure 2.14 – Transverse diffusion as a function of the applied electric field obtained with XEMIS1. Figure taken from [165].

Electron attachment by impurities

Another mechanism that significantly affects the collection of charges is the presence of impurities inside the liquid, particularly electronegative impurities such as O_2, N_2, CO_2 and H_2O. Electron attachment to impurities causes a reduction in the number of collected charge that increases as electrons drift towards the anode. This phenomenon translates into a decrease on the electron lifetime and a degradation of energy resolution of the detector.

The collision between a free electron and electronegative impurity may lead to the capture of the electron by three different processes described in the following:

Three body attachment:

$$e + AB \longleftrightarrow (AB^-)^*$$

$$(AB^-)^* + X \rightarrow AB^- + X \tag{2.13}$$

Dissociative attachment:

$$e \; + \; AB \; \rightarrow \; AB^{*} \; + \; e \; \rightarrow A^{+} \; + \; B^{-} \; + \; e$$

$$e \; + \; AB \; \rightarrow \; AB^{-} \; \rightarrow A \; + \; B^{-} \tag{2.14}$$

Radiative attachment:

$$e \; + \; AB \; \rightarrow \; AB^{-} \; + \; h\nu \tag{2.15}$$

where e denotes a free electron, AB is an impurity (atom or molecule), X stands for a Xe atom or molecule and * represents an excited state. For a more detailed description please refer to [4]. In all three cases, the presence of impurities causes a reduction on the number of produced electrons, which increases over the electron drift time.

The effect of electronegative impurities on the number of collected electrons $N_e(t)$ after a drift time t can be described by the following equation [2]:

$$N_e(t) \; = \; N_0 \, e^{-t \, \sum_i k_i [N_i]} \tag{2.16}$$

where N_0 is the initial number of ionization electrons, k_i is the attachment rate constant of a given contaminant i and $[N_i]$ are the molar concentrations of such impurity. Detailed measurements of the attachment rate constants for different electric fields and molecular contaminants are described in [166]. In order to estimate the amount of impurities the term $\sum_i k_i[N_i]$ is commonly expressed as oxygen equivalent impurity concentration $k.[O_2]_{eq}$ measured in ppb (parts per billion).

The impurity concentration is related to the electron lifetime τ_e, i.e. the average time elapsed before a free electron is captured by an impurity, as follows:

$$\tau_e \; = \; \frac{1}{\sum_i k_i [N_i]} \tag{2.17}$$

According to this, the number of collected electrons $N_e(t)$ can be expressed as a function of the electron lifetime as:

$$N_e(t) \; = \; N_0 \, e^{\left(-\frac{t}{\tau_e}\right)} \tag{2.18}$$

Using Equation 2.18 the free electron lifetime can be directly obtained without prior knowledge of the present concentration of contaminant inside the detector. Moreover, the electron lifetime is related to the electron attenuation length though the expression:

$$\lambda \; = \; v_{drift} \; . \; \tau_e \tag{2.19}$$

Using these equation, the rate of electron attachment of O_2 was calculated in [166]. The results are showed in Figure 2.15. As we can see, the rate of electron attachment of O_2 is reduced by almost a factor of 5 as the applied electric field increased from 1 kV/cm to 10 kV/cm. However, in most cases this reduction is not enough to avoid charge loss. A much greater reduction of electron attachment is achieved by reducing the impurity concentration by means of a purification system. In our LXe TPC a closed re-circulation system was installed to continuously purify the xenon through a SAES MonoTorr Phase II (model PS4-MT3-R) getter. The purification sub-system is described more in detail in Section 3.1.4. The measurement of the attenuation length is further described in Chapter 7. The value of the electron attenuation length is necessary to correct the collected charge for charge losses as a function of the distance to the anode.

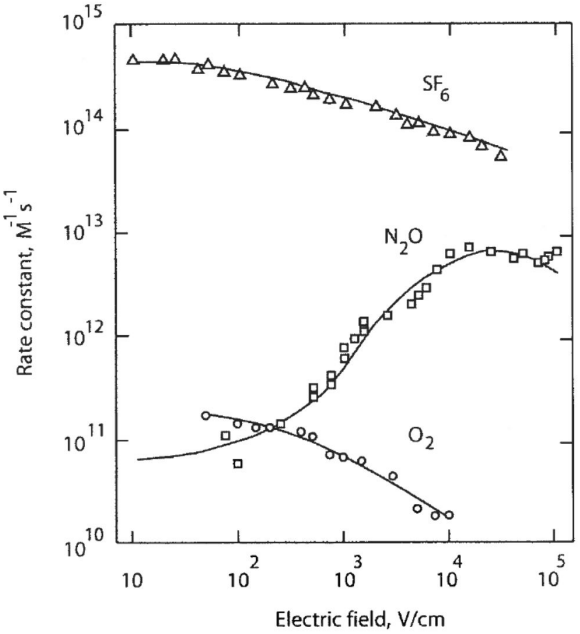

Figure 2.15 – Attachment rate constant of electrons in LXe as a function of the applied electric field for three different contaminant. Figure taken from [166].

2.3 Other mechanisms that affect electron signal detection

Besides the transport properties of charge carriers in LXe, other physical aspects, such as the mean free path of primary electrons, may also contribute to the performances of the detectors. In this section, three aspects related to the production and detection of the ionization signal in LXe are considered. These are the displacement of the electron cloud from the point of interaction due to the mean free path of the recoiling electrons, the emission of fluorescence X-rays after the interaction of a γ-ray with the LXe and the angular resolution limitation due to the non-zero momentum of bound electrons in the atom. The discussion is supported by some experimental results reported by other authors and by a simulation study performed by our group.

2.3.1 Primary Electron Cloud

In general, the electronic cloud produced by ionization is considered as a point-like distribution where all electrons start drifting towards the anode from the same starting point. However, as discussed in Section 2.2, the ionization density is not uniform along the recoiling electron track, which causes a variation in the amount of produced charge along the trajectory of the primary electrons before completely loss their energy. Moreover, electrons do not follow a straight line but they describe erratic trajectories before completely slow down. The spatial extent of the track of the recoiling electrons may affect both the final spatial resolution of the detector and the shape of the collected signal. In this section we perform a detailed study of the primary electron cloud in LXe in order to better understand the physics and limitations of a LXe TPC, and to provide a better description of the charge cloud in LXe.

To estimate the size and shape of the recoil electron cloud in LXe, we performed a Monte Carlo simulation using CASINO V3.2 (CArlo SImulation of electroN trajectory in sOlid) [167]. CASINO is a 3D simulation software developed to simulate electron interactions with matter, which provides information step by step of the trajectory of the primary electrons through the medium until its energy is lower than 50 eV. The program simulates both elastic and inelastic collisions of electron with matter. We used the Mott model for elastic scattering and the Joy-Luo model to describe energy loss rate between two consecutive collisions.

In the simulation, we consider a source of primary electrons with energies between 30 keV to 511 keV and an incident direction normal to the LXe surface ($\vec{p}_z = 1, \vec{p}_x = \vec{p}_y = 0$). At each step, the simulation provides information of the energy loss (E_i) and electron location (x_i, y_i, z_i) where $i = 1, ..., n$ represents the interaction point and n is the total number of collision experienced by the primary electron. Figure 2.16 shows a typical ionization track for a 511 keV primary electron in LXe. High-energy electrons travel a certain distance producing a minimum ionization region, whereas most of their energy is deposited at the end of the trajectory creating a non-uniform distribution of secondary electrons along their track. Moreover, we can see that the electron recoil track is not at all a straight line, but electrons can undergo hard scatters with the primary electron giving several keV to a secondary electron. Even secondary electrons with a few keV of energy may result in a dense ionization blob along the track [44]. This important energy loss in one interaction shared among secondary recoils gives rise to recombination fluctuations along the track of the primary electron.

The penetration depth or Z_{mean} depends on the energy of the recoil electron. The path length is measured as the average value of the distance between two successive collisions over the total number of collisions. The minimum mean free path of electrons between scattering events is around 1 nm. Figure 2.17 shows the spatial extent of the primary electron cloud for 511 keV primary electrons. The recoil electron cloud has an almost spherical shape with an average radius in 3D of the order of $\sim 190\ \mu m$. The barycenter of the charge cloud is displaced of about 100 μm towards the incoming direction from the initial interaction point which represents the γ ray absorption point, whereas no displacement is observed in the X and Y directions. This implies that the photoelectrons created by 511 keV γ-rays are more probably emitted in the forward direction with respect to the incident photon with a small emission angle.

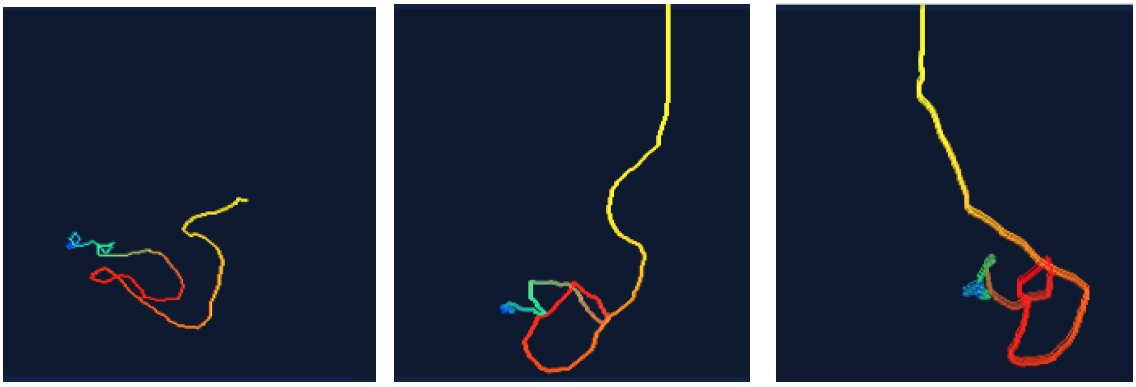

(a) (x, y) **(b)** (x, z) **(c)** (y, z)

Figure 2.16 – Example of an electron recoil track of 511 keV simulated using CASINO. Energy loss along the track is represented by the the color palette from yellow (511 keV) to blue (0 keV) (see Figure 2.17(b)) [21].

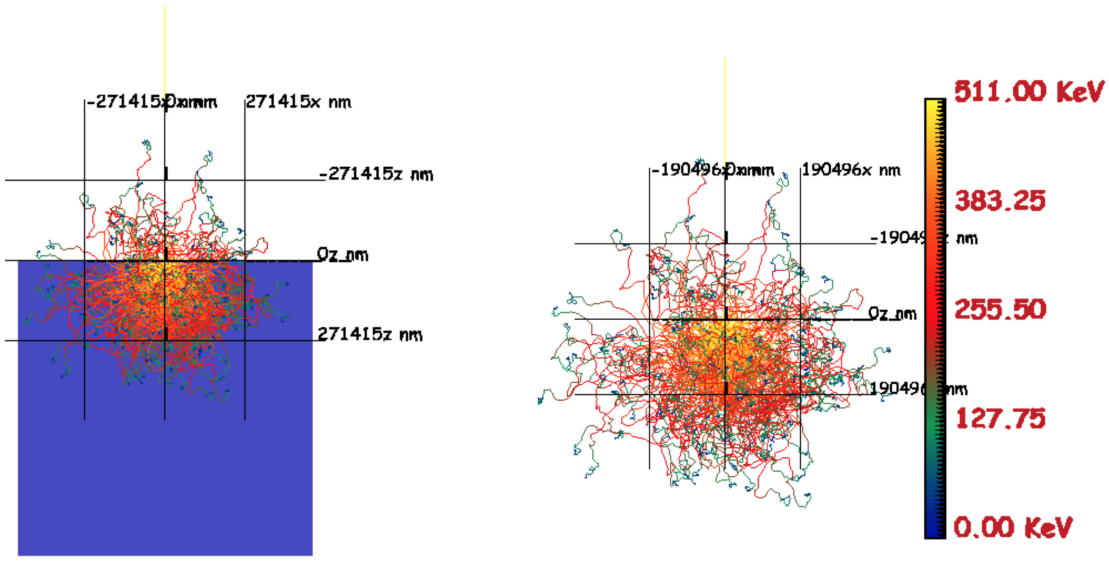

(a) **(b)**

Figure 2.17 – Example of an electron cloud for 2000 simulated 511 keV primary electrons using CASINO.The blue region in (a) represents the LXe surface [21].

The radius in 3D of the primary electron cloud from the barycenter point is estimated according to the following expression:

$$R = \sqrt{(|\bar{x} - \langle\bar{x}\rangle|)^2 + (|\bar{y} - \langle\bar{y}\rangle|)^2 + (|\bar{z} - \langle\bar{z}\rangle|)^2} \tag{2.20}$$

where $\bar{x} = \frac{\sum_1^n x_i E_i}{\sum_1^n E_i}$, $\bar{y} = \frac{\sum_1^n y_i E_i}{\sum_1^n E_i}$ and $\bar{z} = \frac{\sum_1^n z_i E_i}{\sum_1^n E_i}$ represent the mean value over successive interactions along the primary track, and $\langle\bar{x}\rangle$, $\langle\bar{y}\rangle$ and $\langle\bar{z}\rangle$ indicate the mean value

of the $\bar{x}$, $\bar{y}$ and $\bar{z}$ distributions obtained over the total number of simulated events N. The average value of the radius in 3D, which represents the isotropic radial extension of the electron cloud, is then estimated from the mean value of the R distribution obtained for all the simulated events. The shift of the barycenter in the forward direction and the isotropic radial extension as a function of the electron recoil energy are presented in Figure 2.18. The error bars represent the standard deviation of the R distribution. For each energy, 2000 electrons were simulated. We can see that the cloud size increases as the energy of the recoil electron increases and the maximum of ionization, i.e. the center of the cloud, shifts to higher distances as the energy increases. Moreover, for energies near the shell edges (K-shell and L-shell), the size of the electronic cloud is completely negligible and most of the energy is deposited near the X-ray absorption point.

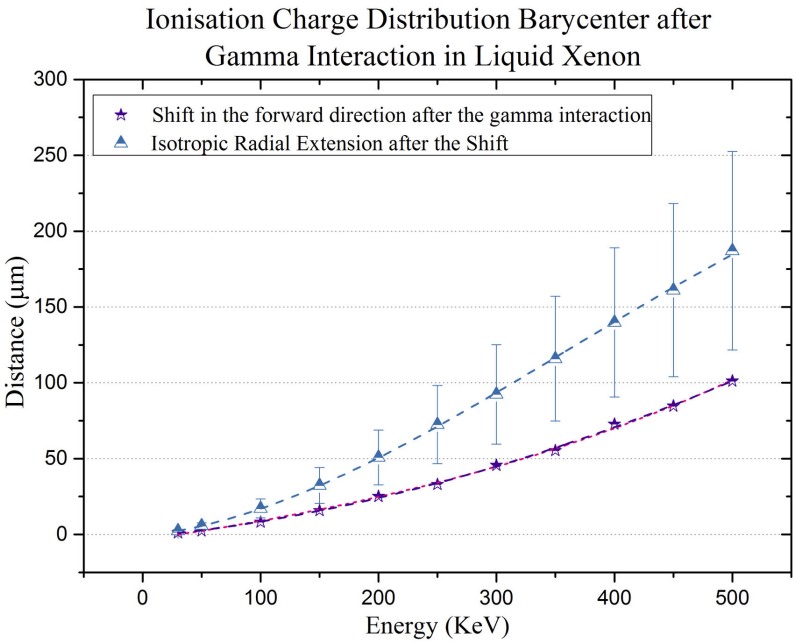

Figure 2.18 – Electron radial distribution in the primary electron cloud obtained as a function of energy [21].

The Monte Carlo simulation demonstrates that the assumption of a uniform distribution of electrons liberated by the primary electron along an electron track is not realistic. Moreover, since electrons do not follow straight line trajectories, the estimation of the length of the electron track from the average path length traveled by a charged particle before coming to rest, called the CSDA range, is not appropriated [168]. For 511 keV electrons, the CSDA range is of the order of 1 mm (0.3012 g/cm^2) [169]. This value is consistent with the total length of the electron track obtained with CASINO. Our results show, however, that a maximal radial extension in 3D of less than 200 μ is expected for 511 keV recoil electrons, although no information about the charge distribution inside the electron cloud is reported. The effect of the size of the electron cloud in the measured signals is further discussed in Chapter 7.

2.3.2 Doppler Broadening Effect

The Compton equation 1.4 is only valid under the assumption that the interaction between the γ-ray and an atomic electron occurs when such electron is unbounded and at rest. However, in a real medium, the Compton scattering takes place with bound and moving electrons. The motion of the atomic electrons around the nucleus produces a broadening of the scattered photon energy $E_{\gamma'}$, which results in a corresponding broadening of the scattering angle. This effect is known as Doppler broadening [170]. The Doppler broadening effect implies an intrinsic limitation on the angular resolution of any Compton telescope.

After a Compton scattering process, the energy conservation leads to: $E_\gamma = E_b + E_{\gamma'}$ where E_γ and $E_{\gamma'}$ are the energies of the incident and scattered photons respectively, and E_b is the binding energy of the electron in the atom for its corresponding subshell. However, the electron momentum inside the atoms introduces an uncertainty in the energy of the deflected photon and the recoil electron. For a given incident photon energy E_γ and a scattering angle θ, a broadening of the possible $E_{\gamma'}$ is produced. The broadened energy distribution is usually called *Compton profile*. Figure 2.19 shows the energy distribution of deflected photons for 140 keV incident γ-rays and a scatter angle of 45° for three different materials [170]. The uncertainty in the scattered photon energy, given by the standard deviation of the Doppler broadening distribution, increases as the atomic number increases [170]. The momentum of such electron p_z before the interaction, projected upon the γ momentum transfer vector is given by Equation 2.21 [126]:

$$\mid \vec{p_z} \mid = \frac{\vec{p_\gamma}.\vec{p_{e^-}}}{\mid \vec{p_\gamma} \mid} \tag{2.21}$$

where $\vec{p_\gamma}$ and $\vec{p_{e^-}}$ are the momentum vector of the incident photon and the ejected electron respectively. Applying energy and momentum conservation:

$$p_z = -m_e c \frac{E_\gamma - E_{\gamma'} - E_\gamma E_{\gamma'} \frac{(1 - cos\theta)}{m_e c^2}}{\sqrt{E_\gamma^2 + E_{\gamma^2}^{'} - 2E_\gamma E_{\gamma'} cos\theta}} \tag{2.22}$$

If the electron is at rest, $p_z = 0$, and Equation 2.21 reduces to the formula of the scattering Compton 1.4.

The Compton scattering interaction probability is characterised by the cross section. The differential cross section for the scattering of photons with unbound and at rest electrons was first derived by O. Klein and Y. Nishina [171], and the angular distribution of the recoil electrons is given by the Klein-Nishina differential cross section presented in Equation 2.23 [20]:

$$\left(\frac{d\sigma}{d\Omega}\right)_{KN} = \frac{r_e^2}{2}\left(\frac{E_\gamma^{'}}{E_\gamma}\right)^2\left(\frac{E_\gamma^{'}}{E_\gamma} + \frac{E_\gamma}{E_\gamma^{'}} - sin^2\theta\right) \quad [cm^2 sr^{-1} electron^{-1}] \tag{2.23}$$

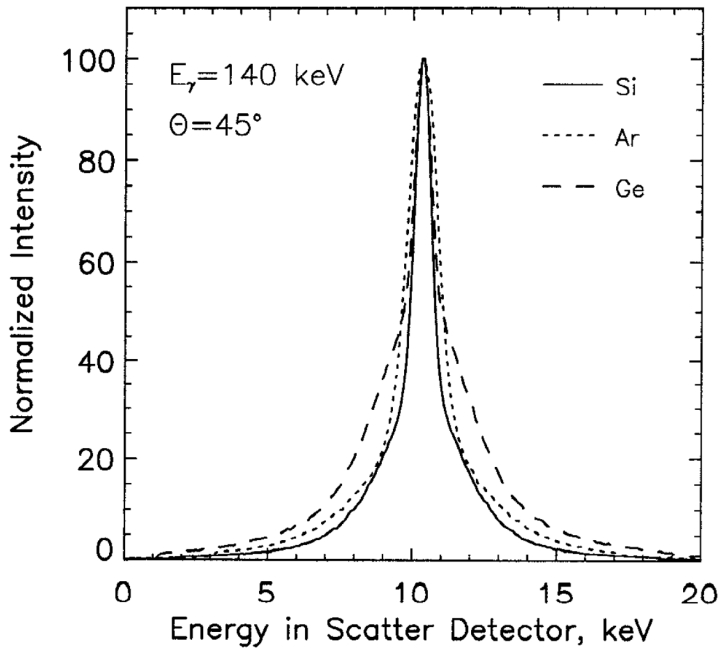

Figure 2.19 – Energy lost distribution for 140 keV γ-rays after a Compton scattering interaction with a bound atomic electron through a 45° deflection angle for Si (Z = 14), Ar (Z = 18) and Ge (Z = 32) [170].

where r_e is the classical electron radius and Ω is the solid angle. The Klein-Nishina equation for Compton scattering is a good approximation for high energy photons ($>$ 1 MeV), especially for low atomic number materials. Figure 2.20 shows the angular distribution of the differential cross section of Compton scattering. For example, 511 keV γ-rays have a high probability to undergo a forward scattering with small deflection angle. However, due to the non-zero momentum of the recoil electrons before the interaction, this is not completely accurate. To account for the momentum distribution of the bound electrons, the atomic shell effects should be taken into account in the Klein-Nishina formula, which leads to the following expression [126]:

$$\left(\frac{d\sigma}{d\Omega}\right)_{DB} = \left(\frac{d\sigma}{d\Omega}\right)_{KN} . S_i(E_\gamma, Z, \theta) \tag{2.24}$$

where $S_i(E_\gamma, Z, \theta)$ is the *incoherent scattering function* of the i-th shell electrons of an atom with atomic number Z, which depends on the momentum transfer of the incident photon. The total scattering cross section for an specific orbital is obtained by integrating Equation 2.24 over all angles. The results show that the Doppler broadening effect is more important for low γ-ray energies, high scattering angles and material with high atomic number.

The uncertainty in the angular resolution introduced by the Doppler broadening can be estimated from the Angular Resolution Measure (ARM) profile, which is obtained from the difference between the scatter angle θ, derived from the Compton equation, and the geometric scatter angle θ_{geo}, calculated from the real position of the photon emission and the position of the interaction in the material. The Doppler broadening effect on a Xe

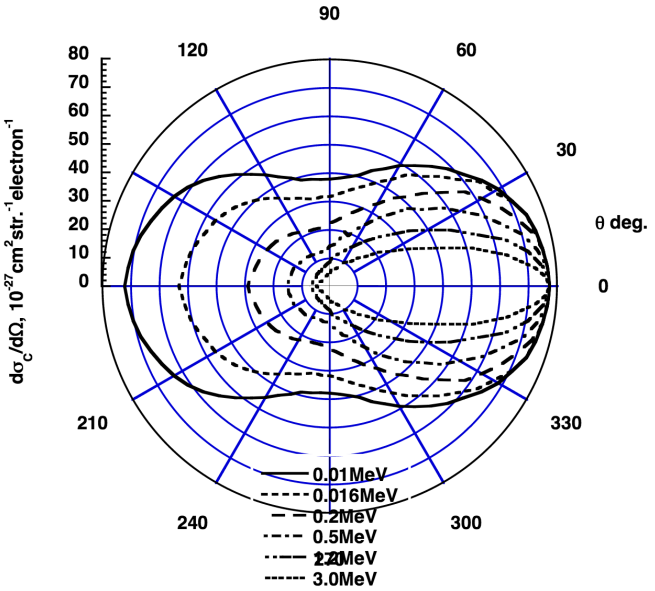

Figure 2.20 – Differential cross section of Compton scattering. Original figure from [172].

Compton telescope was determined by Zoglauer and Kanbach [126]. The angular resolution was estimated from the FWHM of the ARM distribution. Figure 2.21 shows the dependence of the angular resolution on the energy of the incident photon for Xe, Si and Ge. For a Xe Compton camera and 511 keV γ-rays, a minimum angular resolution due to the Doppler broadening of $\sim 1.45°$ was estimated, whereas a resolution of $\sim 0.8°$ was measured for 1 MeV γ-rays [126]. This limitation in the angular resolution is present regardless the energy resolution of the detector.

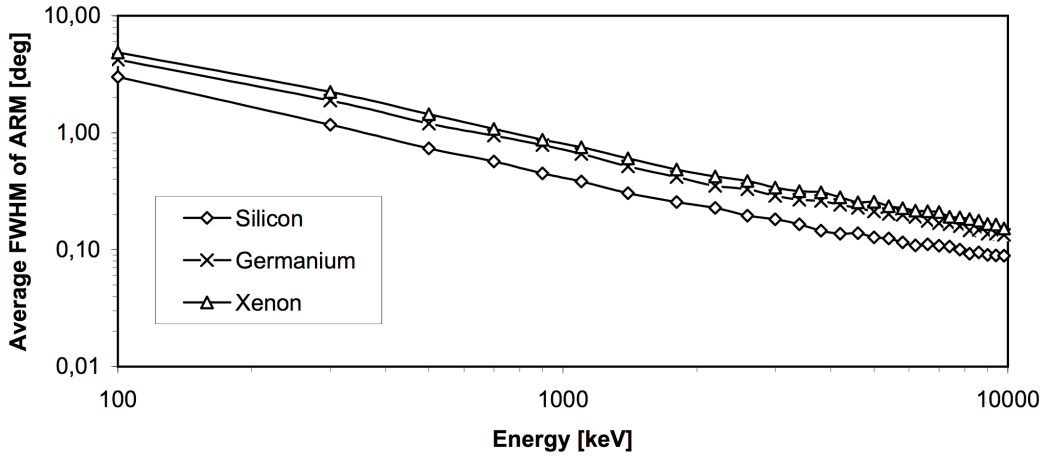

Figure 2.21 – Angular resolution as a function of the energy of the incoming γ-ray for Xenon, Silicon and Germanium. Figure taken from [126].

2.3.3 Isotropic X-ray emission

As discussed in the previous chapter, when a γ-ray interacts with LXe there is a non negligible probability that it will ionize an inner shell of an atom with the consequent emission of a X-ray or an Auger electron. After a photoelectric absorption, for example, the photon is completely absorbed and an inner shell electron, generally from the K or L shells, is ejected from the atom. Part of the energy of the γ-ray is used to overcome the binding energy of the electron and the rest is transferred to the ejected electron. In xenon, the absorption edges corresponding to the K, L and M atomic shells correspond to energies of around 34.5 keV, 5 keV and 2 keV respectively. The ejected electron creates a vacancy leaving the atom in a highly excited state. The atom will rapidly return to its ground state by filling the vacancy with an outershell electron. This de-excitation process is usually accompanied by the emission of a fluorescence X-ray or an Auger electron, with energies equal to the difference in the binding energies between the two atomic levels involved in the transition.

Inner shell excitation and X-ray emission may also be produced after a Compton scattering interaction. However, this process is more unlikely than X-ray emission after a photoelectric effect since the γ-ray must collide with an electron from the inner K or L shells of the atom. Assuming a constant probability of Compton scattering per electron, the probability of interaction with an electron of the K-shell can be roughly estimated as ~ 4 %.

For γ-rays with incident energies above 34.5 keV, the probability of photoabsorption to occur in the K-shell is around 86 %. After the ionization of the K-shell, the probability of atomic relaxation via a K_α (29.7 keV) or a K_β (33.8 keV) fluorescence photons is of the order 87 %, whereas the emission of an Auger electron is almost negligible. On the other hand, if the incident photon has an energy lower than the binding energy of the K-shell, the interaction will more probably occur with an electron from the L-shell or from a higher level. In this case, the de-excitation via the emission of an Auger electron is more likely than the emission of a L fluorescence photon. After the emission of an Auger electron, the atom will return to the ground state by a series of cascade relaxation processes.

In most cases, the emitted X-ray is reabsorbed by the LXe producing a second electron cloud displaced from its production point. Photoelectrons produced with energies of the order of ~ 30 keV will travel a maximum distance of $\sim$370 μm in LXe (CSDA) [13]. Whether or not the two electron clouds are spatially resolved depends on the emission direction of the X-ray photoelectron with respect to the primary electron cloud. While the X-ray emission is isotropic, the primary photoelectron has a certain directionality, which depends on the energy of the incident γ-ray. The electron is emitted forward in the direction of the incoming photon at high incident energies, while it is emitted perpendicular to the γ-ray at low energies [173, 174].

If both electrons are emitted in the same direction, a single electron cloud will be formed and all electrons will drift to the anode at the same time. In this case, the total collected energy will be equal to the energy of the incident γ-ray. On the other hand, if both interactions take place far from each other, two different electron clouds will be formed and electrons will drift towards the anode with a certain time difference. In LXe, since the mean free path of 30 keV γ-rays is small, the production of multiple scattering events due to the emission of a X-ray from the K-shell should not be very significant. An Auger electron can

also produce a considerable amount of secondary electron-ion pairs by ionization. However, due to their small range (see Figure 2.18) only a single electron cloud is expected.

To better understand the implications of X-ray emission in the data analysis, a precise Monte Carlo simulation of the interaction of the 3γ-rays emitted by a ^{44}Sc source with our LXe TPC has been carried out using Geant4 [175, 176]. The physics of photoionization were simulated using the low-energy Penelope model [177]. X-ray fluorescence and Auger electron emission were also considered in the simulation. Figure 2.22(a) shows the energy spectra for photoelectric and Compton scattering processes for all the interactions inside the detector. On the other hand, the energy spectrum for only those interactions with an emitted X-ray is depicted in Figure 2.22(b). The simulation shows that 84 % of the time a photoelectric absorption in the LXe is followed by the emission of a X-ray from the K-shell, whereas only a 4 % of the X-rays are emitted after a Compton scattering. These results are in good agreement with the theoretical expectations. For small deposited energies the emission of a X-ray is more likely due to a Compton interaction than a photoelectric absorption. However, this probability remains small compared to the probability of the emission of a high energy photoelectron. Moreover, a widening of the front Compton due to Doppler broadening is also appreciable in the Figure 2.22(b) compared to the total Compton spectrum. This is because X-ray emission due to a Compton scattering is produced by the interaction with a inner electron, most likely from the K-shell. Inner electrons are, in turn, more affected by the Doppler broadening effect due to their higher momentum compared to outershell electrons.

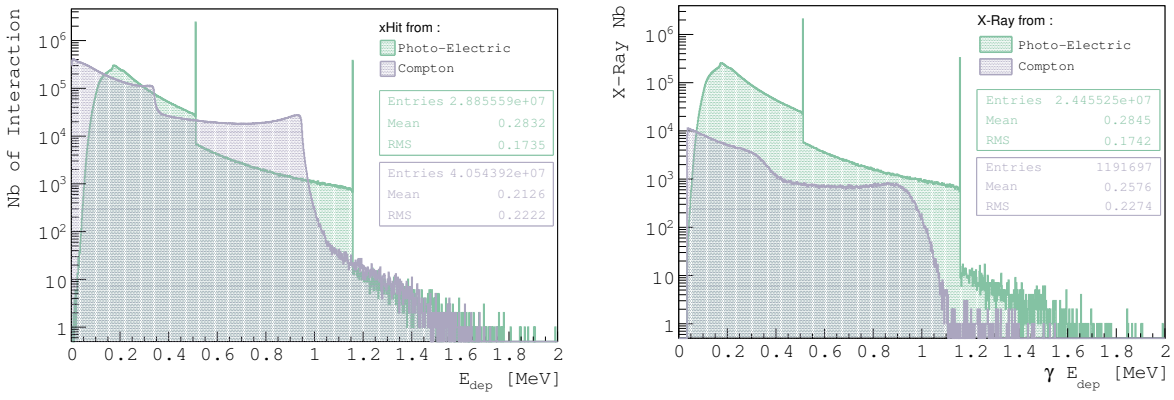

(a) **(b)**

Figure 2.22 – Geant4 simulation of the interaction of the 3γ-rays emitted by a ^{44}Sc source with a LXe TPC. a) all hits and b) only those hits with the emission of a X-ray from the K-shell.

2.4 Conclusions Chapter 2

A LXe TPC combines the detection of the ionization and scintillation light signals to provide information of the 3D position and energy deposit of each individual interaction inside the fiducial volume of the detector. In this chapter we have described the basic principle of a LXe TPC based on a monolithic detector filled with LXe. The detector provides information of

each interaction point along the transverse (X, Y) and longitudinal (Z) coordinates, besides energy loss information along the particle track. The measurement of the Z coordinate requires a precise knowledge of the electron drift velocity, which depends on the applied electric field. The information of the time of interaction t_0 is obtained from the emission of scintillation light, that provides the detector self-triggering capabilities. Therefore, a LXe TPC technology allows for three-dimensional event reconstruction and precise energy measurements, providing good angular and calorimetry resolutions. These characteristics are essential to obtain a good quality image of the source distribution on a medical imaging Compton telescope.

We have seen that the final charge collection depends on the electron-ion recombination rate and on the purity of the xenon. A description of the recombination process in LXe was proposed by Thomas and Imel [143]. In Chapter 7 we analyze our experimental results with the Thomas and Imel model. The obtained results are consistent with the values reported by other authors, as shown in this chapter.

The time evolution of the electron cloud has been also discussed in this chapter. When a electron cloud moves through a liquid under the influence of an electric field, three processes are involved in its time development: electron drift velocity, electron diffusion and electron attachment to electronegative impurities. All three aspects have discussed in detail in this chapter. Other effects such as the initial size of the electron cloud, the emission of fluorescence X-rays and the Doppler broadening effect may also impact the performances of the detector. A simulation using CASINO shows that the barycenter of the electron cloud is shifted by around 100 μm from the γ-ray interaction point, which introduces a small systematic error to the position determination. We have observed that the average size of the electron cloud for 511 keV γ-rays is of the order of 200 μm. The impact of the size of the electron cloud is further discussed in Chapter 7.

The interaction of a γ-ray with the LXe is followed almost the 85 % of the time by the emission of a X-ray from the K-shell after a photoelectric absorption and 4 % of the time after a Compton scattering. This means that there is a high probability that two ionization clouds are generated in the chamber after the interaction of a γ-ray. Due to the small mean free path of X-rays with energy of the order of 30 keV, in most of the cases both interaction will be confused leading to a total collected charge equal to energy of the incident γ-ray. Finally, we have discussed the effect of the Doppler broadening to the final angular resolution of a Xe Compton telescope. In the case of Xe, a minimum angular resolution of $\sim 0.8^\circ$ (FWHM) was estimated for 1 MeV γ-rays [126].

In the next chapter, a detailed description of the two prototypes of a LXe Compton telescopes developed within the XEMIS project is presented.

Chapter 3

XEMIS: A liquid xenon Compton telescope for 3γ imaging

Contents

In order to prove the feasibility of the 3γ imaging technique and consolidate this new imaging modality in the scientific community, a first phase of research and development (R&D) has been performed at Subatech laboratory. This first stage represents the beginning of the XEMIS (XEnon Medical Imaging System) project that started at Subatech in 2006, with the development of a first prototype of a LXe Compton telescope called XEMIS1. The promising results obtained to date with this small dimension device have led to the development of a second prototype dedicated to small animal imaging called XEMIS2. In this chapter, a detailed description of the two prototypes XEMIS1 and XEMIS2 is presented. The main characteristics of the experimental set-up of XEMIS1 are described in Section 3.1. The light detection and charge collection systems are described in Sections 3.1.2 and 3.1.3 respectively, while the cryogenic infrastructure used to liquefied and purified the xenon in XEMIS1 is introduced in Section 3.1.4. Section 3.2 is devoted to give a detailed description of the new prototype XEMIS2 that comprises the experimental set-up and signal detection

systems. The innovative cryogenic infrastructure used to recuperate and store the xenon, especially developed for XEMIS2, is introduced in Section 3.2.4.

3.1 XEMIS1: First prototype of a liquid xenon TPC for 3γ imaging

3.1.1 Detector description

In order to test the possibility of using a LXe Compton telescope for the 3γ imaging technique, a small dimension single-phase LXe TPC, XEMIS1, has been developed and tested. A general view of the experimental set-up of XEMIS1 is presented in Figure 3.1, that includes the XEMIS1 TPC, the data acquisition system, the cryogenic system required to liquefy the xenon, the purification and recirculation systems and the rescue tank used to recuperate the xenon in case of necessity.

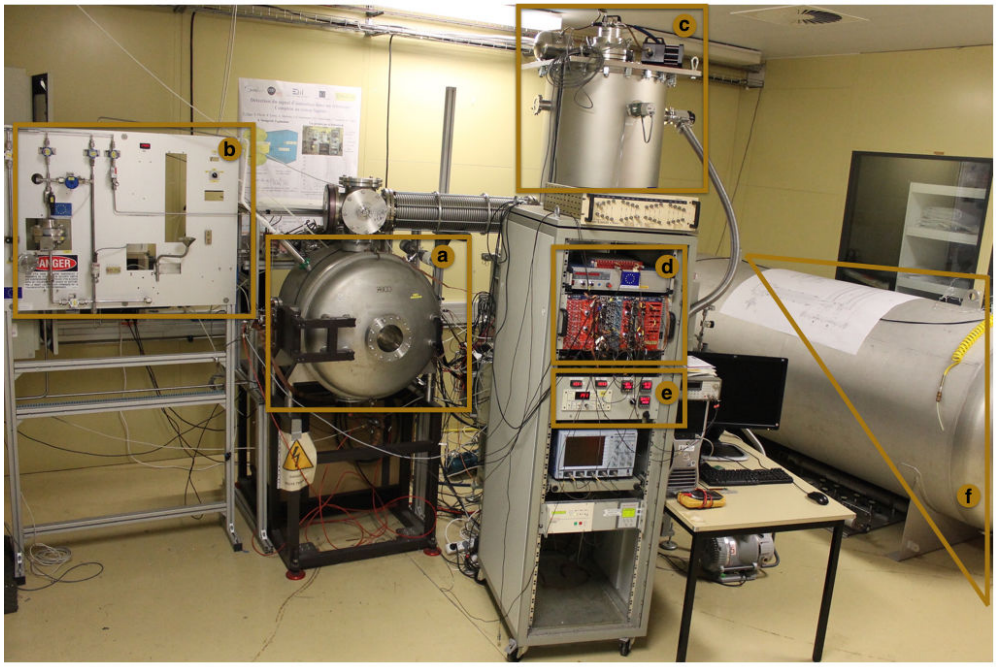

Figure 3.1 – General view of the XEMIS1 experimental set-up installed at Subatech laboratory that comprises: (a) external cryostat that hosts the TPC, (b) injection panel, (c) heat exchanger and pulse tube refrigerator, (d) data acquisition system, (e) control panel and (f) rescue tank.

The XEMIS1 prototype consists of a cylindrical TPC full of liquid xenon with a drift volume of 2.8 x 2.8 x 12 cm^3. Figure 3.2 shows the main parts of the XEMIS1 TPC. A photomultiplier tube (PMT) is placed at the top of the TPC with the aim of detecting the VUV scintillation photons (178 nm) generated after the interaction of a γ-ray with the LXe. The PMT is especially designed to work at LXe temperature and, as previously mentioned in Chapter 2, it is used as a trigger for the signal acquisition. The charge carriers produced

in the ionization process are collected by a segmented anode of 2.5 x 2.5 cm^2. The anode represents the entrance window for the incoming radiation and it is located facing the PMT. The drift length of the TPC is delimited by a micro-mesh placed 1.6 mm below the PMT and the anode. The micro-mesh is used as a cathode for the drift electric field. A set of 24 copper field rings is located around the TPC to provide a homogeneous electric field up to 2.5 kV/cm between the cathode and the anode. A mesh used as a Frisch grid is placed above the anode.

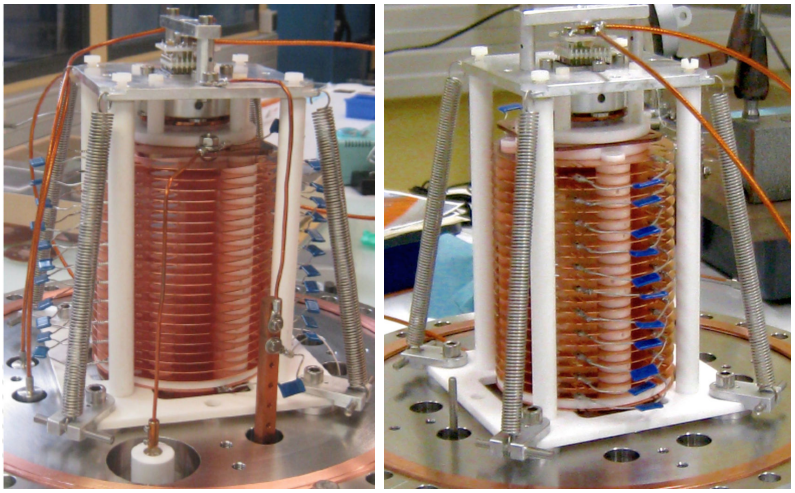

Figure 3.2 – Two different views of the XEMIS1 TPC. In the right side figure the resistive divider chain used to provide an uniform electric field along the drift volume is visible.

To ensure a uniform electric field inside the drift volume, the potential is distributed from the cathode, which is directly connected to a high voltage supply, to the first field shaping ring by means of a resistive divider chain of 24 x 500 MΩ resistors immersed in the LXe (see Figure 3.2). The first resistor of the divider chain is connected to the rim of the high-voltage electrode, while the last one is connected to ground through a 500 MΩ resistor. Two independent power supplies are used to provide a constant voltage to the first copper field ring and to the Frisch grid separately. The pixels are connected to ground via the front-end electronics. To ensure a 100% electron transparency of the Frisch grid, an electric field in the gap of at least 5 to 10 times higher than the electric drift field is necessary. The ratio between the two electric drift fields depends on the kind of Frisch grid. A study of the transparency of the grid as a function of the electric field is presented in Section 5.5.1.

The sensitive volume of XEMIS1 is then defined by the drift length and by the intersection area of the segmented anode, which is 2.5 x 2.5 x 12 cm^3. A drift length of 12 cm was chosen to ensure a high γ-ray detection efficiency with a maximum trigger efficiency. The probability that a 1.157 MeV γ-ray interacts at least once in 12 cm of LXe is 88%. However, due to the trigger system configuration, the PMT, which is responsible of the data acquisition triggering, is located 13.6 cm far from the anode. This implies that a reasonable small solid angle is covered by the light detection system, mostly for those interactions that take place close to the anode. A higher drift length will result in a smaller solid angle, and thus in an important lose of trigger efficiency.

The anode is connected to an ultra-low noise front-end electronics consisting of two standard IDeF-X HD-LXe 32 channels chips that generates 64 independent analog signals [5]. The electronics are placed inside a vacuum container at a temperature lower than -60°, allowing a reduction of the electronic noise ENC (Equivalent Noise Charge) down to 80 electrons.

As we can see in Figure 3.2, the different components of the TPC are mounted on a column structure made of four Macor ceramics rods. The base of the rods are fixed on a stainless steel flange. Furthermore, to compensate for temperature-induced changes in some of the materials, a set of four stainless steel springs is used to support the whole assembly. The ensemble is built inside a stainless steel cylindrical cryostat filled with about 30 kg of high-purity LXe, which is located in a vacuum chamber to ensure good thermal insulation. All materials used to construct the TPC, including the cryostat and the assembly structures, were chosen due to their low outgassing. Moreover, to minimize the effect of thermal contraction of the TPC during cooling, all materials were selected due to their similar coefficients of thermal expansion, excluding the Macor ceramic which undergoes a very small thermal contraction. Table 3.1 lists the different components of the TPC. A more detailed description of the light detection and charge collection systems is presented in the following subsections.

Designation	**Materials**	**Thickness (mm)**	**Tolerance (mm)**
Flange	Stainless steel	0.5	± 0.2
Glue	STYCAST	0.1	± 0.1
Anode	*[a]	2.6	± 0.1
Support Frisch grid	Copper	1	± 0.04
Field rings	Copper	0.5	± 0.03
Lower board	Macor ceramics	4	± 0.05
Column spacer	Macor ceramics	4.5	± 0.05
Cathode	Copper	0.005	± 0.02
Screening mesh	Copper	0.005	± 0.02

Table 3.1 – Assembly components of the XEMIS1 TPC.

[a] See section 3.1.3.

3.1.2 Light detection system

As we have seen in Section 1.1.4, LXe is an excellent scintillator with high photon yield and short decay times consisting of a fast (2 ns) and a slow (27 ns) decay components [36]. In order to detect the scintillation light in XEMIS1, we use a VUV-sensitive Hamamatsu R7600-06MOD-ASSY PMT especially developed to work at LXe temperature. A picture of the PMT is presented in Figure 3.3. The PMT is directly immersed in the LXe, showing a good UV photon sensitivity with a quantum efficiency of 35% at 175 nm. The PMT

has a quartz window of 28 x 28 mm^2 and a bi-alkaline photocathode of 18 x 18 mm^2 that constitutes the active area of the detector. At the LXe temperature the total gain is of the order of 10^6 for a voltage of 750 V.

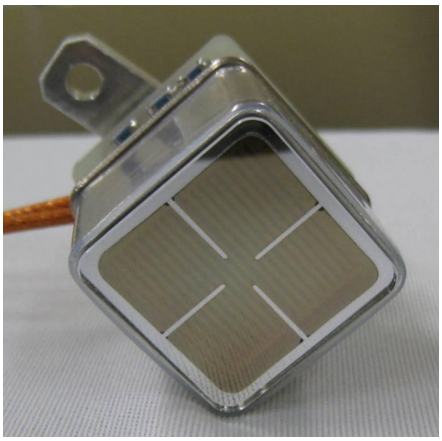

Figure 3.3 – VUV-sensitive Hamamatsu R7600-06MOD-ASSY PMT used in XEMIS1 TPC to detect the scintillation light.

Besides the high scintillation yield of LXe and the relatively large active area of the light detection system with respect to the geometry of XEMIS1, the design of the TPC is not optimal for light detection. In absence of an electric field, a large photon yield of around 42000 UV photons are generated after the interaction of a γ-ray of 1 MeV of energy. However, the necessity of an electric field to collect the charge carries reduces the amount of photons produced after the interaction. At a drift field of 1 kV/cm, which is a standard value used to characterize XEMIS1, the light reduction is about 50% leaving to around 21000 photons/MeV. Even though this value is comparable to those of the best scintillation crystals used in PET [87], only a reduced fraction of the emitted photons reaches the PMT due to the small solid angle coverage, especially for those interactions that take place far from the PMT surface. For example, the interaction of a 1.157 MeV γ-ray at 12 cm from the PMT with an electric field of 1 kV/cm will result in the detection of around 25 photoelectrons. Other effects such as the reflection of the UV photons in the cathode or in the copper field rings, the optical transparency of a screening mesh placed below the PMT surface or the reflection at the PMT window could also affect the fraction of photons that reaches the PMT. As a result, the number of photoelectrons is too small for energy resolution measurements, which is not our goal, but enough to give a suitable signal for triggering of the data acquisition system and for measuring the interaction time t_0.

Signals from the PMT are sent both to an electronic logic chain and to a Flash Analog-to-Digital Converter (FADC). In the FADC the signals are digitized with a sampling rate of 250 MHz and a resolution of 16 bits.

3.1.3 Charge collection system

To collect the electrons produced by the ionization of LXe after the passage of an ionizing particle, XEMIS1 includes: a mesh used as a Frisch grid, a segmented anode divided in 64 pixels and the data acquisition electronics.

Frisch grid

After the interaction of an ionizing particle with the LXe, and in order to collect an ionization signal with an amplitude proportional to the deposited energy and independent of the distance of the interaction with respect to the collecting electrode, a grid is placed between the anode and the cathode. This grid, known as Frisch grid, is then introduced with the aim of removing the position dependency of the collected signals. The grid shields the anode of the motion of the drifting electrons between the cathode and the grid [178]. Therefore, with an ideal Frisch grid no signal is collected in the anode until the electrons pass through the grid. The shielding of the anode from electrons motion is, however, not perfect, which leaves to signal induction on the anode while electrons drift towards the Frisch grid. This effect known as Frisch grid inefficiency affects the time shape of the anode signal and hence, it has a direct impact on the energy resolution [179].

In addition to the charge induction opacity of the Frisch grid, the mesh should be transparent to the drifting electrons. This implies that all electrons created in the ionization process should be able to pass through the grid to be collected by the anode. However, if the transparency is not good enough, and the electrons are collected by the grid, the full ionization charge is not detected, worsening the SNR and hence, negatively affecting the energy resolution. The electron transparency of a grid depends on the geometry of the grid. For this reason, the choice of the Frisch grid in a LXe TPC is of crucial importance for the collection of the ionization signals. During the course of this thesis four different grids have been tested. A more detailed description of the properties of a Frisch grid is presented in Chapter 5.

The Frisch grid is basically a metallic mesh usually made of nickel, aluminium, copper or stainless steel. There are many different types of meshes depending on the manufacture technique that limit the size and shape of the mesh as well as the distance between the anode and the grid. Electroformed and chemical-etched micro-meshes are both commonly used in Micro-Pattern Gas Detectors (MPGD) such as Micro-Mesh Gaseous Structure (Micromegas) [115, 139]. Electroformed micro-meshes manufactured by Precision Eforming LLC are usually very thin meshes with a thickness of 5 μm and a wide variety of geometries. Three different types of electroformed micro-meshes have been tested in XEMIS1. Their main properties are summarized in Table 3.2. The chemical-etched micro-meshes also known as CERN meshes, are also commonly used in a gridded ionization chamber. However, they are not a reasonable option for the XEMIS TPC due to the gap region is generally limited to 25 to 50 μm. Such a small gap is crucial in Micromegas detectors since the amplification gain depends directly on the distance between the micro-mesh and anode. However, in our case no amplification is needed and the mesh is only used as Frisch grid. A very narrow gap will increase the electronic noise reducing the SNR and hence, affecting the energy resolution, in addition to make harder the manage of the mesh.

Mesh	**Electroformed 670 LPI**	**Electroformed 500 LPI**	**Electroformed 70 LPI**
Mesh thickness (μm)	5	5	5
Hole size (μm)	26.2	39.1	344
Bar thickness (μm)	11.7	11.7	18.5
Pitch (μm)	37.9	50.8	362
Material	Copper	Copper	Copper
Optical transparency (%)	48	59	90

Table 3.2 – Properties of three electroformed micro-meshes used in XEMIS1.

Another good option are the metallic woven wire meshes. This kind of grid has the advantage of allowing larger detectors with a more robust structure, which ease the handling of the mesh to achieve good flatness and parallelism with respect to the anode plane. The main characteristics of two different types of woven wire meshes tested during this work are listed in Table 3.3. Figure 3.4 shows a 100 LPI woven wire mesh and a 70 LPI electroformed micro-mesh both used in the development of XEMIS1.

Mesh	**Metallic woven 100 LPI**	**Metallic woven 50.29 LPI**
Mesh thickness (μm)	50	60
Hole size (μm)	230	475
Bar thickness (μm)	25	30
Pitch (μm)	254	505
Material	Stainless steel	Stainless steel
Optical transparency (%)	81	89

Table 3.3 – Properties of the metallic woven meshes used in XEMIS1.

Besides the geometry of the grid, another important parameter to take into account when selecting a Frisch grid for a LXe detector is the material. Due to the TPC is immersed in LXe, all the structures that compose the detector are subjected to extreme temperature changes. This implies that all materials should have similar thermal expansion coefficients, to minimize the expansion and contraction effects. Any deformation of the grid issues from thermal expansion would increase the electronic noise or even cause catastrophic damage to the electronics. Taking this into consideration, stainless steel and copper meshes are good choices for XEMIS1. To preserve the distance between the anode and the Frisch grid, the mesh is stretched and glued on a spacer made of copper to ensure an uniform electric field. Two different gaps of 500 μm and 1 mm have been tested during this thesis.

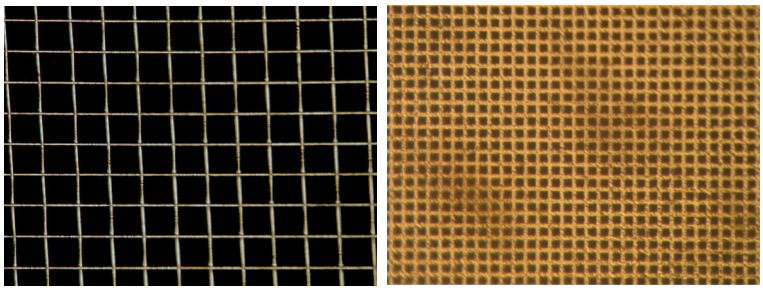

Figure 3.4 – Left) 100 LPI metallic woven wire mesh and right) 70 LPI electroformed micro-mesh.

The cathode

The cathode is based on an electroformed 5 μm thick micro-mesh manufactured by Precision Eforming LLC, that presents an optical transparency of 90 % for the passage of the UV photons to the PMT. It consists of a set of intertwined metallic bars made of copper to form square holes of 344 μm in steps of 365 μm (70 LPI, line per inch). The cathode is placed 1.6 cm below the PMT. Furthermore, to protect the PMT from the high voltages applied to the cathode that can reach 24 kV for a drift field of 2 kV/cm, an additional screening mesh was installed 1 mm below the PMT surface and 1.5 cm above the cathode. The screening mesh is also a 70 LPI electroformed copper micro-mesh. The total transparency for the passage of the UV photons to the PMT of the set of meshes is 81 % [115].

The segmented anode

The pixelized anode gives information of the two-dimensional localization of an interaction inside the active area of the TPC, in addition to the deposited energy in such of interaction. For this reason, its design must be optimized to achieve a compromise between a good energy resolution and a good transverse spatial resolution. Both properties of the detector performance depend, among other things, on the pixel size inside the sensitive area of the anode. A reduction on the pixel size is good to reach a high spatial resolution but at the expense of worsening the energy resolution, since charge sharing effects due to diffusion become more important. Moreover, some technical constraints should be taken into account when selecting the pixels size. The total number of pixels is limited by the number of tracks that can be connected. The granularity is therefore limited by the minimum distance between PCB (Printed Circuit Board) tracks. In the case of XEMIS1, the anode is segmented in 64 pixels or pads of 3.1 x 3.1 mm^2 that gives an active area of 2.5 x 2.5 cm^2. A frontal view of of the anode where the 64 pixels can be identified is presented in Figure 3.5.

Besides the relevance of the anode in terms of energy and spatial resolutions, its mechanical design and the different materials that compose it are also of primary importance. The anode in XEMIS1 is not only used to collected the ionization signal but it also works as the entrance window for the incoming radiation, being responsible for the insulation between LXe and vacuum. This implies that the mechanical structure of the anode has to support both temperatures close to the LXe temperature and pressure differences of the order of 1 to 2 bar without any important deformation or delamination. The anode has therefore represented an important challenge in the development of XEMIS1.

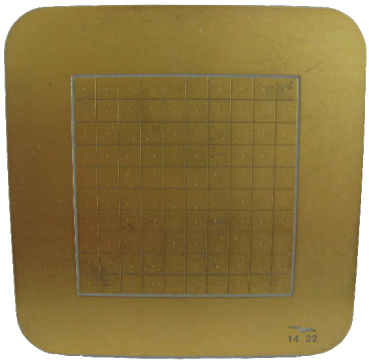

Figure 3.5 – Frontal view of the anode used in XEMIS1. The anode has a total surface of 51 x 51 mm^2 and it is segmented in 100 pixels of 3.1 x 3.1 mm^2. The ionization signal is collected by the 64 internal pixels resulting in an active area of 2.5 x 2.5 cm^2. The 36 pixels at the edges of the anode are connected to ground.

The anode consists of a multilayer structure composed of seven main layers with a total thickness of 2.6 mm. Figure 3.6 shows a schematic design of a transversal cut of the anode. It has four copper layers called Top, Layer2, Layer3 and Bottom. The Top layer, which is directly in contact with the LXe, has a thickness of 40 μm and is responsible for charge collection. To isolate the Top layer from the next copper surface, Layer2, three sheets of prepreg with a total thickness of 147 μm are used. Layer2 has a total thickness of 46 μm. The prepreg, abbreviation of preimpregnated, refers to a fiberglass reinforced substrate which has been preimpregnated with a resin system such as epoxy. The prepeg coat serves also as bonding between the two copper electrodes to form an integrated structure. Equally, between Layer2 and Layer3, there is a 2 mm thick dielectric coating based on alternate layers of Rogers RO4350B ceramic laminates and prepreg. Both ceramics and prepreg present good mechanical resistance and they are good insulators. Moreover, both materials have a thermal expansion coefficient similar to that of the stainless steel and copper, which is important to provide good dimensional stability when the system cools down to the LXe temperature. Layer3 is finally separated from the last copper foil, Bottom, through a prepeg coating of 147 μm in thickness. Layer3 and Bottom are, respectively, 46 μm and 40 μm thick. Figure 3.7 shows the four copper layers that make up the anode.

In this multilayer structure the copper layers serve as the structural units while the prepreg and ceramics provide dielectric insulation between adjacent layers of copper, in addition to minimize electrical signal loss, reduce the crosstalk between conductive layers and reduce the electronic noise. The electrical connection between the copper layers through the dielectrics is made via conductive plated-through holes created by either laser or mechanical drilled. In Figure 3.6 the pathway via are also illustrated. The signal induced in a pixel is transmitted from the Top layer to the Bottom one through this plated-through via. Due to the anode is used as the entrance window for the incoming radiation in the TPC and thus, it is in direct contact with the LXe, to prevent a LXe leak from the TPC to the vacuum container, the different layers are not communicated with one another through the same plated hole. Instead, the layers are communicated through a series of L-shaped drilled holes as depicted in Figure 3.6.

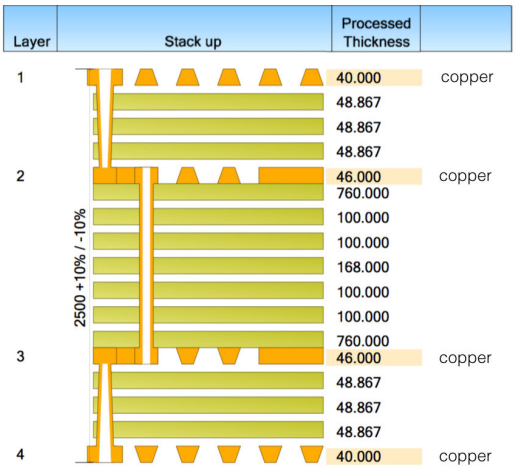

Figure 3.6 – Transversal cut of the segmented anode. The layers 1, 2, 3 and 4 correspond to Top, Layer2, Layer3 and Bottom respectively. Between the four copper layers there are alternate layers made of ceramics and prepeg for insulation and bounding. The thickness of the different layers is expressed in μm.

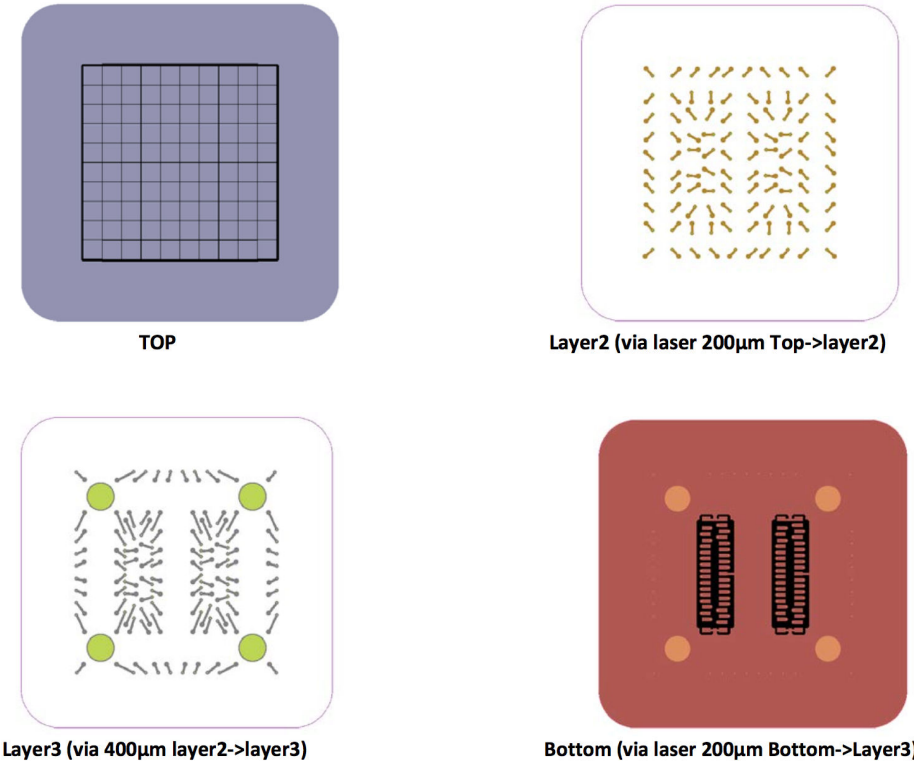

Figure 3.7 – Illustration of the four main layers of the segmented anode used in XEMIS1.

Each pixel of the anode has its own pattern of plated holes between the different layers to collect the ionization signal. The design is made to minimize and equalize the length of the conductive tracks between the copper layer for all the pixels, with the aim of minimizing the electronic noise. In the Bottom layer, pixels are wire bonded directly to the ASIC electronics through two standard 32 channels vertical mini edge card connectors.

3.1.4 Cryogenics Infrastructure

During operation, XEMIS1 runs at a stable temperature of 171 K and a pressure of 1.25 bar. Pressure and temperature stability are crucial to maintain the LXe at a steady state during long data-taking periods, since both ionization and scintillation yields vary with temperature. For this reason, an advanced and reliable cryogenic system is required. A schematic diagram of the XEMIS1 LXe cryogenic installation is shown in Figure 3.8. The cryogenic system consists of: a double-walled stainless steel vessels that host the TPC, an external double-walled vacuum-insulated stainless steel vessels used for thermal insulation, and a *cooling tower*. A Pulse Tube Refrigerator (PTR) especially developed for LXe applications is used to liquefy the xenon and maintain the temperature of the system constant. A gas-phase purification system is used to achieve high purity levels of the LXe, which is essential to measure the ionization signal. This purification system requires the continuous circulation of the xenon to evaporate it and re-condense it after purification. An effective heat transfer between the boiling and condensing xenon during circulation is achieved by means of a coaxial heat exchanger. Because of the narrow temperature margin between xenon normal boiling point (165 K) and the triple point (161 K) (see Figure 6.26), a set of security systems and a rescue tank have been introduced in order to recuperate the xenon in case of necessity. In addition, a Slow Control System allows a continuous control and monitoring of the cryogenic infrastructure.

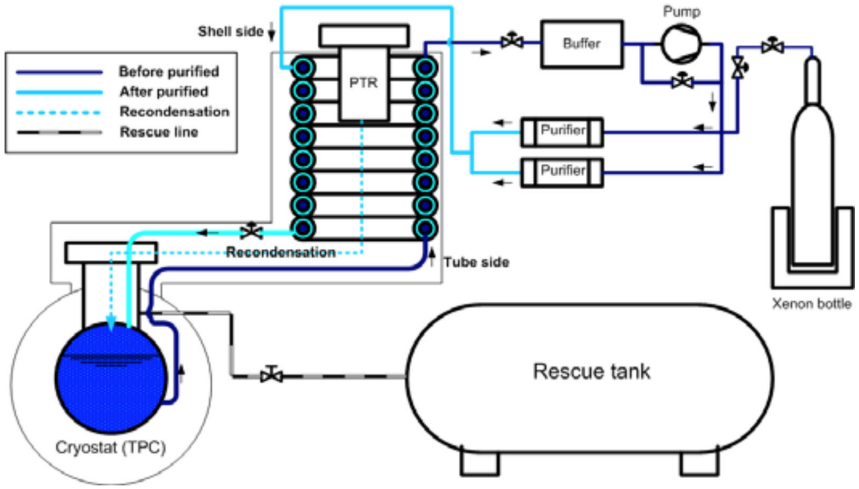

Figure 3.8 – Schematic diagram of the XEMIS1 LXe cryogenic system. Figure taken from [180]

Xenon Cooling System

The main part of the cooling system of XEMIS1, responsible of liquefying and keeping the xenon at constant temperature, is based on a Iwatani PC150 PTR specially developed and optimized for LXe cryogenics. The PTR was originally designed at KEK (The High Energy Accelerator Research Organization in Japan) and it provides stable cooling power up to 200 W at 165 K [181, 182]. The maximum cooling power is achieved when the PTR is connected to

a water-cooled helium compressor (CryoMini Compressor OW404 commercialized by Iwatani / CW701) with nominal input power of 6.5 kW. The PTR provides the necessary cooling power to compensate the expected heat load of 80 W leaked into the detector due to thermal losses. In Figure 3.9, a picture of the Iwatani PC150 PTR and the available cooling power as a function of the cold head temperature are shown. As we can deduce from the plot, a cooling power of 200 W is required to maintain the temperature of the cold head at 165 K.

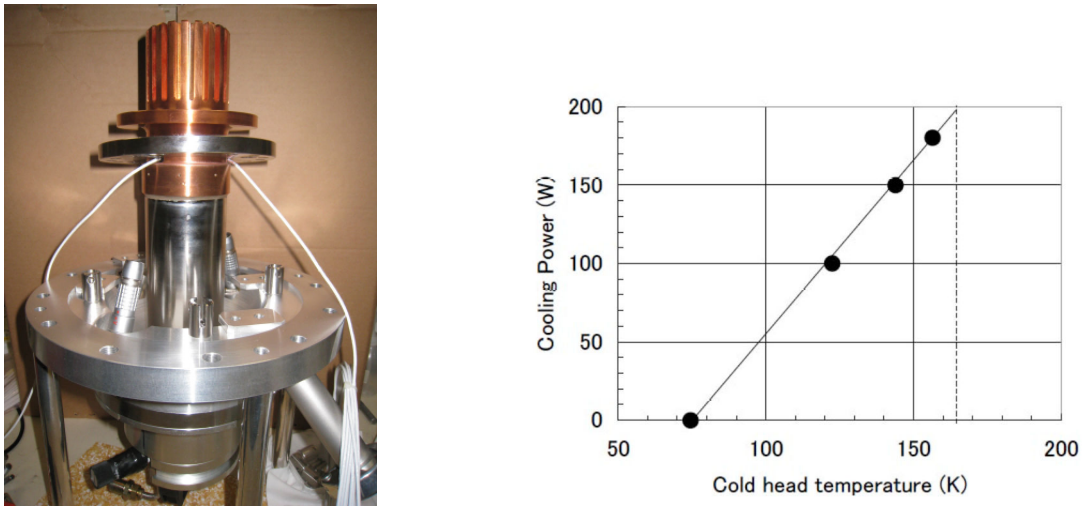

(a) **(b)**

Figure 3.9 – (a) Iwatani PC150 pulse-tube cryocooler and (b) available cooling power (heater power) versus cold head temperature [183] (right).

In XEMIS1, the liquefaction process does not take place in the cryostat itself but in a separate vessel called the *cooling tower*. The cooling tower is located about 50 cm above the detector volume and it consists of a double-walled vacuum-insulated container made of stainless steel. The PTR is placed on top of the cooling tower and outside the vacuum vessel. The cooling power is then transferred to the system via the *cold head* of the PTR which is integrated inside the vacuum enclosure. The distance between the cryostat and the PTR is extended to $\sim$ 2 m to reduce mechanical noise [180]. A cross-section of the cooling tower is shown in Figure 3.10. The vacuum insulation of the cold part of the cryogenic system is important to reduce the heat transfer between the outside and the LXe and hence, to maintain the required temperature constant with a minimum cooling power.

The PTR and the cold head are not in direct contact with the xenon but they are coupled to a copper plate known as *cold finger*, which is the actual responsible of the gas xenon liquefaction (see Figure 3.10). The coupling is made by a set of indium foils for optimal heat transfer. The PTR is then connected to the cryostat via a double-walled tube. This tube allows the gas xenon from the upper part of the cryostat to pass through the cooling tower for liquefaction. If the temperature is low enough, xenon condenses on the cold finger. Afterwards, the drops of liquefied xenon are recuperated in a stainless steel funnel and guided into the tube to return into the cryostat. The cold head of the PTR is also equipped with an ohmic resistor acting as a heater to compensate any excess of cooling power of the PTR. The cold head of the PTR, heater and all temperature sensors are within vacuum insulation

and cover by a Multilayer insulation (MLI) in order to avoid radiative heat transfer. The separation of the PTR from the xenon via the cold finger was first implemented for the XENON10 experiment [184]. This design reduces the number of impurities released into to the LXe and facilitates the replacement of the PTR without exposing the inner vessel into the air since the cold tower is hermetically closed by the cold finger.

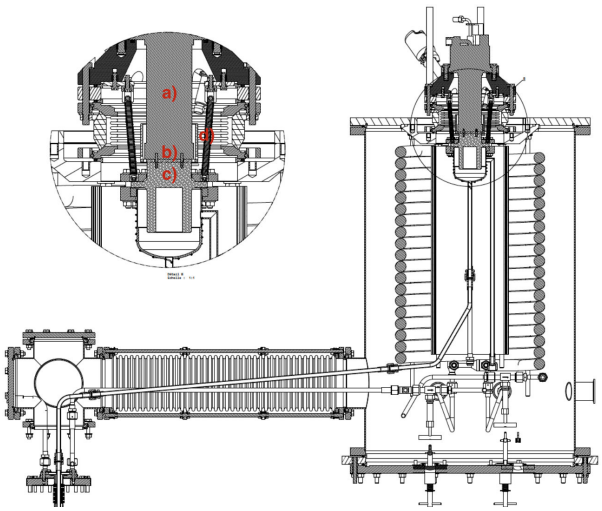

Figure 3.10 – Cross-section of the cooling tower of XEMIS1, showing a) PTR, b) cold head, c) cold finger and d) heater.

In order to control and monitor the overall temperature of the system, a set of 7 pt100 sensors are placed to control the temperature during all cryogenic process. These sensors measure for example, the temperature of the cold head and the cold finger. The cooling power of the PTR can be adjusted by fixing the temperature of the cold head. The desired temperature of the LXe can be set and maintain constant by controlling the power supplied to the heater placed on the cold head using a Proportional-Integral-Derivative (PID). This PID regulator is necessary due to the only way to control the temperature of the cold head is in fact by means of the heater. This means that if the cooling power provided by the PTR to liquefy the xenon is higher than the actual power required to maintain the xenon in liquid state, the temperature of the cold head would reach the freezing point and the xenon would start to freeze. Therefore, the PID can regulate the heater power to maintain the temperature of the cold head on the requested value. The heater has a maximum capacity of 100 W, which is enough to counteract the cooling power at all times.

Internal Cryostat and Vacuum Enclosure

Another important part of the cryogenic system is the cryostat itself. The TPC is placed inside a double-walled stainless steal vessel for thermal insulation. The inner vessel is 20 cm in diameter and 35.4 cm high. It contains around 36.5 kg of LXe and its design was made in order to host the TPC and necessary cables with the minimum extra amount of liquid. Due to thermal exchange by convection, the inner container is maintained at LXe temperature. Additionally, in order to maintain the xenon in liquid state and to avoid the possible evaporation of part of the LXe, the thermal exchanges between the cryostat and the

outside are minimized. Both design and materials of the cryostat were optimized to reduce the thermal losses by conduction. The number of tubes that connect the cryostat with the rest of the system are limited. Moreover, all tubes are made of stainless steel which is a bad heat conductor. The cryostat is mounted on a support made of epoxy with a reduced surface to minimize the contact with the outer wall.

To ensure good thermal insulation the inner vessel is placed inside a vacuum container that consist of a double-walled stainless steal vessel. This outer vessel reduces the heat flow into the detector and thus, reduces the required cooling power. Due to the large volume of the whole system, the containers are first evacuated using a set of two primary vacuum pumps to reduce the pressure down to 10^{-2} bar. Then and in parallel to the primary pumps, two turbo-pumps are used to achieve a vacuum level of the order of 10^{-6} to 10^{-8} bar. During normal operation, only a primary vacuum pump and a turbo-pump are continuously running to maintain the pressure level. In addition to the vacuum insulation, multiple layers of aluminized Mylar foil (MLI) are applied between the inner vessel and the vacuum container and also around all tubes and connexion wires to avoid radiative heat transfer. Figure 3.11 shows an internal view of the vacuum vessel that enclosures the cryostat. The system can be optimized by covering the outer flange with MLI. In this way, we can reduce the radiative heat transfer from the outer vessel to the LXe.

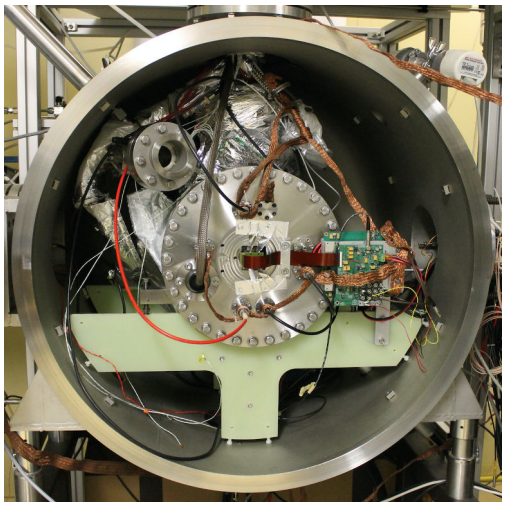

Figure 3.11 – Internal view of the stainless steal vacuum-insulated vessel. The cryostat that contains the TPC is placed inside the vacuum enclosure. All part of the system including the inner vessel, tubes, and the outer flange of the inner vessel that surround the front-end electronics are cover by MLI to reduce the heat load into the detector.

Precooling and Liquefaction Procedures

In addition to the xenon liquefaction, the PTR has the task of lowering the temperature inside the cryostat chamber. The goal of this initial phase, known as precooling, is to reduce the temperature of the cold head and the entire system down to around 165 K in order to start the liquefaction process.

Before starting the precooling the required vacuum level is achieved. Afterwards, 2 bar of xenon are injected into the cryostat. This pressure is enough to reduce the temperature of the whole system without damaging any part of the detector, such as the PMT or the cryostat, that can withstand pressure up to ∼2 bar. Once the gaseous xenon is inside the inner vessel, the PTR is turned on and the temperature of the cold head is set to 165 K. Figure 3.12 shows the temperature variation of the cold finger during the precooling. As we can see, the temperature decreases continuously from room temperature to around 165 K in about 1 hour. At this point the temperature of the cold finger becomes stable, which means that the temperature of the cold head of the PTR is low enough so the xenon starts to condensate in the surface of the cold finger. The drops of liquefied xenon are recuperated by the stainless steel funnel placed below the cold finger which is still warm. This implies that when the liquefied xenon touches the funnel, it will evaporate cooling the funnel progressively. Thanks to these condensation-evaporation cycles of the 2 bar of injected xenon, the temperature of the funnel and the rest of component of the detector including the tubes that connect the cold finger with the cryostat and the cryostat itself, falls to 165 K in less than 24 hours. The time required to cool the whole system depends on the quality of the insulation. Figures 3.13 and 3.14 shows both temperature and pressure profiles during the precooling until achieve stability. The pressure inside the chamber decreases gradually to 0.9 bar. The pressure fluctuations observed at the beginning of the precooling are the result of liquid drops that fall and touch the bottom of the cryostat which is still warm. When this happens, the pressure rises rapidly. However, these pressure increases are far from the pressure security value of 1.8 bar, and thus they are harmless to the detector. The precooling stage can be accelerated by injecting more xenon in gas state once the heater starts to compensate the extra cooling power of the PTR. The cooling power required to liquefy the xenon will be reduced if the temperature of the system is low enough before starting the xenon injection.

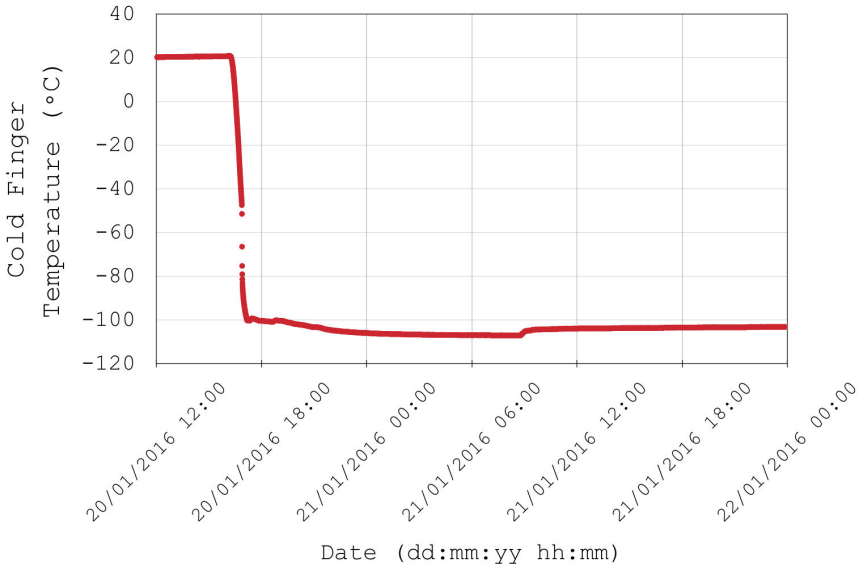

Figure 3.12 – Temperature profile of the cold finger during the precooling phase.

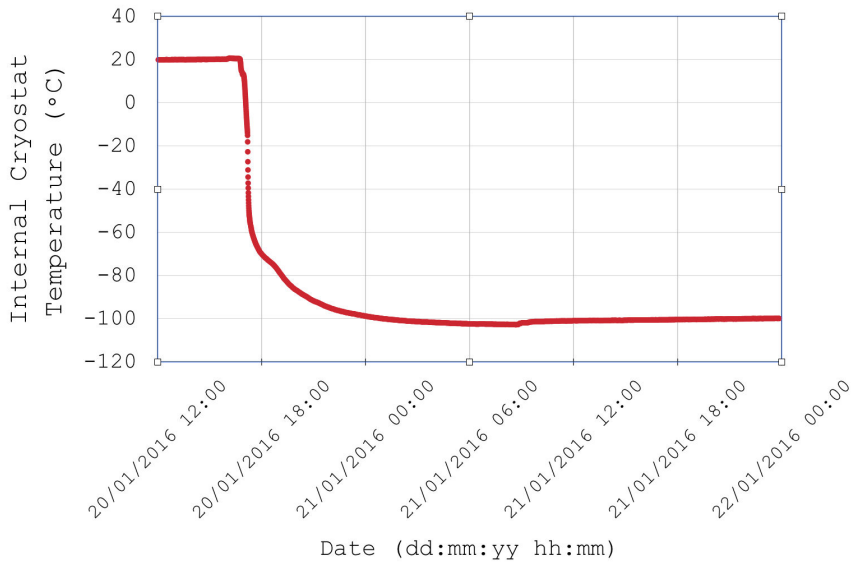

Figure 3.13 – Temperature profile of the internal cryostat during the precooling phase.

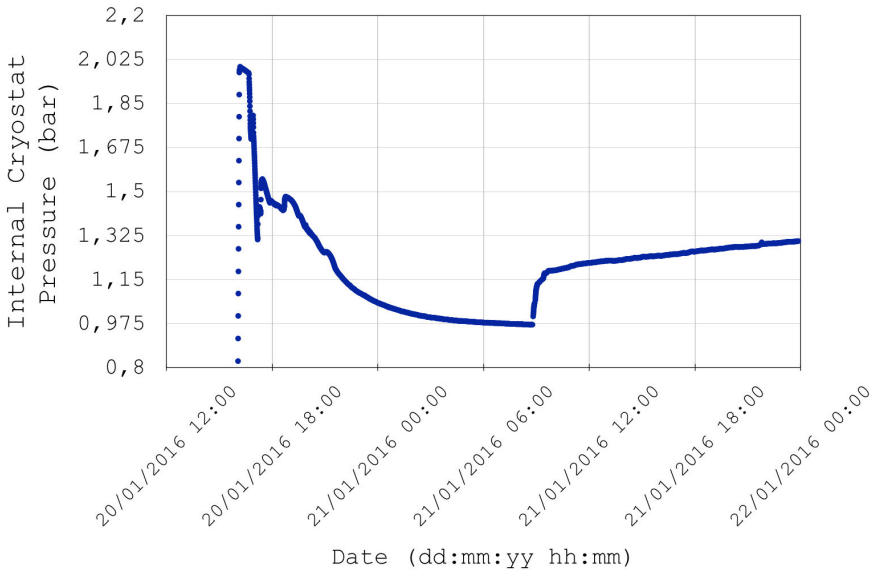

Figure 3.14 – Pressure profile of the internal cryostat during the precooling phase.

Once the cryogenic system is cooled down sufficiently, we can start filling the inner vessel with GXe. The gas injection should be made progressively to avoid an excess of pressure inside the chamber that could damage the detector. The gas flow depends on the pressure difference between the storage bottle and the system. When the pressure inside the bottle decreases, the flow rate into the chamber rises, increasing consequently the pressure inside the cryostat. For this reason, to compensate the pressure variations during gas injection a Mass Flow Controller (MFC) is placed between the injection valve, that regulates the gas flow that gets out the bottle, and the cryostat. The gas flow is set to 5 l/min during all liquefaction process. Since the temperature inside the detector is low enough, the gas is immediately condensed at the cold finger and the detector is completely filled with liquid in

about 24 hours. The amount of LXe can be controlled by monitoring the mass of the storage bottle or by measuring the level of LXe inside the cryostat. The level of LXe is measured thanks to a liquid level meter placed at the bottom of the chamber (see Section 3.24). The xenon mass variation inside the storage bottle and the level of LXe inside the TPC are presented in Figure 3.15(a) and 3.15(b) respectively. In both cases, the amount of xenon varies progressively during the liquefaction process. The drastic variation on the level of LXe inside the chamber from zero to 2.8 cm is due to the position of the liquid level meter with respect to the bottom of the cryostat. In less than 1 day, the detector is full with around 20 cm of LXe. A reduction of about 2 cm in the level of LXe is produced when the circulation process starts, since a constant amount of LXe remains inside the connecting tubes during circulation. The cryogenic system is ready to start the LXe circulation and purification after 36 hours of cooling.

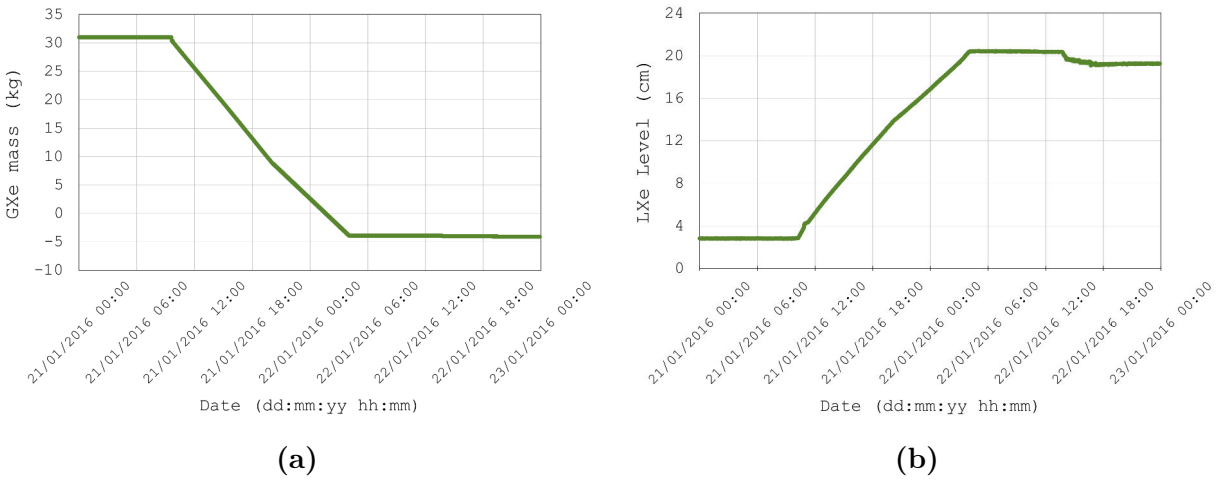

(a) **(b)**

Figure 3.15 – (a) GXe mass variation inside the storage bottle and (b) LXe level variation inside the cryostat during liquefaction.

Xenon Purification and Recirculation Systems

The detector performances are limited by the level of purity of the LXe. If the purity is not good enough, the drifting electrons may be absorbed by electronegative impurities such as O_2 or N_2 before being collected by the anode. Moreover, the presence of water inside the detector, as main contaminant, may also degrade the scintillation signal. For this reason, in order to achieve and maintain an adequate level of purity, constant circulation of the xenon through a purification system is required. In XEMIS1, the purification system is based on two rare-gas purifiers connected in parallel, which consist of a high-temperature SAES MonoTorr Phase II getter, model PS4-MT3-R/N, based on zirconium (see Figure 3.16). This kind of purifier provides output impurity levels below 1 part per billion (ppb) O_2 equivalent [185].

With such a purification system, the xenon must be in a gaseous state, so it has to be continuously evaporated and condensed by a re-circulation system. The circulation is driven by an oil- free membrane pump that creates the required pressure drop to pump up the xenon from the cryostat and send it to the getter (see Figure 3.17) [186]. The pump can provide a maximum circulation rate of 50 NL/min.

Figure 3.16 – XEMIS1 rare-gas purifier.

Figure 3.17 – Oil-free membrane pump used to recirculate the xenon during purification.

The continuous phase changes from gas to liquid and vice versa, require a considerable amount of energy. For a flow rate of 3 liters per minute, the power required to decrease the temperature from 165 K to room temperature is about 13 W (specific heat of xenon is 0.34 kJ/kg°C at 1 bar). Additionally, another 28 W are needed for the phase change from GXe to LXe (latent heat of xenon 96.26 kJ/kg). This means that for a circulation rate of 3 liters per minute at least 41 W are required to re-liquefy the purified xenon. Without a heat exchanger incorporated to the set-up all this cooling power is provided by the PTR, which implies that the flow rate is limited by the available cooling power. For circulation rates higher that 15 liters per minute, even the maximum cooling power delivered by the PTR would not be enough to liquefy the xenon. In fact, if we also take into account the thermal load leaked into the detector, a maximum circulation rate of the order of 3.8 liters per minute is achieved without heat exchanger. With a gas flow of 3.8 liters per minute only ∼38 % of the total volume of LXe is purified per cycle [115].

In order to mitigate the heat load required by these phase changes and to achieve an effective thermal transfer between the boiling and condensing xenon, a coaxial heat exchanger

has been installed in XEMIS1. It consists of a stainless steel 22.5 cm long hollow tube with a diameter of 48.26 mm, which has been bent to form a ∼1 m height cylindrical shape. The XEMIS1 heat exchanger is presented in Figure 3.18(a). The concentric tube is placed inside a vacuum enclosure for thermal insulation as shown in Figure 3.18(b). To optimize the heat transfer between the evaporating liquid stream and condensing gas stream, the gaseous xenon that returns into the detector enters the heat exchanger through a thinner tube of 17.08 mm in diameter. This tube is contained inside the main tube on the side of the exchanger that collects the GXe after purification, known as tube side (see Figure 3.8). Outside the thin tube, the xenon remains in gas state, so the heat transfer to re-condense the xenon is made around this thiner tube. The heat exchanger is placed ∼50 cm above the cryostat and coupled to the PTR to tackle space constraints and also to insulate the PTR through the heat exchanger.

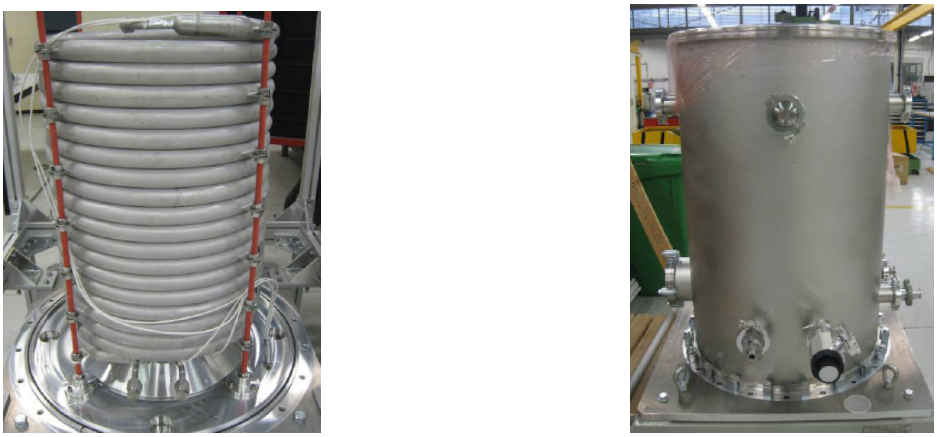

(a) **(b)**

Figure 3.18 – XEMIS1 coaxial heat exchanger.

During normal operation, the xenon is pumped out the cryostat thanks to the circulation pump and passes through the heat exchanger where it is evaporated. Afterwards, the gaseous xenon flows through the getter for purification. The gas flow can be measured by a MFC and controlled manually by a valve placed between the outlet of the heat exchanger and the circulation pump. After purification, the xenon returns into the detector volume through the tube side of the heat exchanger where it is re-condensed. The maximum circulation flow rate achieved with XEMIS1 is 32 liters per minute, which implies that almost the total volume of xenon can be purified continuously. An schematic diagram of the re-circulation process is also illustrated in Figure 3.8. The integration of a coaxial heat exchanger in the circulation system with respect to a previous prototype based on a parallel-plate heat exchanger [115], has led to a great improvement not only on the performances of XEMIS1 but also on the development of a bigger scale LXe Compton telescope prototype such as XEMIS2 [115].

In terms of operational effectiveness, the heat exchanger was designed in order to achieve an efficiency of 95% for a re-circulation rate up to 50 NL/min (4.92 g/s). This efficiency was estimated for a pressure difference of 0.5 bar between both sides of the heat exchanger and a temperature difference of 6 K at the cold end. At detailed study of the performances of the heat exchanger used in XEMIS1 as a function of the gas flow has been performed by Chen

et al. [180]. As we can see in Figure 3.19(a), an efficiency of the order of 99%, better than the expected value, is achieved even at high gas flows. This means that during circulation less than half of the available cooling power is used to compensate heat leaking into the detector (about 80 W of thermal losses has been estimated for XEMIS1), since heat exchange with an efficiency of the order of 99% up to a flow rate of 32 liters per minute is possible. With the XEMIS1 re-circulation and purification systems, we achieve electron drift lengths greater than 1 m after 1 week of circulation. Figure 3.19(b) shows the estimated cooling power required to keep stable the pressure inside the cryostat as a function of the gas flow when using the coaxial heat exchanger. As we can observe thanks to heat exchanger the required cooling power is almost the same regardless the circulation rate, except for very low deliveries. We achieve good stability levels in both pressure and temperature during long data-taking periods. Figure 3.20 and Figure 3.21 shows the evolution of the LXe temperature and pressure, respectively, during several months of continuous operation.

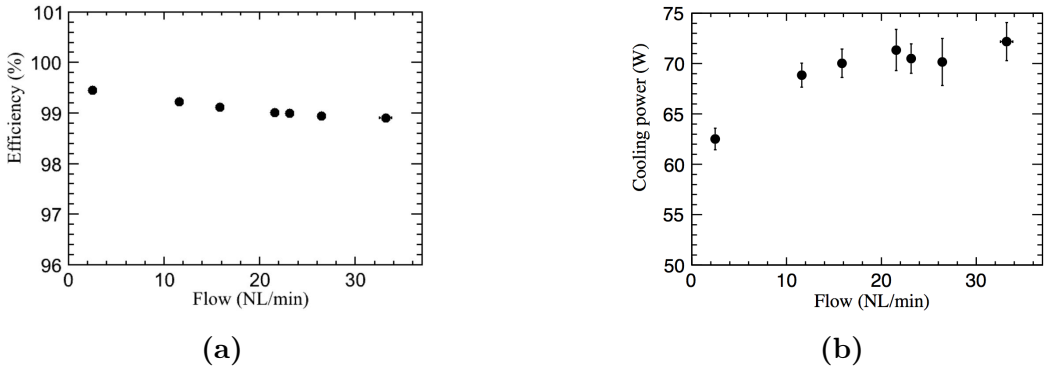

Figure 3.19 – (a) Heat exchanger efficiency calculated as a function of gas flow [180]. (b) Estimated cooling power as a function of gas flow [180].

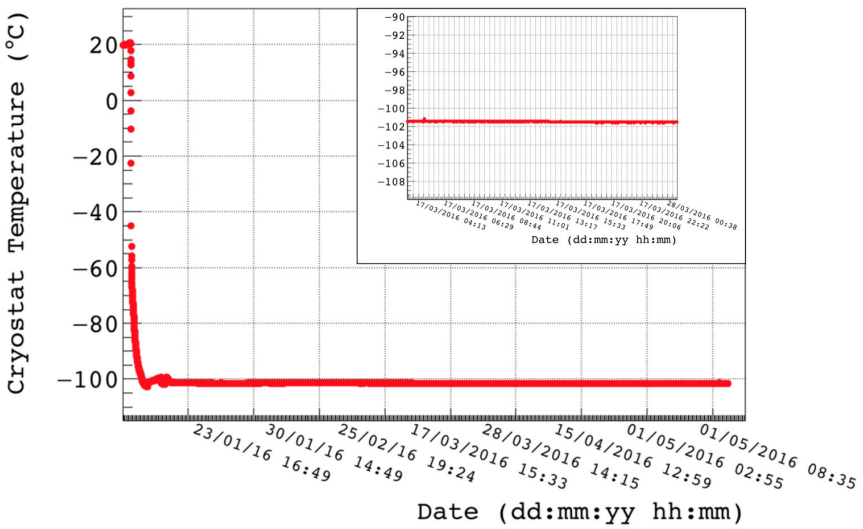

Figure 3.20 – Temperature inside the internal cryostat during circulation.

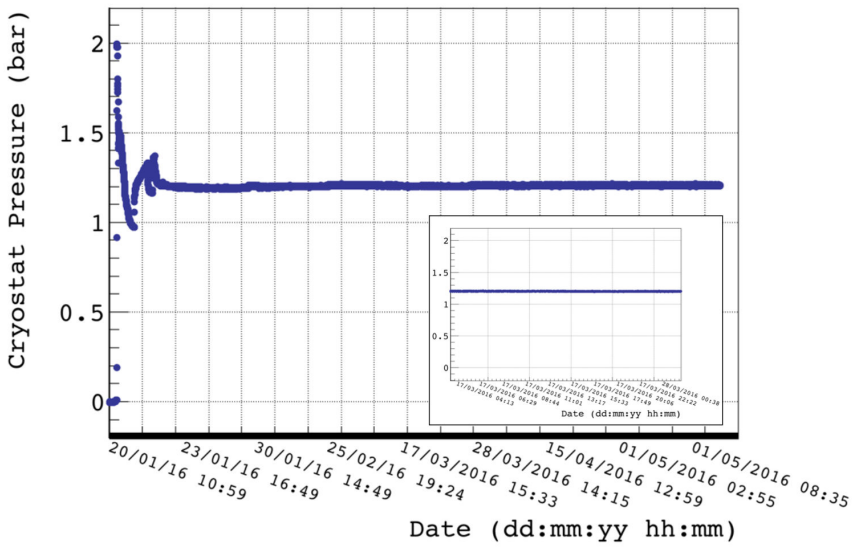

Figure 3.21 – Pressure inside the internal cryostat during circulation.

Xenon Storage and Recuperation

Whenever the detector is not running, the xenon is stored in gaseous state in a stainless steel bottle where the xenon is kept at a pressure of 60 bar. Figure 3.22 shows the high pressure storage bottle and the connexion to the injection valve. During operation the bottle is isolated from the rest of the set-up through this valve. A pressure regulator is used to monitor the pressure inside the bottle. A second empty bottle is also installed in case the xenon has to be immediately recuperated during operation.

Figure 3.22 – High pressure bottles used to store the gaseous xenon when the detector is not in use.

When the cryostat needs to be emptied, the xenon is recuperated during a process known as cryopumping. This process is based on cooling down the temperature of the bottle that contains the xenon when the set-up is not operational, so the pressure difference between the detector and the storage bottle will force the gaseous xenon to flow from the detector to the bottle. For recuperation, a dewar that surrounds the storage bottle is filled with

liquid nitrogen, so the container is cooled down to a temperature of around 77 K. The temperature of the bottle is therefore lower than the xenon freezing point (161 K). The valve that separates the bottle from the system is opened, so GXe from the detector volume flows into the cool bottle and it immediately sublimates on its walls. Since all the gas freezes, the pressure in the bottle remains low and the xenon will keep flowing to the storage vessel. During the cryopumping the PTR is turned off. A second heater also based on an ohmic resistance is located at the bottom of the cryostat to help the xenon evaporation and hence to increase the recuperation rate. The gas flow is limited by the evaporation of the xenon inside the detector, which avoids the xenon to freeze inside the detector. In addition, the primary vacuum pump and the turbo-pump are switched off preserving a static vacuum inside the chamber. After all xenon is recuperated, the injection valve is closed and the bottle starts to heat up. Once the temperature of the bottle drops to room temperature, the xenon will remain inside the storage container in gaseous form. The complete cryopumping procedure takes about 6 hours (see Figure 3.23). The temperature of the outer and inner vessels rises above 0 °C in around 12 hours. At this moment, the chamber can be opened ensuring that no ice is formed on the interior walls.

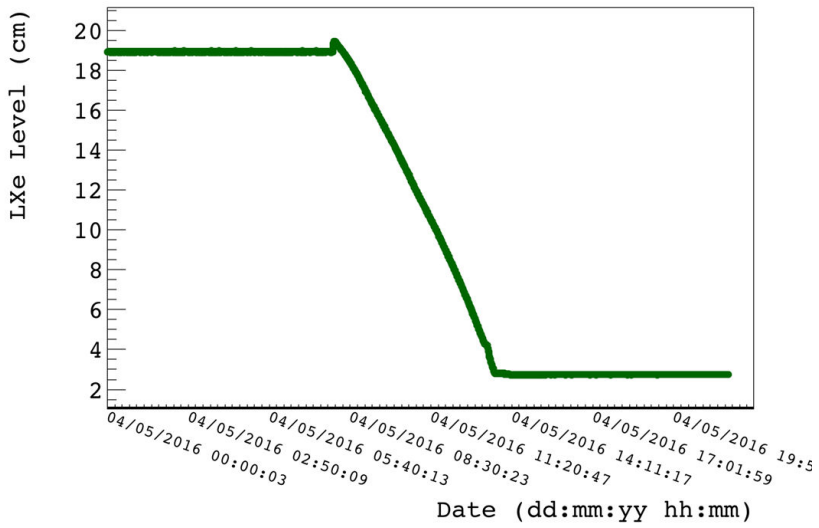

Figure 3.23 – Evolution of the LXe level inside the cryostat during cryopumping.

Slow Control System

A Slow Control System (SCS) was developed using LabView to constantly monitor the essential values of the experimental set-up such as temperature, pressure, LXe level, gas flow rate and heater power. Figure 3.24 shows a screen shot of the slow control system of XEMIS1. A total of 26 parameters are monitored and continuously saved to a file every 1 to 5 seconds. The continuous data acquisition allows the user to access the stored information at any particular moment. In addition, the SCS allows access to all the variables monitored over the last 24 hours and provides real-time plots of the different parameters. The SCS also includes an alarm system that sends a text message when the temperature or pressure inside the cryostat approach a critical value. The alarm is also sent whether the vacuum inside the chamber is altered.

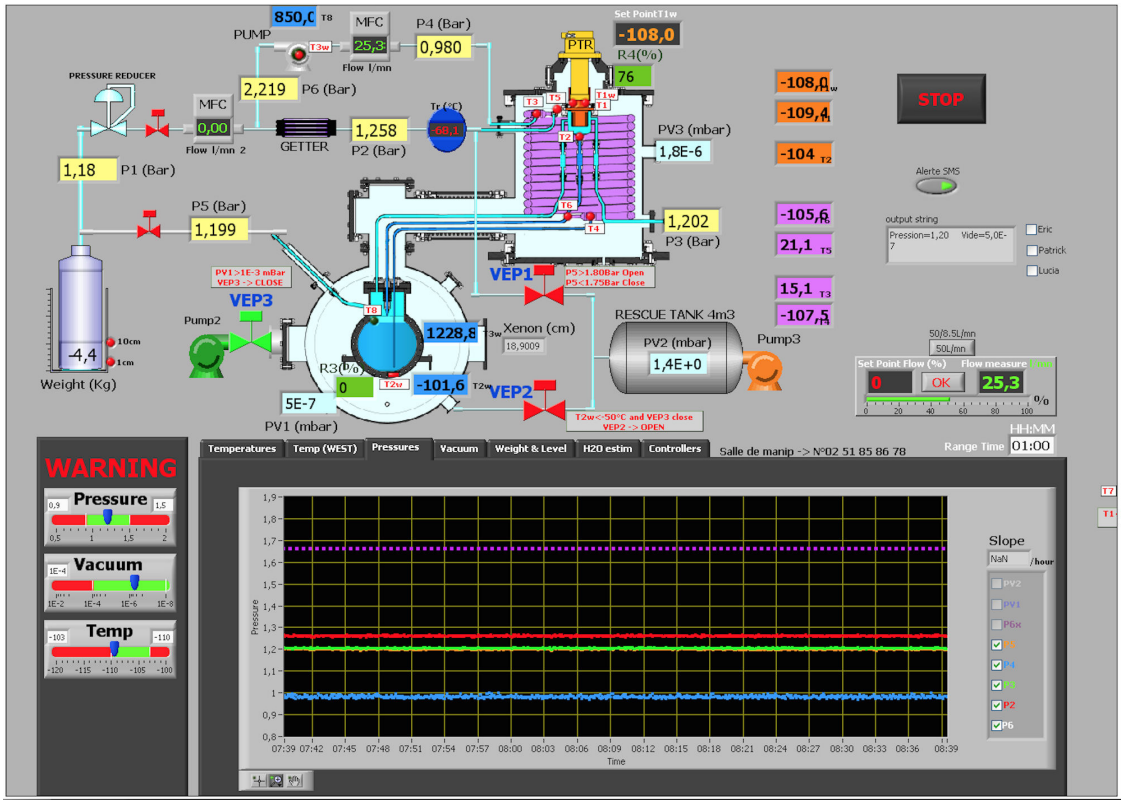

Figure 3.24 – Screen shot of the slow control system used in XEMIS1.

Pressure monitoring inside the system is of crucial importance, not only for operation but also in terms of safety. The PMT and the anode support pressures up to 2 bar. Above this value, permanent damages can be inflected to the detectors. Equally, pressures higher than 3 bar can damage the membrane of the circulation pump. The pressure is controlled inside the chamber, in the purification and circulation systems and also in the storage bottle that collects the GXe when the detectors is not in use. These are measured by an absolute pressure sensor with a pressure range of 0 - 3 bar. The pressure measurement is converted to an electric signal with typical output of 4 - 20 mA. The signal is transmitted to a programmable logic controller and then sent to the computer for monitoring and registering.

Temperature at the main parts of the experimental set-up is controlled by 10 pt100 temperature sensors. We can highlight cold head and cold finger temperature measurements, indispensable during the precooling and liquefaction process, as well as a set of pt100 sensors to control the temperature at heat exchanger inlet and outlet, and at the bottom of the cryostat. Temperature control is important due to the narrow margin between the xenon boiling point and triple point. The freezing of xenon inside the chamber can reduce the performances of the detector and even cause irreversible damages. The level of LXe inside the cryostat is measured by a capacitive sensor manufactured by American Magnetics Inc. The sensor is place around 2 cm above the bottom of the cryostat, which means that no information of the level of LXe inside the chamber are available below this value. Alternatively, the amount of xenon inside the chamber can be controlled by a balance placed under the storage bottle. The difference between the weight of the bottle before and after the injection of GXe into the chamber provides information of the volume of xenon inside

the cryostat. The gas flow is monitored during both the injection phase and re-circulation process by a MFC from Bronkhorst High-Tech. Finally, the vacuum insulation is controlled by means of a standard vacuum gauge.

Safety Systems

During a data-taking period XEMIS1 runs continuously for several weeks or even months, which means that the detector should be able to work in the absence of lab personnel. In case of cooling power failure the system should be ready to recuperate immediately the xenon to protect the workers and the detectors, and also to avoid a potential loss of xenon. If the PTR or any component of the cryogenic system stop running due to, for example, a power outage, the xenon will start to warm up and the pressure inside the detector will start to increase. To limit the pressure inside the chamber a pneumatic valve shown in Figure 3.25(a) is included in the set-up as a safety device. The valve opens at a pressure above 1.8 bar, so the detector is never exposed to pressure levels that could damage the different components of the TPC. When the pneumatic valve opens, the xenon is sent to a $4m^3$ rescue tank (see Figure 3.26). Once the pressure inside the chamber falls below 1.8 bar, the valve closes off. Since this pneumatic valve requires power supply, after an electrical failure the valve will not work. For this reason, a second safety device based on a burst disk is also included (see Figure 3.25(b)). The goal of this disk is exactly the same as the valve. It opens if the pressure inside the cryostat exceeds 2 bar. However, once the burst disk is opened all xenon is recuperated in the rescue tank. The rescue tank can host 35 kg of xenon is gaseous state at a pressure of 1.6 bar. The tank is maintained at a vacuum level of the order of 10^{-2} bar thanks to its own primary vacuum pump. To prevent freezing due to an important pressure drop, a one-way valve is located before the tank inlet.

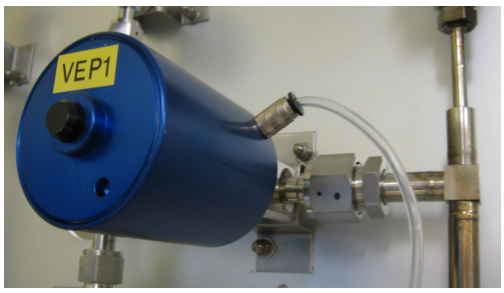

(a) Pneumatic Valve

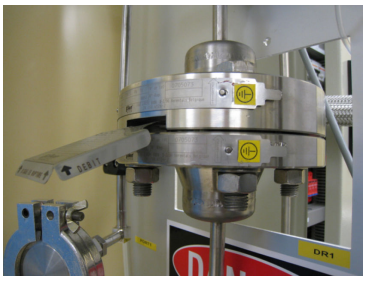

(b) Burst Disk

Figure 3.25 – XEMIS1 pressure security systems

Moreover, to overcome an electricity cut, two backup power supply systems are incorporated to the set-up: an Uninterruptible Power Supply (UPS) and a power generator. The UPS provides emergency power supply with a typical autonomy of 15 minutes after an electrical failure. In addition, the UPS provides near-instantaneous protection from input power interruptions. Immediately after the UPS starts, the generator starts up providing power supply to the detector during a maximum of 12 hours. After a power failure the system is allowed to warm up for at least 2 hours before the pressure achieves a critical value. The laboratory personnel is notified by the slow control alarm system, which means that 12 hours

are enough to restore power or to perform the cryopumping procedure to recuperate the xenon.

Figure 3.26 – 4 m^3 rescue tank used to recuperate the xenon is case of emergency.

3.2 XEMIS2: A small animal imaging LXe detector

3.2.1 Detector description

A small animal imaging LXe Compton telescope called XEMIS2 is currently under development as a prototype for quantifying the potential benefit of the 3γ imaging technique in terms of injected dose. The design of the system is based on a cylindrical camera filled with LXe that completely covers the whole animal. This particular geometry maximizes the FOV and thus, increases the sensitivity. A general view of the experimental set-up of XEMIS2 is presented in Figure 3.27, that includes the XEMIS2 cryostat and the cryogenic infrastructure used to store, liquefy and recuperate the xenon. The purification and recirculation systems are presented in Figure 3.28.

Figure 3.27 – General view of the XEMIS2 experimental set-up installed in Subatech laboratory: right) XEMIS2 cryostat and left) Recovery and Storage of Xenon (ReStoX).

Figure 3.28 – General view of the XEMIS1 experimental set-up installed in Subatech laboratory: right) Recovery and Storage of Xenon (ReStoX) and left) purification system.

XEMIS2 consists of a cylindrical TPC full of LXe with a total drift volume of 26.7 x 26.7 x 24 mm^3. Figure 3.29 illustrates a design of the active zone of XEMIS2. At detection level, the camera is composed by two identical TPC arrays placed back to back and separated by a shared cathode. The active zone of the detector is a cylinder of 7 cm of inner radius, 19 cm of outer radius and 24 cm of total depth (12 cm for each TPC array). The active volume is completely covered by 380 Hamamatsu PMTs to detect the VUV scintillation photons (178 nm) generated after the interaction of a γ-ray with the LXe. Two circular segmented anodes are located at the edges of the active zone. A total amount of 24000 pixels of 3.125 x 3.125 mm^2 size are used to collect the ionization signal. A mesh used as a Frisch grid is placed above each anode. To provide a homogeneous electric field between the cathode and the anode, a set of 104 field rings is located around both sides of each TPC.

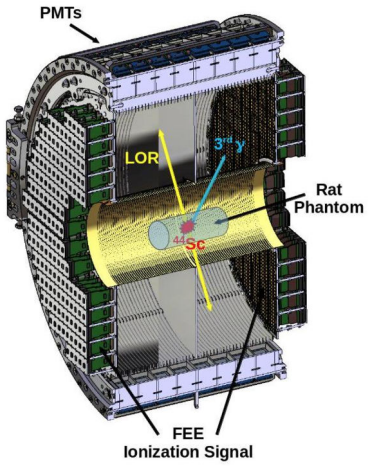

Figure 3.29 – Mechanical design of the active zone of the XEMIS2 prototype for small animal imaging [82].

A schematic diagram of the active zone of XEMIS2 is illustrated in Figure 3.30. For simplicity, the design only shows the upper half of one of the TPCs placed at the right side on the cathode. The other half of the TPC is completely symmetrical. All the dimension are expressed in mm. Each TPC has a drift length of 12 cm between the cathode and the grid. This length is the same as the one used in XEMIS1, and its value was chosen according to the requirements exposed in Section 3.1.1. A gap between the grid and the anode of the order of 100 μm has been chosen in order to reduced the effects of charge sharing. The TPC is divided in two by a hollow 2.5 mm thick tube made of Aluminium. The tube is place outside the chamber and it is in direct contact with the air. In Figure 3.30 only half of the tube is represented. The dimensions of the tube are 100 mm of diameter and a total length of 875 mm. The tube crosses the chamber side to side. The purpose of this tube is to hold the small animal during the medical exam. For this reason, to insulate the animal from the internal temperature of the cryostat and maintain it at room temperature, the tube is separated from the stainless steel inner vessel by a 7.5 cm thick vacuum insulation. The inner container has a thickness of 1.5 mm that separates the LXe from the vacuum. A 7 cm thick Teflon support is added around the inner radius of the stainless steel vessel, that serves both as insulation and to increase the light collection by the PMTs.

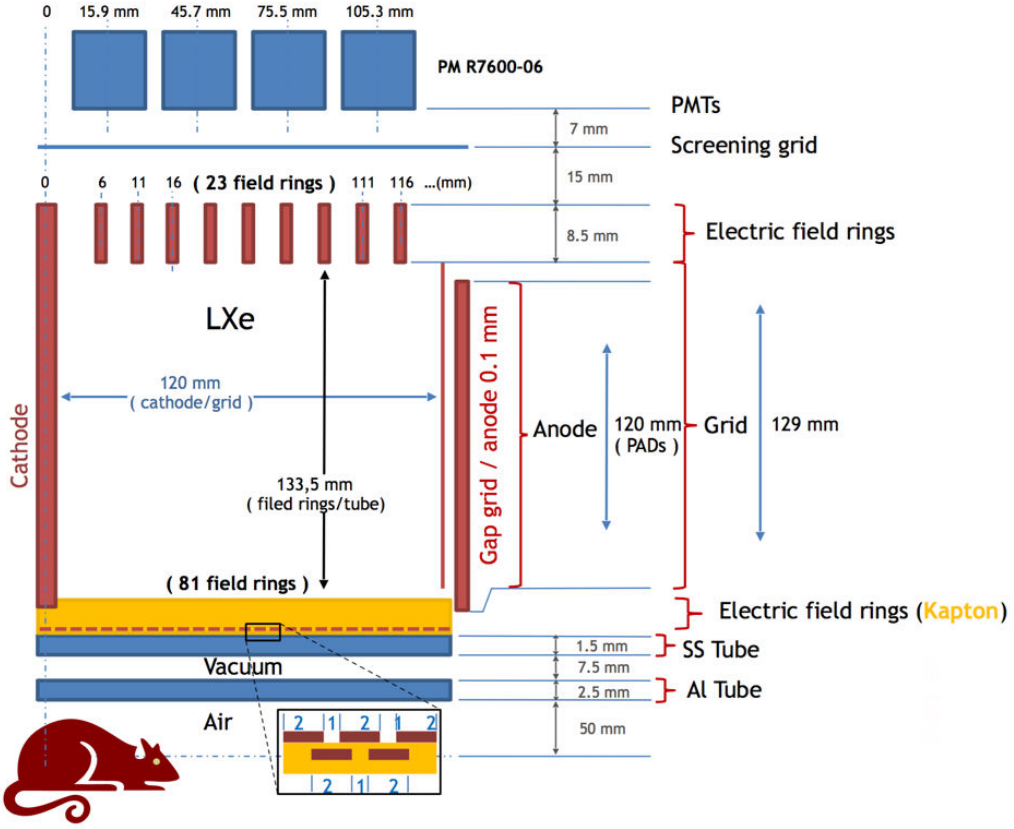

Figure 3.30 – Schematic diagram of the dimensions of XEMIS2. Only half of the right TPC with respect to the cathode is represented.

Each half of the TPC has a radial length of 133.5 mm limited by a external set of 23 stainless steel field rings and an internal set of 81 copper field rings. The external field rings are shown in Figure 3.31. The copper electrodes are a set of interspersed 2 mm tracks with a thickness of 0.35 mm, which are separated 1 mm from each other and located around the inner part of the TPC as illustrated in Figure 3.30. The tracks are directly printed in a kapton support which serves as insulation. These two sets of electrodes are necessary to ensure a homogeneous electric field along the chamber. The sensitive volume of XEMIS2 is then defined by the drift length between the cathode and the grid, and by the intersection area of the segmented anode, which is in total of de order of 24 x 24 x 24 cm^3.

In the same way as in XEMIS1, to ensure a uniform electric field inside the drift volume, two resistive divider chains (one for each set of electric field rings) immersed in the LXe are used to drive the potential from the cathode to the first field ring. Since in XEMIS2 there are two TPC, each of them can be treated independently from one another. Each resistive divider chain is based on 500 MΩ resistors. The last resistor of each chain is connected to ground, whereas the first one is connected to the rim of the high-voltage electrode, which is common for the two detectors. The first copper field ring and the Frisch grid of each TPC are biased through two independent power supplies. Each anode is connected to ground via the front-end electronics.

Figure 3.31 – External 46 stainless steel field rings used to provide an uniform electric field along the drift volume of the detector.

As in XEMIS1, to read-out the collected charge by the pixels of the anode, we use an ultra-low noise front-end electronics based on an IDeF-X HD-LXe 32 channels chips [187]. Each ASIC is connected to 32 pixels, which generates 32 analog signals. To reduce the volume of data produced by 24000 pixels, each IDeF-X is coupled to a new front-end electronics called XTRACT that extracts from each detected signal that crosses a given threshold, the amplitude, time and pixel address. The performances of this ASIC are presented in Section 4.6. The electronics are placed inside a vacuum container allowing a reduction of the electronic noise.

The assemblage and the materials of the different components of the TPCs follows the same principle as the one presented for XEMIS. The device is designed in such a way that the total TPC constituted by the common cathode and the field rings can be mounted independently of the PMTs, which allows a correct adjustment of all the components. The total structure is then assemble together inside a stainless steel cylindrical cryostat. This inner cryostat is located in a vacuum chamber to reduce the convection heat transfer.

3.2.2 Light detection system

In order to detect the scintillation light in XEMIS2, we use a set of 380 VUV-sensitive Hamamatsu R7600-06MOD-ASSY PMT especially developed to work at LXe temperature. The main characteristics of this kind of PMT are reported in Section 3.1.2. The PMTs are located all around the active zone of XEMIS2 and mounted on a stainless steal structure. A picture of the mounting bracket is shown in Figure 3.32. The structure is directly immersed in the LXe. Each PMT has a quartz surface of 26.8 x 26.8 mm^2 with an active area of 18 x 18 mm^2. A distance of 3 mm between PMTs is set by the separation structures, that constitutes a dead zone between PMTs of the order of 20.6 mm.

Figure 3.32 – Mounting bracket for the 380 PMTs used to detect the VUV scintillation photons emitted after the interaction of an ionizing particle with the LXe.

The PMTs surface is place at around 31 mm from the LXe and 22 mm from the external part of the ring shaping rings. To protect the PMTs from the hight voltage applied to the cathode and the copper electrodes, a screening mesh is installed 7 mm below the PMTs surface and 1.5 cm above the electric field rings. The screening grids is based on a copper mesh with a 6.3 mm pitch and an optical transparency of 89 %.

The design of the XEMIS2 has been optimized to increase the light detection with respect to XEMIS1. Every interaction inside the active zone of the detector will produce a certain number of VUV scintillation photons depending on the energy of the γ-ray and the applied electric field. Due to the full coverage of the chamber by photodetectors, we ensure that the produced light will be collected. The scintillation signal will be exclusively used to measure the time of interaction t_0 of the 3γ-ray interaction, which allows to determine the z-position, and not for spectroscopy purposes. In addition, the light detection can be useful to reduce the fraction of pile-up events.

3.2.3 Charge collection system

To collect the ionization signal produced after the passage of an ionizing particle through the LXe, XEMIS2 includes: two meshes used as a Frisch grid, two segmented anodes divided in 12000 pixels each, a shared cathode and the data acquisition electronics.

The cathode is based on a 2 mm thick stainless steel plane electrode (see Figure 3.33). The cathode is completely opaque for the passage of the UV photons, so for a given interaction the produced light is not divided between the tow TPCs. The cathode has a circular shape with an inner radius of 6.3 cm and an outer radius of 20.3 cm, allowing the aluminium tube that holds the small animal to pass through. The cathode is placed in the middle of the two TPC a 12 cm from each anode. Under standard experimental conditions, the cathode will be biased at a high voltages of 25 kV for a drift field of 2 kV/cm.

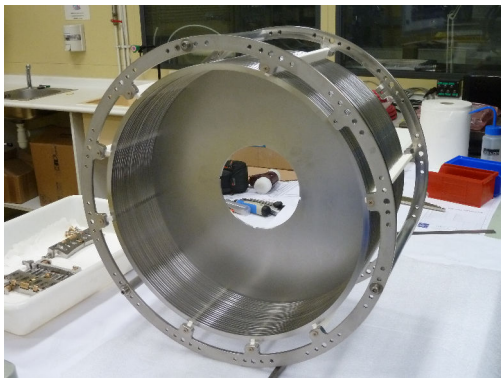

Figure 3.33 – Frontal view of the cathode with the stainless steel field rings.

The generated charges inside the detector are collected by two segmented anodes place diametrically opposed. Based on the results obtained with XEMIS1, the pixel size has been optimized to achieve good energy and spatial resolutions, withstanding the space limitations imposed by the electronic connectors. Each anode is divided in 12000 pixels of 3.1 x 3.1 mm^2 that gives an active area of 24 x 24 cm^2. A frontal view of of the design of one of the anodes is shown in Figure 3.34. The internal structure of the anode is the same as the one reported in Section 3.1.3. The anode has a circular shape with an inner diameter of 135 mm and an outer diameter of 424 mm. The internal and external parts of the anode are based on a copper circular-shaping ring with a thickness of 5.3 mm and 10 mm respectively. Between these copper rims and the first pixels there is a 1 mm thick insulating layers. Due to the circular shape of the anode, a set of smaller pixels is placed around the inner and outer parts of the anode to fill up with electrodes the entire structure. Both internal and external copper rings are connected to a high voltage supply.

Figure 3.34 shows the mechanical design of the anode of XEMIS2 connected to the front-end electronics. The signals from the 24000 pixels are processed via an ultra-low noise front-end electronics. Around 700 read-out IDeF-X LXe ASICs of 32 channels are used to collect the signals. A new analog ASIC has been developed in order to extract only the relevant information of each collected signal reducing the amount of data produced per interaction. The new front-end electronics called XTRACT, performs a CFD[1] operation to

[1]Constant Fraction Discriminator

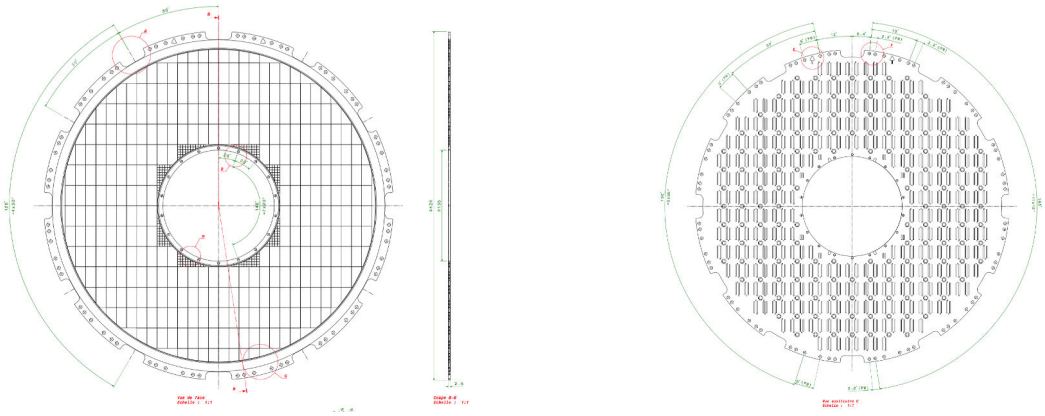

(a) **(b)**

Figure 3.34 – (a) Frontal view and (b) bottom part of the segmented anode used in XEMIS2. The small squares at the center of (a) represents the pixels, whereas in (b) the vertical connectors of the front-end electronics are illustrated.

obtain the charge and timing information of each signals that crosses a certain threshold level. Each set of eight XTRACTs is read-out by a common PU card. This new connexion system significantly reduces the amount of cables that go out from the chamber to the outside, reducing the risk of leak between the vacuum and the air.

Electronics cooling system

On low temperature detectors, a complete knowledge of the heat transfer in the detector is necessary in order to reduce both the power consumption and the possible operational problems caused by liquid variations inside the active volume (see Section 6.4.1). The conduction of heat from the outside surfaces to the LXe imply a major source of heat load. In XEMIS2 the large number of read-out electronics will cause an important heat flow from the electronics towards the inner vessel.

The electronic system used to collect the ionization signal require ∼100 mW per channel, which leads to a heat dissipation problem. In order to minimize the heat load from the front-end electronics to the LXe, two options have been proposed: a cooling system and the installation of the electronics directly inside the LXe. Figure 3.35(a) shows the mechanical design of the cooling system. It is based on an coiled stainless steel pipe design to circulate LXe at a temperature of 168 K and a pressure of 1.2 bar. The LXe is directly extracted from the detector cryostat and evacuated to the surface of the chamber. The tube is placed on a copper structure. Since the cooling is conductive, the heat sink is placed in direct contact with the electronics to remove the dissipated heat. On the other hand, the mechanical design of the chamber with the electronics inside the LXe is depicted in Figure 3.35(b). Only the IDeF-X LXe front-end electronics would be placed inside the liquid, whereas the XTRAC and Pu boards would remain in the vacuum. This option provides better temperature stability, but on the other hand, implies more technological difficulties, especially in the interface vacuum-liquid. Please note that the goal is not to cool down the electronic components themselves, but to minimize the heat flow towards the liquid.

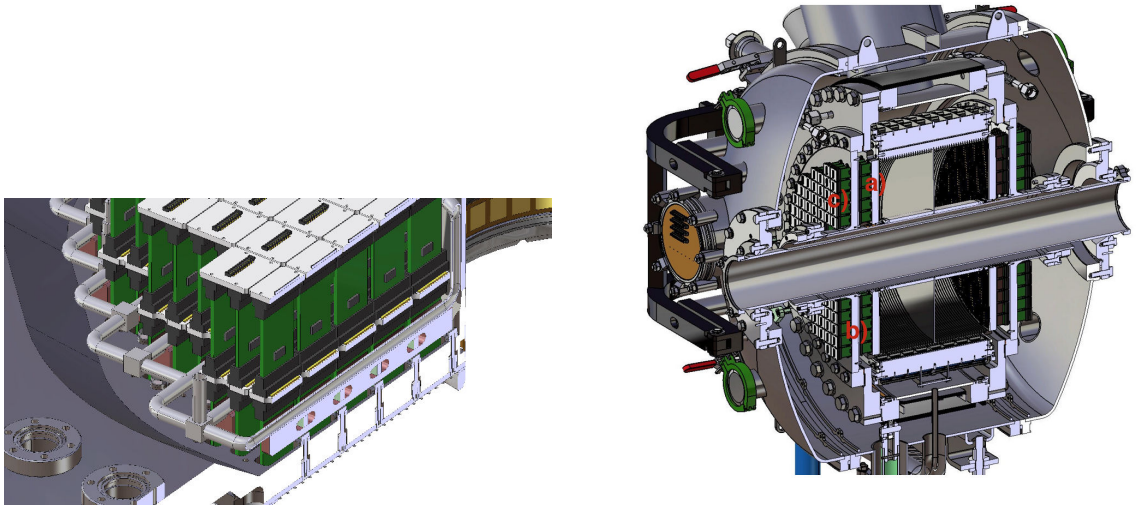

(a) **(b)**

Figure 3.35 – (a) Cooling system design to reduce the heat transfer by conduction between the electronics towards the LXe. (b) Mechanical design of XEMIS2: a) IDeF-X LXe chip inside the LXe, b) interface liquid-vacuum and c) XTRACT in the vacuum.

3.2.4 Cryogenics Infrastructure. ReStoX: Recovery and Storage of Xenon

As discussed in Section 3.1.4, during operation the LXe inside the chamber should be kept under stable temperature and pressure conditions during long data-taking periods. However, temperature and pressure stability becomes more and more difficult as the dimensions of the detector increases. Same cooling and storage systems as the one used in XEMIS1 are no longer a feasible option for XEMIS2, where the amount of LXe increases from 8 l to 70 l.

In this section, we introduce the new cryogenics infrastructure developed for XEMIS2. Figure 3.39 shows an schematic diagram of the XEMIS2 LXe cryogenic installation, that can be divided in three different sub-systems: the cryostat that encloses the TPC, the purification and recirculation systems and a new recovery and storage system called ReStoX (Reservoir Storage Xenon), which is also engaged in the pre-cooling and liquefaction processes.

Internal Cryostat and Vacuum Enclosure

The detector cryostat consists of a double-walled stainless steel vessels that host the TPC. This inner vessel is 60 cm in diameter by 35.4 cm long and it provides thermal insulation to the detection volume. The inside of the cryogenic chamber is illustrated in Figure 3.36. The camera holds 200 kg of LXe and its is placed inside a double-walled vacuum-insulated stainless steel vessels used to improve the thermal insulation.

The design of the chamber has been optimized in order to reduce the amount of liquid xenon, the power consumption and heat transfer into the detector. The vacuum enclosure limits the convective heat transport. To increase the shielding, the vacuum envelope is based on a cylindrical shell 5 mm thick with a diameter of 80 cm and 87.5 cm of length. Under normal operating condition a vacuum level of the order of 10^{-6} *bar* is continuously

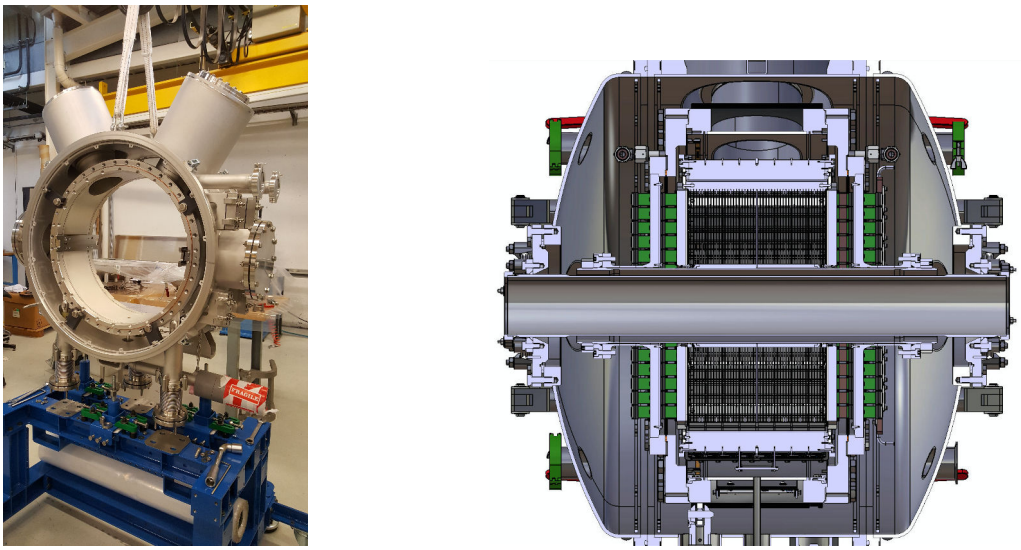

(a) **(b)**

Figure 3.36 – (a) Frontal view and (b) mechanical design of the internal part of the XEMIS2 cryostat.

maintained. This outer vessel reduces the heat load into the detector and thus, reduces the required cooling power.

The conduction of heat from the outside surfaces to the LXe can also occur through the components that supports the inner vessel, cables, detectors, etc. On the worst possible scenario, a thermal loss by conduction of ∼28 W has been estimated through the mechanical components of the chamber including, for example, the three bracket supports, the high voltage lines, the PMT cables and the two upper exit pipes. A small heat transfer of ∼10 W has been estimated from the 380 PMTs to the LXe.

To reduce the thermal radiation, the outside of the inner chamber is wrapped with MLI. Without any kind of insulation, a heat load of 156 W due to radiative losses has been calculated. Most of the thermal losses comes from the stainless steel enclosure, whereas a negligible loss has been determined through the central tube. With an insulation consisting of 20 layers of MLI, a reduction of the radiative heat transfer by a factor of 11 has been estimated, which leads to a total radiative heat load of ∼7.5 W. This improvements against thermal radiation reduces the cooling power consumption and increases the circulation rate.

The cabling inside XEMIS2 is also a challenge compared to a small dimension prototype. 380 cables with a length of 1.5 m from the PMTs must be extracted from the external vessel through the outside avoiding any possible leak, in addition to the 98 cables from the front-end electronics, the high voltage lines and the calibration and monitoring wires from the slow control sensors. XEMIS2 has four side openings around the outer vessel as shown in Figure 3.27. The two upper tubes have a diameter of 270 mm and are designed to exit, on one side the 380 PMTs cables, and on the other side the high voltage line. All these cables are extended toward the top of the cryostat through the exit pipes and they pass through the cap of the outer vessel to out of the chamber. The lateral tubes are equally a 200 mm extraction pipe. One of them is used to host the front-end electronics and exit the read-out signal cables from the two segmented anodes towards the outside, where the data acquisition

systems and computers are located. Once all cables are within their respective exit tubes, the tubes are pumped up to remove the presence of impurities due to the cable outgassing. The other lateral exit tube is connected to the vacuum pump.

ReStoX: Recovery and Storage of Xenon

Same cryogenics infrastructure as the one reported in Section 3.1.4 for the small dimensions prototype XEMIS1 is not longer viable when a 200 kg of LXe detector is developed. The operation principle and purposes are the same, but dealing with a large amount of LXe requires a new technological concept to liquefy, store and transfer the xenon in an efficient and low consuming way. Subatech in collaboration with Air Liquide Advanced Technologies has developed a sophisticated cryogenic storage and recovery system called ReStoX (Reservoir Storage Xenon) that brings together the three last requirements. A storage system of similar characteristics has already been installed and tested in the Gran Sasso Underground Laboratory (LNGS) Laboratory for the dark matter XENON experiment [188].

The design of this new cryogenic infrastructure has to comply with the criteria of a medical imaging facility. The detector should only be operational during medical exams or calibrations tests. Therefore, when the detector is not working, the chamber is empty of LXe, which implies that a reliable and relative fast recovery and transfer system is necessary. Unlike XEMIS1, where the xenon is kept in a gas bottle when the detector is not in use, storing 200 kg of LXe in gas state will require at least 6 standard bottles (60 bar) at ambient temperature, besides the important time required to liquefied this large amount of xenon (see Section 3.1.4). For this reason, one of the main goals of ReStoX is to store the xenon already in liquid state.

ReStoX is based on a double-walled insulated stainless steel tank, that can hold up to 280 l of gaseous xenon. For security reasons, it has been designed in such way that only the 25 % of the total volume should be in liquid state, which makes 70 l (203 kg) of LXe inside ReStoX, while the rest of the volume is occupy by xenon in gas state. The inner vessel that holds the xenon, is 2 cm thick and it has a diameter of 20 cm and a length of 1 m. To protect and insulate the inner vessel from convection heat transfer, it is enclosed in a vacuum insulation container. The vacuum enclosure is a 300 l volume stainless steel cylinder with a wall thickness of 2 cm. The vacuum jacket is 25 cm thick and it is filled with perlite insulation. Both stainless steel containers have total weight of 440 kg.

Precooling and Liquefaction Procedures

To initially liquefy the xenon, ReStoX has a cooling system based on liquid nitrogen (LN2). Instead of using a PTR, the cooling system of XEMIS2 is based on a massive aluminium heat exchanger, which behaves as a thermal buffer. The heat exchanger is a cylinder with a cross section of 600 mm by 205 mm and 260 kg of aluminium. The condenser is located at the top of the reservoir and placed inside the inner vessel. The LN2 circulates in an open loop through the aluminium heat exchanger via a double stainless steel tube of 2 x 12 m long. This continuous circulation of LN2 reduces progressively the temperature of the aluminium block, until it reaches a temperature slightly below the xenon transient temperature. Since the thickness of the tube that holds the liquid nitrogen is small, after some time both surfaces

reach the same temperature. Due to the high thermal inertia of aluminium, the condenser is capable of maintaining the temperature of the system stable over long-term periods without any refrigeration. Moreover, since the inner vessel is also in contact with the aluminium condenser, its temperature is automatically reduced. Around 250 - 300 kg of liquid nitrogen are necessary to reduce the temperature of the heat exchanger, the stainless steel inner vessel and 2 bar of xenon from 300 K to 170 K.

Figure 3.37 shows the liquid nitrogen container, that holds around 3500 kg of LN2. The liquid nitrogen is transferred to the ReStoX though a 50 cm thick stainless steel tube, and the injection rate is regulated by a control valve. Once the liquid nitrogen pass trough the cooling loop, it is evacuated to the open-air. Liquid nitrogen is not only used to initially liquefy the xenon, but also to maintain the temperature and pressure of the system constants by a continuous compensation of the specific heat losses of the whole system. An increase of the LN2 flow reduces the pressure system, whereas no LN2 circulation will imply a progressive increase of the pressure inside the system. Unlike XEMIS1, no heater is used to regulate the temperature inside the chamber. Under equilibrium condition, the xenon is kept at a temperature of 172 K and a pressure of 1.5 bar inside ReStoX.

Figure 3.37 – Liquid nitrogen container.

Same as in XEMIS1, before sending the xenon inside the cryostat, we need to reduce the temperature of the whole system in order to avoid the pressure to increase above the security value of 2 bars. Figure 3.38 illustrates the GXe and LXe injection procedures from ReStoX to the detector cryostat. We use the GXe which is at the surface of ReStoX to inject 2 bar of xenon inside the cryostat though a valve. When the chamber is cold enough, we can start filling the detector vessel with LXe. A UHV manual valve directly connects the inner vessel with the chamber. Since the pressure inside ReStoX is 1.5 bar and the pressure of the connexion tube is approximately ambient pressure ($\sim$ 1 bar), this depression makes the LXe to go naturally towards the cryostat when the valve is opened. The moment the valve is opened, the flow of liquid nitrogen is stopped. However, thanks to the high thermal inertia of the aluminium condenser, the inner pressure of ReStoX is stable. During the injection, the level of xenon and pressure inside the chamber starts to increase. The steady state is

reached when the pressure inside the cryostat is 1.2 bars, whereas the pressure inside ReStoX remains at 1.5 bars. The temperature inside the chamber is therefore ∼168 K. When the injection process is finished, a pressure difference of 300 mbar between the slower point of ReStoX and the LXe surface inside XEMIS2 is reached.

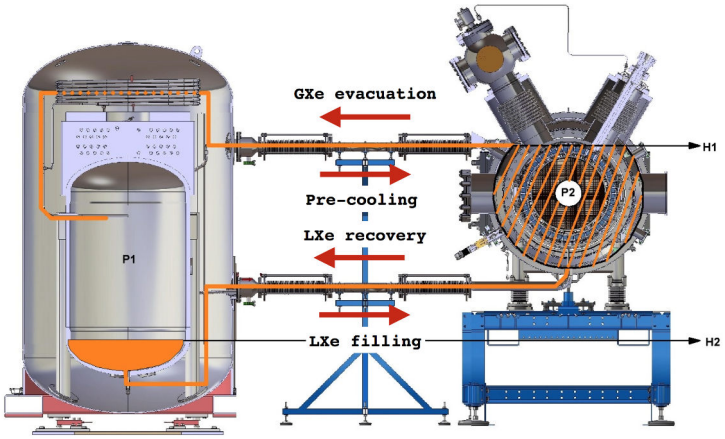

Figure 3.38 – Schematic diagram of the filling process of XEMIS2 with LXe and the GXe evacuation process.

Same stainless steel tube is used to recuperate the xenon. This reversible transfer system allows to drive back the LXe into the ReStoX from the cryostat in case of necessity in a about eight minutes. Moreover, the valve allows to completely separate ReStoX from the rest of the system and used it as a safe storage tank. To recuperate the LXe inside ReStoX, the temperature and pressure of the reservoir is reduced by increasing the flow of LN2. Due to the pressure difference between ReStoX and the cryostat, the LXe naturally returns to the storage tank. The circulation of LN2 continuous until no liquid remains inside the chamber.

Xenon Purification and Recirculation Systems

To accomplish for the high LXe purity levels required for signal detection, the LXe has to be continuously purified during its storage, so the detector cryostat is directly filled up with ultra pure xenon at any moment. The xenon is continuously liquefied and purified thanks to a closed loop that includes the detector cryostat and the storage tank. The purification process is illustrated in Figure 3.39. The purification and re-circulation systems used in XEMIS2 are the same as the one used in XEMIS1 (see Section 3.1.4). The LXe is extracted from the chamber and sent to the purification loop by a double oil free pump [186]. The LXe enters in a 30 m long coaxial heat exchanger placed at the top of the aluminium condenser. No thermal contact between the two heat exchanger is established. The coaxial heat exchanger is placed inside the vacuum enclosure to not disturb the heat transfer. Once in the coaxial heat exchanger, the LXe is evaporated and pumped through a SAES MonoTorr Phase II hot getter, model PS4-MT3-R/N [185]. The pure GXe returns to the ReStoX through the coaxial heat exchanger, where it is cooled and re-condensed with a $\sim$ 99% efficiency. A maximum re-circulation rate of 2.9 g/s is expected due to the pumps.

Under equilibrium conditions, the xenon inside the TPC is at a temperature of 168 K and at a pressure of 1.2 bars. However, the thermal losses due to radiation and conduction

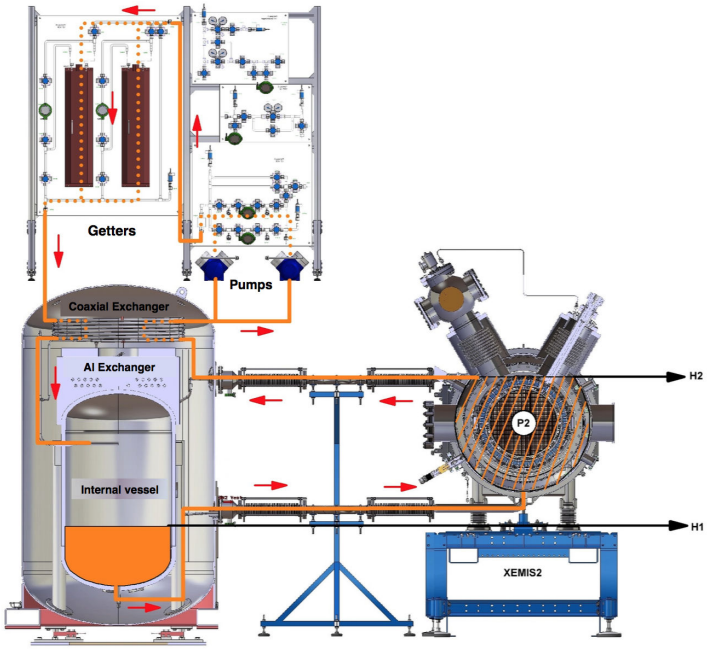

Figure 3.39 – Schematic diagram of the purification and re-circulation process in XEMIS2.

increases the temperature of the liquid above the stationary regime. An estimation of possible heat transfer on the three different sub-system reveals that most of the heat load is due to the cryostat (44 W) and ReStoX (33 W), while only 15 W are lost through the purification system. The heat transfer inside the TPC causes the evaporation of part of the LXe stored inside the chamber. Part of the heat load is directly evacuated through the ReStoX due to the temperature difference between the two systems. However, if the heat load is higher that the heat flow between the cryostat and ReStoX, the GXe accumulated in the surface of the chamber will cause an increase of the pressure. To maintain the pressure at 1.2 bar, the GXe must be evacuated from the chamber. A pump is used to extract the GXe from the cryostat surface towards the purification loop. This evacuation process is illustrated in Figure 3.38. Furthermore, in the process, part of LXe is also removed from the chamber. When the xenon evaporates due to the heat transfer, the equilibrium level required to perform the medical exam decreases. The amount of LXe lost has to be replaced by injecting more LXe from ReStoX to the detector.

Safety System and Slow Control

The narrow operational margin of 4 K (at 1 bar) requires a continuous monitoring of the temperature and pressure inside both ReStoX and the detector. In addition, as discussed in Section 3.1.4, a set of security systems should be introduced in order to recuperate the xenon inside the storage tank in case of emergency.

ReStoX is able to work even in case of a power failure. The continuous liquefaction of xenon is based on the circulation of LN2 through the aluminium heat exchanger. If the LN2 stops, ReStoX is design to withstand about 70 bar of pressure at ambient temperature of around ∼30 °C. This means that the 200 kg of xenon may be stored in gas state safety. Nevertheless, if the pressure inside ReStoX exceeds the design value, a burst disk is included

that will irreversibly open and liberate the xenon to the outside. To prevent the completely loss of all the xenon, another safety valve has been installed. This relief valve opens proportionally with increasing pressure discharging a small quantity of xenon. The valve closes once the pressure falls below a certain reseting value.

Similarly, the pressure inside the cryostat should not exceed 2 bar to avoid damages on neither the detector, nor the cryostat itself. To limit the pressure inside the chamber the same security system as the one installed in XEMIS1 is used. A pneumatic valve and two burst disks open if the pressure reaches 1.8 bar. If that happens, the xenon is evacuated to the outside. As the same way as for ReStoX, the total loss of xenon is prevented through the GXe injection pipe. A control valve closes the purification and re-circulation loop, and regulates the passage of LXe towards ReStoX. The opening and closure of this valve is regulated by a slow control interface.

3.3 Conclusions Chapter 3

In this chapter, a detailed description of the first prototype of a LXe Compton telescope XEMIS1 has been carried out. This small dimension prototype represents the experimental evidence of the feasibility of the 3γ imaging technique. XEMIS1 consists of a time projection chamber of 2.5 $\times$ 2.5 $\times$ 12 cm^3 active volume full of LXe. The VUV scintillation photons generated after the interaction of a γ-ray with the LXe are detected by a PMT, which has been especially designed to work at liquid xenon temperature. The ionization signal, on the other hand, is collected by a 64 pixels segmented anode. A complete description of the internal structure of the anode has been also presented in this chapter. A homogeneous electric field between the cathode a the anode is established thanks to a set of 24 copper field rings connected through a resistive chain. The charge collection system of XEMIS1 is also equipped with a Frisch grid. The properties of four different grids tested during this thesis are presented is this chapter. The advanced cryogenics system, which has contributed to a high liquid xenon purity with a very good stability, described in detail. The different cryogenic processes performed before any data-taking period, such as liquefaction and purification of the xenon are also presented.

In the second part of this chapter, we have presented the characteristics of the second prototype XEMIS2 designed to image small animals. Main properties and materials of both the detector and the cryostat have been described. This new prototype is a monolithic liquid xenon cylindrical camera, which totally surrounds the small animal. XEMIS2 holds around 200 kg of liquid xenon. The active volume of the detector is completely covered by 380 1" PMT to detect the VUV scintillation photons, allowing a pre-localization for the detection of the ionization signal. The ionization signal is collected by two segmented anodes with a total amount of 24000 pixels. This innovative geometry will allow the simultaneous detection of the three γ-rays with a high sensitivity and a high Field-Of-View. Moreover, in order to manage such as important quantity of liquid xenon, an innovative high-pressure subsystem called ReStoX (Reservoir Storage Xenon) has been developed and successfully installed. ReStoX allows to maintain the xenon in liquid state at the desired temperature and pressure, distribute the xenon into the detector and also recover the xenon in case of necessity. A brief

allusion of the possible thermal losses presented in the whole system has been made. Special attention has been paid to the thermal load from the front-end electronics towards the LXe that may cause certain operational problems (see Section 6.4.1).

This new prototype target to obtain good quality images with only 20 kBq of injected activity, 100 less of activity than a conventional small animal functional imaging exam.

Chapter 4

Optimization of Ionization Signal Extraction with a LXe Compton Telescope

Contents

The main goal of a LXe Compton telescope is to provide information of the 3D location of each individual interaction of an ionizing particle with the LXe, as well as to provide a precise measurement of the produced ionization charge in such an interaction. Both the scintillation light and the electron-ion pairs produced by the incoming radiation provide relevant information of the interaction in the medium. For this reason, the data acquisition system should be capable of recording for each interaction point both the ionization and scintillation signals simultaneously and without any dead time. In addition to that, the 3γ imaging technique requires very good energy and spatial resolutions in order to triangulate

the position of the source. Consequently, charge and time determination on the detected signals must be optimized. In this chapter, we focus on the measurement of the ionization signal. The design and performance of the readout front-end electronics used in XEMIS1 is presented in Section 4.1.1. A detailed study of the electronics response is necessary in order to characterize the detector performances. The study of the influence of the charge sensitive pre-amplifier and shaper on the shape of the output signals is reported in Section 4.3. Charge linearity and electronic noise contributions are also discussed in this section. Moreover, the optimization of the time and amplitude measurement on the ionization signals is performed thanks to a Monte Carlo simulation. The goal of this study is to develop an advanced acquisition system for the measurement of the ionization signal in XEMIS2 (see Section 4.4). A description of the main characteristics of this new analog ASIC is presented in Section 4.6.

4.1 General overview

Incident radiation in the detector induces a current pulse on each pixel of the anode that is commonly read-out by means of a charge-sensitive preamplifier (CSA) [189]. The preamplifier generates an output pulse which amplitude is proportional to the integral of the induced current pulse on each pixel. Figure 4.1 shows a basic preamplifier circuit composed of a feedback capacitor C_f. The capacitor integrates the input current signal *i(t)* and generates a voltage step pulse at the CSA output: $V_{out}(t) = \frac{1}{C_f}\int i(t)dt$. A reset system is incorporated to the CSA to discharge the feedback capacitance in order to avoid amplifier saturation. In the configuration shown in Figure 4.1, the reset is based on a feedback resistor, R_f, placed in parallel to the feedback capacitor C_f. The resistor continuously discharges the capacitor without degrading the signal to noise ratio and the linearity performances of the system. Ideally, the rise time of the output pulse generated by the preamplifier depends only on the charge collection time in the detector, and is independent of the characteristics of the preamplifier and the capacitance of the detector [20]. On the other hand, the decay time of the output pulse is determined by the time constant of the CSA: $\tau_p = R_f C_f$. Therefore, the output signal is proportional to the total collected charge on a pixel, as long as the duration of the input pulse, t_c, is short compared with the time constant of the preamplifier ($t_c << R_f C_f$). Consequently, the choice of the feedback capacitor has an influence on the charge collection efficiency and on the shape of the output signals. Large feedback capacitors, i.e. long time constant, are required to achieve a high charge collection efficiency and also to decrease the electronic noise contribution of the CSA. However, if the charge collection time in the detector is smaller than the CSA time constant, consecutive arriving pulses may overlap at the CSA output. This pile-up effect becomes more important for high event rate.

The preamplifier is also a major source of electronic noise to the system. That is why it should be placed as close as possible to the anode to increase the SNR. A brief discussion of the different sources of electronic noise is presented in Section 4.2. A pulse-shaping amplifier or *shaper* is generally added to the signal processing chain in order to filter and shape the CSA output signals (see Figure 4.2). The shaper generally consists of a band-pass filter that limits the available bandwidth by attenuating the undesirable spectral noise components outside the frequency band of interest and thus, increases the SNR. In addition,

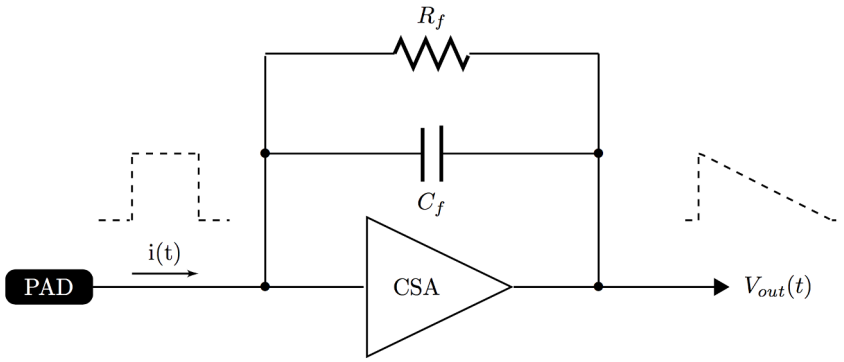

Figure 4.1 – Basic diagram of a charge-sensitive preamplifier with a feedback capacitance C_f and a feedback resistance R_f as reset. An input current pulse *i(t)* is integrated on the CSA that produces an output voltage pulse $V_{out}(t)$ with a time constant $\tau = R_f C_f$.

the shaper contributes to diminish the pile-up effect by shortening the pulse decay time, but preserving the maximum of the signal. In general, shapers are based on a combination of a first order CR high-pass filter also called differentiator, and a n^{th} order RC low-pass filter or integrator (CR-RC^n filter). For example, a second order low-pass filter is used in the front-end electronics of XEMIS1 called IDeF-X (see Section 4.1.1) with equal differentiator and integrator time constants. The resulting output signals generated by the shaper have a quasi-gaussian shape with a rise time that depends on the integration time of the filter or peaking time τ_0, which is usually established by the time constant of the low-pass filter. In the following, the peaking time refers to the time between the moment the output signal reaches 5 % of its amplitude and the maximum. On the other hand, the decay time of the pulse is usually governed by the time constant of the CR filter, which is in general lower than the CSA time constant to reduce the pile-up effect. The choice of the time constants of the shaping circuit affects the maximum amplitude of the output signal. A loss of amplitude on the shaper output pulse compared to the CSA output signal is known as the ballistic deficit of the electronics, and it is discussed more in detailed in Section 4.3.2.

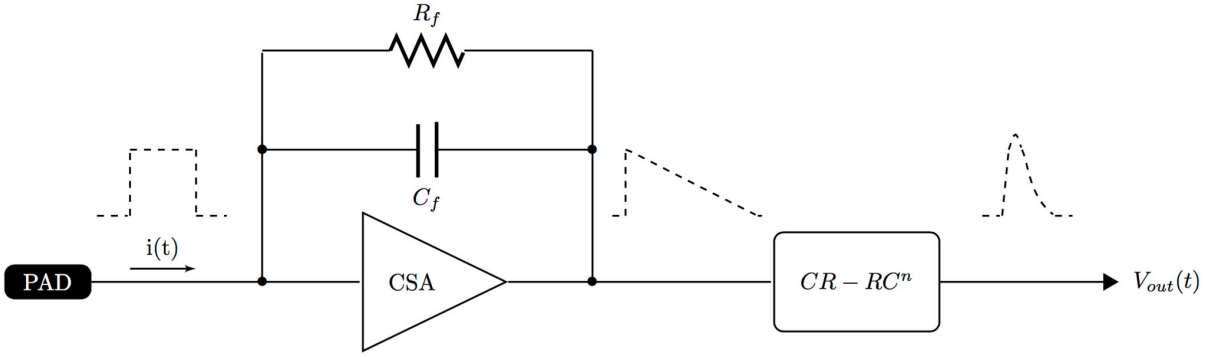

Figure 4.2 – Basic diagram of a charge-sensitive preamplifier with a CR-RC^n filter. The output voltage pulse $V_{out}(t)$ has a quasi-gaussian shape with a rise and decay times that depend on the time properties of the different blocks of the electronic chain.

4.1.1 Front-end electronics: IDeF-X LXe

As discussed in Chapter 3, in the XEMIS1 TPC the ionization signal generated after the interaction of an ionizing particle with the LXe is directly collected by the anode, which means no amplification of the signals is used. This implies that a very low electronic noise is needed in order to maximize the SNR and hence, to achieve a good energy resolution. The location of the electronics close to the anode also reduces the electronic noise, as well as the signal degradation during transmission. However, this implies that they should be able to tolerate temperatures close to the temperature of LXe. In the last version of XEMIS1, the front-end electronics are placed inside the vacuum container reaching temperatures below -60 °C. Several tests with the electronics placed directly inside the LXe have been also performed during this thesis. The coupling between the anode and the ASICs are also of critical importance to maintain the required levels of noise and to withstand low temperatures.

The readout front-end electronics used in XEMIS1 consists of a low-noise 32 channels analog IDeF-X HD-LXe chip (Imaging Detector Front-end for X rays) [187]. This low power ASIC was initially developed by the CEA[1] for X-ray and γ-ray spectroscopy with a Cd(Zn)Te detector named Caliste [190]. The initial IDeF-X HD ASIC has self-triggering capability that includes a baseline restoration circuitry, a peak detector and a discriminator [191]. Subatech has successfully adapted the existing ASIC for the purpose of collecting the ionization signal with a LXe detector. The differential output and multiplexes present on the ASIC have been replaced by 32 analog outputs with no memorization.

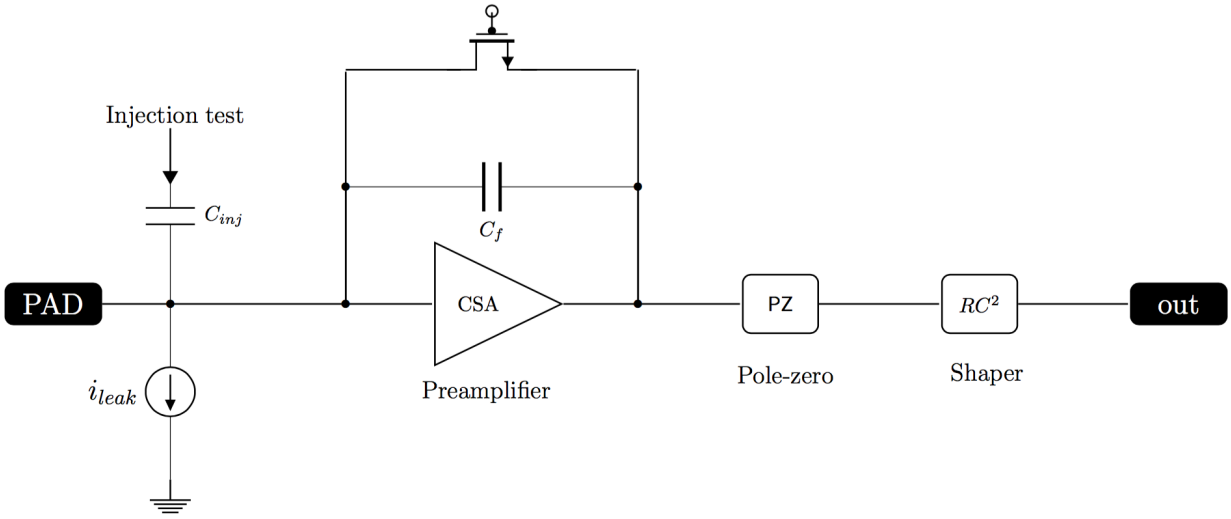

Figure 4.3 – Schematic of the IDeF-X HD-LXe ASIC.

The segmented anode is connected to two IDeF-X HD-LXe of 32 channels each. Every pixel of the anode is then connected to its own ultra low-noise readout channel, generating a total of 64 independent analog signals. A general architecture of a readout channel of the chip is presented in Figure 4.3. Each analog channel includes a charge-sensitive preamplifier that integrates the induced signal on a pixel. To continuously discharge the integration capacitance, C_f, the CSA is provided by a reset system based on a PMOS feedback transistor, which is equivalent to a several GΩ resistor. The output of the CSA

[1]Commissariat à l'énergie atomique et aux énergies alternatives

is fed to a Pole-Zero cancellation (PZC) stage based on a PZ filter [192]. The PCZ is used for baseline restoration by compensating pulse long duration undershoots. It is also used to perform a first signal amplification of the CSA output. The differentiation filter is also included in this module. A shaper based on a RC^2 second order low-pass filter with variable shaping times is also integrated. Each channel is provided with an injection capacitance of 50 fF, C_{inj}, used to inject a well known charge on the input of the CSA of each channel for test and calibration purposes. Furthermore, to emulate the detector dark current each channel includes a adjustable internal current source i_{leak} to polarize the ASIC input.

The main characteristics of the IDeF-X HD-LXe are summarized in Table 4.1. Every parameter of the chip such as the peaking time, the gain and the leakage current among others, are easily tunable with a four wires slow control protocol that is provided with an easy and intuitive graphical user interface [187]. The time constants of the RC^2 filter and hence, the peaking time of the output signals can be varied between 0.73 to 10.73 μs. The gain of each channel can be set from 50 to 200 mV/fC, which means that a dynamic range of around 1.3 MeV can be reached. Moreover, a power consumption of 800 μW per channel has been reported [187]. To reduce the total power consumption or to select only those channels that are needed, the slow control system also allows to switch off every channel independently. The IDeF-X HD-LXe chip includes a temperature sensor with an absolute resolution of 0.5 °C. The technical specifications of the chip are shown in Figure 4.4.

Parameter	**Value**
Chip size	4.34 x 2.00 x 0.16 cm^3
Number of channels	32
Technology	0.35 μm CMOS
Supply voltage	3.3 V
C_f	50 fF
Power consumption	27 mV (800 μW/channels)
Gain	50, 100, 150, 200 mV/fC
Dynamic range	1.3 MeV for LXe at 200 mV/fC
Peak time	0.73 to 10.73 μs (16 values)
ENC (room temperature)	150 e^- RMS [187]
Leakage current tolerance	up to 4 nA

Table 4.1 – Main properties of the IDeF-X HD-LXe chip.

The 32 channels IDeF-X front-end ASIC is bonded on a 4.34 x 2.00 x 0.16 cm^3 PCB (Printed Circuit Board) (see left image in Figure 4.5). In order to comply the temperature and pressure requirements, the different material that compose the PCB circuit are the same as those used to build the anode. The anode and the electronics are directly coupled to two

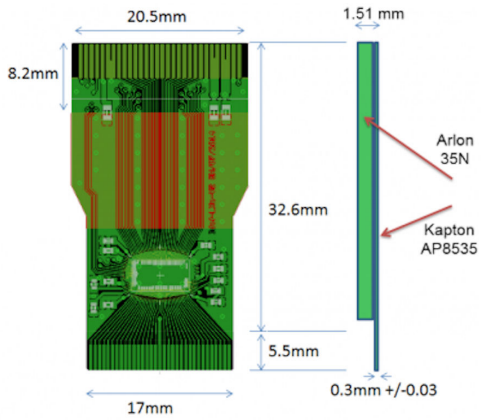

Figure 4.4 – Technical details of the IDeF-X HD-LXe ASIC.

standard 32 channels vertical mini edge card connectors. This type of connectors allow for excellent electrical performances and ensures good signal transmission. Figure 4.5 shows the Bottom layer of the anode with the two 32 channels connectors wire bounded directly to the pixels of the anode. A perpendicular position of the electronics with respect to the anode facilitates the wiring, as well as allowing a reduction of the pixels size. Earlier versions of the segmented anode with a higher pixel size of 3.5 x 3.5 mm^2 and a 1 in^2 PCB board coupled to the anode through a flat Cinch connector, have been also tested during this thesis. However, this oldest configuration led to a higher electronic noise and a worse spatial resolution (see Section 7.6) [187].

The two vertical IDeF-X front-end ASICs are connected together through a 64 channels interface board, as we can see in the right-side image of Figure 4.5. The 64 output signals of the interface board are transferred to an analog buffer through a $\approx$ 20 cm kapton bus. The buffer stage enables the transmission of the analog signals from the vacuum vessel to the outside by increasing the available current. The kapton nap also provides the power supply to the front-end electronics. Figure 4.6 shows the inside part of the outer vessel of XEMIS1 where the kapton nap and buffer are visible. Finally, the 64 analog signals from each pixel are extracted from the vacuum container to the air and transferred to the acquisition board through 64 standard wires. Signals are then digitized with a sampling rate of 12.5 MHz by an external 12 bits FADC. Thanks to the dedicated electronic setup used in XEMIS1 an electronic noise of the order of 80 electrons is achieved.

4.2 Electronic noise

The noise is the result of statistical fluctuations either cause by the detector, the electronics or both, that are superimposed to the output signal. It is clear that the noise limits the smallest detectable charge signal, so it has an important impact on the energy resolution of the detector. Only signals with an amplitude several multiples larger than the noise can be clearly distinguished from random noise fluctuations. The spectral resolution of a detector depends therefore on the SNR. Likewise, timing measurements are also affected by noise. The noise produces an uncertainty or jitter in the time where the maximum of

(a) **(b)** **(c)**

Figure 4.5 – (a) 32 channels IDeF-X front-end ASIC. (b) Bottom layer of the anode with the two standard 32 channels vertical mini edge card connectors. c) Two ASIC chips bounded to the two vertical connectors. The two PCBs are couple through a 64 channels interface board.

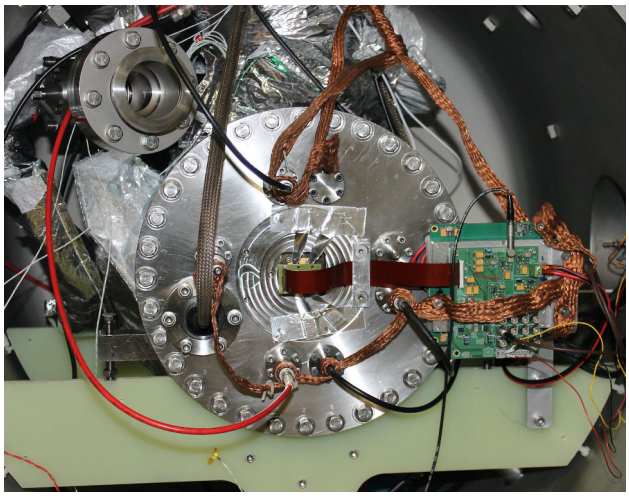

Figure 4.6 – Zoom of the interior view of the outer vessel of XEMIS1. The kapton bus connected to the 64 channels interface board and the buffer are visible.

the signal is measured, so the time resolution depends on the slope/noise ratio according to Equation 4.1 [193]:

$$\sigma_t = \frac{\sigma_N}{\frac{dV}{dt}} \tag{4.1}$$

where dV/dt is the slope of the signal when its leading edge crosses the threshold, and σ_N is the quadratic sum of all non-correlated sources of noise in volt.

The electronic noise causes random fluctuations in the number of collected charges and it is produced by the different components of the read-out electronic system. In general, the higher levels of noise are produced at the beginning of the electronic chain where the signal level is small compared to the noise fluctuations [20]. The charge-sensitive preamplifier

implies, for example, a major source of electronic noise that is in part filtered by the shaper. In a CSA the total input capacitance C_{in}, represented by the inherent pixel capacitance or detector capacitance (C_d), the parasitic capacitance due to the connexion between the pixels and the preamplifier (C_p) and the capacitance at the input of the electronic chain (C_e) are an important source of noise. C_e is the sum of the feedback capacitance C_f and all the parasitic capacitances at the input of the CSA and between the grid and the anode. To reduce the amount of electronic noise is, therefore, important to minimize the total input capacitance. To reduce the input capacitance, the connecting line from the pixel to the CSA has to be as short as possible.

In a detector, there are many different sources of electronic noise that can be classified as *parallel noise* or *serial noise* depending on its coupling with the output signal [194]. For example, detector leakage current shot noise and feedback resistor R_f thermal noise are common noise contributions that are in parallel with the detector at the preamplifier input. On the other hand, thermal noise on the first-stage of the preamplifier is a sort of noise that is in series with the signal source. The different noise contributions are generally expressed in terms of the *voltage* (e_n) or *current* (i_n) spectral density depending on whether the contribution comes from a voltage (series) or current (parallel) noise source [195]. Please note that there are a great variety of noise sources in an electronic circuit and in this section we discuss only the most relevant noise contributions related to the CMOS[2] technology. For a more complete overview of the electronic noise please refer to [196].

The electronic noise added by the read-out electronic system is often expressed in terms of the Equivalent Noise Charge (ENC), which is defined as the charge that must be supplied to the input of the system in order to obtain an output signal equal to the root-mean-square (RMS) due only to noise. Commonly, the ENC is expressed in Coulombs, units of electron charges (e^-) or equivalent deposited energy (eV).

The **Thermal noise** also called Johnson-Nyquist noise is generated by thermal agitation of charge carriers within a conductor [197, 198]. It is produced in the preamplifier input stage due to the input field effect transistor (FET). The thermal noise can be modeled approximately as *white noise* in most real electronic systems, since its Power Spectral Density (PSD) is independent of frequency. The spectral density of the thermal noise contribution is given by [194]:

$$e^2_{thermal} = \frac{8}{3}\frac{kT}{g_m} \quad (V^2/Hz) \tag{4.2}$$

where k is the Boltzmann's constant, T is the absolute temperature and g_m is the transconductance of the first-stage of the preamplifier. The thermal noise on the preamplifier output due to the first-stage FET can be also expressed in terms of the equivalent noise charge as follows [194]:

$$ENC^2_{thermal} = \frac{8}{3}\frac{kT}{g_m}\frac{C_t^2}{q^2\,\tau_0} \tag{4.3}$$

[2]Complementary Metal Oxide Semiconductor

where q is the electron charge, $C_{in} = C_d + Cp + C_e$ is the total input capacitance and τ_0 is the shaping time constant. The contribution of this thermal noise to the detector can be significantly reduced by operating at low temperature.

The **shot noise** is due to random fluctuations of the electric current about its average value and causes fluctuations in the number of charge carriers within a semiconductor or vacuum tube [199]. It comes from the sensor leakage current, and like the thermal serial noise, it also has a white spectrum. The power spectral density of the shot noise is proportional to the average current I given by the gate leakage current of the first-stage of the preamplifier and the dark current of detector:

$$i^2_{shot} = 2qI \quad (A^2/Hz) \tag{4.4}$$

The leakage current shot noise on the preamplifier expressed in terms of the equivalent noise charge is given by the following expressions:

$$ENC^2_{shot} = 2qI\ \tau_0 \tag{4.5}$$

Other significant parallel contributors to the noise is the **thermal noise** associated with the **reset** of the preamplifier R_f, which current power spectral density and ENC are given by:

$$i^2_{Rf} = \frac{4kT}{R_f} \quad (A^2/Hz) \tag{4.6}$$

$$ENC^2_{R_f} = \frac{4kT\ \tau_0}{R_f} \tag{4.7}$$

This noise contribution decreases by increasing the resistance value and its power density is also independent of frequency. However, larger values of R_f implies longer time constants and hence, longer pulse tails that may lead to an increase of pulse pile-up. The ENC of the thermal noise caused by feedback resistance is proportional to the shaping time τ_0 but independent of the input capacitance C_i. Substituting the feedback resistor by a PMOS transistor is a good alternative to reduce this kind of noise.

Flicker noise is another source of inherent noise in a detector. Its contribution also comes from the preamplifier input transistor and may be explained by the charge carriers which are trapped in the impurities or imperfections of the medium, and then released after a characteristic lifetime, producing fluctuations on the number of produced charge carriers. The PSD of the flicker noise is inversely proportional to frequency, and that is why is also called **1/f noise**. The spectrum of the noise depends on the ratio of the upper to lower cutoff frequencies, rather than the absolute bandwidth unlike the thermal serial noise and shot noise. The contribution of the flicker noise is given by:

$$e^2_{1/f} = \frac{K_f\ I^m\ \Delta f}{f} \quad (V^2/Hz) \tag{4.8}$$

where I is the current, K_f is the flicker-noise coefficient, m is the flicker noise coefficient and Δf is the bandwidth in hertz over which the noise is measured [199]. The ENC of the 1/f noise depends on the input capacitance of the detector ($\propto C_{in}$) and it is independent of the shaping time τ_0 [194].

Since all these contributions are uncorrelated noise sources, the total electronic noise is given by the square root of the quadratic sum of the different noise sources:

$$ENC^2_{total} = ENC^2_{parallel} + ENC^2_{series} + ENC^2_{1/f} \tag{4.9}$$

The total electronic noise of a detector can be reduced by choosing the appropriate amplifier shaping time. Figure 4.7 shows the ENC as a function of the shaping time. In general, the series noise contribution such as the thermal noise at the input stage of the preamplifier dominates at short shaping times, while the parallel noise component (shot noise and thermal noise at the preamplifier feedback resistor) increases with the shaping time. Therefore, the selection of the time components of the read-out electronics should be taken under careful consideration in order to minimize the noise contribution. In theory, the minimum noise is obtained when both contributions, series and parallel noise, are equal. The flicker noise on the other hand, is independent of the shaping time and it tends to dominate at low frequencies. However, its contribution does depend on the input capacitance. The relative contribution of series noise also increases with detector capacitance, while the parallel noise does not depend on C_{in}. Consequently, the minimum noise is usually achieved for detectors with long shaping times and small input capacitances.

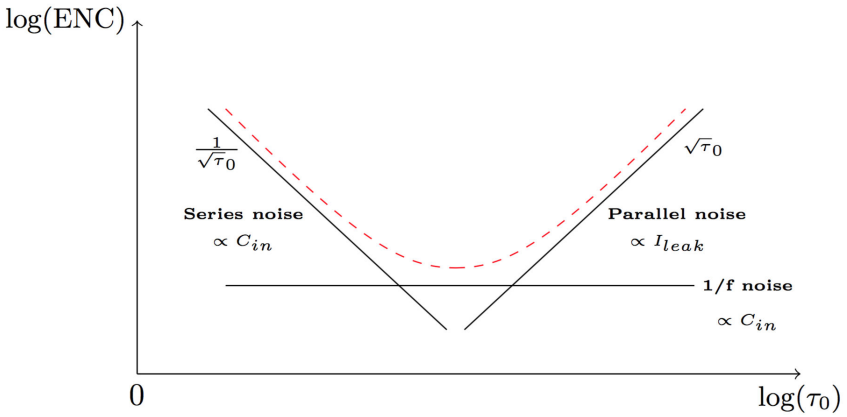

Figure 4.7 – Equivalent noise charge vs. shaping time. At long shaping times the ENC noise is dominated by current or parallel noise, whereas at small shaping times (large bandwidth) the parallel contributions dominates. A minimum of noise is achieved when the series and parallel contributions are equal, so changing any of these noise contributions shifts the noise minimum. The 1/f noise contribution is independent of shaping time. The dependence on the input capacitance and the leakage current is also shown in the figure.

4.3 Effect of the readout electronics on the measurement of the induced ionization signal

As discussed in Section 4.1, in order to measure the full amplitude of the induced signal on a pixel, the shaping time must be larger than the temporal width of the signal. Therefore, for high energy resolution detectors, the best method to measure the energy of an interaction is to use a charge-sensitive amplifier with large shaping times. Timing measurements, on the other hand, require short shaping times to reduce the SNR and the pulse pile-up. When both requirements are necessary, as in the case of a TPC, the choice of the parameters of the front-end electronic requires a thoughtful study. In this section, we study the shape of the output signal of the IDeF-X HD LXe ASIC for an injected test pulse and different peaking times (T_{peak}[3]). Results are compared to the experimental output pulse for 511 keV γ-rays. Moreover, charge loss as a function of the shaping time and the linearity of the chip are also discussed in this section.

4.3.1 Study of the shape of the output signals

The response of the front-end electronics used in XEMIS1 has been tested by injecting a test pulse to the input of the preamplifier. Every channels of the anode, i.e. every preamplifier, includes a 50 fF test pulse capacitor that enables to inject well defined test charges to be integrated by the preamplifier. All measurements were performed under realistic experimental conditions with the LXe TPC completely functional. Figure 4.8 and 4.9 show the output signal of the shaper and preamplifier, respectively, for a step input pulse with an amplitude of 60 mV and a 5 ns rise time. The injected test pulse was provided by a standard waveform generator (Agilent 33250A). The presented signals are the result of averaging over 2000 test pulses to reduce statistical fluctuations. The injection was performed on four different pixels of the anode, two from each IDeF-X chip. The preamplifier output signal was extracted from two of the injected channels. The gain and peaking time of the amplifier were set to 200 mV/fC and 1.39 μs respectively.

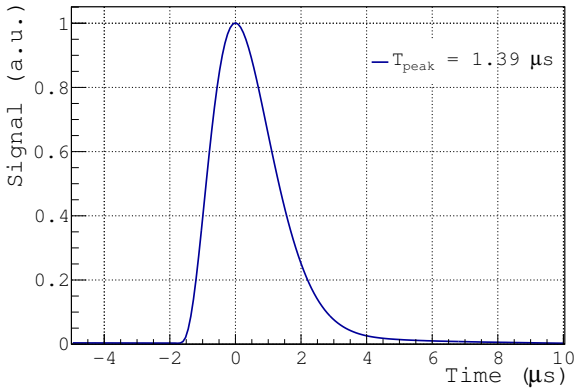

Figure 4.8 – Output signal of the shaper for a 60 mV injected delta-like pulse with 5 ns rise time and a peaking time of 1.39 μs.

[3]The peaking time is defined as the time between the 5 % of the amplitude and the maximum.

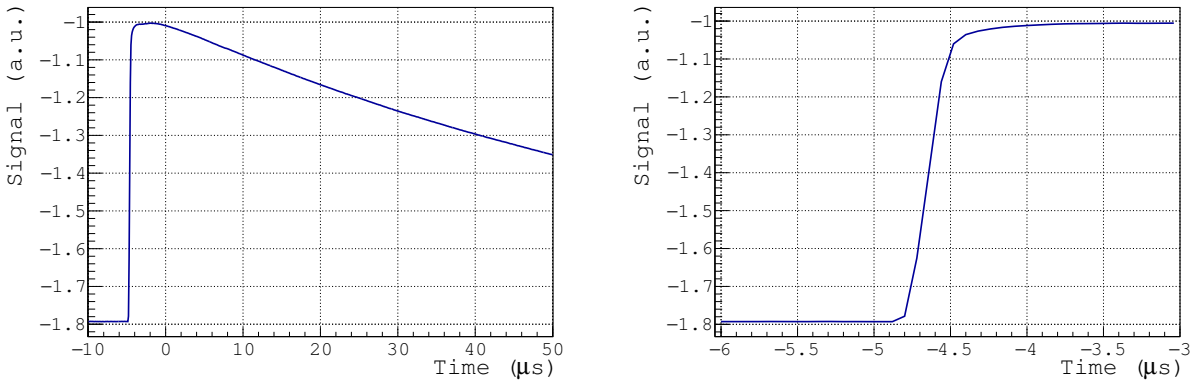

Figure 4.9 – Output signal of the preamplifier for a 60 mV injected delta-like pulse with 5 ns rise time.

As expected, the response of the chip to a Dirac-like current signal is a quasi-gaussian pulse that reaches its maximum value in 1.39 μs (from 5 % to 100 % of the amplitude). Similar results were obtained for different peaking times. Figure 4.10 shows the comparison of the signal at the output of the shaper for four different peaking times: 0.73 μs, 1.39 μs, 2.05 μs and 2.72 μs. Since the same time constant is used on both differentiation and integration stages of the shaper, faster rise times and faster decay times are achieved for slower peaking times. The charge loss due to the ballistic effect is discussed in the next section.

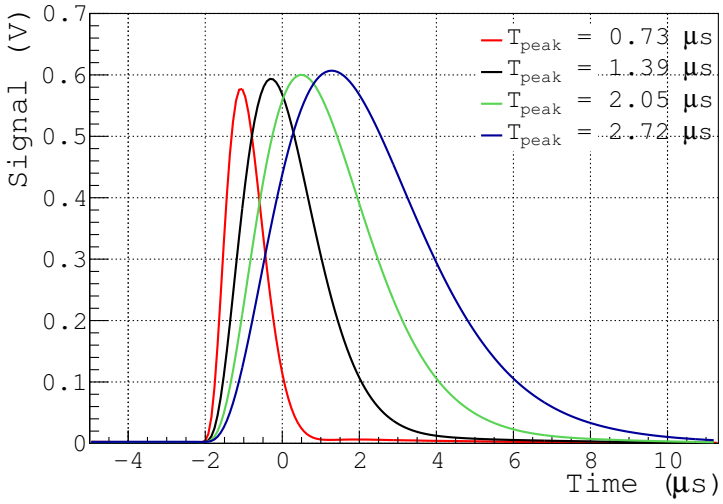

Figure 4.10 – Output signal of the shaper for a 60 mV injected delta-like pulse with 5 ns rise time and four different peaking times.

On the other hand, the shape of the preamplifier signal differs from a delta-like pulse. The preamplifier generates a signal with a rise time of the order of 500 ns when a 5 ns leading edge current pulse is injected. This behavior is due to the fact that a real CSA does not respond instantaneously to an input charge.

In order to reproduce the actual output signal of the front-end electronics when radiation interacts with the LXe, some other aspects besides the shaping time of the amplifier should be taken into account. The rise time of the output signals also depends on the charge collection time. In the case of XEMIS1 and for an ideal Frisch grid, electrons start to induce a signal on the anode from the moment they pass through the grid, so all charges travel the same distance, equal to the gap, before being collected. The effect of the inefficiency of the Frisch grid on the pulse shape is discussed in Chapter 5.

During this thesis two different gaps of 500 μm and 1 mm have been tested. In the LXe, the electron drift velocity for an electric field of 1 kV/cm is around 2 mm/μs, whereas for field strengths higher than ∼3 kV/cm it saturates at around ∼2.3 kV/cm. Although the electric field in the gap is between five to six times the electric drift field (6 kV/cm) (see Section 5.5.1), the total electron drift time was approximated as 250 ns and 500 ns for a 500 μm and a 1 mm gap respectively. The evolution of the preamplifier output signal for three injected delta-like pulses with different rise times of 5 ns, 250 ns and 500 ns, that simulates three different grid-anode distances is presented in Figure 4.11. As the collection time increases, i.e. the slope of the injected step increases, the rise time of the signal at the output of the preamplifier also increases. This implies that, in general, higher gaps require larger shaping times in order to integrate the total charge.

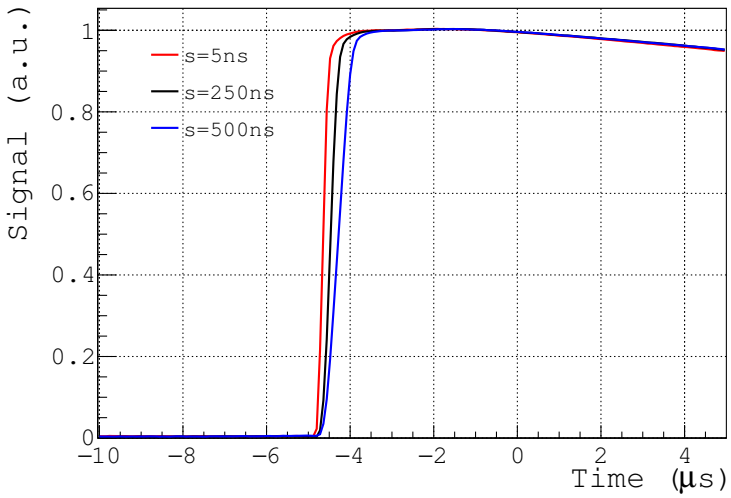

Figure 4.11 – Output signal of the preamplifier for a 60 mV injected delta-like pulse with 5 ns, 250 ns and 500 ns rise time.

However, some discrepancies have been observed on the experimental data. Figure 4.12 shows the comparison between the average output signal for 511 keV events obtained with a 100 LPI metallic woven mesh placed at 500 μm from the anode and a 6 cm long TPC (see Chapter 6, Section 6.2), with a 250 ns slope injected pulse, i.e. $\sim$ 500 μm of gap. The peaking time on both signals was set to 1.39 μs. For the experimental pulse only single-cluster events, i.e. clusters with only one fired pixel, for interactions that took place between 2.6 cm and 6 cm from the grid were selected. Likewise, the signal was averaged over a large enough number of events to increase the SNR. The experimental signal shows a larger peaking time of 1.52 μs compared to the injected pulse ($T_{peak} = 1.46$ μs). The decay

time of the experimental pulse is estimated to be 3.3 μs, obtained between the 100 % to 5 % of the maximum. The shaped pulse from an injected 60 mV step signal with a rise time of 500 ns corresponding to grid-anode distances of approximately 1 mm is also depicted in the figure. The results show that the convolution of a delta-like charge signal with a gap of 500 μm does not mimic the shape of the experimental signal, but instead a gap of 1 mm better reproduces the rise time of the pulse. A difference of ∼80 ns is measured at 5 % of the signal's maximum between the experimental pulse and a 250 ns rise time injected pulse, while no difference is measured for the 500 ns slope pulse.

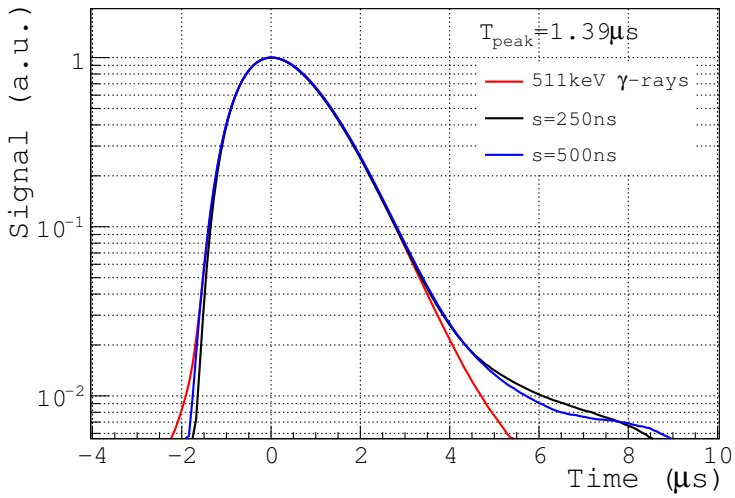

Figure 4.12 – Comparison between the output signal of the shaper for 511 keV events with a 100 LPI Frisch grid placed at 500 μm from the anode (red line) and a 60 mV injected delta-like pulse with 250 ns (black line) and 500 ns (blue line) rise time. The peaking time was set to 1.39 μs.

The comparison of the experimental output signal for two different gaps is presented in Figure 4.13. A large pulse was expected for a higher gap distance due to the added time to the electrons drift. However, we observed that the rise time of the signals does not change when the gap varies by a factor of two, despite of the slow rising tail that it is attributed to the inefficiency of the Frisch grid as discussed in Section 5.5. These results show that the peaking time of the amplifier and the collection time of electrons in the gap cannot explain the shape of the output signals, and denote the presence of an additional effect that affects the charge collection in the anode. This effect seems also independent of the physical characteristics of the Frisch grid since a similar rise time was found for a 50.29 LPI mesh (see Figure 4.14). In fact, it points out that the collected charge depends on the position of the interaction with respect to the anode. This effect is further discussed in Chapter 5.

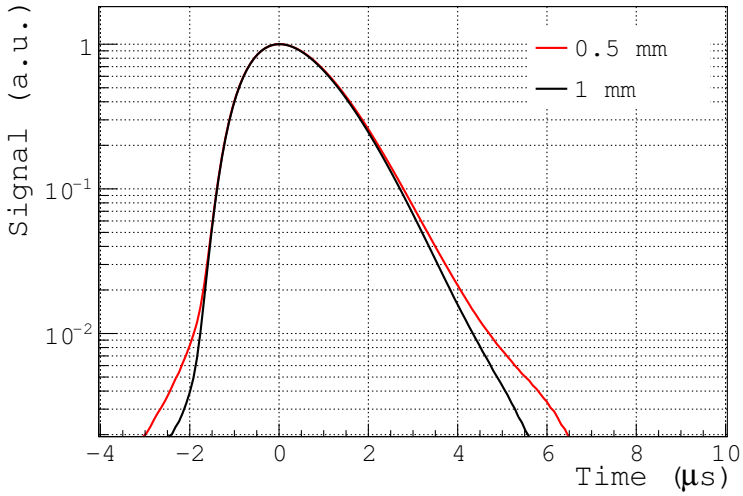

Figure 4.13 – Comparison between the output signal of the shaper for 511 keV events with a 100 LPI Frisch grid placed at 500 μm (red line) and a 1 mm (black line)from the anode. The peaking time was set to 1.39 μs.

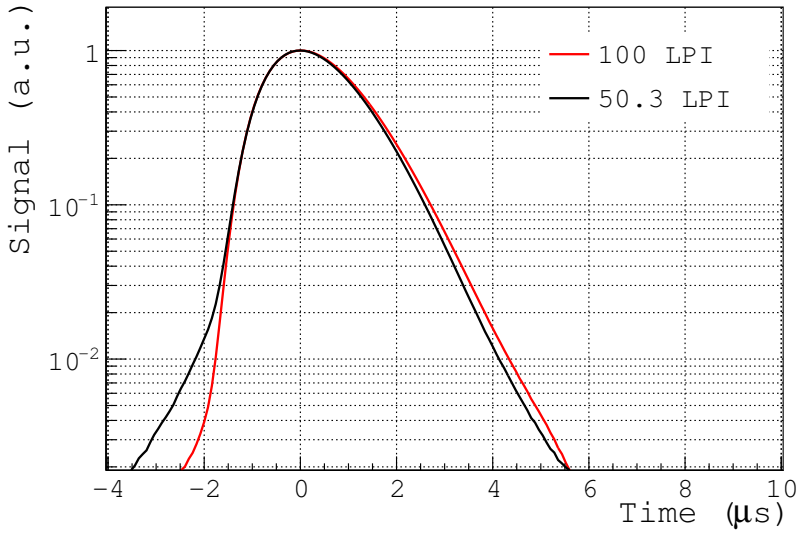

Figure 4.14 – Comparison between the output signal of the shaper for 511 keV events for two different Frisch grids placed at 1 mm from the anode: a 100 LPI Frisch grid (red line) and a 50.3 LPI (black line). The peaking time was set to 1.39 μs.

4.3.2 Ballistic deficit

In a radiation detector the amplitude of the measured signals should be proportional to charge produced after an ionizing particles interacts with the medium. In addition to that, the measured charge should be independent of the charge collecting time within the detector. This means that the maximum amplitude of the preamplifier signal must be preserved after the shaper. This is possible if the shaping time constants of the pulse-shaping amplifier are large compared with the preamplifier pulse rise time. However, if the shaping time constants

are not long enough, part of the collected charge would be lost in the shaping process. This effect is called *ballistic deficit*. The amplitude loss, together with the electronic noise and the statistical fluctuations associated with the charge production process in the detector are the major source that limits the energy resolution on a detector. The ballistic deficit can be corrected by an adequate selection of the shaping time of the linear amplifier. However, the choice of the peaking time cannot be made arbitrarily, but it should be made depending on the detector requirements. For example, on high rate experiments short shaping times are needed in order to minimize pulse pile-up. Equally, short shaping times are necessary to spatially resolve multiple interactions as in a Compton scattering sequence.

Variations in the rise time of the output signals can also affect the amplitude of the shaper output pulse. In an ideal gridded TPC, since all electrons start to induce a signal on the anode from the same point, the shape of the pulse at the output of the shaper is the same regardless the position of the interaction. Thus, the ballistic effect should only depend on the time properties of the combination preamplifier-shaper.

In this section we try to quantify the degree of ballistic deficit as a function of both peaking time and preamplifier output signal rise time. Figure 4.10 shows the average output signal obtained for four different peaking times obtained when a delta-like pulse with a 5 ns slope is injected in the preamplifier input capacitance. The pulses were averaged over 2000 events. When a delta-like current pulse in injected at the input of the preamplifier, no ballistic deficit is expected for an ideal CSA since the rise time of the output signal is, in general, very fast compared to the minimum peaking time provided by the IDeF-X LXe ASIC, which is 0.73 μs. However, as discussed in the previous section, due to the slower rise time of the preamplifier signals which is of the order of 500 ns, a shaping time of 0.73 μs is not enough to integrate all the collected charge. The peak signal deficit increases as the peaking time decreases. Considering that for shaping times larger than 2.72 μs there is not ballistic deficit [191], a 6 % of charge loss has been measured for a peaking time of 0.73 μs. Similarly, at 1.39 μs, 2.3 % of the total charge is lost just due to the time response of the preamplifier, and less than 1 % is expected for a 2.05 μs of peaking time.

The dependence of the ballistic deficit with the preamplifier pulse rise time is presented in Figure 4.15. Since the rise time of the preamplifier output signal depends on the charge collection time, for a fixed peaking time the maximum amplitude of the shaped pulse should depend on the grid-anode distance. The signals presented in Figure 4.15 were obtained with a constant peaking time of 1.39 μs and four different rise time: 5 ns, 250 ns, 500 ns and 750 ns corresponding to a grid-anode distance of approximately 0 mm, 0.5 mm, 1 mm and 1.5 mm for an electron drift velocity of 2 mm/μs at 1 kV/cm. The signals were also injected through the test input capacitance and averaged over 2000 events to reduce the statistical fluctuations. The results show that the amplitude deficit increases as the rise time increases. A loss of the order of 1.7 % on the maximum collected charge is observed for a gap of 1 mm (red line) compared to a gap of 500 μm (black line). On the other hand, for shaping time of 2.72 μs, a maximum ballistic deficit of the order of 1 % is observed as shown in Figure 4.16.

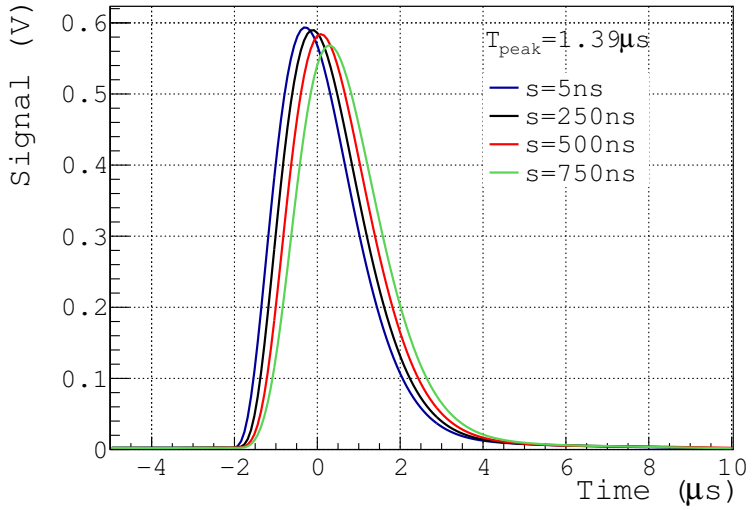

Figure 4.15 – Output signal of the shaper for a peaking time of 1.39 μs as a function of the preamplifier pulse rise time.

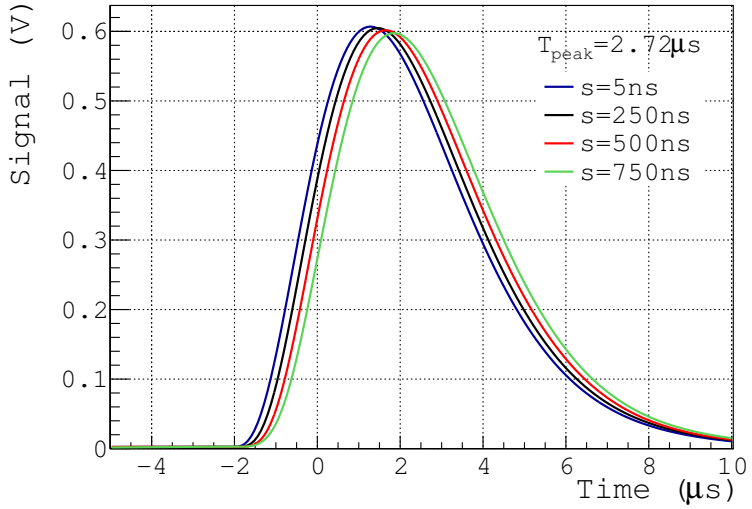

Figure 4.16 – Output signal of the shaper for a peaking time was of 2.72 μs as a function of the preamplifier pulse rise time.

We can conclude that larger peaking times imply both less electronic noise as discussed in Section 4.2, and less ballistic deficit. However, better timing resolutions are in general related to shorter peaking times, since the time resolution on a detector depends on the slope-to-noise ratio. In addition, we have seen that larger gaps also increase the charge loss due to ballistic deficit. For a peaking time of 1.39 μs and a gap-anode distance of 500 μm, which are the standard experimental conditions in XEMIS1, a ballistic deficit of around 3 % is estimated. This effect adds a systematic uncertainty in the measurement of the charge in the detector. In the next section, a study of the amplitude and time measurement precision as a function of the peaking time is carried out in order to optimize the performances of the analog ASIC that would be used in XEMIS2 for the measurement of the ionization signals.

4.3.3 Charge linearity

The study of the linearity range of the IDeF-X LXe ASIC for a given gain of 200 mV/fC and a peaking time of 1.39 μs has been also performed by injecting a charge through the Frisch grid. Since the pulse shape at the output of the shaper is not well reproduced by an ideal delta-like pulse, we opted to inject the preamplifier average signal presented in Figure 4.17(a) obtained for 511 keV events. In this way, we take into account the different effect on the output signal due to the overall system. The average pulse was parametrized and defined as a piece-wise function in the pulse generator and directly injected to the grid. The measurements were taken with a 100 LPI Frisch grid at 1 mm from the anode, a 12 cm long TPC and a shaping time of 1.39 μs. Figure 4.17 shows the comparison between the experimental average pulse and the theoretical one at the output of both the preamplifier and the shaper. We can see that the injected pulse fairly represents the average experimental signal, and the small difference between the preamplifier signals does not affect the shaped pulse. This implies that the shaper is not very sensitive to slight fluctuations in the slope of the preamplifier signal.

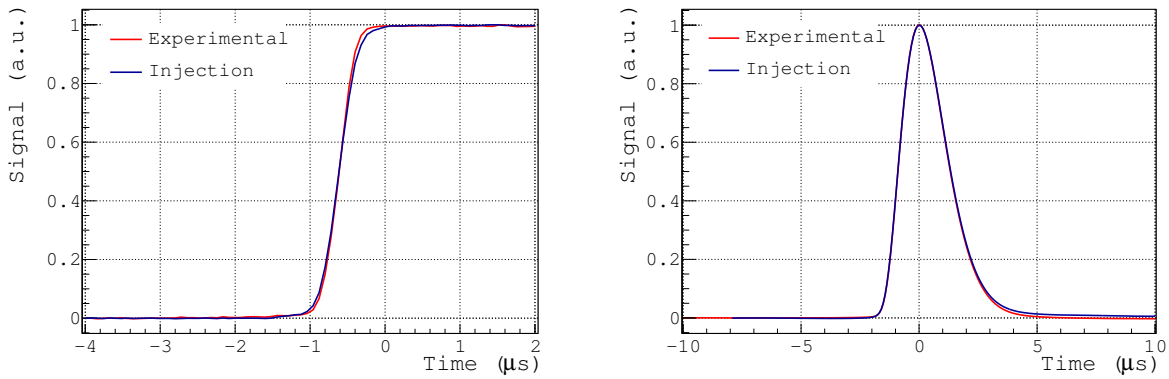

(a) Preamplifier. **(b)** Shaper.

Figure 4.17 – Comparison between the experimental and injected signals at the output of the (a) preamplifier and (b) shaper. The average injected pulse was obtained over a large number of experimental preamplifier output pulses with a total energy of 511 keV.

The amplitude of the injected pulses varied between 100 mV to 3.1 V. For each configuration 1000 events were acquired and analyzed. The maximum amplitude of the signals was determined by a method based on a Constant Fraction Discriminator (CFD) (see Section 4.4.2). Pulse selection was made with a threshold level of 3 times de noise ($\sim$4.5 keV). Figure 4.18 shows the maximum measured amplitude, averaged over the 1000 events, as a function of the injected charge. The data is well described by a first order polynomial and show an excellent linear behavior in all the amplitude range. The dynamic range completely covers the required energy interval for the calibration of the detector, and enables to measure signals of energies up to 1.274 MeV for a gain of 200 mV/fC. The ASIC saturation is observed at $\sim$ 1.3 MeV.

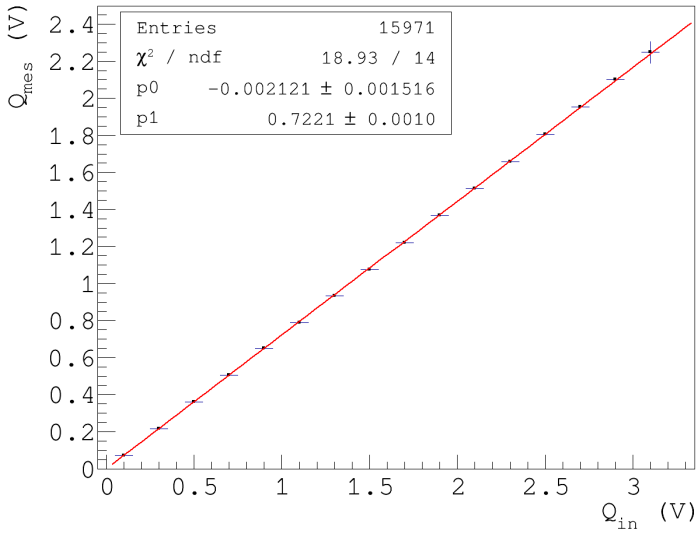

Figure 4.18 – Output amplitude of the IDeF-X LXe chip as a function of the injected charge for the pixel 1 of the anode (peaking time 1.39 μs and gain 200 mV/fC). The red line represents a first order polynomial, which shows a perfect linear response of the electronics in all the dynamic range.

Same study was performed for low measured energies. In this case, the charge of the injected pulses varied between 1 mV to 1 V in steps of 5 mV. Equally, for each configuration 1000 events were acquired and analyzed using a method based on a CFD to measured the maximum of the signals. The data show a good linear behavior in most of the energy internal, which is well fitted by a first order polynomial, as shown in Figure 4.19. A non-linear response was measured, in the other hand, at very low measured charges close to the threshold level (∼4 times the noise). This non linearity, depicted in Figure 4.20, is not related to the response of the electronics, but is due to the electronic noise and the method used to measured the charge. Since the signals are selected with a threshold level set at $3\sigma_{noise}$, only pulses with an amplitude strictly higher than this threshold are registered. The threshold effect generates a bias in the measured charges at low energies. Figure 4.21 shows the ratio between the number of measured signal and the number of injected pulses vs. the measured charge. At amplitudes at around six times the electronic noise (∼9 keV), 100 % of the injected pulses are measured by the CFD method, whereas only 40 % are measured at the threshold level.

Please note that the differences between the two curves for the same injected charge are due to the fact that the injection was performed under different experimental conditions. However, the purpose of this study is to measure the linear behavior of the electronics before saturation and not the gain (no calibration of the injected charges was made).

4.3.4 Equivalent Noise Charge

The noise performances of the IDeF-X LXe ASIC have been also studied during this thesis by measuring the ENC as a function of the peaking time. The ASIC was connected to the detector, that was fully operational and working under standard experimental conditions. The Frisch grid (100 LPI) was biased with a voltage of -300 V. The value of the input

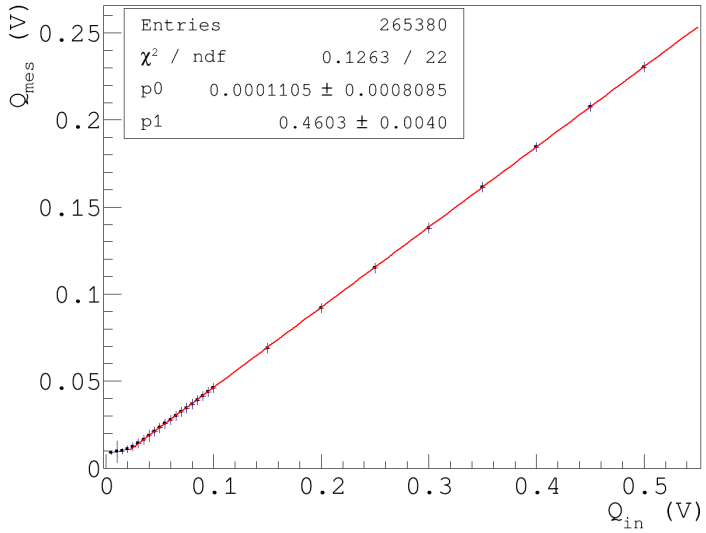

Figure 4.19 – Output amplitude of the IDeF-X LXe chip vs input charge for the pixel 1 of the anode and low injected amplitudes (peaking time 1.39 μs and gain 200 mV/fC). The red line represents a first order polynomial, which shows a perfect linear response of the electronics in almost the entire dynamic range. A lost of linearity due to the measurement method is observed close to the threshold level.

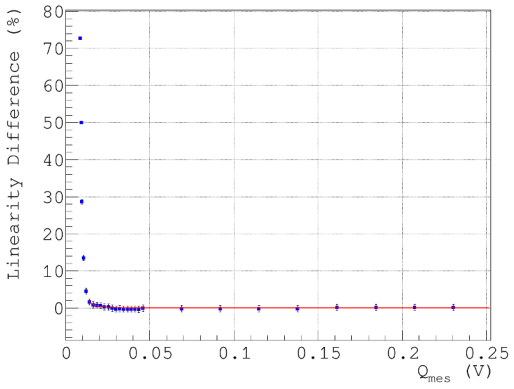

Figure 4.20 – Linearity difference between the measured charge and the first degree polynomial fit. The red line represents an exponential fit.

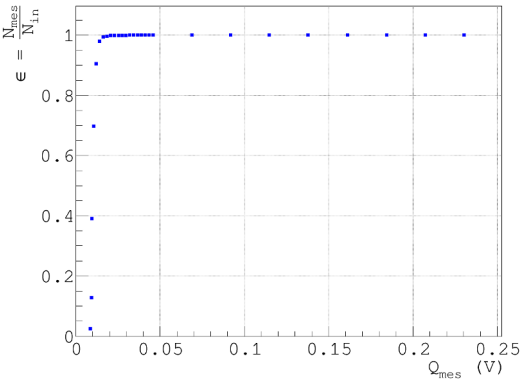

Figure 4.21 – Ratio between the number of measured signal and the number of injected pulses as a function of the measured charge.

capacitance was estimated to be $\sim 15\ pF$ at room temperature [187], and we can assume that this value does not change at lower temperatures of the order of -60°C. The injection capacitance of a channel is 50 fF. The ASIC was programmed with a gain of 200 mV/fC and with the minimum available value of the leakage current (20 pA). We used a waveform generator to inject delta-like pulses of 30 mV and 60 mV. The noise was measured at the maximum of the signals, and all signal are treated after pedestal correction (see Chapter 6, Section 6.4). The conversion from volt to electrons was performed using the injection capacitance.

Figure 4.22 shows the ENC values as a function of the shaping time obtained for one of the pixels of the anode. The system shows excellent noise performances with a minimum of $\sim 100\ e^-$ for a shaping time of 2.05 μs. This level of noise is adequate for 3γ imaging applications. In Figure 4.22 the values of ENC have been fitted to separate the different noise contributions described in Section 4.2 (see Figure 4.7). The dominant contribution to the ENC in the peaking time range of 1.39 μs to 4.06 μs is the 1/f noise, whereas at higher shaping times the parallel noise seems to dominate.

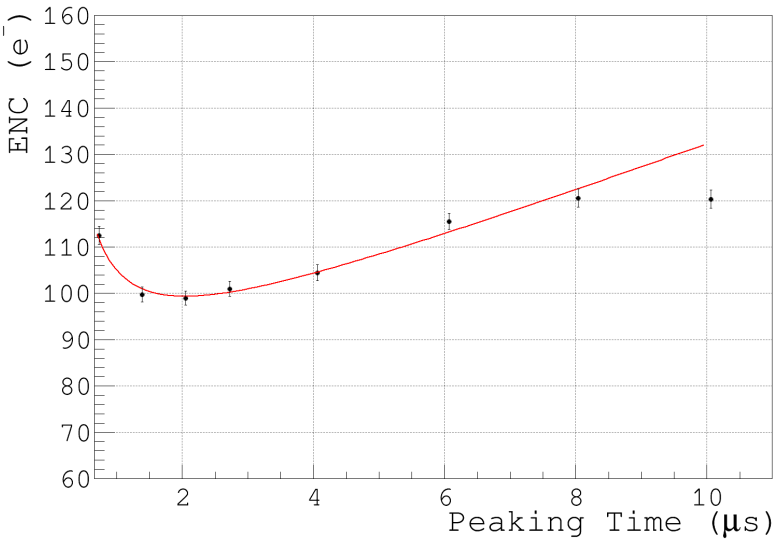

Figure 4.22 – ENC vs. shaping time for a leakage current of 20 pA and a conversion gain of 200 mV/fC.

The thermal noise contribution due to the reset of the CSA is very small due to the high value of the equivalent resistance of the PMOS transistor ($\sim G\Omega$). Moreover, since the dark current of the detector is negligible and the injected leakage current is small, of the order of tens of pA, the expected relative contribution of the parallel noise should be also small. As a result, an almost flat distribution limited by the 1/f noise contribution is expected at high peaking times. However, we see in Figure 4.22 that for peaking times higher than 4.06 μs the parallel noise seems to dominate. Since the parallel noise contribution increases as the leakage current i_{leak} increases, the ENC values as a function of the peaking time have been calculated for two different values of i_{leak}. The results are shown in Figure 4.23. We can see that an increase of the leakage current of the CSA has no impact on the series noise contribution (short peaking times). A minimum noise of the order of 100 e^- is measured for both i_{leak} currents at a shaping time of 2.05 μs. Moreover, no significant difference in the noise performances is observed at long peaking times between the two i_{leak} values. This suggests that the contribution of a correlated noise, mostly due to capacitive coupling between signal and electronics grounding, cannot be neglected.

Figure 4.24 shows the same measurements after correlated noise correction (see Chapter 6, Section 6.5.2). As expected, for the smallest current, the serial noise increases. This is due to the fact that the main source of series noise is the thermal noise at the input of the CSA, which is oppositely proportional to the transconductance of the input transistor, which in

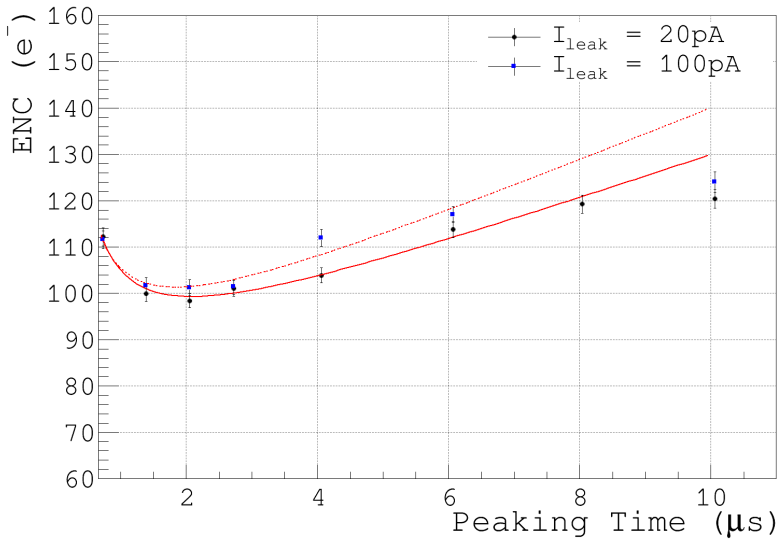

Figure 4.23 – ENC vs. shaping time for two different values of the leakage current of 20 pA and 100 pA, and a conversion gain of 200 mV/fC.

turn is proportional to the total current of the CSA. For long peaking times (above 4.06 μs) the contribution of the shot noise dominates for a leakage current of 100 pA, whereas for 20 pA only the 1/f noise is present. After correlated noise correction the minimum noise for a leakage current of 20 pA, shifts to $\sim 88\ e^-$ at a peaking time of 2.72 μs. Figure 4.25 shows the ENC vs the shaping time with and without correlated noise correction for the two different values of i_{leak}. The estimated contribution of the correlated noise as a function of the peaking time is presented in Figure 4.26.

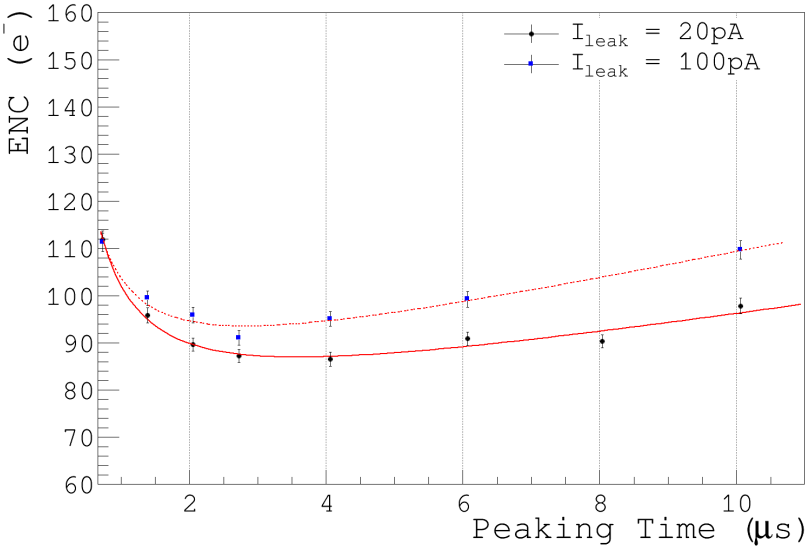

Figure 4.24 – ENC vs. shaping time for two different values of the leakage current of 20 pA and 100 pA (conversion gain of 200 mV/fC) after correlated noise correction.

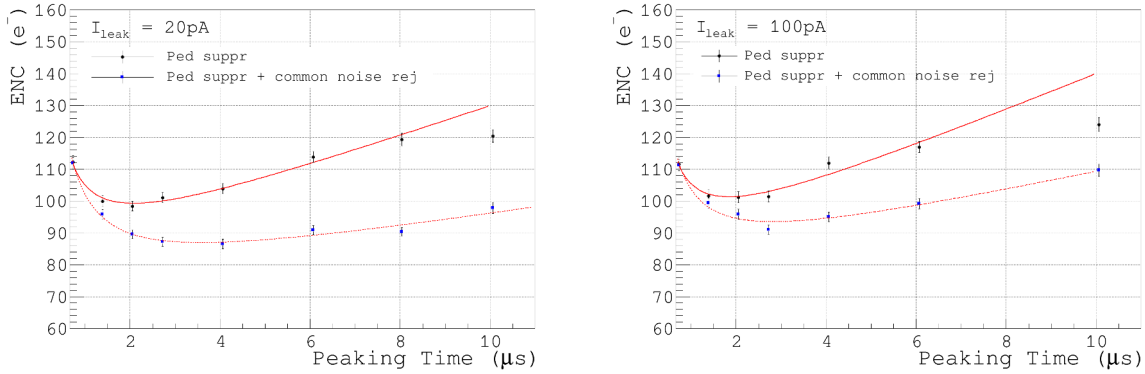

(a) $i_{leak} = 20\ pA$ **(b)** $i_{leak} = 100\ pA$

Figure 4.25 – ENC vs. shaping time for two different values of the leakage current of (a) 20 pA and (b) 100 pA with and without correlated noise correction.

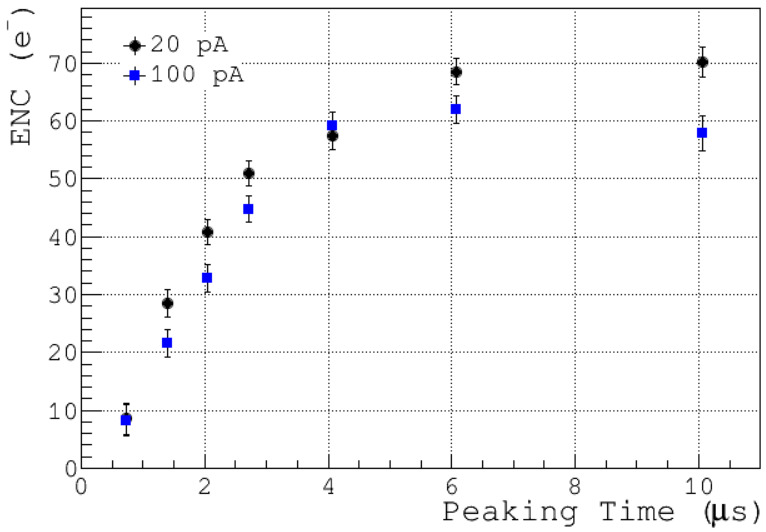

Figure 4.26 – Correlated noise contribution for two different values of the leakage current of 20 pA and 100 pA.

As a conclusion, to minimize the contribution of the electronic noise to the energy and time resolutions, the IDeF-X LXe ASIC should operate at the smallest possible leakage current and at a peaking time of the order of 2 μs. Moreover, a shielding optimization of the chip and the connexion cables will reduce the correlated noise contribution. Results of the ENC as a function of the peaking time at room temperature and as a function of the input capacitance for the IDeF-X LXe ASIC can be found in Lemaire et al. [187].

4.4 Measurement Optimization of the Ionization Signal with a CFD

Excellent energy and spatial resolutions are essential in Compton imaging, where both the deposited energy and the position of each interaction are required for the final reconstruction of the image. As we have discussed in the previous sections, the noise and the ballistic deficit degrade the energy and time resolutions of a detector. However, besides the statistical fluctuations in the number of produced charges, there are other intrinsic effects that may also affect the performances of the detector. For example, the spread of the electronic cloud during the drift process along the TPC due to the electron transverse diffusion, adds some uncertainty in the calculation of the reconstructed interaction position and the final collected charge, which in turn affects the final spatial and energy resolutions.

Because of the electronic cloud diffuses while it drifts towards the anode, due to the long drifting distance, there is a non-negligible probability that the electron cloud would fire multiple neighboring pixels. In this case, the estimated position of the interaction is calculated as the centroid position of the electron cloud, while the final charge is the sum of all the individual charges. Moreover, since not all the neighboring fired pixels must become from the same interaction, an additional condition concerning the drift time should be applied in order to discriminate different interactions that take place very close one from each other. As a result, accuracy on both time and charge measurements are indispensable to ensure good energy and spatial resolutions. The purpose of this study is to determine the optimal method for the measurement of the amplitude and the drift time of the ionization signals in the LXe. Two different methods are presented and compared. To perform the study, a complete Monte Carlo simulation of the output signal of the front-end electronics of XEMIS1 has been performed.

4.4.1 Electronic Noise and Ionization Signal Simulation

As discussed in Section 4.1.1, the read-out electronics of XEMIS1 generates 64 (32 x 2) independent analog signals S(t) corresponding to the 64 pixels of the anode. Each signal is registered over a total period of 102.2 μs and sampled by the FADC at a rate of 12.5 MHz. Consequently, each registered event results in a set of 64 sampled signals S(n), where n = 1,...,N denotes the sampling time index and N is the total number of channels per signal, equal to 1278.

The aim of this section is to accurate simulate the output signal of the IDeF-X ASIC, S(n), by using experimental data. Assuming that the signals can be decomposed as the sum of two statistically independent components, a noiseless signal s(n) and a disturbing noise n(n), the simulation of both contributions was performed individually.

Signal simulation

The shape of the signal s(n) was reconstructed as a result of the parametrization of the average signal obtained over a large enough set of independent experimental events. The goal of using the average signal was to minimize the noise contribution per bin. The experimental

data was taken for a 100 LPI mesh with a 1 mm gap, an electric field of 1 kV/cm and a shaping time of 1.39 μs. To reject noise events, a threshold of 10 time the noise ($\sim 15\ keV$) was set on each individual signal. In this way, we ensured that only events with enough amplitude contributed to the final shape of s(n). The amplitude of s(n) corresponds to the voltage equivalent to an electron. As a result, any amplitude signal (in charge) can be generated by multiplying s(n) by a constant. Figure 4.27 shows the simulated pulse compared to the experimental averaged signal.

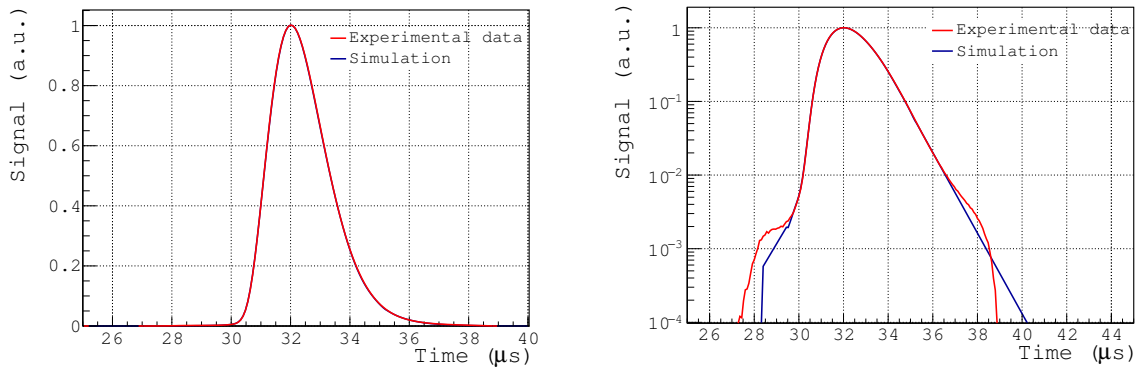

Figure 4.27 – Comparison between the normalized averaged signal obtained from experimental data and the simulated signal, in linear and logarithmic scale ($\tau_0 = 1.39\ \mu$s).

Noise simulation

The noise adversely affects the signal characteristics and complicates the data processing. For this reason, its contribution is very important, especially at low energies. The simulation of the noise n(n), unlike the noiseless signal s(n), is a complicated process that requires a thorough study.

The noise at the output of the IDeF-X LXe has a Gaussian amplitude distribution. The power spectrum of the noise obtained for a set of experimental noise events is depicted in Figure 4.28, which represents the distribution of the noise amplitudes. The equivalent value of the noise can be quantitatively characterized in terms of the root-mean-square (RMS) of the distribution. The experimental noise distribution was fitted by a Gaussian function with a standard deviation of $\sigma_{noise} = 85.42$ electrons.

Time domain representation is useful for noiseless signals. However, a correct simulation of the noise behavior requires the analysis on the frequency domain. This technique allows to extract relevant signal features not perceptible from the time domain representation. A signal can be converted between the time and frequency domains by a mathematical operation call transformation. A common transformation used in data processing is the Fourier transform. For discrete-time and finite-duration signals, the Discrete Fourier Transform (DFT) is commonly used (4.10):

$$X[k] = \sum_{n=0}^{N-1} x[n].e^{-j.k.\omega_0.n} \tag{4.10}$$

where N is the total number of samples, k = 0,1,...N-1 is the frequency bin index[4] and ω_0 is the fundamental frequency given by $\omega_0 = \frac{2\pi}{N}$. We assume that $\sum_{n=0}^{N-1} x^2[n] = 1$ to facilitate our notation and to avoid additional normalization factors.

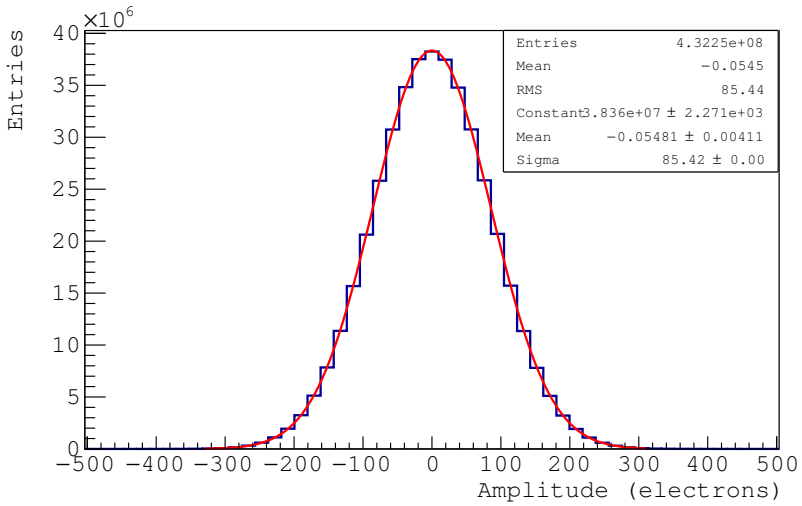

Figure 4.28 – Experimental distribution of the noise amplitudes for a peaking time of 1.39 μs. The red curve represents the Gaussian fit.

Each spectral component of the DFT X[k] is a complex variable that can be expressed as a function of its real and imaginary components: $X[k] = \Re e[k] + i\Im m[k]$:

$$\Re e[k] = \sum_{n=0}^{N-1} x[n].\cos(\omega_0.n.k) \tag{4.11}$$

$$\Im m[k] = \sum_{n=0}^{N-1} x[n].\sin(\omega_0.n.k) \tag{4.12}$$

The effect of applying the DFT over a finite time window results in high fluctuations between different events, especially at low frequencies. In fact, the smaller the time interval and the bigger the sampling period, the higher the inexactitude in the results. A well used method to compensate this limitation and minimize its effect, is to average the DFT coefficients for each bin over a large number of events. For this study, we used a set of 12000 events per pixel recorded under standard experimental conditions over a total time window of 77.3 s. The averaged spectra of the real and imaginary parts of the DFT coefficients are reported in Figure 4.29. Only the positive half of the frequency spectrum is displayed

[4]One frequency channel k equals 10 kHz

due to the symmetry around the DC component. The highest detectable frequency, called Nyquist frequency, is equal to half of the sampling frequency. In our case the Nyquist frequency is 6.25 MHz.

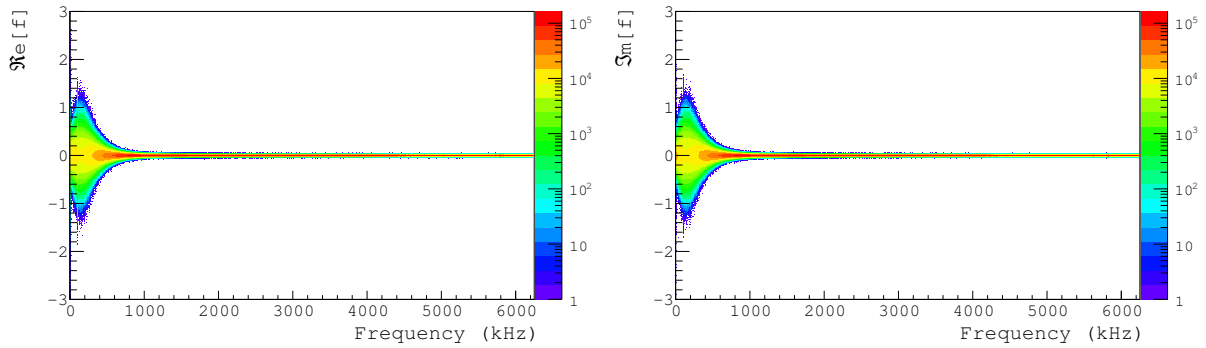

(a) ℜe **(b)** ℑm

Figure 4.29 – Average probability density functions of the (a) real and (b) imaginary parts of the DFT coefficients obtained from experimental noise events registered over a total time window of 77 s.

Figure 4.30 illustrates the probability density function (PDF) of the real and imaginary parts of the Fourier Transform coefficients for a given frequency obtained with experimental data. As we can see, both coefficients obey a zero mean Gaussian probability distribution with equal variance. This fact is derived from the stochastic character of the x[n] coefficients and explained by the Central Limit Theorem [200]. In addition, both coefficients are statistically independent, and hence uncorrelated as we can presume from the Figure 4.31.

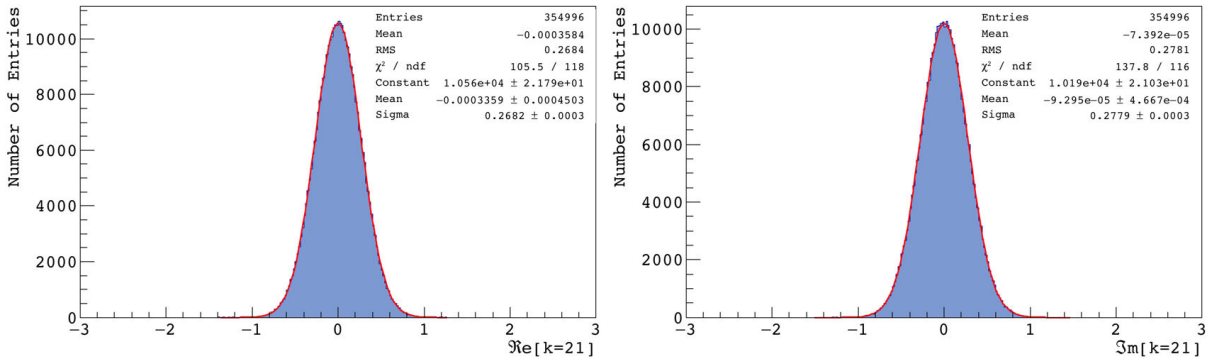

(a) ℜe[k] **(b)** ℑm[k]

Figure 4.30 – Probability density functions of the (a) real and (b) imaginary parts of the DFT coefficients obtained for the same frequency (k = 21). The red curve represents the Gaussian fit.

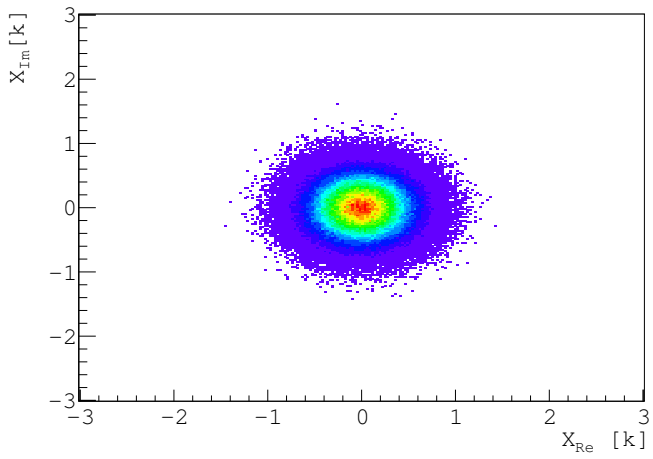

Figure 4.31 – Distribution of the imaginary part of the DFT coefficients as a function of the real part.

Generally, the Fourier transform is expressed in terms of the magnitude (A[k]) and the phase ($\phi[k]$): $X[k] = A[k]e^{i\phi[k]}$, which are directly related to the real and imaginary parts of the DFT coefficients through the following formulas:

$$A[k] = \sqrt{\Re e[k]^2 + \Im m[k]^2} \tag{4.13}$$

$$\phi[k] = \arctan(\frac{\Im m[k]}{\Re e[k]}) \tag{4.14}$$

Because of the independence of the real and imaginary parts of the DFT coefficients, the joint probability density function can be expressed as the product of the individual PDFs: $P(x, y) = P(x)P(y)$, where x and y represent the $\Re e$ and $\Im m$ respectively. The index k has been dropped for simplification. In addition, since both parts are identically distributed modeled by a Gaussian density function, the joint PDF is given by equation (4.15),

$$P(x, y) = P(x)P(y) = \frac{1}{2\pi\sigma^2} e^{-\frac{x^2 + y2}{2\sigma^2}} \tag{4.15}$$

by using $dxdy = AdAd\phi$, we obtain the joint PDF as a function of the magnitude and the phase. Note that A and ϕ are also statistically independent.

$$P(A, \phi) = \frac{A}{2\pi\sigma^2} e^{-\frac{A^2}{2\sigma^2}} \quad with \quad A \in [0, \infty] \ \ and \ \ \phi \in [-\pi, \pi] \tag{4.16}$$

The individual PDFs of the magnitude and the phase are therefore:

$$P(A) = \int_0^{\infty} \frac{1}{2\pi\sigma^2} e^{-\frac{x^2+y2}{2\sigma^2}} \, dA \;\; = \;\; \frac{A}{\sigma^2} e^{-\frac{A^2}{2\sigma^2}} \tag{4.17}$$

$$P(\phi) = \int_{-\pi}^{\pi} \frac{1}{2\pi\sigma^2} e^{-\frac{x^2+y2}{2\sigma^2}} \, d\phi \;\; = \;\; \frac{1}{2\pi} \tag{4.18}$$

This result shows that the magnitude obeys a Rayleigh distribution given by Equation (4.17) [201] while the phase is uniformly distributed over $\pm\pi$. The power spectrum obtained from experimental data is presented in Figure 4.32, whereas the experimental PDFs of the magnitude and the phase obtained for a given frequency are presented in Figure 4.33(a), which are consistent with the expected distributions. Figure 4.33(b) reveals an almost uniform distribution of the phase. Discrepancies with the expected distribution should be associated with the limitations of the method.

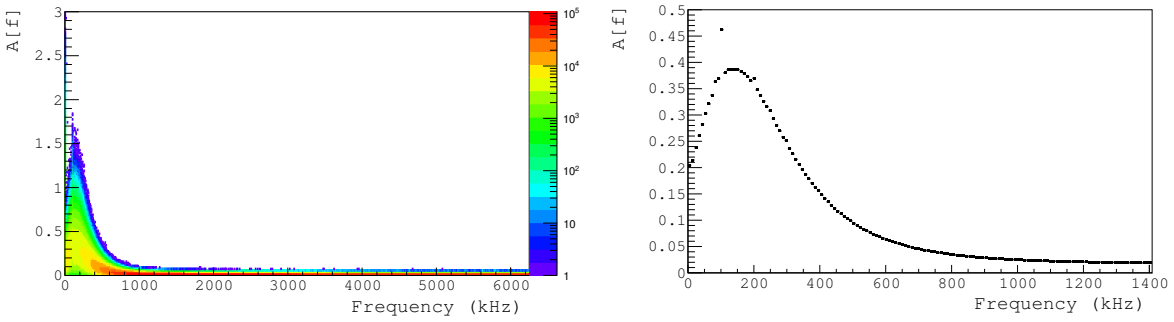

(a) **(b)**

Figure 4.32 – (a) Power spectrum of the magnitude of the DFT as a function of the frequency obtained from experimental noise events registered over a total time window of 77 s. (b) shows the average value per bin.

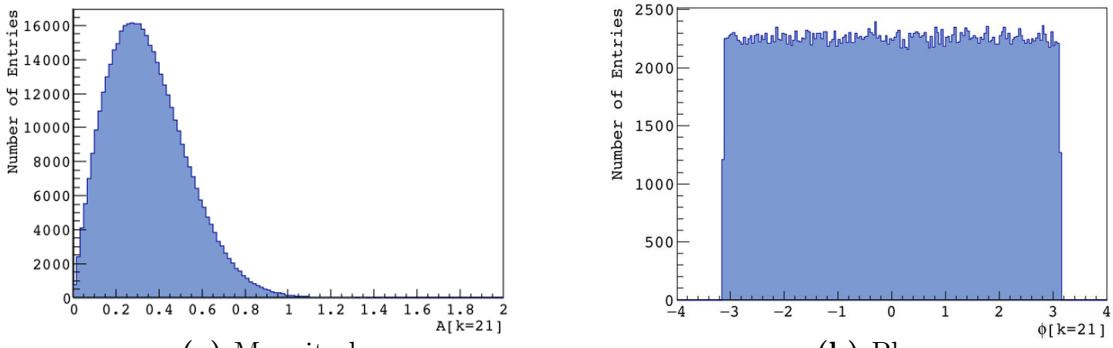

(a) Magnitude **(b)** Phase

Figure 4.33 – Probability density functions of the (a) magnitude and (b) phase of the DFT obtained for the same frequency (k=21).

A Monte Carlo simulation is finally performed to reconstruct the noise signals n(n) using these results. A random number is generated for both coefficients ($\Re$e and $\Im$ m) for each of the N bins. These random numbers are Gaussian distributed with mean and variance given by the averaged PDFs obtained for each individual bin (see example in Figure 4.30 for the frequency 210 kHz ($k = 21$)). The simulated noise signal is then obtained by performing the inverse DFT. An example of a simulated noise signal is presented in Figure 4.34.

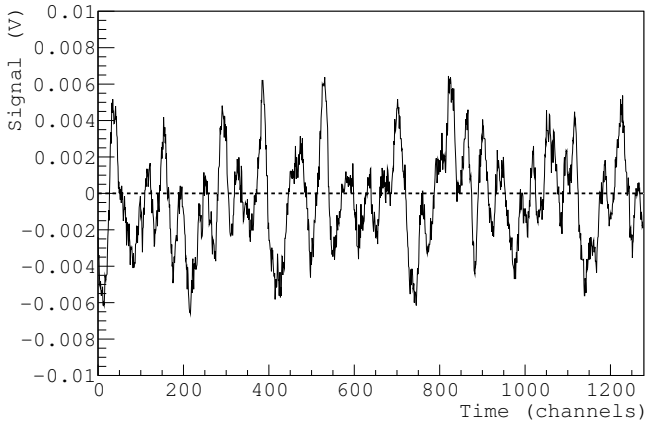

Figure 4.34 – Example of a typical simulated noise signal over a total time of window of 102.2 μs at a sampling rate of 12.5 MHz for a peaking time of 1.39 μs.

The simulated power spectrum of the magnitude of the DFT is presented in Figure 4.35(a). We can verify from Figure 4.35(b) that this method reproduces very well the experimental results. Moreover, the simulated amplitude distribution of noise events is depicted in Figure 4.36. A Gaussian fit to the distribution gives a estimated noise of $\sigma_{noise} = 84.89 \pm 0.02\ e^-$ which is in good agreement with the value obtained with the experimental data. These results confirm that the simulated noise can reproduce, with an excellent approximation, the electronic noise contribution.

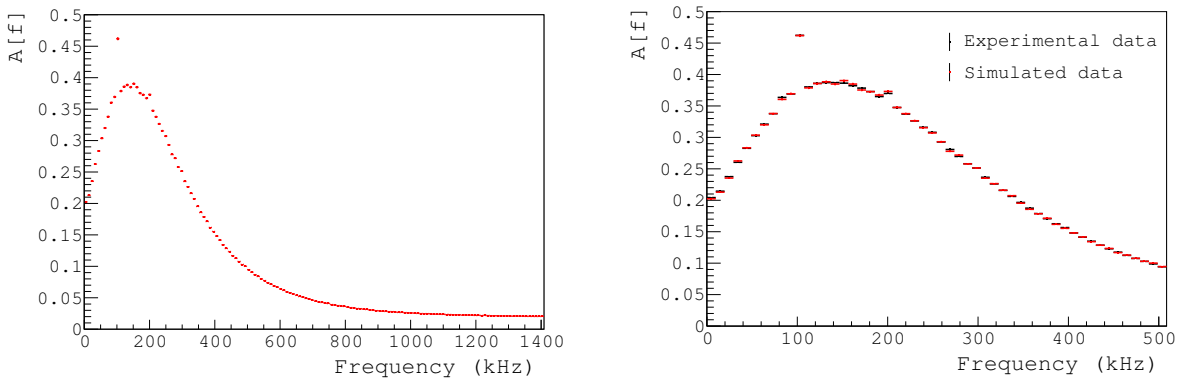

(a) **(b)**

Figure 4.35 – (a) Average power spectrum of the magnitude of the DFT obtained with the Monte Carlo Simulation and (b) Comparison between the experimental and simulated power spectra of the magnitude of the DFT.

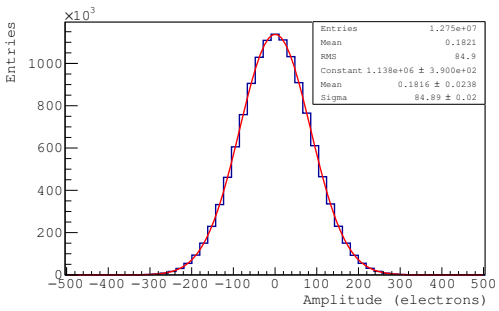

(a)

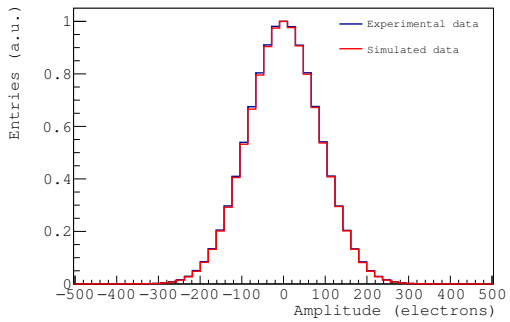

(b)

Figure 4.36 – (a) Simulated distribution of the noise amplitudes obtained for 10000 simulated events for a peaking time of 1.39μs. The red curve represents the Gaussian fit. (b) Comparison between the normalized experimental and simulated noise distributions.

Finally, by summing up both contributions s(n) and n(n) the simulated output signal of XEMIS1 is generated. Figure 4.37 shows an example of a simulated signal with amplitude $20\sigma_{noise}$ (5.4 V). Please note that the amplitudes are commonly expressed in terms of the value of sigma (RMS value) of the noise distribution.

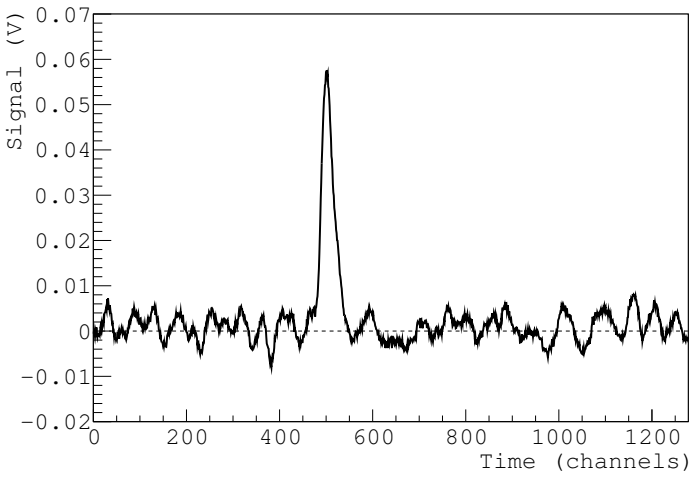

Figure 4.37 – Simulated output signal of XEMIS1 with amplitude $20\sigma_{noise}$ for a peaking time of 1.39μs.

4.4.2 Time and Amplitude measurement optimization

As we have seen the output signals of XEMIS1 consist of a total of 64×1278 samples for each registered ionization event resulting, in average, in an output file of around 2 GB for one hour run. This type of data acquisition is not longer recommendable for a detector with a large number of pixels as the case of XEMIS2, where near 24000 pixels will be present (see Section 4.6). To minimize the readout data volume we have proposed some updates in the front-end electronics. Instead of continuous sampling the analog signals, the new readout system uses an analog ASIC called XTRACT, that registers only the value of the amplitude, the time and the pixel address of those signals that trigger the discriminator. This type of recording requires much less time and power than real-time digitization. However, accurate measurements of time and amplitude are a very delicate issue, mainly for very low energy signals where noise contributions become important. For this reason, a Monte Carlo simulation has been performed in order to determine the method that provides the optimum time and amplitude measurement resolutions.

The simulation can be divided in two different parts. The first part includes of the generation of the output signal of the IDeF-X, as presented in the previous section 4.4.1. Each event corresponds to the simulation of one signal. The pulses are randomly generated inside a time window of 102.2 μs equivalent to the registration time over one pixel. Amplitudes are simulated between $3\sigma_{noise}$ (8 mV) and $20\sigma_{noise}$ (54 mV) because we are mostly interested in performing the analysis at low energies.

The second part consists of the simulation of the ASIC XTRACT, where the time and amplitude of the signals are estimated. Two different methods of measurement have been proposed and compared: a Constant Fraction Discriminator (CFD) and a peak-sensing ADC.

In addition, since the shape of the output signals depend greatly on the time-related parameters of the shaping amplifier such as the the peaking time of the shaper, in order to improve the SNR and to optimize the measurements of the amplitude and time of the signal, two different peaking times of 1.39 μs and 2.05 μs have been tested during this analysis.

Time and Amplitude measurement with a Constant Fraction Discriminator

The concept of the constant fraction triggering technique is illustrated in Figure 4.38. The input signal V_a is split in two parts. One part is inverted and attenuated to a certain fraction k of the original amplitude $V_c = -kV_a$, and the other part is delayed by a time τ_d. These two signals are added to form a bipolar pulse V_{out} with a zero-crossing point that is independent of the amplitude of the signal and is placed always at the same point, that corresponds to the optimum fraction of the signal height [22]. Our purpose is to accurately determine this zero-crossing point at the moment when the original signal reaches its maximum value. Therefore, with the CFD method, the time and amplitude of the signals are determined at the zero-crossing point. Since the precision is related to the proper selection of the delay τ_d and the constant fraction k, different combinations of these two parameters have been considered.

In general, the event selection is done by using a leading-edge discriminator [22]. Only those signals with an amplitude higher than a certain threshold value will be registered. In particular, for this study the discriminator level was set on $3\sigma_{noise}$ to optimize the background

rate (see Section 4.5). A second threshold may be included in the trailing edge of the pulses to reduce the number of noise triggers. Moreover, in the CFD method, the threshold can be set on either the original signal (S1) or directly on the constant-fraction signal (S2) (see Figure 4.39). Both cases are considered in this study.

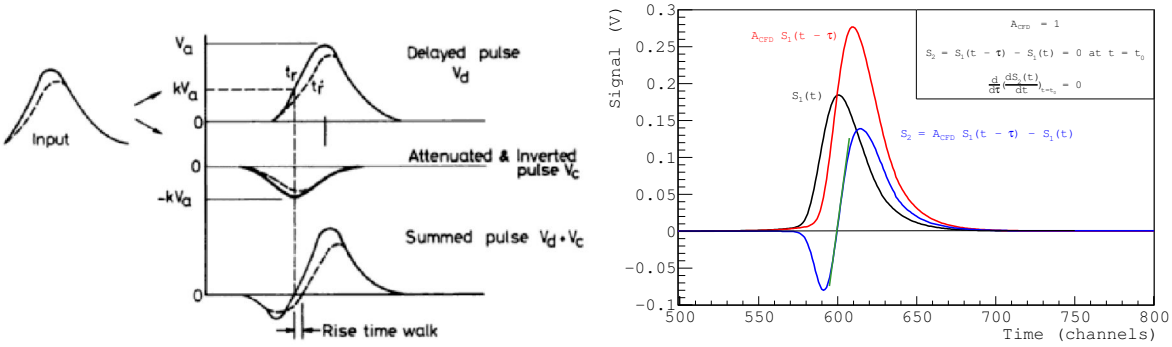

(a) **(b)**

Figure 4.38 – Principle of the Constant Fraction Discriminator. The dotted line in (a) shows the result for a different rise time [22]. In (b) S_1 is the original signal and S_2 the CFD signal.

Setting the discriminator threshold on S2 requires, however, an additional study of the noise in order to determine the optimum threshold level. The CFD amplitude distribution of the noise depends on the chosen values of the time delay and the attenuation fraction. For a delay of $\tau_d = 12$ channels[5] and a factor k = 1.436, an increase of the order of 45.6 % of the noise on the S2 signal was measured compared to S1. For this particular case, the equivalence to the $3\sigma_{noise}$ threshold level on S2 was found at $3.1\sigma'_{noise}$. This value was estimated from the CFD noise distribution at the point where the number of triggers per second agrees with the counting rate at the $3\sigma_{noise}$ level of the S1 noise distribution.

The worsening of the SNR on the CFD signal (S2), implies an important efficiency decrease at low energies compared to the result obtained for a $3\sigma_{noise}$ threshold set on S1 (see Figure 4.40). For an input signal with an amplitude equal to $3\sigma_{noise}$ the efficiency should be around 50%. However, by setting the discriminator on S2, less that 20 % of the simulated signals are measured. This efficiency loss cannot compensate the slight improvement observed at low energies on the measurement of the time and the amplitude resolutions, as shown in Figures 4.41 and 4.42 respectively. The decrease in the amplitude resolution observed for simulated amplitudes lower than $5\sigma_{noise}$ is due to a bias introduced by the method. As the threshold is set to $3\sigma_{noise}$, for example for a signal of amplitude $3\sigma_{noise}$, only half of the amplitude distribution is measured, and therefore, the mean of the distribution is shifted. As a consequence, the CFD method with the discriminator set on the original signal was considered the best option.

[5]One channel corresponds to 80 ns.

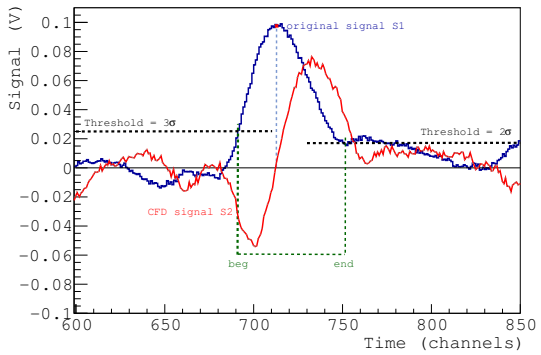

(a)

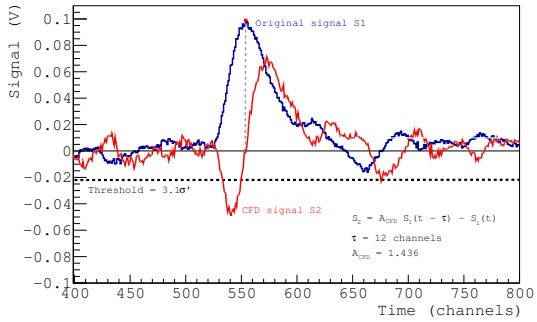

(b)

Figure 4.39 – Example of the CFD technique applied on a simulated signal (blue curve). The red curve is the CFD signal. The dashed black line represents the discriminator threshold. In (a) the threshold is directly applied on the simulated signal S1, while in (b) the threshold is set on the CFD signal S2. The threshold depends on the value of the σ_{noise} of the noise distribution. The x-axis is expressed in time channels, where 1 channel equals to 80 ns.

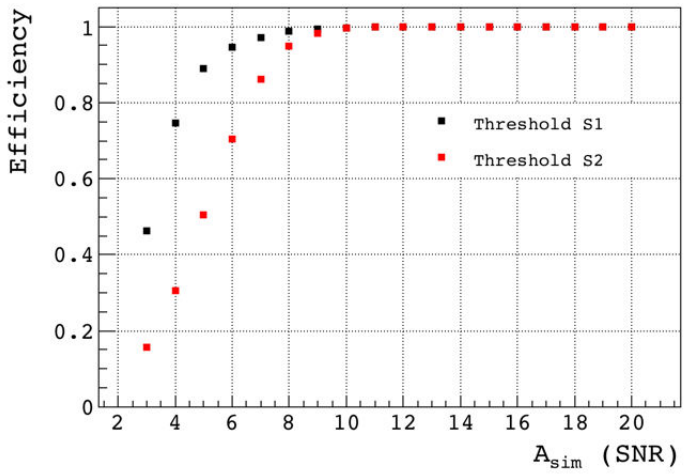

Figure 4.40 – Efficiency results obtained for the CFD technique for a $\tau_d = 12$ channels and a attenuation fraction k = 1.436. The black dots correspond to the case where the threshold level was set on the signal S1, whereas for the red dots the threshold was set on the CFD signal S2. The signal S1 was obtained for a peaking time of 2.05μs.

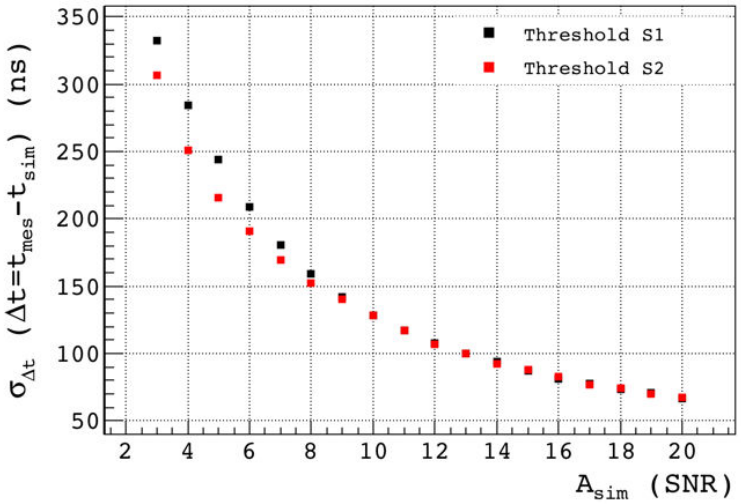

Figure 4.41 – Time resolution measured with the CFD method (τ_d = 12 channels and k = 1.436) for the two possible discriminator situations as a function of the simulated amplitude, expressed in units of SNR. The signal S1 was obtained for a peaking time of 2.05μs.

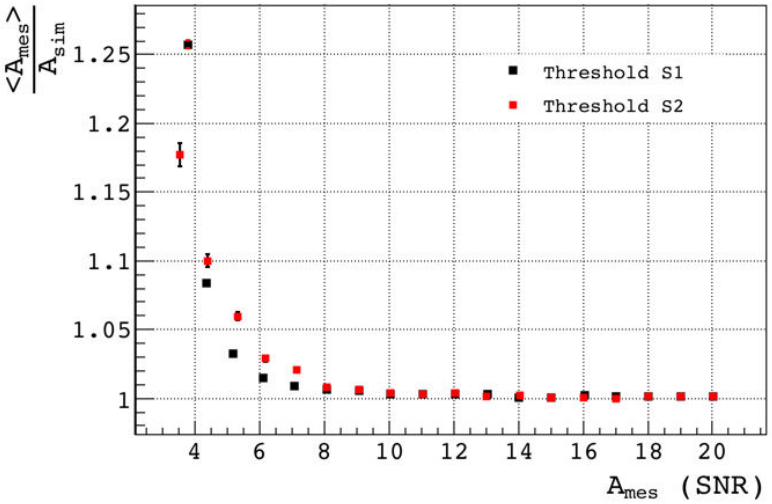

Figure 4.42 – Ratio between the measured averaged amplitude and the simulated amplitudes obtained with the CFD method (τ_d = 12 channels and k = 1.436) for the two possible discriminator situations as a function of the average measured amplitude, expressed in units of SNR. The signal S1 was obtained for a peaking time of 2.05μs.

To discriminate noise events, an additional condition on the zero-crossing point was included. If the zero crossover occurs inside a time window determined by the time interval elapsed from the moment that the input pulse rises above the threshold (*beg*) and the point where the signal trailing edge of the signal crosses again the threshold (*end*), the amplitude and the time of the signal will be measured. If not, the event will be rejected (see Figure 4.39(a)).

Peaking time optimization:

Another aspect to have into account is the role of the peaking time in the time and amplitude resolutions. As we have seen, the minimum ENC value is obtained for a shaping time of the order of 2 μs. However, a better time resolution, is expected at lower values of the peaking time. In this section, we compare two different values of the shaping time: 1.39 μs and 2.05 μs. In both cases, the CFD parameters were selected to obtain the zero-crossing point at the exact moment where the signal reaches its maximum. For a shaping time of 1.39 μs the delay was set to $\tau_d = 9$ channels (720 ns) and the attenuation fraction k = 1.5, while for a peaking time of 2.05 μs the delay was $\tau_d = 12$ channels and the attenuation fraction k = 1.436. Figure 4.43 shows the time resolution, i.e. the difference between the simulated and measured time, for the two values of the peaking time. Greater accuracy in the measurement of the time is observed for a time peaking of 1.39 μs, even at high amplitudes. On the other hand, non significant difference was observed on neither the measurement of the amplitude nor the efficiency, as shown in Figures 4.44 and 4.45 respectively. Based on these results, a shaping time of 1.39 μs is considered as the best option for the measurement of the drift time of the ionization signals in the detector.

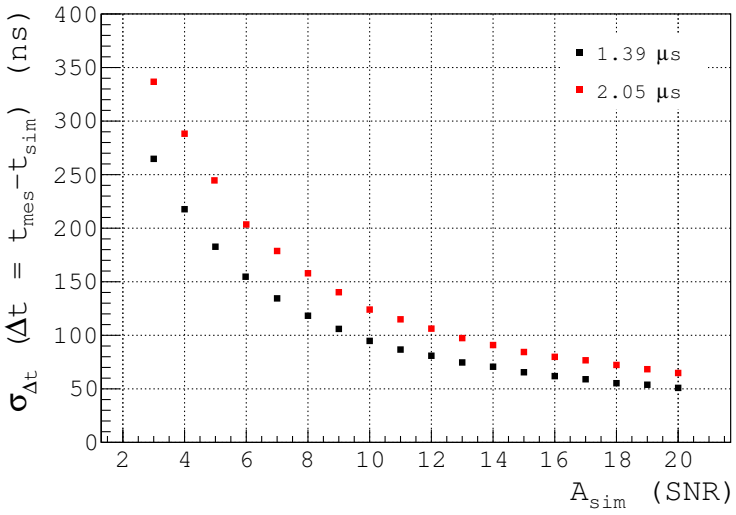

Figure 4.43 – Comparison of the time resolution obtained for two different values of the peaking time.

CFD parameters optimization:

The results are conditioned by the values of the delay and the CFD attenuation fraction. Ideally, this two parameters should be chosen in such a way that the zero-crossing time happens at the point of maximum slope. However, when a non-negligible level of electronic noise is present, fluctuations on the time at which the signal crosses the threshold introduces an uncertainty or jitter in the measurement of the time. Timing uncertainty caused by noise-induced jitter is illustrated in Figure 4.46. This contribution is inversely proportional to the slope of the CFD signal at the zero-crossing point and in general, the greater the

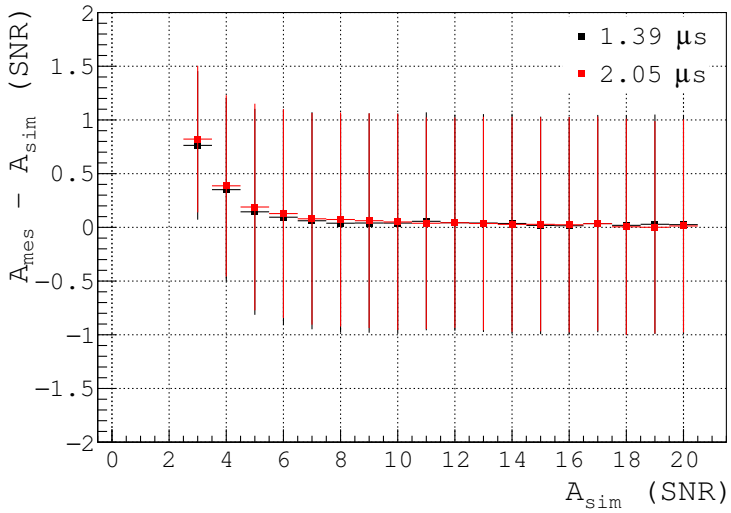

Figure 4.44 – Difference between the average measured amplitude and the simulated amplitude obtained for two different values of the peaking time. The error bars are obtained from the RMS of the distribution.

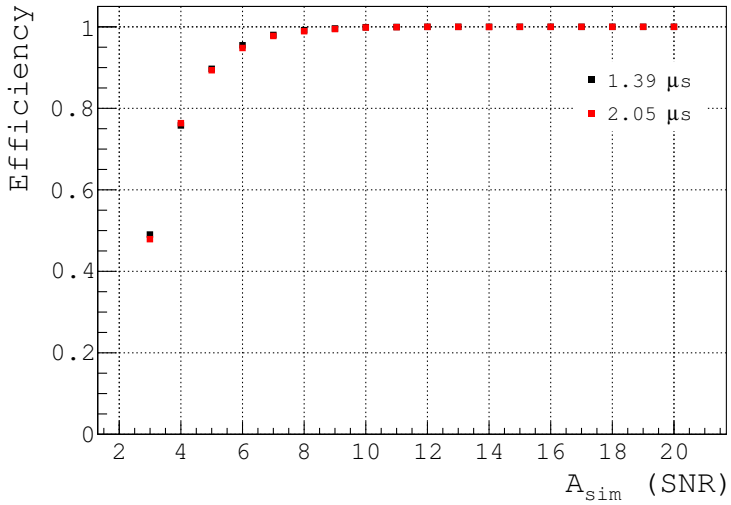

Figure 4.45 – Comparison of the efficiency obtained for two different values of the peaking time.

slope, the smaller the uncertainty introduced by this effect [202]. Equation (4.19) shows the relation between the timing error and the slope:

$$\sigma_t = \frac{\sigma_{N_{cfd}}}{\left.\frac{dV_{cfd}}{dt}\right|_{t=t_0}} \tag{4.19}$$

where $\sigma_{n_{cfd}}$ is the RMS value of the noise distribution of the constant-fraction signal (V_{cfd}) and t_0 is the zero-crossing time.

Figure 4.47 shows the slope of the constant-fraction signal at the zero-crossing point as a function of the delay for two different values of the attenuation fraction. The value of the

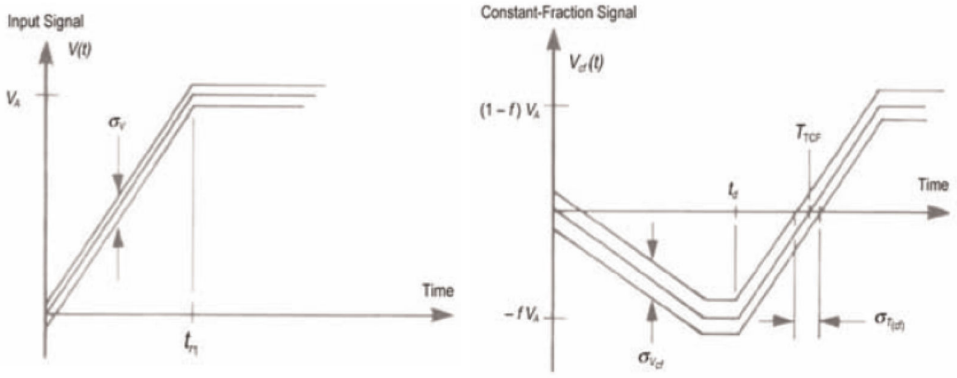

Figure 4.46 – Noise-induced time jitter. Figure adapted from [202].

slope was calculated for the ideal case of a noiseless signal with an amplitude of $20\sigma_{noise}$ amplitude and a peaking time of 1.39 μs. A maximum has been found for a delay of around 28 and 25 channels for an attenuation fraction of 1 and 1.5 respectively.

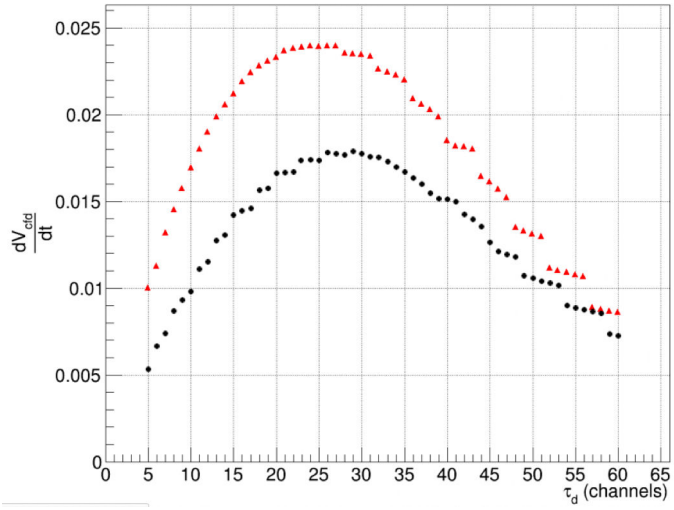

Figure 4.47 – Slope of the constant fraction signal at the zero-crossing point as a function of the time delay τ_d for two different attenuation fraction values: (a) k = 1.5 (red) and k = 1 (black).

However, the important noise contribution at low energies distorts the shape of the input signal compensating the minimization of the jitter contribution achievable at maximum slope. As we can see from Figure 4.48(a), as the value of τ_d delay increases the noise (RMS value) also increases. In addition, the smallest noise contribution found for smaller delays is associated with a worsen in SNR. The timing uncertainty σ_t as a function of the delay is presented in Figure 4.48(b). As a result, the best σ_t is obtained over a large range of delay values, which implies that several combinations of the CFD delay and the attenuation fraction may provide the same time resolution. Comparison of the time and amplitude resolutions for three different configurations of the CFD parameters are shown in Figure 4.49 and Figure 4.50 respectively. For the same attenuation fraction ($k = 1$), two different values

of the delay have been tested. In both cases the zero-crossing point occurs after the input signal reaches its maximum, so an additional delay, called numerical delay, was necessary to ensure that the measurement of the time is performed at the maximum of the signal. The results for a different value of k ($k = 1.5$) are also presented in the same figures. In this case, the crossover point occurs at the exact moment where the signal reaches its maximum and thus, no additional delay is needed. In all cases, a better precision in the measurement of time and amplitude is achieved for a delay of 9 channels and a gain of 1.5.

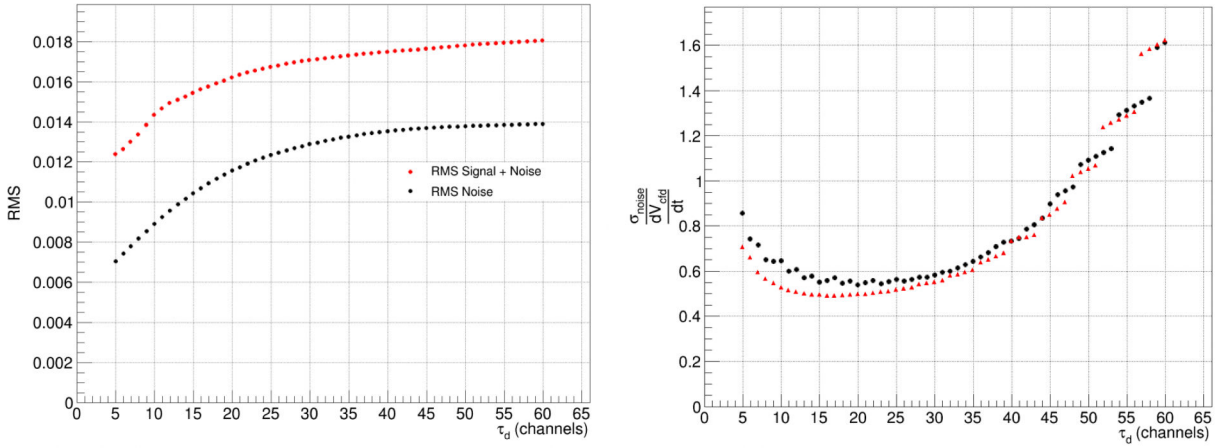

(a) **(b)**

Figure 4.48 – (a) Signal-to-noise ratio (RMS values) of the constant-fraction signal as a function of the delay τ_d for two different attenuation fraction values. (a) $k = 1.5$ (red) and $k = 1$ (black). and (b) Value of σ_t as a function of the delay τ_d for two different attenuation fraction values. (a) k = 1.5 (red) and k = 1 (black).

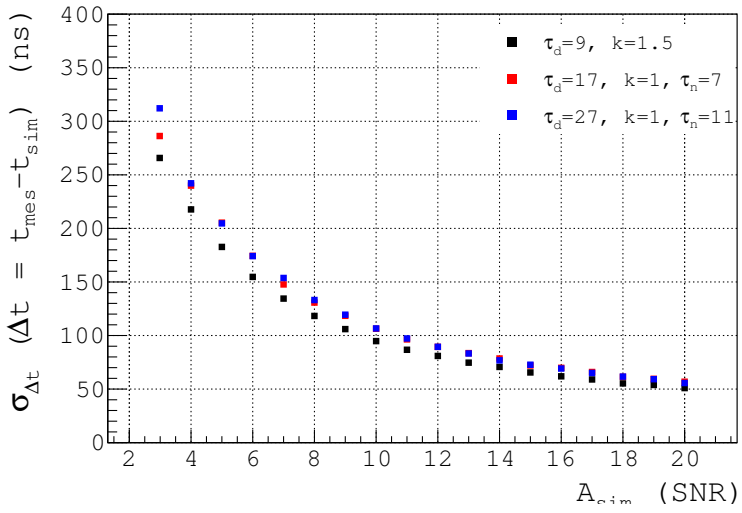

Figure 4.49 – Time resolution obtained for three different values of the delay τ_d and the attenuation fraction k. τ_n represents the additional numerical delay added to measure the maximum amplitude of the signals.

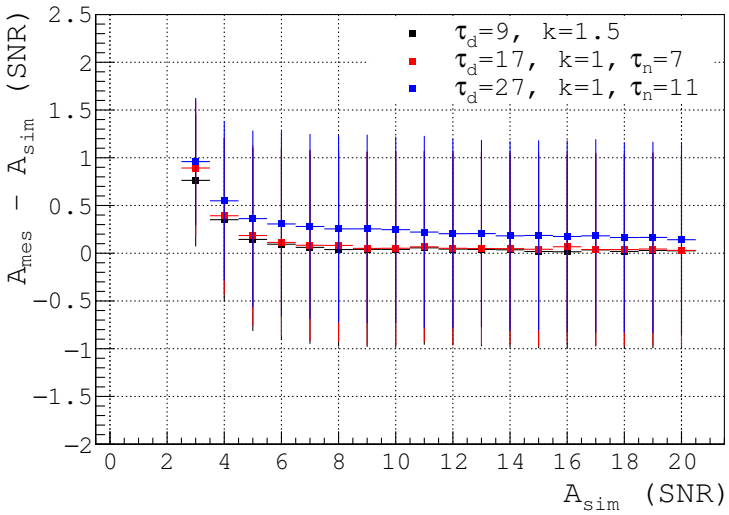

Figure 4.50 – Difference between the average measured amplitude and the simulated charge for three different values of the delay τ_d and the attenuation fraction k. τ_n represents the additional numerical delay added to measure the maximum amplitude of the signals. The error bars are obtained from the RMS of the distribution.

Time and Amplitude measurement with a Peak-sensing ADC

The second method to measure the time and the amplitude of the signals is based on a peak-sensing ADC [22], for which the amplitude and the time are directly measured from its maximum value as illustrated in Figure 4.51. For simplicity we will refer to this method as Max.

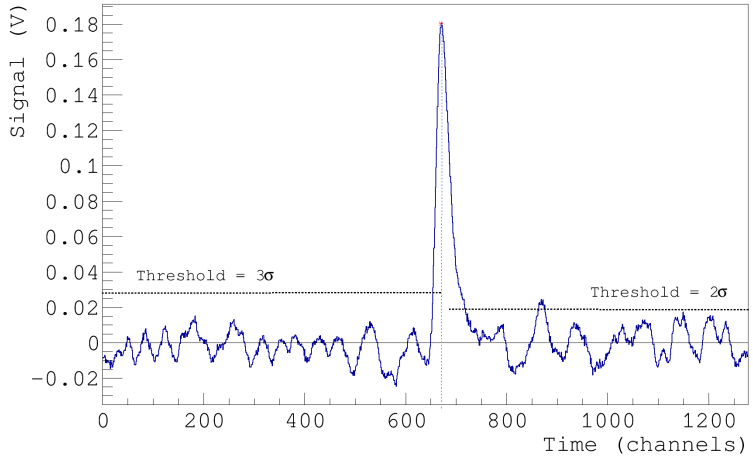

Figure 4.51 – Time and amplitude measurement on a simulated signal using the method of a peak sensing ADC. The leading threshold was set on $3\sigma_{noise}$, whereas the trailing edge threshold was $2\sigma_{noise}$. The maximum was found at 0.18 V (red star) corresponding to a drift time of 53 μs (670 channels).

In Figure 4.52 and 4.53 the comparison between both techniques is presented. The peaking time of the input signal was set to 1.39 μs and the CFD was performed for a delay

of 9 channels and an attenuation fraction of 1.5. A better time resolution has been observed for the CFD method for all amplitudes. The best result obtained for the Max technique was around 100 ns, in comparison with a resolution of 50 ns obtained with the CFD. Additionally, a better amplitude resolution has been obtained for the CFD method for the entire amplitude interval, especially at low energies. The worsening in the time and charge resolutions with the Max technique is due to fact that this method depends on the amplitude of the input signal. This effect is most important at low energies and results in a higher detection efficiency are shown in Figure 4.54.

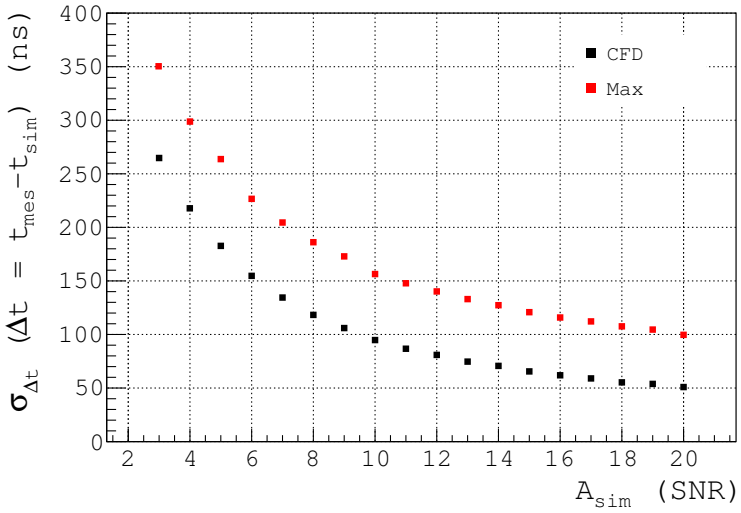

Figure 4.52 – Comparison of the time resolution obtained for the Max and CFD methods. The CFD was performed for a delay of $\tau_d = 9$ and an attenuation fraction $k = 1.5$.

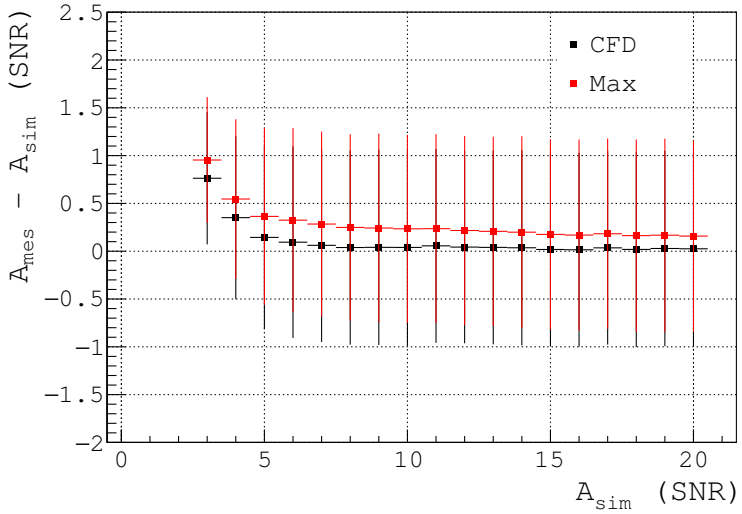

Figure 4.53 – Difference between the average measured amplitude and the simulated amplitude obtained for both techniques. The CFD was performed for a delay of $\tau_d = 9$ and an attenuation fraction $k = 1.5$. The error bars are obtained from the RMS of the distribution.

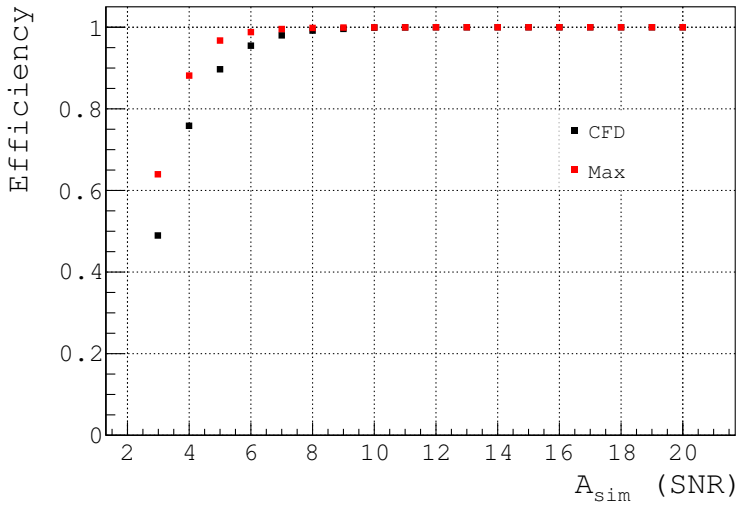

Figure 4.54 – Comparison of the efficiency obtained for both techniques. The CFD was performed for a delay of $\tau_d = 9$ and an attenuation fraction $k = 1.5$.

4.5 Noise counting rate

The noise not only affects the time and amplitudes resolutions, but also determines the minimum detectable signal threshold. The discriminator threshold should be as low as possible to ensure the best resolution and the maximum detection efficiency, but also it should be compatible with an acceptable noise rate. High background rates may cause besides a huge readout data volume, an important degradation of the quality of the acquired data, as well as a dead time increase. If the time interval between two consecutive triggers is smaller than the time required by the electronics to process the information of the first signal, the second pulse will be ignored. This could lead to the loss of relevant information coming from a real interaction and the addition of noise events. The aim of this section is to determine the optimal threshold level by measuring the electronic noise rate at different discriminator threshold levels.

Since the amplitude distribution of the noise is Gaussian distributed with a standard deviation given by σ_{noise} (see Section 4.4.1), the dependency of the noise counting rate on the threshold can be estimated with the Rice's formula [195, 203]:

$$f_n \;=\; f_{n0}\, e^{-\dfrac{V_{th}^2}{2\sigma_{noise}^2}}, \tag{4.20}$$

where f_{n0} represents the counting rate at zero threshold and V_{th} is the threshold level. Assuming a positive threshold, a trigger will registered only when a signal crosses the threshold with positive slope, see example in Figure 4.55. As a result, the noise rate f_{n0} is half of the frequency at zero threshold f_0, and its value depends on the timing characteristics of the electronics.

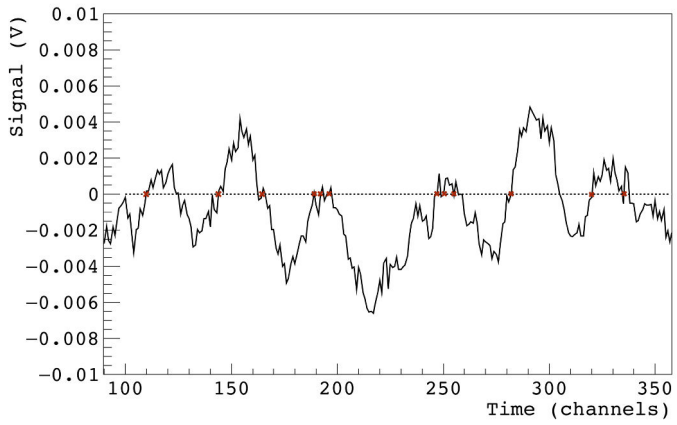

Figure 4.55 – Example of a typical noise signal. The red cross represents a trigger for a zero threshold level. A trigger is considered when the signal crosses the threshold with positive slope.

For a fast amplifier with peaking time τ_0, the noise rate at zero threshold can be approximated by the following expression [204]:

$$f_{n0} = \frac{1}{2\tau_0}, \tag{4.21}$$

The result of the noise counting rate as a function of the threshold is reported in Figure 4.56. The threshold scan was performed over a total period of 7 s. The result shows that the experimental counting rate distribution is in very good agreement with the theoretical prediction and can be described by a Gaussian distribution with excellent precision up to $\sim 5\sigma$.

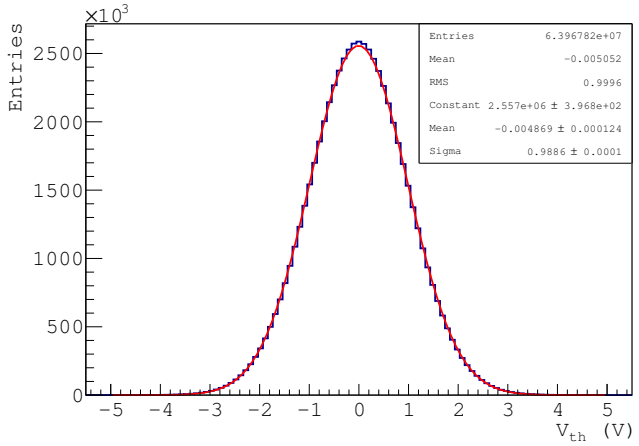

Figure 4.56 – Counting rate as a function of the discriminator threshold. The red line represents the Gaussian fit to the distribution.

Table 4.2 summarizes the average noise counting rates obtained for five different thresholds. The value obtained for the zero-threshold rate is consistent with equation (4.21) for a peaking

time of 1.39 μs. The results presented in the table are compatible with the values obtained directly from Equation (4.20) for a fixed $f_{n0} = 365$ kHz measured experimentally:

$$f_{n0} = \frac{1}{2\tau_0} = \frac{1}{2 \times 1.39\mu s} = 360\ kHz, \tag{4.22}$$

Threshold (SNR)	Threshold (mV)	Exp Rate (Hz)	Rice's formula(Hz)
0	0	365x10^3	365x10^3
1	2.27	220x10^3	222x10^3
2	4.54	49x10^3	51x10^3
3	6.81	4263	4286
4	9.08	229	143

Table 4.2 – Experimental noise rate as a function of the discriminator threshold level. The last column shows the expected values from the Rice's formula for a f_{n0} given by the experimental data.

The noise counting rate at very low threshold is too high, which implies the registration of a large number of noise event and an important increment of the dead time. The minimum acceptable threshold level is 3 times the noise, that results in a noise rate of around 4000 triggers/s. This threshold is low enough to have into account almost all physical signals, even those with low amplitude, without saturating the readout electronics.

However, the results obtained for the noise counting rate do not reproduce the real behavior of the discriminator. Figure 4.57 reveals the time difference between two consecutive triggers for a $3\sigma_{noise}$ threshold. Because of the time discretization, the minimum acceptable time difference is 2 time channels (160 ns) due to the signal needs to go below the threshold to re-trigger the discriminator. This high frequency comes from the fact that the ADC also discretizes in amplitude. The registered values of the charge depends on the amplitude resolution of the ADC. The higher the resolution, the higher the fluctuation in the amplitude. To compensate for this effect we introduced a lower threshold on the trailing edge of the signal. The difference between these two threshold is called *hysteresis* [205].

Taking into account that one ADC channels corresponds to $\sim 0.2\sigma_{noise}$[6], the minimum trailing edge threshold should be set at $(V_{th} - 0.4)\sigma_{noise}$, where V_{th} is the leading edge threshold. The noise counting rate obtained by including this second threshold is presented in Figure 4.58. Note that in this case the noise rate distribution is not longer modeled by a Gaussian distribution. The shape of the distribution is due to the asymmetric threshold, which makes that the discriminator is never centered around zero. By including a second threshold level, the time interval between two consecutive triggers for a threshold of $3\sigma_{noise}$ is, in general, higher than τ_0 (see Figure 4.59). The noise rate for a leading edge threshold of 3 times the noise is now given by ~ 3300 triggers/s. This value is significantly reduced by using the CFD method described in the previous section. For an asymmetric threshold of $3\sigma_{noise} - 2\sigma_{noise}$,

[6]One ADC channel corresponds to 0.6 mV

the number of noise events is reduced by ∼10 % with the CFD (∼ 1790 $triggers/s$), compared to the standard peak sensing ADC. In the following, the trailing edge threshold is set at $(V_{th} - 1)\sigma_{noise}$.

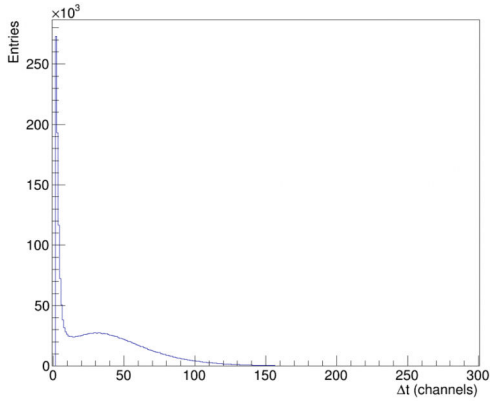

Figure 4.57 – Time interval between two consecutive threshold crossing for a $3\sigma_{noise}$threshold level.

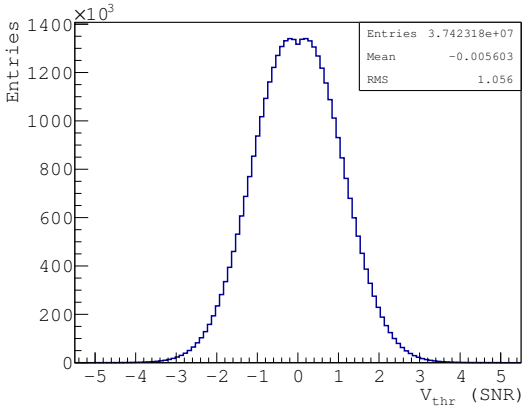

Figure 4.58 – Counting rate as a function of the discriminator threshold. The leading edge threshold was set a $3\sigma_{noise}$ and the trailing edge threshold a $2.6\sigma_{noise}$.

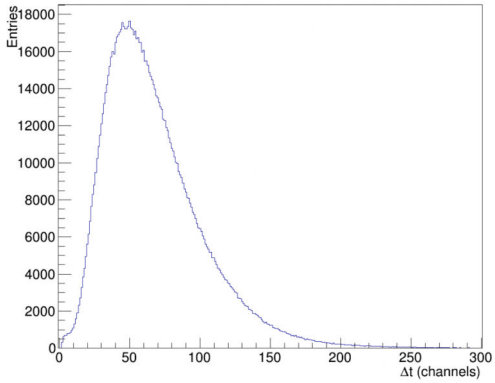

Figure 4.59 – Time interval between two consecutive threshold crossing for a $3\sigma_{noise}$threshold level with a leading edge threshold at $3\sigma_{noise}$ and a trailing edge threshold at $2.6\sigma_{noise}$.

4.6 XTRACT: A New Front-End Electronics for XEMIS2

The continuous sampling of the analog signal performed in XEMIS1 for the data acquisition, provides a complete picture of what happens at every moment of time, allowing a robust event identification, pedestal and common noise correction and other analysis-related capabilities. However, in XEMIS2, due to the large amount of channels used to collect the ionization signal, the data output from the the whole system would be difficult to manage in real time. Assuming that each signal is sampled at a frequency of 12.5 MHz with a resolution of 12 bits, a trigger rate of 2 Hz and a total amount of 24000 pixels, the readout system would produce a data collection rate of around 10 Tb for a 20 min medical imaging exam. This enormous volume of data is impossible to handle with a standard computer.

For detectors with a large number of readout channels, the solution is to reduce down to the minimum the information necessary to describe an interaction inside the chamber. In addition, when a large number of channels is present, efficient power supply and data traffic management are also required. In this section, we introduce a new circuit called XTRACT (Xenon TPC Readout for extrAction of Charge and Time), that has been developed for the data acquisition of XEMIS2, with the goal of extracting the amplitude and time information of each signal derived from the IDeF-X LXe ASIC. Moreover, this new front-end electronics allows to reduce the number of connexions between the inside and the outside of the chamber, which is of crucial importance on a system in which the thermal losses may affect the performances of the detector, and the risk of a leak from the outside through the vacuum contained is elevated.

XTRACT is a low power 32-channel front-end ASIC design to withstand temperatures of the order of -80 °C. This new ASIC is coupled to the 32 outputs channels of the IDeF-X LXe chip through a standard connector. This implies that in XEMIS2 around 700 XTRACTs will be present inside the chamber (350 chips per anode). Each XTRACT provides only timing and charge information of those signals delivered by the IDeF-X that exceeds a certain threshold level, and the pixel address in which the charge is collected. The value of this threshold can be externally fixed for each individual pixel via a slow control interface, which allows the configuration of each ASIC independently. Other parameters such as the DC offset are also accessible via the slow control protocol. Individual selection of the 32 channels of a certain XTRACT is also possible. The channel 31 of each ASIC includes analogical and digital test points to verify the proper functioning of the chip, in addition to provide information of its temperature. The XTRACs are grouped together in blocks of 8 ASICs through a PU card, which is responsible of reading-out the data. A total of 46 PU boards are used per anode. Time, amplitude and pixel address for each detected event is extracted from the PU card to the outside of the cryostat via high-speed LVDS lines at a rate of 96 Mb/s, to be directly stored on a disk. Figure 4.60 shows a diagram of the XEMIS2 data acquisition system. This design was made to optimize power consumption and communication schemes by reducing the number of output channels from 24000 to 94 digital outputs.

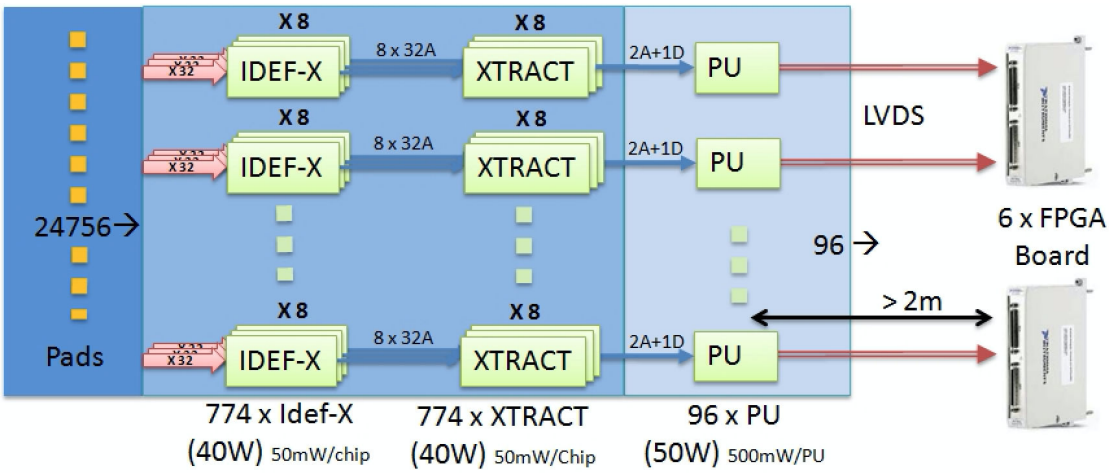

Figure 4.60 – Schematic diagram of the data acquisition system of XEMIS2. The collected signals by the segmented anode are read-out by an IDeF-X ASIC in the same way as in XEMIS1. The information of time, amplitude and pixel address is extracted from each detected signal thanks to the XTRACT. The information is then read by a PU card that groups together 8 XTRACT ASICs. The information from the PU card is extracted towards the outside of the chamber via a LVDS connexion and stored in a disk.

Figure 4.61 shows a schematic diagram of the XTRACT ASIC. It consists of five main blocks: a constant fraction discriminator or CFD, a ramp generator for event-tagging, an analog memory circuit per channel to store the value of time and amplitude of each event, a time derandomizer or Asynchronous Binary Tree Multiplexer (ATBM) and a control digital module.

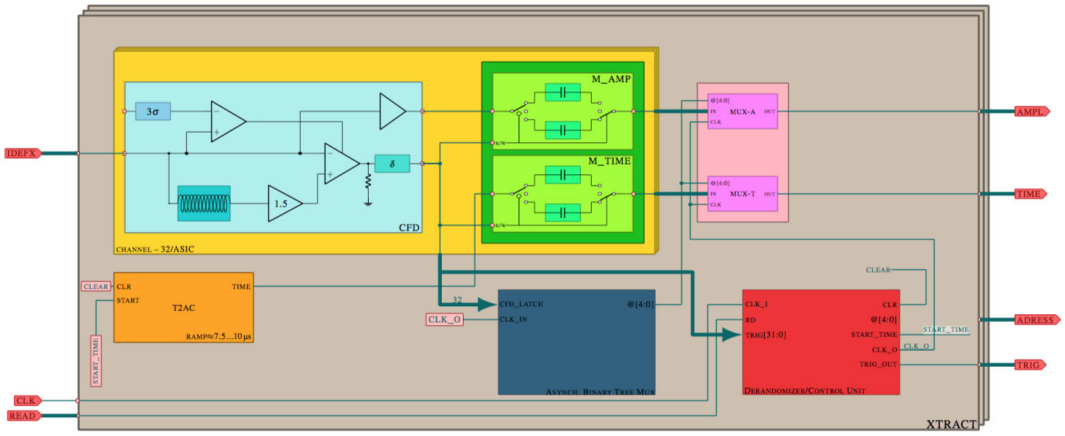

Figure 4.61 – Illustration of the XTRACT architecture.

As discussed in Section 4.4.2, a CFD is the best option to determine the amplitude and time of the collected ionization signals. The **CFD block** was designed in order to accomplish for the time and amplitude resolutions reported in Section 4.4.2. The output signals of the shaper located inside the IDeF-X LXe chip are fed to the input of the CFD module. The shaper is set with a peaking time of 1.39 μs. An example of the CFD method is illustrated in Figure 4.62. The analog signal is split and send, on one side to a voltage comparator

that verifies whether the pulse triggers the discriminator threshold level, and on the other side, the analog signal is delayed by a second order Bessel filter and attenuated a 30 % of its maximum amplitude by a voltage divider. The delay introduced by the filter is around 600 ns to achieve a timing resolution of 300 ns at $3\sigma_{noise}$. If the input signal crosses the threshold, the outputs of both the voltage comparator and filter are send to a zero-crossing detector circuit (ZCD). The ZCD comparator subtracts both input signals and produces an output the moment the generated bipolar pulse crosses a reference value. The DC offset of the ZCD circuit is set by a 6 bits digital-to-analog converter (DAC) adjustable between $\pm 43\ mV$ via the slow control. A different value of this offset can be set per pixel. A second threshold, normally at (n - 1) times the noise where n is the leading edge discriminator, is added to avoid a new CFD at the same pixel outside the interval of interest. A veto is included to lock the CFD output, so the amplitude and time of a signal can be directly registered independently of the CFD.

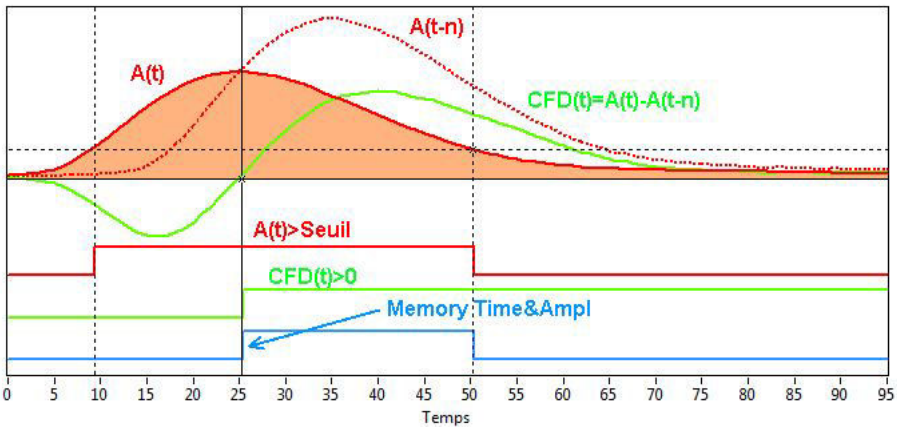

Figure 4.62 – Example of a signal measured by the CFD method. The original signal is described by A(t). An attenuated and delayed signal A(t-n) is subtracted from the original signal, to produce a bipolar pulse designed by CFD(t). The zero-crossing point of the CFD signal corresponds to the moment A(t) reaches its maximum value. The signals are sent to the zero-crossing comparator only if A(t) crosses a certain threshold level (referred as *seuil* in the figure).

If the CFD module detects a pulse, the *flag* signal of this particular pixels changes from *0* to *1*, and a trigger is sent to the rest to the electronic chain to inform that a pulse have been detected. At this point, a **voltage ramp** with constant slope is generated. The ramp generator (T2AC[7] in Figure 4.61) is based on a capacitor that is charged linearly through a constant current circuit until the input current ends. The output of the ramp generator is then a voltage pulse, which provides information of the arrival time of the events inside the detector relative to the first detected event. The time t_0 is, therefore, the arrival time of the first event or *trigger event*. The ramp returns to its zero value the moment the trigger signal ends. The ramp lasts between 7 to 10 μs, and its duration can be regulated with the slow control interface.

[7]Time-to-amplitude converter

Equally, at the moment the CFD block detects a signal, the time and amplitude informations are stored in an **analog memory**. Each analog memory contains two different cell, one for the time and another one for the charge. The value of the amplitude corresponds to the analog value of the charge at the zero-crossing point, whereas the time is the analog value delivered by the voltage ramp. Each pixel has its own analog memory.

Every time a flag signal from a pixel states *1*, it is sent and stored in the **derandomizer**. This block handles the arrival of information in case several pixels are fired, preventing a loss of information in the case a new flag arrives during the reading procedure. The derandomizer also provides addressing information to the **control unit**. This module performs a logical OR operation between the received flags and sends a trigger signal to the **PU card** presented in Figure 4.63. When the PU card is ready, one of the eight XTRACTS driven by the same board is selected by a signal Chip Select (CS). Afterwards, a reading order is sent to recuperate the information stored in the analog memory via a multiplexer. When a pixel is read, the control unit sends a reset to the derandomizer, and the flag of the pixel in question changes from *1* to *0*.

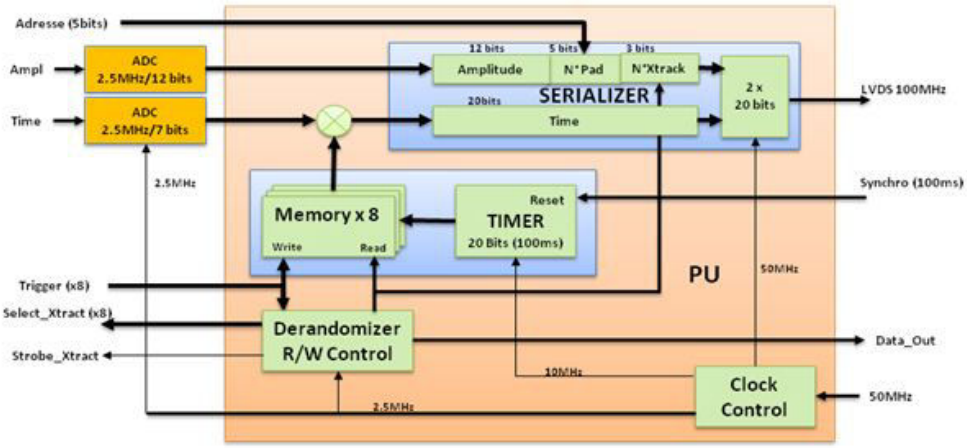

Figure 4.63 – Schematic diagram of the PU card.

Figure 4.64 illustrates an example of the XTRACT detection and read-out processes. In the example, three different pixels, corresponding to the channels 22, 3 and 4, collect a signal. When the first arriving pulse is detected by the CFD module, a trigger signal is generated and the flag of the pixel 22 states *1*. At this moment the voltage ramp generator also starts. If another pulse is detected while the ramp generator is still on (pixels 3 and 4 in Figure 4.64), their arrival times are obtained from the analog value of the ramp at the zero-crossing point. This time value is not the absolute time of the interaction inside the TPC but it is relative to the moment the first pulse is detected (trigger). The flag signals of the three fired pixels are also sent to the control unit to later be read by the PU card. The trigger warns the PU board that at least an event has been detected. When the card is ready, a CS is sent in order to start reading the information stored in the analog memory. The derandomizer selects the reading sequence, that can be different from the detecting one, i.e. the pixels may be read-out in a different order than that of detection. In the example presented in Figure 4.64 channels are read-out starting from pixel 3 to pixel 22. When a pixel is read by the PU card, its flag signal states *0*. A new reading order is sent from the

PU board to the derandomizer until the last flag changes to *0*. At this moment, the trigger and CS signal return to its zero value and the PU board is free to start reading another XTRACT ASIC. A reset signal is also sent to the ramp generator which remains at zero until a new event is detected.

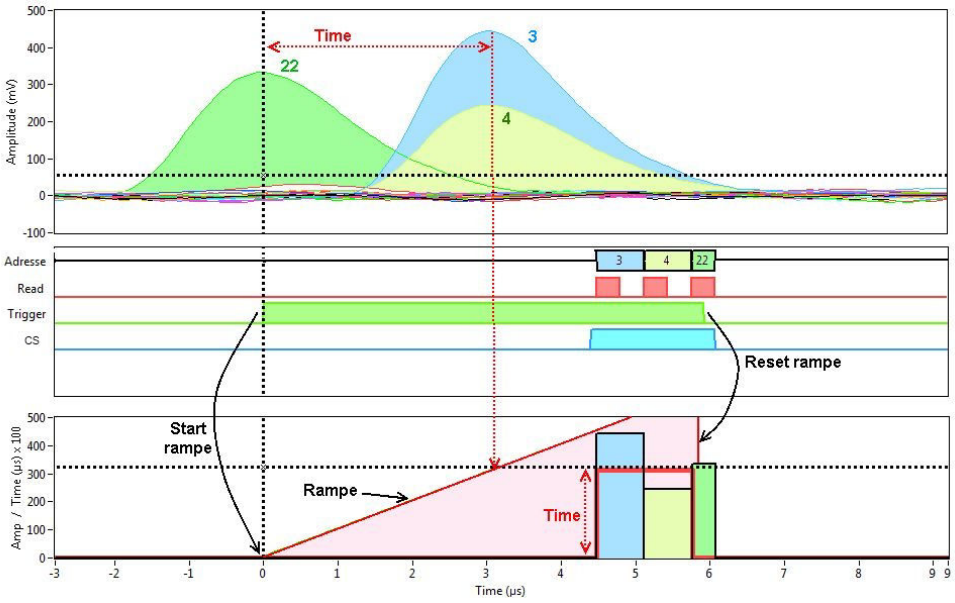

Figure 4.64 – Example of the detection and read-out process of three different signals.

As discussed in the previous chapters, a very low threshold level of at least three times the electronic noise is required in order to perform the Compton sequence reconstruction and triangulate the position of the radioactive source. A low threshold, however, is accompanied by a high noise trigger rate that should be handle by the read-out system. The design of the data acquisition system of XEMIS2 was made to support a noise rate of around 4096 trigger per second and per pixel at $3\sigma_{noise}$. At this trigger rate, each XTRACT will receive, in average, an event every 7.6 μs. Since the ASICs are grouped in sets of 8 XTRACTs, the PU board will be receive, in average, a noise trigged every 950 ns. With a 3 MHz reading rate, XEMIS2 is capable of reading without dead time 11700 events per second and per pixel. In average, ∼7400 of the registered events will come from an interaction of an ionizing particle inside the TPC.

4.7 Conclusions Chapter 4

In this chapter we have presented the performances of the readout front-end electronics used in XEMIS1 for the measurement of the ionization signal. In order to optimize the signal extraction, we have carried out a detailed study of the electronics response. The study of the influence of the charge sensitive pre-amplifier and shaper on the shape of the output signals has been reported in Section 4.3, as function of both the shaping time of the linear amplifier and the collection time of electrons in the TPC. Charge linearity and electronic noise contributions have been also discussed in this section.

In a large number of applications, precise information of the arrival time of the electrons in the detector is of particular interest. When timing information is the major goal, pulses are often handled differently than when accurate charge measurement is the purpose. The accuracy with which timing and amplitude measurements can be performed depends both on the properties of the detector and on the performances of the electronics used to process the signal. In 3γ imaging both good energy and spatial resolutions are required in order to reconstruct the 3D distribution of a radioactive source. Consequently, the measurement of the charge and time on the detected signals must be optimized. In this chapter, we have presented a complete study of the measurement of the timing and amplitude information of the ionization signals based on a Monte Carlo simulation that reproduces the output signal of the IDeF-X LXe front-end electronics. Special attention has been paid to the simulation of the noise. The study has been performed for two different methods based on a Constant Fraction Discriminator (CFD) and a Peak-sensing ADC. The obtained results with the CFD method, for an optimized selection of the CFD parameters, showed a clear improvement of the time and amplitude resolutions in comparison with a peak-sensing ADC. We have showed that the Max method is not useful to measure the amplitude of low energy signals due to the important amplitude fluctuations caused by the electronic noise. Moreover, we have also found that a small peaking time provides an improvement of the time and amplitude resolution regardless the slightly higher ENC noise. Taking into account these results, together with the electronic limitations, we found that the best results are obtained for a delay of 9 channels (720 ns) and a attenuation fraction of 1.5.

The results obtained with this study have contributed to the development of a specific acquisition system for the measurement of the ionization signal in XEMIS2. A description of the main characteristics of this new analog ASIC called XTRACT has been presented in Section 4.6.

Chapter 5

Study of the Performances of a Frisch Grid

Contents

When radiation pass through the LXe, it ionizes the medium producing a track of electrons-ion pairs. The resulting charge carriers rapidly recombine unless an external electric field is applied. In this case, electrons and ions immediately drift in opposite directions by the action of the electric field. In order to determine the energy deposited by the incoming radiation, the detector should be sensitive to the produced charge carriers in the interaction. Ionization detectors, such as ionization chambers, Geiger-Müller tubes and proportional counters have been commonly used since the first half of the 20th century to detect ionizing particles [135]. In an ionization detector, the formation of a signal is caused by the charge induced in one or more electrodes. The induced signal is in fact produced by the displacement of electrons and positive ions through the medium. Considering the simplest structure of an ionization detector, which is based on two parallel electrodes separated by a distance d and immersed in a dielectric medium, the total induced charge depends on the distance travelled by the charges before being collected. This implies that the collected signal

depends on the position of the interaction in the active zone of the detector with respect to the collecting electrode. To overcome this pulse-amplitude dependence with the position of the interaction, a third electrode known as Frisch grid is usually incorporated between the two electrodes [178]. Gridded ionization chambers are commonly used in nuclear and particle physics to measure ionization radiation. More sophisticated designs including strip electrodes or pixelated anodes make this kind of ionization detectors interesting not only for γ spectroscopy but also for position determination. The XEMIS camera is based on the principle of a Frisch grid ionization chamber.

In this chapter, we discuss the basic theory of signal induction in a parallel plate ionization chamber. The advantages of using a gridded ionization chamber and the basic principle of signal formation are discussed in Section 5.1. The signal generated in an ionization detector depends on the transport of the charge carriers through the active volume. For this reason, when using a Frisch grid ionization chamber the properties of the collected signal also depend on the characteristics of the grid. In order to improve the performances of future devices, during this work, we have tried to understand and study the main effects associated with a gridded ionization chamber. Electron transparency and charge collection efficiency of a Frisch grid are discussed in Section 5.2 and 5.3, respectively. Charge sharing between neighboring pixels is discussed in Section 5.4. The theoretical discussion is supported by experimental results and by simulation. The results obtained with XEMIS1 for different Frisch grids are reported in Section 5.5.

5.1 Theoretical background

The phenomenon of charge induction by moving charges in an ionized medium is well-described in the literature [20, 195, 206, 207]. However, the commonly used term *charge collection* instead of charge induction sometimes leads to a misinterpretation. In presence of an electric field, the displacement of electrons and ions in a detector induces a current signal on the readout electrodes. This implies that the signal on an electrode is formed from the moment the charges start to move, and not from the actual collection of the charges when they arrive to the electrode.

In order to better understand the physics of signal formation on an electrode, a general overview of the theory of charge induction due to the motion of charge porters in an ionization detector is given in this section. A brief introduction to the Shockley-Ramo theorem is presented in Section 5.1.1. Furthermore, more specific examples of charge induction on a parallel plate ionization chamber and a Frisch grid ionization chamber are discussed in Sections 5.1.2 and 5.1.3 respectively.

5.1.1 Charge induction and the Shockley-Ramo theorem

The current induced on an electrode by a single charge produced in a detector can be determined from the Shockley-Ramo theorem [156, 208]. This theorem was first developed for charge induction in vacuum tubes but it has been demonstrated that it can be applied to

any detector configuration, from gas ionization chambers to semiconductor detectors. The Shockley-Ramo theorem states that the instant current induced on a single electrode can be evaluated as follows:

$$i \;=\; -q \,.\, \vec{v} \,.\, \vec{E_w} \tag{5.1}$$

where $\vec{v}$ is the velocity of the charge q in the medium and $\vec{E_w}$ is the weighting field at the position of q. Similarly, the charge Q induced on an electrode due to the movement of a point charge q can be determined by the following expression [156]:

$$Q \;=\; -q \,.\, \Delta\varphi_w \tag{5.2}$$

where $\Delta\varphi_w$ represents the weighting potential difference. $\vec{E_w}$ and φ_w are, respectively, the electric field and the electric potential at the position of q when the electrode that collects the charge is set to a potential of 1 V, all other electrodes are grounded and all charges are removed [207, 209]. The weighting field and weighting potential only depend on the geometry of the detector and in general, they differ from the actual applied electric field and electric potential except for the basic case of a two infinite parallel plate ionization chamber.

According to the Shockley-Ramo theorem, while the trajectory of the charge q follows the real electric field lines (if diffusion is neglected), the charge Q induced on the electrode of interest can be obtained from the weighting potential. The distribution of the weighting potential does not influence the motion of the charge but it represents the electrostatic coupling between the moving charge and the collecting electrodes. The weighting potential is determined by solving the Laplace equation $\nabla^2\varphi_w \;=\; 0$ with spatial boundary conditions that only depend on the detector's geometry. As a result, the value of the charge induced by the motion of q does not depend on the potential applied to the electrodes, but it only depends on the position of q with respect to the collecting electrode.

5.1.2 Principle of a parallel plate ionization chamber

One of the simplest methods to measure the charge produced in a liquefied noble gas detector is by using a parallel plate ionization chamber. Its basic design consist of two parallel plane electrodes (anode and cathode) separated by a certain distance d and filled with a suitable medium, normally a gas or a liquid. The electrodes are maintained at a potential difference V_b in order to create an electric field between them. The distance between the electrodes should be small with respect to the length and width of the electrodes to generate an uniform electric field. A schematic drawing of a parallel plate ionization chamber is illustrated in Figure 5.1. The cathode is generally kept at a potential of -V_b, while the anode or collecting electrode is grounded through a resistance R. Electrons and ions generated after the passage of radiation through the medium are immediately drift apart by the action of the electric field. The current induced on the anode is converted into an electrical pulse with an external electronic chain usually composed by a charge sensitive preamplifier.

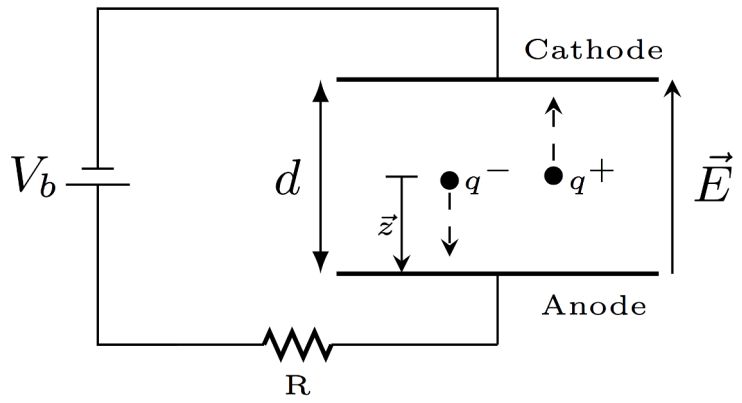

Figure 5.1 – Schematic drawing of a conventional parallel plate ionization chamber.

The Shockley-Ramo theorem states that the weighting field of the anode can be calculated by setting the anode at unity potential and the cathode to ground. The result of the Laplace equation for a two parallel plate detector with this boundary conditions results on a weighting field, $\vec{E_w}$, that varies linearly with the distance from the anode over the drift length d and it is zero otherwise [195]:

$$\vec{E_w} \;=\; \frac{1}{d}\,\vec{z} \tag{5.3}$$

where $\vec{z}$ represents the drift direction of charges in the detector. Applying Equation 5.1, the current induced on the anode by a single electron of charge q is given by:

$$i \;=\; -q\,.\,\frac{\vec{v^-}}{d} \tag{5.4}$$

where $\vec{v^-}$ is the electron velocity in the medium. Equation 5.4 shows that the current induced on the anode only depends on the real applied electric field and the distance between electrodes.

If we now consider a certain number N^- of drifting electrons produced by ionization after the passage of radiation through the space between the plates, Equation 5.4 results in:

$$i^-(t) \;=\; -q\,.\,N^-\,.\,\frac{v^-(t)}{d} \tag{5.5}$$

Assuming that all charges are produced at the same position, both the electric and the weighting fields are uniform between the electrodes and electrons move at constant velocity, Equation 5.5 implies that the current induced on the anode by the displacement of N^- electrons in the drift region is constant during the time the electrons drift towards the anode, and becomes zero the moment the electrons reach the electrode.

After a γ-ray of energy E_γ interacts with the LXe, a number N of electron-ion pairs is produced according to: $N \;=\; \frac{E_0}{W}$, where W is the average energy required to produce an electron-ion pair and E_0 is the energy deposited in the interaction. Same as for the

electrons, the current induced on the anode due to the displacement of N^+ positive ions can be expressed as:

$$i^+(t) \;=\; -q \,.\, N^+ \,.\, \frac{v^+(t)}{d} \tag{5.6}$$

where v^+ is the velocity of ions in the medium. Since ions also drift with constant speed in a homogeneous electric field, the current induced on the anode by the displacement of positive ions between the two plates is also constant during the drift time and it ceases the moment the charges reach the cathode. Considering that the same number of ions and electrons is produced with the same absolute charge, the total induced current by the movement of both electrons and ions can be approximated as:

$$I(t) \;=\; i^-(t) \;+\; i^+(t) \;=\; q \,.\, N \,.\, \left(\frac{v^-(t) \;+\; v^+(t)}{d}\right) \tag{5.7}$$

If the interaction occurs at a position z from the anode (Figure 5.1), the electrons will drift a distance z before being collected, while the positive ions will travel a distance $(d \;-\; z)$ to the cathode. Likewise, the traveled distances can be represented as $z \;=\; v^- \,.\, t^-$ and $(d \;-\; z) \;=\; v^+ \,.\, t^+$ where t^- and t^+ are the drift time or collecting time of electrons and positive ions respectively, which represents the time required by the charges to reach the electrodes from the point of interaction. The induced charge is then obtained by integrating the induced current over the collecting time as presented in Equations 5.8 and 5.9:

$$Q^-(t) \;=\; \int_0^{t^-} i^-(t) \,.\, dt \;=\; -q \,.\, N^- \,.\, \frac{z}{d} \tag{5.8}$$

$$Q^+(t) \;=\; \int_0^{t^+} i^+(t) \,.\, dt \;=\; -q \,.\, N^+ \,.\, \left(1 \;-\; \frac{z}{d}\right) \tag{5.9}$$

The sum of these two contributions gives the total charge induced on the anode: $q(t) \;=\; Q^-(t) \;+\; Q^+(t)$, and the corresponding voltage difference between the anode and the cathode is given by $V(t) \;=\; \frac{q(t)}{C}$ where C is the capacitance between both electrodes.

Signal shape:

The slope of the induced signal depends on the drift velocity of the charges, and the signal duration depends on the position of the interaction. Since the mobility of ions is about three orders of magnitude slower than that of electrons, all electrons reach the anode in a short time compared to ions and therefore, their motion can be almost neglected while electrons drift towards the anode. As a result, the induced signal has a double contribution with a fast rise time due to the deriving electrons, and a slower component that comes from the fact that the ions are still traveling after all electrons have been collected. An example of the current and voltage induced on a parallel plate ionization chamber as a function of time is illustrated in Figure 5.2. Even though both electrons and positive ions induce a signal

on the collecting electrode during the electrons' drift time t^-, the fast rise time observed in the output signal is mostly due to the migration of electrons since the slow drift of the positive ions provides an almost negligible contribution to the signal. Once all electrons are collected, a more gradual rise is observed in the output signal due to the ions still induce a voltage $\frac{qN}{dC}t(v^+ + z)$ during a time t^+, which is much longer than t^-. Finally, when all charge carriers are collected, the maximum induced charge on the anode is achieved:

$$Q = q \,.\, N \,.\, \left(\frac{(d-z)+z}{d}\right)$$

$$Q = q \,.\, N \tag{5.10}$$

The total induced charge on the anode is independent of the interaction depth and only depends on the number of electron-ion pairs, which is proportional to the deposited energy. However, in real experimental conditions, only the contribution to the induced signal due to electron motion is registered, whereas the contribution of positive ions is generally suppressed by the integration time of the external electronic readout system. As a result, the total induced charge becomes dependent on the position of the interaction with respect to the anode according to Equation 5.11:

$$Q \approx q \,.\, N \,.\, z \tag{5.11}$$

Depending on where the electron-ion pairs are created, the amplitude of the induced pulse will vary from *0* to $V_{max} \approx \frac{q \,.\, N}{C}$. This variations of the signal amplitude with the position of the interaction severely degrade the detector's energy resolution [209]. To avoid this z-dependence of the induced signals, the incorporation of a third electrode between the cathode and the anode was proposed by Frisch [178]. The principle of a Frisch grid ionization chamber is presented in the following section.

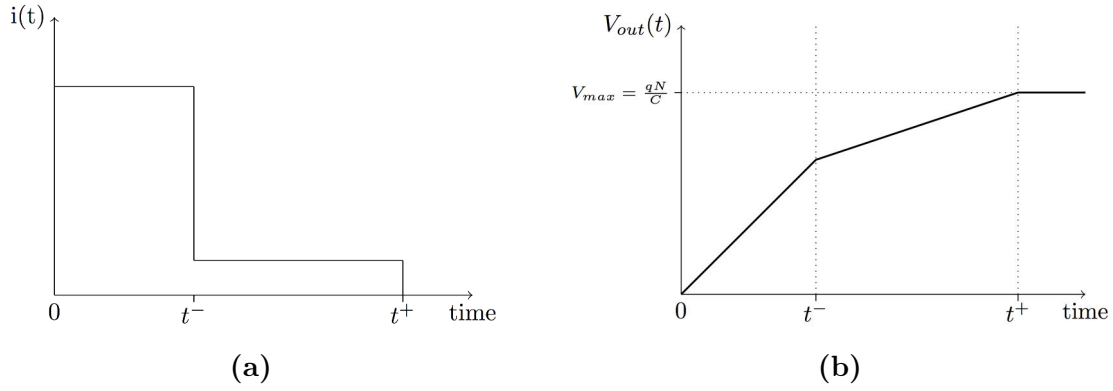

(a) **(b)**

Figure 5.2 – Illustration of the time development of the induced current (a) and voltage (b) on the anode on a two infinite parallel plate detector. In the figure, t^- and t^+ are the electron and positive ion collecting times respectively.

5.1.3 Frisch Grid Ionization Chamber

In order to improve the performances of an ionization chamber and remove the position dependence of the induced signal due to the motion of charge carriers in the medium, a gridded electrode is incorporated between the cathode and the anode. This method was first proposed by O. Frisch in 1944 for a gas ionization chamber [178]. Figure 5.6 shows a schematic diagram on a Frisch grid ionization chamber. This third electrode, known as Frisch grid, is placed at a distance p close to the anode and set at an intermediate potential between the potentials of the cathode and the anode. Under this conditions, the grid shields the anode from the induction of charges generated in the region between the cathode and the grid. Ideally, this configuration divides the active area of the detector in two independent chambers: the *drift region* and the *gap*. Since the gap is small compared to the drift region, most of the interactions take place between the cathode and the grid. Electrons and ions created in this region migrate in opposite directions by the action of the electric field. While the positive ions induce a current on the cathode in the same way as explained in the previous section, the electrons, on the other hand, pass through the grid. The actual signal induced on the anode starts from the moment the electrons crosses the grid and stops when they reach the collecting electrode. Positive ions on the other hand, are shielded by the grid and hence, they induced no current on the anode.

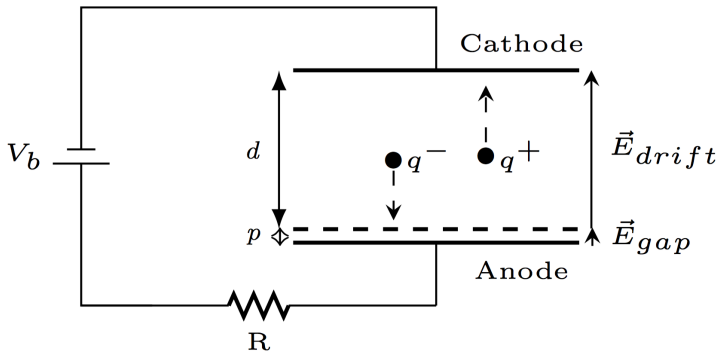

Figure 5.3 – Illustration of a conventional Frisch plate ionization chamber. The grid is represented as a dashed line close to the anode.

The charge induced on the anode can also be determined from the Shockley-Ramo theorem. The weighting potential of the anode is obtained by applying a potential of 1 V to the electrode and setting both the cathode and the Frisch grid to ground. An illustration of the weighting potential for an ideal Frisch grid ionization chamber as a function of the distance between electrodes is presented in Figure 5.4. The weighting potential is zero in the region between the cathode and the grid, and varies linearly to 1 between the grid and the anode. As a result, the total induced charge does not depend on the position of the interaction because now, all the electrons travel the same distance p within the detector. Figure 5.5 shows an example of the induced voltage on a Frisch grid ionization chamber. Compared to Figure 5.2, the induced signal is zero while electrons migrate towards the grid, followed by a fast rise time from the moment the electrons pass through the grid. The amplitude of the output signal is now proportional to the number of collected electrons, since

carriers, that are created at any position in the cathode-grid region, induce a maximum signal on the anode as long as they all pass through the grid. Moreover, the signal is independent of whether or not the positive ions are collected [210]. Since the slow moving ions do not affect the output signal, the rise time of the induced pulse only depends on the distance between the Frisch grid and the anode and on the electronics used to integrate the induced current. In general, for the same electronics system, smaller gap distances result in faster rise times.

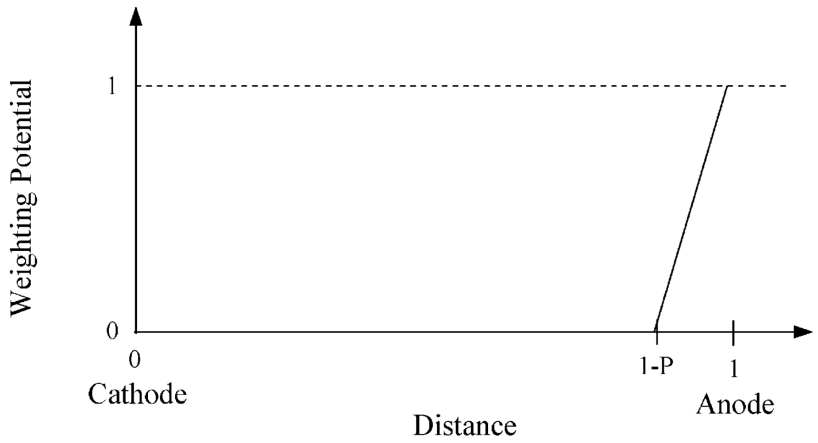

Figure 5.4 – Illustration of the weighting potential of the anode for an ideal Frisch grid ionization chamber. The grid is placed at a distance *1-P* from the anode [135].

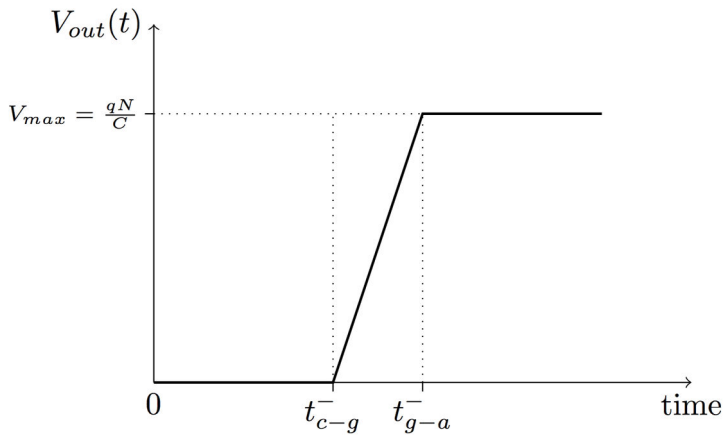

Figure 5.5 – Example of the output voltage as a function of time in a Frisch-gridded ionization chamber. Only the signal induced by electrons is considered. In figure, t^-_{c-g} and t^-_{g-a} are the electron drift time from the point of interaction to the Frisch grid and the drift time between the grid and the anode respectively.

Taking this into account, with an ideal Frisch grid placed between the cathode and the anode, the amplitude of the induced signal is directly proportional to the deposited energy in the detector, although the total induced charge still depends on the number of collected electrons. The fraction of electrons that reaches the anode depends on many factors such as detector design, the purity of the medium and the applied electric field. Under real

experimental conditions, a certain number of electrons may be collected by the grid reducing the total number of collected charges. This effect is related to the electron collection efficiency of the grid. In addition, the shielding of the Frisch grid to the movement of charges in the drift region is not perfect. In fact, electrons induce a current on the anode before they pass through the grid. This effect referred as inefficiency of the Frisch grid affects both the total induced charge and the shape of the output signals. A more detailed description of the electron transparency and inefficiency of the Frisch grid are presented in Sections 5.2 and 5.3 respectively.

5.2 Electrons collection by the Frisch Grid

Electron transparency of a grid refers to the fraction of electrons produced after the interaction of an ionizing particle with the medium that passes through the grid under the influence of an electric field. If the transport properties of the grid are good, no electrons are trapped during migration between the point of interaction and the grid and hence, the amplitude of the measured signal at the anode does not depend on the position of the interaction. On the other hand, if a fraction of electrons are collected before reaching the anode, the shape and amplitude of the output signals would be reduced degrading the energy resolution of the detector [179]. Electron transparency of a grid depends mostly on the choice of the potentials applied to the electrodes in the detector, but it also depends on the gap and the geometrical characteristics of the grid as is discussed in this section. The reduction on the number of drifting electrons due to recombination is omitted in this chapter.

The grid is maintained at an intermediate potential of those of the cathode and the anode. With an appropriate biasing of the electrodes, the overall electric field within the chamber remain substantially uniform so electrons can pass through the grid with high efficiency. For this to happen, the electric field in the gap, E_{gap}, should be higher than the electric field in the drift region, E_{drift}. When the electric field ratio $\frac{E_{gap}}{E_{drift}}$ is large enough, all field lines will pass through the grid and electrons (if diffusion is neglected), that in fact drift along the electric field line, will arrive to the anode without being collected by the grid. On the other hand, if the ratio is not enough, some electric field lines may terminate on the grid and a fraction of electrons would be collected before they actually cross the grid. Bunemann et al. [179] established a minimum bias condition that should be satisfied in a Frisch grid ionization chamber in order to avoid electron collection:

$$\frac{E_g}{E_d} \geq \frac{1 + \frac{2\pi r}{a}}{1 - \frac{2\pi r}{a}} \tag{5.12}$$

where r is the grid wire radius and a is grid pitch, i.e., the center-to-center distance between adjacent wires. The geometry of a Frisch grid ionization chamber is shown schematically in Figure 5.6. It should be noticed that Equation 5.12 is valid for a specific kind of grid based on 1D parallel wire grid. In our LXe TPC, the Frisch grid is a mesh wire grid that consists of a set of parallel and perpendicular wires. Hence, although this condition cannot be directly applied to our detector, it gives an idea of the direct relationship between the

electric fields required to avoid electron collection by the grid and the characteristics of the experimental setup and the physical properties of the grid.

Equation 5.12 relates, in fact, to the fraction of field lines that ends on the collecting electrode where E_g and E_d do not directly represent the electric field in the gap and drift region, but they represent the number of lines per unit area that ends and leave the grid respectively. Substituting E_g and E_d by the actual potential difference on the electrodes, Equation 5.12 results in:

$$\frac{V_{anode} - V_{grid}}{V_{grid} - V_{cathode}} \geq \frac{p + p\rho + 2l\rho}{d - d\rho - 2l\rho} \tag{5.13}$$

where p is the grid-anode distance, $\rho = \frac{2\pi r}{a}$, $l = \frac{a}{2\pi}(\frac{1}{4}\rho^2 - \log\rho)$ and $V_{cathode}$, V_{anode} and V_{grid} are the voltages applied to the cathode, anode and Frisch grid respectively [179]. The local distribution of the electric field lines that pass through the grid and terminates on the anode depends, therefore, on the geometry of the grid. By decreasing the wire radius or increasing the pitch of the grid a smaller electric field ratio is required to achieve a maximum electron collection efficiency.

Moreover, according to Equation 5.13, for the same applied electric drift field and same Frisch grid, halving the gap implies a reduction by a factor of two on the potential applied to the grid in order to have the same electron transparency. However, smaller gaps imply some severe mechanical constraints. Although a mesh grid is in general mechanically resistant, the handling of the grid to achieve good flatness and parallelism with respect to the anode-cathode plane may be quite challenging. When an intense potential is applied to the grid, the electric field pulls down the mesh. In order to maintain the flatness of the grid and hence, the gap distance between the grid and the anode, the grid should be uniformly stretched over a frame. A small deflection of the grid with respect to the anode plane may cause capacitance variations, and thereby produce an increase of the electronic noise. Moreover, small gap distances and high electric fields imply large capacitances per unit area that makes the grid very sensitive to mechanical vibrations. A small variation of the distance between the grid and the anode produced by a vibration may create a large transitory fluctuation in the capacitance producing a charge pulse spike at the input of the readout electronics. In a worst-case scenario, if the grid-anode distance is too small and the grid is not well stretched, a mechanical vibration may cause the direct contact between electrodes producing irreversible damages to the electronics.

In addition, the possibility of sparks in the gap when working at high voltages and small gaps should be taken into account. This effect limits the maximum potential that can be applied to the Frisch grid and hence, it limits the maximum electric drift field.

5.3 Frisch Grid Inefficiency

As discussed in Section 5.1.3, the Frisch grid should act as an electrostatic shielding between the drift region and the gap, removing the position dependence from the charge induced on the collecting electrode. If the shielding is perfect, electrons will induce a current on the anode from the moment they pass through the grid while no signal is induced by the

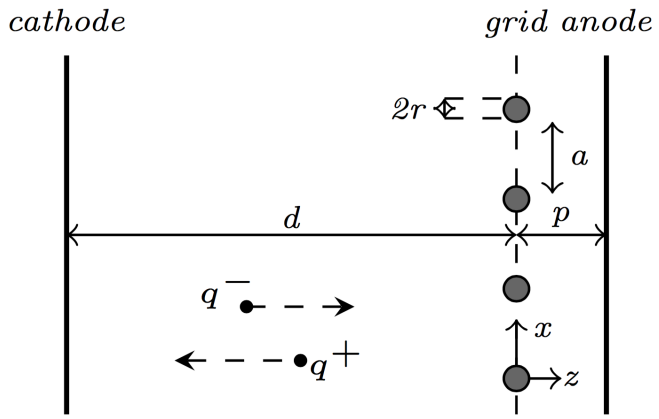

Figure 5.6 – Schematic illustration of the geometry of a Frisch grid ionization chamber.

positive ions. However, in real experimental conditions, a slightly position-dependence on the induced signals is always present due to the limited shielding of the grid. This effect known as inefficiency of the Frisch grid implies that electrons start inducing a current on the anode before they actually pass through the grid. If so, the weighting potential of the anode is not strictly zero in the drift region as presented in Section 5.1.3. Numerical calculations of the weighting potential on a Frisch grid ionization chamber have been reported in [211]. Authors show that the weighting potential of the anode at distances far from the grid, i.e. $z > a$ where a represents the grid pitch, is not zero but it increases slowly as the distance from the grid decreases. In the vicinity of the grid its value deviates abruptly from zero and rapidly increases as the distance to the anode decreases. Figure 5.7 shows an example of the weighting potential reported by [211] for a parallel wire grid. The weighting potential on the anode can be approximated as a function of z according to Equation 5.14:

$$\varphi_{anode} = \begin{cases} \sigma\left(1 - \dfrac{z}{d}\right), & \text{if} \quad p < z < d \\ \sigma + \left(1 - \sigma\right)\dfrac{p - z}{p}, & \text{if} \quad 0 < z < p \end{cases} \tag{5.14}$$

The inefficiency of the Frisch grid is determined by a linear extrapolation of the obtained weighting potential distribution at the position of the grid. These results describe fairly well the weighting potential in the regions between electrodes although they do not reproduce the inhomogeneities observed around the Frisch grid. Equation 5.14 assumes that the weighting potential only varies with depth. However, in the proximity of the grid the weighting potential lightly fluctuates in the region between wires. As shown in Figure 5.7 this y-dependency disappears almost completely at distances higher than the grid pitch ($x > p$). However, these fluctuations strongly depends on the gap, increasing as the gap decreases. This approximation is therefore valid for detectors with large gaps compared to the pitch of the grid, and otherwise the lateral dependence of the weighting potential should be taken into account on the induced signal.

In Equation 5.14 σ is the inefficiency factor for a parallel-wired grid calculated by Bunemann et al.. The inefficiency parameter σ depends on the grid-anode distance p, the wire radius r and the pith between wires a according to:

$$\sigma \approx \frac{a}{2\pi p} \log\left(\frac{a}{2\pi r}\right) \tag{5.15}$$

Values of the grid inefficiency factor σ determined experimentally for a parallel wire grid and a mesh grid are also reported in [211]. The results are in good agreement with the values of σ obtained by numerical calculations and also predicted by Equation 5.15 for the case of a parallel wire grid. Authors show that for both kind of grids, the inefficiency factor σ does not vary linearly with the ratio $\frac{a}{p}$. For a constant value of r and a, when the gap is large compared to the grid pitch, the grid inefficiency increases by almost a factor of two when the gap is reduced from 10 mm to 6 mm as expected from Equation 5.15. However, when the gap distance becomes comparable to the pitch, a larger increase of σ is observed for the same gap variation. Nevertheless, this increase is less important for a mesh of crossed wires than that of a parallel wire grid, although the variation is smaller than the one expected in the case of both set of parallel and perpendicular wires would act as independent shields to the anode. Based on the results obtained by Göök et al., for a metallic woven mesh with 254 μm pitch, bar thickness of 25 μm and placed at 500 μm from the anode, an inefficiency of around 5 % is estimated ($\frac{a}{p} \approx 0.5$). On the other hand, an inefficiency factor of the order of 2 % is estimated for the same grid but with a 1 mm gap.

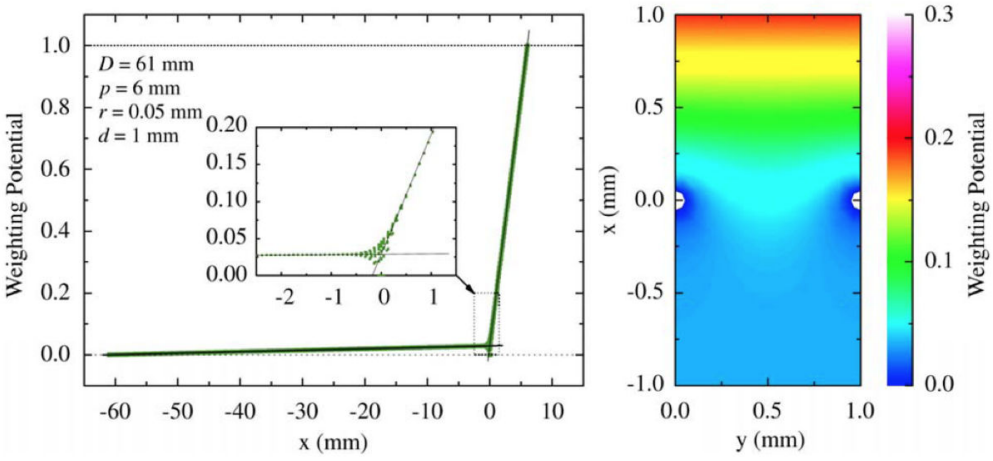

Figure 5.7 – Left: Weighting potential distribution of the Frisch grid detector along the drift direction. The physical properties of the grid are listed in the figure, where D and p are cathode-grid and anode-grid distances respectively, d is the distance between the grid elements and r is the wire radius. Right: 2-D map of weighting potential around the Frisch grid. Image courtesy of [211]

The choice of a Frisch grid and the gap distance on a gridded ionization chamber should be a compromise between the improve of the grid efficiency and the requirements related to a good electron collection efficiency as discussed in Section 5.2. In Section 5.5 a detailed

study of the effect of the inefficiency of the Frisch grid on the shape of the output signals for different type of grid geometries and grid-anode distances is presented.

5.4 Charge induction on a pixelated anode

So far we have discussed the charge induction on a planar electrode so the total charge collected by the anode is always equal to the charge produced in the interaction (if electrons are not collected by the grid or trapped by the impurities of the medium). However, in our LXe TPC the collecting electrode is based on a segmented anode divided in 3.125 x 3.125 mm^2 pixels. The advantage of using a pixelated anode is that it provides two-dimensional information of the position of the interaction in the detector and therefore, we can measure both the energy and the position. However, pixelated electrodes are also sensitive to other effects such charge sharing between neighboring pixels or indirect charge induction, that affects the performances of the detector.

Charge sharing between adjacent pixels is mainly related to the transverse diffusion of electrons in the medium, which determines the size of the electronic cloud. If the pixel size is smaller that the size of electron cloud, the charge will be always collected by several pixels. Otherwise, the charge sharing between pixels will depend on the relative position of the cloud with respect to the center of the pixel. X-ray emission after a photoelectric interaction and the mean free path of the primary electrons may also contribute to charge sharing between neighboring pixels. Either way, charge sharing increases the number of fired pixels per interaction. Multiple-pixel events, i.e. events with at least one cluster composed by more than one fired pixel, can be used to improve the spatial resolution by measuring the center of gravity of the interaction. However, multiple-pixel events also have poorer energy resolution. Charge sharing implies lower amplitude signals collected per pixel, which makes the device more sensitive to the noise discrimination level. Very low threshold levels are therefore required, in order to collect all the charge from a single electron cloud shared between several pixels. The number of triggered pixels depends on the pixel size (see Section 7.3). In this respect, larger pixel dimensions are recommended for better energy measurement performances.

In LXe, the spread of the electron cloud due to transverse diffusion is $\sim 200\ \mu m\sqrt{cm}$ for an applied electric field of 1 kV/cm. The simulated lateral extension of the electron cloud at 511 keV was found to be around 200 μm, and the mean free path of K-shell X-rays is $\sim 400\ \mu m$. Note that the last two effects are small compared to a $3.1 \times 3.1\ mm^2$ pixel size, so its contribution can be neglected. The lateral spread of the electron cloud is only significant if the distance between the point of interaction and the adjacent pixel boundary is smaller than 3 times the transverse diffusion coefficient. Other effects such as electronic noise or charge induction on the neighboring pixels may also generate multiple-pixel events even though the charge produced in the interaction is collected by a single pixel of the anode. These two effects degrade the energy resolution of the detector since an additional charge is added to the real charge produced by the ionizing particle. The effect of the electronic noise is discussed in Section 6.4. In this section, we study the charge induced on a pixel that neighbors a direct signal collecting electrode.

The charge induced on a pixelated anode by a moving charge q in general differs from the one induced on a planar electrode. Figure 5.8 shows the weighting potential distribution for a parallel plate electrode and for two different pixel pitch. As we have seen, on a two parallel plate detector the weighting potential is a linear function of the distance from the electrode surface. However, on a pixelated anode the weighting potential start to bend in the proximity of the pixel. The inhomogeneities of the weighting potential close to the pixel become more significant as the size of the pixel decreases [212].

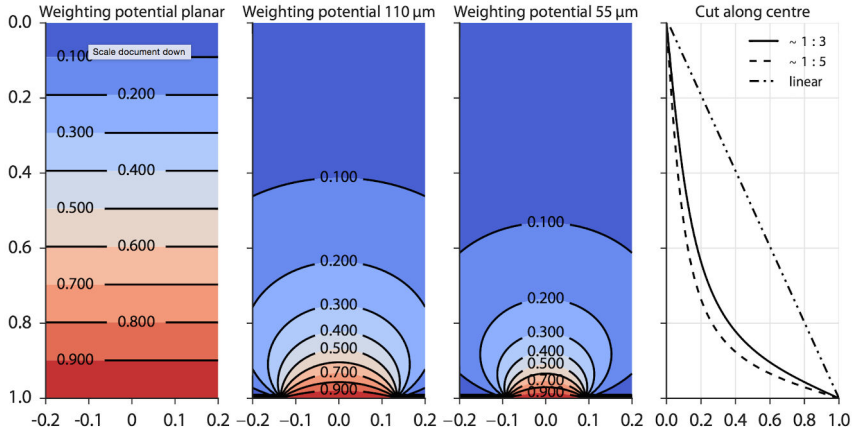

Figure 5.8 – Weighting potential of an infinite parallel plate electrode and two different pixel pitch of 55 μm and 100 μm. Figure taken from [213].

According to the Shockley-Ramo theorem, the weighting potential of a certain pixel of the anode is obtained by solving the Laplace equation $\nabla^2\varphi_w = 0$ when the pixel of interest is set at unity potential and the rest of pixels, the Frisch grid and the cathode are grounded [209]. If the pixel size is much larger than the gap distance, the weighting potential can be approximated as a linear function of depth so it increases linearly from zero to unity as electrons drift between the grid and the anode. Under this conditions, the same charge is induced independently of position of the interaction [212]. However, if the pixel size is comparable or smaller than the gap, the weighting potential is no longer linear with distance, but it shows a gradient that becomes steeper in the immediate vicinity of the pixel. The induced current is small when q is far from the pixel, i.e. $z > s$ where s is the size of the pixel, due to the charge sharing among many pixels of the anode and it becomes significant only when the charge is very close to the pixel. This non-linear behavior of the weighting potential on a segmented electrode varies with the pixel size. Smaller pixels with respect to the detector dimensions show a more rough deflection from linearity. This effect is known as *small pixel effect* [209].

Since the weighting potential is not uniform on a pixelated anode and it bends around the pixel, the weighting potential reaches into the neighboring pixel volume. This leads to the induction of a transient signal on the neighboring pixel, even if the charge is drifting only in the actual collecting pixel through the electric field lines. Since these neighboring pixels do not collect charge, their weighting potential should be zero. However, it rises and shows a maximum value before dropping to zero as illustrated in Figure 5.9 [20]. The transient signal is a bipolar pulse, which is positive as the electrons pass close to the non-collecting

pixel and then becomes negative as the electrons are collected by the collecting pixel leading to a net zero integral. If the shaper has a long integration time the induced transient signal will give a zero output pulse. However, if the integration time is short, the output signal of the electronics may gives a positive pulse with enough amplitude to trigger the threshold level. Consequently, these transient signals are considered as real deposited charge in the interaction and then added to the total energy of the cluster. In some cases, this transient signal will be mixed with direct collected charge, resulting in a deformed pulses with a biased value of the time and the amplitude.

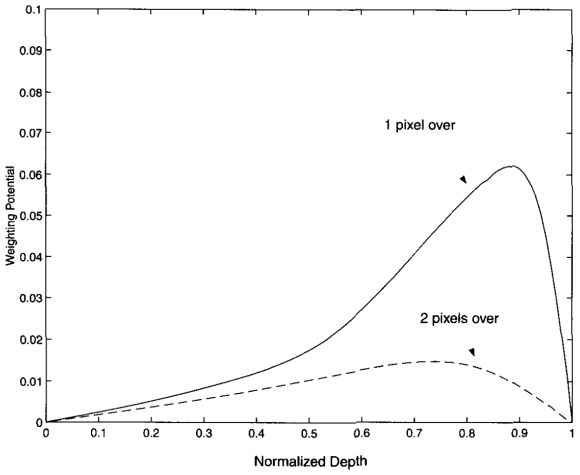

Figure 5.9 – Weighting potential of a neighbor pixel along the drift direction. The dashed line shows the same variation of a pixel that is located two pixels away of the actual collecting pixel. Figure taken from [20].

The contribution of the induced charge on a non-collecting electrode depends on the weighting potential. Smaller pixel size lead to stronger charge induction in the neighboring pixels due to the small pixel effect, but also give rise to the multiple-pixel events due to the diffusion and the charge cloud distribution. Moreover, the amplitude of the transient signal induced on a non-collecting electrode depends on the lateral position of the electronic cloud with respect to the pixel center.

5.5 Results and Discussion

5.5.1 Measurement of the electron transparency of the Frisch grid

In LXe after the interaction of a 511 keV γ-ray around 27200 electrons are produced in the medium if an electric drift field of 1 kV/cm is applied [115]. For an ideal Frisch grid and if any of the electrons are collected by the grid i.e. the transparency of the grid is 100 %, the total charge collected by the anode is equal to the number of electrons produced in the interaction. However, if the transport properties of the grid are not good, a fraction of the electrons are collected before passing through the grid and the total induced charge on the anode will be reduced. Since the transparency of a Frisch grid depends on the fraction of

electric field lines intercepted by the grid [179], it can be measured by comparing the 511 keV photoelectric peak for different electric field ratios ($\frac{E_{gap}}{E_{drift}}$).

The electron collection efficiency of a Frisch grid can be thus determined by keeping the potential applied to the cathode constant, i.e. same electric drift field, the anode to ground and by varying the potential applied to the the grid. In the particular case of XEMIS1, to maintain the same electric field along the drift region the voltages applied to the grid, the cathode and the first electric field ring should vary while the anode is kept to ground. The results presented in this section were obtained for a constant electric drift field of 1 kV/cm with a 6 cm TPC. The cathode was biased from -6300 V to a maximum voltage of -7000 V, while the potential applied to the Frisch grid varied from 50 V to 500 V corresponding to electric field ratios from 2 to 8. The Frisch grid used for this study was a 100 LPI metallic woven mesh placed at 500 μm from the anode. The experimental set-up used to have a mono-energetic beam of 511 keV γ-rays and the data acquisition system are introduced in Chapter 6.

Figures 5.10 shows two examples of the 511 keV γ-ray spectrum obtained with a low activity ^{22}Na source at 1 kV/cm. In Figure 5.10(a) the Frisch grid was set to a potential of 50 V corresponding to an electric field ratio of 2, while the spectrum shown in Figure 5.10(b) was obtained for a ratio of 6. In both cases the event selection was performed according to the method presented in Chapter 6. Only those events that take place at least 5 mm from the grid were selected for the analysis. Moreover, the measured energies were corrected by electron attenuation as discussed in Chapter 7 (Section 7.1). The maximum position of the photoelectric peak was obtained by fitting the distribution by a Gaussian function. The mean value of the peak represents the average charge measured by the detector after a 511 keV energy deposit in the TPC.

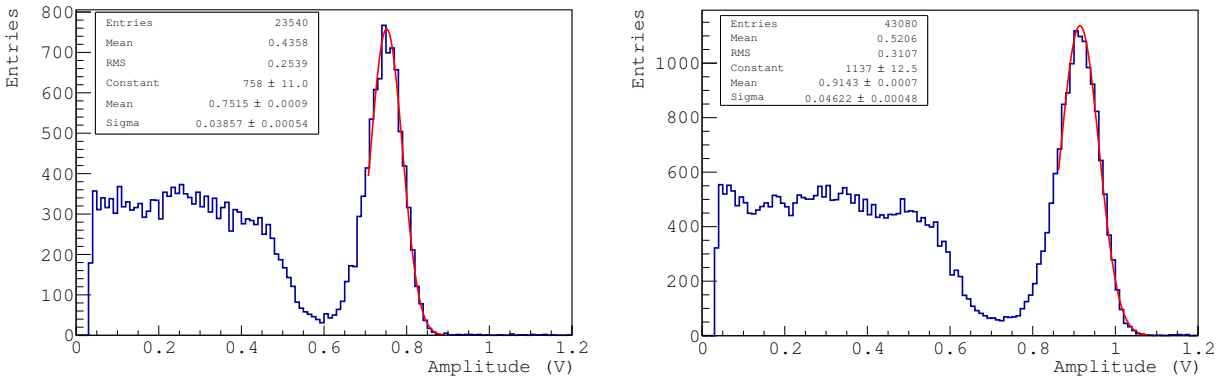

(a) R = 2 **(b)** R = 6

Figure 5.10 – Energy spectrum of the 511 keV γ-rays obtained with a 100 LPI mesh placed at 500 μm from the anode at an electric drift field of 1 kV/cm and two different electric field ratios of (a) R = 2 and (b) R = 6.

We can observe from Figure 5.10 that the position of the 511 keV peak varies with the voltage applied to the grid. When the ratio is low the mean of the photoelectric peak is around 0.75 V. However, by increasing the electric field in the grid-anode region by a factor

of 3 the collected charge increases to 0.91 V. This implies that a fraction of the electrons are lost during motion towards the anode when an electric field of 2 kV/cm is applied in the gap region compared to an electric field of 6 kV/cm.

In order to determine the optimal bias voltage that should be applied to the grid to obtained a 100 % electron transparency, the same study was performed for different electric field ratios. Figure 5.11 shows the evolution of the amplitude of the photoelectric peak as a function of the electric field ratio for a constant electric drift field of 1 kV/cm. The collected charge was normalized to the maximum charge measured for a field ratio of 8. We can see that a maximum electron collection efficiency is already achieved for a ratio of 5.5. Lower electric fields in the gap implies that a fraction of the produced electrons are lost before reaching the anode. For an electric field ratio of 2 the loss is of the order of 18 % and decreases rapidly as the ratio increases. The statistical error, estimated from the Gaussian fit of the photoelectric peak, is too small to be seen in the figure.

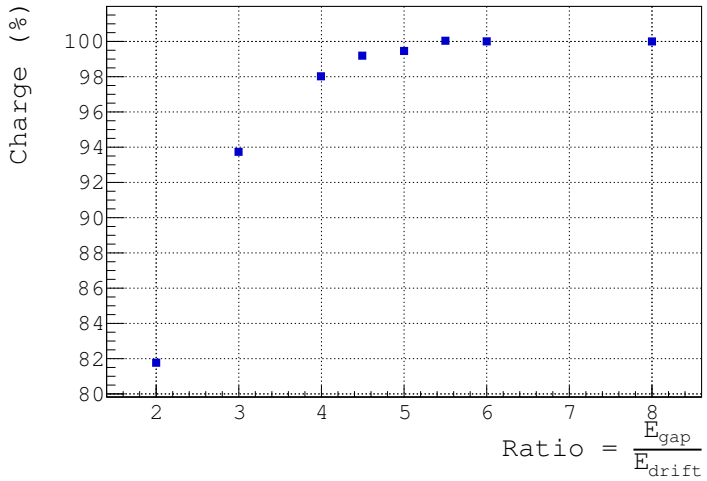

Figure 5.11 – Collected charge for 511 keV events as a function of the electric field ratio for a constant electric drift field of 1 kV/cm. The results were obtained for a 100 LPI Frisch grid located at 500 μm from the segmented anode.

As discussed in Section 5.2 the optimal bias to the electrodes depend both on the physical properties of the grid and on the distance between the grid and the anode. The results presented in Figure 5.11 were obtained for a 100 LPI metallic woven mesh which has a 50 μm thickness and 254 μm pitch between wires. Figure 5.12 shows the comparison of the electron collection efficiency of this kind of Frisch grid for two different gap sizes as a function of the potential applied to the grid. As expected, for a 1 mm gap, same levels of electron transparency are obtained by increasing by a factor of two the potential applied to the grid. Similarly, the collected charges were normalized to the maximum charge measured at the highest electric field ratio.

This study was performed for each of the grids tested during this thesis. For example, the results obtained for a 50.29 LPI mesh are shown in Figure 5.13. For this mesh, which has a pitch of around 2 times bigger than that of the 100 LPI (505 μm) mesh, the optimal electric field ratio is 3 instead of 6 for the same electric drift field of 1 kV/cm. In this case, the influence of the thickness is assumed to be negligible since the variation is small (50 μm

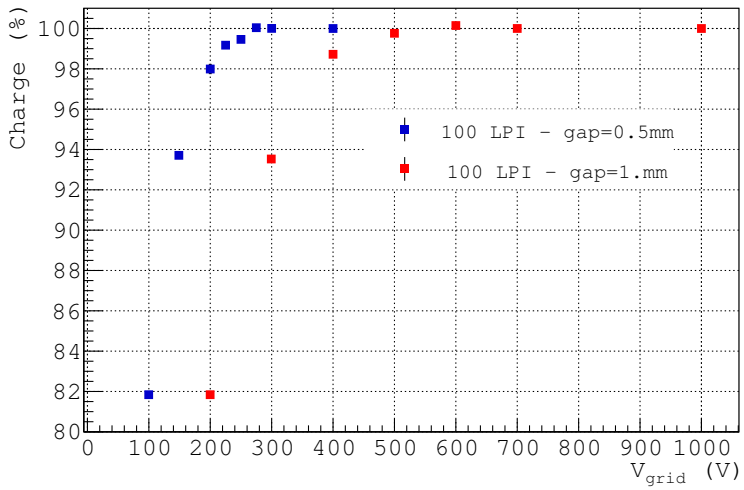

Figure 5.12 – Collected charge for 511 keV events as a function of V_{grid}, for a constant electric drift field of 1 kV/cm. The results were obtained for a 100 LPI Frisch grid for two different gaps of 500 μm and 1 mm.

and 60 μm thick respectively). Therefore, increasing the mesh hole size by a factor of 2, halves the electric field on the gap required to achieve an electron transparency of 100 %. This reduction could be interesting when high electric drift fields are required as in the case of XEMIS2 where electric fields up to 3 kV/cm are expected.

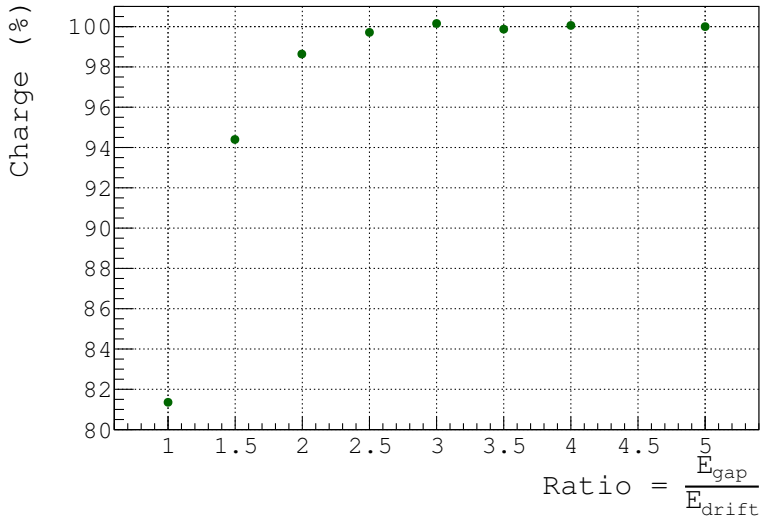

Figure 5.13 – Collected charge for 511 keV events as a function of the ratio between the electric field in the gap and the electric drift field for a constant electric drift field of 1 kV/cm. The results were obtained for a 50.29 LPI Frisch grid located at 1 mm from the segmented anode.

5.5.2 Influence of the Frisch grid inefficiency on the pulse shape

In Section 4.3.1, we performed the study of the shape of the output signal for 511 keV events in order to understand the slower rise time of the signals compared to an ideal step-like pulse injected to the front-end electronics. A rise time[1] of 1.52 μs was measured regardless the gap distance between the grid and the anode, while a rise time of 1.39 μs is expected from the shaping time of the electronics. Our hypothesis is that this increase of the pulse rise time is attributed to the inefficiency of the Frisch grid. Moreover, in addition to the larger rise time, a long rising edge is also observed on the pulses that is also attributed to the inefficiency of the grid.

The charge induced on an electrode on an ideal Frisch grid ionization chamber is zero in the drift region and increases linearly as the electrons move from the grid to the anode. In this case, the total collected charge is equal to the number of generated electrons, and the shape of the signal is given by the collection time of the electrons in the detector and the integration time of the electronics. This is the case of an ideal step-like pulse injected into the injection capacitance of the IDeF-X chip as presented in Figure 4.8, where the signal reaches its maximum value in 1.39 μs. However, as reported in Section 5.3, the shielding of the grid to the motion of charges in the drift region is not perfect due to the inefficiency of the grid, so electrons start inducing a signal on the anode before they pass through the grid [179]. Figure 5.14 shows the comparison between the average output signal for 511 keV photoelectric events measured with a 100 LPI metallic woven grid placed at 500 μm from the anode, and the output signal obtained after the injection of a test pulse to the front-end electronics through the 50 fF test capacitance. To simulate the drift in the gap, the test signal was a step pulse with a slope of 250 ns that corresponds to a pre-amplifier output signal over a gap of 500 μm (for an electron drift velocity of 2 mm/μs and an electric field of 1 kV/cm). The injection was performed on two different pixels of the anode, one from each IDeF-X chip, under the standard experimental conditions. The injected signal presented in Figure 5.14 corresponds to the average pulse over 2000 injected signals to reduce statistical fluctuations. For the case of the 100 LPI output signal, only single-cluster events i.e. events with only one reconstructed cluster, that correspond to an unique signal with an amplitude of 511 keV collected by just one pixel of the anode were selected. Isolated pixels refers to interactions where the electronic cloud drifts just above the center of the pixel that collects the charge. Likewise, the signal was averaged over a sufficient number of events to increase the SNR. In addition, to remove the z-dependence, only signals with a drift time between 2.6 cm and 6 cm from the anode were considered. The 511 keV anode signal presents an early rise time that reaches 5 % of the maximum amplitude. This early rising edge suggests that electrons start to induce a current on the anode around 3.5 μs before they pass through the grid, which is equivalent to a distance of 7 mm (at 1 kV/cm).

By direct extrapolation, the rising edge of the pulse matches with a grid inefficiency of 5 %, compatible with the value of the inefficiency factor σ estimated in Section 5.3. Equation 5.15 and the results obtained by Göök et al., also state that by increasing the ratio $\frac{a}{p}$ (ratio grid pitch - gap) the grid inefficiency factor decreases. This means that if the long rising edge is actually due to the inefficiency of the Frisch grid, it should vary with the type

[1]The rise time is defined as the time required by the pulse to rise from 5 % to 100 % of its amplitude

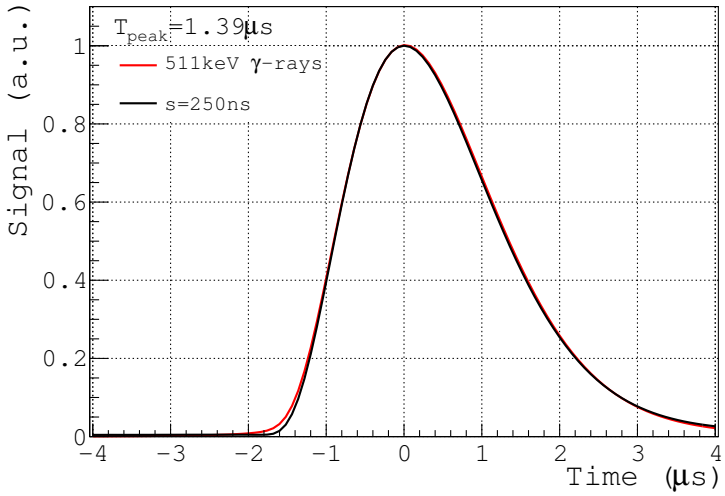

Figure 5.14 – Comparison between the output signal of the shaper for 511 keV events with a 100 LPI Frisch grid placed at 500 μm from the anode (red line) and a 60 mV injected step-like pulse with a slope of 250 ns (black line). The peaking time was set to 1.39 μs.

of grid. Figure 5.15 shows the average output signal for 511 keV photoelectric events for four different Frisch grids (see Tables 3.2 and 3.3). The grid-anode distance was set to 1 mm in all cases. Different pulse shapes are clearly obtained for the different type of meshes. As expected, the smallest inefficiency factor, i.e. the smaller rising edge, is obtained for the 500 LPI micro-mesh that presents the smallest pitch of 50.8 μm ($\frac{a}{p} = 0.05$). On the other hand, the worst efficiency, of the order of 10 %, is estimated for the 70 LPI electroformed micro-mesh, which has a large pitch of 362 μm with a small thickness of 5 μm. The 50.29 LPI has the largest pitch (505 μm) but it presents an intermediate inefficiency factor of 8 % due to its high thickness. Consequently, unlike for electron collection efficiency, which increases as the pitch of the mesh increases, the best Frisch grid in terms of shielding efficiency is the one with the smallest pitch. Please note that the inefficiency factors are just an estimation, since our experimental set-up is not optimal for inefficiency measurements. The differences in the trailing edge of the pulses is attributed to the different coupling AC - DC selected during the consecutive data taking periods.

As discussed in Section 5.3, the inefficiency of a Frisch grid not only depends on the physical properties of the grid but it also depends on the grid-anode distance. Figure 5.15 also shows the comparison of the output signal for the 100 LPI mesh for two different gaps. As expected, the inefficiency of the grid increases with decreasing the gap. In addition, by comparing the 100 LPI at 500 μm from the anode with the 50.29 LPI at 1 mm, we can state that the inefficiency loss due to a reduction of the gap by a factor of 2 is less significant that the loss due to an increase by the same factor of the pitch size, as expected.

Frisch grid inefficiency as a function of the distance from the anode

In an ionization chamber, the induced signals on the anode show a strong dependency on the z-position. The rise time of the signals is shortened as the drift distance decreases, and the

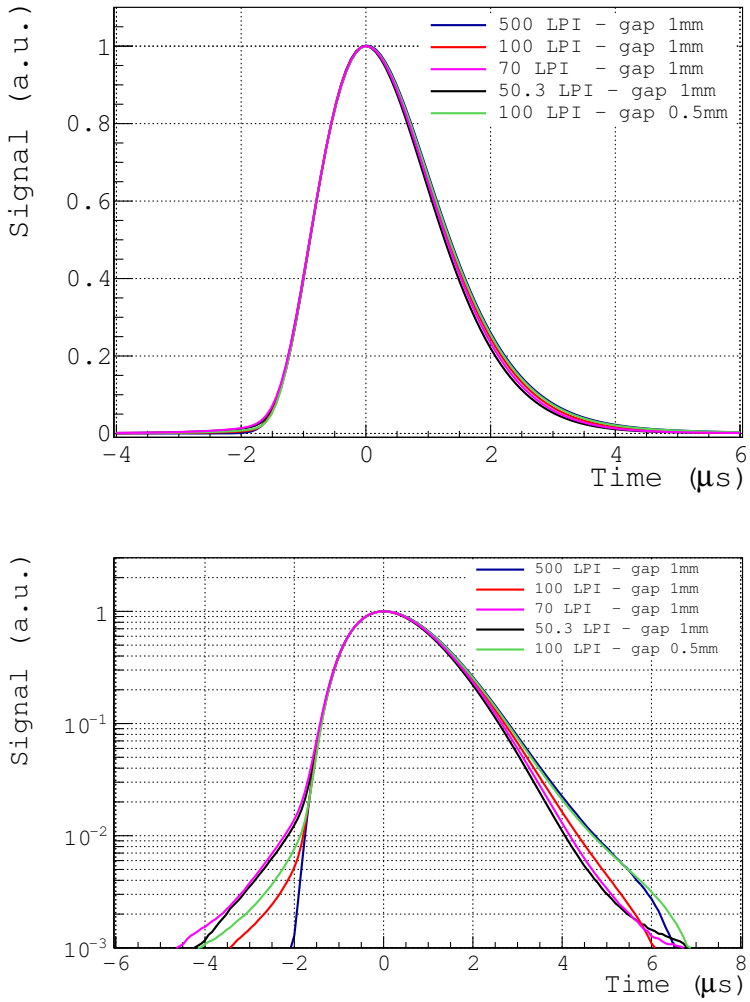

Figure 5.15 – Average output signal for 511 keV events and four different Frisch grids in linear and logarithmic scales. The peaking time was set to 1.39 μs.

amount of induced current also decreases due to the weighting potential. In Figure 5.16, the shaped signals of charge clouds for different z-intervals above the pixelated anode are shown. These results are obtained for a 100 LPI Frisch grid located at 500 μm from the anode. The rise time increases with increasing the z-position. At positions close to the Frisch grid, the shape of the pulse matches with the injected pulse convolved with a gap of 500 μm. As the distance from the anode increases, the shape of the signals differs from the ideal pulse. Non significant variation is, however, observed from distances of around 7 mm from the grid. The early rise time also varies with the position. Close to the grid, no early rising edge is observed, while it increases as the z-position increases. These results support the hypothesis that both the larger pulse width and the early rise time are due to a defective shielding of the grid to the electrons.

The resulting signals can be integrated over time to obtain the total induced charge. To minimize the charge loss at high distances due to diffusion, the pulses showed in Figure 5.16 were integrated over a virtual cluster formed by 9 pixels. We considered only events with a total charge of 511 keV collected by the 3×3 virtual electrode. The presence of the parasitic

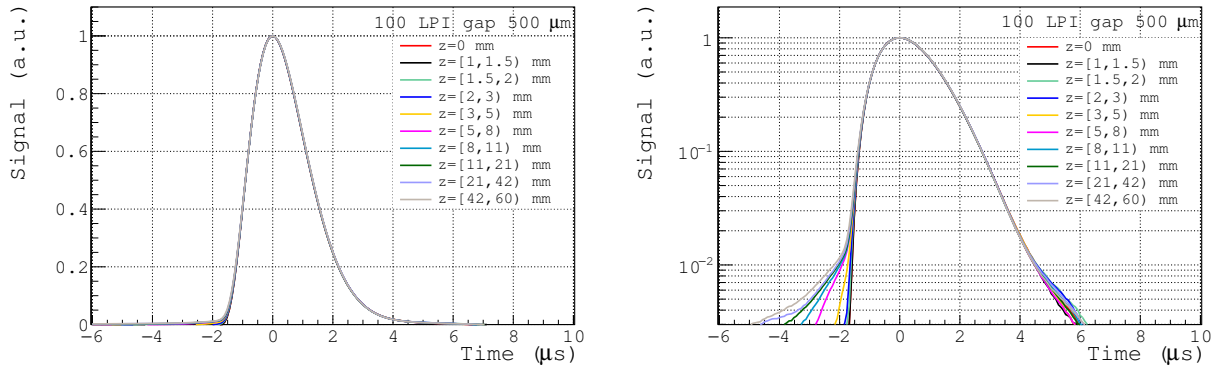

Figure 5.16 – Average output signal for 511 keV events obtained with the 100 LPI Frisch grid located at 500 μm from the anode, as a function of the drift time for different z-intervals along the drift length. The signals are shown in linear (left) and logarithmic (right) scales. The peaking time was set to 1.39 μs.

signal reported in Section 6.4.2 was corrected to avoid a bias due to the non-collecting pixels. Figure 5.17 shows the pulse integral as a function of drift time for different z-intervals. The total integrated charge as a function of the average position of the z-distribution obtained for each position interval is depicted in Figure 5.18. The maximum of the induced charge is a function of the interaction depth, due to the dependency of the weighting potential with the position. The collected charge increases with increasing the position from the anode, and it tends to saturate at a distance of the order of 7 mm. This is most likely due to the ballistic deficit produced by the induced charge before the grid. Therefore, assuming a 100 % electron transparency, we can state that the difference in the pulse shape, i.e. in the collected charge, with the z-position can be associated to the inefficiency of the grid.

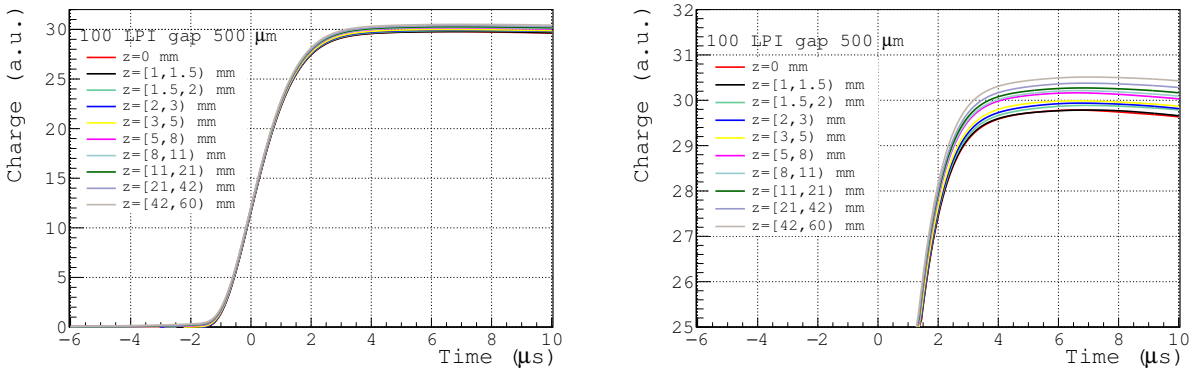

Figure 5.17 – Pulse integral as a function of the drift time for different z-intervals along the drift length. Figure on the right is a zoom of the figure on the left.

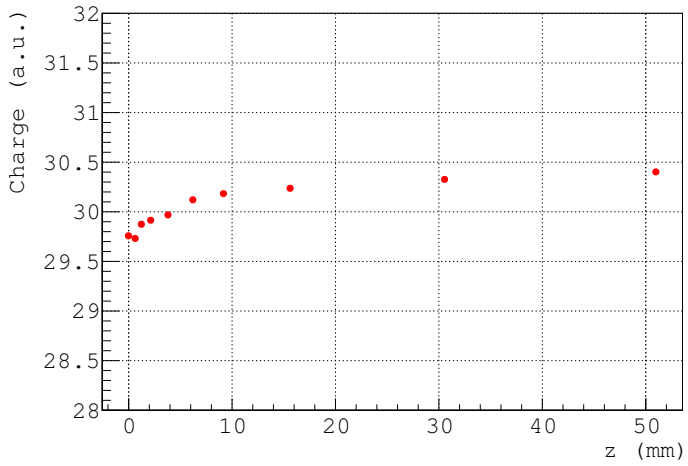

Figure 5.18 – Total integrated charge as a function of the distance from the anode.

5.5.3 Charge sharing and charge induction between neighboring pixels

In a segmented anode, multiple-pixel events are produced by either charge sharing from a single electron cloud or from multiple γ-ray interactions in the detector. Due to the nature of the interactions in the LXe, for 511 keV γ-rays 2.1 pixels are triggered, in average, per cluster for a energy threshold level of $3\sigma_{noise}$. If these multiple-pixel events are actually produced from a single electron cloud the arrival time of the electrons onto the pixels, determined from the maximum of the shaped signals, should be the same. In our case, the maximum of the signals is determined from the time of CFD as reported in Section 4.4.2. The study of the time of CFD of the signal from pixels that form a same cluster is, in fact, an useful tool to determine the minimum timing separation to resolve two different interaction that occurred close in space, such as Compton scattering followed by a photoelectric effect. This timing condition, also called cluster time window, takes into account the precision in the time measurement, which can depend on the collected charge.

Charge induction study with a 1 mm gap

The simulation of the output signal of the IDeF-X LXe chip presented in Section 4.4 showed a timing resolution of the other of 260 ns for an amplitude of 3 times the electronic noise (σ_{noise}). This result was obtained with the CFD method and an optimal configuration of the CFD parameters; time delay and attenuation fraction. For the same measurement conditions, higher time differences have been measured, however, from real data between the pixels of the same cluster. Figure 5.19 shows the total time difference distribution between the pixels of the same cluster for a total measured charge of 511 keV. The cluster time window was fixed to 2 μs, i.e. if two neighboring signals have a drift time difference smaller than 2 μs, both signals are grouped into the same cluster. The value of Δt was obtained as the difference between the time of CFD of the pixel with maximum amplitude and the time of the CFD of the rest of neighboring pixels of a cluster. The distribution is non-symmetric and does not agree with to a normal distribution. The distribution shows a sort of double-peak

structure centered at $\Delta t \approx 0$ with a plateau at positive time differences and a second peak at around 9 time channels. To better understand this result, we obtained the time difference Δt distribution as a function of the amplitude of the neighboring pixel (see Figure 5.20). For simplicity, we will refer to the amplitude of the neighboring pixels as $A_{neighbor}$. For signal amplitudes 3 times the electronic noise, an average time difference of 720 ns (9 time channels) is observed, which is around 3 times higher than the value estimated by simulation. Moreover, a cluster of events is also visible around this value at higher amplitudes.

The distribution of average values of Δt is depicted in the bottom part of Figure 5.20. The mean value of Δt was measured by dividing the scatter plot presented in the top part of Figure 5.20 in slices of $1\sigma_{noise}$ up to to an amplitude of $18\sigma_{noise}$, and in slices of $10\sigma_{noise}$ for higher amplitudes to increases the statistics per charge interval. Each of the charge distributions are fitted by a double-Gaussian function with a constant background (see Figure 5.21). The value of Δt is directly deduced from the mean of the fit. The experimental time difference between adjacent pixels decreases exponentially as the amplitude of the signals increases and tends to zero for a value of $A_{neighbor}$ higher than $50\sigma_{noise}$. On the other hand and according to the simulation results, a time delay of less than 80 ns was expected at amplitudes higher than $10\sigma_{noise}$. The observed decay was well fitted by a triple exponential function (blue line) that can be used to corrected the systematic time shift at low energy signals.

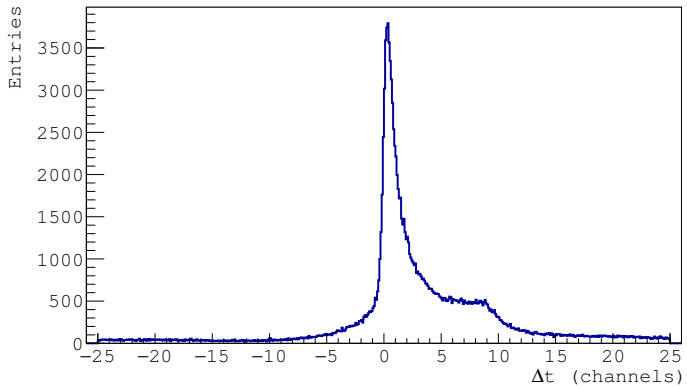

Figure 5.19 – Time difference between the pixels of the same cluster, for cluster with a total measured energy of 511 keV and a cluster time window of 2 μs.

The accumulation of events observed at low energies at around 9 time channels is due to a double-peak distribution observed at very low amplitude signals. In fact, for amplitudes up to $\sim$10 σ_{noise}, a fraction of the detected signals are delayed by around 720 ns from the pixels of reference. This result was not observed on the simulated data. Figure 5.21 shows two Δt distributions for constant amplitudes of 3 and 6 times σ_{noise}. For amplitudes of $3\sigma_{noise}$, an unique peak with a mean value of 9 channels (720 ns) stands out from the background. On the other hand, at $6\sigma_{noise}$ the mean value of the distribution is shifted to 7 channels, while a constant peak with mean at 9 channels remains present. This constant peak is still present at higher amplitudes, while the mean of the distribution moves towards zero. As the amplitude of the neighboring signals increases, the fraction of delayed events by 720 ns decreases until the peak is no longer visible in the Δt distribution. This important difference

between the electron arrival time to neighboring pixels cannot be explained by neither the presence of the electronic noise nor the size of the electron cloud nor the fluorescence X-ray emission. A time difference of 720 ns represents a separation of almost 1.5 mm for an electric field of 1 kV/cm.

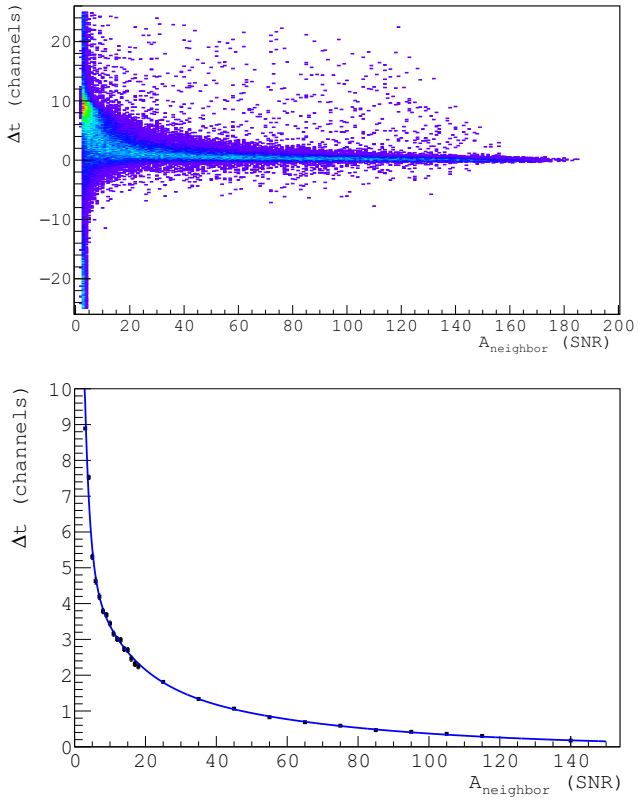

Figure 5.20 – Time difference distribution between the pixels of the same cluster as a function of $A_{neighbor}$. Only cluster with a total measured energy of 511 keV are included in the distribution. In the bottom figure the mean value of Δt per slice in charge is represented.

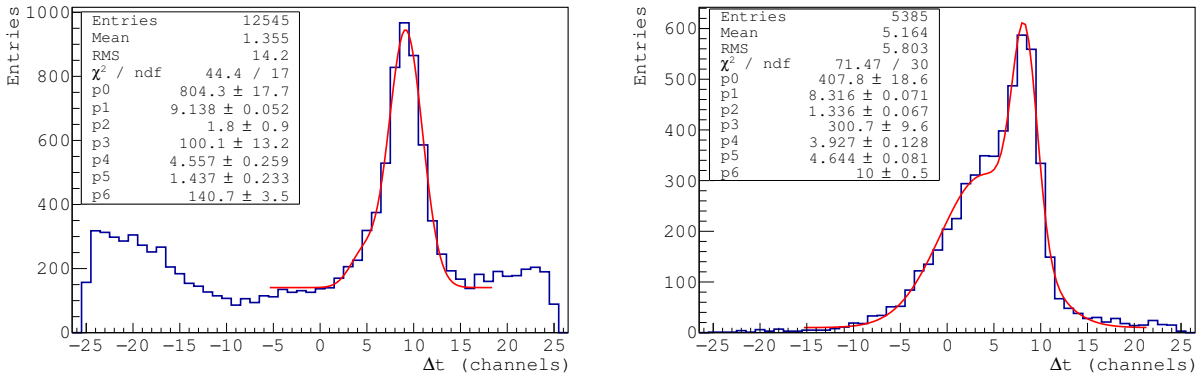

(a) $< A_{neighbor} > = 3\sigma_{noise}$ **(b)** $< A_{neighbor} > = 5\sigma_{noise}$

Figure 5.21 – Example of the Δt between pixels of the same cluster for a total charge of 511 keV and a $A_{neighbor}$ of $3\sigma_{noise}$ and $5\sigma_{noise}$ respectively.

The time difference between triggered pixel of the same cluster also varies with the depth of interaction. We observed that the time delay decreased as the distance from the anode increased. Figure 5.22 shows the average time delay as a function of $A_{neighbor}$ for three different slices of 1 cm each along the drift length. This effect is consistent with the increase of the spread of the electron cloud due to the lateral diffusion, and suggests that as the direct collected charge per pixel increases, the delay between adjacent pixels decreases. As discussed bellow, this effect is due to the indirect current induction between neighboring pixels. On the contrary, no significant variations were observed as a function of the total charge per cluster.

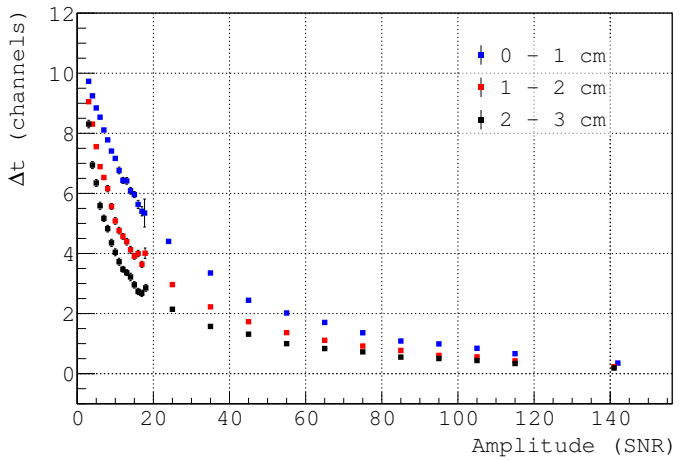

Figure 5.22 – Time difference between the pixels of the same cluster as a function of $A_{neighbor}$ for three different interaction positions with respect to the anode.

Simulation of charge induction in a segmented anode

In a real detector, the impact of charge sharing is difficult to isolate from other contributions. This makes simulation an excellent choice for studying these effects. In this section we present a simulation study performed with the aim of better understand charge sharing effects and charge induction between neighboring pixels in a detector with the same characteristics as XEMIS. It is important to note that the simulation study reported in this section does not attempt a detailed simulation of the charge induction in the anode but to provide a better understanding of the charge sharing effects and the indirect charge induction in the adjacent pixels. Thanks to this study, some questions related to the experimental setup of XEMIS1 have been exposed, which have contributed to the optimization of the future detector XEMIS2.

For the simulation, we defined the geometry of 9 adjacent pixels, each of them defined as a unit cell with an area of $3.1 \times 3.1\ mm^2$. The cathode was defined as a plane electrode of $9.3 \times 9.3\ mm^2$ placed at 0.5 mm or 1 mm from de anode surface. Since the goal of the simulation is to study the effect of charge induction in a pixelated anode, the Frisch grid was not included. The geometry definition and the 3D finite element grid generation was performed using Gmsh [214] (see Figure 5.23).

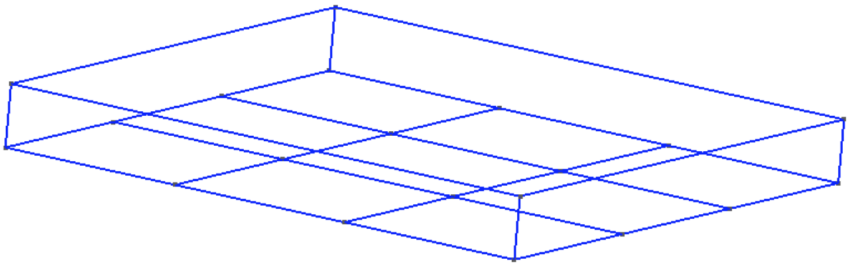

Figure 5.23 – Simulation of the geometry of 9 adjacent pixels of $3.1 \times 3.1\ mm^2$ obtained with gmsh. The cathode is considered a plane electrode of $9.3 \times 9.3\ mm^2$ located at 1 mm from the segmented electrode.

According to the Shockley-Ramo theorem, charge induction in a pixelated anode can be determined from the weighting potential distribution along the drift length. The maps of the electric, potential and weighing fields were calculated with a finite element electrostatic solver using Elmer [215]. The drift electric field was fixed at 1.0 kV/cm. To calculate the weighting field and weighting potential, the central pixel was set to unity potential while the rest of the pixels and the cathode were grounded. The electric field and the weighting potential are identical for every pixel with identical geometry, so the mapping fields of the rest of the detector surfaces are directly determined by symmetry.

The electric field and weighting potential maps for the central pixel were exported to Garfield++ [216]. The transport of the electrons through the LXe and the induced current signals caused by the drifting electrons in the gap were finally calculated by a homemade simulation based on Garfield++. For every simulated charge, the instantaneous induced current in the central pixel is calculated as the scalar product of the charge and the weighting field in every time step until the charge reaches the anode according to Equation 5.1. The resulting pulse corresponds to the current signal at the entrance of the preamplifier. The total induced charge is finally determined as the integral of the induced current along the total drift length for all the simulated charges, assuming a perfect current integration of the front-end electronics. This signal is then convolved with the transfer function of the shaper used in the IDeF-X LXe ASIC to generate the signal at the output of the front-end electronics.

In a segmented anode with pixels much smaller than the gap, the weighting potential becomes denser closer to the electrode. The smaller the pixels are, the closer the weighting potential lines and thus, moving charges far from the anode has nearly no influence on the induced signal. This means that most of the signal is induced by the charges moving close to the electrode. However, this also means that the weighting potential lines extend far from the pixel's area and reach into the adjacent pixel. Figure 5.24 shows the weighting potential distribution in the x-z plane (y = 0), for two different gap distances of 0.5 mm and 1 mm obtained with Elmer. For the larger gap, we can see that the inhomogeneities of the weighting potential in the vicinity of the electrode are more important, and the potential lines reach the surface of the two nearest neighboring pixel. Weighting potential cross-talk between pixels leads to charge induction in the adjacent pixels, even if the charge carriers only drift in the central pixel. This effect almost disappears for a gap of 0.5 mm. The ratio

between the pixel size and the gap is therefore crucial in the shape of the weighting potential and hence, in the charge induction in the non-collecting electrodes.

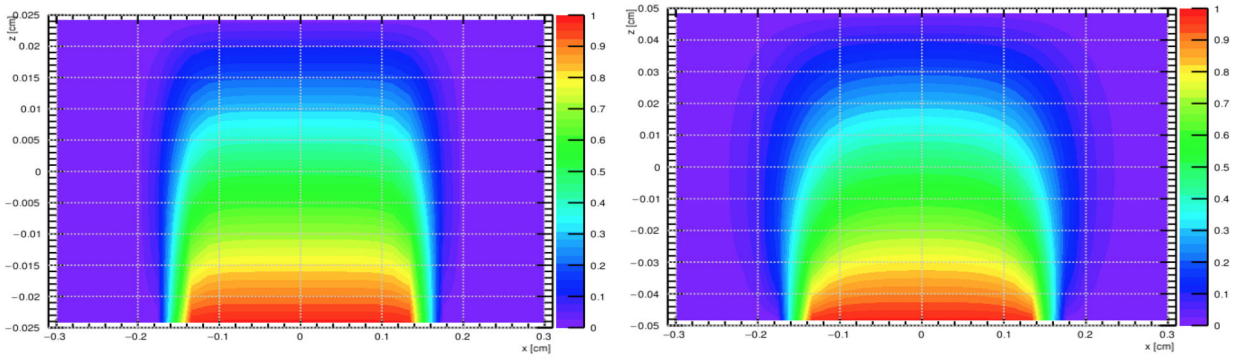

(a) gap = 0.5 mm **(b)** gap = 1 mm

Figure 5.24 – Weighting potential distribution for a 3.1 × 3.1 mm^2 pixel size and two different gaps. The distribution was obtained with Elmer by setting the pixel of interest at unity potential and the rest of the pixels and the cathode to ground.

To better understand the effect of charge induction in the neighboring pixels, we calculated the amplitude of the induced signals as a function of the interaction position along the x-axis (y = 0). The electron cloud was placed at different positions inside the pixel volume starting at the center of the pixel (x = 0). Since moving charges can also induce a current in the neighboring pixels, the maximum distance was chosen to be equal to the pixel dimensions (x = 3.1 mm). In order to correctly simulate the charge sharing, a lateral electron diffusion of 200 μm was included in the simulation. The range of the primary electrons was also taken into account. Each electron cloud consisted of 10000 ionization electrons uniformly distributed within a sphere of radius $< 300\ \mu m$. The simulation was performed over 1000 events.

In Figure 5.25, the induced signal in the central pixel is plotted as a function of the distance to the pixel center (x = 0). The amplitude was determined at the maximum of the signal. The impact of the weighting potential cross-talk between adjacent pixels increases as the charge is closer to the pixel boundary. When the electron cloud is produced at the center of a pixel, the charge is fully collected by the electrode, and no charge is induced on the neighboring pixels. However, as the electron cloud moves towards the border of the pixel, the collected charge decreases. Half of the charge is collected by the central pixel when the cloud is located between two pixel, which means that the other half is induced on the nearest neighboring pixels. In the most extreme case, when the charge carriers drift into the neighboring pixel (x > 1.55 mm), some charge is still induced in the central pixel. The amplitude of the induced signal decreases as the electron cloud moves towards the center of the neighboring pixel. This effect is more significant for a bigger gap. The transient signal induced in the pixel should result in a zero net charge. However, due to the fast shaping time of the amplifier, the induced signal may result in an additional charge that bias the total measured charge per cluster. This effect is almost negligible for a gap of 0.5 mm.

The shape of the resulting signal at the output of the front-end electronics depends on the amount of real collected charge with respect of the transient amplitude of the transient

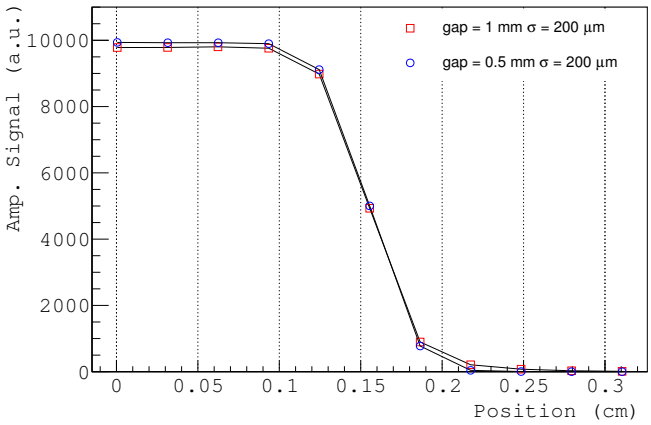

Figure 5.25 – Amplitude of the induced signal as a function of the interaction position along the x-axis (y = 0), for a simulated transverse diffusion of 200 μm.

induced signal. The higher the collected charge the smaller the contribution of the induced signal. To study the effect of charge induction in the collected signal, we took as reference the signal produced by an interaction produced at the center of a pixel. Figure 5.26 shows the difference between the time of the induced signals and the time of the signal of reference as a function of the relative amplitude. The value of the time was measured at the maximum of the induced signal. This time represents the collection time of the electrons onto the anode. When the amplitude of the transient signal is small and all the measured charge is due to direct collection, i.e. the electron cloud drift into the central pixel surface, no discrepancies are observed between the measured and the reference times. However, as the position of the interaction approaches the boundary of the pixel, the time difference increases. A maximum time difference of 800 ns (10 time channels) is obtained when almost no direct charge is collected by the central pixel. This means that the integration of both direct and indirect induced charges by the front-end electronics, deforms the shape of the output signal with respect to the ideal pulse.

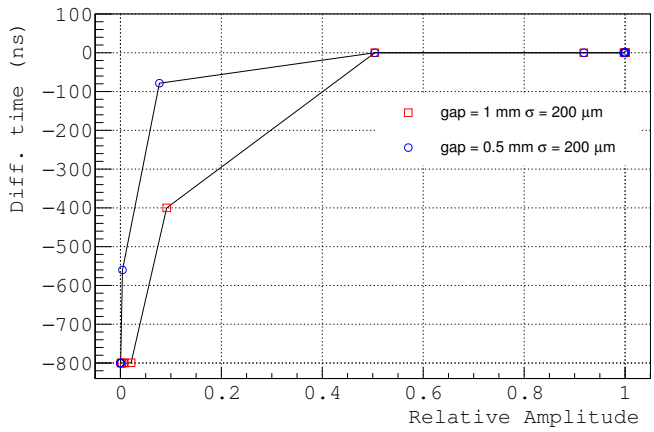

Figure 5.26 – Time difference between the signal of reference measured at the center of the collecting pixel and the induced signal as a function of the relative amplitude, for a simulated transverse diffusion of 200 μm.

In order to estimate the contribution from lateral diffusion to the induced signal, the simulation was repeated for a transverse diffusion coefficient of 300 μm. The value of the lateral diffusion is directly related to the position of the interaction with respect to the anode. In LXe, the transverse diffusion coefficient is $\sigma_{x,y} \approx 200\ \mu m\sqrt{cm}$. Figures 5.27 and 5.28 shows the amplitude and time of the induced signals as a function of the interaction position along the X-axis. In this case, the amplitude of the induced signal decreases more rapidly as the electron cloud approaches the pixel's boundary. On the contrary, the time difference decreases slowly with the position of the interaction. Both effects are directly related to the charge sharing between neighboring pixels due to diffusion. As the amount of real collected charge increases, the effect of charge induction in the shape of the collected signals decreases.

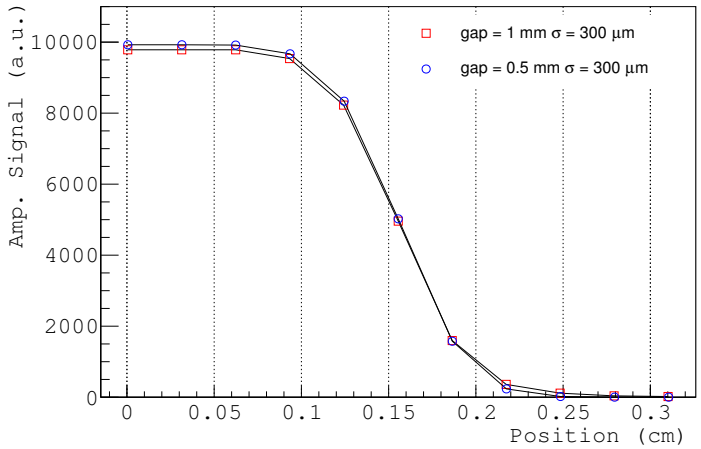

Figure 5.27 – Amplitude of the induced signal as a function of the interaction position along x-axis (y = 0) for a simulated transverse diffusion of 300 μm.

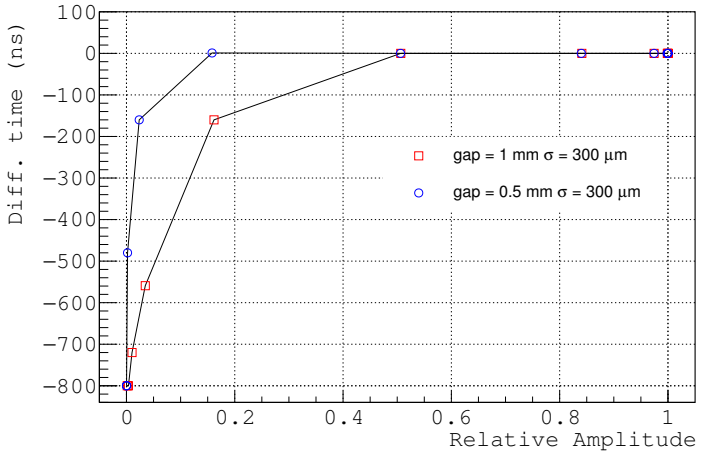

Figure 5.28 – Time difference between the signal of reference measured at the center of the collecting pixel and the induced signal as a function of the relative amplitude, for a simulated transverse diffusion of 300 μm.

The results of the simulation showed that charge sharing and weighting potential cross-talk between neighboring pixels affect the performances of a pixelated detector. The induced signal in a pixel depends on the position of the electron cloud with respect to the center of the pixel. As the charge carriers move away from the pixel's surface, the amount of collected charge decreases and the induced charge in the neighboring pixels increases. The induction of a transient signal on a pixel affects the shape of the output signal and introduces a bias in the measured time and amplitude of the signals. The simulation showed a maximum time delay of 800 ns which is consistent with the results obtained with real data. Both the time difference and the induced signal increases as the ratio gap-pixel size decreases. Moreover, we have seen that the charge sharing between adjacent pixels due to lateral diffusion reduces the effect of charge induction in a non-collecting electrode. This result is also consistent with the time difference variation with the depth of interaction observed in the experimental data.

Charge induction study with a 500 μm gap

According to the simulation, a significant reduction on the time difference between the pixels of a cluster should be observed for a gap of 0.5 mm with respect to the results obtained for a 1 mm gap (see Figure 6.42). To corroborate these results we installed in XEMIS1 the 100 LPI Frisch grid at 0.5 mm from the segmented anode. Figure 5.29 shows the time difference Δt between the pixel of reference and the rest of the pixel of a cluster as a function of the amplitude of the neighboring pixel $A_{neighbor}$, for a total measured charge of 511 keV. The population of events at around 9 time channels (720 ns) is no longer present but instead, for small amplitudes the value of Δt becomes negative due to the presence of the parasitic signal presented in Section 6.4.2. This negative signal explains the lack of events observed at positive values of Δt. This result implies that for a gap of 0.5 mm, the effect of charge induction in the neighboring pixels has been significantly reduced with respect to a gap of 1 mm, and other effects such as baseline fluctuations come to light at very low energies. At amplitudes higher than $10\sigma_{noise}$, a time delay of less than 80 ns is observed instead of 240 ns measured with a gap of 1 mm. The comparison between the mean value of Δt as a function of $A_{neighbor}$ for the two different gaps is shown in the right part in Figure 5.29.

Since the parasitic signal is only present in the same IDeF-X LXe chip, to remove its impact from the distribution we selected only those clusters with at least two triggered pixel, each of them in a different chip. As we can see in Figure 5.30, the negative values of Δt for low amplitudes become positive, the lack of statistic at low energies and positive time differences disappears, and the Δt distribution follows an exponential function with a value of 240 ns (3 time channels) for an amplitude of $4\sigma_{noise}$. The comparison between clusters which pixels are shared by the two IDeF-X LXe ASICs and cluster which all pixels belong to the right side chip is shown in Figure 5.31. These results suggest that for low energy signals the contribution of the parasitic signal dominates over indirect charge induction. No significant variation has been observed, on the other hand, with a gap of 1 mm (see Figure 5.32). Consequently, with a gap of 0.5 mm and no contribution of the parasitic signal, the time difference distribution between the pixels of the same clusters is less than 1 time channel at amplitudes of the neighboring pixel higher than 10 times the electronic noise. These results agrees with the results obtained with the simulation (see Section 4.4).

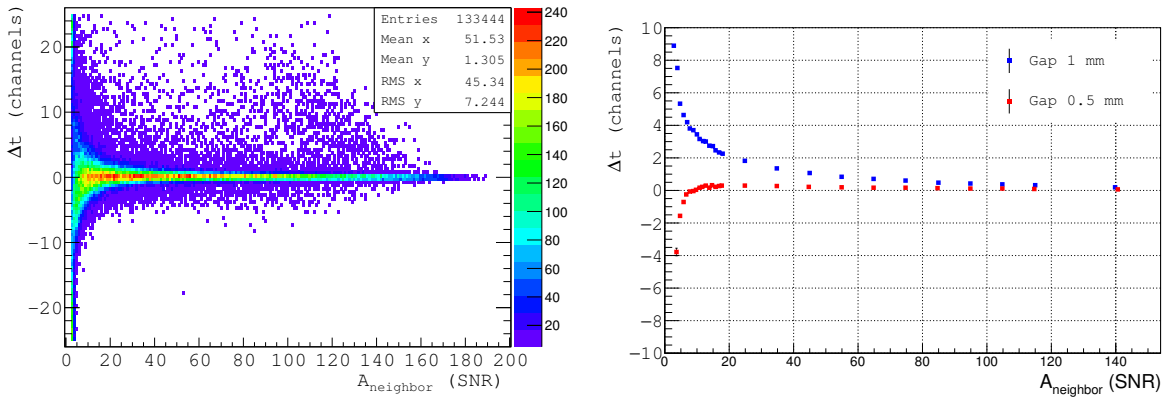

Figure 5.29 – (Left) Time difference distribution between the pixels of the same cluster as a function of $A_{neighbor}$ for a gap of 0.5 mm. (Right) Comparison of the average Δt as a function of $A_{neighbor}$ for two different gap distances.

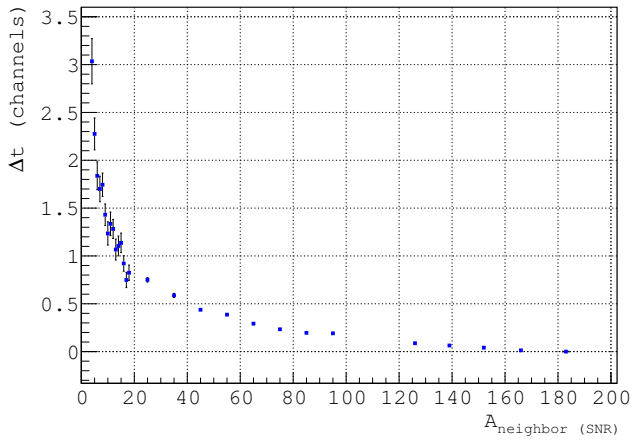

Figure 5.30 – Mean time difference between the pixels of the same cluster as a function of $A_{neighbor}$ for cluster with a total measured energy of 511 keV and which pixels are shared between the two IDeF-X LXe front-end electronics.

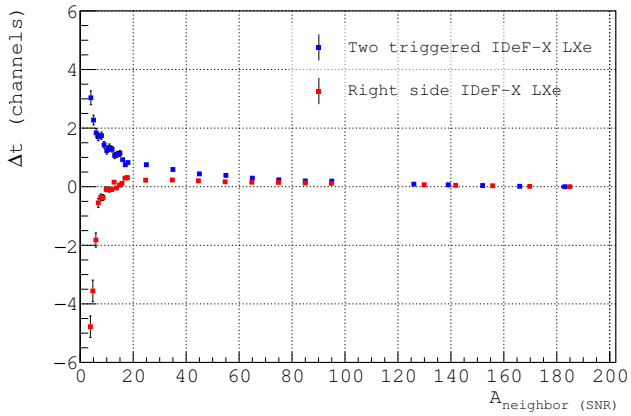

Figure 5.31 – Average time difference between the pixels of the same cluster as a function of $A_{neighbor}$, for cluster with a total measured energy of 511 keV and a Frisch grid located at 500 μm from the anode, for two different pixel configurations.

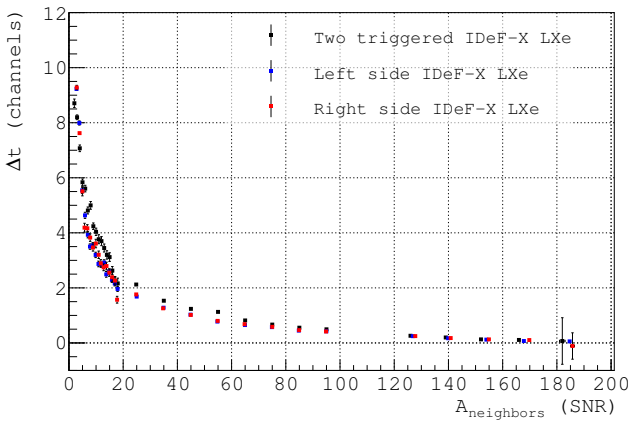

Figure 5.32 – Average time difference between the pixels of the same cluster as a function of $A_{neighbor}$, for clusters with a total measured energy of 511 keV and a Frisch grid located at 1 mm from the anode, for two different pixel configurations.

5.6 Conclusions Chapter 5

Understanding of signal formation in a detector is crucial to optimize the measurement of the time, energy and position of the detected signals. In this chapter we discussed the principle of signal induction in a detector. We have seen that the total charge induced on an electrode by a moving charge can be determined from the Shockley-Ramo theorem, which depends on two crucial parameters, the weighting field and the weighting potential.

In a parallel-plate ionization chamber the total induced charge depends on the drift distance of the electrons. This position-dependence can be efficiently removed by including a third electrode, called Frisch grid, between the cathode and the anode. In this chapter, we focused in the principle of a gridded ionization chamber and the effects of the Frisch grid on the collected signals. We have seen that the properties of the induced signals depend on the characteristics of the grid. For example, electron transparency of a Frisch grid is directly related to the number of collected charges per interaction and affects the energy resolution of the detector. An optimized set-up requires an adequate biasing of the electrodes in order maximize the charge collection, which indeed depends on the geometrical properties of the grid. Detailed measurements for two different type of grids are presented in this chapter. In XEMIS1 and for a 100 LPI mesh, the electric field in the gap should be at least five times the electric drift field. The electric field ratio depends on the gap distance and on the pitch and thickness of the grid. Larger gaps require higher bias voltages to obtain the same electron transparency conditions. On the contrary, a smaller electric field ratio is necessary with a more open grid.

Another aspect that affects the performances of a gridded ionization chamber is the inefficiency of the grid. An ideal Frisch grid shields the anode from the movement of positive ions in the space between the cathode and the grid, and removes the position-dependence of the induced signals. Theoretically, a charge is induced on the anode from the moment the electrons start passing through the grid. As a result the slope of the signals only depends on the grid-anode distance and on the timing characteristics of the front-end electronics used to process the information. However, under real experimental conditions, the electrons

start inducing a signal on the anode before they actually pass through the grid. Although our experimental set-up is not optimal for the determination of the inefficiency of a Frisch grid, its impact is clearly visible on the shape of the output signals. To investigate this effect we compared the shape of the output signals for a set of different meshes and different gap-pitch ratios. The results presented in this chapter imply experimental confirmation of the inefficiency of the Frisch grid on the induced signals. A rough estimation of the inefficiency of the Frisch grid has been performed based on the results of other authors [179, 211]. A grid inefficiency of the order of a few percent is expected for all the kind of meshes tested during this thesis.

Charge sharing between several pixels due to lateral diffusion, the size of the primary electron cloud or the emission of fluorescence X-rays is useful to improve the spatial resolution of a pixelated detector. However, multiple-pixel events degrade the energy resolution. The probability of charge sharing depends on many factors such as the pixel size and the electronic noise. To better understand the physics of charge induction on a pixelated anode, we presented a simulation study. We have shown that the shape of the output signals changes depending on the relative position of the electron cloud inside the pixel due to the weighting potential cross-talk between neighboring pixels. Charge clouds produced close to the boundaries of a pixel may induce a signal on the neighboring pixel even if all the ionization electrons are collected by the central pixels. The induced transient signal on the adjacent pixels introduces a bias on the amplitude and time of the shaped signals. These effects become more important for smaller pixel sizes compared to the gap distance. Moreover, the results obtained by simulation confirm the time difference observed between the triggered pixels of the same cluster observed on the real data.

The results presented in this chapter have been essential to understand the effect of signal formation on a gridded ionization chamber based on a segmented anode for charge collection. These results are crucial to improve the performances of the future Compton camera XEMIS2.

CHAPTER 6

Performance Evaluation of XEMIS1 for 511 keV γ-rays. Data Acquisition and Data treatment

Contents

The small dimension prototype XEMIS1 was developed with the purpose of testing the feasibility of the 3γ imaging technique with a LXe Compton telescope. The design of XEMIS1 is not optimal for tracking Compton, but it provides relevant information of the potential of a LXe Compton camera for 3γ imaging. In this chapter, we present the experimental set-up used to detect the 511 keV γ-rays generated after the annihilation of a β^+ with an electron. In order to carry out the characterization of XEMIS a low activity ^{22}Na source was used. The data acquisition and trigger systems used to register the data are presented in Section 6.2. The efficiency of the trigger for 511 keV events as a function of the characteristics of the TPC is also studied in this section. Furthermore, a detailed analysis and calibration of the noise for each individual pixel is discussed in Section 6.4. The

results obtained from this analysis are used to correct the raw data and to set a threshold level for event selection. Finally, the off-line method used for data analysis and clustering is presented in Section 6.5.

6.1 Experimental setup

In order to test the feasibility of using a LXe TPC for 3γ imaging we have been carried out the performance characterization of XEMIS1 with a 511 keV γ-ray source. A schematic view of the experimental setup is shown in Figure 6.1. This includes the XEMIS1 TPC described in Section 3.1, the charge and light detection systems and an external PMT used for triggering. The detector is calibrated using a low activity ^{22}Na source of about 10 kBq. The ^{22}Na is a 3γ emitter radionuclide with similar characteristics to those of the ^{44}Sc, that emits a γ-ray of 1.274 MeV and a positron in quasi-coincidence. The source is encapsulated in a plastic casing of 1 mm thick with a diameter of 2 cm and placed inside a 15 mm diameter stainless steel hollow tube. The tube, visible in Figure 6.1, is located outside the vacuum enclosure and in front of the cryostat entrance. To minimize the γ-ray attenuation before entering into the TPC, the entrance flange consists of a 1 mm aluminium wall that is placed at around 15 cm from the anode. The position of the source with respect to the TPC, located inside the inner vessel, can vary thanks to a sample holder within the external tube.

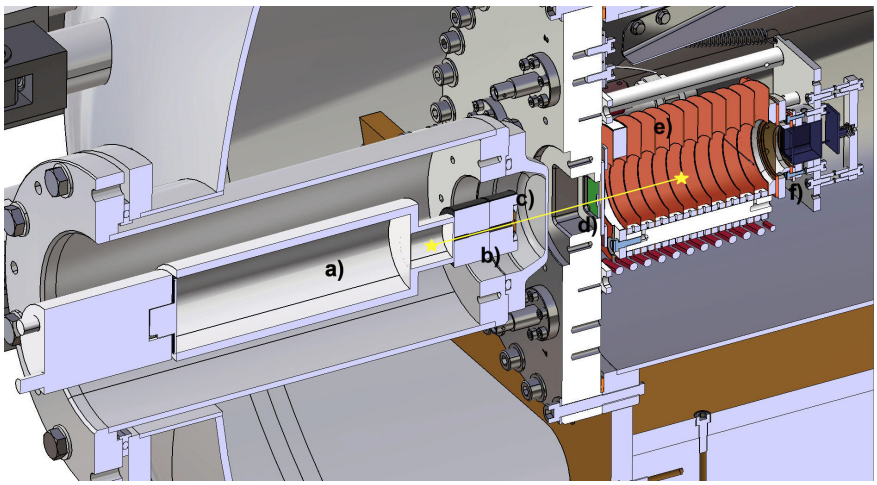

Figure 6.1 – Schematic drawing of XEMIS1 experimental set-up: a) BaF_2 crystal and PMT, b) collimators, c) ^{22}Na source, d) entrance window, e) TPC and f) LXe PMT. The yellow line emulates the emission and detection of the 2 back-to-back 511 keV γ-rays.

The detector energy response and time resolution was first calibrated using the two 511 keV γ-rays produced after the annihilation of a β^+ with an electron. A coincidence trigger between the TPC and a BaF_2 scintillation crystal coupled to a PMT was set to trigger on the 2 back-to-back 511 keV γ-rays events. The PMT is set to a high voltage of -850 V. Both the BaF_2 crystal and PMT are located inside the stainless steel tube after the source holder. Two collimators made of lead and antimony with an external diameter

of 4 cm and a total length of 3.5 cm are placed between the BaF_2 crystal and the source. The collimator coupled to the BaF_2 crystal is a cone shaped hole collimator with a top diameter of 1 mm and a cone base diameter of 1.5 mm. On the other hand, the one coupled to the ^{22}Na source is a parallel hole collimator with an internal diameter of 2 mm. The collimators are used to optimize the solid angle of the beam source covered by the BaF_2 crystal. Moreover, the ensemble BaF_2, collimators and source is positioned in such a way that the solid angle subtended by the beam completely covers the active area of the TPC, so for almost the 100 % of the 511 keV γ-rays detected by the BaF_2, the other 511 keV photon deposits its energy inside the TPC. With respect to the anode, the beam is centered in the x-y plane to maximize the charge collection. To prevent bad energy reconstruction only the 36 central pixels of the segmented anode are considered during data analysis. For this reason, to minimize event loss by border rejection a calibration of the position of the beam with respect to the anode is made at the beginning of each data-taking period.
Additionally, the TPC has been calibrated for different electric fields varying between 0.25 kV/cm to 2.5 kV/cm. Higher electric fields result in better energy resolution [115]. However, it also implies that greater voltages must be applied to the Frisch grid to ensure a 100 % electron transparency. As discussed in Section 5.2, the transparency of a Frisch grid depends on the ratio between the drift field and the collection field, which in turn depends on the characteristics of the grid. A 100 % transparency requires, in some cases, very high bias voltages that in fact can limit the performance of the detector. By decreasing the grid-anode distance we can also reduce the applied potential. Halving the gap implies a reduction by a factor of two on the voltage required by the Frisch grid for the same electric drift field. However, some mechanical constraints come into play when the gap is too small. Consequently, the maximum electric drift field on a LXe TPC is in part limited by the Frisch grid and the mechanical design of the TPC. The cathode, on the other hand, is an electroformed 70 LPI micro-mesh that supports voltages from 0 V up to -24 kV. A more detailed description of the performances of the TPC as a function of the electric drift field for different configurations is reported in Chapter 7.

6.2 Data Acquisition and Trigger Description

A diagram of the triggering system used in XEMIS1 for the 511 keV performance characterization is shown in Figure 6.2. Signals from both the BaF_2 scintillation crystal and the LXe PMT are sent to an electronic logic chain where the signals are discriminated and logically combined. A trigger requires the coincidence of both PMT signals within a time window of 10 ns. To select the 511 keV photons a low discriminator threshold is used on both PMTs to suppress noise events. On the other hand, no high threshold has been used to reject high-energy signals that exceed the energy of a 511 keV γ-ray.

Figure 6.3 shows an example of two typical scintillation signals detected by the two PMTs. The PMT coupled to the BaF_2 scintillation crystal has a good time resolution of the order of 200 ps. The BaF_2 output is fed into a discriminator, which transforms the analog signal into a digital pulse. The output signal of the LXe PMT is, on the other hand, split by a

linear fan in/out unit and sent, on one side to an ADC[1] where the signal is digitized and recorded, and on the other side to the discriminator for event selection. Timing is now set by the leading edge of the discriminator signals and not on the PMT output signals themselves.

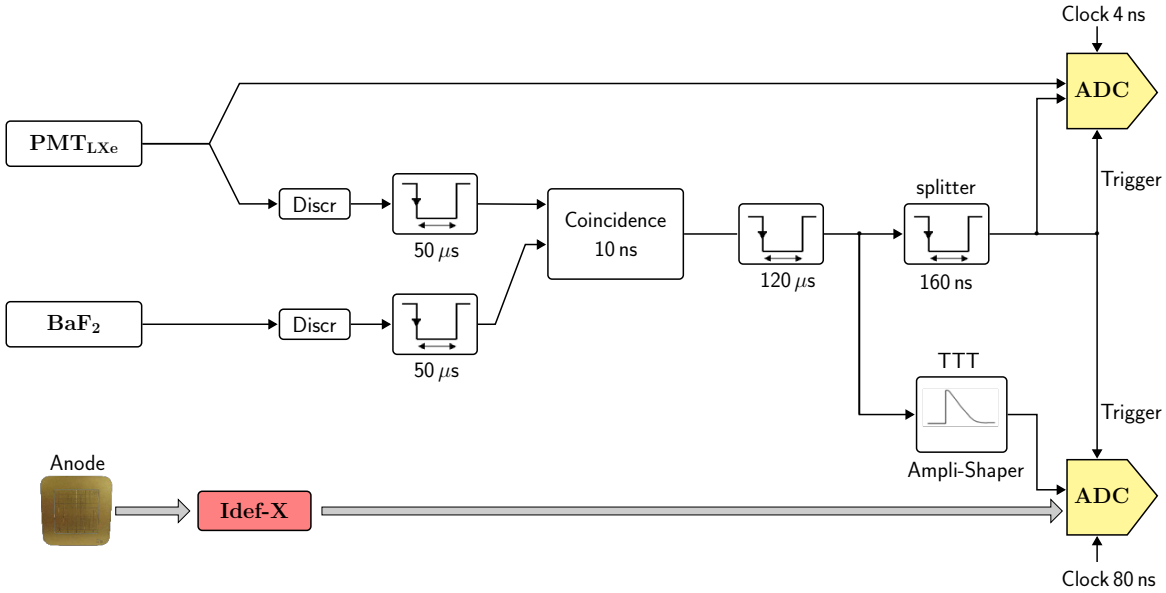

Figure 6.2 – Schematic drawing of XEMIS1 trigger setup.

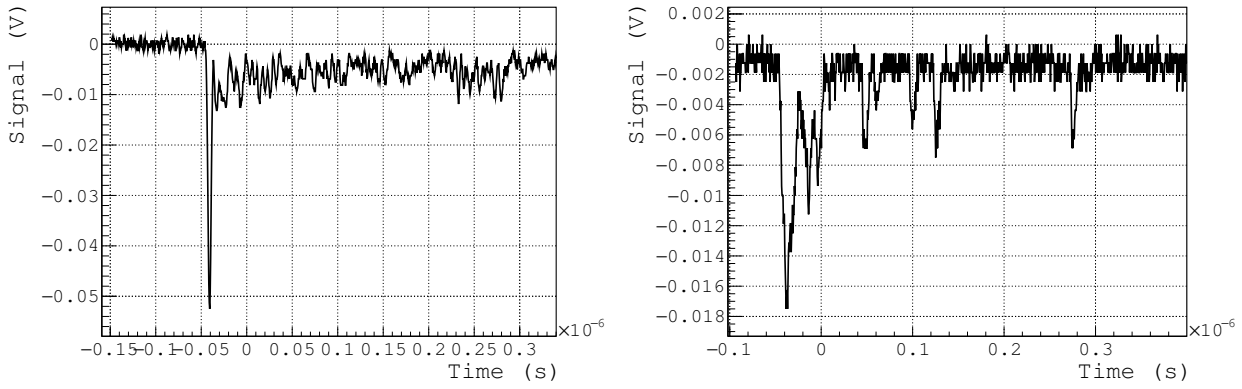

(a) BaF_2 scintillation crystal **(b)** LXe PMT

Figure 6.3 – Example of two typical scintillation signals from the (a) BaF_2 crystal and (b) LXe PMT.

The slow decay component (45 ns at 173 K) of LXe due to recombination can introduce a considerable time delay between the arriving photoelectrons that form the output signal [38]. This results in long decay tail signals as shown in Figure 6.3(b). The impact of this slow decay component depends on the applied electric field, decreasing as the electric field increases [37, 115]. For example, for an electric field of 2 kV/cm, the 63 % of the scintillation light is emitted due to direct excitation with a time constant of 2.2 ns or 27 ns

[1] Analog to Digital Converter

depending on whether the emission comes from the de-excitation of the singlet or triplet states respectively [36, 37]. A non negligible 37 % of the scintillation yield comes, however, from recombination and it is emitted with a slower decay time of 45 ns. The distribution of photon arrival times in LXe can be roughly approximated by a triple exponential decay corresponding to the three LXe lifetimes:

$$A_f . \exp\left(\frac{-t}{\tau_f}\right) + A_s . \exp\left(\frac{-t}{\tau_s}\right) + A_r . \exp\left(\frac{-t}{\tau_r}\right) \tag{6.1}$$

where $A_f = 0.03$, $A_s = 0.60$ and $A_r = 0.37$ are the relative scintillation rates for the fast, slow and recombination components respectively at an electric field of 2 kV/cm, and τ_f, τ_s and τ_r are the scintillation decay times of the three components.

The long tail in the photoelectrons arrival time distribution implies that photons may arrive to the detector with a delay of several hundreds of ns. Since we work at the minimum possible threshold level, single photons from the signal tail may re-trigger the discriminator even though they come from the same interaction. This can increase the number of accidental triggers. For this reason, in order to avoid the possibility of re-triggering, a veto of 50 μs is set on both PMT signals. This 50 μs logic gate completely covers the 45 ns photoelectron extraction.

Since the scintillation light yield due to direct excitation does not depend on the applied electric field, triggering on the fast component of the scintillation light minimizes the electric field dependency of the trigger system, in addition to allow small coincidence time windows of the order of several ns. However, due to the small number of photons that reach the LXe PMT, the trigger window should be large enough to cover almost completely the photoelectron distribution. In order to suppress accidental coincidences after the veto signal, the resulting pulses from both PMTs are transformed into standard logic pulses of 10 ns and 80 ns width for the LXe PMT and BaF_2 respectively, before entering into the coincidence module. The width of the windows was optimized to reduce the number of accidental triggers but preserving a high trigger efficiency. An event is then accepted if the two narrowed pulses arrive within a time window of 10 ns. Figure 6.4 shows the time distribution of the PMT signals after a coincidence. Most of the events are triggered by the fast scintillation component, whereas a small fraction of the coincidences are triggered by the recombination component.

Since the principle of the TPC is to detect both ionization and scintillation signals, an unique light pulse should be associated to each ionization signal. For this reason, to guarantee that only one trigger is accepted during the time the signals are still being recorded by the Data Acquisition Systems (DAQ), a 120 μs logic gate is established after the logical AND of the two PMTs. This window is enough to cover the time needed to record both signals (102 μs for the ionization signal and 2 μs for the scintillation light). The 120 μs logic pulse does not act as a veto but instead, if an event happens while the window is still opened, the event will not only be missed but it will re-open a new 120 μs logic signal ensuring that any new information is registered. This paralyzable behavior maintains the synchronization between charge and light.

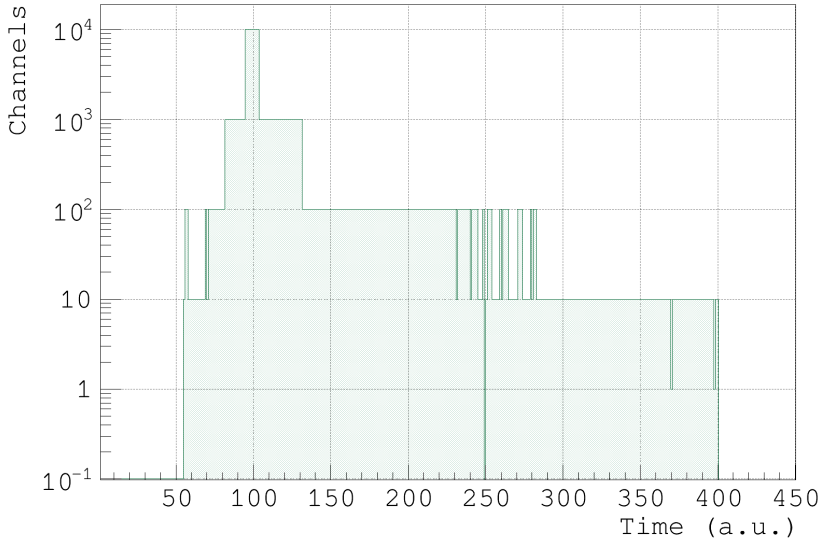

Figure 6.4 – Coincidence time distribution at 1 kV/cm.

If a trigger is accepted, signals from both scintillation (PMT) and ionization (anode) processes are recorded. The scintillation light waveforms from the PMT immersed in the LXe are continuously fed into a CAEN v1720 Flash ADC where they are digitized with 12 bit precision at a sampling rate of 250 MHz. Figure 6.5 shows an example of a typical scintillation and ionization waveforms of a 511 keV γ-ray event from the ^{22}Na source. The digitization pass through a ring buffer where they are sequentially stored. After a trigger a block of data containing 512 samples is automatically transfer from the ring buffer to an event buffer where the event is stored for further processing. The event buffer can store a maximum of 1024 events of 2 μs each before being read. This means that readout and signal processing are in general deadtimeless unless the trigger rate is too high so the entire memory is filled up. An additional 200 ns of baseline presamples are registered to ensure that the event is completely stored regardless the delay added by the electronic chain itself. Besides the scintillation signal, the trigger logic pulse is also stored and digitized every 4 ns in one of the channels of the FADC to correct the jitter introduced by the acquisition systems relative to the trigger start time.

The charges collected by the segmented anode are processed by the two 32 channels IDeF-X ASICs as explained in Section 3.1.3. Output analog signals from 63 pixels are registered during a time window of 102.2 μs by a waveform digitizer (CAEN v1740 Flash ADC) at a sampling rate of 12.5 MHz with a resolution of 8 bits. The registration period is large enough to cover the entire drift length of the TPC that it is of the order of 60 μs for an electron drift velocity of 2 mm/μs (electric field of 1 kV/cm). Same as for the scintillation signal, the charge collection waveforms are continuously digitized and written in a circular memory buffer. When a trigger signal arrives to the FADC, the event is transferred and stored into the event buffer. Equally, data are stored from the time the trigger occurs back to 50 previous samples. The event buffer can hold 1024 event of 1278 samples each that in principle can be read with a negligible dead time, if the trigger rate is less than 20 Hz. Since the charge FADC only has 64 available channels, signals collected by the pixel 29 placed at

the border of the anode (see Appendix B) are not registered. Instead a tag signal called TTT (Trigger Time Tag) is stored for further jitter correction during data analysis. The TTT signal keeps track of the timing information of the trigger and is generated by integrating the coincidence output pulse in a preamplifier-shaper module.

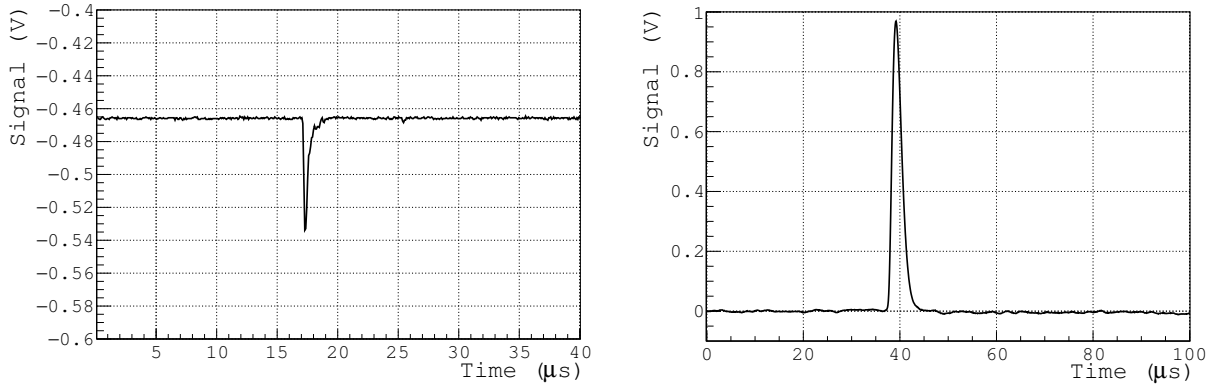

(a) Scintillation light **(b)** Ionization signal

Figure 6.5 – Example of a typical (a) scintillation and (b) ionization waveforms of a 511 keV γ-ray event from the ^{22}Na source.

Trigger Efficiency and Calibration for 511 keV γ-ray events

The trigger system should be able to distinguish physically interesting events from background. In particular, the discriminator threshold level used to select the 511 keV events has a big impact on the trigger efficiency so its value should be optimized to decrease the number of accidental triggers. For the BaF_2 signal, a discriminator was set to 10 mV equivalent to $12\sigma_{noise}$, where σ_{noise} represents the SNR, in order to trigger on the 511 keV signals. The value of the noise was calculated from the amplitude distribution spectrum of the PMT output signal when no threshold is applied.

Amplitude of the LXe PMT signals is, however, dominated by solid angle effects resulting on a small fraction of UV photons reaching the PMT photocathode. A detailed simulation of the geometry of XEMIS1 and the scintillation light collection efficiency is presented in [123]. Results show an important decrease of the number of photons detected by the PMT as the distance from the intersection point to the PMT increases. Figure 6.6 shows the distribution of detected photons as a function of the distance of the interaction point with respect to the PMT. Please note that in this simulation the quantum efficiency of the PMT (35 % for the Hamamatsu R7600-06MOD-ASSY PMT) and the optical transparency of the set of meshes placed just before the PMT surface (81 %) are not taken into account. In addition, the results were obtained for a zero electric drift field. For an electric field of 1 kV/cm, 3.5 photons are detected in average by the PMT if the interaction occurs close to the anode (13.5 cm from the PMT).

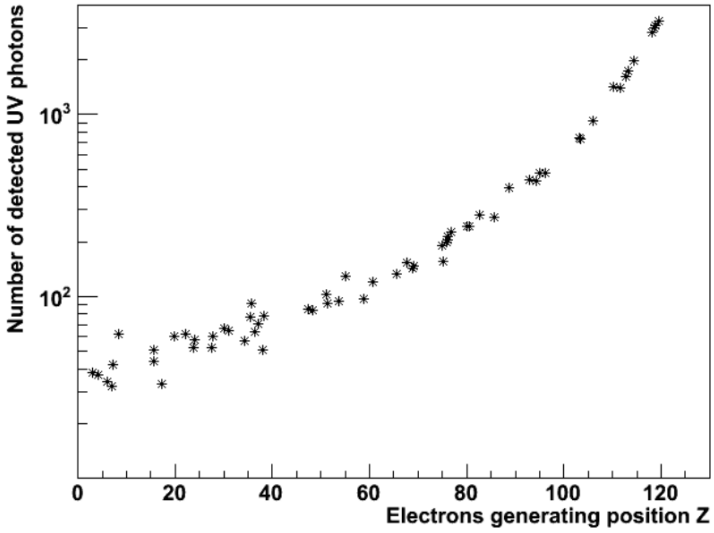

Figure 6.6 – Evolution of the number of VUV scintillation photons that arrives to the LXe PMT as a function of the interaction point of the 511 keV ionization electrons. Figure taken from [123].

This strong dependency of the light collection efficiency with the position of the interaction inside de TPC requires a very low threshold level in order to ensure a relatively uniform response of the detector along the drift direction. Adequate results were obtained for a threshold of 5 mV ($5\sigma_{noise}$).

Figure 6.7 shows the z-dependence of the light yield for 511 keV events for an electric drift field of 1 kV/cm. The amplitude of the PMT signals is calculated at the maximum of the pulse over a time window of 10 ns from the moment the signal crosses a fixed threshold. The TPC has an active area of 12 cm. The value of z = 0 cm on the distribution corresponds to the position of the grid. The end of the fiducial volume is represented at z = 12 cm. The results were obtained for a 100 LPI metallic woven Frisch grid placed at 1 mm from the anode. As expected, the light detection efficiency increases as the distance to the PMT decreases. The shape of the distribution is related to the geometry of the TPC and the position of the source with respect to the PMT, resulting on a decrease of the solid angle of the PMT with increasing z. At low z-position ($z \leq 3\ cm$) a deterioration of the light collection efficiency is observed. This is because at distances far enough from the PMT the effect of solid angle becomes important and a fraction of the events may be rejected due to the discriminator threshold level.

Trigger efficiency can be improved, on one side by decreasing the threshold level and, on the other side by decreasing the active area of the TPC. Lowering the threshold increases the number of accidental triggers without a significant improvement on the efficiency. Figure 6.8 shows the amplitude distribution of the LXe PMT signals for a threshold level of 5 mV. At lower threshold levels, we observed an increase of the dead time of the detector without a significant increasing of the trigger efficiency.

A better option to improve the efficiency of the trigger system is to reduce the length of the chamber. A rough calculation indicates that halving the size of the TPC may improve the light detection efficiency in a factor of 4. Figure 6.9 shows the light amplitude distribution as

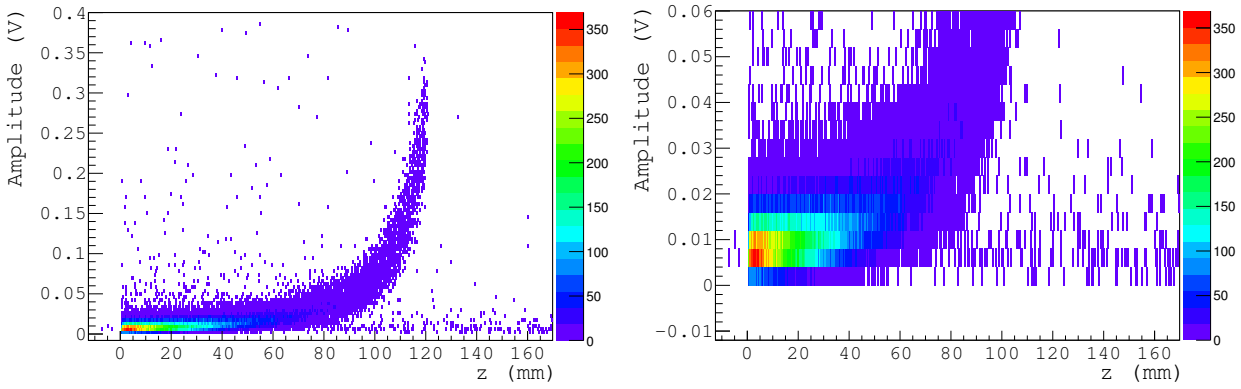

(a) **(b)**

Figure 6.7 – Scintillation light distribution as a function of the time of CFD of 511 keV events. (b) Zoom in the region of interest. The results were obtained for a 100 LPI metallic woven Frisch grid placed 1 mm from the anode and a 12 cm long TPC.

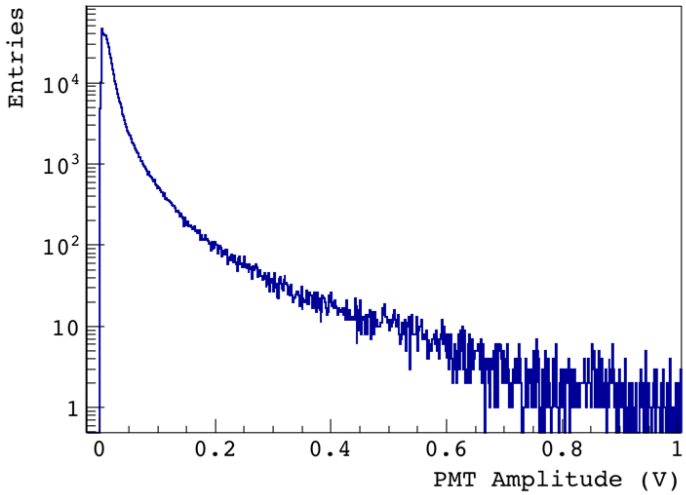

Figure 6.8 – Scintillation light amplitude for a discriminator threshold level of 5 mV.

a function of z for a 6 cm long TPC. No loss of light collection efficiency is observed at low z compared to the 12 cm TPC, which means that the number of photons that reaches the PMT has notably increased. The effect of the threshold is visible in the distribution. The end of the chamber is visible at around 6 cm of the grid. The entries outside the chamber ($z > 60\ mm$) are accidental triggers inside the 10 ns coincidence window.

The characteristics of the new TPC are exactly the same as the 12 cm long TPC described in Chapter 3, except for the active length of the detector which is reduced from 12 cm to 6 cm. The material and the distance between the rest of the components of the TPC remain unchanged and the light and charge collection systems are also the same. The Frisch grid is also a 100 LPI metallic woven mesh but it is placed at 500 μm from the anode. Figure 6.10 shows the geometry of the new 6 cm TPC.

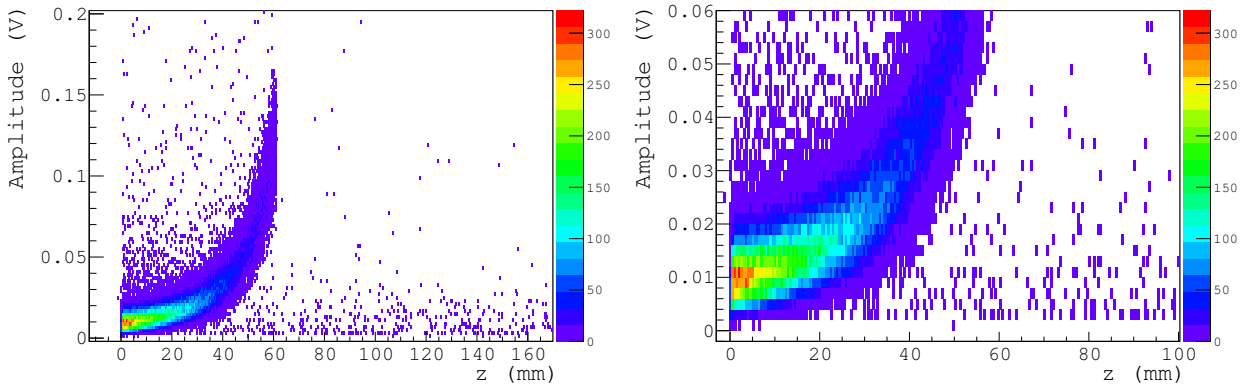

(a) **(b)**

Figure 6.9 – Scintillation light distribution as a function of the time of CFD of 511 keV events. (b) Zoom in the region of interest. The results were obtained for a 100 LPI metallic woven Frisch grid placed 0.5 mm from the anode and a 6 cm long TPC.

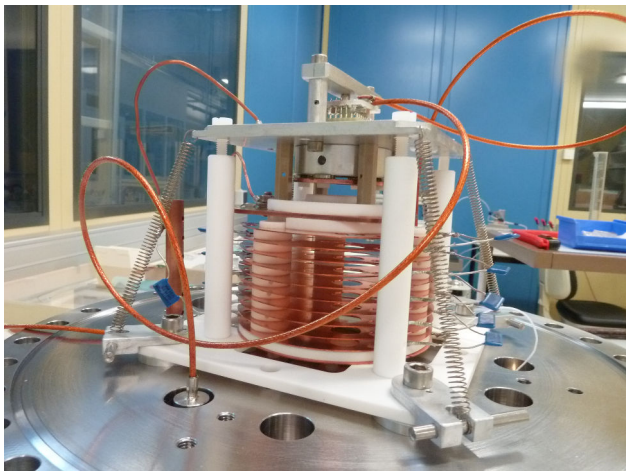

Figure 6.10 – Experimental set-up of XEMIS1 for a 6 cm long TPC.

A negligible rate of accidental coincidences (20 accidental triggers in 5 hours) has been measured for a 5 mV threshold. This result is in good agreement with the expected value for a 10 ns coincidence window, obtained from the individual counting rate of both PMTs. A trigger rate of $\sim$ 120 triggers/s was measured for the BaF_2 (N_{BaF_2}) and $\sim$ 1200/s for the LXe PMT (N_{LXe}):

$$N_{acc} \;=\; N_{LXe} \,.\, N_{BaF_2} \,.\, 10\ ns \;\simeq\; 1.4\ 10^{-3}\ triggers/s \tag{6.2}$$

6.3 Data processing

After a valid trigger, data from both ionization and scintillation processes are stored into the event buffer before being stored on disk. Once in the buffer, data is read by the DAQ computer via a fiber optical cable starting from the first registered event. The optical link supports data transfer of 80 MB/s for both FADCs. The DAQ software is written in LabVIEW using the software libraries provided by CAEN. The software can be used as a second level trigger since it was design to perform a rough analysis of the raw data by applying topological cuts to the events. The program includes a simple framework which allows to start/end a run and to apply cuts to the signal waveforms. Charge and light signals can be treated and registered independently. Moreover, rough noise calculations are implemented to control the overall state of the electronics. The noise is determined from the amplitude distribution obtained for the first registered sample ($\sim$ 200 ns before the trigger). Additionally, preliminary baseline suppression can be performed to the individual ionization signals, so a threshold can be used for event selection allowing a reduction of the data volume. The pedestal is calculated by averaging over the first 50 samples before the trigger start time. Cuts on the total charge deposited inside the TPC during an event or individual selection of the pixels that are actually written on disk are also possible. In addition, real time monitoring of the detector is included, that generates plots of charge and light waveforms, hit map of the anode and trigger rate.

Data collected by the DAQ software are then saved in two independent binary files (one for the charge and another one for the light). Relevant data acquisition information such as the registration time window, sampling rate, shaper peaking time, etc ... are also registered on the header of the files. The software is programmed to generate files with a maximum size of 2 Gb. The DAQ software is able to readout data at a rate of 20 Hz without adding dead time, enough to support the trigger rate of 2 events/s estimated with the actual trigger system. A one hour run generates 2 Gb of data with around 12000 registered events. This means that around 1 Tb is registered for a 1 month data-taking period.

6.4 Noise Analysis and Calibration

On a pixelated detector with individual read-out channels unavoidable differences in noise behavior, baseline and gain between the channels are normal. This variations come from the fabrication process of the electronics and affects the event selection in terms of collected charge and signal threshold. For this reason, an individual characterization of each pixel of the anode is necessary in order to study and, in some cases correct, the influence of these variations before starting the event reconstruction.

To perform a precise estimations of the noise and pedestal per pixel, we used a set of experimental data that contains only noise events. The data acquisition and data processing are performed according to the method reported in this chapter, but with a random external trigger. In the following this kind of data acquisition will be referred as *noise run*. A complete noise run consists of a 2 Gb binary file with around 12000 events in average. For each event, 63 waveforms corresponding to 63 pixels of the anode are recorder over a time window of 102.2 μs. The pixel 64 is used to register the TTT signal (see Appendix B). The

results presented in this section were taken with an electric field of 1 kV/cm and a peaking time of 1.39 μs.

Figure 6.11 shows a diagram that illustrates the procedure followed for the noise analysis. To keep a constant alignment of the source with respect to the anode, all the noise runs were taken with the ^{22}Na source. However, the presence of the source during the noise runs implies that some pulses are registered in coincidence with the random external trigger (see Figure 6.12(a)). These signals would bias the measured noise distribution providing a wrong value of the pedestal and noise per pixel. To remove the contribution from charge generating particles, a initial peak selection is performed. A preliminary estimation of the pedestal and noise value signal per signal is determined from the 50 first and 50 last samples of the signal. A relatively high threshold of around 10 times the noise ($\sim 30\ mV$) is set for peak selection to ensure that only physical events are rejected. In average, the number of rejected pulses per noise file is less than 2%. Figure 6.12(b) shows the noise events after pulse rejection. As we can see, there is a border effect due to the pulse search method. To avoid this effect, we exclude from the noise distribution study the latest 8 μs of the time window.

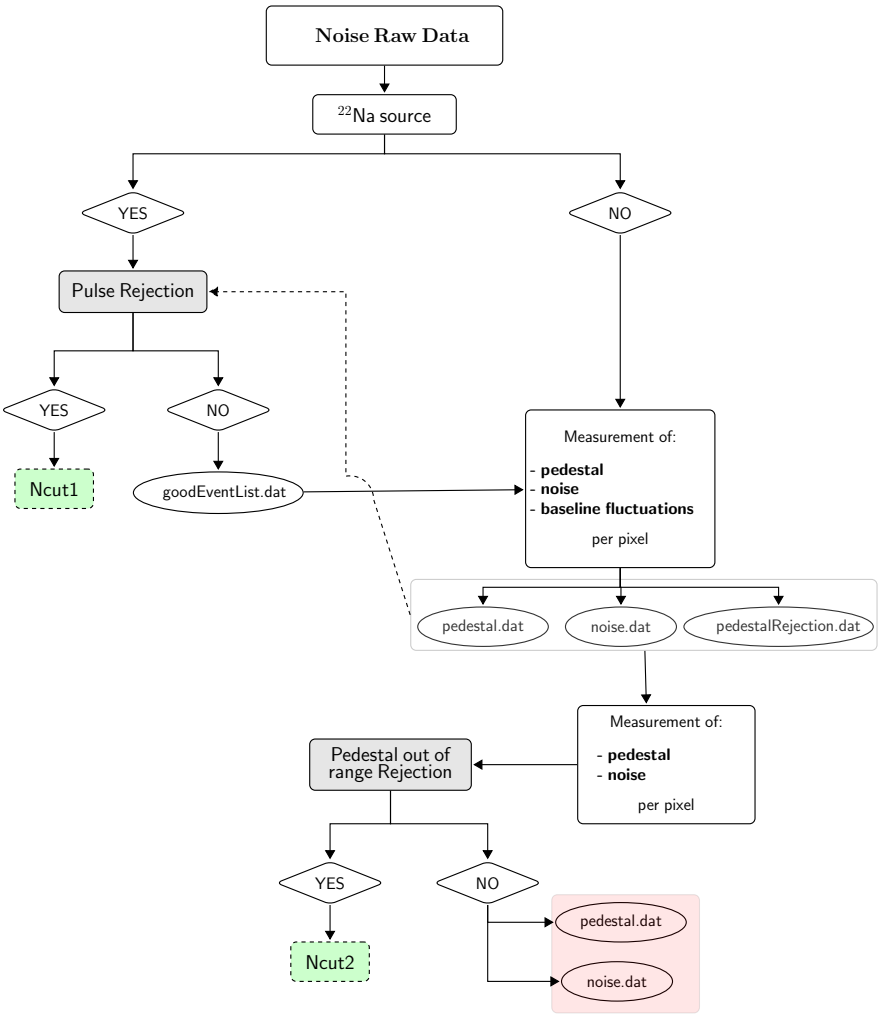

Figure 6.11 – Noise signal analysis diagram.

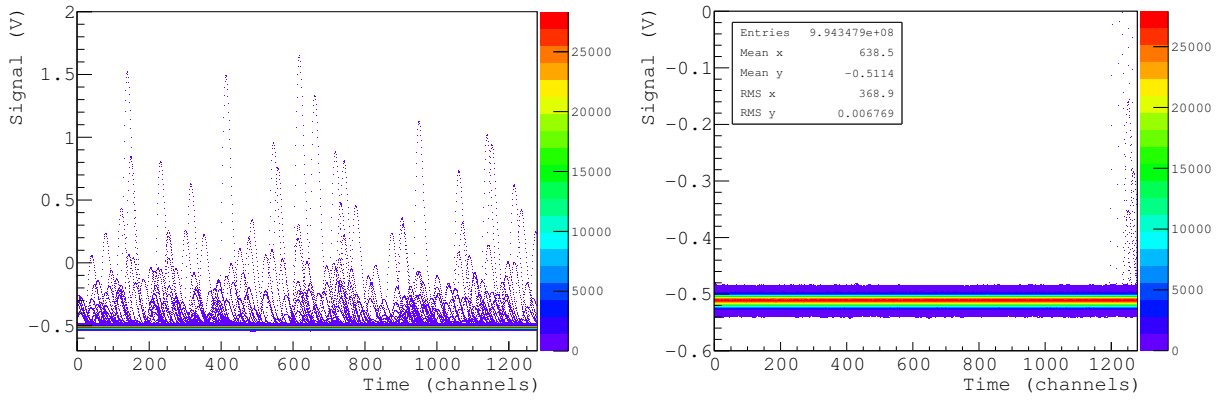

(a) **(b)**

Figure 6.12 – Raw signals distribution as a function of time (a) before and (b) after pulse rejection.

Pedestal and Noise determination

We can see from Figure 6.12 that the preamplifier produces an offset of the order of -0.5 V in the recorded signals, with a certain baseline dispersion for the same read-out channel. To correct this baseline shift, the mean value of the pedestal per pixel should be estimated. Figure 6.13 shows a typical amplitude noise distribution of two pixels of the anode. Assuming that the distributions follows a Gaussian probability density distribution, as good approximation, the pedestal is obtained from the mean value of the distribution, whereas the noise is determined from the standard deviation (RMS) of the pedestal data sample. The distribution shown in Figure 6.13 was measured for a random time sample over the ∼12000 raw signals collected in the noise file. By fitting the distribution by a Gaussian function, a mean pedestal values of -0.51 V and -0.50 V, and an electronic noise of 2.59 mV and 2.72 mV were obtained for the two pixels respectively.

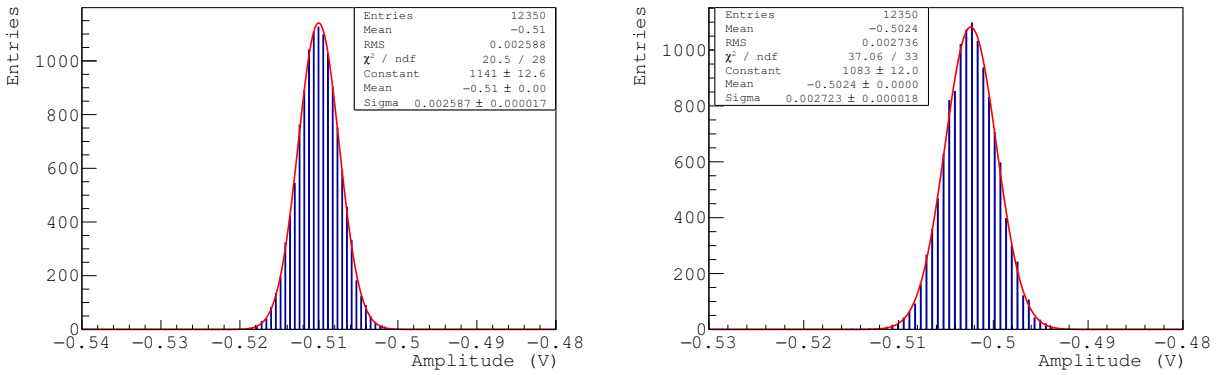

Figure 6.13 – Noise distribution of the pixels 63 and 19 respectively (see Appendix B). Each pixel belong to a different IDeF-X LXe ASIC. The solid red line is a Gaussian fit.

Pedestal values for the rest of the pixels of the anode are presented in Figure 6.14 and 6.15. The offset is not uniform over the anode. A maximum pixel-to-pixel dispersion of the order of 15 mV was measured. The mean pedestal values for the two IDeF-X ASICs separately are shown in Figure 6.17. The relative position of the pixels with respect to the read-out electronic channels is illustrated in Figure 6.16, where each IDeF-X is connected to 32 different pixels. The baseline is almost uniform among the pixels of the left side IDeF-X chip with a dispersion of less than 5 mV. On the other hand, a higher baseline dispersion of the order of 8 mV was obtained for the right-side chip. The pedestal dispersion among the two different chips varies within 7%, which is mostly associated to the connector.

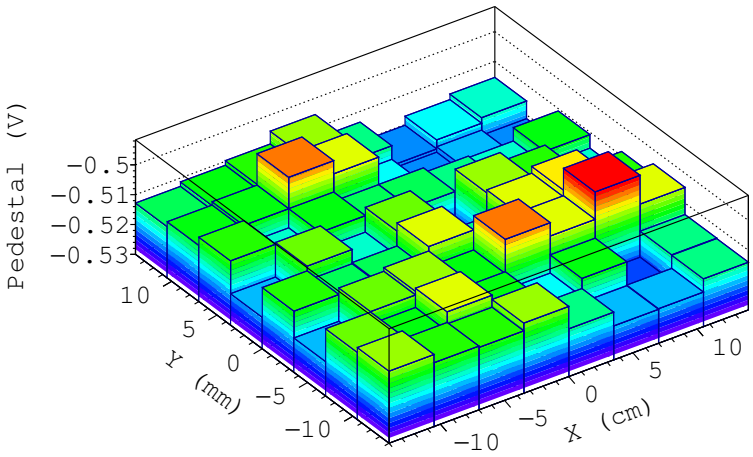

Figure 6.14 – Pedestal map obtained from the mean value of the pedestal per pixel.

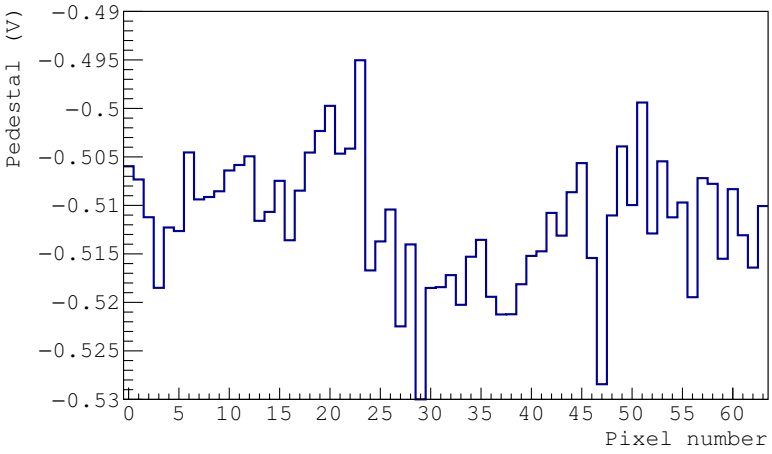

Figure 6.15 – Pedestal value per pixel.

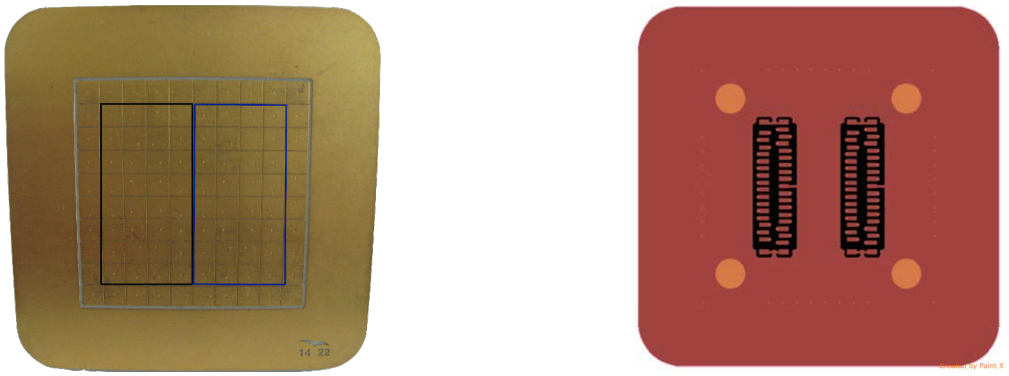

Figure 6.16 – Relative position of the two IDeF-X LXe chips (black and blue line) with respect to the pixels in the anode. In the right figure the location of the connectors directly wire bounded to the 32 pixels of each ASIC is illustrated.

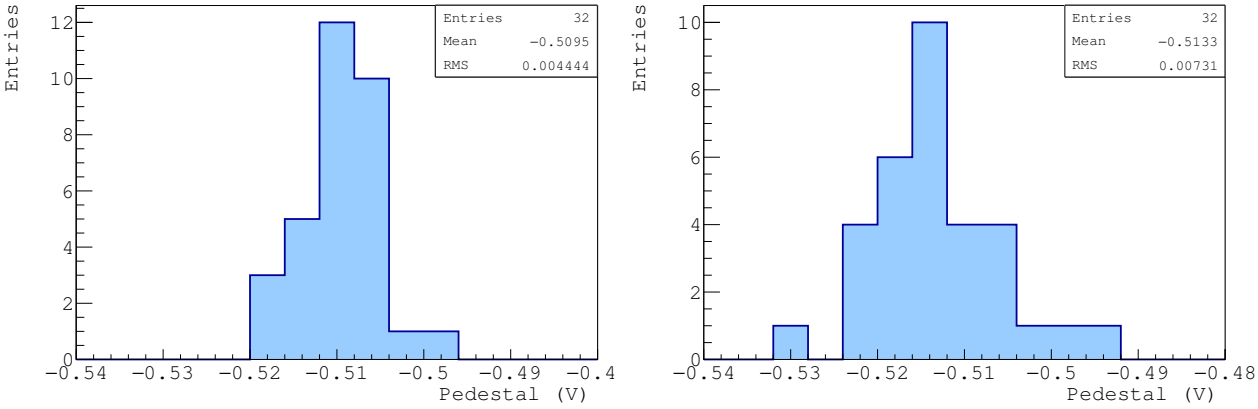

(a) Left IDeF-X LXe chip.

(b) Right IDeF-X LXe chip.

Figure 6.17 – Pedestal value per pixel for the two IDeF-X LXe ASICs. Each chip is coupled to 32 pixels of the anode. The ASICs are identified according to the configuration shows in Figure 6.16.

In principle, pedestal subtraction can be made by either using a constant value per pixel or by using the same average value per IDeF-X. However, since the pedestal dispersion between the different pixels of the same IDeF-X is bigger than the final electronic noise measured once the pedestal correction is applied, the correction should be made by using the mean pedestal value per pixel.

The noise map is presented in Figure 6.18. Higher values of the noise are obtained at the edges of the anode and between the two connectors. This noise distribution is due to the length of the electronic tracks with respect to the pixels. Longer tracks implies higher electronic noise. In addition, the noise increase observed at the four corners of the anode is due to the position of a ground connector as we can see in Figure 6.16. Figure 6.19 shows the noise distribution for the 63 pixels. The noise is expressed in unit of electrons. The electron-V conversion was made using the 511 keV photoelectric peak as described in Section 7.4. We measured an average value of the noise of $\sim 85\ e^-$.

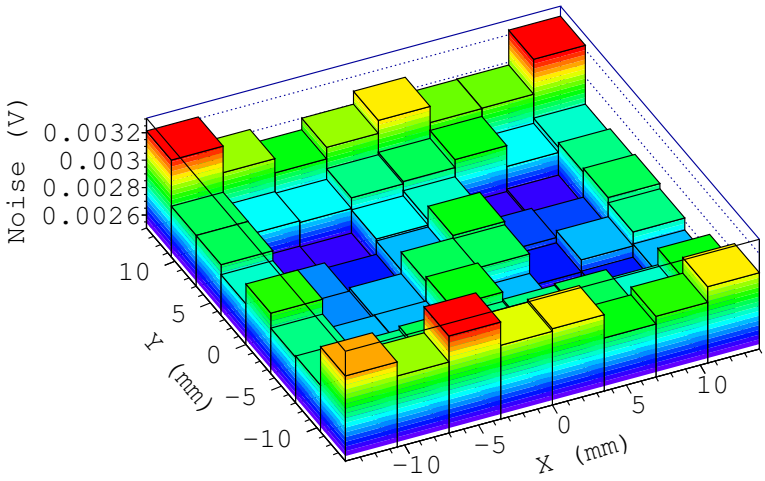

Figure 6.18 – Noise map distribution per pixel.

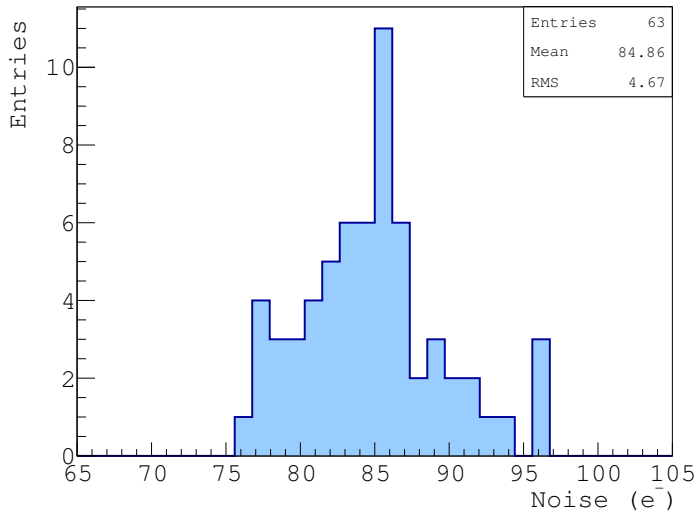

Figure 6.19 – Noise distribution per pixel.

Rejection of fluctuating baselines

In general, each preamplifier, i.e. each pixel of the anode, has a baseline value that should be constant over time and also independent of temperature. However, thermal fluctuations inside the LXe produce prompt baseline variations (see Section 6.4.1). These pedestal fluctuations distort the average value of the pedestal and noise per pixel. Several signals with the baseline out of the average value are visible in Figure 6.20. To remove those events with a bad pedestal, we calculate the baseline rejection interval per pixel from the distribution of the mean values calculated for all the raw signal registered for each individual pixel. Figure 6.21 shows the mean distribution for two pixels of the anode. Unlike the amplitude noise distribution presented in Figure 6.13, the distribution of the mean pedestal value per signal does not have a Gaussian shape, but instead the distribution can be described by a

double Gaussian function that can be defined as follows:

$$A(x) \;=\; A_{core}.\exp\frac{(x-\mu_{core})^2}{2\sigma_{core}^2} \;+\; A_{tail}.\exp\frac{(x-\mu_{tail})^2}{2\sigma_{tail}^2} \tag{6.3}$$

where μ and σ are the mean and the width of the two Gaussian functions, identified as *core* and *tail* (red and green lines in Figure 6.21). As we can see, both distributions have a zero mean value. The mean noise distribution can therefore be described by three parameters σ_{core}, σ_{tail} and the relative share between the two Gaussian functions.

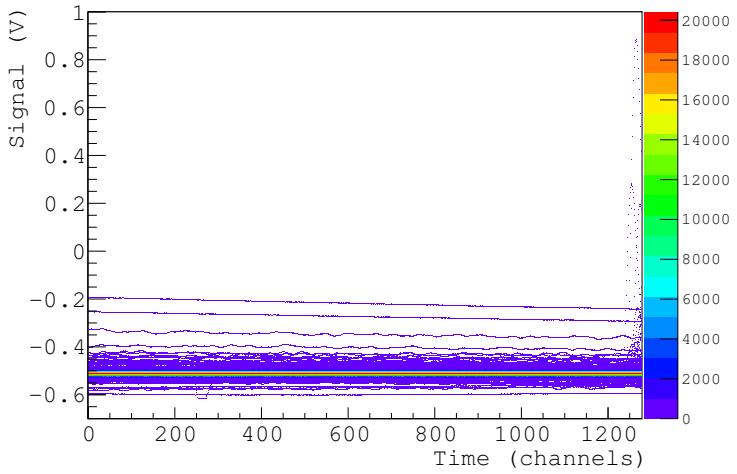

Figure 6.20 – Raw noise distribution with no MLI insulation around the front flange of the TPC.

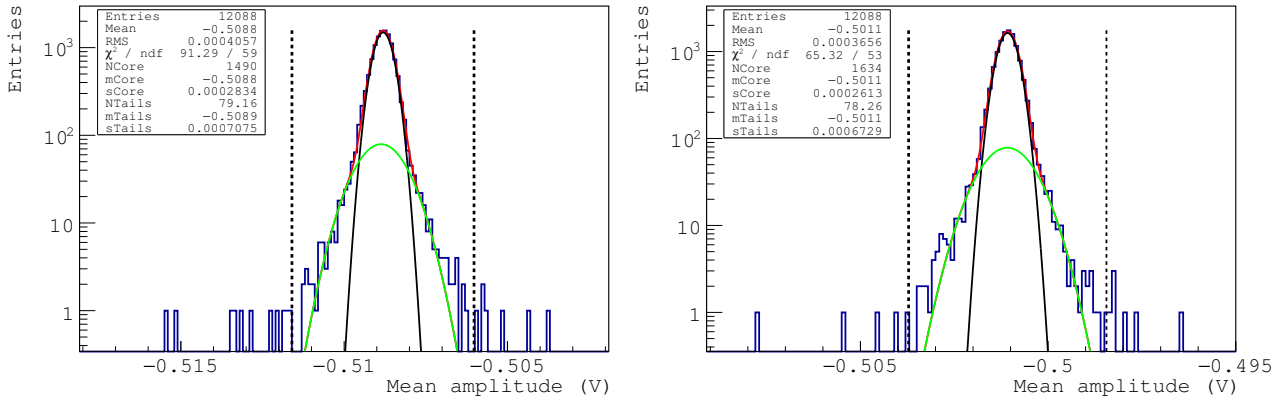

Figure 6.21 – Mean pedestal distribution of the pixels 63 and 19 respectively (see Appendix B). The distributions are fitted by a double Gaussian function given by Equation 6.3.

This wider tail with a σ_{tail} value of ∼0.7 mV is mostly due to the presence of bad pedestal, but it can be also due to undesirable large signals that were not rejected during peak selection and correlated noise. All these contributions cause fluctuation in the mean value of the pedestal. Figure 6.22(a) shows the ratio between the width of the two Gaussian functions for all the pixels of the anode. An almost uniform distribution is observed over the anode. Higher values of σ_{tail} are, on the other hand, measured at the upper part of the anode, which implies correlation between these kind of events and the position of the read-out channels. The red line in Figure 6.21 represents the final double Gaussian fit of the mean noise distribution. The results of the fit are also shown in the figure. A fixed criteria of a maximum rejection of 1/1000 in total due to statistical fluctuations is established, that makes $\sim 1.6\ 10^{-3}$ % of rejected events per pixel. The vertical dashed lines in Figure 6.21 represent the rejection interval due to this cut. The analysis is made in such a way as the integral of the distribution outside these bounds must be larger than the statistical cut. For simplicity in the following, this offline cut is called *bad pedestal interval*. To reject the bad baselines per event, we calculate the median value of the pedestal per pixel, i.e. per individual signal, and we check whether this value exceeds the value of the bad pedestal interval. If so, the entire event is excluded from the analysis. The cut is applied on the median value of each individual signal to ensure that only pedestals out of range are rejected, and the selection is not biased by the presence of large pulses. In average, less than a 10% of the events were rejected due to pedestal fluctuations. Figure 6.22(b) shows the number of rejected pedestals per pixel. As we can observe, most of the rejected baselines are at the top of the anode. This result is consistent with the fact that these baseline fluctuations are due to the presence of bubbles in the liquid xenon as reported in Section 6.4.1. Important improvements have been achieved by including MLI insulation around the front flange of the chamber and around the electronics, that have led as to a pedestal rejection of less than 2 % instead of 10 % in absence of MLI.

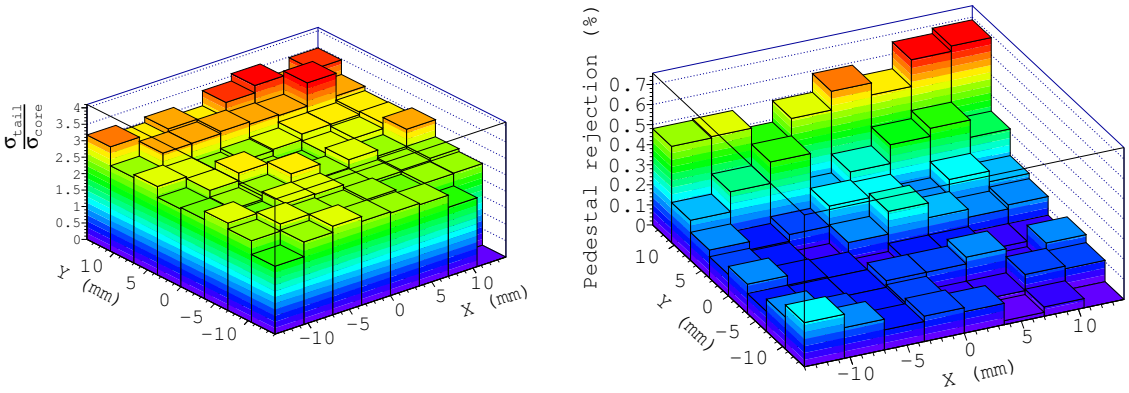

(a) **(b)**

Figure 6.22 – (a) $\dfrac{\sigma_{tail}}{\sigma_{core}}$ per pixel and (b) Mapping of the fraction of rejected pedestals per pixels obtained with no MLI insulation on the front flange of the TPC.

The value of the pedestal per pixel is finally obtained after *bad* pedestal rejection. This value is then used in the data analysis. In addition, the final value of the noise per pixel is also estimated from the baseline fluctuations after pedestal subtraction. The final charge distribution is described by a Gaussian function with zero mean as shown in Figure 6.23. The standard deviation of the distribution gives a value of the electronic noise of the order of 88 e^- and 85 e^- is the borders of the anode are excluded.

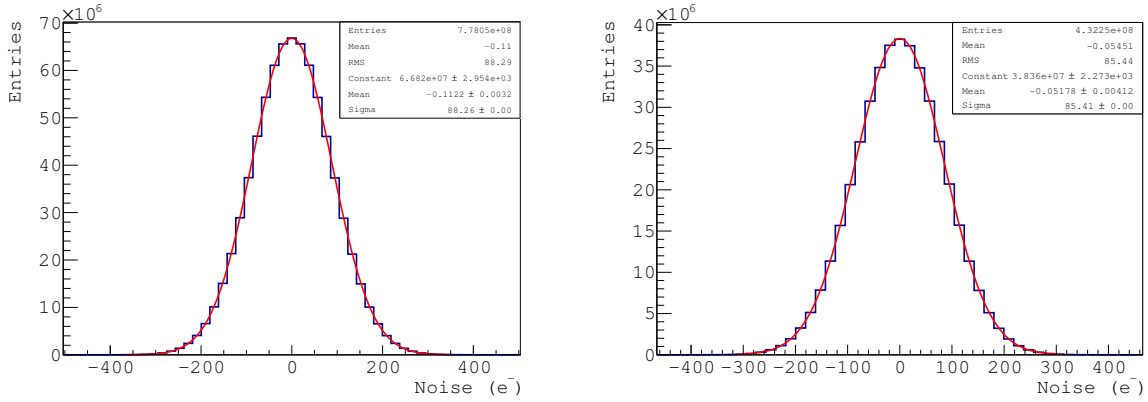

Figure 6.23 – Noise distribution after pedestal subtraction extracted from one random sample for all the pixels with (left) and without (right) the pixels on the borders of the anode.

Event selection depends on the threshold level as much as on the shape of the baseline over the time window. Irregularities on the baseline caused by a trigger perturbation may bias the number of selected events. Figure 6.24 shows the mean pedestal for all the pixels. A reduction of the mean value of the pedestal is observed over a time interval of around 16 μs (200 time channels[2]), with a maximum deviation of the order of 0.25 ADC channel[3] at 20 μs. This baseline reduction is due to the trigger's time position with respect to the data acquisition window and it varies from pixel to pixel. Although this fluctuations is almost negligible, at very low threshold levels it produces a small reduction on the number of triggered events due to the slightly higher equivalent threshold value.

This noise analysis provides the value of the pedestal and electronic noise per pixel that will be used in the data analysis of XEMIS1 and in the data acquisition of XEMIS2. For this reason, the results should be stable over time. Figure 6.25 shows the values of the pedestal and noise obtained during several months of data acquisition for one of the read-out channels. Noise is quite stable over time, with a maximum variation of around 5 electrons. Furthermore, no significant variations have been observed in the pedestal value. Same results have been obtained for the rest of the pixels of the anode.

[2]One time channels corresponds to 80 ns
[3]One ADC channels corresponds to 0.6 mV

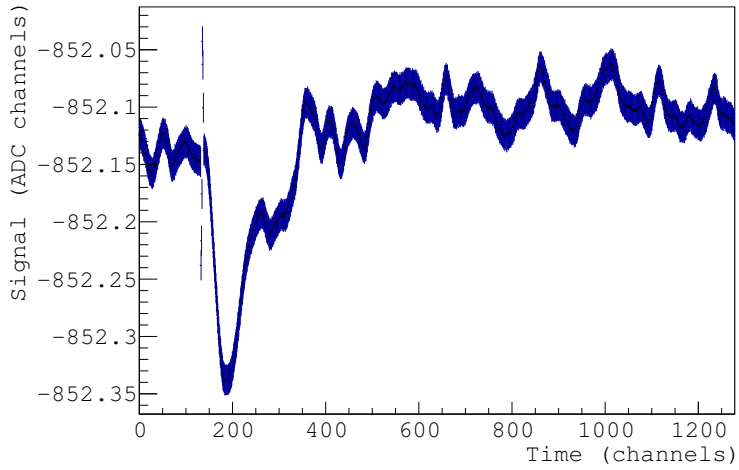

Figure 6.24 – Average baseline over the 64 pixels.

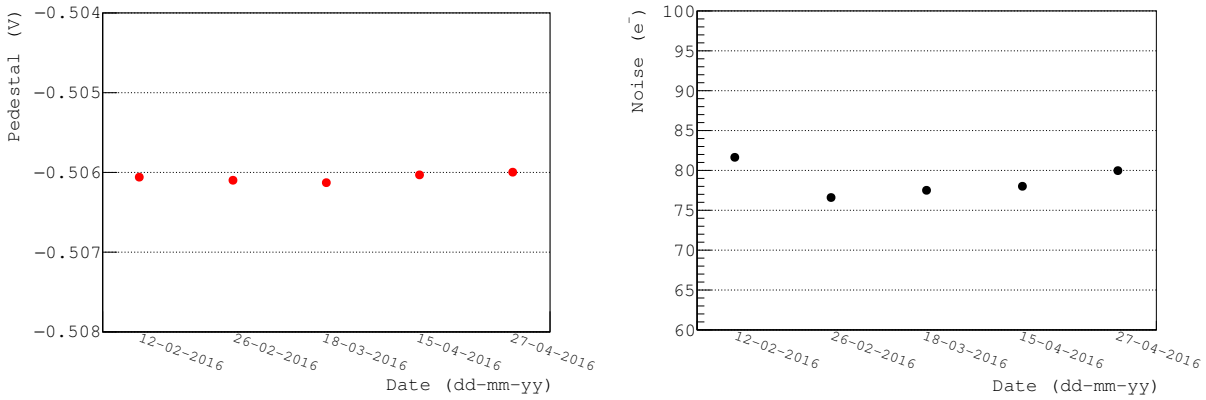

(a) Pedestal **(b)** Noise

Figure 6.25 – Pedestal and noise values for the pixel 0 over several months of data-taking.

6.4.1 Temperature effect on the measured signals

The LXe inside the TPC is in conditions of vapor-liquid equilibrium, which means that the temperature of the liquid inside the cryostat depends on the pressure according to the saturation curve (see Figure 6.26). The amount of heat needed to change from liquid state to gas is given by the specific latent heat L_v. In the particular case of Xe, a small latent heat of 95.587 kJ/kg at a pressure of 1 bar is required in order to change the phase [217]. Moreover, vapor bubbles generation inside a liquid is possible if the temperature of the surface that contains the liquid is warmer than the saturation temperature of the medium. For this reason, the generation of vapor bubbles in the LXe is more important than in conventional liquids such as water[4].

[4]The specific latent heat of water at 1 bar is around 2258 kJ/kg.

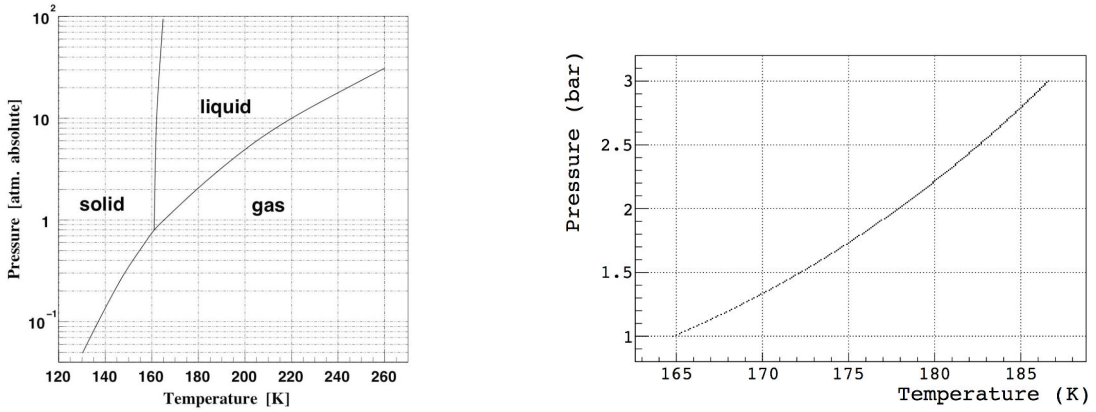

Figure 6.26 – Phase diagram and vapor pressure curve of xenon [2]. The left side figure shows a zoom on the range of interest.

In XEMIS1 the main heat transfer is due to radiation and thermal conduction between the chamber walls and the LXe. Although the design of XEMIS1 was made in order to minimize the contact surface between the TPC and the rest of the components of the detector, thermal conduction through the electronics used to read-out the ionization signal constitutes an inevitable source of heat flow. The most sensitive part of XEMIS1 to heat transfer is the anode. Ideally the anode, which is in contact with the LXe, is kept at the same temperature as the liquid. However, an external heat flow mainly coming from radiation and in lesser extent, from the electronic connectors towards the xenon, increases the temperature of the anode's surface. A small temperature variation of 0.1 °C is enough to produce spontaneous bubbles formation in LXe.

The presence of bubbles inside the TPC may cause important operational problems that degrade the performances of the detector. Spontaneous bubble formation in the anode's surface may affect the stability of the liquid in the collection region. Presumably, the motion of gas bubbles around the anode causes liquid perturbations that in turn produces transient variations of the detector capacitance that give rise to charge induction in the anode. Since the induced signals have a very long tail due to the slow motion of the bubbles in the liquid, after being integrated by the preamplifier the signals would appear as a long-term baseline fluctuations out of the average value, as presented in Figure 6.20. In the worst case scenario, bubble accumulation between the grid and the anode may be a possible cause of discharges due to the high bias voltages usually applied to the grid. This effect is most likely to occur when working with micro-meshes. Small-pitch grids facilitate bubble accumulation in the gap, since bubbles are prevented from evacuation towards the bulk volume and they require, in general, higher voltages to accomplish for electron transparency requirements. The issue of vapor bubbles formation inside the LXe has been also reported by other authors [218, 219].

The evidence leading to the bubble hypothesis has been verified by studying the response of the TPC to pressure and temperature variations. Changes in the cryostat pressure and temperature can be induced by modifying the temperature of the cold finger (see Section 3.1.4). The dynamics of the bubbles were observed for some tens of minutes. Since the migration of the bubbles inside the LXe is slow, the study should be made over long-time registration periods. For each event the 63 waveforms corresponding to the 63 pixels of the

anode are recorded over a time window of 15.36 μs at a frequency of 2.5 kHz. The signals are registered in loops of 1000 events, resulting in 400 ms of data without dead time. The sequence is repeated every 20 s, which is the time necessary to empty the buffer and start a new acquisition process. A total time window of ∼13 minutes is registered on a 2 Gb data file. Due to the limitation of the data acquisition system used in XEMIS1 it is not possible to calculate the fraction of bubbles per event, but instead we could estimated the number of times the average baseline exceed a certain value. The cut interval is obtained from the distribution of the median value of each event, according to the method presented in the previous section. The rejection interval for each pixel was determined under experimental conditions in which the rate of bubble formation is minimum. If the median of each baseline is ±7 times this value of reference, the signal is rejected. Figure 6.27 shows the evolution of the median value of the pedestal as a function of the event number obtained under standard experimental condition for one of the pixels of the anode. The large prompt pulses are important fluctuations of the baseline that occur during several ms, which are associated with the formation of a bubble inside the chamber. These kind of signals populate the tail of the median distribution presented in Figure 6.28. The dashed lines represents the rejection cut interval. 13.5 % of the registered events are excluded due to the baseline rejection cut. The same fraction of bad pedestals has been estimated for different runs under the same experimental condition.

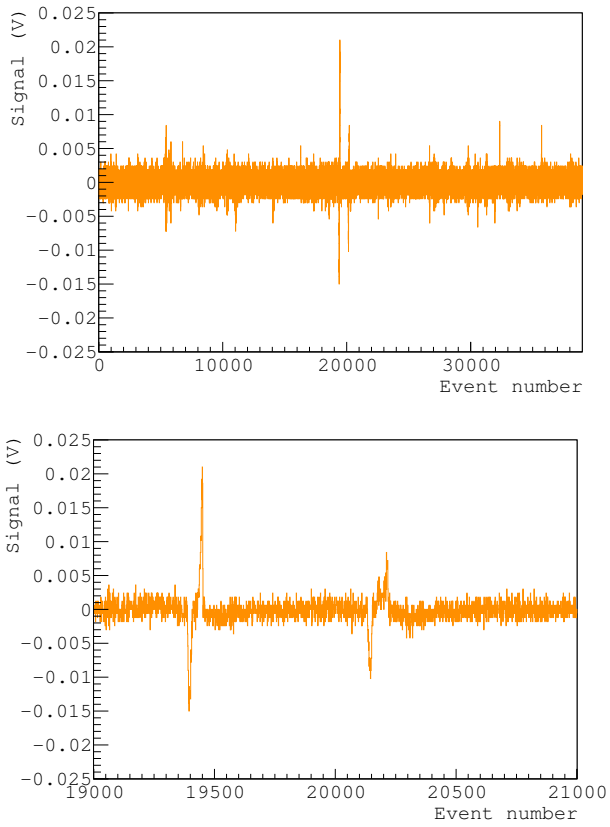

Figure 6.27 – Evolution of the median value of the raw signals with the event number for the pixel 63 of the anode. Each event was registered over a time window of 15.36 μs. The bottom figure shows a zoom on a region of interest where two baseline perturbations are clearly visible.

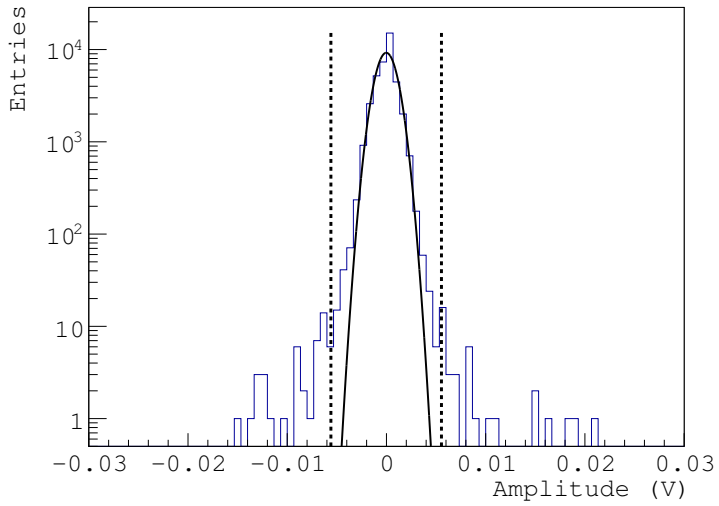

Figure 6.28 – Median distribution of the pixel 63. The black line is the Gaussian fit. The two black dashed lines represents the rejection interval cut obtained from the method presented in Section 6.4.

Figure 6.29 shows the median baseline per event over the total registration time window for the eight pixels of the same column in the anode. Each color represent a given pixel. The vertical axis does not indicate the actual offset of the signals, but a fixed separation of 0.05 V was introduce between them to ease the representation. As we can see from Figure 6.30, the prompt signals follows a clear pattern starting from the bottom of the anode towards the top part. This behavior is consistent with the dynamics of a bubbles inside the LXe. Bubbles created at the bottom of the TPC, detach from the nucleation site and reach the bottom surface of the anode. The bubbles continue ascending until they collapse within a few minutes. In addition, we have also observed that the duration of the baseline fluctuation, represented by the amplitude of the signal, increases by ascending towards the top of the anode. This behavior is also coherent with the enlargement of the bubbles during migration.

Bubble formation can be inhibited by a rapid increase of the cryostat pressure. This can be done by either injecting more xenon inside the cryostat, by increasing the recirculation rate or by changing the system temperature. When the temperature of cold finger increases for example from 164 K to 165 K, the pressure inside the cryostat starts rising immediately in order to maintain the system in thermal equilibrium. The already existing bubbles formed during normal experimental conditions should disappear, whereas the formation of new bubbles is avoided due to the pressure difference between the bottom part of the cryostat and the liquid's surface. Under pressurization conditions, the number of rejected baselines is reduced to 1.3 %. The presence of bubble reappears immediately after the pressure returns to its normal value.

The formation of bubbles, on the other hand, can be enhanced by decreasing the system pressure, i.e. by decreasing the temperature of the cold finger. When the temperature of the PTR decreases by at least 1 K, the pressure inside the cryostat decreases adiabatically below the vapor pressure. The xenon is still in liquid state, but at a pressure where it should be gaseous. Under these thermal condition, a small heat transfer to the LXe may trigger a phase transition from liquid to gas state with the consequent formation of a bubble.

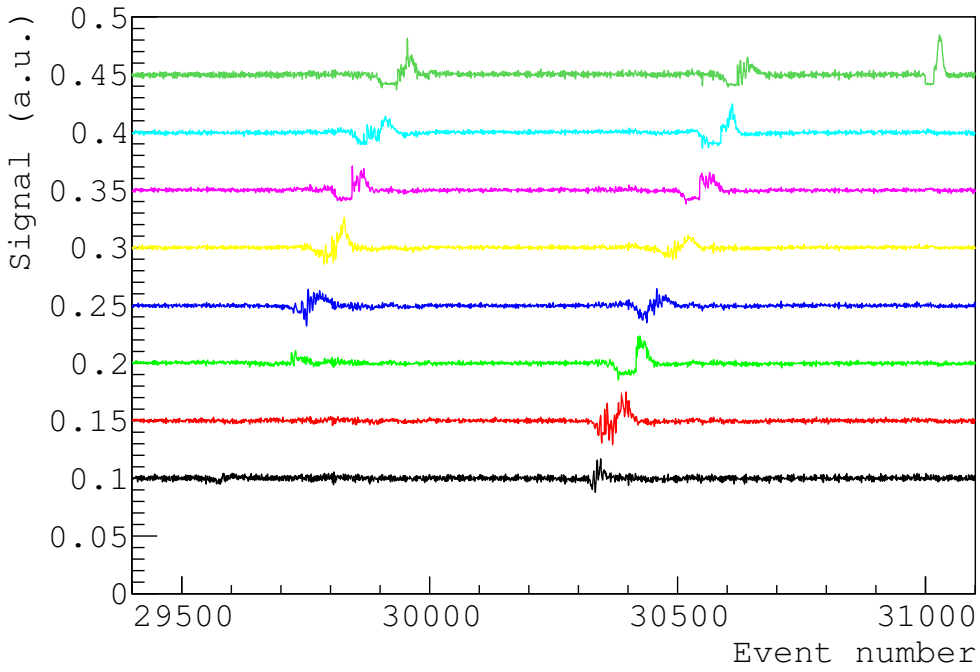

Figure 6.29 – Evolution of the median value of the raw signals with the event number for eight pixels of the column 7 of the anode. The pixels are represented in ascending order.

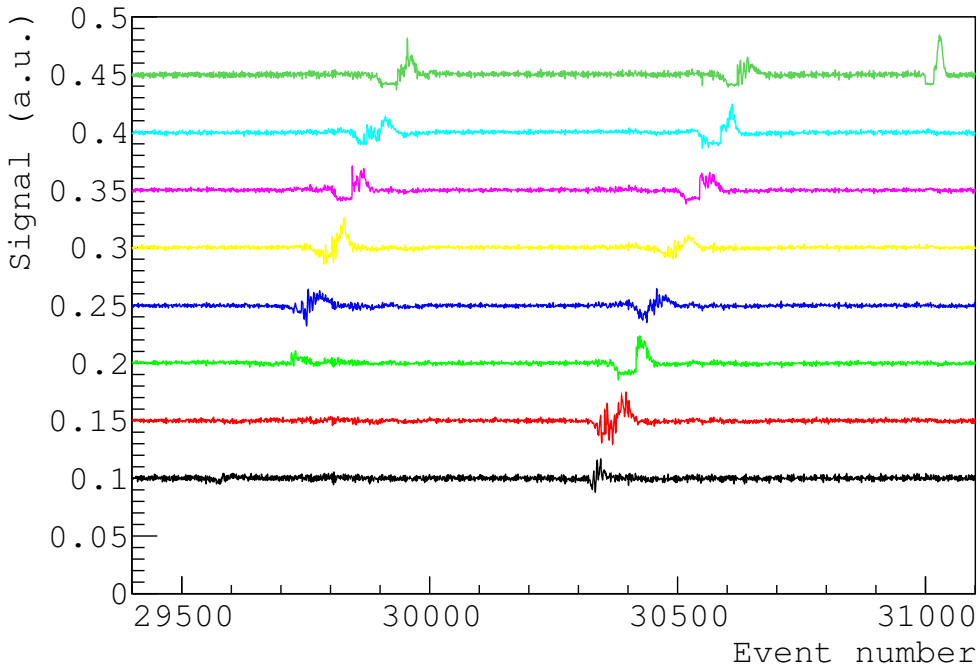

Figure 6.30 – Evolution of the median value of the raw signals with the event number for eight pixels of the column 7 of the anode over a time interval of the total time window. The fluctuations of the baseline follow an ascending pattern from the bottom to the top part of the anode.

Figure 6.31(a) shows the median baseline evolution as a function of the event number for the same pixels column, when the temperature of the cold finger was set to 163 K. We can observe an important increase in the number of bubbles in the chamber compared to pressurization conditions (Figure 6.31(b)). At low pressure, a 25 % of the events where rejected due to baseline rejection cut.

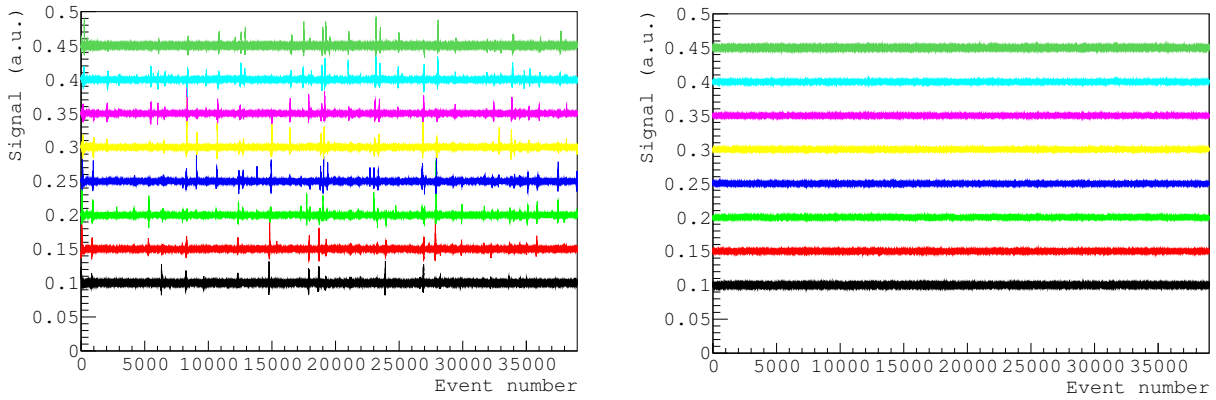

(a) De-pressurization **(b)** Pressurization

Figure 6.31 – Evolution of the median value of the raw signals with the event number for eight pixels of the column 7 of the anode under pressurization and de-pressurization conditions respectively.

Since working under pressurization conditions with the aim of reducing the presence of bubbles in the liquid is not an option, we studied the response of the system as a function of the temperature of the anode. Figure 6.32 shows the experimental set-up used to modify and monitor the temperature of the anode. To decrease the temperature we used a continuous liquid nitrogen cooling system. The liquid nitrogen was stored in an external container at atmospheric pressure. A vacuum pump was used in order to pump out the nitrogens toward the cryostat through a stainless steel tube. Once inside the cryostat, the liquid nitrogen circulate through a copper structure that was screwed onto the front flange of the TPC in such a way that it was in direct contact with the anode and the electronics. The temperature of the copper piece and hence, the temperature of the anode, decreased as the the liquid nitrogens passed through the copper tube placed inside the piece. A sheet of indium metal was included between the copper and the stainless steel to improve the thermal conductivity between the surfaces. A temperature sensor located between the copper piece and the flange allowed for temperature monitoring. An external temperature regulator was used to fix and keep the temperature of the anode at a certain value. A valve placed before the pump controlled the flow of nitrogen towards the chamber. The valve closed the moment the temperature of the anode decreased below the fixed value. Equally, the valve re-opened once the temperature increased above the set point.

This study showed that the presence of strong baseline fluctuations varies with the pressure and temperature conditions of the system, that points out to the formation of bubbles inside the LXe. The number of bubbles inside the TPC decreased as the temperature of the anode decreased. A reduction by a factor of two on the number of rejected events due to baseline out of range rejection was observed when the temperature of the anode was

reduced to 169 K compared to standard experimental conditions (172 K). Moreover, only a 1.6 % of the events were rejected at a temperature of 168 K. Due to the limitations of the set-up the temperature could not be reduce under this value. However, we can presume from these results that the complete inhibition of bubble generation inside the TPC can be achieve by keeping the surface of the anode at the temperature of the liquid. Very satisfactory results were obtained with the electronics completely immersed inside the LXe and by a more complete insulation of the front part of the TPC by using a Multilayer insulation (MLI).

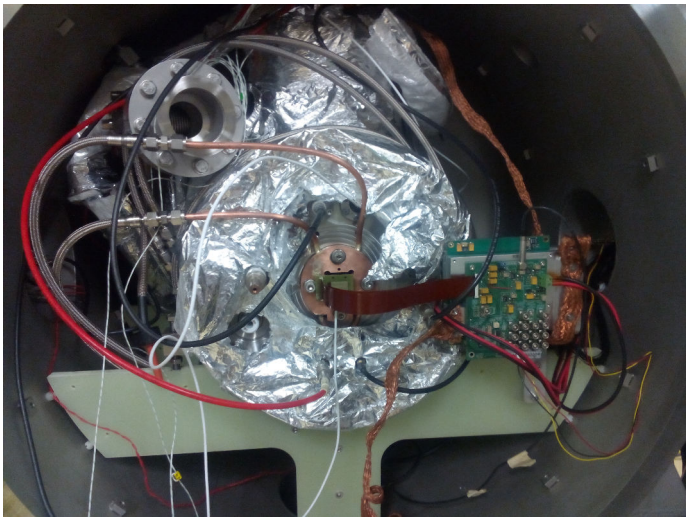

Figure 6.32 – Front view of the XEMIS1 TPC. The copper structure place around the electronic cards was installed to reduced the temperature of the anode and electronics thanks to a liquid nitrogen circuit.

6.4.2 Charge-induced perturbations of the baseline

An additional effect has also been identified on the baseline when a relative high charge is deposited in one of the readout chips. As shown in Figure 6.33, a parasitic signal is observed in all the pixels of the same ASIC after an energy deposition. If all the charge is collected by one of the two IDeF-X LXe chips, no effect has been observed on the other ASIC.

This parasitic signal has a bipolar shape. The negative pole has an average amplitude which is of the order of 0.7 % of the total collected charge by a given chip. A variation of the average amplitude of around 30 % has, however, been observed between the two IDeF-X LXe ASICs. The minimum of the negative pulse arrives around 560 ns before the maximum of the real collected signal. The positive pole, on the other hand, shows a much smaller amplitude, which has almost no effect on the measured signals. The shape and amplitude of the perturbation depends on the peaking time, increasing as the peaking time decreases.

We have noticed that only at low signal amplitudes, of the order of 3 to 5 times de electronic noise, the presence of the parasitic signal results in an appreciable loss of the collected charge, decreasing the number of triggered events. In addition, we realized a distortion on the shape of the measured signal, which affects the measured drift time. At high amplitudes the effect of the perturbation is small and it can be neglected

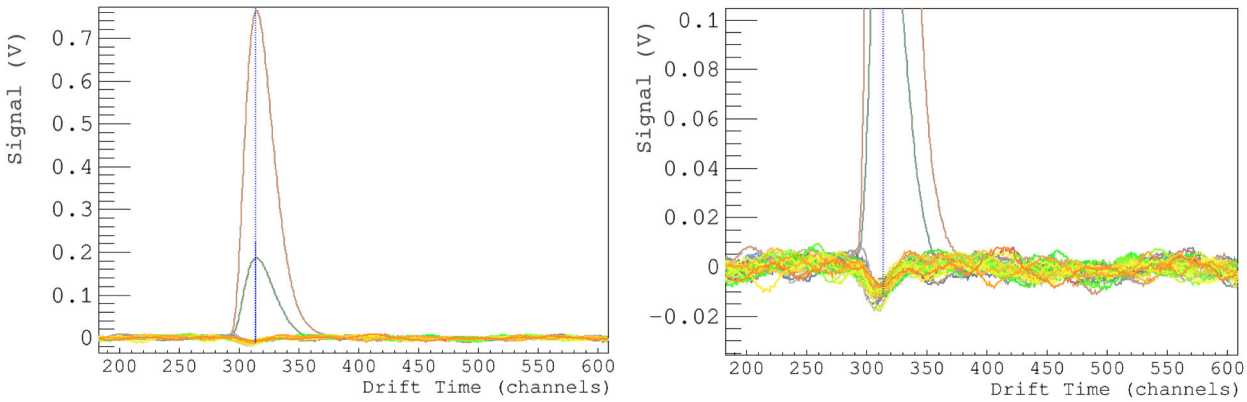

Figure 6.33 – Baseline perturbation caused during the gain stage of the IDeF-X LXe. The left side figure is a zoom on the region of interest.

A complete simulation of the response of the IDeF-X LXe front-end electronics showed that this baseline perturbation is associated to the amplifier that fixes the gain conversion, which is common to all the channels of the same chip. It is important to notice that this baseline perturbation has been observed exclusively in the IDeF-X LXe version of the chip. This effect is currently in the adjustment phase, so it will no longer present in the future versions.

6.5 Data Analysis

This section describes the data analysis steps performed before event reconstruction. A schematic diagram of the data analysis procedure is illustrated in Figure 6.34. The method consists of four main steps: pedestal subtraction, gain correction, pulse selection and clusterization. We use the pedestal and noise results obtained per pixel from the noise analysis to correct the pedestal per signal and to find the pulses. In general, each run with data from the radioactive source is alternated with a noise run, in order to monitor possible variations in pixel pedestal and noise. A threshold level is established for pulse discrimination. The amplitude and time of the signals are calculated using the method of the CFD. After pulse finding, the detected signals from the same interaction are recombine together to form a *cluster*. Several topological cuts are finally applied to these cluster in order to make the final data selection.

6.5.1 Baseline subtraction

As presented in Section 6.4 every signal suffers from an offset, which in general comes from the front-end electronics. Each pixel of the anode can be characterized by a constant pedestal value which is used to correct the data. The pedestal per pixel is obtained from a noise run by averaging over a sufficient number of events. Afterwards, in order to estimate the charge collected in a given pixel, the pedestal is subtracted from the raw signal to compensate from this constant offset.

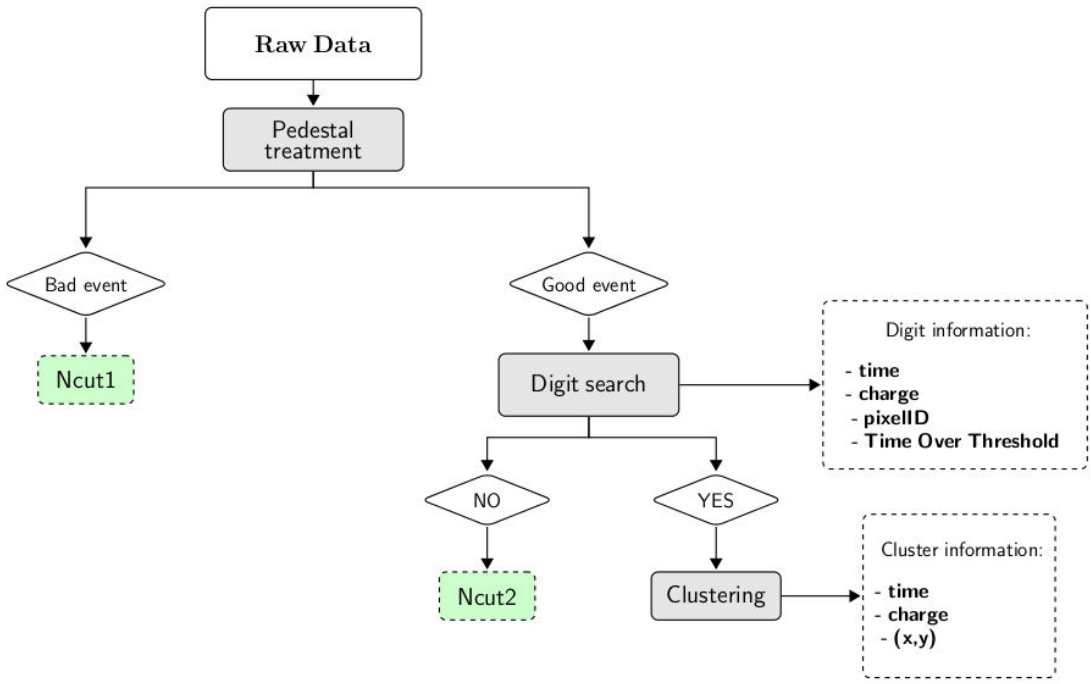

Figure 6.34 – Schematic diagram of the data analysis procedure.

If the probability of the presence of bubbles inside the chamber is high, baseline exclusion can be performed using the rejection interval calculated from the noise events. The median of each individual signal is determined from the first 50 samples and the last 50 samples, and compared to the baseline rejection limits. If the median is above or below three times the value of the rejection cut, the entire event is eliminated from the data analysis. Thanks to an adequate insulation of the detector, we have seen that the formation of bubbles inside the LXe can be neglected and thus this pedestal cut is no longer necessary.

6.5.2 Common noise correction

A common baseline variation may occur in all pixels at the same time, typically due to an imperfect shielding of the components of the detector. Unlike pedestal which is stable over long time periods, common mode noise might vary between consecutive events. Therefore, the second step is the common noise correction event per event. To estimate its contribution, the median value of each sample over all the pixels of the anode is determined event per event. These values are then subtracted from the raw signals of each pixels. The correction is made sample by sample.

The presence of this kind of correlated noise is very sensitive to the grounding of the components as much as the Frisch grid and the first field ring filtering. An important improvement during the course of the thesis has been carried out, so the implementation of this corrections is no longer necessary. Figure 6.35 shows the common noise contribution compared to raw noise and after pedestal correction before the improvement of the system's filtering.

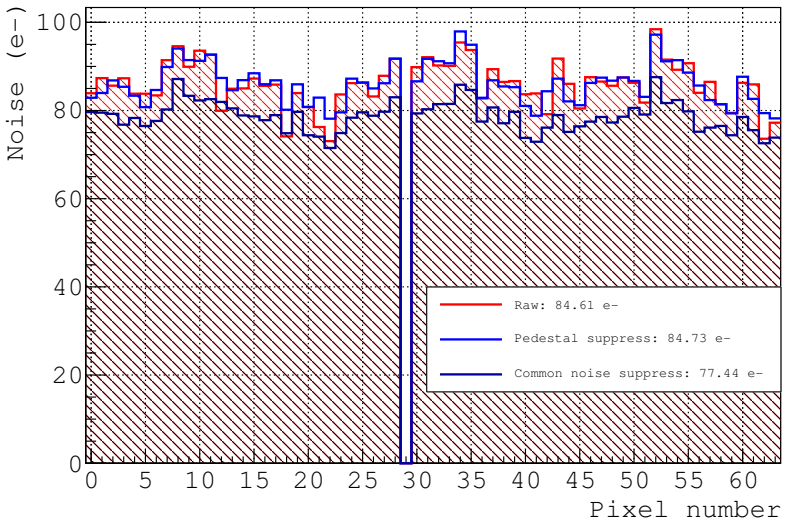

Figure 6.35 – Value of the noise per pixel after pedestal subtraction and common noise rejection.

6.5.3 Gain Correction

So far we have seen that all pixels of the anode do not have the same behavior in terms of DC offset and baseline fluctuations. These variations are mostly due to production differences during the fabrication process where not all the components of the front-end electronics are exactly the same. Equally, pixel to pixel variations of the gain are usually present. In this section, the gain of each individual pixel is calibrated for further correction of the measured amplitude per signal. To obtain an accurate value of the gain of each pixels of the anode an uniform beam is required. To do so, one of the lead collimators placed between the BaF_2 scintillation crystal and the ^{22}Na source was removed in order to increase the solid angle coverage seen by the anode. In addition, to reduce the relative error on the mean value of the amplitude distribution, a high amount of collected events per pixel was necessary.

We obtained the energy spectrum of each pixel. Only clusters with a total measured energy of 511 keV on which 95 % of the charge is collected by a specific pixel were considered. The measured charge per cluster was corrected by electron attenuation to remove the z-position dependence (see Section 7.1). The photoelectric peak obtained per pixel was fitted by a Gaussian function, so the gain of each individual pixels was obtain from the mean value of the Gaussian, which corresponds to the amplitude measured for an energy deposit of 511 keV. The standard deviation, on the other hand, shows the energy resolution per pixel for 511 keV events at 1 kV/cm. Figure 6.36 shows the mean value of the photoelectric peak for the 35 central pixels of the anode. The two different IDeF-X ASICs are represented by a different color. The edges of the anode where removed from the analysis to avoid a possible bias in the collected charge. A maximum pixel-to-pixel difference of 4 % has been measured, whereas a maximum dispersion of 2 % and 2.3 % has been estimated between the pixels of the same IDeF-X LXe chip, respectively. A constant fit per IDeF-X gives an average value of 0.915 V and 0.930 V respectively resulting in a difference of the order of 1.6 %.

The position signal distribution averaged over all the pixels of the same column has been

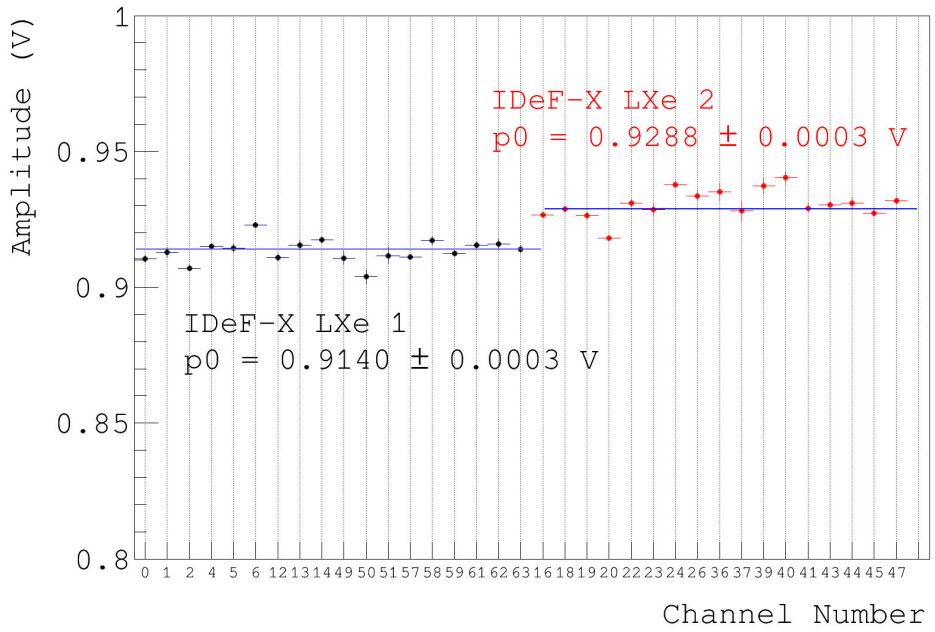

Figure 6.36 – 511 keV peak position as a function of the channel number.

also measured in order to study the contribution of the parasitic signal (see Section 6.4.2). The parasitic signal is proportional to the charge deposited per chip and therefore, its contribution depends on the position of the pixels of a cluster with respect to the maximum energy deposition. For a cluster which pixels are shared between both ASICs, we may expect a non-uniform response of the measured energy. The gain as a function of the column is shown in Figure 6.37. No significant deviation of the columns 3 and 4, i.e. columns at the edge between both chips, is observed with respect of the rest of the columns of the same IDeF-X. A constant fit per IDeF-X shows the same dispersion between ASIC as the one obtained by fitting the value of the gain per pixel.

Gain correction can be applied either pixel by pixel or chip by chip depending on the dispersion between the pixels of the same ASIC. Although a pixel wise correction seem more optimal, it requires a very high statistics per pixel to ensure a correct calibration. To obtain the same precision in the measurement of the gain as the one measured in XEMIS1, we need at least 1000 entries in the photoelectric peak per pixel. This is hardly achievable in XEMIS2 where 24000 electronic channels are present. For this reason, we opted to perform an ASIC wise correction using as average value the one obtained by the fit of the two IDeF-X independently. The measured energy per digit is then normalized by 0.914 V and 0.928 V before clusterization depending of whether the charge is deposited on the left or right side IDeF-X respectively.

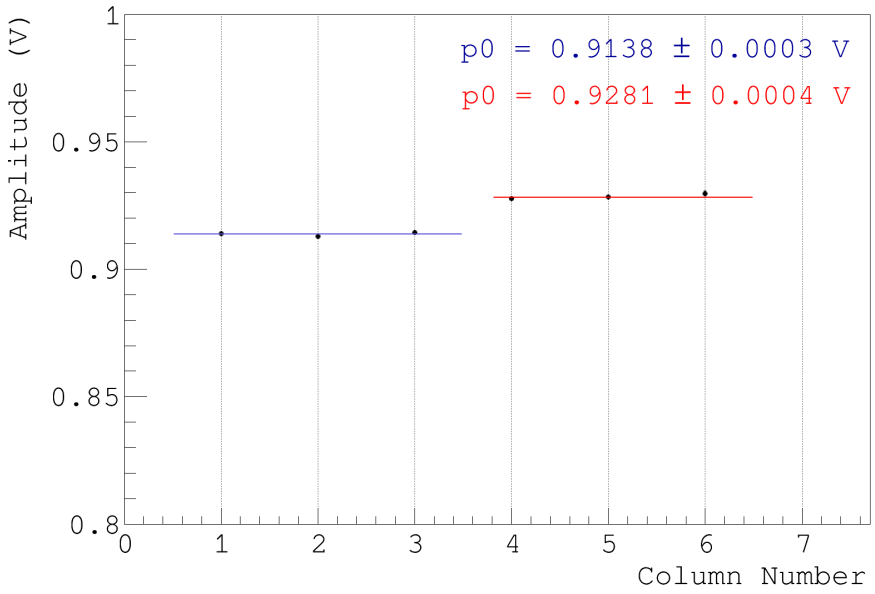

Figure 6.37 – Pixel signal distribution for 511 keV events as a function of the column number.

6.5.4 Signal selection and Clustering

The next step in the data analysis after pedestal (and common noise) correction is signal finding. The goal is to determine the number of interactions per event detected above an energy threshold, which are spatially resolved. A *digit* is found if the amplitude of the pulse is higher than this threshold. In our case, the signal over noise ratio should be higher than $SNR > 3\sigma_{noise}$ (*or* $4\sigma_{noise}$). Such a low threshold is necessary because of the charge spread between adjacent pixels mainly due to electron transverse diffusion and the size of the primary electron cloud. An hysteresis of $n\sigma_{noise}$ to $(n-1)\sigma_{noise}$ was used to determine the time of CFD.

The energy threshold implies an unavoidable loss of detection efficiency. The amount of shared charge depends both on the position of the electronic cloud with respect to the pixel edge, and on the distance of the interaction in the active volume with respect to the anode. In most cases, a high charge is collected by a certain pixel while a very small amount of the total charge is deposited on one or more neighboring pixels. A low threshold level is then required in order to recuperate all the deposited charge shared between the different pixels. During this thesis two different thresholds of 3 and 4 times the noise have been considered as the best option between charge recovery and noise counting rate (see Section 4.5). A $3\sigma_{noise}$ threshold implies that at least an energy deposit of around 4.5 keV inside the fiducial volume of the detector is necessary to be measured. Higher thresholds, on the other hand, would reduce the amount of collected charge per interaction, which would deteriorate both the energy and transverse spatial resolutions of the detector, especially for low energy deposits. Figure 6.38 shows the position of the photoelectric peak as a function of the energy selection threshold. A reduction of around 0.3 % of the collected charge has been calculated with an energy threshold of $10\sigma_{noise}$. The measured charge at 3 and 4 σ_{noise} is compatible within the

statistical uncertainties.

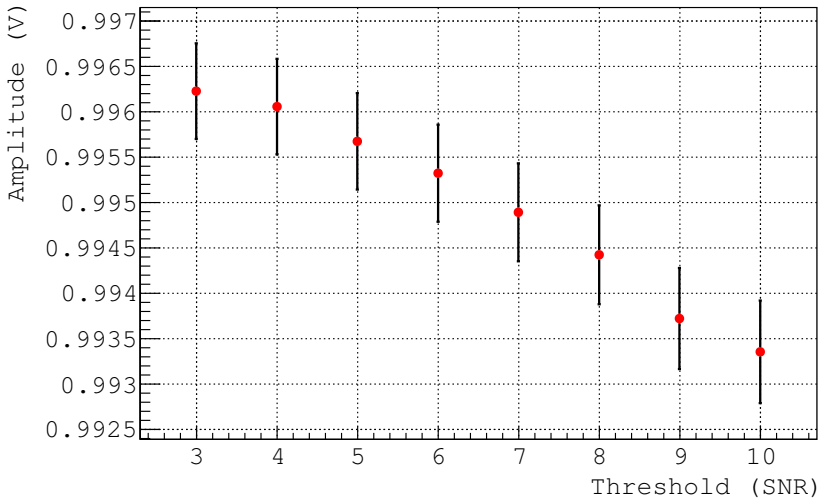

Figure 6.38 – Collected charge as a function of the energy threshold level for 511 keV events at 1 kV/cm.

Each of the selected digits contain the information of the time (z-coordinate), charge, x-y position, pixel address and time over threshold (TOT). The amplitude and time of the signals are calculated using the method of the CFD with a delay of 9 channels and a gain of 1.5. The zero-crossing point of the CFD signal gives directly the position of the maximum amplitude. The jitter introduced in the time measurement by the data acquisition system is corrected by using the TTT signal. Moreover, the amplitude of the signals is corrected by gain linearity (see Section 6.5.3). The TOT is calculated between the nσ_{noise} threshold and a second threshold at (n - 1)σ_{noise}. Only pulses with a calculated time using the CFD method inside this double threshold interval are kept. A 2 % of the signals are lost due to the hysteresis cut. No further assumptions are considered for the peak selection.

Clustering

In the next step, digits coming from the same interaction should be aggregated in the same *cluster*. Pixel clusters are formed by combining neighboring pixels with charge above the pixel threshold. Both side and corner adjacent pixels are included in the cluster. The list of digit is sorted by signal amplitude in descending order. Starting from the first digit, i.e. higher amplitude, a list of neighboring fired pixels is created. The pixel with the maximum amplitude is now considered as the *pixel of reference*. Only pixels which are closest neighbors by side or by the corner to the pixel of reference are possible candidates to the same cluster. The clusterization algorithm loops over all the detected digits and it searches for unclustered digits within a pre-defined time window until no more digits are found in the vicinity of the pixel of reference. The time condition between adjacent pixel is necessary since not all the neighboring fired pixels must come from the same interaction. The selection of this cluster time window is explained below. After a cluster is formed, the digits associated to this cluster are removed from the list for the remaining cluster search in the same event.

The next maximum digit in the list become the new pixel of reference of a new cluster and the search for possible neighboring pixel re-starts. The procedure continues until no digits are left in the list.

Figure 6.39 shows an example of a photoelectric effect, where the total charge is shared by four different pixels. All the signals are collected on the anode after the same drift time of the order of 43 μs (∼540 time channels). The waveforms are presented in Figure 6.40. An almost uniform charge sharing is obtained between the four pixels, that implies that the charge cloud should be located close to the intersection point between the four pixels. The total charge of a cluster is then calculated as the sum of all the individual charges Q_i. The time of the interaction, i.e. the z coordinate, is given by the time measured by the CFD for the pixel of reference. The x and y positions of the interaction, on the other hand, depend on the number of pixels inside the cluster, also called *multiplicity*. If the cluster has multiplicity equal to one pixel, the position of the interaction is measured at the center of the pixel. However, if the charge is shared by more than one pixel, the position is calculated, as first approximation, as the centroid position of the electron cloud:

$$x_{rec} = \frac{\sum_i Q_i \,.\, x_i}{\sum_i Q_i} \tag{6.4}$$

$$y_{rec} = \frac{\sum_i Q_i \,.\, y_i}{\sum_i Q_i} \tag{6.5}$$

where x_i and y_i are the x and y coordinates of the center of each pixel. The center of gravity method is not a good estimator of the true position since the pixel size is larger than the electron cloud. A correction is then necessary in order to obtain a more realistic position distribution. A more detailed study of the x-y position reconstruction is performed in Section 7.6.

After clustering, interactions are classified in single-cluster events, double-cluster events, etc ... or more generally, multi-cluster events, according to the number of clusters per event. This classification is essential for further Compton sequence reconstruction.

Cluster Time Window

Clustering is one of the most delicate parts of the data analysis given the complexity and variety of possible event topologies. A missassociation of digits inside the clusters leads to a degradation of both energy and spatial resolutions.

The adjacency condition between pixels is not always enough to distinguish two interactions produced by the same ionizing particle. For this reason, an additional matching based on the drift time is applied. Two digits measured in two adjacent pixels belong to the same cluster, if the difference between the time of CFD of each of the pulses is smaller than a certain value. If a cluster candidate has more than two pixels, the time difference is always calculated with respect to the *pixel of reference*, i.e. the pixel with the maximum amplitude.

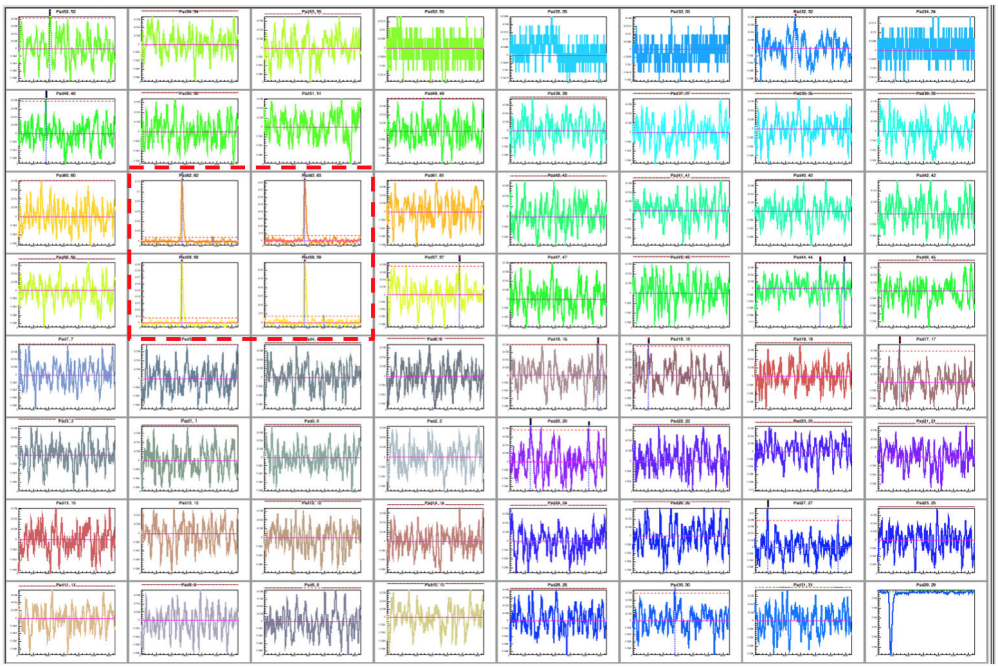

Figure 6.39 – Pixel signal distribution of the segmented anode where a deposit of 511 keV is shared between four adjacent pixels. The waveform registered by the right bottom pixels is the TTT signal.

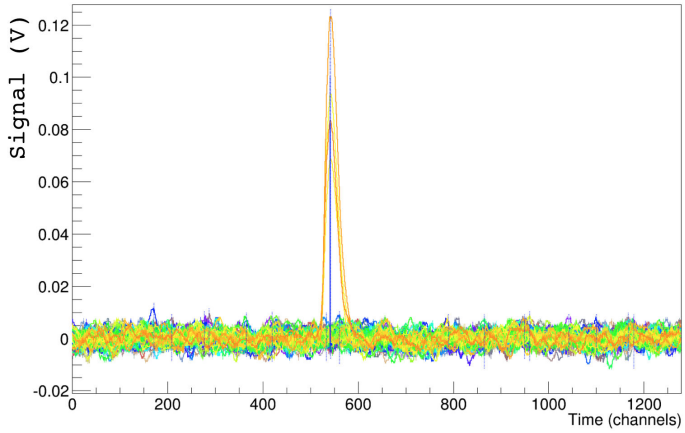

Figure 6.40 – Example of a 511 keV energy deposited shared by four adjacent pixels of the anode.

Clustering with respect to the pixel of reference, is an efficient way to avoid random noise digit to be regrouped with real charge deposits, in addition to enhance the separation of clusters that come from two different interactions produced close in time and space.

To determine the optimum value of the cluster time window, we performed a preliminary study where a large fixed window of 2 μs is set, i.e. if two adjacent digits have a drift time difference smaller than 2 μs, both signals are assumed to come from the same interaction point. The results presented in this section were obtained with the 6 cm TPC, a 100 LPI Frisch grid placed at 500 μm from the anode and an electric drift field of 1 kV/cm. Only single-cluster events with a total energy of 511 keV are selected. No additional condition is set on the clusters multiplicity. The cumulated time difference distribution between two

pixels of the same cluster is shown in Figure 6.41. The value of Δt is calculated as the difference between the time of CFD of the pixel of reference, minus the time of CFD of a neighboring pixel of the cluster. The sharp peak centered at $\Delta t = 0$ is due to the well reconstructed digits and less likely due to two different interactions at the same z-position. A constant background is observed at the tail of the distribution caused by noise digits. The cumulated time difference distribution is presented in Figure 6.42 as a function of the neighbors amplitude expressed in unit of SNR. For simplicity, we will refer to the amplitude of the neighboring pixels as $A_{neighbor}$. For a $A_{neighbor}$ higher than $20\sigma_{noise}$ the distribution seems uniform with a time difference between digits of less than 1 time channel (one channels is equivalent to 80 ns). The dispersion from zero is due to the limited precision because of the time sampling. At amplitudes smaller than $20\sigma_{noise}$, the time difference between adjacent pixels increases as the amplitude of the neighboring pixel decreases. At very low $A_{neighbor}$, of the order of the pulse selection threshold, the distribution is dominated by noise digits. The lack of events at $\Delta t > 0$ is probably due to the parasitic signal reported in Section 6.4.2. Figure 6.43(a) shows the time difference distribution for an amplitude of $4\sigma_{noise}$. A peak with a delay of ∼-4 time channels (∼320 s) with respect to $\Delta t = 0$ is clearly visible, which exceeds from a constant background. The peak was fitted with a Gaussian function plus a background. The time delay of 4 channels disappears at higher amplitudes as presented in Figure 6.43(b). Under this experimental conditions, this time delay is more probably due to the presence of the parasitic signal (see Section 6.4.2). Other possibles causes of signal delay such as indirect signal induction are discussed in Chapter 5.

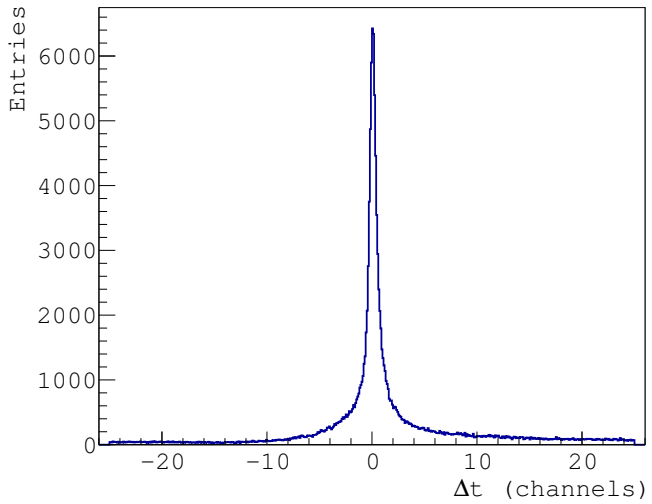

Figure 6.41 – Time difference between the pixels of the same cluster, for cluster with a total measured energy of 511 keV.

The average time difference as a function $A_{neighbor}$ is depicted in Figure 6.42. The value of Δt was obtained by fitting the time difference distribution for each value of $A_{neighbor}$ by a Gaussian function. Moreover, the timing resolution as a function of the deposited energy was deduced from the standard deviation of the Gaussian fit (see Figure 6.44). The higher time dispersion observed at low amplitudes is due to the precision of the CFD method due

to the influence of the electronic noise. For small energy signals, a resolution of the order of 400 ns was calculated.

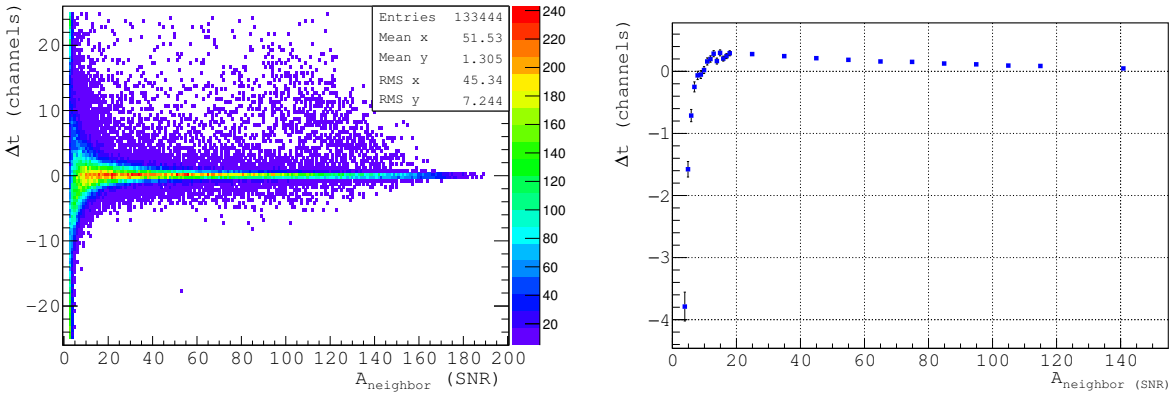

Figure 6.42 – Time difference distribution between pixels of the same cluster as a function of $A_{neighbor}$. Only cluster with a total measured energy of 511 keV are included in the distribution. In the left side figure the mean value of Δt with respect to $A_{neighbor}$ is presented.

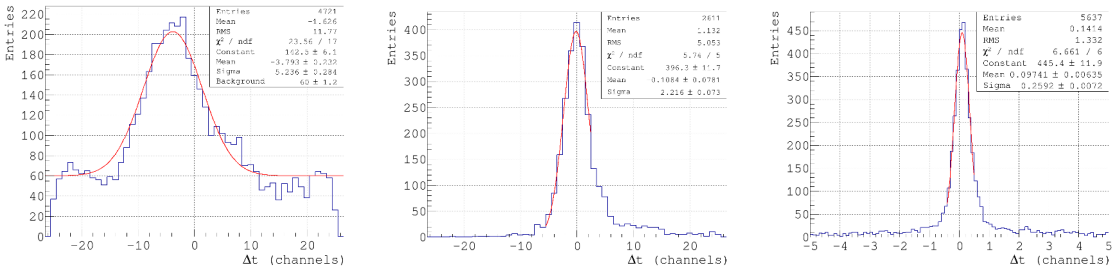

(a) $4\sigma_{noise}$ **(b)** $10\sigma_{noise}$ **(c)** $95\sigma_{noise}$

Figure 6.43 – Example of the Δt between pixels of the same cluster for a total charge of 511 keV and a $A_{neighbor}$ of $4\sigma_{noise}$, $10\sigma_{noise}$ and $95\sigma_{noise}$ respectively.

The time window of clusterization can be set either using a fixed value ($\sigma_{mean} \approx$ 0.5 channels) given by the average standard deviation of the Δt distribution as in [115], or a variable value which depends on the amplitude of the digits of a cluster. Due to the important amplitude-dependency of the precision of the time measurement, a variable time window seems the best option. The dependence of the timing resolution as a function of the amplitude is obtained by fitting the distribution presented in Figure 6.44 by a triple exponential. The cluster time window is then given by the relation: $TW = \pm 3\sigma_{TW}$, where σ_{TW} is given by Equation 6.6:

$$\sigma_{TW} = \sqrt{\sigma_{P_r}^2 + \sigma_{P_a}^2} \tag{6.6}$$

where σ_{P_r} and σ_{P_a} are the values of the time resolution obtained from the triple exponential fit for the pixel of reference and the adjacent pixel respectively. Since the Δt distribution is well described with a Gaussian distribution a $\pm 3\sigma$ time window accounts for 99.7 % of the events for a given collected charge.

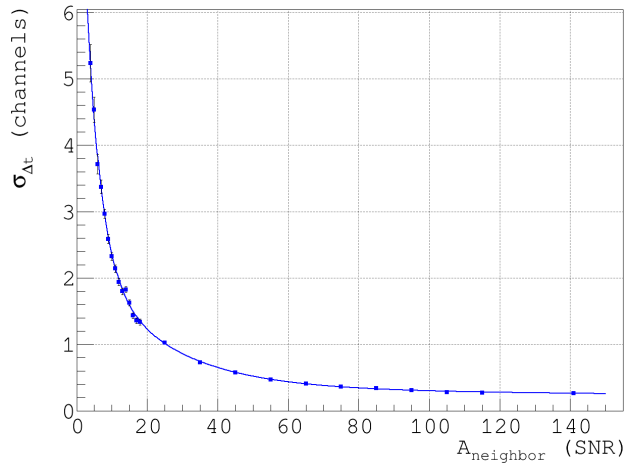

Figure 6.44 – Time resolution as a function of SNR.

The comparison between two different time windows is presented in Figure 6.45. For a constant time window of $\pm 3\sigma_{mean}$, the photoelectric peak is less symmetrical in the region close to the Compton edge. This asymmetry is in part due to a bad clusterization of two different interactions with similar energies that are regrouped together in the same cluster. Moreover, the number of single-cluster events is reduced by a ~ 5 % when a fixed cluster time window of 1.5 time channels (120 ns) is used. A missassociation of the interaction points have detrimental effects on the tracking Compton reconstruction, where the first and second interaction points must be well defined. For this reason, the results presented in this thesis have been obtained by using a variable cluster time window according to the dependency presented in Figure 6.44

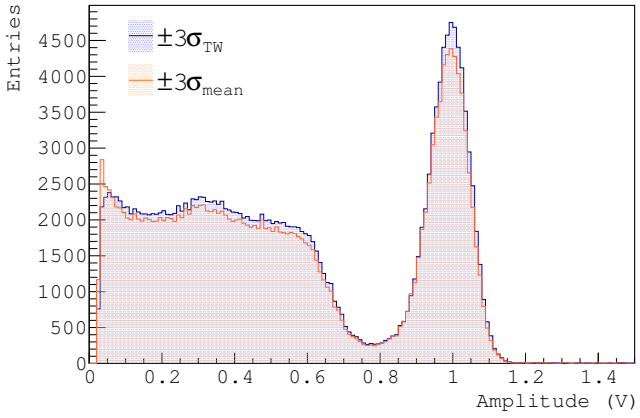

Figure 6.45 – Energy spectrum of single-cluster events for two different cluster time windows.

6.5.5 Off-line Analysis: event selection

Border Rejection

A series of topological cuts were added to the data analysis in order to make an adequate selection of the reconstructed clusters. First of all, clusters which center of gravity is calculated at one of the pixels situated at the borders of the anode are excluded from the analysis. The borders consist of the first and last rows and columns of the segmented anode. This cut is necessary because for these kind of events we cannot conclude that all the charge was deposited inside the active zone of the detector. Similarly, clusters with a reconstructed position around the right bottom corner of the anode are also rejected. The pixel placed at this position is used to register the TTT signal and hence, no real charge is collected. In average, less than 2 % of the measured cluster are removed by these two cuts.

Event Topology and Energy Cut

The number of cluster per events is related to the nature of the interactions inside the detector. For 511 keV events, the probability that a γ-ray undergoes a photoelectric effect is $\sim$20 %, while the probability of Compton scattering is $\sim$80 %. In some cases, when photons interact within the LXe, they may undergo multiple Compton scattering before they are fully absorbed by the medium. Consequently, we expect to reconstruct, in average, around two clusters per event.

The number of detected clusters per event may be affected by both an incomplete clustering algorithm and the presence of electronic noise. Moreover, not every scattering point is necessarily registered by the detector. This effect is directly related to the size of the active area of the detector. When two interactions are spatially close, the clusterization algorithm may not be able to separate them, and a single cluster would be register instead. A bad clusterization affects the measurement of the position and energy of the γ-ray interactions. In addition, if an interaction point do not deposit sufficient energy to trigger the minimum energy detection threshold, it would be treated as electronic noise and the interaction will not be recorded. All these factors affects the event topologies and had the effect of reducing the actual number of cluster per event. On the contrary, a low threshold level will increases the number of clusters per event due to the incorporation of noise clusters. The blue distribution in Figure 6.46(a) shows the number of clusters per event for a charge detection threshold of $3\sigma_{noise}$. In average, 14 clusters are reconstructed after the interaction of a 511 keV γ-ray inside the detector, with no single-cluster events which prevents the calibration of the detector. The shape of the distribution is consistent with the number of noise triggers per event. If we consider that for the CFD method, the number of noise triggers per second and per pixel for a $3\sigma_{noise}$ threshold is around 2200, the average value of the total number of noise triggers in the anode during the 102μs time window is $\sim$14. The number of clusters per event is highly reduced for a $4\sigma_{noise}$ threshold as shown in the blue distribution of Figure 6.46(b).

To reduce the presence of noise events due to the low threshold level, a cut on the clusters energy is necessary. Isolated clusters with an amplitude smaller than 20 keV are excluded. The limit of 20 keV was chosen due to the important loss of angular resolution at low energies. This energy limitation is crucial for tracking Compton. However, to avoid the loss of true

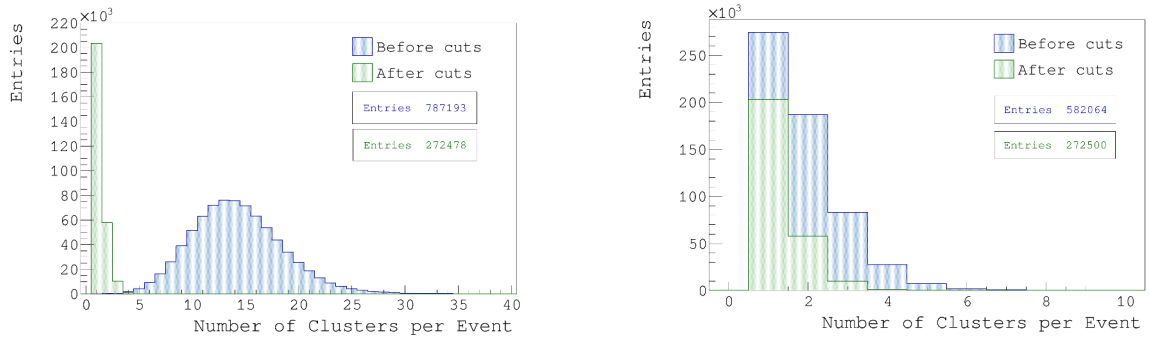

(a) $3\sigma_{noise}$ **(b)** $4\sigma_{noise}$

Figure 6.46 – Distribution of the number of clusters before and after cluster rejection.

events, a more complex cut concerning the multiplicity of clusters is applied. Figure 6.47(a) shows the energy distribution of those clusters rejected due to the energy cut for a threshold of $3\sigma_{noise}$. As we can observe, three clear peaks are present in the distribution. These peaks correspond mostly to clusters with one, two and three pixels per cluster respectively. The multiplicity distribution for the three peaks is depicted in Figure 6.47(b). For the events with energies comprised in the third peak, around 65 % of the clusters have three triggered pixels, whereas 25 % have multiplicity one. Those clusters with around 20 keV deposited on a single pixel cannot be considered as noise clusters and should not be rejected. Therefore, an additional condition concerning the number of pixels per clusters was included to improve the quality of the selection. If the 20 keV of energy are collected by a single pixel the cluster is conserved. Otherwise, the cluster is considered as noise and it is removed from the analysis.

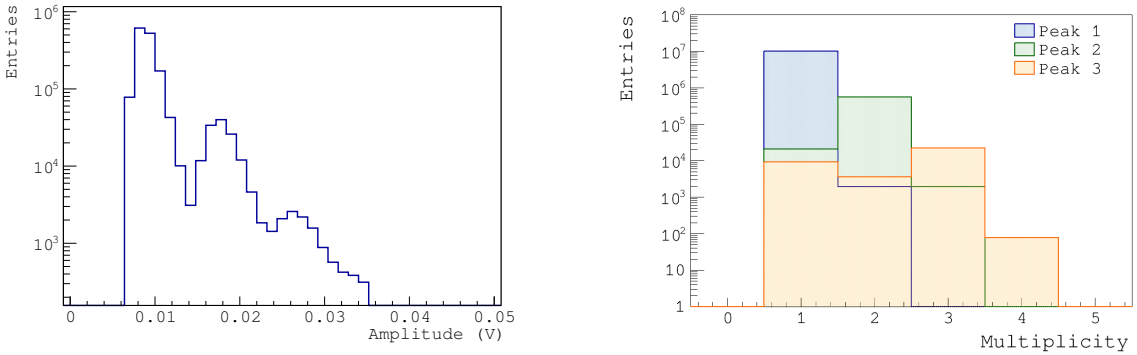

(a) **(b)**

Figure 6.47 – (a) Energy spectrum and (b) number of pixels per cluster for those clusters with an energy smaller than 20 keV with amplitude threshold level of $3.0\sigma_{noise}$.

For a $3\sigma_{noise}$ threshold, 94 % of the reconstructed clusters are rejected due to the energy cut, while for a threshold of $4\sigma_{noise}$, the clusters rejection is reduced by almost a factor of 2 (55 %). Figure 6.48 shows the number of rejected cluster due to the energy cut as a function of electron drift time. As expected, since most of the rejected cluster are isolated noise triggers, the clusters are randomly distributed along the time window. The z-dependence of rejected events is almost flat with a slight fluctuation due to the presence of correlated noise.

A small reduction of the number of trigger is observed at the beginning of time window, which is consistent with the position of the trigger as reported in Section 6.4. Finally, after border and energy cuts, a 6 % of the registered events are, in average, removed from the analysis, while an almost 96 % of the clusters are dropped for a $3\sigma_{noise}$ threshold level. On the other hand, for a $4\sigma_{noise}$ threshold level only 60 % of the clusters are removed from the analysis. The green distribution in Figure 6.46 shows the number of cluster per event after the different selection cuts. In average, we expect a number of clusters per event of 1.3 for both threshold levels, which is more consistent with the nature of the 511 keV γ-ray interactions.

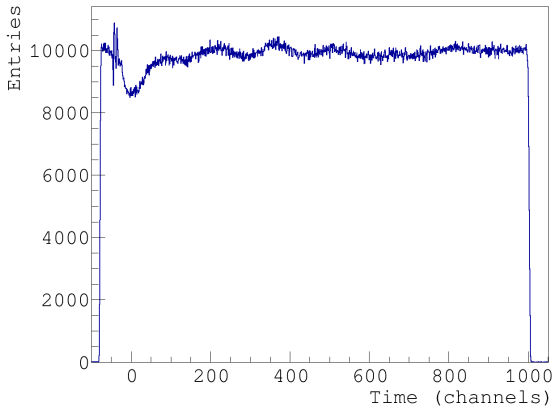

Figure 6.48 – Distribution of the rejected clusters due to the energy exclusion.

Ionization and Scintillation Light Correlation

The correlation between light and ionization can be used to reject 511 keV event which are not related to the charge deposited inside the TPC after a trigger. Those events are present outside the dimension of the TPC and outside the average distribution in the light charge distribution as shown in Figure 6.49. A cut along the scintillation light profile illustrated by the red dashed line in the figure can be used to exclude these events from the data analysis.

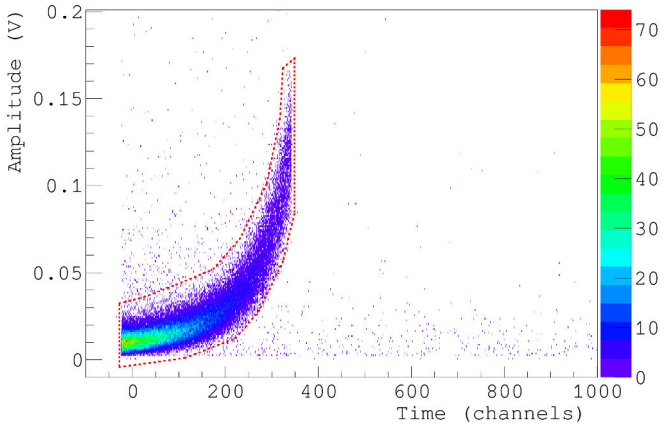

Figure 6.49 – Scintillation light amplitude as a function of the time of the CFD of 511 keV. The red dashed line represents a cut to reject uncorrelated events with the ionization charge as well as noise events. All those events outside the cut are excluded from the analysis.

6.6 Conclusions Chapter 6

In this chapter we have presented the experimental set-up used to measured the 511 keV γ-ray for the performance characterization of XEMIS1. A coincidental trigger between the TPC and a BaF_2 scintillation crystal coupled to a PMT is used to trigger on the two back-to-back 511 keV γ-rays events emitted by a low activity ^{22}Na source. The optimal coincidence time window and threshold level for the LXe PMT has been studied in order to maximize the trigger efficiency. We have confirmed that the trigger efficiency for 511 keV events improves when the active length of the TPC is reduced by a factor of two from 12 cm to 6 cm, due to the geometry of the chamber with respect to the position of the PMT inside the LXe. This new drift length of 6 cm is used from now on for the calibration of the detector.

We have presented a precise study of the noise with the aim of correcting the raw data from the DC offset and set the optimal threshold level for pulse finding. The noise and pedestal calibration is made pixel per pixel. An average noise of around 80 e^- is measured thanks to the low-noise front-end electronics used to collect the ionization signal. Each run with data from the radioactive source was alternated with a noise run, in order to monitor possible variations in pixel baseline and noise, and to calculate the pedestal. A method to reject the pedestal out of range due to the presence of bubbles inside the LXe has been also introduced. We have shown that an adequate insulation of the detector reduces significantly the fraction of bubbles inside the liquid which corroborates the hypothesis that the origin of these bad pedestal is heat transfer from the outside towards the LXe.

A very low threshold level of the order of 3 to 4 times the value of the noise is set on the pedestal-corrected signals to measure a very small charge deposited in the detector. The amplitude and time of the signal that triggers the discriminator are measured by using the CFD method with a constant delay of 720 ns and a gain of 1.5. Since the deposited charge can be collected by more than one pixel, an event reconstruction algorithm is required. The selected pulses are then clustered in order to regrouped digits that come from the same interaction point. A cluster is therefore a set of neighboring pixels that have collected an amount of charge higher than a certain threshold. The total charge collected by all the pixels in a cluster, is proportional to the deposited energy. The optimal time window to match two different signals in the same cluster was deduced from the difference time distribution between the pixels of the cluster. An amplitude variable time window is the best option to avoid the missassotiation of digits that leads to energy and spatial resolutions degradations. Additional topological cuts on the selected events were included in the data analysis to perform a more accurate characterization of the TPC. In Chapter 7 the results obtained using the experimental set-up and methods presented in this chapter are presented.

Chapter 7

Experimental Results and Discussion

Contents

In this chapter, the results obtained from the calibration of the response of XEMIS1 are presented and discussed. These results are a compilation of the work performed during this thesis. All aspects related to the characterization of a LXe Compton camera have been identified and addressed. Energy, timing, position and angular resolutions are studied with a monochromatic beam of 511 keV γ-rays emitted from a low activity ^{22}Na source. The evolution of the energy resolution and ionization charge yield with the applied electric field and the drift length are analyzed in detail. Transport properties of electrons in LXe such as electron drift velocity and cluster multiplicity have also been studied. Finally, in Section 7.5, we present a Monte Carlo simulation that helped to understand the effect of charge sharing on a pixelated detector, and to estimate the position resolution.

The results presented in this chapter were obtained with the last experimental configuration of XEMIS1 based on a 6 cm long TPC to increase the trigger efficiency. We used a 100 LPI metallic woven Frisch grid with an electric field ratio of 6 to achieve a 100 % electron transparency and a gap of 500 μm. For any other kind of configuration it will be explicitly indicated. Most of the results were obtained for an applied electric field of 1 kV/cm. Measurements at different electric fields are expressly mentioned. Noise determination and pedestal subtraction per pixel are performed according to the method reported in Section 6.4. Signals are selected with a $4\sigma_{noise}$ energy threshold equivalent to around 6 keV. The deposited energy and the drift time per interaction is determined with the CFD method with a delay of 720 ns (9 time channels) and an attenuation fraction of 1.5. The measured charge is corrected by gain variations as a function of the IDeF-X LXe readout electronics. Cluster formation is performed with the algorithm presented in Section 6.5.4, with a cluster time window which depends on the energy deposited per pixel. *Good events* are selected according to the offline selection cuts described in Section 6.5.5. Only single-cluster events are selected for the analysis unless otherwise is mentioned. Due to the inhomogeneities close to the Frisch grid, the first 5 mm after the grid are excluded from the analysis. Finally, the collected charge is corrected by electron attenuation using the method presented in Section 7.1.

7.1 Measurement of the liquid xenon purity and attenuation length determination

As discussed in Chapter 2, the purity of the LXe is an important factor that affects the charge collection measurement. The attachment of the ionization electrons to electronegative impurities may result in an important reduction of the collected charge, which deteriorate the energy resolution of the detector. The electron lifetime, τ, is proportional to the concentration of the electronegative impurities present in the medium [166]. Therefore, the measurement of the electron lifetime or electron attenuation length, λ, gives an idea of the purity of the LXe during the data taking. Electron attenuation length determination is also essential to correct the measured charges as a function of the position of the interaction. If the charges are not corrected, even a few percent dependence of the collected charge on the distance would degrade the energy resolution. XEMIS is designed to reduce the concentration of electronegative impurities to less than 1 ppb O_2 equivalent, to ensure the detection of very low energy deposits regardless the interaction point inside the fiducial volume. A detector

with a maximum drift distance of the order of 12 cm requires an attenuation length of drifting electrons longer than 1 m. We achieve a charge loss smaller than 10 %. An attenuation length of 1 m is equivalent to an electron lifetime of the order of 500 μs at 1 kV/cm. That is $\sim$8 times greater than the full drift time between the cathode and the Frisch grid.

To measure the electron attenuation length in our short TPC, we used the ionization signal produced by 511 keV γ-rays emitted from a ^{22}Na source. The goal of this study is to measure the evolution of the 511 keV photoelectric peak as a function of the distance from the anode. The amplitude distribution as a function of the drift time (i.e. z) was divided into 20 time intervals of equal number of events. The collected charge, Q, is then calculated by fitting the 511 keV photoelectric peak by a Gaussian function on each of the different time slices. In presence of electronegative impurities the charge Q induced at a certain distance from the anode, follows an exponential decay as a function of the drift time according to the relation:

$$Q(t) \;=\; Q_0 \, e^{\frac{-t}{\tau}} \tag{7.1}$$

where Q_0 is the total deposited charge at time $t = 0$. The attenuation length is directly calculated by fitting the photopeak vs. z distribution with the Equation 7.1.

To correct the possible attenuation inside each time interval, an iterative algorithm was used. A first value of τ was obtained from the position of the photoelectric peak as a function of the drift time. This value was used to correct the measured charge per bin, providing a second value of the attenuation length:

$$Q(t) \;=\; Q_0 \, e^{\frac{-(t-<t>)}{\tau}} \tag{7.2}$$

where $<t>$ is the average value of each slice weighted by the exponential shape of γ-ray attenuation. This process is repeated until convergence is achieved. The converged value is usually reached after three iterations, with a variation of less than 5 % between the first and last attenuation lengths. Attenuation lengths higher than 1 m have been determined after one week of circulation with the current purification system at 1 kV/cm. The scatter plot of the measured amplitude for single-cluster events as a function of the drift time at 1 kV/cm is shown in Figure 7.1. We can see that the 511 keV photoelectric peak moves to lower pulse heights for longer drift times. The black points represent the mean position of the photoelectric peak per slice and the red line is the resulting fit. The best fit results give an attenuation length of 1742.11 ± 97.58 mm at 1 kV/cm, which ensures less than 3 % of charge loss from events occurring close to the cathode.

To remove the dependence of the signal amplitude on the distance from the anode, the correction due to electron attachment to electronegative impurities is applied to the cluster energy during event reconstruction. This correction significantly improves the spectral performance of the detector. The technique reported in this section provides an accurate method for estimation of the attenuation length in a LXe TPC. The precision on the value of the attenuation length is limited by fluctuations on the measurement of the electron charge, which is related to the signal amplitude.

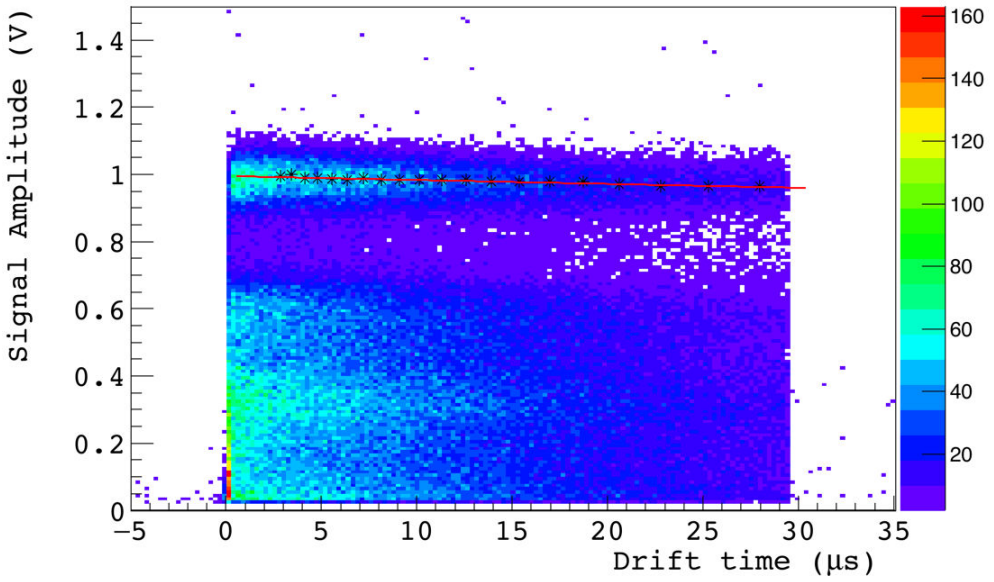

Figure 7.1 – Scatter plot of the measured charge as a function of the electron drift time for 511 keV γ-rays events at 1 kV/cm after two weeks of re-circulation. The black points represents the collected charge per slice, and the solid red line represents the fit of the collected charge to Equation 7.1.

7.2 Drift time distribution and measurement of the electron drift velocity

The drift time distribution of 511 keV photoelectric events at 1 kV/cm is shown in Figure 7.2. The majority of the interactions are produced near the anode due to the position of the radioactive source with respect to the TPC. The observed time-dependent rate follows an exponential decay consistent with the absorption of γ-ray in the medium. An exponential fit to the distribution gives a mean free path of 3.23 ± 0.24 cm, which is in good agreement with the theoretical value of $\lambda = 3.5$ cm for 511 keV γ-rays in LXe at a temperature of 168 K [13]. We emphasize that both edges of the TPC are sharply distributed, with some random events present outside the boundaries of the chamber. The beginning of the TPC is systematically corrected by using the absolute position of the anode with respect to the trigger start time.

The z-coordinate of each interaction point is determined from the electron drift time measurement referred to the light trigger. Therefore, an accurate knowledge of both electron drift time and electron drift velocity are essential for event reconstruction. The measurement of the drift time is mainly limited by the measurement method based on a CFD, and the SNR. The timing resolution worsen for low energy signals. According to the results presented in Section 6.5.4, a maximum timing resolution of 400 ns is expected for signals with an amplitude of $4\sigma_{noise}$, whereas for pulse heights larger that $20\sigma_{noise}$ the precision on the measurement of the time of CFD is less than 80 ns.

The electron drift velocity can be directly inferred from the drift time distribution depicted in Figure 7.2. By measuring the beginning and the end of the TPC we can calculate the

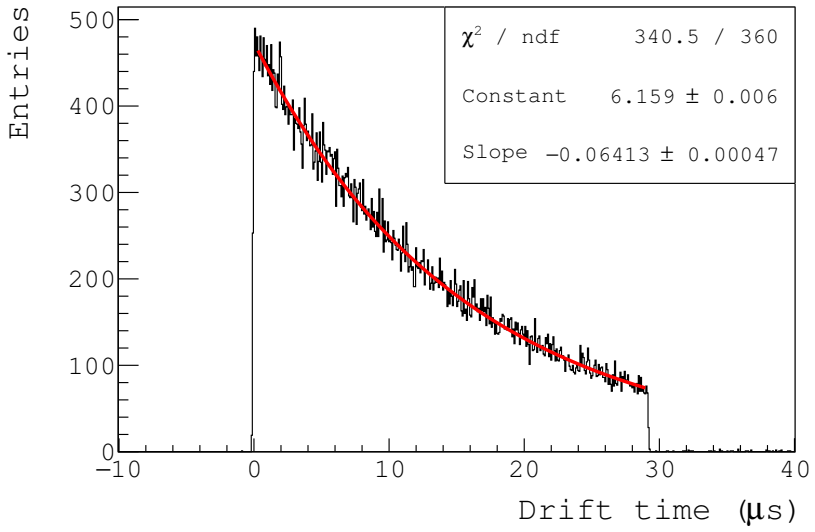

Figure 7.2 – Drift time distribution of 511 keV single-cluster events at 1 kV/cm. The solid red line represents the exponential fit to the distribution.

total collection time needed by the electrons to drift all along the drift length of the detector. The size of the TPC divided by the total collection time gives an estimation of the electron drift velocity at a given electric field. The mechanical length of the TPC between the Frisch grid and the cathode is well known, $60.8 \pm 0.5\ mm$. The error was directly calculated from the uncertainty in the measurement of the different components of the TPC (see Table 3.1). Moreover, a size variation of the order of $\sim$80 μm has been estimated for the 6 cm long TPC due to the thermal contraction of the materials at 168 K in comparison with the length at room temperature. This value has been obtained from the thermal expansion coefficients of the different material.

The position of the beginning and the end of the TPC was measured by fitting the electron drift time distribution for 511 keV photoelectric events by an Error (Erf) function: $\frac{p_0}{2}(1 + Erf(\frac{t-p_1}{\sqrt{2}\,p_2}))$, as shown in Figure 7.3. The position of the anode and the cathode was found to be at $-0.085\ \mu s$ and $29.19\ \mu s$ with a precision of the order of 40 ns and 100 ns respectively. The determination of the beginning of the TPC is also limited by the start-time correction due to the offset induced by the DAQ. The standard deviation of both fits gives also an estimated value of the timing resolution for 511 keV signals of around 44.4 ± 3.0 ns obtained as the weighted arithmetic mean between the two measurements. This value is independent of the applied electric field.

Two effects have been, however, identified that may bias the measurement of the total drift length. As seen in Section 2.3.1, the range of the primary electrons in LXe introduces a shift of around 100 μm, for an incoming energy of 511 keV, in the position of the electron cloud with respect to the interaction vertex. This is an indication that the measured position is systematically shifted from the actual interaction point, which introduces an error in the determination of the electron drift time. The difference between the real and measured position depends on the energy of the ejected electron and the incoming angle of the γ-ray. In addition, a border effect due to the extension of the electron cloud is expected at both

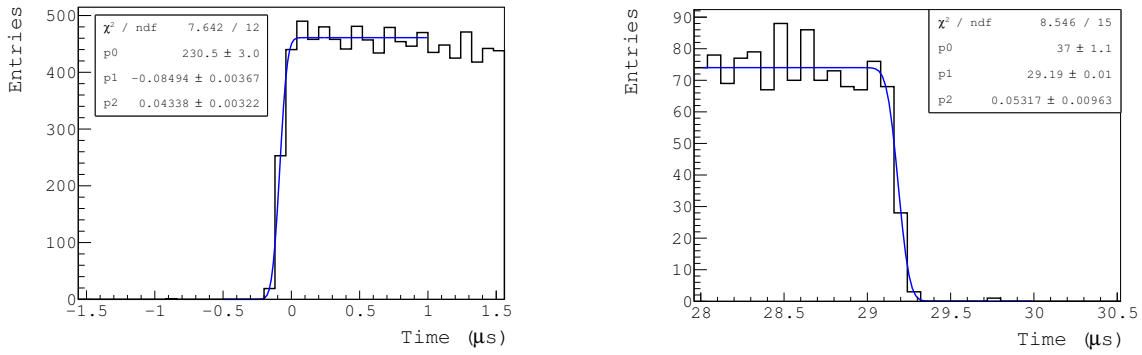

(a) Beginning of the TPC **(b)** End of the TPC

Figure 7.3 – Beginning and end of the TPC at 1 kV/cm for single-cluster 511 keV events. The solid blue lines are the Error function fit to the drift time distribution at both edges of the chamber.

ends of the TPC. Indeed, the simulation of the extension of the primary electron cloud reported in Section 2.3.1, also shows that part of the ionization cloud is not collected by the anode if the interaction occurs very close to the cathode. Some of the electrons may escape the drift region towards the gap between the cathode and the PMT. Figure 7.4 shows the collected charge as a function of the z-position obtained by simulation for the last 2 mm of the TPC. The TPC was simulated with a total length of 6 cm between the anode and the cathode. The collected charge is normalized to the total charge at infinite electric field for an incident energy of 511 keV ($Q_0 = E_\gamma/W$). At 511 keV, the measured position at the end of the TPC is always smaller than 6 cm. Only at small deposited energies, when the electron mean free path is small enough, we can measure interactions exactly at the position of the cathode. Including the error in the measured position due to the shift in the barycenter of the charge cloud, a difference of 200 μm is estimated between the measured end of the TPC and the real position of the cathode for an energy of 511 keV. Likewise, a similar effect is observed close to the Frisch grid. Comparing the experimental data to the simulation results we can deduce the absolute position of the Frisch grid. Both effects have been taken into account when calculating the electron drift velocity. The inhomogeneities in the region close to the Frisch grid due the mesh inefficiency, electron transparency and the indirect charge induction were not included in the simulation. Nevertheless, these results can be considered as a good approximation for the determination of the size of the detector.

The ratio between the length of the TPC and the time difference between the end and the beginning of the TPC results in a electron drift velocity of 2.07 ± 0.01 $mm/\mu s$ at an electric field of 1 kV/cm. This value is consistent with the results previously reported by other authors [220, 221]. Figure 7.5 shows the electron drift velocity for different electric fields from 0.25 kV/cm up to 2.5 kV/cm. The statistical error bars are too small to be visible. As expected, the electron drift velocity increases as the electric field increases, with a slower growth from an electric field of the order to 2 kV/cm. The results reported in this section where taken at a LXe temperature of 168 K. Slight variations of the electron drift velocity are expected with temperature [158].

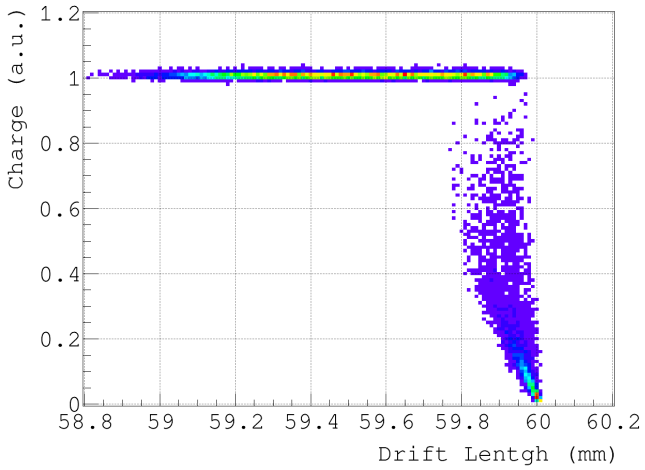

Figure 7.4 – Scatter plot of the normalized charge as a function of the z-position obtained by simulation using the results of CASINO (see Section 2.3.1).

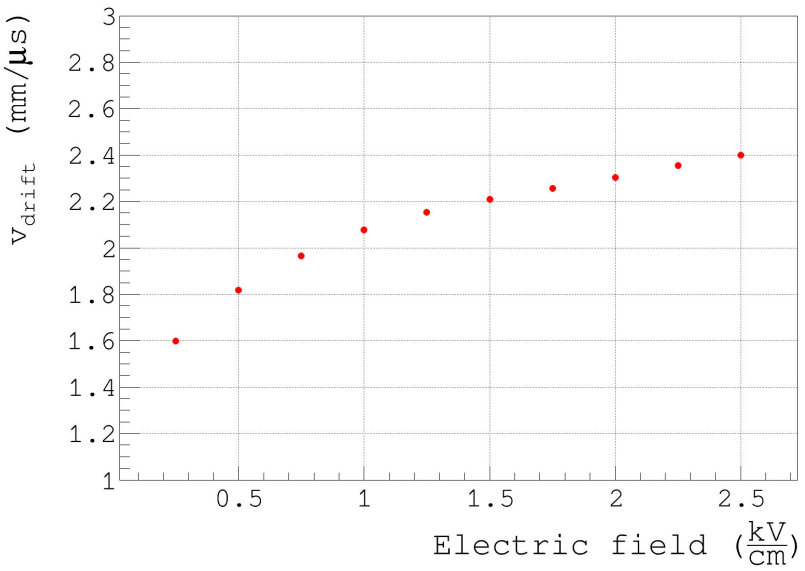

Figure 7.5 – Electron drift velocity as a function of the applied electric field at a temperature of 168 K.

7.3 Event topology and cluster multiplicity

LXe has a high atomic number (54) and high density ($\sim 2.92 g/cm^3$ at 168 K) which makes it very efficient for stopping penetrating radiations. The total mass attenuation coefficient for 511 keV γ-rays in LXe is 0.097 cm^2/g [13], corresponding to a mean-free-path of around 3.5 cm. With a detector drift length of 6 cm, the probability that a 511 keV γ-ray interacts, at least once, inside the active volume of the detector is around 82 %. Compton scattering is the dominant effect for 511 keV γ-rays in LXe with a probability of interaction of 60 %.

Due to the experimental configuration of XEMIS1, all γ-rays from the source enters the TPC with approximately the same incoming angle. At 511 keV, Compton interactions with small scattering angles are most likely ($< 45°$), which means that the deflected photon

moves forward along the direction of the incoming particle. If the scatter photon deposits its energy in the detector bulk, both interaction points will be close in the xy-plane. Moreover, due to the small mean free path of the 511 keV γ-rays in LXe, timing information is not always enough to separate both interactions. Transverse diffusion increases the lateral spread of the charge cloud during the drift. This means that the number of triggered pixels per interaction increases with the electron drift time, which hinders the separation of vertex. The complexity of the event topology requires a high granularity collecting anode. In addition, a very good spatial resolution along the three directions is necessary in order to fully reconstruct multiple-site events with several fired pixels per cluster. The number of pixels per reconstructed cluster also called *cluster multiplicity* is strongly dependent on the energy selection threshold and on the cluster reconstruction algorithm. A low energy threshold results in large cluster sizes since pixels with small charge deposits are also included in the cluster.

The cluster multiplicity along the y-coordinate as a function of drift length for 511 keV events at 1 kV/cm is shown in Figure 7.6. The slices of variable size along the drift length to keep constant statistics, where selected in the same way as reported in Section 7.1. To avoid confusion, Figure 7.7 shows an schematic design of the definition of multiplicity in the XY transverse plane.

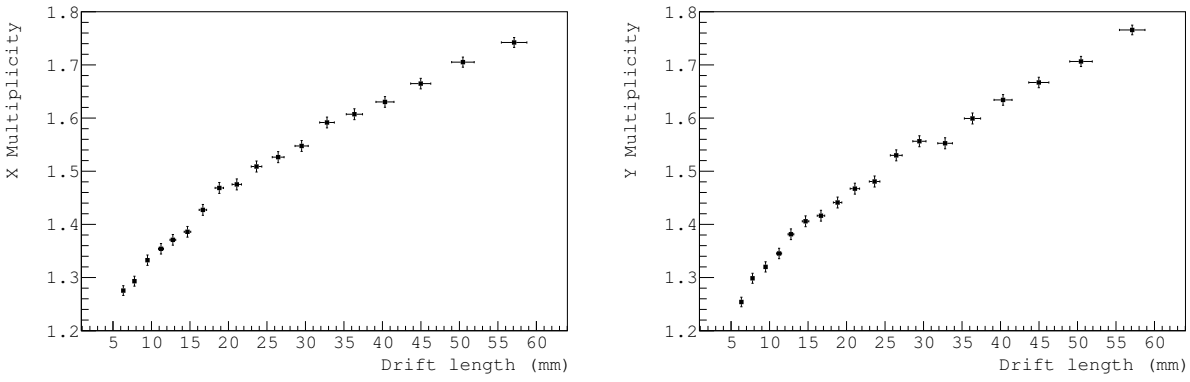

Figure 7.6 – X and Y multiplicities as a function of the drift length for single-cluster 511 keV events at 1 kV/cm and a $4\sigma_{noise}$ selection threshold. The pixel size is 3.125×3.125 mm^2.

When photons interact very close to the Frisch grid, the generated electrons are mostly collected by an unique pixel, resulting in a single-pixel cluster. The size of the reconstructed clusters increases as the electron drift time increases. This result is consistent with the spread of the electron cloud as the electrons drift towards the anode due to the transverse diffusion. In average, the number of pixels per cluster along both directions (x and y) with a signal selection threshold of $4\sigma_{noise}$, is around 1.5 with a total fraction of single-pixel clusters of 70 %. Close to the Frisch grid the total fraction of clusters with only one pixel per cluster is of the order of 50 % as we can see from Figure 7.8, and it decreases as the distance from the anode increases due to the lateral diffusion of the ionization cloud.

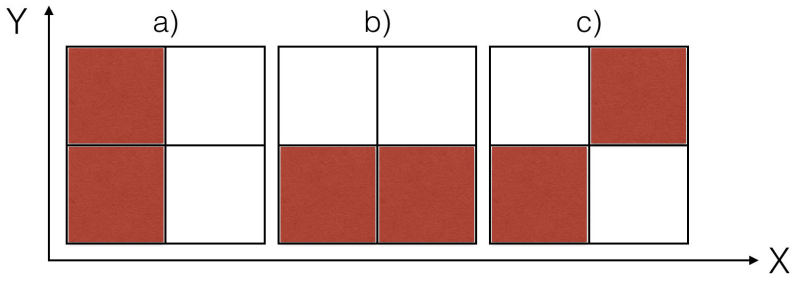

Figure 7.7 – Schematic drawing of the concept of multiplicity in a segmented anode. In the three illustrated examples the *total multiplicity* is equal to 2. In a) the multiplicity along the y-axis (*Y multiplicity*) is 2, while the multiplicity along the x-axis or *X multiplicity* is 1. On the other hand, in b) X multiplicity is equal to 2 and Y multiplicity is 1.

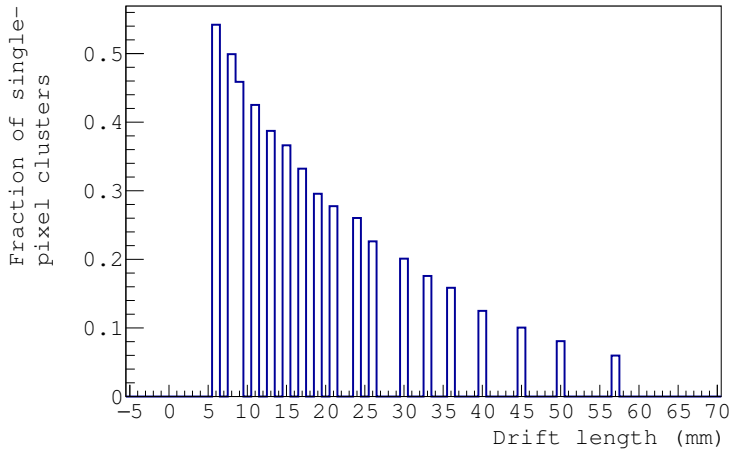

Figure 7.8 – Fraction of cluster with only one triggered pixel as a function of the drift length in the xy-plane for single-cluster 511 keV events at 1 kV/cm and a $4\sigma_{noise}$ selection threshold. The pixel size is 3.125×3.125 mm^2.

7.4 Measurement of the ionization charge yield and the energy resolution

The pulse height spectrum of 511 keV γ-rays from the ^{22}Na source has been measured at different electric drift fields between 0.25 to 2.5 kV/cm. Figure 7.9 shows the results obtained at two different field values. The photoelectric peak at 511 keV can be seen clearly, and the backscattered peak and the Compton edge are also strongly identified. The charge yield and peak width are obtained by fitting the photoelectric peak by a Gaussian function. Due to the difficulty of performing an absolute calibration of the measured charge, we assumed that the number of electrons per energy deposit for 511 keV γ-rays at 1 kV/cm is 27200 electrons [145]. This V-to-electron conversion has been used during the course of this work. The noise contribution, which is directly inferred from the analysis of a *noise run*, is negligible (about 80 electrons) and then ignored from the energy resolution determination. The contribution of the inefficiency of the Frisch grid and the pulse rise time dependence with the position of the interaction are substantially reduced by rejecting those interactions that take place close

to the grid. This leaves the intrinsic energy resolution of LXe as the dominant component. The energy resolution was deduced from the ratio between the standard deviation and the mean of the fit. For an electric field of 1 kV/cm we obtained an energy resolution of 4.92 ± 0.03 % (σ/E). The slightly non-symmetrical behavior at lower amplitude values can be in part attributed to events where the γ-ray was scattered before reaching the LXe. The γ-ray loses part of its energy during the scattering process and will therefore produce a smaller signal in the detector. If the energy loss in the interaction is small, some of these events will be included in the photoelectric peak, which will irretrievably contaminate the low energy part of the spectrum. The contribution of the scattered photons increases at lower electric fields due to the broadened distribution, and for interactions that occur close to the anode. To partially reduce the effect of the scattered events and the non linear behaviour of LXe with the energy (see next section), only the right part of the energy spectrum was fitted for the energy resolution determination.

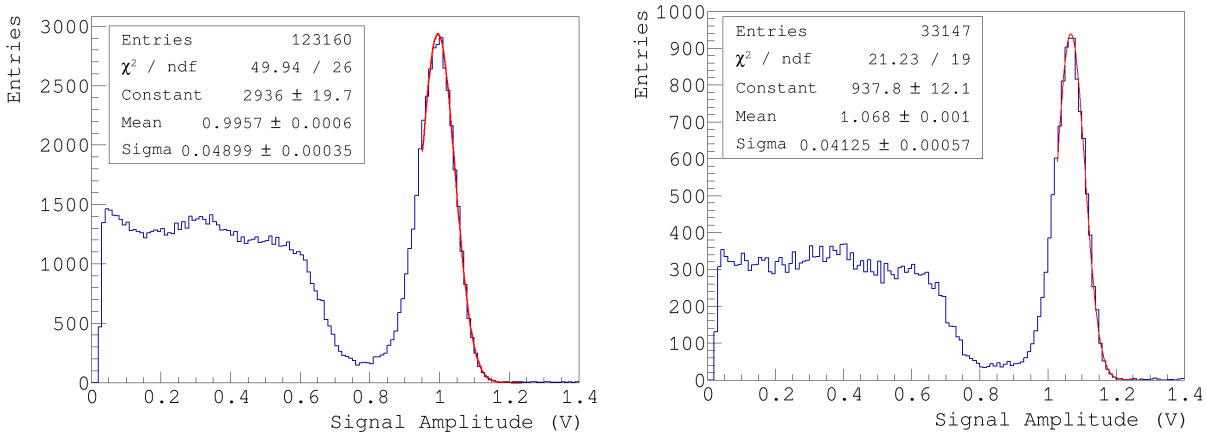

(a) 1 kV/cm **(b)** 2.5 kV/cm

Figure 7.9 – Pulse height spectra of 511 keV γ-rays at (a) 1 kV/cm and (b) 2.5 kV/cm.

7.4.1 Field dependence of ionization yield and energy resolution

Figures 7.10 and 7.11 show the ionization yield and energy resolution (σ/E) as a function of the electric field corresponding to the 511 keV photopeak. The collected charge Q was normalized to the total charge $Q_0 = 32756$ electrons calculated by dividing the energy of the γ-rays by the W-value (15.6 eV [15]). The collected charge increases with the applied electric field. This effect is directly related to the electron-ion recombination quenching produced by the electric field. As the electric field increases, more electrons escape recombination and leave the interaction site. Additionally, the improvement of the energy resolution with increasing the electric field is clearly visible in Figure 7.11. An energy resolution of 3.86 ± 0.05 % (σ/E) is obtained at 2.5 kV/cm. Associated errors were obtained by adding in quadrature the statistical error from the fit of the photoelectric peak, although there are too small to be shown in the figure.

The results reported in this section are consistent with the values measured by other authors [221]. The value of the energy resolution for 511 keV γ-rays as a function of the

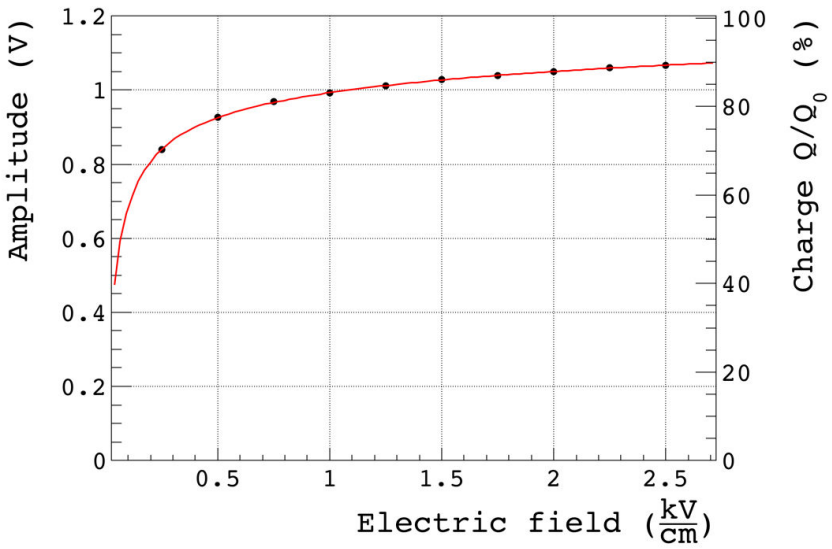

Figure 7.10 – Ionization yield as a function of the electric field for 511 keV γ-rays. The red line represents the fit to Equation 2.4.

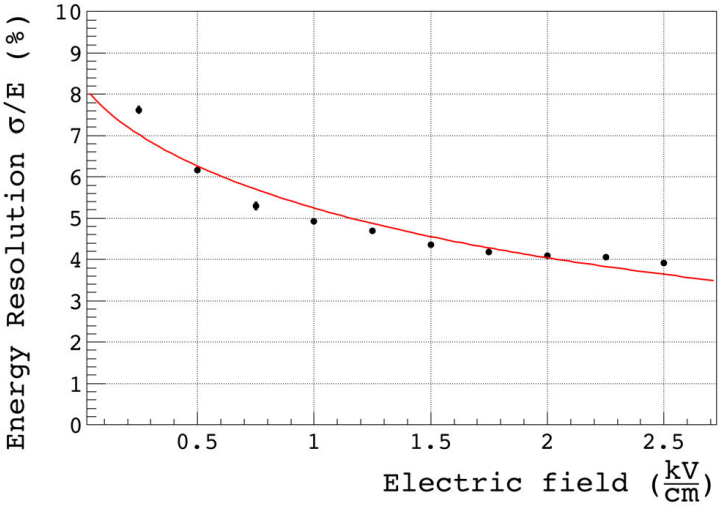

Figure 7.11 – Energy resolution as a function of the electric field for 511 keV γ-rays. The red line represents the fit to Equation 2.7.

electric field is much worse than both the Fano limit and the Poisson statistic predictions. As discussed in Chapter 2, the discrepancies between the predicted and experimental results are due to recombination fluctuations due to ionization density variations along the track of the primary electrons and the presence of δ-electrons that affect the recombination mechanism. We applied the recombination model of Thomas and Imel [142, 143] to analyze the electric field dependence of the ionization charge yield and energy resolution for 511 keV γ-rays. The collected charge and the energy resolution are fitted simultaneously with Equations 2.4 and 2.7 respectively, where E_0 is fixed to 4.2 eV [143] and E_p is the energy of the incoming particle (511 keV). The solid red lines in Figures 7.10 and 7.11 represent the simultaneous fit to experimental data. The best fit parameters are: $\xi_0 E = 4.87 \pm 0.51$, $\xi_1 E = 0.098 \pm 0.008$, $a = 0.207 \pm 0.012$ and $b = 1.705 \pm 0.04$, where E is the magnitude of the electric field.

We can conclude that the Thomas and Imel model does not reproduce our experimental data. The hypothesis that recombination limits the energy resolution in LXe seems realistic since it can better reproduce the experimental results and it points in the right direction to explain the electric field and energy dependence of the charge and light yields in LXe.

Discrepancies between the existing recombination models and the experimental data have been pointed out by many authors [44, 145, 222], which has forced a reinterpretation of the models. For example, Dahl [44] proposed a new recombination model that attempt to reproduce the results obtained for both electronic and nuclear recoils at low energies in LXe. In addition, the Noble Element Simulation Technique (NEST) has been recently developed to provide a complete modeling of the response of liquid noble gases detectors, in particular LXe, with a comprehensible explanation of both ionization and scintillation yields, based on the study carried out by Dahl [44] [222, 223]. The fundamentals of NEST is that it considers two different models to describe the recombination probability depending on energy. For *long particle tracks*, i.e. in the high energy region, they propose the Doke-Birks approach, which directly depends on the linear energy transfer (LET), dE/dx,. On the other hand, for *short tracks*, the recombination probability is calculated using the Thomas-Imel box model, which is independent of dE/dx. A more detailed description of the recombination process in LXe can be found in Chapter 2, Section 2.2.1. According to NEST, *short tracks* are considered when they are shorter than the mean thermalization distance of ionization electron-ion pairs in LXe (4.6 μm). Thus, the Thomas and Imel model dominates at energies below 15 keV.

The probability of recombination is indeed responsible of the non-linear charge and scintillation yields with energy, electric field and type of incident particle observed in LXe. The use of a two-model approach to explain the scintillation and ionization yields in LXe is justified by the experimental results observed in the low energy region. For low-energy deposits ($<$ 10 keV) the scintillation yield decreases instead of increasing. This suggests that at low energies the probability of recombination becomes independent of the ionization density and the Thomas-Imel model provides a more suitable description of the recombination rate [44]. The model provided by NEST can be implemented using a Geant4 simulation, and in the future it can be an excellent tool to test our own experimental data.

So far we have assumed no difference between electronic recoil and γ-rays. The relative ionization yield presented in this section was directly obtained by assuming an electron recoil of 511 keV after the interaction of a 511 keV γ-ray with the LXe. However, it is well known that after a photoelectric absorption a 29.8 keV K_{α_1} X-ray is emitted with a branching ratio of 85 %. This would not be an issue if the probability of the recombination was linear with the energy. However, the non-linear response of the ionization and scintillation yields in LXe with respect to the energy (see Section 7.4.2) results in a variation in the number of collected electrons depending on the type of interaction, i.e. the number of electrons collected after a photoelectric effect with the emission of a X-ray from the K-shell, differs from that measured if no X-ray is emitted. Moreover, this implies that for the same incoming particle and same incident energy, the ionization yield in LXe is different for a photoelectric absorption than for a Compton interaction where the probability of emission of a X-ray is less than 4 %. A future calibration of our detector for electronic recoils especially at low energies is therefore necessary to fully understand the performances of XEMIS1 as Compton camera.

7.4.2 Energy dependence of ionization yield and energy resolution

The charge yield and energy resolution was studied for different γ-ray energies at two different applied electric fields. The radioactive sources used in this study are ^{137}Cs and ^{22}Na with lines at 662 keV, 511 keV and 1274 keV, respectively. For the 511 keV and 662 keV energy calibrations, the sources were collimated with a lead collimator and placed at a distance of around 13 cm from the center of the TPC. Unlike for the 511 keV events, the 662 keV γ-rays from the ^{137}Cs source were triggered using exclusively the scintillation signal in LXe. To avoid the saturation of the DAQ due to the low discriminator threshold level on the PMT signals, a dead time was included to ensure a maximum trigger rate of 2 Hz.

To measure the third photon of energy 1274 keV emitted by the ^{22}Na source, the BaF_2 scintillation crystal coupled to the PMTs was displaced laterally with respect to the radioactive source as illustrated in Figure 7.12. The source was kept in front of the entrance window without any collimator, at the center of the anode but at one of the sides of the BaF_2 crystal. With this new experimental configuration, if one of the two 511 keV γ-rays is detected by the BaF_2 crystal and since the other 511 keV photon is more likely emitted with an angle of 180°, we expect that the signal on the LXe PMT is coming from the third γ-ray. The coincidence between the external PMT and the LXe PMT triggers the registration of the signal (see Section 6.2).

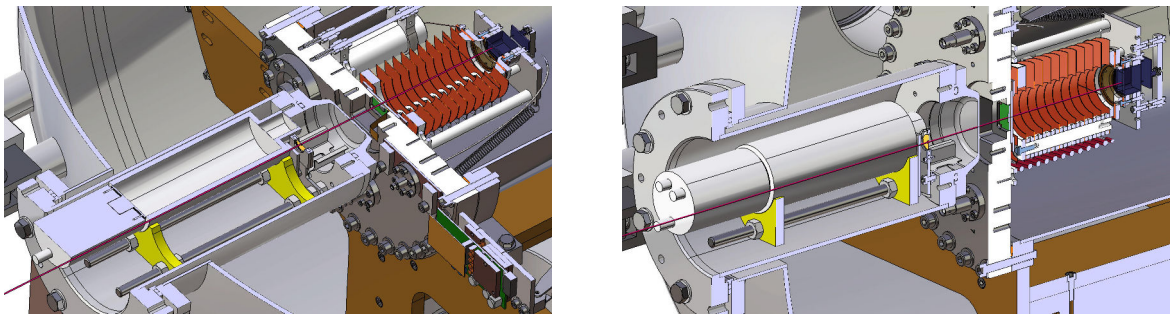

Figure 7.12 – Two different views of the experimental set-up used to detect the 1274 keV γ-ray emitted by the ^{22}Na source. The solid red line represents the axis along the center of the TPC. The source (yellow) is centered with respect to the anode (green), while the BaF_2 and PMT are laterally shifted with respect to the central axis.

The pulse height spectra for the γ-ray lines of 511 keV, 662 keV and 1274 keV at 1.5 kV/cm are shown in Figure 7.13. For the ^{137}Cs, since no coincidental trigger is used, the background was extracted from the charge spectrum. The photoelectric peak is fitted with a Gaussian function. Both pulse height and width are deduced from the results of the fit. The measured charge was corrected by electron attenuation obtained for the 511 keV events.

The measured energy dependence of the energy resolution and the charge yield at two difference applied electric fields is shown in Figure 7.14 and 7.15, respectively. The results are listed in Table 7.1. For higher energy γ-rays, the energy resolution improves. Likewise, a better energy resolution was measured at 1.5 kV/cm with regard to 1 kV/cm, although the improvement as increasing the electric field seems less marked at higher energies.

Assuming that the ionization yield is proportional to the deposited energy, the collected charge for 1274 keV γ-rays is around 60 % larger than that of 511 keV at an electric field

of 1.5 kV/cm. This difference is the result of a recombination effect between electrons and ions since it is more significant for an electric field of 1 kV/cm. In fact, the ionization yield decreases with increasing dE/dx due to an increase in the recombination rate. The energy loss dE/dx increases, in general, with decreasing energy for electrons with energies below 1 MeV [222]. Thus, the ionization yield should decrease with decreasing energy. This is consistent with our results. The statistical errors of less than 0.5 % are deduced from the fit. The collected charge vs. energy was fitted with a first degree polynomial. As expected, the ionization charge yield is non-linear with energy, being more significant at lower field strength.

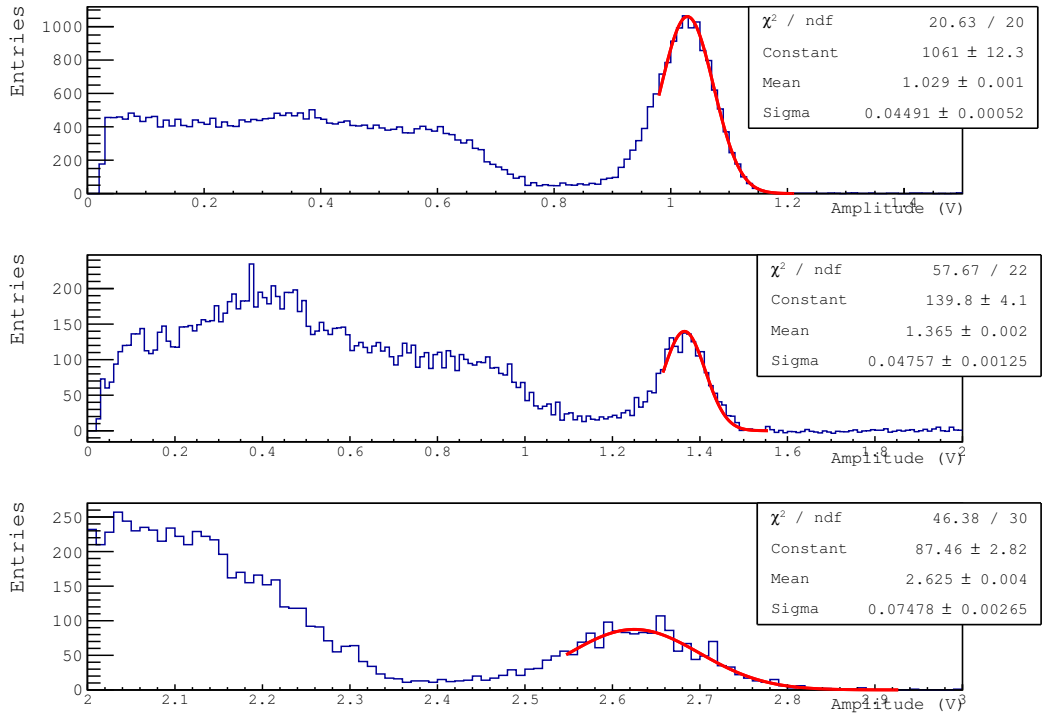

Figure 7.13 – Pulse height spectra for three different γ-ray energies from the lines of 511 keV, 662 keV and 1274 keV of ^{22}Na and ^{137}Cs at 1.5 kV/cm. The red lines represent the Gaussian fit to the photoelectric peak.

		Amplitude (V)		**Energy resolution (σ/E)**	
Source	**Energy (keV)**	1 kV/cm	1.5 kV/cm	1 kV/cm	1.5 kV/cm
^{22}Na	511	0.9957 ± 0.001	1.027 ± 0.001	4.97 ± 0.03 %	4.37 ± 0.05 %
^{137}Cs	662	1.324 ± 0.001	1.364 ± 0.002	4.04 ± 0.06 %	3.49 ± 0.09 %
^{22}Na	1274	2.553 ± 0.005	2.624 ± 0.004	2.92 ± 0.14 %	2.85 ± 0.10 %

Table 7.1 – Ionization yield and energy resolution of γ-rays in LXe at 1.5 kV/cm and 1 kV/cm.

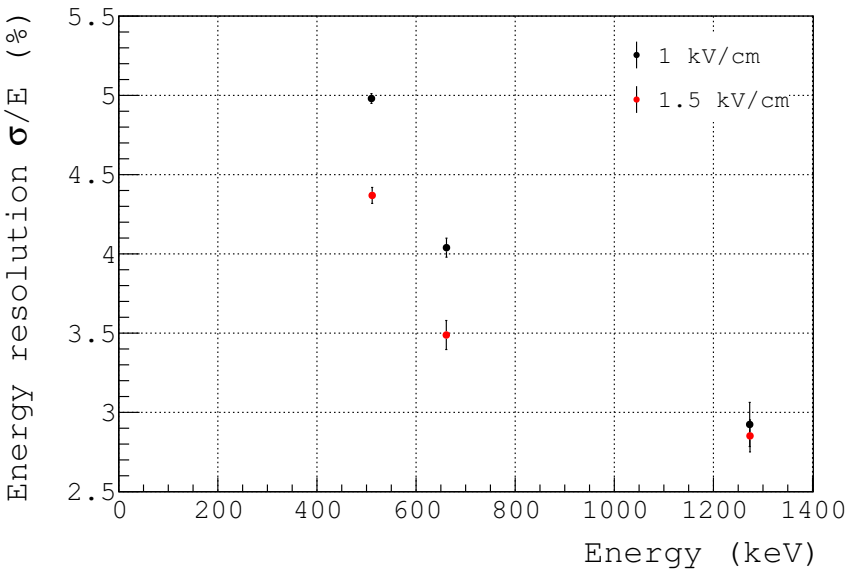

Figure 7.14 – Energy resolution as a function of the energy for two different applied electric fields.

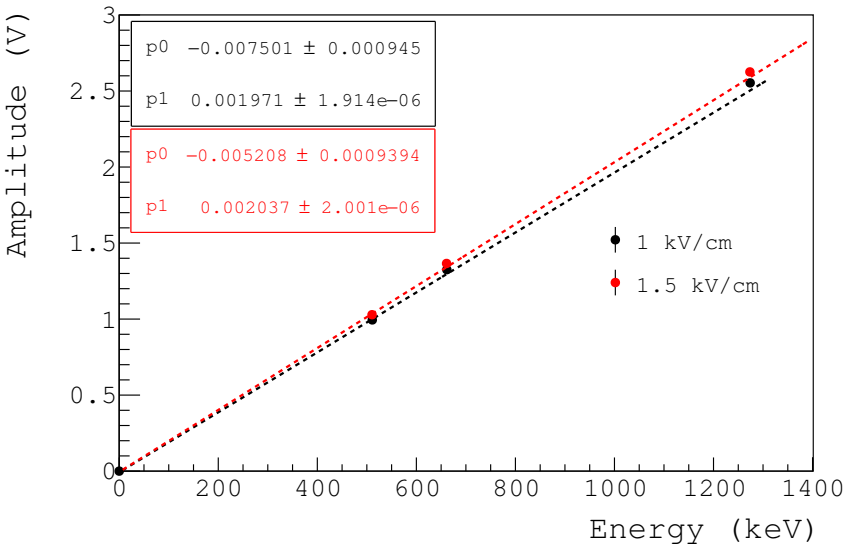

Figure 7.15 – Collected charge as a function of the energy for two different applied electric fields. The dashed lines represent the first degree polynomial fit to data considering the point at (0,0).

This non-linear response of the collected charge with the energy was also identified when two-cluster 511 keV events were selected instead of single-cluster events. We observed that the position of the photoelectric peak for 511 keV γ-rays was shifted by around 4 %, which indicated a loss of collected charge (see Figure 7.16). The two populations of events in Figure 7.16 at 0.65 V and 0.32 V, correspond to backscattering events and the following photoelectric effect, respectively.

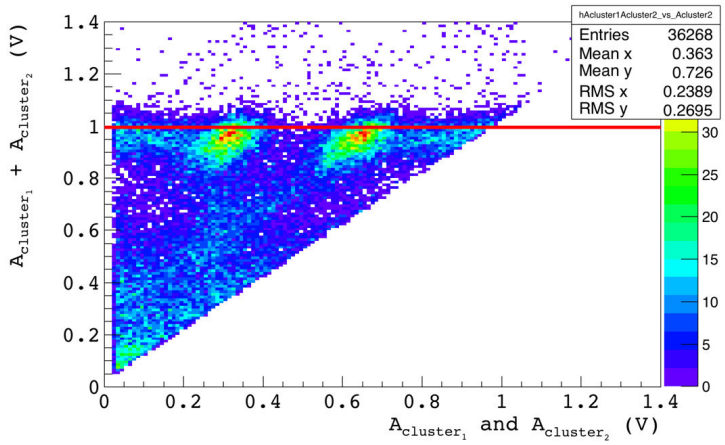

Figure 7.16 – Total charge for two-cluster 511 keV events as a function of the collected charge per clusters. A minimum distance cut between clusters of 1 cm was included in order to avoid pile-up events. The solid red line represents the collected charge for single-clusters 511 keV events.

The non-linear energy dependence of the ionization and scintillation yields for both electronic and nuclear recoils in LXe may be disadvantageous, especially at low energies [224, 225]. At energies of the order of 30 keV, a non-linearity of several tens of percent has been identified by other authors [222]. Understanding the response of LXe at low energies is of crucial importance in low background experiments such as direct dark matter experiments and neutrino detection. That is why, a precise measurement of the charge and light yields in LXe for low energy electronic recoil has become of great interest in the last few years. The calibration of XEMIS with a lower energy source is also important to extend the study of the response of XEMIS as a Compton camera. As discussed in Section 1.3.6, for an incoming γ-ray of energy 1157 keV, fair values of the angular resolution are obtained for scattering angles between $\sim 10°$ to $60°$, which translates into electronic recoils in the energy range of 40 keV to 610 keV, with a maximum in the differential cross section at the scattering angle of 26.4°. Therefore, the experimental study of the ionization yield and energy resolution of electron recoils with energies below 200 keV should be performed in the future.

7.4.3 Ionization yield and energy resolution as a function of the drift length

The ionization yield and the energy resolution as a function of the drift time for an applied electric field of 1 kV/cm are shown is Figure 7.17 and 7.18, respectively. The drift time (i.e. z) distribution was divided into 13 time intervals of equal number of events per bin. The pulse height for a given drift time is obtained from the photoelectric peak of 511 keV γ-rays of each energy spectra in each selected slice. Each pulse height spectra is fitted with a Gaussian function. The collected charge and the energy resolution are directly deduced from the mean and standard deviation of the fit. As we can see, both the charge ionization yield and the energy resolution are constant with the drift length within the uncertainties. Therefore, the attenuation length correction of the experimental data successfully removes the dependency with the drift length. A systematic error of 3 % for the energy resolution

and 1 % for the measurement of the yield have been deduced from the accuracy of the Gaussian fit to the full energy peak by changing the fit boundaries around the mean value. The systematic uncertainty is taken as the maximum difference between the most different results.

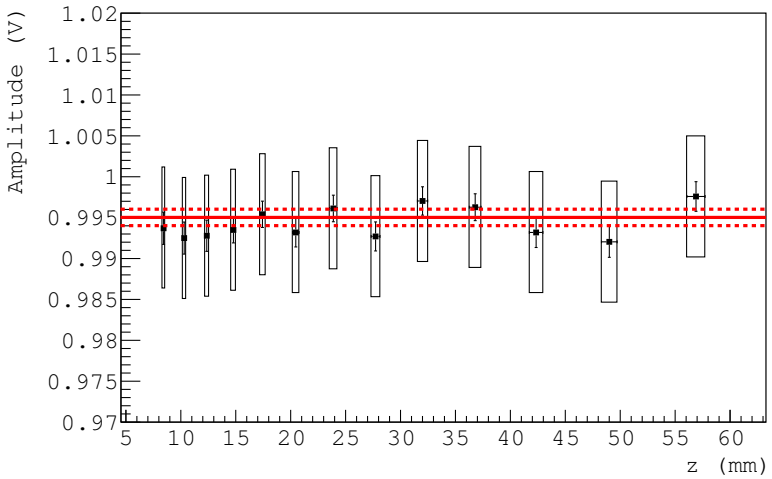

Figure 7.17 – Ionization yield as a function of the drift length at 1 kV/cm. The red solid line represents the value of the ionization yield obtained from the total charge spectrum integrated over all z-values, and the red dashed line shows the 1-σ statistical uncertainty. The error bars represent the statistical uncertainties deduced from the fit and the boxes represent the systematic uncertainties.

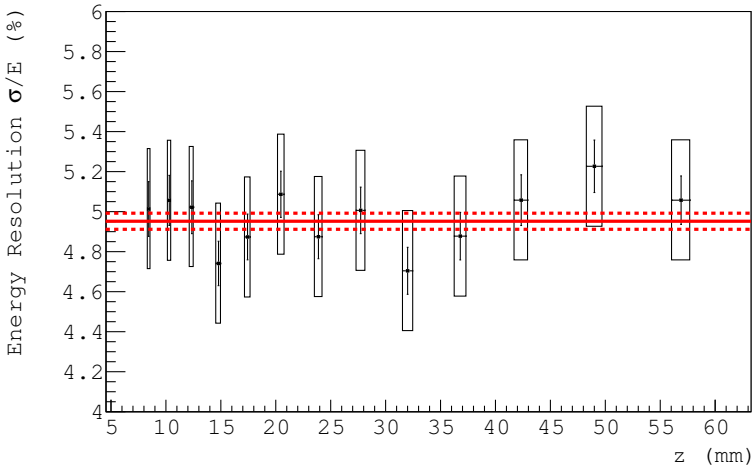

Figure 7.18 – Energy resolution (σ/E) as a function of the drift length at 1 kV/cm. The red solid line represents the value of the ionization yield obtained from the total charge spectrum integrated over all z-values, and the red dashed line shows the 1-σ statistical uncertainty. The error bars represent the statistical uncertainties deduced from the fit and the boxes represent the systematic uncertainties.

7.4.4 Charge collection efficiency

Charge collection efficiency can be defined as the ability of the segmented anode to collect all the deposited charge by a single interaction regardless the number of triggered pixels in the anode. To verify that no charge is lost depending on the topology of the events, we calculated the position of the photoelectric peak for 511 keV single-cluster events as a function of the cluster multiplicity. From this study, we obtained a difference of less than 1 % in the collected charge between one and four pixel clusters. A bigger charge loss of 1.5 % was, however, observed for clusters with a multiplicity of 3. This difference is most likely due to a bias caused by the threshold level. Based on this results, no additional correction as a function of the cluster topology is required. In addition, no significant variations in the energy resolution were observed for the different multiplicity configurations.

7.5 Monte Carlo simulation of the response of XEMIS1 to 511 keV γ-rays

In order to have a complete understanding of the detector performances, a simulation of the detector response was carried out and compared to experimental data. The simulation is focused on the charge carrier transport in LXe and on the ionization signal formation. The simulation is performed by means of a stand-alone code using ROOT. To reduce the computational time, each interaction point is simulated as a point-like cloud, i.e. the mean free path of the primary electrons is neglected and the energy is assumed to be deposited at the same point inside the detector. The goal of this study is to understand the effect of charge sharing between neighboring pixels, and to estimate the spatial resolution of the detector. A point-like source simulation also allows to study indirectly the effect of the mean free path of the primary electrons and the effect of charge induction in the neighboring pixels.

The active zone of the TPC is just defined as $12 \times 2.5 \times 2.5$ cm^3, with 64 pixel of 3.125×3.125 mm^2 defined to collect the simulated ionization signal. Neither the cathode nor the Frisch grid were included in the simulation. The distribution of the interaction position, z_0, follows an exponential decay with a characteristic linear attenuation length of 3.4 cm. In order to simulate the electron transport inside the LXe, energy fluctuations, the spread of the electron cloud due to lateral diffusion and electron attenuation are considered.

7.5.1 Electron transport simulation in LXe

A stand-alone code using ROOT has been developed during this thesis, in order to simulate the transport of electrons inside the LXe and the signal formation in the segmented anode. This program takes into account the energy fluctuations due to the charge density fluctuations caused by changes in the production of electrons along the track of the initial electron, which results in variable ionization densities. This is simulated by applying the Thomas and Imel model of charge recombination (see Section 2.2.1).

Each energy deposition is transformed to a charge electron cloud. The energy fluctuations predicted by the Thomas and Imel model are taken into account through Equation 2.7,

where σ_E represents the energy resolution. The parameters of the model ξ_0, ξ_1, a and b were deduced from the combined fit of the charge yield and energy resolution as a function of the electric field, E, for an incident energy of $E_p = 511\ keV$. The value of the parameters are: $\xi_0 = (4.87 \pm 0.51)/E$, $\xi_1 = (0.098 \pm 0.008)/E$, $a = 0.207 \pm 0.012$ and $b = 1.705 \pm 0.04$. E_0 was fixed as 4.2 eV and E_1 and E_2 are deduced from the values of a and b, being $4.55 \pm 0.73\ keV$ and $16.16 \pm 1.06\ keV$ respectively. The number of electrons per interaction is generated as a random number from a Gaussian distribution with a mean value given by the energy deposited in the interaction E_p and a standard deviation given by the value of σ_E.

The number of ionization electrons generated after the absorption of a 511 keV γ-ray in LXe is around 27200 electrons at 1 kV/cm [145]. Therefore, charge transport along the TPC electron by electron requires a very high computational time. In order to reduce the time of the simulation, we performed a simplified Monte Carlo simulation. As discussed in Chapter 2, charge carrier transport is governed by the electron drift velocity in the medium and the transverse diffusion, both of them dependent of the applied electric field. Instead of drifting electrons individually towards the anode, by knowing the initial position of the interaction z_0 ($t_{drift} = \frac{z_0}{v_{drift}}$), the number of triggered pixels is deduced from the direct projection of the electron cloud onto the anode surface according to Equation 7.3:

$$f(x,y) = \frac{1}{4\pi D_T.t_{drift}}\, exp\left(-\frac{x^2 + y^2}{4D_T.t_{drift}}\right) \tag{7.3}$$

where D_T is the transverse diffusion coefficient and t_{drift} is the electron drift time ($t_{drift} = z_0/v_{drift}$). The longitudinal diffusion along the drift direction is neglected. Each pixel with at least one collected electron is identified from the fraction of the Gaussian distribution that falls into the pixel surface. Statistical fluctuations on the number of electrons per pixel are also ignored. The electron drift time is calculated from the position of the interaction z_0 and the electron drift velocity for a given electric field strength. The number of electrons that reaches the anode is attenuated according to Equation 7.1, in order to reproduce electron attachment to electronegative impurities during the drifting process.

The simulation of the electronics and readout system is carried out separately. The electronics simulation is performed in two steps as reported in Section 4.4. In the first step, a 80-electron random noise signal is created for each pixel. Assuming a linear behavior of the electronics response, for each collected electron, the output signal of the readout IDeF-X LXe chip is generated. Moreover the parasitic signal reported in Section 6.4.2 is added to every waveform to account for its effect, especially for low amplitude signals. The position of the maximum of each pulse is defined by the initial simulated position. Thus, the effect of the mean free path of the primary electrons in neglected. The resulting signal of a given pixel is proportional to the number of collected electrons in such pixel.

The final step of the simulation consists of generating a output file with exactly the same characteristics as the experimental file obtained with the DAQ of XEMIS1. The waveform of the 64 pixels is stored into a binary file. Both experimental and simulated data are treated with the same analysis code and with exactly the same initial conditions and offline treatment.

7.5.2 Simulation results and Comparison with experimental Data

In this section we present the results obtained with the simplified Monte Carlo simulation for a point-like 511 keV electron cloud uniformly distributed over the surface of a pixel placed at the center of the anode. The comparison of the experimental drift length distribution with the simulation is depicted in Figure 7.19. An exponential distribution of the charge cloud along the length of the TPC with a slope of 3.4 cm successfully reproduces the evolution of the photoelectric interaction points with the distance obtained with the experimental data.

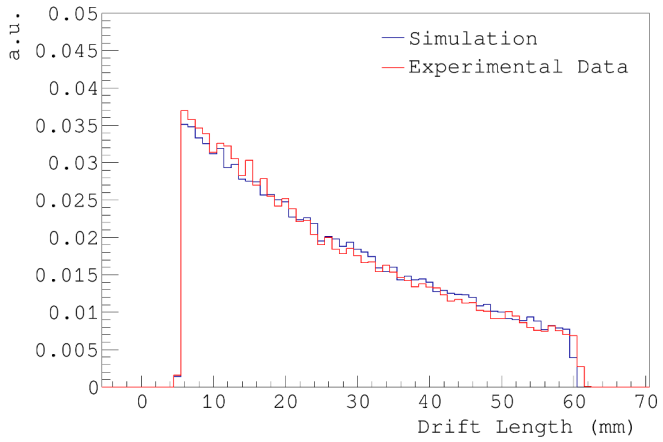

Figure 7.19 – Drift length distribution obtained with experimental and simulated data.

Figure 7.20 shows excellent agreement between the measured and simulated pixel multiplicity as a function of the drift length at 511 keV and 1 kV/cm, for different energy threshold levels. These results were obtained for a transverse diffusion of 230 $\mu m\sqrt{z\ (cm)}$, compatible with the published values [3]. The transport of electrons along the TPC was attenuated with an attenuation length of 1750 mm, similar to that measured experimentally. During data treatment same attenuation correction was applied to both simulated and measured signals. As expected, when the γ-ray interacts close to the Frisch grid, electrons drift a short distance before being collected by the anode and thus, the contribution of diffusion to charge sharing is small. The simulation also shows a remarkable coincidence of the fraction of single-pixel clusters as a function of the z-position for different threshold levels (see Figure 7.21). Close to the grid and for a pulse selection threshold of $4\sigma_{noise}$, the fraction of full energy peak events collected by a single pixel is 54 %, whereas it increases to 60 % for a $10\sigma_{noise}$ threshold.

These results indicate that charge sharing between neighboring pixels can be described by a Gaussian spread that varies with the drift distance as $\sqrt{z\ (cm)}$. Other factors such as the range of the primary electrons and the transport of fluorescence X-ray can be neglected in the simulation, at distances at least 5 mm far from the Frisch grid. Close to the Frisch grid, where the lateral diffusion of carrier electrons become small, the primary charge cloud size may become not negligible, which means that there is a non-zero probability that the electron cloud will be collected by multiple pixels, increasing the clusters multiplicity. A further simulation, where both effects are included, should be performed in the future.

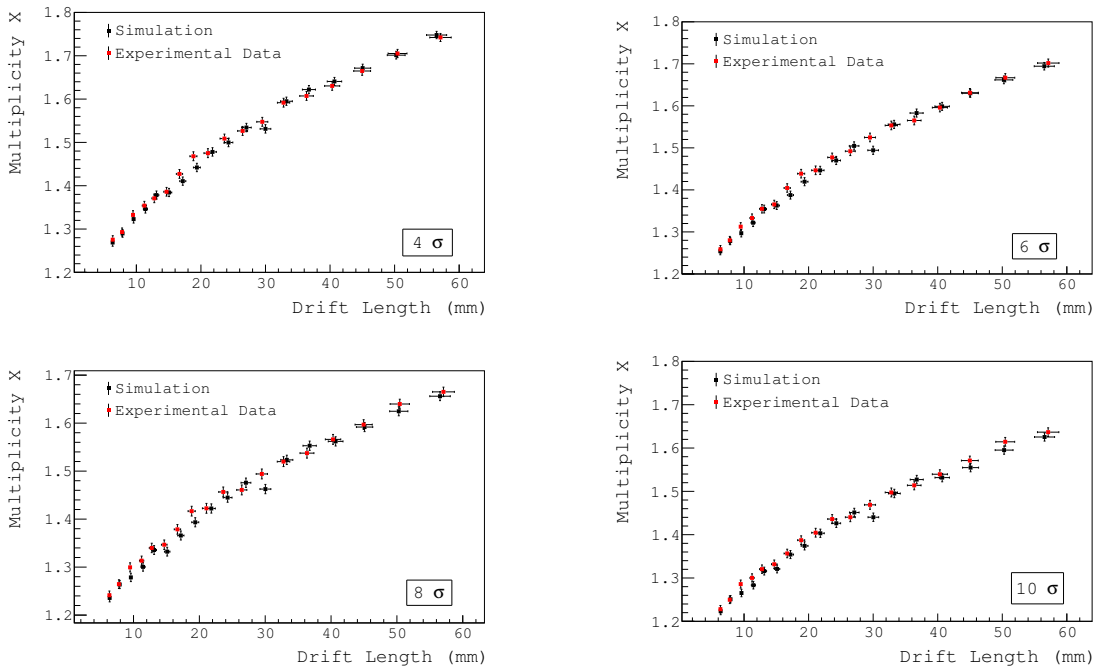

Figure 7.20 – Comparison between the number of triggered pixels as a function of the drift length for four different threshold levels along the y-coordinate obtained with experimental and simulated data.

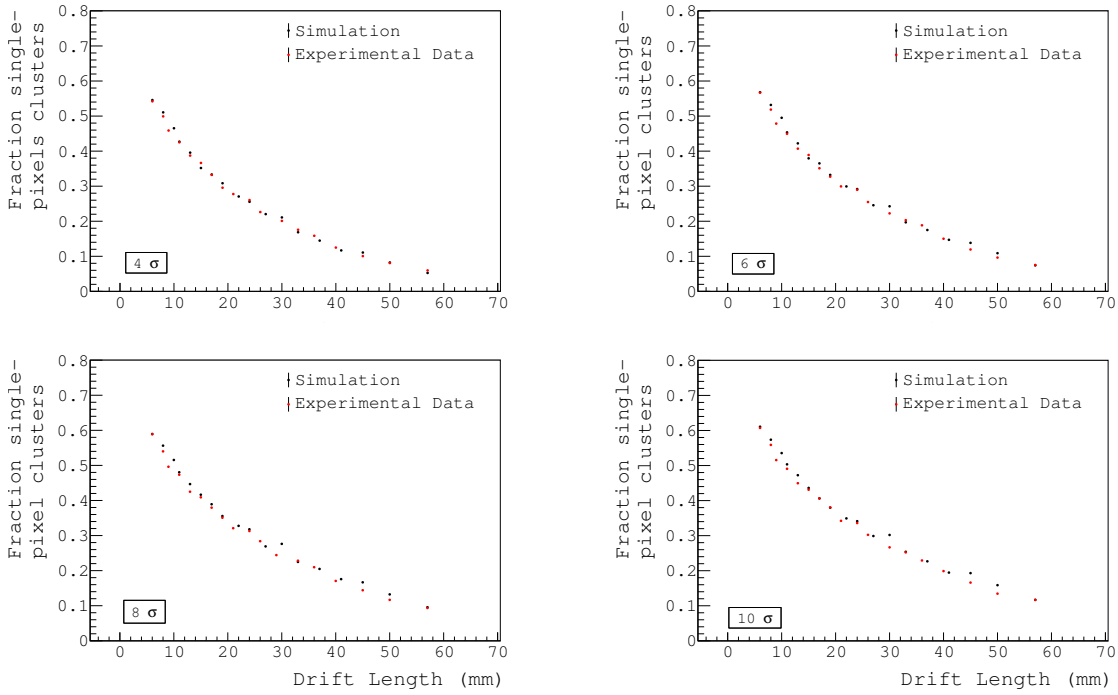

Figure 7.21 – Comparison between the fraction of single-pixel clusters as a function of the drift length for four different threshold levels obtained with experimental and simulated data.

The evolution of the time difference distribution (Δt) between the pixel of the same cluster with the collected charge has been also studied with the simulation. The results showed that the simulation of the parasitic signal is essential to reproduce the shape of the Δt distribution at low amplitude signals when all pixels are collected by the same IDeF-X LXe ASIC (see Figure 5.32). If the baseline variation was not included, a zero time difference was obtained even for amplitudes close to the threshold level. Figure 7.22 shows the comparison of the time difference distribution with the prediction from simulation. The distribution is presented as a function of the neighbors amplitude ($A_{neighbor}$), selected with respect to the pixel of reference or pixel with the maximum collected charge in the cluster. The experimental data was measured with a 100 LPI Frisch grid located at 500 μm from the anode. Good agreement between simulated and experimental data is found for low amplitude signals, whereas an underestimated value of the time difference between pixels is measured with the simulation at amplitudes higher than 15 times the electronic noise ($\sim$ 22 keV). These discrepancies are most likely due to the absence of indirect charge induction in the simulation, since the difference between data and simulation decreases at higher z-values. Similarly, the timing resolution as a function of the measured charge is shown in Figure 7.23. The simulation suggests a better timing resolution for all measured amplitudes, and better agrees with the experimental results for interactions that take place far from the Frisch grid. As reported in Chapter 5, indirect charge induction in non-collecting electrodes due to the weighting potential crosstalk between adjacent pixels, plays an important role in the formation of the ionization signal on a pixelated detector. Charge sharing would affect not only the timing distribution between the pixels of a cluster, but also the clusters multiplicity at distances close to the anode. A detailed simulation that includes all above mentioned effects should be therefore performed in order to fully understand the principle of signal formation in the vicinity of the Frisch grid.

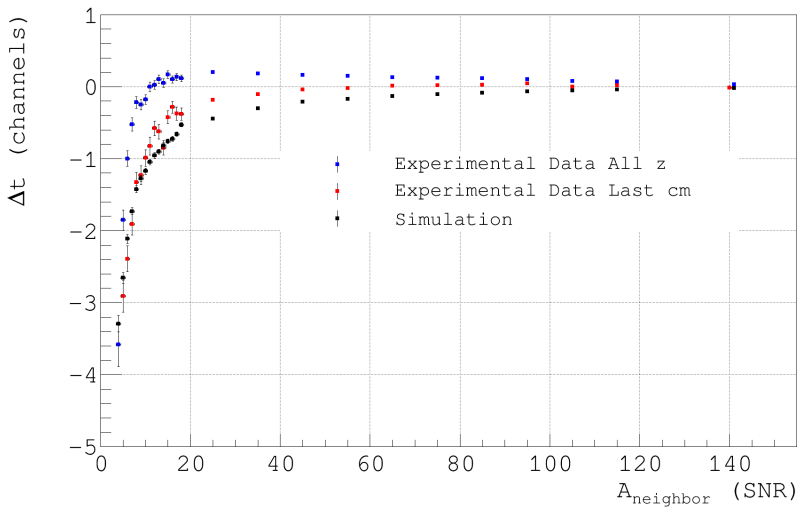

Figure 7.22 – Average time difference between the pixels of the same cluster as a function of $A_{neighbor}$. Distributions were obtained for single-cluster events with a total measured energy of 511 keV.

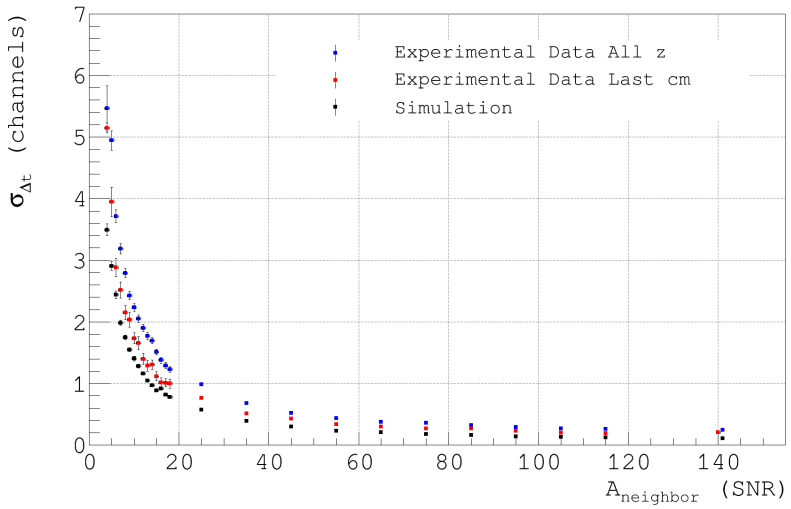

Figure 7.23 – Time resolution as a function of the collected charge in the neighboring pixel ($A_{neighbor}$). Distributions were obtained for single-cluster events with a total measured energy of 511 keV.

7.6 Position reconstruction and Spatial resolution

A cluster is defined as an interaction that is distributed over one or more pixels in the anode. Therefore, the reconstructed position of a cluster depends on the cluster's multiplicity. When a cluster is formed by just one triggered pixel, and assuming a uniform pixel response, the reconstructed position is given by the center of the pixel, and the transverse spatial resolution depends only on the effective pixel size s:

$$\sigma_{x,y} = \frac{s}{\sqrt{12}} \tag{7.4}$$

For a pixel of $3.1 \times 3.1\ mm^2$, the theoretical transverse spatial resolution is about 0.9 mm. If the charge is shared by more than one pixel, the cluster position is reconstructed from the center of gravity. With this method the cluster center is determined by weighting the position of every pixel of the cluster by the fraction of collected charge (Equations 6.4 and 6.5).

Figure 7.24 shows a histogram of the experimental reconstructed y-position with the center of gravity method. The entries at around ± 1.56, ± 4.69, ± 7.81 and $\pm 10.94\ mm$ represent the central position of the pixels, which corresponds to the reconstructed position of single-pixel clusters. Due to the applied energy threshold for hit selection and the size of the electron cloud, a minimum distance between the reconstructed position for single-pixel clusters and multiple-pixel clusters is naturally expected. The position of clusters with more than one triggered pixel should be reconstructed towards the edges of a pixel with a uniform distribution over almost the entire surface. However, with the center of gravity method, the position of multiple-pixel events is mostly distributed around the center of the pixel with a reduced number of entries between two neighboring pixels. This result is a clear example of the fact that the center of gravity method provides a wrong reconstructed position of multiple-pixel clusters.

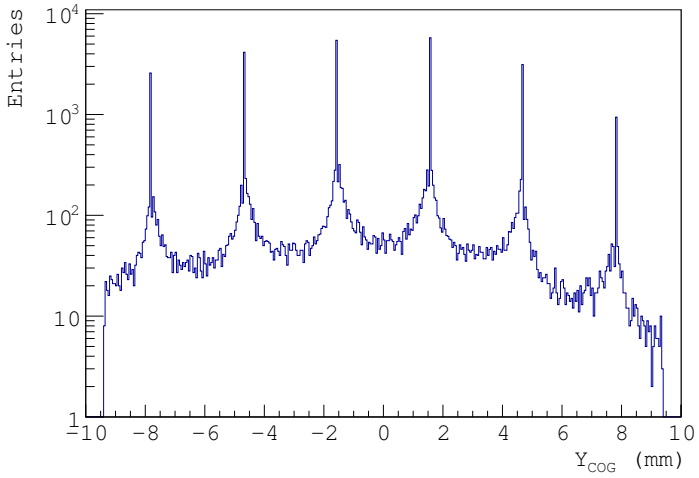

Figure 7.24 – Reconstructed position along the y-coordinate using the center of gravity method for 511 keV events at 1 kV/cm and for all drift times.

In order to study the non-linearity effect observed for multiple-pixel clusters, and to estimate the transverse spatial resolution, we used the simulated data reported in the previous section. A point-like energy deposit is uniformly distributed between the four central pixel of the anode, with a total surface equal to the size of a pixel. The position of the interaction is uniformly simulated along the length of the TPC with a transverse diffusion of 230 $\mu m\sqrt{z\ (cm)}$.

Figure 7.25 shows the residual distribution, defined as the difference between the measured position using the center of gravity method and the real position of the interaction (simulated position), $y_{cog} - y_0$, for an energy deposit of 511 keV and four different initial positions along the drift length of the TPC (z_0). The double peak structure is due to multiple-pixel clusters. For interactions close to the anode ($z_0 = 10\ cm$), the fraction of multiple-pixel clusters is small and the distribution of the residuals is almost uniform due to the dominant contribution of single-pixel clusters. As z increases, the fraction of clusters with more than one triggered pixel increases due to diffusion and thus, the spatial resolution increases, i.e. the residuals tend to zero. This effect becomes more clear in the residual distribution as a function of the reconstructed position presented in Figure 7.26. The two vertical lines at y = -1.56 mm and y = 1.56 mm correspond to clusters with only one triggered pixels. The position y = 0 corresponds to the center of the anode, positioned in the middle between the two central pixels. The pixels have a size of $3.125 \times 3.125\ mm^2$. As we can observe, as the distance from the anode increases, the deviation from zero of the residuals decreases due to the increase of the charge sharing between adjacent pixels. However, even for interactions close to the cathode the reconstructed position differs from the simulated position. This supports the hypothesis that the estimation of the transverse position as the centroid of the charged pixels is not accurate enough. Moreover, this effect depends on the electron cloud to pixel size ratio, being smaller for smaller pixel sizes. To improve the calculation of the position of multiple-pixel clusters along the x and y coordinates, we studied two possible optimization methods.

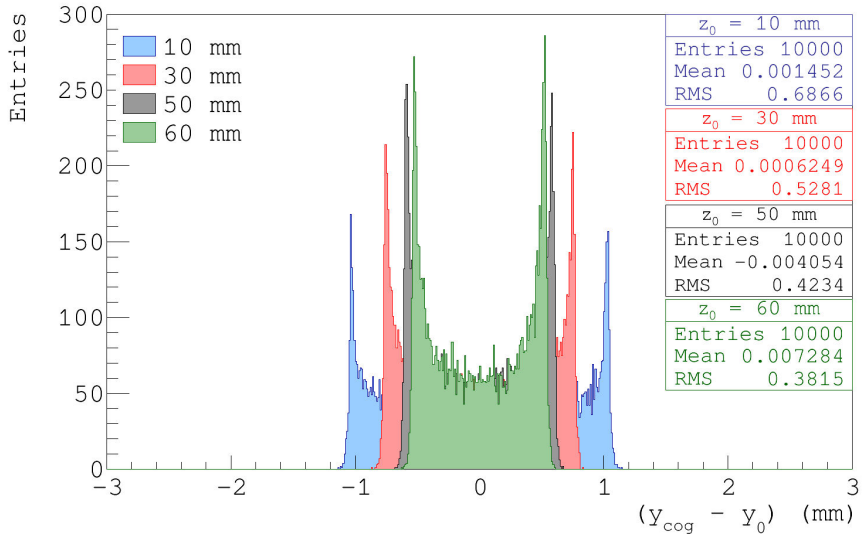

Figure 7.25 – Center of gravity residuals for four different z-positions, obtained by simulation.

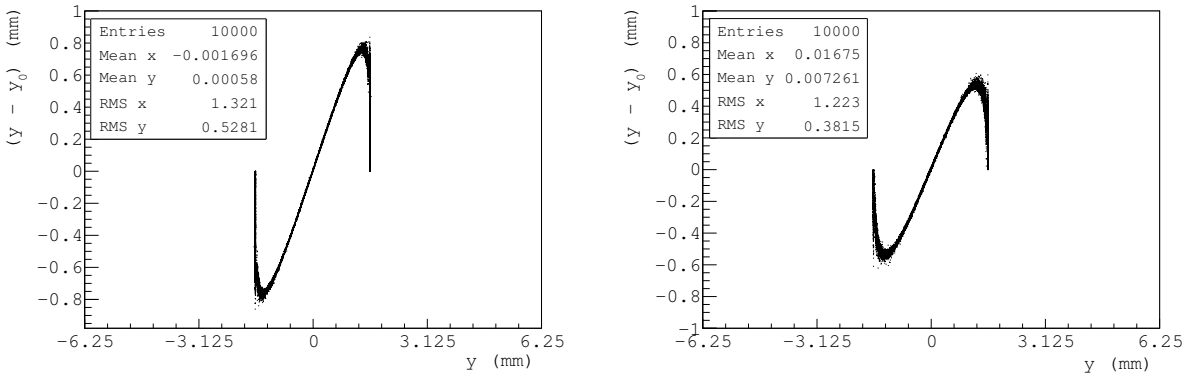

(a) $z_0 = 30\ cm$ **(b)** $z_0 = 60\ cm$

Figure 7.26 – Center of gravity residuals as a function of the reconstructed position for two different interaction points, obtained by simulation.

7.6.1 Gaussian Correction

The center of gravity method, which improves the position reconstruction by weighting the position with the charge collected per pixel, assumes that the position can be obtained from a linear interpolation of the charge distribution between two neighboring pixels, i.e. the charge sharing between adjacent pixels is assumed to be uniform, and the collected charge per pixel is uniformly distributed over the surface of a pixel. However, due to the transverse diffusion that causes the spread of the electron cloud, the charge distribution is more accurately described by a Gaussian probability distribution.

The correction from a linear distribution between adjacent pixels to a Gaussian distribution is applied to the experimental data. This correction is exclusively applied to those clusters with a maximum of two pixels in the x or y directions. Multiple-pixel clusters with more

than two pixels along the same direction are not corrected and its positions is determined by the center of gravity method. The position of single-pixel clusters is given by the center of the pixel.

The first step in the correction method consists of calculating the total collected charge per column or row depending on whether the correction is applied along the x or y direction respectively. The pixels of the anode are grouped together in strips along the perpendicular direction from which the correction is applied. The total charge per strip is calculated as the sum of all the individual charges per pixel above the energy threshold. A pixel hit contains the coordinate of the pixel in which the charge is collected. Assuming a linear system, where the probability of the highest amplitude pixel being to the left or to the right of the edge between two neighboring pixels should be equal, the center of the *left* pixel is taken as position of reference. The charge collected per cluster is approximated by a Gaussian distribution with mean value at the center of the pixel of reference, and a standard deviation given by the lateral diffusion coefficient which depends on the position of the interaction. The charge in each pixel can be therefore estimated from how much of the Gaussian distribution falls into each of the pixels (see Figure 7.27).

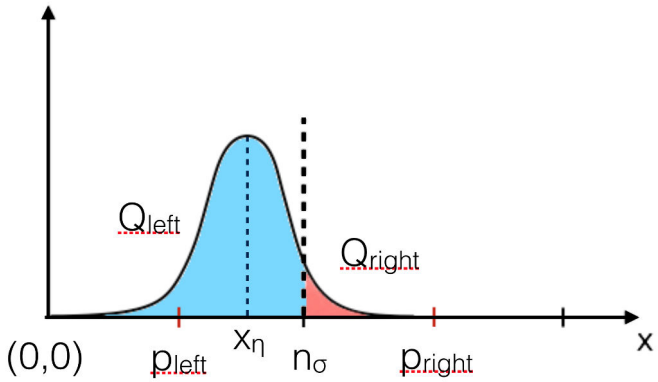

Figure 7.27 – Schematic diagram of the Gaussian correction between to neighboring pixels. p_{right} and p_{left} represent the center of both pixels, n_σ is the number of sigmas of the Gaussian distribution at the inter-pixel position, and x_η is the final reconstructed position. The standard deviation of the Gaussian distribution is given by the lateral diffusion coefficient.

The correction factor depends on the fraction of collected charge per pixel:

$$\eta = \frac{Q_{right}}{Q_{right} + Q_{left}} \tag{7.5}$$

The probability density function is calculated by integrating a Gaussian distribution over the size of the pixel, given by the Error function *Erf*. The η distribution goes from 0 when all the charge is collected by the left pixel, to 1 in the case when no charge is collected by the left pixel and the whole signal is induced in the right pixel. Assuming that the size of the electron cloud is much smaller than the pixel size, the η distribution can be expressed in terms of the probability density function according to the following expression:

$$\eta = \frac{1 + Erf(x)}{2} \tag{7.6}$$

In addition, the correction function can be expressed in terms of the equivalent number of sigmas of the Gaussian distribution that falls in the left pixel:

$$n_\sigma = Erf^{-1}(2\eta - 1) \tag{7.7}$$

Finally, the corrected positions x_η and y_η are given by Equation 7.8, where x_{IP} is the inter-pixel position:

$$x_\eta = x_{IP} - \sqrt{2}\, n_\sigma . \sigma_{diffusion} \tag{7.8}$$

In Equation 7.8, $\sigma_{diffusion}$ represents the transverse diffusion estimated as 230 $\mu m \sqrt{z\ (cm)}$. Figure 7.28 shows the experimental reconstructed y-position after the η correction. No entries are reconstructed at a certain distance from the center of the pixels due to the energy threshold effect. Moreover, the position distribution appears more uniform between pixels. This shows that charge sharing mainly occurs across the pixel borders, whereas for reconstructed positions at the pixel center no charge sharing occurs. The reconstructed position after correction is in better agreement with the expected positions. Even though Figure 7.28 is for the y-coordinate, the correction procedure is also applied to the x-coordinate.

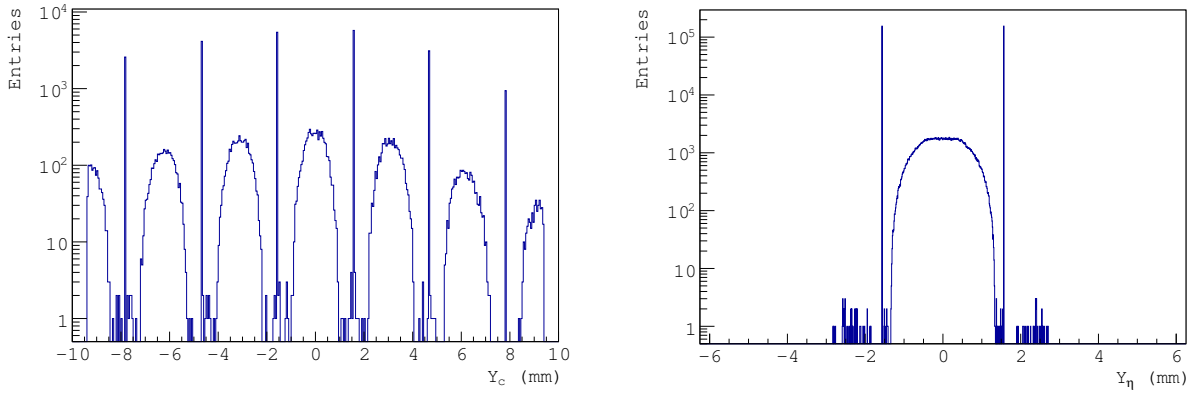

(a) Experimental data **(b)** Simulated data

Figure 7.28 – Reconstructed position along the y-coordinate for 511 keV events at 1 kV/cm for experimental and simulated data. Two-pixel clusters along the y-direction are corrected using the Gaussian method.

The accuracy of the Gaussian correction can be studied by means of the simulation. The residuals distribution as a function of the y-position is depicted in Figure 7.29. Compared to Figure 7.26, we can see a clear improvement of the reconstructed position with a flatter distribution around zero. This translates in an improvement of the position resolution. A small non-linear effect is however present between pixels, most likely due to those events with more than two pixels along the same direction which are not corrected.

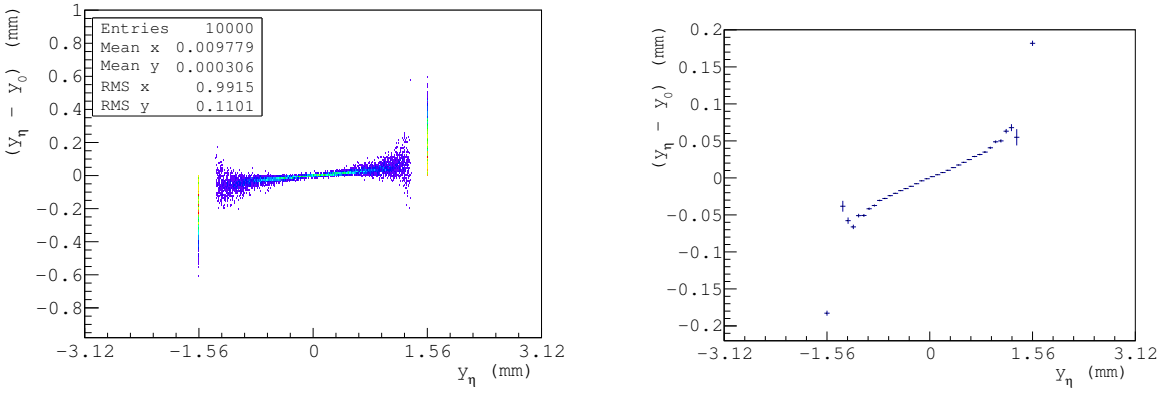

Figure 7.29 – Residuals as a function of the reconstructed position for a simulated point-like electron cloud of 511 keV at 6 cm from the anode. Two-pixel clusters are corrected with the Gaussian method. Left) Mean value of the residuals as a function of the reconstructed position. The error bars represent the RMS. The position $y = 0$ correspond to the center of the anode, located between the two central pixels of size $3.125 \times 3.125\ mm^2$.

7.6.2 Polynomial Correction

The Gaussian correction improves the reconstruction of the cluster positions with respect to the center of gravity method. However, this technique is only applicable to clusters with a multiplicity of two along the same direction. In an attempt to improve the spatial resolution, another correction method has been tested. Figure 7.30 shows the mean of the residuals obtained by simulation, as a function of the reconstructed position using the center of gravity method. The error bars represent the RMS value. The distribution is fitted by a three degree polynomial, so the cluster position can be directly deduced from Equation 7.9, where p_0, p_1 and p_2 are the parameters of the fit:

$$x_c = x_{cog} - p_0 x - p_1 x^2 - p_2 x^3 \tag{7.9}$$

The effectiveness of this correction method is illustrated in Figure 7.31. A zero value of the residuals is obtained for multiple-pixel clusters, which charge distribution falls close to the inter-pixel position. However, when the charge ratio between pixels is important, i.e. most of the charge is collected by one of the pixels, while almost no signal is collected by the other pixels of the cluster, this method is not able to properly reconstruct the position of the cluster. Nevertheless, a better spatial resolution is expected with respect to the center of gravity method.

Because the transverse spatial resolution depends on the energy (the higher the energy the higher the number of electrons in the electronic cloud and thus, the probability of firing more than one pixel increases) and the source position (the transverse diffusion is proportional to the square root of the distance between the interaction point and the anode), we studied the polynomial correction for different positions of the source inside the chamber and different energies. Figure 7.32 shows the mean values of the center of gravity residual distribution as a function of the measured position obtained for multiple-pixel clusters and six different

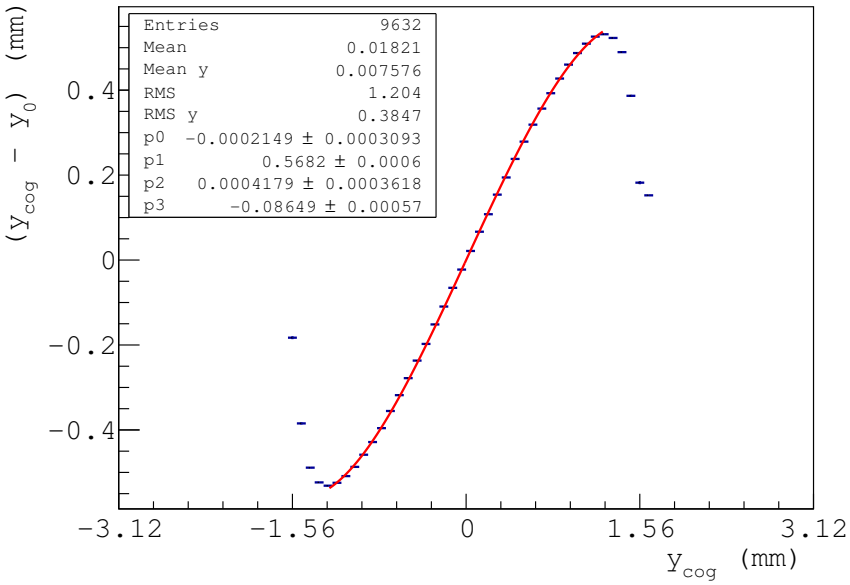

Figure 7.30 – Mean value of the residuals as a function of the center of gravity position, obtained by simulation. The error bars represent the RMS.

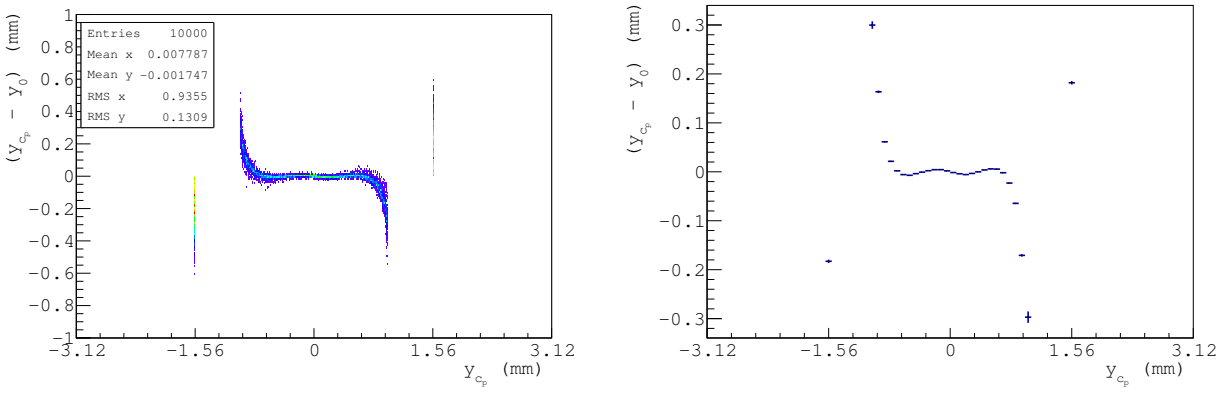

Figure 7.31 – Residuals as a function of the reconstructed position for a simulated point-like electron cloud of 511 keV at 6 cm from the anode. The center of gravity position is corrected with the polynomial correction. Left) Mean value of the residuals as a function of the reconstructed position. The error bars represent the RMS. The position $y = 0$ correspond to the center of the anode, located between the two central pixels of size $3.125 \times 3.125\ mm^2$.

z positions along the drift length. As we can see, a flatter distribution is obtained with increasing z. This effect is directly related to the spread of the electron cloud due to the lateral diffusion. However, even at high z-values the center of gravity method does not well reconstruct the position of the clusters. A different correction if therefore required as a function of the position of the interaction with respect to the anode. On the other hand, no significant variations were observed as a function of the energy (see Figure 7.33).

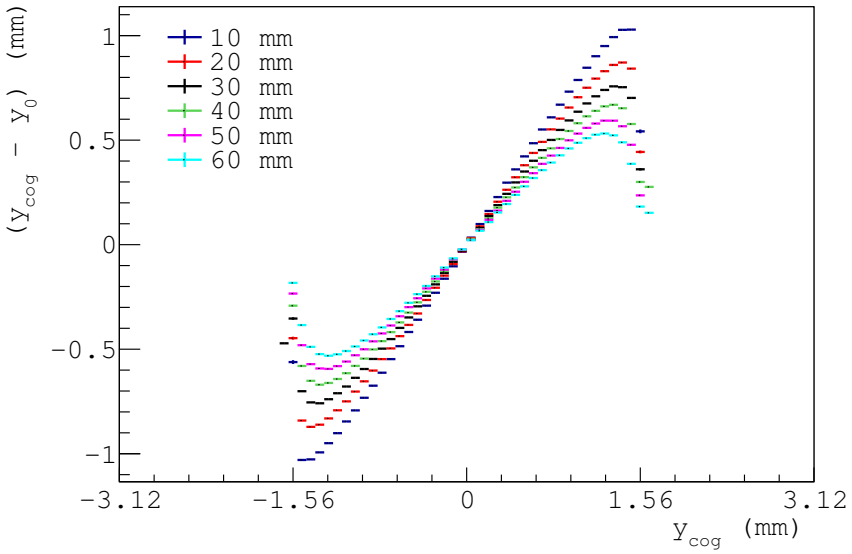

Figure 7.32 – Residuals as a function of the reconstructed position for a simulated point-like electron cloud of 511 keV for six different initial positions.

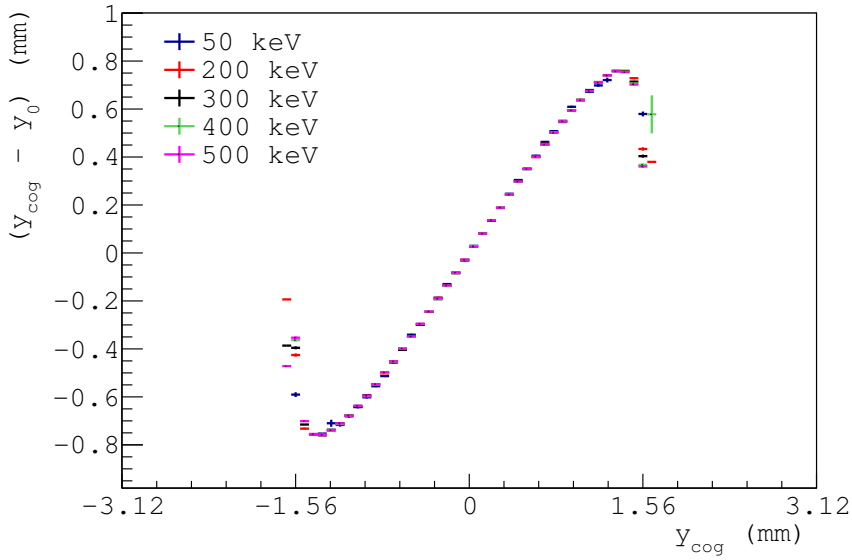

Figure 7.33 – Residuals as a function of the reconstructed position for a simulated point-like electron cloud at 3 cm from the anode, and five different energies.

7.6.3 Position Resolution

A non-linear interpolation between two adjacent pixels seems a more accurate way to reconstruct the position of an interaction inside the chamber. The spatial resolution is defined as the RMS of the 1D distribution of the residuals. Figure 7.34 shows the results obtained with the center of gravity method and the two correction methods presented in this chapter along the transverse y-axis. The results were obtained for a pixel size of $3.125 \times 3.125\ mm^2$. The position resolution is significantly improved after the correction of the reconstructed position of multiple-pixel clusters. Moreover, even though the polynomial

correction gives a flatter distribution of the residuals around zero, since it is not able to well reconstruct those interaction with the barycenter position close the center of a pixel, the Gaussian correction provides, in average, a better position resolution. In addition, since the lateral diffusion term already takes into account the position of the interaction along the drift length, the Gaussian correction is easier to apply that the polynomial correction. After correction, a spatial resolution of the order 500 μm is obtained for interaction at 10 mm from the anode, whereas 100 μm of resolution is deduced close to the cathode. The effective pixel size becomes approximately 1.73 mm and 350μm, respectively, for multiple-pixel clusters. Please note that not all possible effect, such as the contribution of the electron range, are included in the simulation. These results show that larger cluster sizes provide a better position resolution since the charge sharing between pixels allows a more accurate determination of the cluster position.

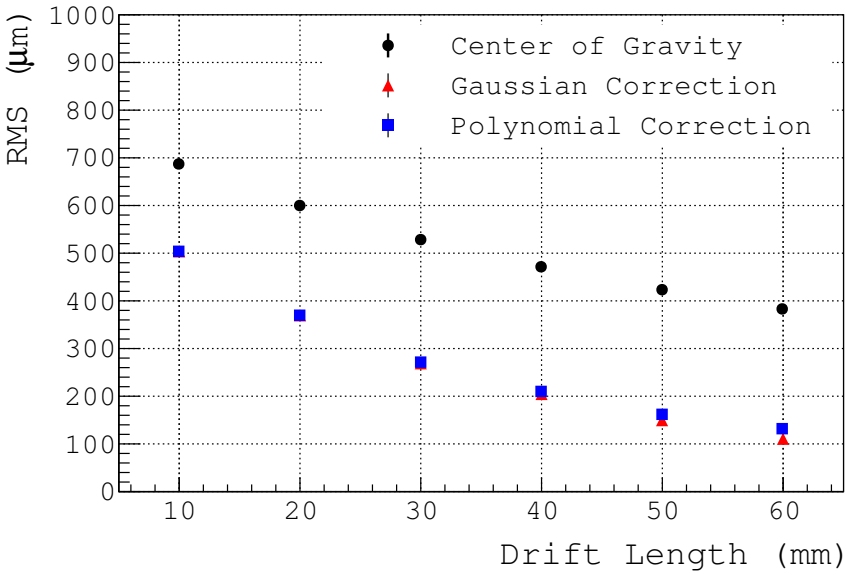

Figure 7.34 – Comparison of the spatial resolution estimated from the RMS of the residuals for the center of gravity method and the two correction methods: Gaussian and Polynomial for 511 keV γ-rays, obtained by simulation.

Figure 7.35 shows the same results for different energy values after the Gaussian correction. The position resolution increases as the energy increases, since the fraction of multiple-pixel clusters increases with the number of generated electrons. A RMS value of 700 μm was measured for a 50 keV energy deposit close to the anode, compared to 500 μm measured for the same energy but at 6 cm. We can conclude that for a pixel size of 3.125×3.125 mm^2 a spatial resolution of less than 1 mm, along both x and y direction, is expected regardless the deposit energy and the position of the interaction.

During the course of this thesis, two different pixel sizes have been tested: 3.125×3.125 mm^2 and 3.5×3.5 mm^2. As the pixel pitch increases, the position resolution also increases. For a pith of 3.5 mm we measured a resolution of $\sim$200 μm for a simulated energy of 511 keV close to the cathode (6 cm), which is around 50 % times worse that the one obtained for a 3.125 μm pixel size. This improvement decreases as the distance from the anode decreases, being of the order of 10 % at 1 cm.

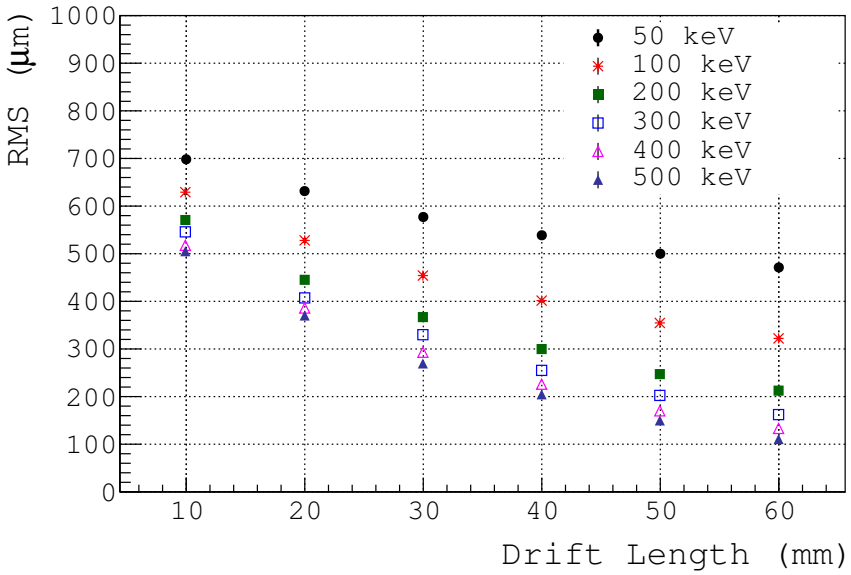

Figure 7.35 – Comparison of the spatial resolution estimated from the RMS of the residuals for the center of gravity method corrected with the Gaussian method for six different energies, obtained by simulation.

7.7 Compton Imaging and Angular Resolution

To test the tracking Compton performance of XEMIS1, the TPC was irradiated with a non-collimated ^{22}Na source placed at around 13 cm from the anode. Unlike for the 511 keV calibration, we did not use a coincidental trigger between the two back-to-back 511 keV events, but instead a coincidental trigger between the two 511 keV γ-rays and the 1274 keV photons is implemented. The third γ-ray should undergo at least two interactions inside the active zone of the TPC to start the reconstruction of the source. In this section a brief summary of the 3-γ reconstruction algorithm is carried out, and the experimental results obtained with the ^{22}Na source at an electric fields of 0.75 kV/cm is presented.

7.7.1 Compton Sequence Reconstruction

The goal of the reconstruction algorithm is to transform clusters into LORs or cones to triangulate the position of the source in 3D. The intersection between a Compton cone and a LOR allows to localize a single decay of the radioactive source. These are the basics of the proposed 3γ imaging technique. Every step of the reconstruction algorithm is illustrated in Figure 7.36. The code summarized in this section was originally developed for simulation purposes but it has already been successfully tested with experimental data [82, 123]. The step number 3 is not necessary in XEMIS1 since only one γ-ray interacts in the active zone of the TPC.

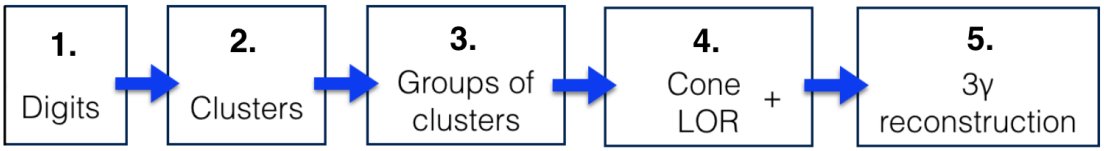

Figure 7.36 – Diagram of the steps used in the event reconstruction algorithm.

LOR Reconstruction

To proof the feasibility of the 3γ imaging reconstruction algorithm with XEMIS1, we modified the experimental set-up presented in Chapter 6. To measure the third photon of energy 1274 keV emitted by the ^{22}Na source we used the experimental set-up described in Section 7.4.2.

The BaF_2 crystal gives temporal information of the 511 keV events but they do not provide information about the position of the interaction. For this reason, we reconstruct the point of intersection using a virtual LOR traced at the position of the radioactive source, which is located at about 13 cm of the center of the TPC. For each event, a virtual LOR is generated with fixed angle θ and a random angle ϕ to enhance the intersection between the LOR and the cone. For the LOR reconstruction in XEMIS2 please refer to [121, 123].

Cone Reconstruction

The next step in the 3γ reconstruction process is to build a cone with the 1274 keV γ-ray. A cone is defined only for those events with at least two measured clusters. In the case of XEMIS1 and for an energy selection threshold of $4\sigma_{noise}$ (6 keV), most of the events ends up with only one interaction event. This result is mostly related to the small dimension of the active zone of the detector. A large fraction of the multi-site events, i.e. Compton scattering followed by a photoelectric effect results in one of the interactions depositing its energy outside the fiducial volume. This leaves to a reduce statistics for the final position reconstruction. Among the conserved multiple-cluster events, the fraction of the events with three or more interaction points is very small.

As discussed in Chapter 1 (Section 1.3.6), the aperture angle of the cone is obtained from the Compton kinematics (Equation 1.18), whereas the axis of the cone is defined from the intersection between the first and second interaction points of the 1274 keV photon (see Figure 7.37). One of the major difficulties of the method is in fact, the tracking sequence identification. Both the aperture angle and the apex of the cone depend on the deposited energy and position of the first interaction vertex, respectively, which means that a correct identification between the first and second interactions is mandatory to perform the Compton image reconstruction. Due to the complexity of the interaction point identification, as first approximation, two different cones are reconstructed for each selected group composed by two different clusters. If the group is composed by more than two clusters, all possible combinations of two hits are considered. Some criteria based on the Compton kinematics can be also applied for hit identification. A cone is accepted if the Compton kinematics is respected. Otherwise, the cone is directly rejected from the reconstruction process. If

more than one combination is a valid candidate, they can be evaluated through a statistical hypothesis test based on a Chi-square, χ^2, test. The most likely first hit in a tracking sequence is the one that gives by the smaller χ^2 value. However, there are some limitations directly associated with the Compton kinematics. In certain cases, the two possible sequences of the first and second interactions are equally valid producing an ambiguity in the hit selection. The aperture angle for which a tracking ambiguity may exist depends in fact on the energy of the incoming γ-ray. In order to minimize the presence of ambiguities in the Compton sequence reconstruction we require a very good energy and spatial resolutions.

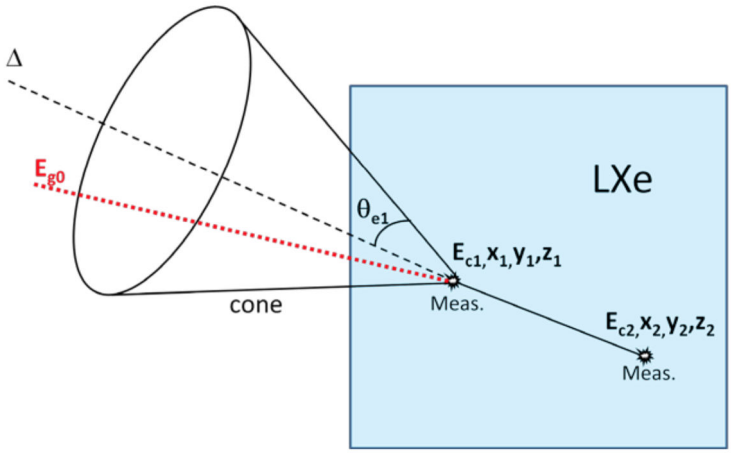

Figure 7.37 – Schematic diagram of the Compton cone reconstruction process. Figure taken from [123].

Cone-LOR Intersection

The position of the radioactive source is finally calculated from the intersection point between the Compton cone and the LOR. A schematic diagram of the cone-LOR intersection process is presented in Figure 7.38. For each event, every intersection between the LOR and all candidate cones is calculated. Cone-LOR intersection is also useful for cone selection. Those cones that do not intersect the LOR are directly rejected. Moreover, those intersection points that are outside a defined FOV are also removed from the final 3D position reconstruction. Finally, only events with one validated intersection point are kept. Otherwise, the event is dismissed.

One of the advantages of the 3γ imaging technique compared to other functional imaging techniques is the rejection of those events in which at least one of the emitted photons undergo a diffusion process before arriving into the detector. Photon attenuation is in fact one of the major drawbacks of PET imaging. In the 3γ imaging technique, the cone-LOR reconstruction is a natural method to reject an important fraction of these diffused events.

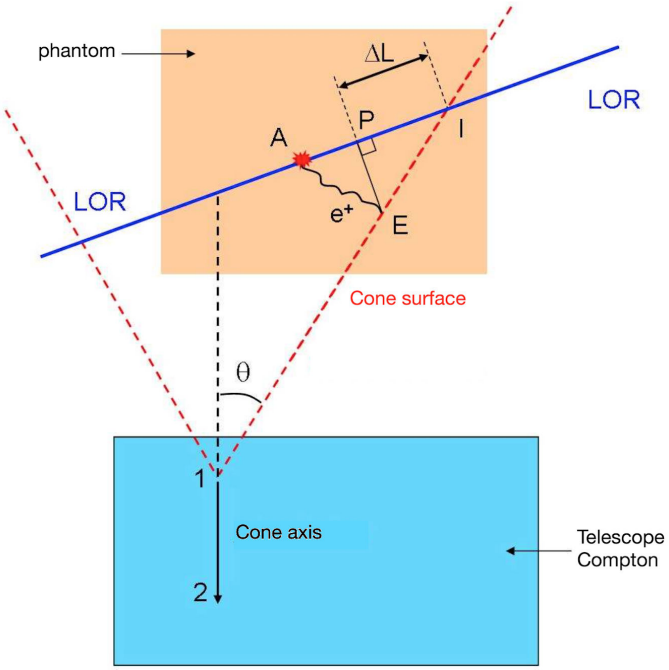

Figure 7.38 – Schematic diagram of the cone-LOR intersection, where E is the emission point, A is the positron annihilation point which differs from E due to the mean free path of the positron inside the LXe, P is the projection of the emission point on the reconstructed LOR and I is the reconstructed intersection point. The distance between P and I represents the resolution along the LOR, ΔL. Figure adapted from [121].

7.7.2 Angular Resolution

As discussed in Section 1.3.6, the precision on the intersection point (ΔL in Figure 7.38) depends on many factors such as the spatial resolution of the two first interaction points, the distance between the two vertex, the energy resolution of the first interaction point and the angle between the LOR and the cone surface. Certain selection cuts may be directly applied to these parameters in order to increase the resolution along the LOR. For example, a cut on the scattering angle can be implemented to enhance the angular resolution. As showed in Figure 1.25, a good angular resolution is expected for scattering angles between $\sim 10°$ to $60°$, which translates into an interval of the deposited energy of the first hit between 40 keV to 610 keV. Moreover, a minimum separation in 3D between the vertex of about 1.5 cm can be imposed in order to reduce the contribution of the spatial resolution to ΔL.

A more sophisticated estimation of the error in the intersection point localization, σ_I, can numerically computed using error propagation. Every contribution to the error is evaluated by infinitesimal variation of each measured parameter:

$$\sigma_I = \sum_i \left(\frac{\Delta I(v_i)}{\Delta v_i} \sigma_{v_i} \right)^2 \tag{7.10}$$

where I represents the intersection point and the index 1 and 2 represents the first and second interactions of the Compton sequence respectively and $v_i \in \{x_i, y_i, z_i, E_i\}$. A new cone is reconstructed and a new intersection point is therefore calculated. No correlation

between the measured parameters is assumed in the calculation. Moreover, we assumed that the uncertainty in the LOR reconstruction is negligible. A detailed study of the spatial resolution along the LOR was performed in [123] using simulated data. The results showed that σ_I can be indeed considered as a good estimator of the spatial resolution along the LOR, ΔL, with an almost linear relationship between both parameters.

The resolution along the LOR is directly related to the angular resolution, which in turn is one of the most important parameter of the performances of the 3γ imaging technique. The difference between the real position of the source, given by the known incident direction of the γ-ray, and the reconstructed point defines an angle α (see Figure 1.24). This angle is directly related to the resolution along the LOR. A first estimation of the angular resolution has been performed with XEMIS1. Figure 7.39 shows the α-distribution obtained for an electric field of 0.75 kV/cm. An angular resolution of 4° has been measured, which implies a resolution along the LOR smaller than 10 mm for a 5 cm distant source.

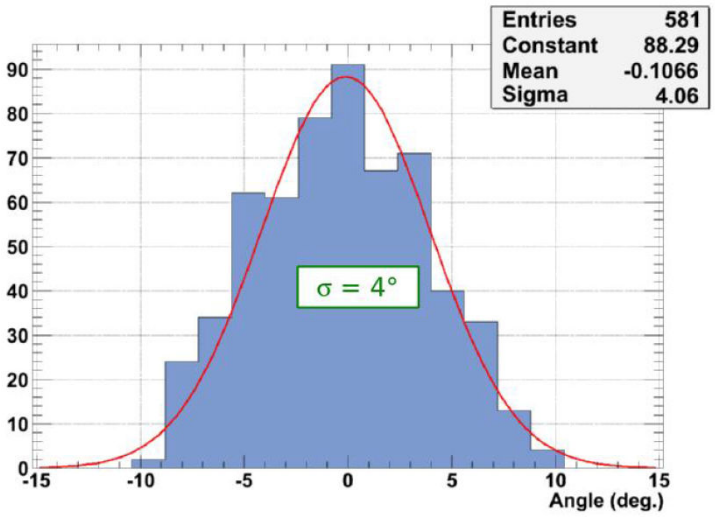

Figure 7.39 – Angular distribution obtained for a preliminary study of the intersection LOR-Compton cone for an electric field of 0.75 kV/cm. Figure adapted from [82].

Unfortunately, the design of XEMIS1 is not optimal to perform an accurate measurement of the angular resolution. Due to the small dimensions of the active zone of the chamber, the number of events with an adequate topology for the Compton sequence reconstruction is extremely reduced. Moreover, for those events with at least two interaction inside the fiducial volume, the angular resolution is limited by the distance between interactions. For this reason, no significant variations have been observed in the angular resolution with the applied electric field. A detailed simulation of the response of XEMIS2 shows very promising results for the angular resolution and sensitivity of the detector [123]. Therefore, considering the excellent performances of the detector in terms of energy and spatial resolution, we expect to obtain a very good angular resolution with XEMIS2.

7.8 Conclusions Chapter 7

In this chapter we have presented and discussed the results obtained with XEMIS1 for the performances characterization of the detector. We have addressed all main aspects related to the development of a Compton camera dedicated to 3γ medical imaging. A full understanding of the properties of LXe as γ-ray detector medium is essential for the development of a bigger scale detector, where some additional challenges will be present. For this reason, in this chapter, we have tried to study the main features related to electron transport and ionization signal extraction on a LXe TPC.

A fundamental requirement for a LXe TPC is that the electrons produced by ionization must travel undisturbed over relative long distances inside the detector. For this reason, the presence of electronegative impurity diluted in the medium should be reduced to very low levels. With the purification and circulation systems used in XEMIS1, attenuation lengths higher than 1 m are achieved after one week of circulation. The correction of the collected charges by attenuation is essential to improve the spectral performance of the detector. To this extent, we showed that after correction a constant collected charge is measured along the length of the detector within the uncertainties.

A timing resolution of 44.4 ± 3.0 ns for 511 keV photoelectric events has been estimated from the drift length distribution, equivalent to a spatial resolution of 100 μm along the z-axis. To determine the beginning and the end of the TPC two effects has been identified and taken into account. The range of the primary electrons in the LXe introduces a shift in the measured position along the z-axis. A Monte Carlo simulation showed that this deviation is of the order of 100 μm for 511 keV, which varies with the energy and the incoming angle of the γ-ray. Moreover, the extension of the electron cloud introduces a bias in the position of the ends of the TPC, that was considered for the determination of the total length of the chamber. Using the measurement of the drift time, we have determined the electron drift velocity as a function the electric field. At 1 kV/cm we obtained a drift velocity of 2.07 $mm/\mu s$, which is consistent with the reported values [220, 221].

The electric field and energy dependence of the ionization charge yield is a complicated issue that has been addressed by many authors in the last few decades, and unfortunately it is still not fully understood. A realistic model of charge recombination proposed by Thomas and Imel [142, 143] points in the good direction to explain the worse intrinsic energy resolution of LXe with respect to the Fano limit and Poisson expectations. In this chapter, we have studied the evolution of the energy resolution and ionization charge yield with the applied electric field, the drift length and γ-ray energy. The collected charge increases with the applied electric field and the γ-ray energy. These effects are directly related to fluctuations in the recombination rate along the track of the primary electrons. The obtained results are consistent with what was published by other authors [145, 146], showing some discrepancies with the theoretical model of Thomas and Imel. Moreover, we observed a non-linear response of the collected charge with the energy, being more significant at lower field strength.

The non-linearity of the ionization charge yield with the energy is an important subject that should be studied more in detail in the future. A small deviation of around 1 % was found at high energies (1274 keV). However, a higher deviation of tens of percents is expected

at low energies($\sim 30\ keV$), which may impact the Compton sequence reconstruction. It should be pointed out that the calibration presented in this chapter was made for γ-rays as incident particles. The non-linear response of the ionization and scintillation yields in LXe with respect to the energy results in a variation in the number of collected electrons depending on the type of interaction. The X-ray emission from the K-shell with a branching ration of 85 %, implies that the number of ionization electrons produced after a photoelectric absorption differs from the one produced after a Compton effect. This is especially important for Compton sequence reconstruction. The calibration of XEMIS for electronic recoils, in particular at energies below 200 keV, should be performed in the future to extend the understanding of the response of the detector.

We also observed an improvement of the energy resolution with the electric field strength and the energy of the γ-ray. Both effects are also related to the electron-ion recombination rate. For an electric field of 2.5 kV/cm we measured an energy resolution of 3.9 % (σ/E) for 511 keV γ-rays. For an energy of 1274 keV and an electric field of 1.5 kV/cm, an energy resolution of 2.85 % (σ/E) is achieved.

Cluster multiplicity has been studied as a function of the drift length for 511 keV events at 1 kV/cm. We showed that when photons interact very close to the Frisch grid, the generated electrons are mostly collected by an unique pixel, whereas as the electron drift time increases, the number of triggered pixels per cluster also increases. These results are consistent with the spread of the electron cloud as the electrons drift towards the anode due to the transverse diffusion. The evolution of the clusters multiplicity with the z-position has been successfully reproduced by a Monte Carlo simulation of the transport of electrons inside the TPC. The variation of the number of triggered pixels per clusters and the fraction of single-pixel clusters are remarkably well reproduced by simulation as a function of the energy selection threshold. These results indicate that charge sharing between neighboring pixels can be easily described by a Gaussian spread that varies with the drift distance as $\sqrt{z\ (cm)}$. The time difference distribution of the pixels of the same cluster is, however, not fully reproduced by the simulation. Indirect charge induction in non-collecting electrodes due to the inhomogeneities of the weighting potential between adjacent pixels, the range of the primary electrons and the X-ray emission should be included in a future simulation to account for other effects that affect the process of signal induction on a detector of the characteristics of XEMIS.

The presented simulation has also helped to estimate the transverse spatial resolution. The spatial resolution on a pixelated detector is limited by single-pixel clusters, where the position is irremediably reconstructed at the center of the pixel. The position of multiple-pixel clusters is, in general, reconstructed by means of the center of gravity method, that used the collected charge per pixel to weight . However, this method is not a good estimator of the real position since the size of the pixels is bigger that the electron cloud. To improve the spatial resolution along the x and y axis, two correction method have been tested with the simulation. The Gaussian correction method, that assumes a Gaussian distribution of the charge cloud, provides better results. For an anode segmented in pixels of size $3.125 \times 3.125\ mm^2$, we found a position resolution of the order of 100 μm for an energy deposit of 511 keV at 6 cm from the anode. The spatial resolution decreases for low energies and small z-position. We conclude that for a pixel size of $3.125 \times 3.125\ mm^2$ a spatial resolution of less than 1 mm,

along both x and y direction, is expected regardless the deposit energy and the position of the interaction.

Finally, we presented the Compton reconstruction algorithm used to triangulate the position of the source in 3D. This algorithm was originally developed for simulation purposes showing very promising results [121, 123], but we have showed that it can be successfully applied to experimental data. An angular resolution of 4° is measured for an electric field of 0.75 kV/cm. Besides the constraints of XEMIS1 to perform the Compton sequence reconstruction, we have showed the potential of the 3γ imaging technique.

Conclusion and Outlook

The rapid evolution of the technologies associated to the development of liquid xenon-based detectors in the past few years, has made this fascinating material one of the principal choices as radiation detection medium in many state-of-art experiments, in the fields of particle physics, astrophysics and medical imaging. The use of liquid xenon for medical applications is not new. In fact, the first attempts of developing a device for functional medical imaging date back from the 1970s, and from the very beginning, the potential of the use of liquid xenon as detection medium was clearly revealed.

In the contest of modern medicine, new challenges continuously ahead with the same purpose of increasing the quality of life and welfare of the patients. For example, in the recent years, the radiation exposure of patients during a medical exam has become a hot topic. It is around this subject that many groups from around the world pursue efforts to improve and develop new technologies in nuclear medicine. The 3γ imaging technique is a clear example of an innovative imaging modality, which main purpose is to reduce the activity injected to the patient to unprecedented limits. The development of the 3γ imaging technique requires the collaboration between different research fields from the development of a new detector system and technologies associated with the used of liquid xenon, through new radiopharmaceuticals labeled with Sc-44 to the development of new reconstruction algorithms to provide a direct 3D reconstruction of the distribution of the source inside the patient. The fundamentals of the 3γ imaging technique are based on the reconstruction of the position of the radioactive source by applying Compton scatter kinetics to the three γ-rays emitted by a specific 3γ-emitter radionuclide. Compton imaging has proven to be an extremely useful tool in γ-spectroscopy, and it seems also a perfect candidate for medical applications.

The experimental demonstration of the potential of the 3γ imaging has been performed with a small dimension Compton camera, XEMIS1, that holds 30 kg of liquid xenon. In this thesis, we have presented, studied and discussed the main performances of XEMIS1. This work is mainly focused in the detection of the ionization signal in liquid xenon and the device optimization. To this extent, we have described in Chapter 2 the main steps related to the production, transport and detection of the ionization electrons in liquid xenon. The discussion is supported by some experimental results reported by other authors and by our own. The studies presented here are complementary to those performed by T. Oger [115], Grignon [121], Hadi [123]. A detailed description of the experimental characteristic of XEMIS1 is carried out in Chapter 3. The basic cryogenics stages involved in setting up de detector before a data taking run, such as xenon liquefaction and liquid xenon purification and circulation processes are also presented in this chapter.

The main challenge associated with the development of a detector of the characteristics of XEMIS is that it requires information about the deposited energy, position and drift time of every individual interaction inside the detector with very good energy and spatial resolutions, both of them necessary for the Compton sequence reconstruction. These criteria demand an

extremely low electronic noise. We have achieved an electronic noise below 100 electrons thanks to an ultra-low noise front-end electronics, IDeF-X LXe, which has been adapted to work at the liquid xenon temperature. The ASIC shows good performances in terms of gain linearity (in the energy range up to 2 MeV), electronic noise and baseline stability. A detailed study of the response of the IDeF-X LXe chip is presented in Chapter 4. In addition, we presented the simulation of the output signal of the IDeF-X LXe chip, that includes a precise simulation of the electronic noise. The simulated data have been extremely useful to study the optimal threshold level for the data acquisition and to optimize the measurement of the amplitude and drift time of the registered signals. A constant fraction discriminator provides the best values in terms of timing and amplitude resolutions. These results have been used in the development of a new front-end electronics called XTRACT. This new ASIC is especially developed to measure the charge and time of the ionization signals in the second prototype of a liquid xenon Compton camera developed for preclinical applications.

The main characteristics of this new camera called XEMIS2 are also presented in Chapter 3. This new prototype is a monolithic liquid xenon cylindrical camera that holds 200 kg of liquid xenon. The geometry of XEMIS2 is optimized to provide a full coverage of the small animal thanks to its 24 cm axial field of view. To detect both the ionization signal and the VUV scintillation photons produced in the liquid xenon after the interaction of ionizing radiation, the active volume of the detector is covered by 380 1" PMTs and two end segmented anodes with a total number of 24000 pixels. To meet the requirements of a detector designed for future clinical applications in hospital centers, particular emphasis was paid in the development of a very compact liquid xenon cryogenics infrastructure and a fast data acquisition system. The work presented in this document has contributed to substantial advancements in our understanding of the detector performances, which has lead to the final design and construction of this second prototype.

One of the most delicate part of the experimental configuration of XEMIS is the Frisch grid. It is obvious that the incorporation of a grid between the cathode and anode is necessary to remove the position-dependence of the collected signals. However, some not so obvious effects are associated with the use of a gridded ionization chamber. Charge loss is one of the major constraints that may limit the spectroscopy performances of a detector. During the development of XEMIS, all the aspects related to the loss of collected charge have been minimized. Electron attachment to electronegative impurities has been reduced thanks to an advanced purification system presented in Chapter 3. Attenuation lengths higher than 1 m are achieved after a short circulation period, which translates into a good charge collection uniformity along the drift length after correction. The method used to estimate the attenuation length is presented in Chapter 7. The loss of charge carriers due to recombination can be reduced by increasing the applied electric field. During this work, the performances of XEMIS1 have been tested for different electric field strengths from 0.25 kV/cm to 2.5 kV/cm. Another aspect that affects the charge collection is the transparency of the Frisch grid to electrons. A good electron transparency requires an adequate bias of the electrodes. However, this depends not only of the experimental configuration of the TPC, i.e. the gap distance between the grid and the anode, but also on the geometrical characteristics of the grid. The pitch of the grid as much as its thickness affect the applied voltages. Larger gaps require higher bias voltages to obtain the same electron transparency conditions. On the contrary,

a smaller electric field ratio between the drift region and the gap is necessary with a more open grid. A more detailed description of the electron transparency of a Frisch grid and the experimental results obtained with XEMIS1 are presented in Chapter 5.

The defective shielding of the Frisch grid causes that electrons start inducing a signal in the anode before they actually pass through the grid. This affects the shape of the processed signals and introduces a certain dependency of the shape of the pulses with the position of the interaction. Better performances in terms of efficiency are achieved for higher gap distances and smaller pitch grids. The necessary requirements to reduce the inefficiency of the Frisch grid oppose to those necessary to increase the electron transparency. Therefore, an exhaustive study is required to achieve the best possible compromise between both effects. The results presented in Chapter 5 provide experimental evidence of the impact of the Frisch grid on the collected signals. The study has been performed in four different kind of meshes and two different gaps.

We presented a simulation study that helped to understand the effect of charge induction on the non-collecting pixels due to the weighting potential cross-talk between neighboring pixels. We showed that the induced transient signal on the adjacent pixels introduces a bias on the amplitude and time of the shaped signals. This effect becomes more important for smaller pixel sizes compared to the gap distance. The results obtained by simulation confirm that the time difference observed between the triggered pixels of the same cluster on the real data. This time difference considerably hinders the clusterization process and increases the possibility of mixing different interaction vertex. Thanks to this detailed study of the Frisch grid, some questions related to the experimental setup of XEMIS1 have been exposed, which has contributed to the optimization of the future detector XEMIS2.

In Chapter 6 we have introduced the experimental set-up used to measured the 511 keV γ-ray emitted from a low activity ^{22}Na source for the performance characterization of XEMIS1. We have presented a precise study of the noise, with the aim of correcting the raw data from the DC offset and set the optimal threshold level for pulse finding. The noise and pedestal calibration is made pixel per pixel. A very low threshold level of the order of four times the value of the noise is set on the pedestal-corrected signals to measure very small charge deposits in the detector. We presented the event reconstruction algorithm used to regroup those signals that come from the same interaction point but are collected by more than one pixel. A study to determine the optimal time window to match two different signals in the same cluster has been carried out. The results showed that an amplitude variable time window is the best option to avoid the missassotiation of signal that leads to energy and spatial resolution degradations.

Finally, in Chapter 7 we have presented and discussed the results obtained with XEMIS1 for the performances characterization of the detector. We have addressed all main aspects related to the development of a Compton camera dedicated to 3γ medical imaging. A timing resolution of 44.3 ± 3.0 ns for 511 keV photoelectric events has been estimated from the drift length distribution, equivalent to a spatial resolution along the z-axis of the order of 100 μm. To determine the beginning and the end of the TPC two effects have been identified and taken into account. The range of the primary electrons in the LXe introduces a shift in the measured position along the z-axis. A Monte Carlo simulation showed that for 511 keV γ-rays, this deviation is of the order of 100 μm and it decreases with decreasing energy.

Moreover, the extension of the electron cloud introduces a bias in the position of the ends of the TPC. Both effects were considered in the determination of the total length of the chamber, used to determined the electron drift velocity as a function the electric field. At 1 kV/cm we obtained a drift velocity of 2.07 $mm/\mu s$.

We studied the electric field and energy dependence of the ionization charge yield and energy resolution for 511 keV γ-rays. The collected charge increases with the applied electric field and the γ-ray energy. We also observed an increase of the energy resolution with the electric field strength and the energy of the γ-ray. These effects are directly related to fluctuations in the recombination rate along the track of the primary electrons. For an electric field of 2.5 kV/cm, we measured an energy resolution of 3.9 % (σ/E). For an energy of 1274 keV and an electric field of 1.5 kV/cm, an energy resolution of 2.85 % (σ/E) is achieved. We observed a non-linear response of the collected charge with the energy, being more significant at lower field strength.

The results of the cluster multiplicity as a function of the drift length for 511 keV events at 1 kV/cm and different thresholds levels are consistent with the spread of the electron cloud as the electrons drift towards the anode due to the transverse diffusion. These results indicate that charge sharing between neighboring pixels can be easily described by a Gaussian spread that varies with the drift distance as $\sqrt{z\ (cm)}$. This dependency has been successfully reproduced by a Monte Carlo simulation of the electron transport inside the TPC. The simulation has been also used to estimate the transverse spatial resolution in the detector. As a first approximation, the reconstructed position of clusters with more than one fired pixel is deduced from the center of gravity method. However, this technique is not a good estimator of the real position, since the size of the pixels is bigger that the electron cloud. To improve the spatial resolution along the x and y axis, two correction method have been tested. The Gaussian correction method, that assumes a Gaussian distribution of the charge cloud, provides better results with respect to the polynomial correction method. For a segmented anode with pixels of size $3.125 \times 3.125\ mm^2$, we found a position resolution of the order of 100 μm for an energy deposit of 511 keV at 6 cm from the anode. The spatial resolution decreases for low energies and small z-positions. We conclude that for a pixel size of $3.125 \times 3.125\ mm^2$ a spatial resolution of less than 1 mm, along both x and y directions, is expected regardless the deposit energy and the position of the interaction.

Finally, we presented the Compton reconstruction algorithm used to triangulate the position of the source in 3D. Besides the constraints of XEMIS1 to perform the Compton sequence reconstruction, we have showed the potential of the 3γ imaging technique. An angular the resolution of 4° is measured for an electric field of 1.5 kV/cm.

The results presented in this document provide a recapitulation of the main characteristics of the XEMIS detector, which provide the proof of concept of the 3γ imaging technique with a liquid xenon Compton camera. A very low electronic noise, a good energy and spatial resolutions and a very promising angular resolution for 511 keV γ-rays are compatible with the necessary requirements.

During this work, some limitations of the camera have been also identified allowing the optimization of XEMIS2. The use of a Frisch grid is necessary to remove the position dependence of the induced signals in the anode. However, some mechanical constraints may arise when migrating to a larger scale detector. The handling of the grid to achieve good

flatness and parallelism with respect to the anode-cathode plane may be quite challenging for an anode of the dimension of XEMIS2. A new anode that includes vertical metallic columns will be tested for the first time. The pillars would support the grid, allowing to put the mesh directly over the anode with high precision. This system will allow smaller gaps of less than 200 μm. Moreover, the advanced cooling system of the electronics installed in XEMIS2 and a complete insulation of the detector will reduce the probability of the presence of bubble inside the fiducial volume, which will allow the use of a Frisch grid with a small pith of less than 100 μm. This experimental configuration is optimal to reduce the inefficiency of the Frisch grid and the effect of charge induction.

During this work, we have been focused in the detection of the ionization signal. The UV scintillation photons emitted after the interaction of an ionizing particle with the medium are exclusively used to provide triggering capabilities to the detector. In XEMIS2, the full coverage of the active zone with PMTs can be used to reduce the pile-up that comes from two different decays of the radioactive source. This can be possible by performing a pre-localization of the ionization signals inside the detector. A simulation of the geometry of XEMIS2 and the response to the scintillation signal is being carried out to optimize the scintillation signal extraction.

We have showed that charge sharing between neighboring pixels can be described by a Gaussian distribution that varies with the drift distance as $\sqrt{z\ (cm)}$, with a transverse diffusion of 230 μs. However, we have also presented that the simulation is not able to fully reproduce the time difference distribution of the pixels of the same cluster. In this thesis, we have identified three factors that may affect the collection of the ionization signal in the detector: indirect charge induction in non-collecting electrodes due to the inhomogeneities of the weighting potential between adjacent pixels, the range of the primary electrons and the X-ray emission. Experimentally, the impact of these factors is very difficult to isolate from other contributions. That is why, all these aspects should be considered and included in the simulation. A simulation of this level is, however, a very difficult task since it should account for physics of particle interaction in LXe, atomic de-excitation simulation, electron transport in LXe and electric field and charge induction simulations.

The non-linearity of the ionization charge yield with the energy is an important subject that should be studied more in detail in the future. During this work, we found a small deviation of around 1 % at high energies (1274 keV) at 1 kV/cm. However, at low energies ($<$ 30 keV), we expect a non-linearity of the order of tens of percents, which may impact the Compton sequence reconstruction. As discussed in Chapter 2, for an incoming γ-ray of energy 1157 keV coming from the decay of the ^{44}Sc, a good angular resolution is obtained for scattering angles between $\sim 10^{\circ}$ to 60°. Applying Compton kinematics, a scattering angle of these values implies a electronic recoil in the energy range between 40 keV to 610 keV, with a maximum in the differential cross section at the scattering angle of 26.4°. This means that the calibration at energies below 200 keV should be carried out in the future.

In addition, the non-linear response of the ionization and scintillation yields in LXe with respect to the energy, results in a variation in the number of collected electrons depending on the type of interaction. The results presented in this document exclusively refer to the interaction of a γ-ray with the LXe. However, the X-ray emission from the K-shell with a branching ration of 85 %, suggests that the number of ionization electrons produced after a

photoelectric absorption differs from the one produced after a Compton effect, where the probability of emission of a X-ray is less than 4 %. The distinction between a photoelectric absorption and electronic recoil can substantially help the Compton sequence reconstruction. Therefore, a calibration of XEMIS for electronic recoils, especially at low energies, is necessary to fully understand the performances of the detector as Compton camera, and to exploits the benefits of the Compton imaging. Due to the quantity of matter present between the outside and the liquid xenon, a low energy source should be placed inside the liquid xenon in order to avoid γ-ray attenuation. However, even a small deposit inside the TPC will disturb the electric field. The Compton coincidence technique could be a good option [226, 227]. This method is based on measuring the energy of the Compton scattered γ-rays emitted from a source of ^{22}Na or ^{137}Cs from different deflection angles. Using the formulas of the Compton kinematics, we can determine the geometrical scattered angle from the Compton sequence reconstruction and determine the energy of the recoiling electron. The calculated energy can be, thus, compared with the measured energy. Due to the continuous spectrum of Compton electrons, the Compton coincidence technique can provide a wide range of energies from different scattering angles.

The XEMIS2 camera should be completely qualified this year and it will be operational and available from 2017 for preclinical research at the Center for Applied Medical Research (CIMA) located in the Nantes Hospital. XEMIS2 will provide the first images of a small animal obtained with a liquid xenon Compton camera. This images will be the conclusive evidence of the potential of the 3γ imaging technique in nuclear medicine.

Optimisation d'une camera Compton au xénon liquide à simple phase pour l'imagerie médicale 3γ

La rapide évolution des différentes techniques d'imagerie médicale, particulièrement dans les domaines de l'instrumentation de détection et de l'analyse de l'image, a marqué le début du 21ième siècle. Elle est en partie due aux importants progrès technologiques réalisés par la société, et aux liens très étroits caractérisant les mondes de la recherche et de l'industrie. Dans les thématiques de la physique expérimentale, où le but est d'investiguer la structure de la matière, l'origine de l'univers ou les lois fondamentales régissant les propriétés de la nature sont au coeur des recherches scientifiques. De nouveaux instruments de mesure sont constamment imaginés pour appréhender de nouvelles observations où les limites de nos connaissances sont testées. Ainsi, de nombreux outils utilisés actuellement en pratique clinique ont des origines directement empruntées à la communauté scientifique autour d'expériences de physique fondamentale. Cependant, malgré les très bonnes images diagnostiques obtenues actuellement en routine clinique, les progrès technologiques ne cessent d'évoluer. L'augmentation de l'espérance de vie et la volonté de toujours progresser dans ce sens lancent de nouveaux défis, en particulier pour les techniques d'imagerie fonctionnelle pratiquées en médecine nucléaire. La réduction de la dose de radiation administrée au patient, la diminution du temps de pause des caméras utilisées en imagerie et la nécessité d'un suivi thérapeutique plus personaliè comptent parmi les principaux vecteurs pour orienter les futures améliorations. C'est autour de ces objectifs que le laboratoire Subatech propose depuis 2004 la mise au point d'une nouvelle technique d'imagerie médicale, baptisée imagerie à 3 photons. L'imagerie à 3 photons est basée sur deux nouveaux concepts : l'utilisation conjointe d'une nouvelle technologie de caméra, un télescope Compton au xénon liquide, et d'un nouveau médicament radioactif basé sur le ^{44g}Sc.

Le principe de l'imagerie à 3 photons est basé sur l'utilisation d'un isotope radioactif spécifique, le ^{44}Sc, qui émet un positron et un photon d'énergie 1,157 MeV en coïncidence spatiale et temporelle. Après l'annihilation du positron avec un électron rencontré à l'intérieur du corps du patient, deux photons γ d'énergie 511 keV sont émis à 180° l'un de l'autre. La détection simultanée de ces deux photons permet de tracer une ligne entre les deux interactions. Cette ligne est appelée ligne de réponse (LOR). L'imagerie à 3 photons a pour but de localiser directement la position des sources d'émission en trois dimensions, pour chacune des désintégrations mesurées, grâce à l'intersection entre la LOR et un cône Compton. Ce cône est obtenu suite à l'interaction du photon d'énergie 1.157 MeV émis lors de la décroissance du ^{44g}Sc avec un télescope Compton. L'information additionnelle apportée par ce troisième photon permet de localiser la position de l'émetteur le long de la LOR et ainsi d'obtenir la distribution de la source en 3D. Le bénéfice de cette nouvelle technique

s'exprime directement en termes de réduction du nombre de désintégrations nécessaires pour l'obtention de l'image. Le temps des examens et/ou l'activité injecté au patient se voient ainsi diminués.

Dans le but de consolider et de fournir une démonstration expérimentale de l'utilisation d'une caméra Compton au xénon liquide pour l'imagerie 3γ, une première phase de recherche et développement (R&D) a été effectuée. Cette première phase représente le point de départ du projet XEMIS (XEnon Medical Imaging System) né à Subatech. Elle implique la recherche fondamentale et ainsi la mise en application de technologies innovantes. Un premier prototype d'un télescope Compton au xénon liquide, appelé XEMIS1, a été développé avec succès par le laboratoire Subatech. Le choix du xénon liquide comme milieu de détection est motivé par le fait que les techniques de détection disponibles actuellement en imagerie, basées sur les cristaux scintillateurs pour la détection des photons γ, ne sont pas adaptées pour l'imagerie à 3 photons. Par ailleurs, les propriétés physiques fondamentales du xénon liquide, haute densité et son numéro atomique élevé, confèrent un pouvoir d'arrêt élevé aux rayonnements ionisants, ce qui fait le xénon liquide très bon candidat en tant que détecteur de rayons γ dans la gamme d'énergie allant de quelques dizaines de keV à plusieurs dizaines de MeV. Le xénon liquide est à la fois un excellent milieu actif pour la détection de rayonnements ionisants et un excellent scintillateur, avec l'avantage de rendre possible la construction de détecteurs grande taille avec un milieu sensible homogène. Ce sont les principales raisons pour lesquelles le xénon liquide a été choisi comme milieu de détection, non seulement pour l'imagerie médicale, mais aussi dans d'autres domaines tels que la physique des particules et l'astrophysique.

Les travaux présentés dans ce document ont été réalisés au sein du laboratoire Subatech sous l'avis scientifique du Dr. Jean-Pierre Cussonneau et la supervision du Dr. Ginés Martinez. Ce document est divisé en sept chapitres rendus aussi indépendants que possible. Ce manuscrit détaille la caractérisation et l'optimisation d'une caméra Compton au xénon liquide à phase unique pour l'imagerie 3γ. Il fournit la preuve expérimentale de sa faisabilité à travers un prototype à petite échelle, XEMIS1. Ce travail a été centré sur l'extraction du signal d'ionisation produit dans le xénon liquide et à l'optimisation du détecteur. Les résultats obtenus ont contribué à d'importantes avancées sur les performances du détecteur et sur l'extraction du signal d'ionisation, ce qui a conduit à la conception et la construction d'un second prototype dédié à l'imagerie du petit animal. Ce dispositif de plus grande taille, baptisé XEMIS2, est une caméra cylindrique monolithique remplie de xénon liquide placée autour du petit animal. La géométrie de XEMIS2 a été optimisée pour la mesure simultanée des trois rayons γ issus du ^{44g}Sc, avec une très grande sensibilité et un large champ de vision.

Le **Chapitre 1** est consacré à une introduction sur les propriétés générales du xénon liquide en tant que milieu de détection de rayonnement ionisantes. Nous présentons de façon génerale la physique de l'interaction des particules avec le xénon liquide, et la production des signaux d'ionisation et de scintillation. Un résumé général de divers détecteurs basés sur le xénon liquide utilisés dans des différents domaines de recherche expérimentale, est présenté. Ce chapitre se poursuit avec une brève introduction à l'imagerie en médecine nucléaire et en particulier sur les deux techniques les plus utilisées en imagerie fonctionnelle, la Tomographie à Emission Mono-Photonique (TEMP) et la Tomographie à Emission de Positons (TEP). Il intègre ensuite les bases de l'imagerie Compton et une description détaillée du principe de

la technique d'imagerie 3γ. Enfin, les exigences de base d'une caméra Compton au xénon liquide consacrée à l'imagerie médicale sont exposées.

Dans le **Chapitre 2**, nous présentons le principe de base d'une chambre à projection temporelle au xénon liquide. Les chambres à projection temporel comptent parmi les technologies les plus prometteuses pour l'étude des phénomènes rares, comme la recherche de la matière noire ou la détection de neutrinos. XEMIS est une chambre à projection temporelle à simple phase, dont la conception a été optimisée pour des applications médicales. Ce chapitre présente le principe de base et les avantages de ce type de détecteur pour l'imagerie médicale. Les différents mécanismes qui peuvent affecter la production et la détection du signal d'ionisation dans le xénon liquide tel que la diffusion, la recombinaison et la présence d'impuretés sont discutés. Enfin, ce chapitre donne un bref résumé du processus de formation du signal d'ionisation dans l'anode segmentée, allant de l'interaction d'une particule ionisante avec le détecteur à la collection du signal par l'électronique front-end. La discussion est soutenue par nos résultats expérimentaux ainsi que par des résultats issus de la littérature.

Le **Chapitre 3** donne une description détaillée de la caméra XEMIS1. Cela comprend une description des systèmes de détection de la lumière et de collection de charges, ainsi que de l'infrastructure cryogénique mise au point pour liquéfier et maintenir le xénon dans des conditions de température et de pression stables pendant de longues périodes de prise de données. La pureté du xénon liquide est une préoccupation majeure dans des détecteurs où les électrons doivent parcourir de longues distances sans rencontrer d'impuretés. Le système de purification et de circulation utilisé dans XEMIS est présenté dans ce chapitre. Ensuite, nous présentons les principales caractéristiques de la nouvelle caméra Compton au xénon liquide, XEMIS2. Ce nouveau prototype est une caméra cylindrique monolithique qui contient $\sim$200 kg de xénon liquide. La géométrie de XEMIS2 est optimisée pour fournir une couverture complète des petits animaux grâce à son champ de vue axiale de 24 cm. Afin de détecter à la fois le signal d'ionisation et les photons VUV de scintillation produits dans le xénon liquide après l'interaction des rayonnements ionisants, le volume actif du détecteur est couvert par 380 1' PMTs et menu deux anodes segmentées avec un nombre total de 24000 pixels. La construction et l'exploitation d'un détecteur de grande envergure pour des applications médicales soulève un ensemble de défis. Pour répondre aux exigences de ce détecteur dont l'utilisation est envisagée dans des centres hospitaliers, un effort particulier a été porté sur le développement d'une infrastructure très compacte autour de la cryogénie du xénon liquide et d'un système d'acquisition de données rapide et performant.

Le **Chapitre 4** est consacré au système d'acquisition de données utilisé avec XEMIS1. Le système a été développé pour enregistrer les deux signaux d'ionisation et scintillation avec un temps mort le plus faible possible. La conception et les performances de l'électronique *front-end* utilisée dans XEMIS1 y sont discutées, ainsi qu'une étude détaillée de la réponse de l'électronique. L'*ASIC* présente d'excellentes propriétés en termes de linéarité du gain (dans une game d'énergie jusqu'à 2 MeV), de stabilité de la ligne de base et du bruit électronique. Mon travail de thèse a notamment porté sur la mesure du signal d'ionisation. Une attention particulière est portée à l'optimisation de la mesure d'amplitude et du temps des signaux d'ionisation. Dans cette thèse, une simulation Monte Carlo du signal de sortie du IDeF-X LXe a été mis en ouvre. Les résultats obtenus ont contribué au développement d'un système d'acquisition avancé pour la mesure du signal d'ionisation dans XEMIS2. Enfin, ce chapitre

présente une description des principales caractéristiques de ce nouveau *ASIC* analogique, appelé XTRACT, est présenté.

Une des parties les plus sensibles de la configuration expérimentale de XEMIS est la grille Frisch. L'incorporation d'une grille entre la cathode et l'anode est nécessaire pour s'affranchir de la dépendance avec la position des signaux recueillis. Cependant, certains effets sont liés à l'utilisation d'une chambre d'ionisation de ses caractéristiques. Une étude complète des performances d'un chambre d'ionisation avec une grille de Frisch est présentée au **Chapitre 5**. Au cours de ce travail, trois effets ont été identifiés comme facteurs possibles ayant un impact direct sur l'extraction du signal d'ionisation : la transparence au passage des électrons, l'inefficacité de la grille de Frisch et l'induction de charge indirecte dans des pixels adjacents. Ces processus et les études réalisés dans cette thèse y sont expliqués en détail dans ce chapitre. Des données expérimentales ont été obtenues dans le but de fixer une limite supérieure de leur impact sur la qualité des signaux recueillis.

La perte de la charge collectée est l'une des principales contraintes pouvant limiter les performances spectroscopiques d'un détecteur. Au cours du développement de XEMIS, tous les aspects liés à la perte de charges recueillies ont été minimisés. La présence d'impuretés a été réduite grâce à un système de purification avancé présenté dans le Chapitre 5. Des longueurs d'atténuation supérieures à 1 m sont atteintes après une courte période de circulation, ce qui se traduit par une bonne uniformité de la collection de charge sur toute la longueur de dérive de la chambre. La méthode utilisée pour estimer la longueur d'atténuation est présentée dans le Chapitre 7. La perte des porteurs de charge due à la recombinaison peut être réduite par l'augmentation du champ électrique. Au cours de ce travail, les performances de XEMIS1 ont été évaluées pour différentes intensités de champ électrique de 0,25 kV/cm à 2,5 kV/cm. Un autre phénomène influant sur la collection de charges est la transparence de la grille de Frisch aux électrons. Une bonne transparence électronique nécessite une polarisation appropriée des électrodes. Cependant, elle ne dépend pas que de la configuration expérimentale du TPC, i.e. la distance entre la grille et l'anode, mais également des caractéristiques géométriques de la grille. Le pas de la grille et son épaisseur affectent les tensions appliquées. Une description plus détaillée de la transparence électronique d'une grille de Frisch du dispositif expérimental ainsi que des résultats obtenus avec XEMIS1 est présentée au Chapitre 5. Un blindage défectueux de la grille Frisch induit un signal dans l'anode dû à la présence d'électrons, avant leur passage à travers la grille. Cela affecte la forme des signaux traités et introduit une certaine dépendance dans la forme des impulsions avec la position de l'interaction. Les facteurs contribuant à l'amélioration de l'efficacité de la grille de Frisch détériorent la transparence des électrons. Par conséquent, un étude exhaustive est nécessaire pour trover le meilleur compromis possible entre les deux effets. Les résultats présentés dans le Chapitre 5 fournissent la preuve expérimentale de l'impact de la grille de Frisch sur les signaux recueillis. L'étude a été réalisée dans quatre différents types de mailles et deux gaps différents. Enfin, nous avons présenté une étude de simulation qui favorise la compression de l'effet de l'induction de charge dans les pixels voisins. Nous avons montré que le signal transitoire induit sur les pixels adjacents introduit un biais sur l'amplitude et le temps des signaux. Cet effet devient plus important pour des tailles des pixels de petite taille par rapport à la distance entre la grille et l'anode. Les résultats obtenus par simulation confirment la différence de temps observée entre les pixels à d'un même cluster dans les

données éxperimentales. Cette différence de temps affecte considérablement le processus de clusterisation et augmente la possibilité de mélanger différentes vertex d'interaction. Grâce à cette étude détaillée de la grille de Frisch, des questions relatives à la configuration expérimentale de XEMIS1 ont été exposé, ce qui a contribué à l'optimisation du futur du détecteur XEMIS2.

Dans le **Chapitre 6**, nous présentons une description détaillée du système expérimental et de déclenchement de l'acquisiton des données pour la détection de rayons gamma d'énergie 511 keV provenant d'une source de ^{22}Na avec XEMIS1. Le protocole du système d'acquisition de données et du traitement des données de XEMIS1, est décrit. Cette partie inclue une présentation complète de la méthode d'analyse et d'étalonnage mise au point au cours de ce travail de thèse pour déterminer la bruit dans chaque pixel. Les résultats obtenus dans cette étude sont utilisés pour corriger les données brutes et fixer un niveau de seuil pour la sélection de l'événement. Un seuil très bas, de l'ordre de quatre fois la valeur du bruit, est réglé sur des signaux corrigés de la ligne de base pour mesurer de très petits dépôts de charge dans le détecteur. L'algorithme de reconstruction des événements utilisé pour regrouper les signaux provenant du même point d'interaction, mais collectées par plusieurs pixels, est présenté. Une étude a été réalisée, visant à déterminer la fenêtre temporelle optimale pour discriminer deux signaux différents détectés dans un même cluster. Les résultats ont montré qu'une fenÍtre variant avec l'amplitude du signal est la meilleure option pour éviter la mauvaise association des signaux et ainsi éviter la dégradation de la résolution en énergie et de la résolution spatiale.

Le **Chapitre 7** est consacré à la présentation et la discussion des résultats obtenus au cours de ce travail de thèse, avec XEMIS1. Les résultats présentés dans cette section visent à fournir une compréhension complète de la réponse de XEMIS1 aux rayons gamma de 511 keV. Ce chapitre montre l'étude détaillée de la résolution en énergie, la résolution temporelle, la résolution spatiale et la résolution angulaire avec un faisceau mono-énergétique de rayons gamma de 511 keV émis par une source de ^{22}Na de faible activité. L'évolution du rendement de charges d'ionisation ainsi que l'évolution de la résolution en énergie avec le champ électrique appliqué et la longueur de dérive ont été analysées. Un étalonnage préliminaire de la réponse du détecteur pour différentes énergies de rayons γ est présenté. Il a été observé une augmentation de la charge recueillie avec le champ électrique appliqué et l'énergie des rayons γ, ainsi qu'une augmentation de la résolution en énergie avec l'intensité du champ électrique et l'énergie du rayon γ. Ces effets sont directement liés aux fluctuations du taux de recombinaison tout au long de la trace des électrons primaires. Pour un champ électrique de 2,5 kV/cm, une résolution en énergie de 4 % (σ/E) a été mesurée. Pour une énergie de 1274 keV et un champ électrique de 1,5 kV/cm, une résolution en énergie de 2,85 % (σ/E) a été atteinte. Une réponse non-linéaire de la charge collectée a été observée en fonction de l'énergie, et est d'autant plus significative à faible intensité de champ. Les propriétés de transport des électrons dans le xénon liquide, telles que la vitesse de dérive des électrons et la diffusion, sont discutées. Les résultats obtenus sur la multiplicité des clusters en fonction de la longueur de dérive pour des événements de 511 keV à 1 kV/cm et pour différents seuils sont conformes avec la propagation du nuage d'électrons vers l'anode due à la diffusion transversale. Ces résultats indiquent que le partage de charges entre les pixels voisins peut être facilement décrit par une Gaussienne variant avec la distance de

dérive $\sqrt{z\ (cm)}$. Ces résultats ont été reproduits avec succès par une simulation Monte Carlo du transport d'électrons à l'intérieur d'une TPC. La simulation a également été utilisée pour estimer la résolution spatiale transverse dans le détecteur. En première approximation, la position reconstituée de clusters avec plus d'un pixel est déduite à partir du centre de gravité. Cependant, cette technique ne permet pas une bonne estimation de la position réelle, étant donné que la taille des pixels est plus grande que la taille du nuage d'électrons. Afin d'améliorer la résolution spatiale le long des axes x et y, deux méthodes de correction ont été testées. La méthode de correction Gaussienne, qui suppose une distribution Gaussienne du nuage de charge, donne de meilleurs résultats que la méthode de correction polynomiale. Pour une anode segmentée avec des pixels de taille $3,125 \times 3,125\ mm^2$, une résolution sur la position de l'ordre de 100 μm pour un dépôt d'énergie de 511 keV à 6 cm de l'anode, a été obtenue. La résolution spatiale diminue pour des énergies plus faibles et de petites positions le long de l'axe z. En conclusion, pour une taille de pixel de $3,125 \times 3,125\ mm^2$, une résolution spatiale inférieure à 1 mm le long des directions x et y, est prévue quelle que soit l'énergie déposée et la position de l'interaction. Enfin, l'algorithme de reconstruction Compton utilisé pour trianguler la position de la source en 3D est présenté. Malgré les contraintes géométriques de XEMIS1 pour effectuer la reconstruction Compton, le potentiel de la technique d'imagerie de 3γ a été prouvé. Une résolution angulaire de 4° a été mesurée pour un champ électrique de 0,75 kV/cm.

En conclusion, le travail realisé au cours de cette thèse a permis d'atteindre un très faible bruit électronique (inférieure à 100 électrons), une résolution temporelle de 44 ns pour des événements photoélectriques de 511 keV, une résolution en énergie de 4% (σ/E) à 511 keV et un champ électrique de 2,5 kV/cm, et une résolution spatiale transversale inférieure à 1 mm. Tous ces résultats sont compatible avec les exigences nécessaires à l'imagerie du petit animal avec XEMIS2, et ils s'avèrent très prometteurs pour l'avenir de l'imagerie 3γ.

Appendix A

Noise counting rate simulation

A Monte Carlo simulation of the noise counting rate has been implemented in order to crosscheck the accuracy of the method reported in Section 4.4.1 to simulate the noise from experimental data. Figure A.1(a) shows the results for 10000 simulated event over a total period of 18 s. The zero-crossing rate is about 402 kHz which agrees with the value obtained for the experimental data (see Chapter 4, Section 4.5). The comparison with the experimental noise rate distribution is presented in Figure A.1(b). The values of the noise rate as a function of the threshold for both experimental and simulated noise events are listed in Table A.1.

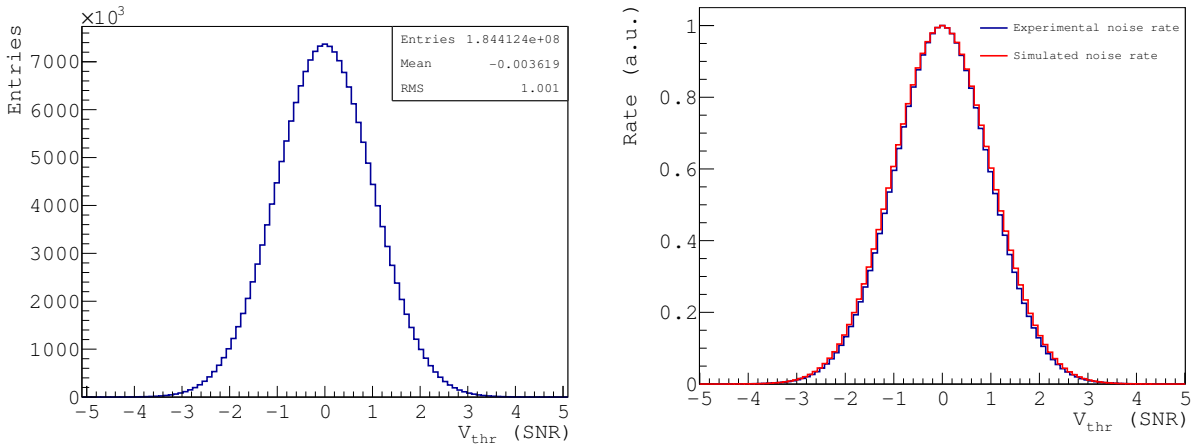

(a) **(b)**

Figure A.1 – (a)Monte Carlo prediction of the counting rate distribution as a function of the discriminator threshold. (b) Comparison between the experimental and simulated noise rate distributions.

In order to take into account the electronic limitations, a second threshold on the trailing edge of the signals was included. Figure A.2 shows the noise rate vs. an asymmetric threshold between $n\sigma_{noise} - (n-0.4)\sigma_{noise}$. Consistency in the results with respect to the experimental results is conserved (Table A.2).

Threshold (SNR)	Sim Noise Rate (Hz)	Exp Noise Rate (Hz)
0	402×10^3	365×10^3
1	242×10^3	220×10^3
2	54×10^3	49×10^3
3	4640	4263
4	140	115

Table A.1 – Noise counting rate as a function of the discriminator threshold level obtained from experimental and simulated data.

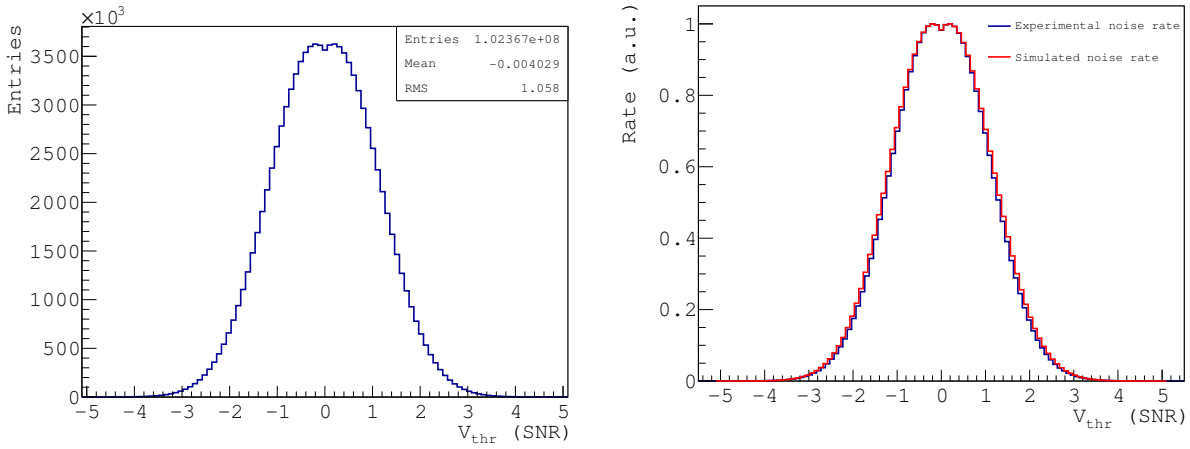

(a) **(b)**

Figure A.2 – (a)Monte Carlo prediction of the counting rate distribution as a function of the discriminator threshold. The leading edge threshold was set a $3\sigma_{noise}$ and the trailing edge threshold a $2.6\sigma_{noise}$. (b) Comparison between the experimental and simulated noise rate distributions.

Threshold (SNR)	Sim Noise Rate (Hz)	Exp Noise Rate (Hz)
0	$189\text{x}10^3$	$195\text{x}10^3$
1	$133\text{x}10^3$	$140\text{x}10^3$
2	$33\text{x}10^3$	$36\text{x}10^3$
3	3453	3214
4	140	229

Table A.2 – Noise counting rate as a function of the discriminator threshold level obtained from experimental and simulated data. The leading edge threshold was set a $3\sigma_{noise}$ and the trailing edge threshold a $2.6\sigma_{noise}$.

Appendix B

XEMIS1 Mapping

Figure B.1 shows the complete mapping of XEMIS1. The anode is segmented in 64 pixels of $3.125 \times 3.125\ mm^2$ that gives a total detection area of $2.5 \times 2.5\ cm^2$. The white region depicts the active region. The numbers represent the pixel address, used to access a specific electronic channel. The reference system (0,0) was chosen to be at the center of the anode. The left bottom pixel is used to register the TTT signal.

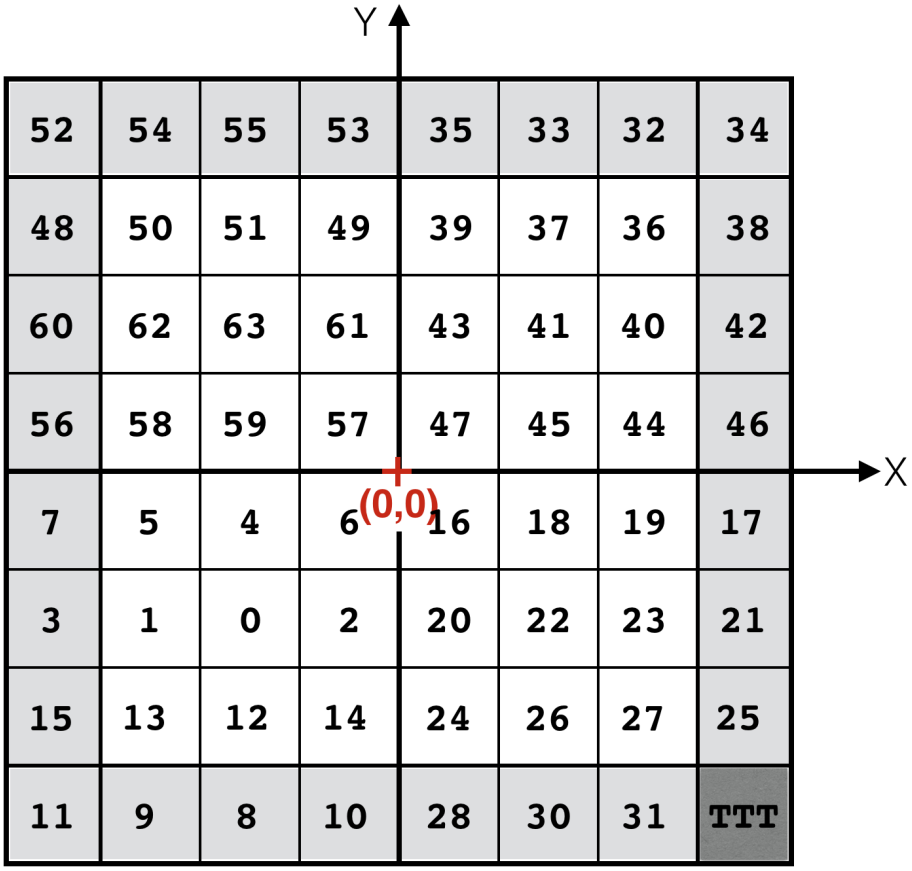

Figure B.1 – Mapping of XEMIS1.

List of Tables

List of Figures

Figure **Page**

List of Abbreviations

ADC	Analog to Digital Converter
$ATBM$	Asynchronous Binary Tree Multiplexer
CFD	Constant Fraction Discriminator
CS	Chip select
CT	Computed Tomography
ENC	Equivalent Noise Charge
FET	Field Effect Transistor
FOV	Field of View
$LAAPD$	Large Area Avalanche Photodiodes
LAr	Liquid argon
LET	Linear Energy Transfer
$LN2$	Liquid nitrogen
LSO	Lutetium Oxyorthosilicate
LXe	Liquid xenon
MFC	Mass Flow Controller
MLI	Multilayer insulation
$MPGD$	Micro-Pattern Gas Detectors
MRI	Magnetic Resonance Imaging
PET	Positron Emission Tomography
PID	Proportional-Integral-Derivative
PMT	Photomultiplier Tube
PSD	Power Spectral Density
PTR	Pulse Tube Refrigerator
PZC	Pole-Zero Cancellation
$ReStoX$	Reservoir Storage Xenon

RMS	Root-Mean Square
SCS	Slow Control System
$SiPM$	Silicon PhotoMultiplier
SNR	Signal to Noise Ratio
$SPECT$	Single Positron Emission Computed Tomography
TPC	Time Projection Chamber
UPS	Uninterruptible Power Supply
$XEMIS$	XEnon Medical Imaging System
ZCD	Zero-crossing detector

Bibliography

[1] T. Doke, "Fundamental Properties of Liquid Argon, Krypton and Xenon as Radiation Detector Media," *Portugal. Phys.*, vol. 12, pp. 9–48, 1981.

[2] E. Aprile and T. Doke, "Liquid Xenon Detectors for Particle Physics and Astrophysics," *Rev. Mod. Phys.*, vol. 82, pp. 2053–2097, 2010.

[3] T. Doke *et al.*, "Recent Developments of Liquid Xenon Detectors," *Nucl. Instrum. Meth.*, vol. 196, pp. 87–96, 1982.

[4] E. Aprile, A. Bolotnikov, A. Bolozdynya, and T. Doke, *Noble Gas Detectors*. Wiley, 2006.

[5] L. M.I. and C. V., "Liquid rare gas detectors: recent developments and applicstions," *IEEE Transaction on Dielectrics and Electrical Insulation*, 2004.

[6] M. Bramson, *Infrared Radiation: A Handbook for Applications*. Springer, 1968.

[7] D. McKinsey and J. Doyle, "Liquid Helium and Liquid Neon - Sensitive, Low Background Scintillation Media For The Detection Of Low Energy Neutrinos," *Journal of Low Temperature Physics*, vol. 118, no. 3/4, 2000.

[8] J. Kwong, "Liquefied Noble Gas Detectors for Detection of Nuclear Materials," *Nuclear Science, IEEE Transactions on* , vol. 60, pp. 652–657, 2013.

[9] M. Korzhik *et al.*, "Development of scintillation materials for PET scanners," *Nuclear Instruments and Methods in Physics Research A*, vol. 571, pp. 122–125, 2007.

[10] T. Doke *et al.*, "Time-of-flight positron emission tomography using liquid xenon scintillation," *Nuclear Instruments and Methods in Physics Research A*, vol. 569, pp. 863–871, 2006.

[11] J. Nikkel *et al.*, "Liquefied Noble Gas (LNG) detectors for detection of nuclear materials," *Journal of Instrumentation*, vol. 7, 2012.

[12] *Handbook of Chemistry & Physics*. The Chemical Rubber Company.

[13] National institute of standards and technology. [Online]. Available: http://www.itl.nist.gov/fipspubs/fip180-1.htm

[14] K. Hagiwara and others (Particle Data Group), "Review of Particle Physics," *Physical Review D*, vol. 66, 2002.

[15] T. Takahashi *et al.*, "Average energy expended per ion pair in liquid xenon," *Phys.Rev. A*, vol. 12, pp. 1771–1775, 1975.

[16] T. Doke *et al.*, "Present status of liquid rare gas scintillation detectors and their new application to gamma-ray calorimeters," *Nucl.Instrum.Meth. A*, vol. 420, pp. 60–80, 1999.

[17] L. Barkov *et al.*, "Measurement of the refractive index of liquid xenon for intrinsic scintillation light," *Nucl. Instrum. Meth.*, vol. A379, no. 482, 1996.

[18] V. Solovov *et al.*, " Measurement of the refractive index of liquid xenon for intrinsic scintillation light," *Nucl. Instrum. Meth. A*, vol. 516, pp. 462–474, 2004.

[19] R. Evans, *The Atomic Nucleus*. Tata McGraw-Hill Publishing Company Limited, 1955.

[20] G. Knoll, *Radiation Detection and Measurements*. Wiley, 2000.

[21] Y. Xing, "Etudes et Simulations du Signal d'ionisation induit par l'interaction de rayon gamma avec le xénon liquide d'une caméra XEMIS," Master's thesis, Ecole des Mines de Nantes, 2016.

[22] W. Leo, *Techniques for Nuclear and Particle Physics Experiments*. Springer-Verlag.

[23] F. Sauter, "Über den atomaren Photoeffekt in der K-Schale nach der relativistischen Wellenmechanik Diracs. ," *Ann. Phys.*, vol. 11, no. 454, 1931.

[24] C. Davisson and R. Evans, "Gamma-Ray Absorption Coefficients," *Revs. Mod. Phys.*, vol. 24:79, 1952.

[25] A. Compton, "A Quantum Theory of the Scattering of X-rays by Light Elements," *Phys. Rev.*, vol. 21, 1923.

[26] Lord Rayleigh and J. W. Strutt, "On the light from the sky, its polarization and color," *Philosophical Magazine*, vol. 41, pp. 107 – 120, 1871.

[27] Lord Rayleigh and J. W. Strutt, "On the scattering of light by small particles," *Philosophical Magazine*, vol. 41, pp. 447 – 454, 1871.

[28] W. Hayes and R. Loudon, *Scattering of light by crystals*. Dover Publications, Inc., 2004.

[29] R. E. Kleinman and T. B. A. Senior, "Rayleigh Scattering," *V. K. Varadan, V. V. Varadan (Eds.), Low and High Frequency Asymptotics, North Holland.*, 1986.

[30] C. Anderson, "Energies of Cosmic-Ray Particles," *Phys.Rev.*, vol. 41, pp. 405–421, 1932.

[31] J. Hubbell, "Electron–positron pair production by photons: A historical overview," *Radiation Physics and Chemistry*, vol. 75, no. 6, pp. 614–623, 2006.

[32] R. L. Platzman, "Total ionization in gases by high energy particles: an appraisal of our understanding," *The International Journal of Applied Radiation and Isotopes*, vol. 10, 1961.

[33] M. Miyajima *et al.*, "Average energy expended per ion pair in liquid argon," *Physical Review A*, vol. 10, 1974.

[34] A. Incicchitti, P. Belli, and M. Scafi, "Liquid Xenon as a Detector Medium," *Nuclear Instruments and Methods in Physics Research A*, vol. 289, pp. 236 – 242, 1990.

[35] G. Plante, "The XENON100 Dark Matter Experiment: Design, Construction, Calibration and 2010 Search Results with Improved Measurement of the Scintillation Response of Liquid Xenon to Low-Energy Nuclear Recoils," Ph.D. dissertation, Columbia University, 2012.

[36] S. Kubota, H. M., and R. J., "Dynamic behavior of free electrons in the recombination process in liquid argon, krypton and xenon," *J. Phys. C: Solid State Phys.*, vol. 11, pp. 2645–2651, 1978.

[37] S. Kubota, H. M., S. M., and R. J., "Dynamic behavior of free electrons in the recombination process in liquid argon, krypton and xenon," *Physical Review B*, vol. 20, pp. 3486–3496, 1979.

[38] A. Hitachi *et al.*, "Effect of ionization density on the time dependence of luminescence from liquid argon and xenon," *Physical Review B*, vol. 27, pp. 5279–5285, 1983.

[39] S. Kubota and A. Nakamoto, "Recombination luminiscence in liquid argon and in liquid xenon," *Physical Review B*, vol. 17, no. 6, 1978.

[40] E. Aprile *et al.*, "Simultaneous Measurement of Ionization and Scintillation from Nuclear Recoils in Liquid Xenon as Target for a Darl Matter Experiment," *Phys. Rev. Lett.*, vol. 97, 2006.

[41] V. Chepel and H. Araújo, "Liquid noble gas detectors for low energy particle physics," *Journal of Instrumentation*, 2013.

[42] T. Doke *et al.*, "Absolute Scintillation Yields in Liquid Argon and Xenon for Various Particles," *Japanese Journal of Applied Physics*, 2002.

[43] T. Shutt, C. E. Dahl, J. Kwong, A. Bolozdynya, and P. Brusov, "Performance and fundamental processes at low energy in a two-phase liquid xenon dark matter detector," *Nucl. Phys. B: Proc. Suppl.*, vol. 173, pp. 160 – 163, 2007.

[44] C. E. Dahl, "The physics of background discrimination in liquid xenon, and first results from XENON10 in the hunt for WIMP Dark Matter," Ph.D. dissertation, Princeton University, 2009.

[45] E. Aprile and M. Suzuki, "Development of liquid xenon detectors for gamma ray astronomy," *IEEE Trans. Nucl. Sci.*, vol. 36, no. 1, pp. 311–315, 1989.

[46] N. Schwentner, E. E. Koch, and J. Jortner, "Electronic Excitations in Condensed Rare Gases," *Springer Tracts in Modern Physics*, vol. 107, 1985.

[47] K. Ozone, "Liquid xenon scintillation detector for the $\mu \rightarrow \gamma$ search experiment," Ph.D. dissertation, Department of Physics, Faculty if Science, University of Tokyo, 2005.

[48] N. Ishida *et al.*, "Attenuation length measurements of scintillation light in liquid rare gases and their mixtures using an improved reflection suppresser," *Nuclear Instruments and Methods in Physics Research A*, vol. 384, 1997.

[49] K. Griest, M. Kamionkowski, and M. S. Turner, "Supersymmetric dark matter above the w mass," *Phys. Rev. D*, vol. 41, pp. 3565 – 3582, 1990.

[50] S. Lindemann, "Intrinsic ^{85}Kr and ^{222}Rn Backgrounds in the XENON Dark Matter Search," Ph.D. dissertation, Ruperto-Carola-University of Heidelberg, Germany, 2013.

[51] E. Aprile, "The XENON100 dark matter experiment," *Astropart. Phys.*, vol. 35, pp. 573 – 590, 2012.

[52] D. S. Akerib, X. Bai, S. Bedikian, E. Bernard, A. Bernstein, A. Bolozdynya *et al.*, "The large underground xenon (LUX) experiment," *Nuclear Instruments and Methods in Physics Research A*, vol. 704, pp. 111 – 126, 2013.

[53] L. C. D. S. Akerib, "LUX-ZEPLIN (LZ) Conceptual Design Report," *arXiv:1509.02910*, 2015.

[54] X. C. J. Liu, "The XMASS 800 kg detector," *J. Phys.: Conf. Ser.*, vol. 375, 2012.

[55] A. Aprile *et al.*, *Nuclear Instruments and Methods in Physics Research A*, vol. 412, 1998.

[56] E. Aprile, "An Upgraded Data-Acquisition System for the Balloon-Borne Liquid Xenon γ-ray imaging telescope LXeGRIT," *IEEE Transactions on Nuclear Science*, vol. 48, no. 4, 2001.

[57] E. Aprile, "Calibration and In-Flight Performance of the Compton Telescope prototype LXeGRIT," *Preprint. New Astronomy*, 2003.

[58] A. Curioni, "Laboratory and Balloon Flight Performance of the Liquid Xenon Gamma Ray Imaging Telescope (LXeGRIT)," Ph.D. dissertation, Columbia University, 2004.

[59] E. Aprile, "Compton Imaging of MeV Gamma-Rays with Liquid Xenon Gamma-Ray Imaging Telescope (LXeGRIT)," *Nuclear Instruments and Methods in Physics Research A*, vol. 593, 2008.

[60] R. Gornea, "Double beta decay in liquid xenon," *Fourth Symposium on Large TPCs for Low Energy Rare Event Detection*, 2009.

[61] E.-. C. J. Albert, "Search for Majorana neutrinos with the first two years of EXO-200 data," *Nature 510*, vol. 510, no. 229 - 234, 2014.

[62] J. Albert, "Status and Results from the EXO Collaboration," *EPJ Web of Conferences*, vol. 66, 2014.

[63] V. V. Erogov *et al.*, *Preprint Lebedev Physical Institute*, vol. 166, 1983.

[64] V. Chepel, "Liquid Xenon Detectors for Medical Imaging," *Revista Do DETUA*, vol. 4, no. 7, 2007.

[65] L. Lavoie, *Medical Physics*, vol. 3, no. 5, 1976.

[66] V. Chepel, "New liquid xenon scintillation detector for positron emission tomography," *Nucl. Tracks and Rad. Meas.*, vol. 21, 1993.

[67] V. Chepel, M. I. Lopes, R. Kuchenkov, R. Ferreira Marques, and A. J. P. L. Policarpo, "Performance study of liquid xenon detector for PET," *Nuclear Instruments and Methods in Physics Research A*, vol. 392, pp. 427 – 432, 1997.

[68] K. Giboni *et al.*, "Compton Positron Emission Tomography with a Liquid Xenon Time Projection Chamber," *Journal of Instrumentation*, vol. 2, 2007.

[69] D. Thers *et al.*, "A Positron Emission Tomography (PET) based on a liquid Xenon Time Projection Chamber and Microestructure Devices for Compton tracking," *Workshop on LXe-PET Camera, Subatech, Nantes*, 2003.

[70] A. Miceli *et al.*, "Liquid Xenon Detectors for Positron Emission Tomography," *Journal of Physics: Conference Series*, vol. 312, no. 6, 2011.

[71] M.-L. Gallin-Martel *et al.*, "A liquid xenon positron emission tomograph for small animal imaging: First experimental results of a prototype cell," *Nuclear Instruments and Methods in Physics Research A*, vol. 599, 2009.

[72] C. Grignon *et al.*, "Nuclear medical imaging using $\beta+$ γ coincidences from Sc-44 radio-nuclide with liquid xenon as detector medium," *Nucl. Instrum. Meth. A*, vol. 571, pp. 142–145, 2007.

[73] M. MacManus *et al.*, "Use of PET and PET/CT for radiation therapy planning: IAEA expert report 2006-2007," *Radiother Oncol*, vol. 91, pp. 85–94, 2009.

[74] R. F. Mould, *A Century of X-Rays and Radioactivity in medicine 1993.* Bristol, Institute of Physics, 1993.

[75] K. Rootwelt, "Henri Beckquerel's discovery of radioactivity, and history of nuclear medicine. 100 years in the shadow or on the shoulder of Röntgen," *Tidsskr Nor Laegeforen*, vol. 116, pp. 3625–3629, 1996.

[76] J. H. Means, "Historical Background of the Use of Radioactive Iodine in Medicine," *N. Engl. J. Med.*, 1955.

[77] J. W. van Iseelt, "The philosophy of science: a history of radioiodine and nuclear medicine," *Tijdschr Nucl Geneeskd*, 2010.

[78] Institute of Medicine and National Research Council, *Advancing Nuclear Medicine Through Innovation*. The National Academies Press, 2007.

[79] R. W. Todd, J. Nightingale, and D. Everett, "A Proposed Gamma Camera," *Nature*, vol. 251, pp. 132–134, 1974.

[80] P. Lale, "The examination of internal organs using gamma ray scatter with extension to megavoltage radiotherapy," *Phys. Med. Biol.*, vol. 4, 1959.

[81] H. J. Muller, "Artificial Transmutation of the Gene," *Science*, vol. 66, 1927.

[82] L. Gallego Manzano *et al.*, "XEMIS: A liquid xenon detector for medical imaging," *Nuclear Instruments and Methods in Physics Research A*, vol. 787, pp. 89–93, 2015.

[83] G. B. Saha, *Physics and Radiobiology of Nuclear Medecine*. Springer, 2006.

[84] H. O. Anger, "Scintillation camera," *Rev. Sci. Instr.*, vol. 29, no. 1, pp. 27 – 33, 1958.

[85] H. Zaidi, "Recent developments and future trends in nuclear medicine instrumentation," *Z. Med. Phys.*, vol. 16, pp. 5 – 17, 2006.

[86] F. Kharfi, "Principles and Applications of Nuclear Medical Imaging: A Survey on Recent Developments," 20013.

[87] Melcher, Charles L., "Scintillation Crystals for PET," *J Nucl Med*, vol. 41, pp. 1051–1055, 2000.

[88] D. Renker and E. Lorenz, "Advances in solid state photon detectors," *Journal of Instrumentation*, vol. 4, 2009.

[89] C. Tsoumpas, D. Visvikis, and G. Loudos, "Innovations in Small-Animal PET/MR Imaging Instrumentation," *PET Clin.*, pp. 105 – 118, 2016.

[90] S. R. Cherry *et al.*, "Treatment of axial data in three-dimensional PET," *J Nucl Med*, vol. 28, 2003.

[91] D. Papathanassiou *et al.*, "Positron Emission Tomography in oncology: present and future of PET and PET/CT," *Crit Rev Oncol Hematol*, vol. 72, pp. 239–54, 2009.

[92] H. Peng and C. S. Levin, "Recent Developments in PET instrumentation," *Curr. Pharm. Biotechnol.*, vol. 11, pp. 555–571, 2010.

[93] T. Lewellen, "Recent developments in PET detector technology," *Phys Med Biol*, vol. 53, 2008.

[94] C. S. Levin and E. J. Hoffman, "Calculation of positron range and its effect on the fundamental limit of positron emission tomography system spatial resolution." *Phys. Med. Biol.*, vol. 44, pp. 781–799, 1999.

[95] S. DeBenedetti, C. E. Cowan, W. R. Konneker, and H. Primakoff, "On the angular distribution of two-photon annihilation radiation." *Physical Review*, vol. 77, pp. 205–212, 1950.

[96] R. Allemand, C. Gresset, and J. Vacher, "Potential advantages of a Cesium Floride scintillator for time-of-flight positron camera." *J. Nucl. Med.*, vol. 21, pp. 153–155, 1980.

[97] N. A. Mullani, D. C. Ficke, R. Hartz, J. Markham, and G. Wong, "System design of a fast PET scanner utilizing time- of-flight." *IEEE Trans. Nuc. Sci., NS-28*, pp. 104–107, 1981.

[98] M. Moszynski, M. Kapusta, A. Nassalski, T. Szczesniak, D. Wolski, L. Eriksson, and C. L. Melcher, "New Prospects for Time-of-Flight PET with LSO Scintillators," *IEEE Trans. Nuc. Sci.*, vol. 53, pp. 2484–2488, 2006.

[99] S. Surti, "Update on time-of-flight PET imaging," *J Nucl Med*, vol. 56, pp. 98 – 105, 2015.

[100] C. Lois *et al.*, "An assessment of the impact of incorporating time-of-flight information into clinical PET/CT imaging," *J Nucl Med*, vol. 51, pp. 237–45, 2010.

[101] B. Jakoby *et al.*, "Physical and clinical performance of the mCT time-of-flight PET/CT scanner," *Phys Med Biol*, vol. 56, pp. 2375–89, 2011.

[102] S. Vandenberghe *et al.*, "Recent developments in time-of-flight PET," *EJNMMI Phys*, Published online 2016 Feb 16.

[103] G. L. Brownell, C. A. Burnham, S. Wilensky, S. Aronow, H. Kazemi, and D. Streider, "New developments in positron scintigraphy and the application of cyclotron produced positron emitters," *Medical Radioisotope Scintigraphy*, 1969.

[104] M. M. Ter-Pogossian, "Positron emission tomography (PET)," *J Med Syst*, vol. 6, pp. 569 – 577, 1982.

[105] V. C. Spanoudaki and C. S. Levin, "Photo-Detectors for Time of Flight Positron Emission Tomography (ToF-PET)," *Sensors*, vol. 10, pp. 10 484 – 10 505, 2010.

[106] C. Levin *et al.*, "Potrotype time-of-flight PET ring integrated with a 3T MRI system for simultaneous, whole-body PET/MR imaging," *Society of Nuclear Medicine Annual Meeting Abstracts*, vol. 54, 2013.

[107] E. Vicente Torrico, "Caracterización, Mejora y Diseño de Escáneres PET Preclínicos," Ph.D. dissertation, Universidad Complutense de Madrid, 2012.

[108] T. Beyer *et al.*, "A combined PET/CT scanner for clinical oncology," *J Nucl Med*, vol. 41, pp. 1369–1379, 2000.

[109] G. Mariani *et al.*, "A review on the clinical uses of SPECT/CT." *Eur J Nucl Med Mol Imaging*, vol. 37, pp. 1959–1985, 2010.

[110] H. Jadvar and P. Colletti, "Competitive advantage of PET/MRI," *Eur J Radiol.*, 2013.

[111] T. Beyer *et al.*, "Putting 'clear' into nuclear medicine: a decade of PET/CT development," *Eur J Nucl Med Mol Imaging*, vol. 33, pp. 857–861, 2006.

[112] D. B. Everett, J. S. Fleming, R. W. Todd, and J. Nightingale, "Gamma-radiation imaging system based on the Compton effect," *Proc.IEEE*, vol. 124, pp. 995–1000, 1977.

[113] R. Kohara, "Advanced Comton Camera System for Nuclear Medicine: Prototype System Study," *IEEE Nuclear Science Symposium*, 2008.

[114] A. Curioni *et al.*, "A Study of the LXeGRIT Detection Efficiency for MeV Gamma-Rays during the 2000 Balloon Flight Campaign," *Nuclear Instruments and Methods in Physics Research A*, vol. 576, 2007.

[115] T. Oger, "Dévelopment expérimental d'un télescope Compton au xénon liquide pour l'imagerie médicale fonctionnelle," Ph.D. dissertation, Ecole des Mines de Nantes, 2012.

[116] L. K. Shankar, "Consensus Recommendations for the Use of 18F-FDG PET as an Indicator of Therapeutic Response in Patients in National Cancer Institute Trials," *J. Nucl Med*, vol. 47, no. 6, pp. 1059–1066, 2006.

[117] R. Simon, R. D. Cherry, and J. Q. Badawi, *Essentials of In Vivo Biomedical Imaging*. CRC Press, 2015.

[118] Z. Liang, H. Hart, and A. Schoenfeld, "Triple coincidence tomographic imaging without image processing," *IEEE Conf. on Engineering in Medicine and Biology*, pp. 825–826, 1987.

[119] J. D. Kurfess and B. F. Phlips, "Coincident Compton nuclear medical imager ," *IEEE Nuclear Science Symposium*, 2001.

[120] C. Lang, D. Habs, P. G. Thirolf, and A. Zoglauer, "Submillimeter nuclear medical imaging with a Compton Camera using triple coincidences of collinear β^+ annihilation photons and γ-rays," *Radiotherapy and Oncology*, vol. 102, 2012.

[121] C. Grignon, "Étude et développement d'un télescope Compton au xénon liquide dédié à l'imagerie médicale fonctionnelle," Ph.D. dissertation, Ecole des Mines de Nantes, 2007.

[122] G. D. Hutchins *et al.*, "Small Animal PET Imaging," *ILAR Journal*, vol. 49, no. 1, 2008.

[123] A. F. M. Hadi, "Simulation de l'imagerie à 3γ avec un télescope Compton au xénon liquide," Ph.D. dissertation, Ecole des Mines de Nantes, 2013.

[124] U. Fano, "Ionization Yield of Radiations. 2. The Fluctuations of the Number of Ions," *Phys. Rev.*, vol. 72, pp. 26–29, 1947.

[125] S. Stephenson *et al.*, "MiX: A Position Sensitive Dual-Phase Liquid Xenon Detector," *Journal of Instrumentation*, 2015.

[126] A. Zoglauer and G. Kanbach, *Doppler Broadening as a Lower Limit to the Angular Resolution of Next Generation Compton Telescopes*, Truemper, J. E. and Tananbaum, H. D., Ed., 2003, vol. 4851.

[127] N. N. D. Center. [Online]. Available: http://nndc.bnl.gov

[128] D. V. Filosofov, N. S. Loktionova, and F. Rösch, "A $^{44}Ti/^{44}Sc$ radionuclide generator for potential application of ^{44}Sc-based PET-radiopharmaceuticals," *Radiochimica Acta*, vol. 98, pp. 149 – 156, 2010.

[129] G. W. Severin *et al.*, "Cyclotron Produced ^{44g}Sc from Natural Calcium," *Appl Radiat Isot.*, vol. 70, no. 8, pp. 1526–1530, 2012.

[130] C. Duchemin *et al.*, "Production of scandium-44m and scandium-44g with deuterons on calcium-44: cross section measurements and production yield calculations," *Physics in Medicine & Biology*, 2015.

[131] C. Duchemin, "Etude de voies alternatives pour la production de radionucléides innovants pour les applications médicales," Ph.D. dissertation, Université de Nantes, 2015.

[132] M. Miederer *et al.*, "Small animal PET-imaging with Scandium-44-DOTATOC," *Radiother Oncol*, vol. 102, 2012.

[133] F. Rösch and R. P. Baum, "Generator-based PET radiopharmaceuticals for molecular imaging of tumors: on the way to THERANOSTICS," *Dalton Trans*, vol. 40, no. 23, pp. 6104 – 6111, 2011.

[134] R. Walczak *et al.*, "Cyclotron production of ^{43}Sc for PET imaging," *EJNMMI Phys*, 2015.

[135] F. Sauli, *Gaseous Radiation Detectors. Fundamentals and Applications.* Cambridge University Press, 2014.

[136] D. Nygren, "The time-projection chamber: A new 4π detector for charged particles," *PEP*, vol. 144, 1976.

[137] C. Rubbia, "The Liquid-Argon Time Projection Chamber: a new concept for neutrino detectors," *CERN EP Internal Report*, vol. 77, no. 8, 1977.

[138] F. Sauli, "GEM: A new concept for electron amplification in gas detectors," *Nucl.Instrum.Meth. A*, vol. 386, pp. 531–534, 1997.

[139] Y. Giomataris, P. Rebourgeard, J. Robert, and G. Charpak, "MICROMEGAS : A high-granularity position-sensitive gaseous detector for high particle-flux environment," *Nucl. Instrum. Meth. A*, vol. 376, pp. 29–35, 1996.

[140] L. Onsanger, "Initial Recombination of Ions," *Phys. Rev.*, vol. 54, 1938.

[141] G. Jaffé, "Zur Theorie der Ionisation in Kolonnen," *Ann. Phys.*, vol. 42, 1913.

[142] J. Thomas and D. Imel, "Recombination of electron-ion pairs in liquid argon and liquid xenon," *Phys. Rev. A*, vol. 36, no. 2, pp. 614–616, 1987.

[143] J. Thomas, D. Imel, and B. Biller, "Statistics of charge collection in liquid argon and liquid xenon," *Phys.Rev. A*, vol. 38, no. 11, pp. 5793–5801, 1988.

[144] T. Doke *et al.*, "Estimation of Fano factors in liquid argon, krypton, xenon and xenon-doped liquid argon," *Nucl. Instrum. Meth.*, vol. 134, pp. 353–357, 1976.

[145] E. Aprile and R. Mukherjee and M. Suzuki, "Performance of a liquid xenon ionization chamber irradiated with electrons and gamma-rays," *Nuclear Instruments and Methods in Physics Research A*, vol. 302, pp. 177 – 185, 1991.

[146] E. Aprile and others, "Detection of γ-rays with a 3.5 l liquid xenon ionization chamber triggered by the primary scintillation light," *Nuclear Instruments and Methods in Physics Research A*, vol. 480, pp. 636 – 650, 2002.

[147] E. Conti *et al.*, "Correlated Fluctuations between Luminiscence and Ionization in Liquid Xenon," *Physical Review B*, vol. 68, 2003.

[148] E. Aprile *et al.*, "Observation of Anti-correlation between Scintillation and Ionization for MeV Gamma-Rays in Liquid Xenon," *Physical Review B*, vol. 76, 2007.

[149] W. Shockley, *Bell Sys. Tech.*, vol. 30, 1951.

[150] L. S. Miller, S. Howe, and W. E. Spear, "Charge Transport in Solid and Liquid Ar, Kr, and Xe," *Physical Review*, vol. 166, no. 3, 1967.

[151] J. Lekner, *Phys. Rev.*, vol. 158, no. 130-137, 1967.

[152] M. H. Cohen and J. Lekner, *Phys. Rev.*, vol. 158, pp. 130–137, 1967.

[153] H. D. Pruett and H. D. Broida, *Phys. Rev.*, vol. 164, 1967.

[154] G. Ascarelli, *J. Chem. Phys.*, vol. 71, pp. 5030–5033, 1979.

[155] V. Atrazhev *et al.*, "Electron Transport Coefficients in Liquid Xenon," *IEEE International conference of dielectric liquids*, pp. 329–332, 2005.

[156] W. Shockley, "Currents to Conductors Induced by a Moving Point Charge," *Journal of Applied Physics*, vol. 9, no. 10, pp. 635–636, 1938.

[157] S. S.-S. Huang and G.R. Freeman, "Electron transport in gaseous and liquid argon: Effects of density and temperature," *Physical Review A*, vol. 24, no. 2, 1981.

[158] E. Gushchin, A. Kruglov, and I. Obodovsky, *Sov. Phys., JETP*, vol. 55, no. 650 - 660, 1980.

[159] E. Wagner, F. Davis, and G. Hurst, "Time-of-flight investigations of electron transport in some atomic molecular gases," *The Journal of Chemical Physics*, vol. 47, no. 9, pp. 3138 – 3147, 1967.

[160] J. Pack, "Longitudinal electron diffusion coefficients in gases:Noble gases," *Journal of Applied Physics*, vol. 71, no. 11, pp. 5363 – 5371, 1992.

[161] T. Kimura and G.R. Freeman, "Electron Transport in Liquids: Conduction Bands and Localized States," *Canadian Journal of Physics*, vol. 52.

[162] S. R. H. Schnyders and L. Meyer, "Electron drift velocities in liquefied argon and kypton at low electric field strengths," *Physical Review*, vol. 150, pp. 127–145, 1966.

[163] Y. Suzuki, M. Nakahata, Y. Koshio, and S. Moriyama, *Technique and Application of Xenon Detectors*. World Scientific, 2003.

[164] O. Hilt and W. F. Schmidt, "Positive-hole mobility in liquid xenon as a funtion of temperature," *J. Phys. Condens. Matter.*, vol. 6, pp. L735 – L738, 1994.

[165] W.-T. Chen *et al.*, "Measurement of the Transverse Diffusion Coefficient of Charge in Liquid Xenon," *Diffusion in Solids and Liquids*, vol. VII, p. 567, 2011.

[166] G. Bakale, U. Sowada, and W. F. Schmidt, "Rate constant for Electron Attachment to O2, N2O and SF6 in LXe at 165K," *J. Chem. Phys.*, vol. 80, pp. 2556–2559, 1976.

[167] CASINO. monte CArlo SImulation of electroN trajectory in sOlids. [Online]. Available: http://www.gel.usherbrooke.ca/casino/What.html

[168] H. Zhu, "Electric Field Calculation and Ionization Signal Simulation in Liquid Xenon Detectors for PET," Master's thesis, University of British Columbia, Vancouver, 2012.

[169] E. L. update: 03 Sep 2013.

[170] Ordonez, C. E. and Bolozdynya, A. and Chang, W., "Doppler Broadening of Energy Spectra in Compton Cameras," *IEEE*, 1998.

[171] Klein, O. and Nishina, Y., "Über die streuung von strahlung durch freie elektronen nach der neuen relativistischen quantendynamik von dirac," *Zeitschrift für Physil*, vol. 52, pp. 853 – 868, 1929.

[172] R. Evans, *Compton Effect*, T. Handbuch der Physik XXXIV, Ed. Springer-Verlag, 1958.

[173] M. Gavrila, *Phys. Rev.*, vol. 124, 1961.

[174] F. Sauter, *Ann. Phys.*, vol. 11, 1931.

[175] S. Agostinelli *et al.*, "Geant4 - a simulation toolkit," *Nuclear Instruments and Methods in Physics Research A*, vol. 506, no. 3, pp. 250 – 303, 2003.

[176] J. Allison *et al.*, "Geant4 Developments and Applications," *IEEE Trans. Nucl. Sci.*, vol. 53, no. 1, pp. 270 – 278, 2006.

[177] F. Salvat, J. M. Fernandez-Varea, and J. Sempau, "Penelope - A code system for Monte Carlo simulation of electron and photon transport," *Proc. Workshop NEA 6416*, 2008.

[178] O. Frisch, "Isotope analysis of uranium samples by means of their α-ray groups," *Brithish Atomic Energy Respot BR-49*, 1944.

[179] O. Bunemann *et al.*, "Design of Grid Ionization Chambers," *Canadian Journal of Research Sec. A*, vol. 27, 80.

[180] W.-T. Chen *et al.*, "Improvement of xenon purification system using a combination of a pulse tube refrigerator and a coaxial heat exchanger," *Proceeding of ICEC24-ICMC2012*, 2012.

[181] T. Haruyama *et al.*, "High-power pulse tube cryocooler for liquid xenon particle detectors," *Cryocoolers 13*, pp. 689–694, 2005.

[182] T. Haruyama, K. Kasami, H. Inoue, S. Mihara, and Y. Matsubara, "Development of a high-power coaxial pulse tube refrigerator for a liquid xenon calorimeter," *Advances in Cryogenic Engineering, AIP Conf. Proc. 49*, pp. 1459–1466, 2004.

[183] T. Haruyama *et al.*, "Performance of a liquid xenon calorimeter cryogenic system for the MEG experiment," *Advances in Cryogenic Engineering, AIP Conf.Proc. 985*, pp. 1193–1200, 2008.

[184] T. Haruyama *et al.*, "Design and Performance of the XENON10 Dark Matter Experiment," *Astropart. Phys.*, vol. 34, pp. 679–698, 2011.

[185] *Model MonoTorr PS3-MT3-R-1*, SAES Pure Gas, Inc., p.A. Viale Italia 77 20020 Lainate (Milan) Italy.

[186] *Model N 186.3 SN.12E*, KNF Neuberger GmbH, Alter Weg 3 D 79112 Freiburg, Germany.

[187] O. Lemaire *et al.*, "Developement of a Readout Electronic for the Measurement of Ionization in Liquid Xenon Compton Telescope Containing Micro-patterns," *IEEE Nuclear Science Symposium Conference Record (NSS/MIC)*, 2012.

[188] [Online]. Available: http://science.purdue.edu/xenon1t/?tag=cryogenics

[189] H. Spieler, "Radiation Detectors and Signal Processing," Lecture Notes - VII. Heidelberger Graduate Lectures in Physics, University of Heidelberg, 2001.

[190] A. Meuris, "Étude et optimisation du plan de détection de haute énergie en Cd(Zn)Te de la mission spatiale d'astronomie et gamma Simbol-X," Ph.D. dissertation, Université Paris 7 Diderot, 2009.

[191] A. Michalowska *et al.*, "IDeF-X HD: A low power Multi-Gain CMOS ASIC for the readout of Cd(Zn)Te Detectors," *IEEE Nuclear Science Symposium Conference Record (NSS/MIC)*, 2010.

[192] G. De Geronimo and P. O'Connor, "A CMOS Fully Compensated Continuous Reset System," *IEEE Nuclear Science Symposium Conference Record (NSS/MIC)*, no. 584-588, 1999.

[193] K. Iniewski, *Electronics for Radiation Detection.* CRC Press, 2010.

[194] V. Radeka, "Low-Noise Techniques in Detectors," *Ann. Rev. Nucl. Part. Sci.*, vol. 38, pp. 217–277, 1988.

[195] H. Spieler, *Semiconductor Detector Systems.* Oxford Science Publications, 2005.

[196] A. Gillespie, *Signal, Noise and Resolution in Nuclear Counter Amplifiers.* Pergamon Press, London, 1953.

[197] H. Nyquist, "Thermal agitation of electric charge in conductors," *Phys. Rev.*, vol. 32, no. 1, pp. 110–113, 1928.

[198] J. Johnson, "Thermal agitation of electricity in conductors," *Phys. Rev.*, vol. 32, no. 1, pp. 97–109, 1928.

[199] W. Marshall Leach, "Fundamentals of Low-Noise Analog Circuit Design," *IEEE*, 1994.

[200] J. Schoukens and J. Renneboog, "Modeling the Noise Influence on the Fourier Coefficients After a Discrete Fourier Transform," *IEEE Transaction on Instrumentation and Measurements*, vol. IM-35, no. 3, 1986.

[201] R. Kulak, "Accuracy and Repeatability of Noise Measurements with a Discrete Fourier Transform," *IEEE Circuits and Systems Workshop: System-on-Chip - Design, Applications, Integration and Software*, 2008.

[202] ORTEC, *Application note AN42. Priciples and Applications of Timing Spectroscopy.*

[203] S. Rice, "Mathematical analysis of random noise," *Bell Sys. Tech. J. 23 (1944) 282. Bell Sys. Tech. J.*, vol. 24, no. 46, 1945.

[204] I. Sorokin, W. Müller, and C. Schmidt, "Rice Formula Applicability for Noise Rate Estimation in the CBM and other experiments with self-triggered electronics: comparing the calculation to a measurement on example of N-XYTER CHIP," *PHN-NQM-CBM-18.*

[205] W. Riegler, "MDT Resolution Simulation Frontend Electronics Requirements," *ATLAS Internal note MUON-NO-137*, 1997.

[206] B. Rossi and H. Staub, *Ionization Chambers And Counters.* Mcgraw Hill Book Company Inc., 1949.

[207] W. Blum, W. Riegler, and L. Rolandi, *Particle Detection with Drift Chambers.* Springer, 2008.

[208] S. Ramo, "Currents induced by Electron Motion," *Proceedings of the IRE*, vol. 27, no. 9, pp. 584–585, 1939.

[209] Z. He, "Review of the Shockley-Ramo theorem and its application in semiconductor gamma-ray detectors," *Nuclear Instruments and Methods in Physics Research A*, vol. 463, pp. 250–267, 2001.

[210] P. Luke, "Unipolar Charge Sensing with Coplanar Electrodes Application to Semiconductor Detectors," *IEEE TRANSACTIONS ON NUCLEAR SCIENCE*, vol. 42, no. 4, 1995.

[211] A. Göök, F.-J. Hambsch, A. Oberstedt, and S. Oberstedt, "Application of the Shockley-Ramo theorem on the grid inefficiency of Frisch grid ionization chambers," *Nuclear Instruments and Methods in Physics Research A*, vol. 664, pp. 289–293, 2012.

[212] L. Rossi, P. Fischer, T. Rohe, and N. Wermes, *Pixel Detectors: From Fundamentals to Applications*. Springer, 2006.

[213] D. Krapohl, "Monte Carlo and Charge Transport Simulation of Pixel Detector Systems," Ph.D. dissertation, Mittuniversitetet, Mid Sweden University, 2015.

[214] C. Geuzaine and J.-F. Remacle, "Gmsh: A 3-D finite element mesh generator with built-in pre- and post-processing facilities," *International Journal for Numerical Methods in Engineering*, 2009.

[215] M. Lyly, J. Ruokolainen, and P. Råback. (2008) Computer Code Elmer 6.0. [Online]. Available: http://www.csc.fi/english/pages/elemer

[216] Garfield++ – simulation of tracking detectors. [Online]. Available: https://garfieldpp.web.cern.ch/garfieldpp/

[217] Airliquide gas encyclopedia. [Online]. Available: http://encyclopedia.airliquide.com/encyclopedia.asp

[218] A. Denat *et al.*, "Generation of bubbles in liquid argon and nitrogen in divergent electric fields," *Proceeding of ICDL*, 1999.

[219] E. Erdal *et al.*, "Direct observation of bubble-assisted electroluminescence in liquid xenon," *Journal of Instrumentation*, vol. 10, no. 11, 2015.

[220] E. Aprile, R. Mukherjee, and S. M., "Measurement of the lifetime of conduction electrons in liquid xenon," *Nuclear Instruments and Methods in Physics Research A*, vol. 300, pp. 343 – 350, 1990.

[221] M. Ichige, E. Aprile, T. Doke, K. Hasuike, K. Itoh, J. Kikuchi, and K. Masuda, "Measurement of attenuation length of drifting electrons in liquid xenon," *Nuclear Instruments and Methods in Physics Research A*, vol. 333, pp. 355–363, 1993.

[222] M. Szydagis, N. Barry, K. Kazkaz, J. Mock, D. Stolp, M. Sweany, M. Tripathi, S. Uvarov, N. Walsh, and M. Woods, "NEST: A Comprehensive Model for Scintillation Yield in Liquid Xenon," *Journal of Instrumentation*, 2011.

[223] B. Lenardo, K. Kazkaz, A. Manalaysay, J. Mock, M. Szydagis, and M. Tripathi, "A Global Analysis of Light and Charge Yields in Liquid Xenon," *IEEE Trans. Nucl. Sci.*, vol. 62, 2015.

[224] Q. Lin, J. Fei, F. Gao, J. Hu, Y. Wei, X. Xiao, H. Wang, and K. Ni, "Scintillation and ionization responses of liquid xenon to low energy electronic and nuclear recoils at drift fields from 236,Äâ,ÄâV/cm to 3.93,Äâ,ÄâkV/cm," *Phys. Rev.*, vol. D92, no. 3, 2015.

[225] D. Y. Akimov *et al.*, "Experimental study of ionization yield of liquid xenon for electron recoils in the energy range 2.8-80 keV," *Journal of Instrumentation*, vol. 9, 2014.

[226] J. Valentine and B. Rooney, "Desing of a Compton spectrometer experiment for studying scintillator nonlinearity and intrinsic energy resolution," *Nuclear Instruments and Methods in Physics Research A*, vol. 353, pp. 37 – 40, 1994.

[227] J. Valentine and B. Rooney, "Benchmarking the Compton coincidence technique for measuring electron response nonproportionality in inorganic scintillators," *IEEE Trans. Nuc. Sci.*, vol. 43, no. 3, pp. 1271 – 1276, 1996.

Thèse de Doctorat

Lucía Gallego Manzano

Optimisation d'une camera Compton au xénon liquide à simple phase pour l'imagerie médicale 3γ

Optimization of a single-phase liquid xenon Compton camera for 3γ medical imaging

Résumé

Les travaux décrits dans cette thèse sont centrés sur la caractérisation et l'optimisation d'une camera Compton à phase unique au xénon liquide pour des applications médicales. Le détecteur a été conçu pour exploiter les avantages d'une technique d'imagerie médicale innovante appelée l'imagerie 3γ. Elle vise à l'obtention de la position en 3D d'une source radioactive avec une très haute sensibilité et une réduction importante de la dose administrée au patient. L'imagerie 3γ est basée sur la détection en coïncidence de 3 photons gamma émis par un émetteur spécifique (+β, γ), le ^{44}Sc. Un premier prototype de camera Compton au xénon liquide a été développé par le laboratoire Subatech à travers le projet XEMIS (Xenon Medical Imaging System), pour démontrer la faisabilité de l'imagerie 3γ. Ce nouveau système de détection comporte un système de cryogénie avancé et une électronique front-end à très faible bruit qui fonctionne à la température du xénon liquide. Ce travail a contribué à la caractérisation de la réponse du détecteur et à l'optimisation de la mesure du signal d'ionisation. L'influence de la grille de Frisch sur le signal mesuré a été particulièrement étudiée. Les premières preuves de la reconstruction Compton en utilisant une source de ^{22}Na (β+, Eγ = 1.274 MeV) sont aussi rapportées dans cette thèse et valident la preuve de concept de la faisabilité de l'imagerie 3γ. Les résultats présentés dans cette thèse ont joué un rôle essentiel dans le développement d'une camera Compton au xénon liquide de grandes dimensions pour l'imagerie des petits animaux. Ce nouveau détecteur, appelée XEMIS2, est maintenant en phase de construction.

Mots clés
Xénon liquide, camera Compton, imagerie médicale, imagerie 3γ, TPC, 44Sc.

Abstract

The work described in this thesis is focused on the characterization and optimization of a single-phase liquid xenon Compton camera for medical imaging applications. The detector has been conceived to exploit the advantages of an innovative medical imaging technique called 3γ imaging, which aims to obtain a precise 3D location of a radioactive source with high sensitivity and an important reduction of the dose administered to the patient. The 3γ imaging technique is based on the detection in coincidence of 3gamma rays emitted by a specific (+β, γ) emitter radionuclide, the ^{44}Sc. A first prototype of a liquid xenon Compton camera has been developed by Subatech laboratory within the XEMIS (Xenon Medical Imaging System) project, to proof the feasibility of the 3γ imaging technique. This new detection framework is based on an advanced cryogenic system and an ultra-low noise front-end electronics operating at liquid xenon temperature. This work has contributed to the characterization of the detector response and the optimization of the ionization signal extraction. A particular interest has been given to the influence of the Frisch grid on the measured signals. First experimental evidences of the Compton cone reconstruction using a source of ^{22}Na (β+, Eγ = 1.274 MeV) are also reported in this thesis, which demonstrate the proof of concept of the feasibility of the 3γ imaging. The results reported in this thesis have been essential for the development of a larger scale liquid xenon Compton camera for small animal imaging. This new detector, called XEMIS2, is now in phase of construction.

Key Words
Liquid xenon, Compton camera, medical imaging, 3γ imaging, TPC, 44Sc.